# DEVELOPMENT OF SMALL MOLECULES TO IMPAIR AND IMAGE MITOCHONDRIA IN CANCER CELLS

**A THESIS**

**SUBMITTED TO PARTIAL FULFILMENT OF THE DEGREE**

**OF**

**DOCTOR OF PHILOSOPHY**

**IN CHEMISTRY**

**BY**

**SOHAN DILIP PATIL**

**ID: 20143330**

**UNDER THE GUIDANCE OF DR. SUDIPTA BASU**


**INDIAN INSTITUTE OF SCIENCE EDUCATION AND RESEARCH, PUNE**

**2019**

# CERTIFICATE

Certified that the work incorporated in the thesis entitled, "**Development of Small Molecules to Impair and Image Mitochondria in Cancer Cells**". Submitted by **Mr. SOHAN DILIP PATIL** was carried out by the candidate, under my supervision. The work presented here or any part of it has not been included in any other thesis submitted previously for the award of any degree or diploma from any other University or institution.

**Date**: 22-10-2019

Sudipta Basu

**Dr. Sudipta Basu**

**(Research Supervisor)**

Nirmalya Ballav

**Dr. Nirmalya Ballav**

**(Co-Supervisor)** 22/10/19

# DECLARATION

I declare that this written submission represents my ideas in my own words and where others' ideas have been included; I have adequately cited and referenced the original sources. I also declare that I have adhered to all principles of academic honesty and integrity and have not misrepresented or fabricated or falsified any idea/data/fact/source in my submission. I understand that violation of the above will be cause for disciplinary action by the Institute and can also evoke penal action from the sources which have thus not been properly cited or from whom proper permission has not been taken when needed.

Date: 22-10-2019

**Sohan Dilip Patil**
ID-20143330
(Senior Research Fellow)
Department of Chemistry
IISER, Pune- 411008, India

# ACKNOWLEDGMENTS

Foremost, I would like to express my sincere gratitude to my advisor **Dr. Sudipta Basu** for the continuous support of my Ph.D. study and research, for his patience, motivation, enthusiasm, and immense knowledge. His guidance helped me in all the time of research and writing of this thesis. I could not have imagined having a better advisor and mentor for my Ph.D. study. I want to offer my special thanks to **Dr. Nirmalya Ballav** for being my administrative advisor. I owe Ballav sir, and I cannot forget the valuable help and support from him.

Besides my advisors, I would like to thank the Research Advisory Committee (RAC): Dr. D. S. Reddy, Dr. R. Kikkeri and Dr. N. Ballav for their encouragement, insightful comments, and hard questions during the RAC meetings. I thank former director Prof. K.N. Ganesh and current director Prof. Jayant B. Udgaonkar of IISER-Pune, for the academic support and the facilities provided to carry out the research work at the Institute. I am thankful to the University Grants Commission (UGC) and IISER Pune for financial support.

I am extremely thankful to my collaborator Dr. Mithun Radhakrishna and Amit Singh (IIT Gandhinagar) for performing the theoretical experiments in chapter 3. I am also grateful to all my other collaborators: Dr. Shailza Singh (NCCS, Pune), Dr. Vineetha Mandlik (NCCS, Pune), Dr. B. Gnanaprakasam (IISER Pune), Mr. Moreshwar B. Chaudhari (IISER Pune) for the immense trust they have shown on me. I also want to thank Dr. Poulomi Sengupta for helping in chapter 2. I also thank Dr. Mayurikha Lahiri and her lab members from IISER Pune, Biology Department for constructive discussions and extending research facilities in their laboratory. I thank Prof. M. Jayakannan, Dr. Harinath Chakrapani, for allowing me to work in a biology laboratory. I am grateful to Dr. Amol B. Gade and Mr. Ravindra Raut for helping in HPLC and X-ray crystal analysis.

It is my pleasure to thank all my labmates; Dr. Sandeep, Dr. Abhik, Dr. Chandramouli, Aditi, Shalini, Aman, Meenu, Kamil, Ankur, Sainath, Piyush, Sumer, Suhas, Nikunj and Deepali for devoting their precious time and made many valuable suggestions, which indeed helped me during this research work. A special thanks to Dr. Sandeep for teaching me biological experiments and stimulating discussions. I am grateful to Shalini for helping me in chapter 3. I would like take the opportunity to thank to all my friends for providing an inspiring and fun-filled environment around me especially, Amol, Tushar, Sandip, Pavan, Gorakhnath, Rupal, Kishor, Aslam, Prabhakar, Ravi, Moreshwar, Shahaji, Iranna, Pramod, Ganesh, Sainath and all

other IISER Pune's friends. I would like to thanks all my enthusiastic cricket mates for allowing me to play; I enjoyed a lot during all IISER Premier Leagues (IPL) being as a keeper and a bowler. I want to thank all instruments technicians and purchase department people of IISER Pune for their support especially in the Chemistry Department, Mr. Sandeep Kanade, Mr. Mahesh Jadhav, Mr. Yatish T. S, Ms. Megha Paygude and Mr. Ganesh Dimber.

My acknowledgment would be incomplete without thanking the biggest source of my strength, my family. The blessings of my father Dilip and mother Latika and the love and care of my sisters Shweta and Nisha and their husbands Dr.Pramod Sabale and Mr. Vikas Kolhe have all made a tremendous contribution in helping me reach this stage in my life. I must thank my wonderful wife Balika, as without her support (mental, motivational, and emotional) I may never have completed this thesis.

Finally, I dedicate this thesis to my dear family and naughty nephew, Advik.

With sincere thanks,
Sohan Dilip Patil

*Dedicated to*

*My Beloved Family*

# CONTENTS

**Chapter 3: Hydrazide-Hydrazone Small Molecules as AIEgens: Illuminating Mitochondria in Cancer Cells**

**Chapter 4: Cyanobax: Small Molecules for Mitochondrial Dysfunction upon Inhibiting Bcl-2 Family Proteins in Cancer Cells**

# Synopsis

## Title: Development of small molecules to impair and image mitochondria in cancer cells

Cancer is believed to be ranked as one of the leading causes of death worldwide in the upcoming years. Over the centuries, lots of efforts have been made to understand the function of mitochondria in the cancer cell. Unfortunately, due to make the wrong interpretation, the mitochondrial role in cancer was overlooked in cancer therapy for a long time. Recently, Hanahan and Weinberg discussed the ten hallmarks of cancer, which provide a useful framework for understanding the complexities of cancer. However, mitochondria are strongly associated with most of the cancer hallmarks, especially resisting cell death and deregulation of cellular energetics which are fully controlled by mitochondria. Therefore, the mitochondrion has emerged as one of the unconventional targets in next-generation cancer therapy.

Mitochondrion, a central metabolic organelle, is known as the powerhouse of the cells, required for bioenergetics, biosynthesis, and signaling. Overall, the collective finding suggests that these functions of mitochondria are mainly responsible for tumorigenesis. Hence, illuminating and targeting the mitochondria in cancer cells with novel small molecules have immense potential for the next generational anticancer therapy. However, there are three significant challenges that need to be considered to develop small molecules which can impair and or illuminate mitochondria: (a) *selectively impairing of mitochondria of cancer cells over normal cells*, (b) *selectively illuminate mitochondria in cancer cell* and (c) *selectively impair and image mitochondria*. In this thesis, we have addressed these challenges by developing small organic molecules to target mitochondria in cancer cell and validate their action of mechanism (Scheme 1).

In **chapter 2**, we have synthesized a library of hydrazide-hydrazone based small molecules and identified a novel compound which induced mitochondrial outer membrane permeabilization (MOMP) by inhibiting anti-apoptotic B-cell CLL/Lymphoma 2 (Bcl-2) family proteins followed by sequestration of pro-apoptotic cytochrome c. The new small molecule triggered programmed cell death (early and late apoptosis) through cell cycle arrest in G2/M phase and caspase-9/3 cleavage in HCT-116 colon cancer cells confirmed by an array of

fluorescence confocal microscopy, cell sorting and immuno-blotting analysis. Furthermore, cell viability studies verified that the small molecule rendered toxicity to a panel of colon cancer cells (HCT-116, DLD-1 and SW-620) keeping healthy L929 fibroblast cells unharmed. In this chapter, we have achieved first challenge, selectively impairing of mitochondria of cancer cells over normal cells. The novel small molecule has the potential to form a new understudied class of mitochondria targeting anti-cancer agent.

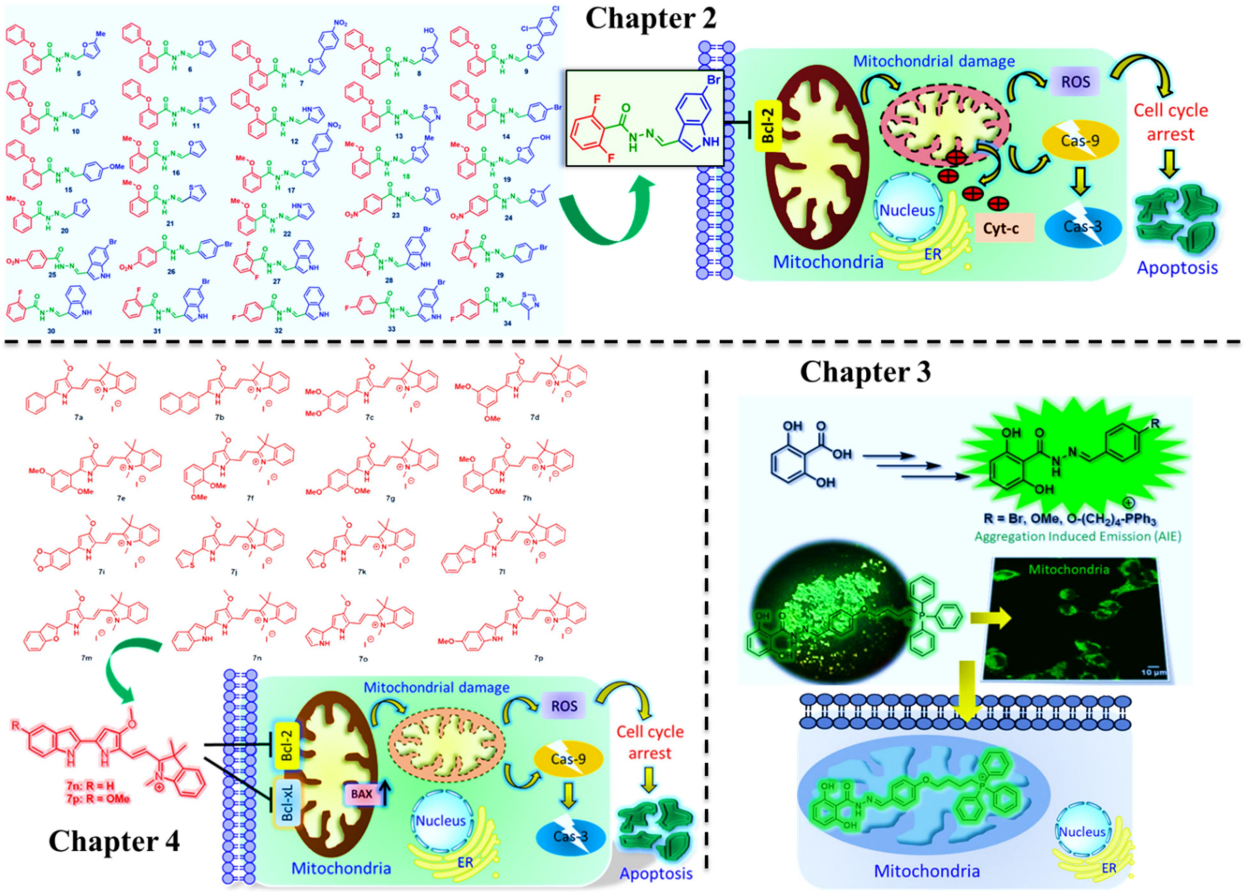


**Scheme 1:** Development of small molecules to impair and image mitochondria in cancer cells

Aggregation-induced emission probes (AIEgens) have gained lots of attention as interesting tools for ample biomedical applications, especially bio-imaging due to their brightness and photo-stability. Numerous AIEgens have been developed for lighting up the sub-cellular organelles to understand their forms and functions in healthy as well as diseased states like cancer. However, there is a serious absence of easily synthesizable, biocompatible small molecules for illuminating mitochondria, also known as power houses of the cell. To address

this, in **chapter 3** we describe an easy and short synthesis of novel biocompatible hydrazide-hydrazone based small molecules with remarkable aggregation-induced emission (AIE) property. These small molecule AIEgens showed hitherto unobserved AIE property due to dual intra-molecular H-bonding confirmed by theoretical calculation, pH and temperature dependent fluorescence and NMR spectroscopy as well as X-ray crystallography studies. Confocal microscopy showed that these AIEgens were internalized into the HeLa cervical cancer cells without showing any cytotoxicity. One of the AIEgens was tagged with triphenylphosphine (TPP) moiety, which successfully localized into mitochondria of HeLa cells selectively compared to L929 non-cancerous fibroblast cells at 12 h. These unique hydrazide-hydrazone based biocompatible AIEgens can serve as powerful tools to illuminate multiple sub-cellular organelles to elucidate their forms, functions and interactions with other organelles in cancer cells for next-generation biomedical applications. By developing this novel AIEgen we have addressed the second challenge, selectively illuminate mitochondria in cancer cells.

To address the third challenge, selectively impair and image mitochondria, in **chapter 4**, we have developed a novel cyanine-based positive charge containing small molecules library to target mitochondria in cancer cells. All the molecules were found having $IC_{50}$ values less than 5 μM. Two highly active molecules were thoroughly studied in the HeLa cervical cancer cells. They were colocalized in mitochondria leading to mitochondrial dysfunction in HeLa cells, validated with the formation of mitochondrial permeability transition pore (MPTP) upon inhibiting the anti-apoptotic Bcl-2 and Bcl-xl protein and enhanced the expression of BAX proteins. Finally, these molecules induced mitochondrial-dependent apoptosis by producing reactive oxygen species (ROS) and cleaved caspase-9/3. These findings were confirmed with confocal imaging, immunostaining, and immunoblot experiments. These molecules have the potential to illustrate mitochondria targeted, next generational anticancer agent.

## Noteworthy Finding

1. Validate the first time hydrazide-hydrazone small molecules are able to impair mitochondria in colon cancer cells
2. First time report that hydrazide–hydrazone as an AIEgn
3. Developed cyanine-based, positive charge, red florescence molecule library to image and impair mitochondria.

## List of Publications

1 **S. Patil**, M. M. Kuman, S. Palvai, P. Sengupta and S. Basu. *Impairing the Powerhouse in Colon Cancer Cells by Hydrazide-Hydrazone based Small Molecule*. ***ACS Omega*, 2018, 3, 1470-1481**

2 **S. Patil**, S. Pandey, A. Singh, M. Radhakrishna, and S. Basu. *Hydrazide-Hydrazone Small Molecules as AIEgens: Illuminating Mitochondria in Cancer Cells*. ***Chemistry: A European Journal*, 2019, 25, 8229-8235** (***Hot Paper***)

3 **S. Patil** and S. Basu. *Development of Cyanine-based Small Molecules for Mitochondrial Impairment upon Inhibiting Bcl-2 Family Proteins in Cancer Cells*. (Manuscript under minor revision in ACS Medicinal Chemistry Letters)

# Chapter 1

# Relation between Mitochondria and Cancer

## 1.1 Cancer

Cancer is a group of more than 277 varieties of diseases, in which abnormal cells divide without control and invade nearby tissue or organ. Cancer is the second leading cause of mortality. According to International Agency for Research on Cancer (IARC), over 9.5 million people died from cancer (about 26000 per day) worldwide in 2018.[1] Moreover, by 2040, the global burden is expected to grow to 27.5 million new cancer cases and 16.3 million cancer deaths.[2] Therefore, cancer is a big issue affecting the heath of all human beings. Unfortunately, it is a group disease at the tissue level, creates significant challenges not only for its specific diagnosis but also for the efficacy of treatment.[3,4]

Cancer occurs through a series of consecutive mutations of genes altering cellular functions. Chemical compounds play a prominent role in the formation of gene mutations and cancer cells. Also, various carcinogenic chemical compounds that cause lung cancer are involved in smoking.[5,6] In addition, environmental chemicals with carcinogenic properties have a direct or indirect influence on the cytoplasmic proteins, mitochondria, endoplasmic reticulum, and nucleus of the cells lead to gene mutation.[7,9] However, with most cancers, it takes months and years for these mutations to accumulate in the DNA and become detectable. The landscape of cancer treatment has changed dramatically in the last five decades. The classic traditional cancer therapies include surgery, radiation, endocrine therapy, and chemotherapy.

These therapies are old but still useful in some cancer treatments. Currently, targeted therapy has been known for its better efficacy and diagnosis rate.[10-12] The targeted therapy is a drug-based cancer therapy, which, however, differs from conventional chemotherapy upon focuses on cancer-specific genes, their proteins, or the tissue environment that contributes to cancer growth and survival. Mostly, it has two types; first, monoclonal antibodies that block a specific target on the outside of cancer cells and/or the target might be in the area around cancer and second, small-molecule drugs which block the process that helps cancer cells multiply and spread.

## 1.2 Mitochondria

The mitochondrion (plural mitochondria) is an unusual organelle found in most eukaryotic organisms. The mitochondria have two outer and inner membranes that are structurally and

functionally different (Figure 1.1). A significant difference lies in the permeability properties: the outer membrane allows the free passage of most molecules with a molecular weight below about 10,000 Daltons, while the inner membrane forms an effective barrier against even small molecules and ions.[13-15]

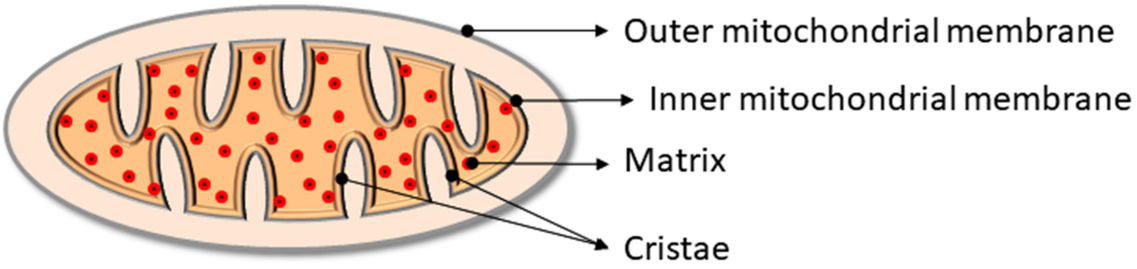


**Figure 1.1**: Structure of mitochondria

In addition, mitochondria are unique organelles among the cytoplasmic organelles because they have their independent genome (double-stranded circular mitochondrial DNA; mtDNA). The mtDNA contains instructions for several proteins and other cell support materials for 37 genes, among which 13 encode polypeptides involved in OXPHOS, 2 encode rRNAs, and the remaining 22 genes encode tRNAs.[16] With the help of mtDNA, mitochondria constantly replicate by dividing in two using the process prokaryotic binary fission. Mitochondrial fission has important implications for the response to stress and apoptosis, a programmed cell death.[15]

### 1.2.1 Bioenergetics and biosynthetic function of mitochondria

A mitochondrion is often known as the powerhouse of the cells by playing a crucial role in the production of metabolic energy in eukaryotic cells. The main function of mitochondria is the production of adenosine triphosphate (ATP) via tricarboxylic acid cycle (TCA or Krebs or citric acid cycle) (Figure 1.2).[16-20] By using multiple carbon fuels, mitochondria produce ATP and metabolites such as pyruvate, glutamine, and fatty acids. The TCA cycle utilizes acetyl-CoA and water, reduces NADH and $FADH_2$, and produces carbon dioxide as a waste by-product. The NADH and $FADH_2$ generated by the citric acid cycle deliver their electrons to the electron transport chain (ETC). These electrons are coupled with hydrogen ions, which create a proton gradient that is used for the production of ATP (known as oxidative phosphorylation). Also, the TCA cycle generates other intermediates that can act in multiple biosynthetic metabolic

pathways to produce glucose, amino acids, lipids, heme, and nucleotides. In this way, the mitochondria work as a central hub of both catabolic (breakdown macromolecules to smaller units to generate energy) and anabolic (builds macromolecules from small metabolic intermediates by utilizing energy) metabolism.[17-20]

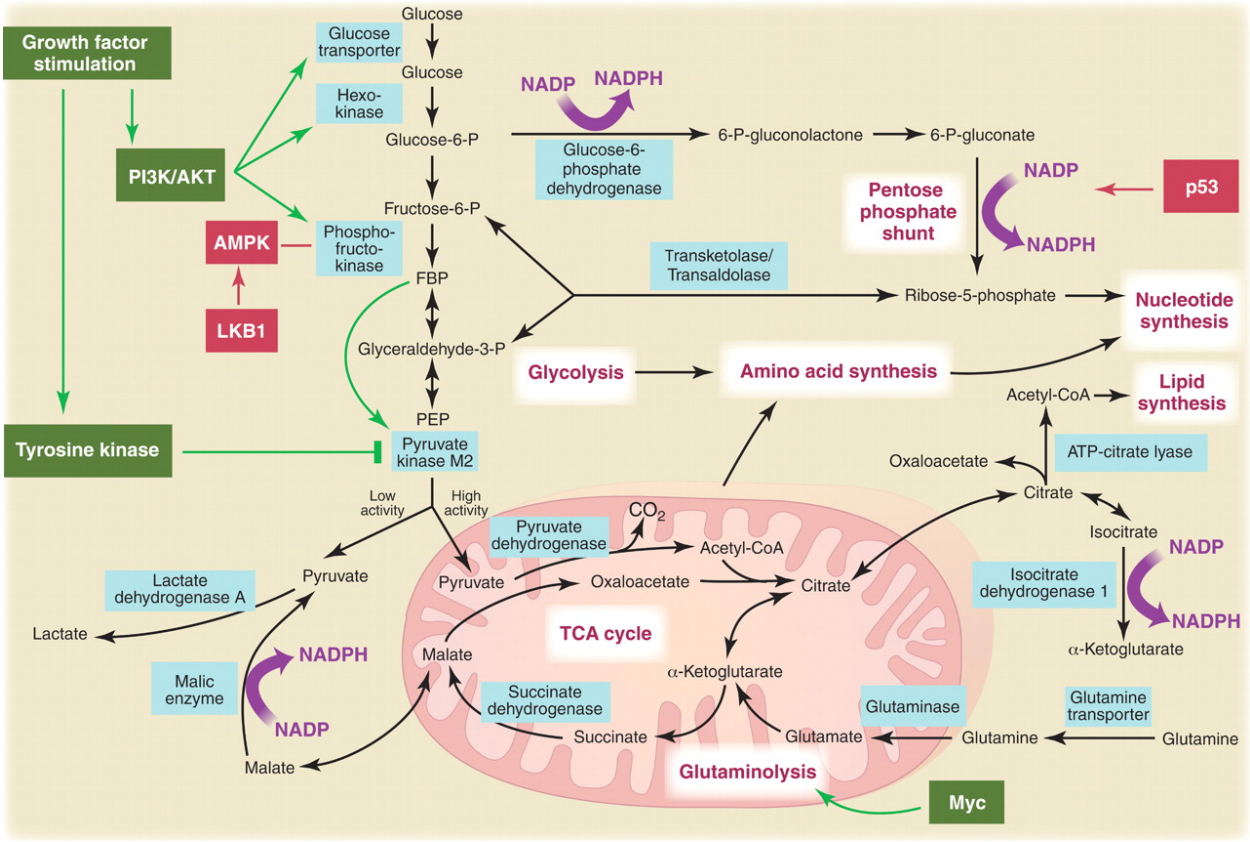


**Figure 1.2**: Mitochondrial functions[20] (Adapted from *Science*, 2009, *334*, 1029-1033)

### 1.2.2 Mitochondria and signalling

Mitochondria have been considered as crucial organelles, mainly due to their role in bioenergetics and biosynthesis. However, the past two decades have provided evidence that mitochondria are closely involved in cellular signaling pathways (Figure 1.2).[20,22] They are continually communicating with the cytosol to initiate biological events under homeostatic and stress conditions. Moreover, mitochondrial membranes also linked with other organelle membranes such as endoplasmic reticulum recognized as mitochondria-associated membranes

(MAMs) also serve as a signaling platform.[21] Generally, there are two forms of communication between the mitochondria and the rest of the cell: anterograde and retrograde signaling.[19] Signal transduction from the cytosol to mitochondria is known as anterograde whereas signal transduction from mitochondria to cytosol denoted as retrograde signalling. The anterograde signal caused by the accumulation of calcium in the mitochondrial matrix from high cytosolic calcium. This accumulated mitochondrial calcium triggers multiple enzymes of the TCA cycle to stimulate mitochondrial oxidative metabolism. Initially, the release of cytochrome c from mitochondria to the cytosol to initiate apoptosis known for retrograde signalling but there are several mechanisms of retrograde signalling include the release of reactive oxygen species (ROS) and other metabolites. Here, ROS, such as hydrogen peroxide ($H_2O_2$), releases from mitochondria in the cytosol in a nanomolar range, which oxidized specific thiol-containing proteins to modify their functions. Metabolites such as citrate can be released into the cytosol and cleaved by ATP citrate lyase to obtain acetyl-CoA and oxaloacetate. The acetyl-CoA levels can modulate protein acetylation, a reversible post-translational modification that modifies protein activity. Besides these signalling, mitochondrial signalling also helps for the expression of phosphatases and kinases (Figure 1.2).[19,22]

## 1.3 Mitochondria and Cancer

Every cell requires energy, and most of the energy comes through mitochondria in ATP form and some from the cytoplasm by glycolysis. Glycolysis is a metabolic process in which glucose converted into pyruvate in aerobic situations and lactate in anaerobic conditions, i.e. burning off the glucose to generate energy. Then, pyruvate enters the Krebs cycle for further energy production.

Mitochondrial function is essential for cancer cells. In healthy cells, mitochondrial functions known for bioenergetics, biosynthesis, signalling, and apoptosis. However, dysfunctions in the mitochondrial metabolism or genome, such as the TCA cycle, electron transport, and mtDNA mutations, are directly associated with cancer.[23,24] These mitochondrial defects lead to tumorigenesis and impaired apoptosis. To proliferate the cancer cell, most of the metabolic pathways get hijacked. Different types of cancer cells undergo various bioenergetics changes, some more glycolytic and others more oxidative, partly according to the state of development of the cell undergoing neoplastic transformation.

### 1.3.1 Warburg effect

The role of mitochondria in cancer has long been ignored due to laudable studies by german physiologist Otto Warburg (1883-1970), who received the Nobel Prize in Physiology for his discovery of the type and mode of action of respiratory enzymes in 1931. He found a strange thing while he was studying cancer cells.[20,25] He observed that cancer cells had an increased rate of glycolysis that was despite the availability of adequate oxygen levels (Figure 1.3). Therefore cancer cells preferably use glycolysis for energy by producing a large amount of lactic acid in the presence of oxygen.[20] This unusual metabolism became known as "aerobic glycolysis." The observation led Warburg to suspect that cancer is due to mitochondrial dysfunction, as cancerous cells select glucose fermentation and subsequent lactic acid production under conditions of abundant oxygen.[25]

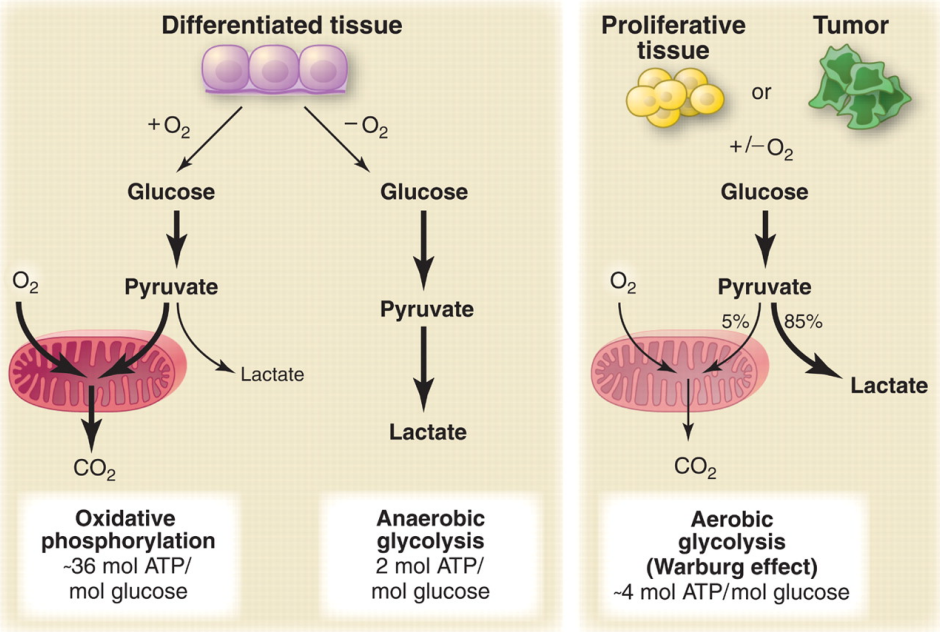


**Figure 1.3**: Warburg effect[20] (Adapted from *Science*, 2009, *334*, 1029-1033**)**

Due to this misinterpretation, the mitochondrial role in cancer was overlooked in cancer therapy for a long time. However, many studies have shown over time that mitochondria play a crucial role in cancer cell proliferation and apoptosis or necrosis because the elimination of mtDNAs reduces their growth rate and tumorigenicity.[25-27]

### 1.3.2 Hallmarks of cancer and mitochondria

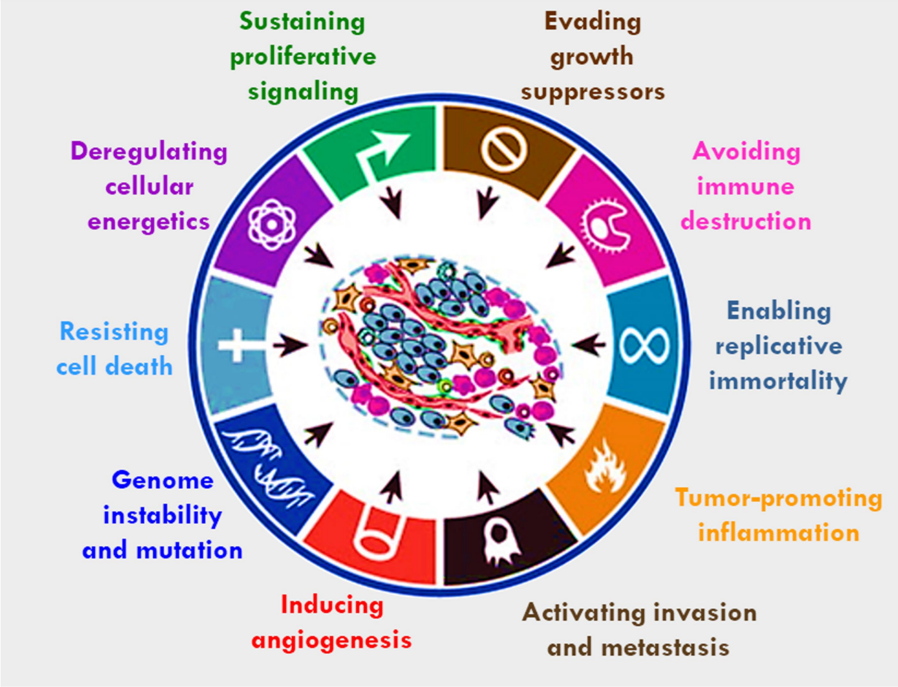


**Figure 1.4**: Hallmarks of cancer[28,29] (Adapted from *Cell* **2011**, *144*, 646 674)

In the early 2000s, Hanahan and Weinberg suggested that cells develop distinctive capabilities when they develop into a neoplastic condition.[28] These have been termed hallmarks of cancer and provide a useful framework for understanding the complexities of cancer (Figure 1.4). They consist of six hallmarks, namely, sustaining proliferative signaling, evading growth suppressors, resisting cell death, enabling replicative immortality, inducing angiogenesis, and activating invasion and metastasis. All were validated by genomic instability and mutation. Later in 2011, they added two emerging hallmarks include, deregulating cellular energetics, avoiding immune destruction and two enabling characteristics, genome instability and mutation, tumor-promoting inflammation.[29] However, mitochondria are strongly associated with most of the cancer hallmarks especially resisting cell death and deregulation of cellular energetics which are fully controlled by mitochondria.

### 1.3.3 Mitochondrial function required for cancer growth

Currently, it is clear that cancer cell firmly engages not only glycolysis but also its metabolism to supply the essential building blocks for macromolecules synthesis as well as ATP and NADPH for cell proliferation.[30] The high level of glycolysis in tumor cells is the result of

signal dysregulation pathways, such as the PI3K pathway, and the activation of oncogenes such as MYC and KRAS, which support cancer growth (Figure 1.2).[20] Moreover, oncogenic stimulation also increases mitochondrial metabolism to produce ATP and TCA cycle intermediates used as precursors to macromolecule synthesis.[31] Most of the cancer cells are addicted to glucose, and glutamine ultimately increases the workload of mitochondrial metabolism.[32] As a result, a large amount of ROS production by mitochondrial ETC, which activates signaling pathways associated with the mitochondria to encourage cancer cell proliferation and tumorigenesis.[33] However, the accumulation of excess ROS leads to cancer death.[34] As a result, cancer cells produce an abundance of NADPH in the mitochondria and cytosol to maintain high levels of antioxidant activity and prevent the formation of potentially harmful ROS.[35,36] Thus, mitochondrial metabolisms, as well as glucose-dependent metabolic pathways, are crucial for cancer cell proliferation. Overall these suggest that in some cancer cells, mitochondrial function bioenergetics can be compensating by glycolysis, but the mitochondrial function remains necessary to meet the biosynthesis requirements and generation of ROS required for cancer cell proliferation.

## 1.4 Mitochondria and apoptosis in cancer cell

Apoptosis is an irreversible, systematic process of programmed cell death. It can be triggered via one of the two routes, the intrinsic; the cell kills itself because it detects cellular stress. While, in the extrinsic, the cell is killed by signals from other cells.[37] Mitochondria play a vital role in the intrinsic pathway by releasing proteins from the intermembrane space of mitochondria or when cells are in stress or mitochondrial damage.[38,39] In mitochondrial apoptosis, the pro-apoptotic Bcl-2 family proteins Bax/Bak are translocated to the outer mitochondrial membrane resulting in oligomerization. Then occurs the formation of mitochondrial outer membrane permeabilization (MOMP), mitochondrial transition pores formation (MTP), and release of stored cytochrome c from mitochondria into the cytosol (Figure 1.5). This released cytochrome c irreversibly activates the caspases (the executors of apoptosis) that executes the apoptotic process to completion.[39]

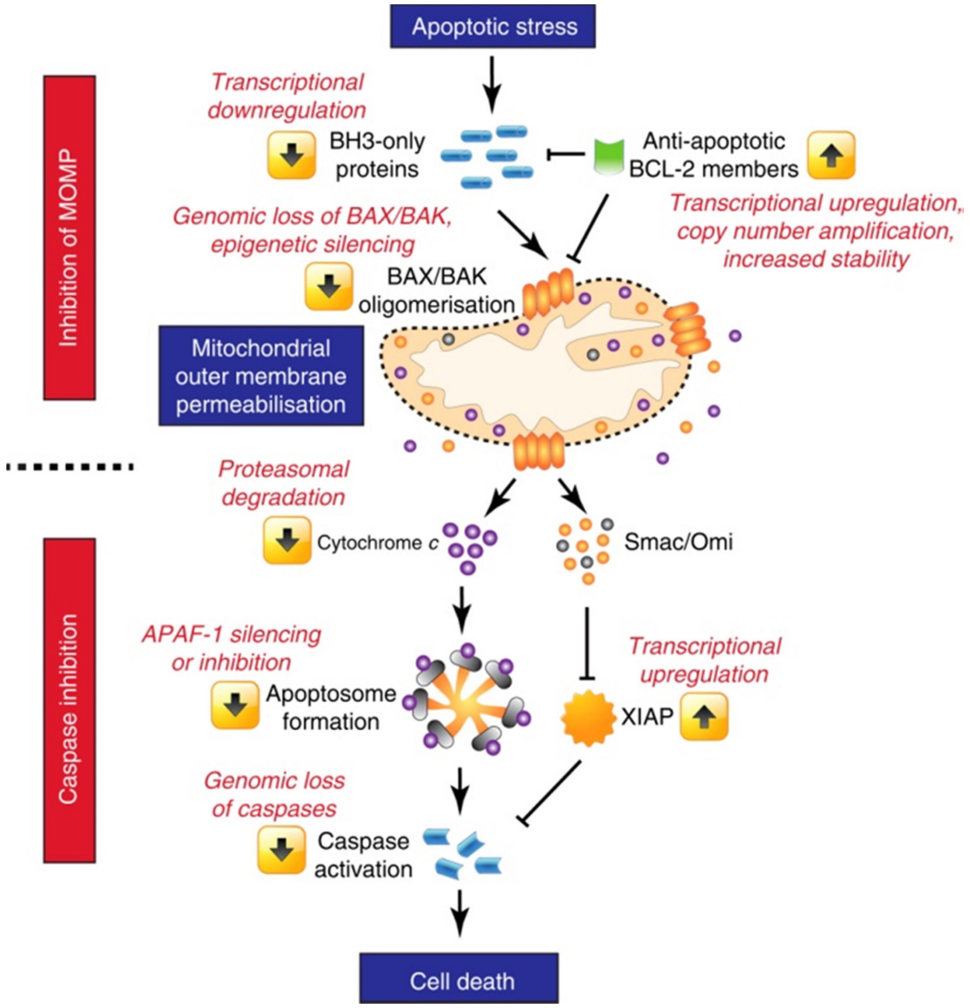


**Figure 1.5**: Mitochondrial apoptosis[39] (Adapted from *Br J Cancer* **2015**, *112*, 957-962)

### 1.4.1 Bcl-2 Protein family

The BCL-2 protein family is identified as an essential guardian of the apoptotic response.[40-46] This group of structurally related proteins contains pro-apoptotic and anti-apoptotic members that cooperate (Figure 1.6). The short sequences of amino acids that are mutual to BCL-2 and other members of this protein family are known as the Bcl-2 homology (BH) motif.[41,43] Each of the Bcl-2 family members contains at least one BH region, which is responsible for contributing the function of each member.[43] Members of the Bcl-2 family can be divided into three functional groups first, the anti-apoptotic proteins contains Bcl-2, Bcl-$X_L$, Bcl-w, Al, Mcl-1, Bcl-B, second, the pro-apoptotic activators such as Bid, Bim, Bik, Bad, Puma, Noxa and Bmf and third, pro-apoptotic effectors such as Bax and Bak.[44] Activators that contain

only a single BH3 motif are essential mediators in the cellular response to stress such as DNA damage. Whereas effectors are closely associated with the mitochondrial membrane, upon stimulation by BH3-only activators, these effectors initiate the apoptosis process by forming pores in the mitochondrial membranes.[40-46]

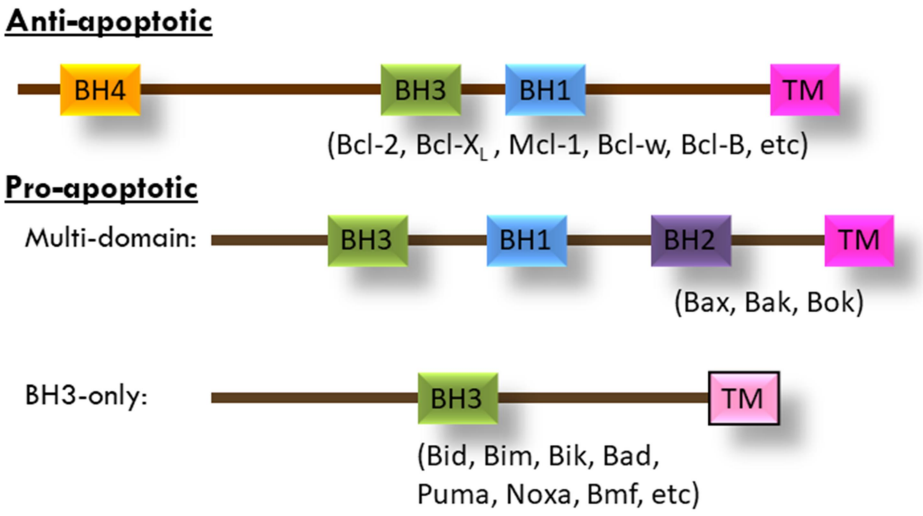


**Figure 1.6**: Bcl-2 family proteins

### 1.4.2 MOMP, MTP, and cytochrome c release

MOMP is the point-of-no-return process in which mitochondrial outer membrane becomes porous to allow high molecular weight proteins (cytochrome c) and other molecules from intermembrane space to the cytosol upon apoptotic signal.[47,48] It is caused by oligomerization of Bax / Bak proteins on the outer membrane-initiated by Bid. MOMP leads to the opening of mitochondrial transition pores (MTP). MTP is the complex of membrane proteins at the inner and outer membrane that believed to form large pores. Formation MTP, mitochondria compromise the inner membrane result translocation of cytochrome c and other molecules towards cytosol through MOMP and leads mitochondrial swelling and loss of mitochondrial potential $\Delta\Psi m$ (Figure 1.5).[49] The released essential protein cytochrome c activates the caspase cascade (sequential activation of caspase-9, then caspase-3 and caspase-7) to bring the apoptotic process to completion. Other than cytochrome c variety of molecules such as SMAC (Diablo) and Omi (HtrA2) are release from MOMP which also promote caspases activity by antagonized XIAP which is an endogenous inhibitor of caspase function (Figure

1.5).[38] However, since Cytochrome c is the only one involved in ETC, it is potential to explain the link between bioenergetics and apoptosis.[49]

### 1.4.3 Reactive Oxygen Species (ROS)

Reactive oxygen species (ROS) is a collective term to unstable, reactive, and partially reduced oxygen derivatives, which are produced as a by-product of normal metabolic processes. Mostly, they include hydrogen peroxide ($H_2O_2$), superoxide anion ($O_2^-$), hypochlorous acid (HOCl), singlet oxygen ($^1O_2$), and hydroxyl radical ($^{\cdot}OH$) play a critical role not only in the mitochondrial metabolic process but also mitochondrial intrinsic apoptosis pathway.[23,33] During cancer treatment, most anticancer drugs candidates, produce excess ROS in cancer cells. The high production of cellular ROS during chemotherapy can be attributed to two main reasons: the production of mitochondrial ROS upon disruption of ETC also electronic leakage and the inhibition of the cellular antioxidant system such as the depletion of glutathione (GSH) or inhibition of superoxide dismutase (SOD). Currently, it is proven that ROS production upon drug treatment amplifies the apoptosis process.[50]

## 1.5 Targeting mitochondria in cancer

Mitochondria are increasingly renowned as imperative targets in cancer owing to their fundamental role in apoptosis pathways and cellular metabolism. Therefore, initiate apoptotic signals, alter metabolic pathways ultimately impair mitochondria provides excellent opportunities for the development of next-generational anticancer agents. To target mitochondria in cancer cells, different strategies have been explored mainly by targeting mitochondrial bioenergetics, biosynthetic production, and redox signalling.

### 1.5.1 Targeting bioenergetics

As noted in the previous section, most of the cancer cells can compensate for the lack of mitochondrial ATP through the upregulation of glycolysis. Thus, targeting mitochondrial production of ATP for cancer treatment may not be a practical approach. However, the cores of many solid tumors are poorly perfused with a lack of nutrient, glucose, but enough oxygen to produce only mitochondria ATP over glycolysis.[19,51,52] Therefore, any drug candidate that blocks the production of mitochondrial ATP would induce cell death in this tumor. Moreover, some

cancers that strongly depend on the OXPHOS for the ATP, which can be controlled by inhibiting mitochondrial ATP production.[53] Adding to this, inhibitors of PI3k pathways demonstrated to diminish the glycolysis.[54] Despite these observations, the main challenge for this strategy, which limits its therapeutic index is healthy cells also entirely depends on the mitochondrial ATP for survival. However, few molecules have been validated in preclinical models of cancer without toxicity in healthy non-cancerous cells (Figure 1.7).[19] All the molecules are listed in figure 1.7 and share the same consequence is to decrease mitochondrial bioenergetics ability.

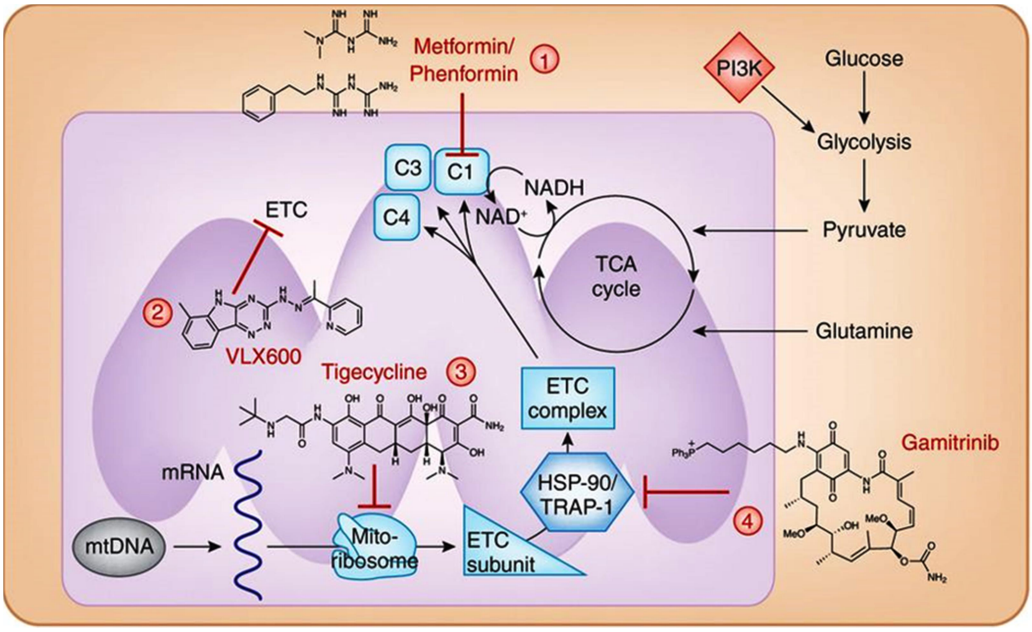


**Figure 1.7**: Targeting mitochondrial bioenergetics.[19] (1) Metformin and phenformin inhibit mitochondrial complex I; (2) VLX600 inhibits ETC; (3) Tigecycline inhibits the mitochondrial ribosomes; (4) Gamitrinib inhibits mitochondrial chaperone proteins. (Adapted from *Nat. Chem. Biol.* **2015**, *11*, 9-15)

### 1.5.2 Targeting biosynthetic production

The most important feature of cancer cells is their rapid growth compared to healthy cells. For this reason, they continuously need building blocks molecules such as amino acids, lipids, nucleotides, glutathione, heme, and other components that are produced by the biosynthetic method. Most of the TCA intermediates are used for biosynthesis to build the building blocks molecules. Glutamine, the most abundant amino acid in the cell, is an important

carbon source for supplementing TCA intermediates and supporting their use for biosynthesis in many tumor cells. Many cancer cells are addicted to the glutamine especially MYC and KRAS-induced cancer cells.[55-58] Glutaminase (GLSs) translates glutamine to glutamate, a precursor to glutathione synthesis. After that, the formation of TCA cycle intermediate α-ketoglutarate by using either by glutamate dehydrogenase (GLUD) or by aminotransferases (TA). Therefore, the inhibition of GLS or GLUD / TA is effective in preclinical cancer models (Figure 1.8). Moreover, Autophagy is another approach to reduce the production of TCA intermediates. Autophagy produces metabolic substrates mainly glutamine for mitochondrial metabolism (Figure 1.8).[59]

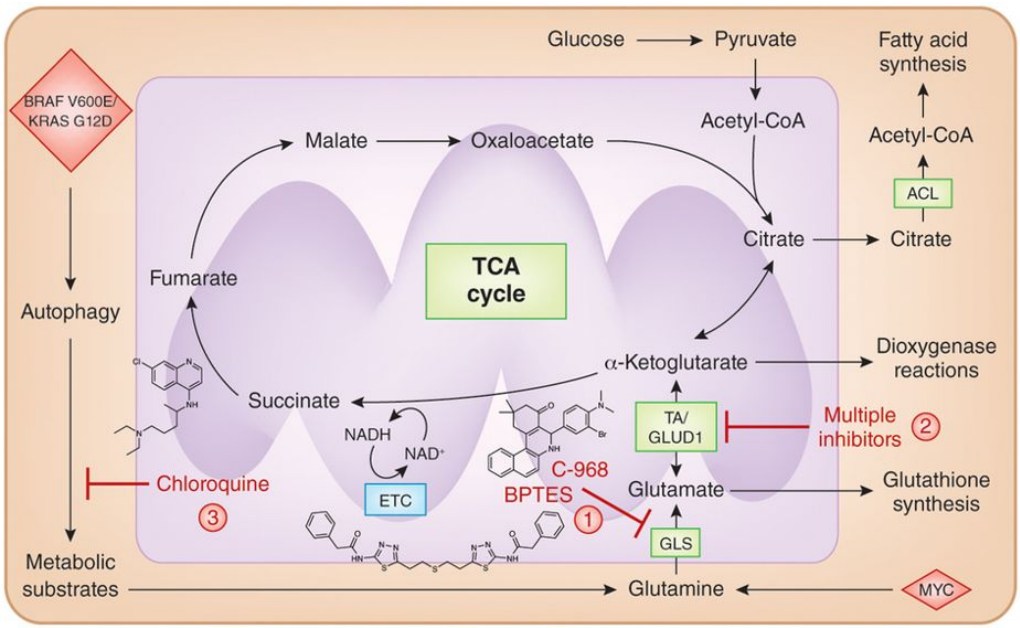


**Figure 1.8**: Targeting mitochondrial biosynthetic production.[19] (1) Compound 968 and compound BPTES inhibits glutamine catabolism. (2)Inhibiting TA/GLUD1 reduces the production of glutamine. (3) Chloroquine is an inhibitor of autophagy, known for impair mitochondrial metabolism. (Adapted from *Nat. Chem. Biol.* **2015**, *11*, 9-15)

### 1.5.3 Targeting mitochondrial redox capacity

Many natural antioxidants are known for their anticancer activity, but their effectiveness in reducing the tumor is always controversial.[60] One of the reasons for their lack of efficacy is that they are unable to minimize the localized mitochondrial ROS. In the previous section, we know

that mitochondrial ROS are responsible for many signalling pathways in cancer cells. Hence mitochondrial-targeted antioxidants effectively reduce cell proliferation.[61] However, Cancer cells neutralize the ROS production by increasing their antioxidant capacity, and this leads to an increase in the amount of $H_2O_2$ to activate the mitochondrial signaling pathway.[62] Also, the enzymes of one-carbon metabolism, SHMT2, and MTHFD2, maybe another therapeutic target as they help maintain redox balance in the mitochondria (Figure 1.9).[63]

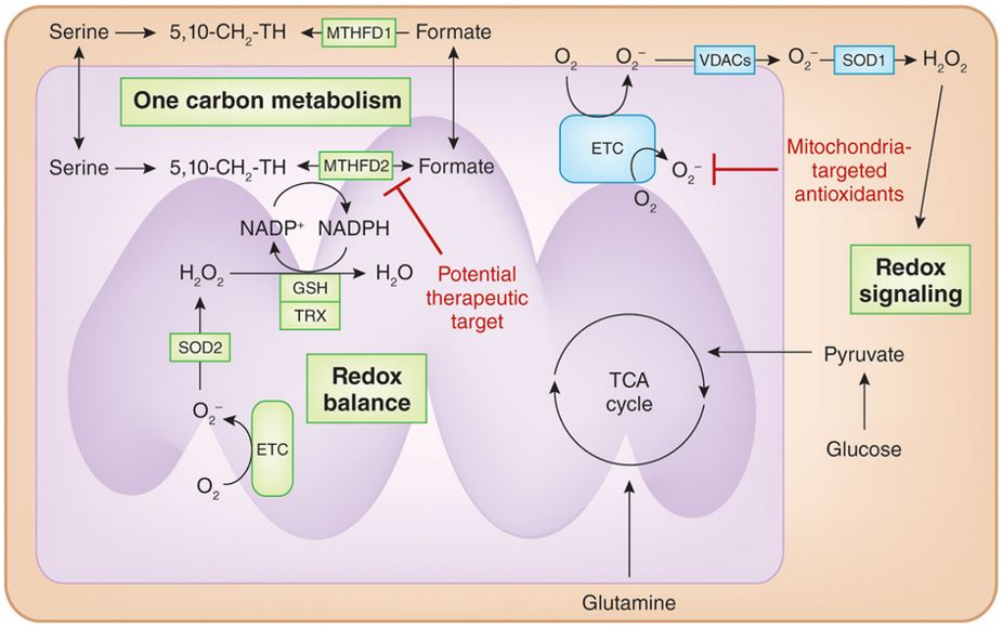


**Figure 1.9**: Targeting mitochondrial redox capacity.[19] (Adapted from *Nat. Chem. Biol.* **2015**, *11*, 9-15).

## 1.6 Specific targeting mitochondria

Despite advances in targeting mitochondrial bioenergetics, biosynthesis, and redox capacity, some critical challenges still need to be addressed. First, any drug to target mitochondria, toxicity must be established in a normal cell. Second, any drug must have properties to penetrate the cell membrane as well as two mitochondrial membranes. And the last challenge is to understand basic mitochondrial biology in cancer to design the novel molecules.

Over the last decade, the covalent modification of the compounds to the vectors directed to the mitochondria has become immensely attractive owing to the direct chemical synthesis and the high efficiency of the targets. Due to the immense negative membrane potential generated by

ETC to the inner mitochondrial membrane, delocalized positively charged compounds accumulate in the mitochondrial matrix, 1,000-fold greater in concentration than outside the cell (Figure 1.10).[19] Therefore, several delocalized lipophilic cationic molecules, including alkyltriphenylphosphonium cations, rhodamine, cyanine, and cationic peptides, have been extensively used to target mitochondria selectively in cancer cells.[64]

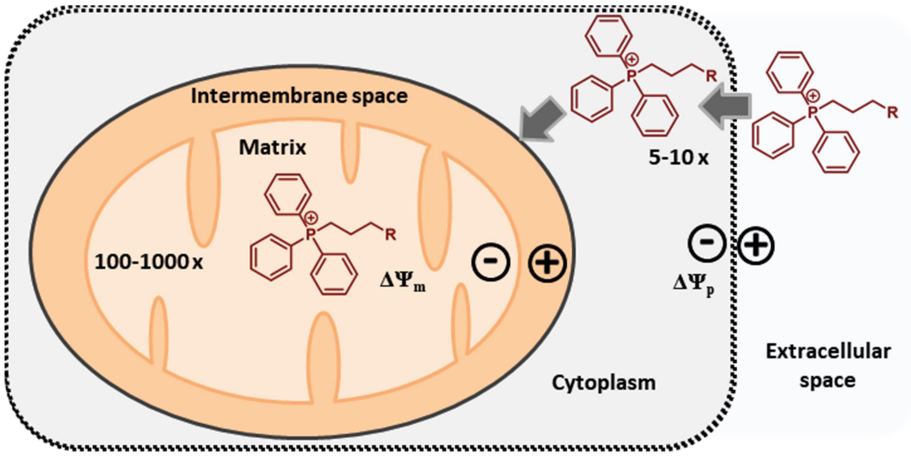


**Figure1.10**: Specific targeting mitochondria[19,65]

### 1.6.1 Triphenylphosphonium cation (TPP)

Triphenylphosphonium (TPP), a delocalized lipophilic cation molecule, is the most well-known for selective accumulation in the mitochondria (Figure 110).[65] Initially, alkylated triphenylphosphonium cations were used to investigate the mechanism of coupling of the mitochondrial membrane potential with OXPHOS, then, were used to determine the mitochondrial membrane potential. Murphy and coworker, first demonstrate the conjugate bioactive molecules to TPP for successful accumulation into mitochondria.[66] TPP cations have been used to transport the probes, antioxidants, and pharmacophores into the mitochondria (Figure 1.11). The TPP molecule has many advantages over any other targeting moiety to the mitochondria, such as biocompatible, both natures hydrophilic as well as hydrophobic, easy to synthesize and purify, stable in a biological system and photo-physically stable. Generally, the basic design of any TPP based mitochondria-targeting agent consists of a TPP cation, a linker sequence, and a functional moiety (Figure 1.11).[64, 65]

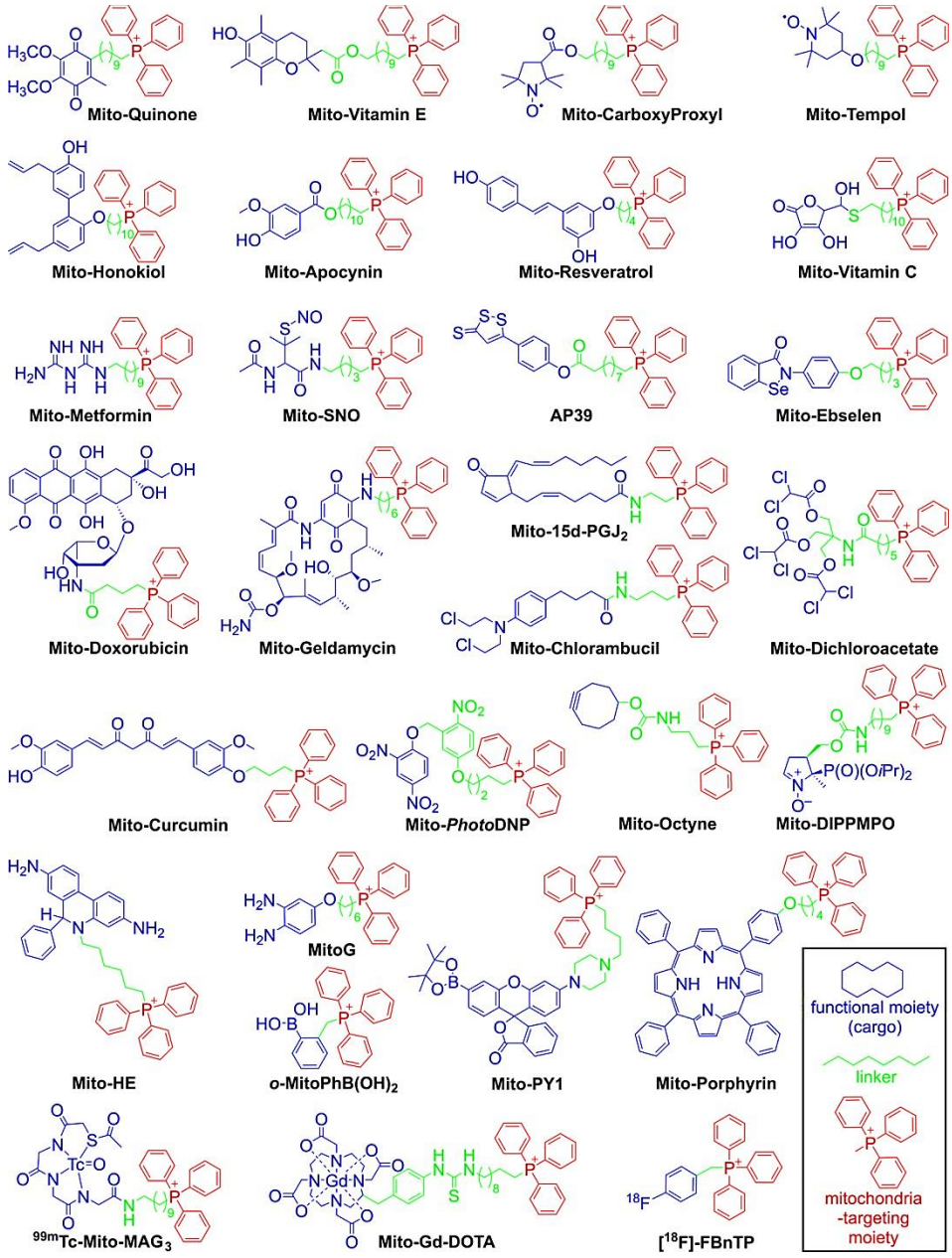


**Figure 1.11**: Examples of $TPP^{+}$ [64,65] ( Adapted from *Chem. Rev.* **2017**, *117*, 10043−10120)

### 1.6.2 Heterocyclic aromatic cations

It has been shown that many heterocyclic, lipophilic, small molecule cations accumulate into cellular mitochondria mainly, rhodamine, pyridinium, and cyanine derivatives.[64,65] Cationic fluorophores such as rhodamine and cyanine dyes are often used for mitochondrial visualization and to monitor mitochondrial membrane potential. Some examples of heterocyclic compounds

that are used as mitochondria-targeting vehicles include the cations berberine, rhodamine, indolium, pyridinium and guanidinium (Figure 1.12A).[65]

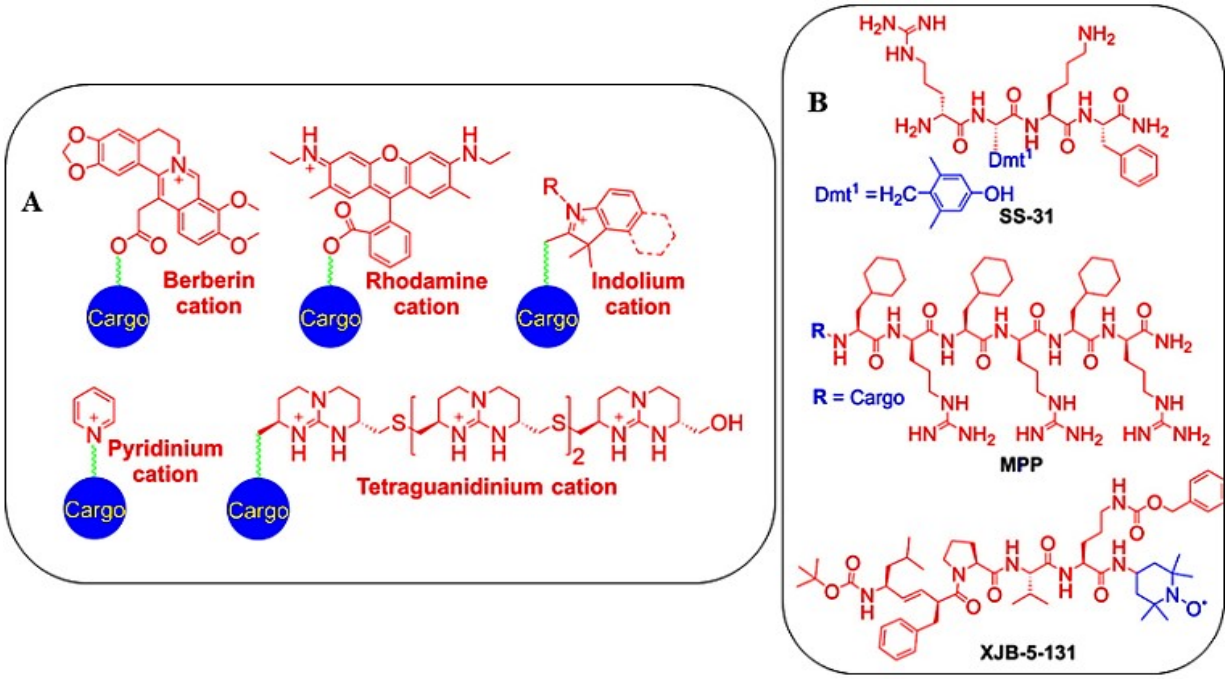


**Figure 1.12**: (A) Examples of heterocyclic cations (B) Examples of mitochondria-targeted peptides [64,65] ( Adapted from *Chem. Rev.* **2017**, *117*, 10043−10120)

### 1.6.3 Mitochondria-targeted peptides

Mitochondrial-targeted peptides have been suggested as an alternative to delocalized lipophilic cations to deliver bioactive molecules into mitochondria selectively.[64,65] Mostly, these peptides typically contain hydrophobic (phenylalanine, tyrosine, isoleucine) and positively charged amino acids (arginine, lysine). Some of the examples are Szeto−Schiller (SS) peptides, mitochondria-penetrating peptides (MPP), Hemigramicidin S-linked nitroxide (XJB-5-131) (Figure 1.12B).[64,65]

## 1.7 The objective of the thesis

Mitochondrion, a central metabolic organelle, is known as the powerhouse of the cells required for bioenergetics, biosynthesis, and signaling. Overall, the collective finding suggests that these functions of mitochondria are mainly responsible for cancer proliferation and tumorigenesis.

Hence, illuminating and targeting the mitochondria in cancer cells with novel small molecules have immense potential for the next generational anticancer therapy.

However, there are three significant challenges that need to be considered to develop small molecules which can impair and or illuminate mitochondria: *(a) selectively impairing of mitochondria of cancer cells over healthy cells*, *(b) selectively illuminate mitochondria in cancer cells and (c) small molecule has to traverse not only the cell membrane but also the two mitochondria membranes.*

To address these challenges, first, we have developed a library of hydrazide-hydrazone-based small molecules and identified novel a compound in the panel of three colon cancer cell lines. The compound induces mitochondrial outer membrane permeabilization by inhibiting anti-apoptotic B-cell CLL/lymphoma 2 (Bcl-2) family proteins followed by sequestration of pro-apoptotic cytochrome C and triggered programmed cell death in HCT-116. Cell viability studies have verified that the small molecule rendered toxicity in a panel of colon cancer cells, keeping non-cancerous L929 fibroblast cells unharmed. The novel small molecule has the potential to form a new understudied class of mitochondria targeting anticancer agents (Chapter 2).

Subsequently, we have developed a facile and short synthesis of novel hydrazide-hydrazone-based small molecules, which demonstrate for the first time remarkable aggregation-Induced emission (AIE) property in water as well as in the solid-state. These molecules internalized selectively into the HeLa cervical cancer cells over non-cancerous L929 fibroblast cells. One of the molecules was tagged with triphenylphosphonium (TPP) moiety, which successfully localized into mitochondria. These unique hydrazide-hydrazone-based biocompatible AIEgens can serve as powerful tools that illuminate not only mitochondria but also other subcellular organelles to elucidate their form and function in cancer cells for next-generation biomedical application (Chapter 3).

Finally, we have developed a delocalized positively charged, cyanine-based red fluorescence small molecules library. All the compounds were found highly active in the HeLa cells. Two molecules in the library were able to home into mitochondria at less than 200 nM concentrations. These compounds induced mitochondrial impairment validated with the formation of mitochondrial permeability transition pore (MPTP) upon inhibiting the anti-apoptotic Bcl-2 and Bcl-xl proteins and enhanced the expression of pro-apoptotic Bax protein

which leads to triggering mitochondrial-dependent apoptosis. We anticipate that this finding will be helpful to explore the future mitochondria-targeted therapeutics in cancer (Chapter 4).

In summary, this thesis attempts the design, synthesis, and validation of novel classes of small organic molecules to illuminate and impair mitochondria in cancer cells.

## 1.8 References


1. American Cancer Society. Global Cancer Facts and Figures 4th Edition. Atlanta: American Cancer Society; **2018**.
2. J. Ferlay, I. Soerjomataram, R. Dikshit S. Eser, C. Mathers, M. Rebelo, D. M. Parkin, D. Forman and F. Bray. Cancer Incidence and Mortality Worldwide: Sources, Methods and Major Patterns in GLOBOCAN 2012. *Int. J. Cancer* **2015**, *136*, E359-386.
3. C. E. Meacham and S. J. Morrison. Tumour Heterogeneity and Cancer Cell Plasticity. *Nature* **2013**, *501*, 328-337.
4. R. Fisher, L. Pusztai, and C. Swanton. Cancer Heterogeneity: Implications for Targeted Therapeutics. *Br. J. Cancer* **2013**, *108*, 479-485.
5. K. Aizawa, C. Liu, S. Tang S. Veeramachaneni, K. Hu, D. E. Smith, and X. Wang. Tobacco Carcinogen Induces Both Lung Cancer and Non-alcoholic Steatohepatitis and Hepatocellular Carcinomas in Ferrets Which Can be Attenuated by Lycopene Supplementation. *Int. J. Cancer* **2016**, *139*, 1171-1181.
6. L. A. Loeb and C. C. Harris. Advances in Chemical Carcinogenesis: A Historical Review and Prospective. *Cancer Res.* **2008**, *68*, 6863–6872.
7. N. Parsa. Environmental Factors Inducing Human Cancers. *Iran. J. Public Health* **2012**, *41,* 1 9.
8. US Department of Health and Human Services. Public Health Service, National Toxicology Program. Report on Carcinogens, Fourteenth Edition. **2016**. Accessed at *http://ntp.niehs.nih.gov/pubhealth/roc/index-1.html on November 3, 2016*
9. International Agency for Research on Cancer (IARC). Agents Classified by the IARC Monographs, **2015**, Volumes 1 – 114. Accessed at *http://monographs.iarc.fr/ENG/Classification/List_of_Classifications_Vol1-114.pdf on October 27, 2015*
10. C. Sawyers. Targeted Cancer Therapy. *Nature* **2004**, *432*, 294–297.
11. American Society of Clinical Oncology. Understanding Targeted Therapy. 10/**2015**. Accessed at *www.cancer.net/navigating-cancer-care/how-cancer-treated/personalized-and-targeted therapies/understanding-targeted-therapy on May 10, 2016*

12. National Cancer Institute. Targeted Cancer Therapies. **2014.** Accessed at *www.cancer.gov/cancertopics/factsheet/Therapy/targeted on May 4, 2016*
13. W. Kühlbrandt. Structure and Function of Mitochondrial Membrane Protein Complexes. *BMC Biology* **2015***,* **13**, 89. DOI 10.1186/s12915-015-0201-x
14. D. D. Newmeyer and S. Ferguson-Miller, Mitochondria: Releasing Power for Life and Unleashing the Machineries of Death. *Cell* **2003**, *112*, 481–490.
15. J. R. Friedman and J. Nunnari. Mitochondrial form and function. *Nature* **2014**, *505*, 335–343.
16. S. Anderson, A. T. Bankier, B. G. Barrell, M. H. L. de Bruijn, A. R. Coulson, J. Drouin, I. C. Eperon, D. P. Nierlich, B. A. Roe, F. Sanger, P. H. Schreier, A. J. H. Smith, R. Staden and I. G. Young. Sequence and Organization of the Human Mitochondrial Genome. *Nature* **1981**, *290*, 457–465.
17. D. G. Nicholls. Mitochondrial Function and Dysfunction in the Cell: it's Relevance to Aging and Aging-Related Disease. *Int J Biochem*. *Cell Biol.* **2002**, 34, 1372-1381.
18. E. Murphy, H. Ardehali, R. S. Balaban, F. DiLisa, G. W. Dorn, R. N. Kitsis, K. Otsu, P. Ping, R. Rizzuto, M. N. Sack, D. Wallace and R. J. Youle. Mitochondrial Function, Biology, and Role in Disease. *Circ. Res*. **2016**, *118*, 1960–1991.
19. S. E Weinberg and N. S Chandel. Targeting Mitochondria Metabolism for Cancer Therapy. *Nat. Chem. Biol*. **2015**, *11*, 9-15.
20. M. G. V. Heiden, L. C. Cantley and C. B. Thompson. Understanding the Warburg Effect: The Metabolic Requirements of Cell Proliferation. *Science*, **2009**, *334*, 1029-1033.
21. N. S. Chandel. Mitochondria as Signaling Organelles. *BMC Biology* **2014**, *12*, 34. doi: 10.1186/1741-7007-12-34
22. N. S. Chandel. Evolution of Mitochondria as Signaling Organelles. *Cell Metab*. **2015**, 22, 204 206.
23. S. S. Sabharwal and P. T. Schumacker. Mitochondrial ROS in Cancer: Initiators, Amplifiers or an Achilles' heel? *Nat. Rev. Cancer* **2014**, *14*, 709–721.
24. N. Badrinath and S. Y. Yoo. Mitochondria in Cancer: In the Aspects of Tumorigenesis and Targeted Therapy. *Carcinogenesis*, **2018**, *39*, 1419–1430.
25. D. C. Wallace, Mitochondria and Cancer. *Nat. Rev. Cancer* **2012**, *12*, 685–698.
26. W. Zong, J. D. Rabinowitz, and E. White. Mitochondria and Cancer. *Mol. Cell.* **2016** *61*, 667 676.
27. S. Vyas, E. Zaganjor, and M. C. Haigis. Mitochondria and Cancer. *Cell* **2016**, *166*, 555–566.
28. D. Hanahan and R. A.Weinberg. The Hallmarks of Cancer. *Cell* **2000**, *100*, 57-70.
29. D. Hanahan and R. A.Weinberg. Hallmarks of Cancer: The Next Generation. *Cell* **2011**, *144*, 646 674.
30. P. S. Ward and C. B. Thompson. Metabolic Reprogramming: A Cancer Hallmark Even Warburg Did Not Anticipate. *Cancer Cell* **2012**, *21*, 297–308.

31. C. V. Dang. Links between Metabolism and Cancer. *Genes Dev.* **2012**, *26*, 877–890.
32. R. J. DeBerardinis and T. Cheng. Q's next: the diverse functions of glutamine in metabolism, cell biology and cancer. *Oncogene* **2010**, *29*, 313–324.
33. M. Schieber and N. S. Chandel. ROS Function in Redox Signaling and Oxidative Stress. *Curr. Biol.* **2014**, *24*, 453–462.
34. C. Gorrini, I. S. Harris and T. W. Mak. Modulation of Oxidative Stress as an Anticancer Strategy. *Nat. Rev. Drug Discov.* **2013**, *12*, 931–947.
35. J. Fan, J. Ye, J. J. Kamphorst, T. Shlomi, C. B. Thompson and J. D. Rabinowitz. Quantitative Flux Analysis Reveals Folate-Dependent NADPH Production. *Nature* **2014**, *510*, 298–302.
36. C. A. Lewis, S. J. Parker, B. P. Fiske, A. M. Feist, M. G. V. Heiden and C. M. Metallo. Tracing Compartmentalized NADPH Metabolism in the Cytosol and Mitochondria of Mammalian Cells. *Mol. Cell* **2014**, *55*, 253–263.
37. S. Elmore. Apoptosis: A Review of Programmed Cell Death. *Toxicol. Pathol*. **2007**, *35*, 495 516.
38. D. R. Green and J. C. Reed. Mitochondria and Apoptosis. *Science* **1998**, *28*, 281, 1309-1312.
39. J. Lopez and S. W. G. Tait. Mitochondrial Apoptosis: Killing Cancer Using the Enemy Within. *Br. J. Cancer* **2015**, *112*, 957–962.
40. L. Campos, J. P. Rouault, O. Sabido, P. Oriol, N. Roubi, C. Vasselon, E. Archimbaud, J. P. Magaud and D. Guyotat. High Expression of Bcl-2 Protein in Acute Myeloid Leukemia Cells is Associated with Poor Response to Chemotherapy. *Blood* **1993**, *81*, 3091-3096.
41. A. J. García-Sáez. The Secrets of the Bcl-2 Family. Cell Death Differ. **2012**, *19*, 1733–1740.
42. S. Cory, D. C. S. Huang and J. M. Adams. The Bcl-2 Family: Roles in Cell Survival and Oncogenesis. *Oncogene* **2003**, *22*, 8590-8607.
43. A. Strasser, S. Cory, J. M. Adams. Deciphering the Rules of Programmed Cell Death to Improve Therapy of Cancer and Other Diseases. *EMBO J*. **2011**, *30*, 3667-3683.
44. MichaCerto, V. D. G. Moore, M. Nishino, G. Wei, S. Korsmeyer, S. A. Armstrong, A. Letai. Mitochondria Primed by Death Signals Determine Cellular Addiction to Antiapoptotic BCL-2 Family Members. *Cancer Cell* **2006**, *9*, 351-365.
45. R. J. Youle and A. Strasser. The BCL-2 Protein Family: Opposing Activities That Mediate Cell Death. *Nat. Rev. Mol. Cell Biol*. **2008**, *9*, 47–59.
46. J. E. Chipu, T. Moldoveanu, F. Llambi, M. J. Parsons and D. R. Green. The BCL 2 Family Reunion. *Mol. Cell.* **2010** *37*, 299-310.
47. J. E. Chipuk, L. Bouchier-Hayes and D. R. Green. Mitochondrial Outer Membrane Permeabilization during Apoptosis: The Innocent Bystander Scenario. *Cell Death Differ*. **2006**, *13*, 1396–1402.

48. S. W. G. Tait and D. R. Green. Mitochondria and Cell Death: Outer Membrane Permeabilization and Beyond. *Nat. Rev. Mol. Cell Biol*. **2010**, *11*, 621–632.
49. P. J. Burke. Mitochondria, Bioenergetics and Apoptosis in Cancer. *Trends Cancer* **2017,** *3*, 857-870.
50. H. Yang, R. M. Villani, H. Wang, M. J. Simpson. M. S. Roberts, M. Tang and X. Liang. The Role of Cellular Reactive Oxygen Species in Cancer Chemotherapy. *J. Exp. Clin. Cancer Res*. **2018**, *37*, 266.
51. R. K. Jain, L. L. Munn and D. Fukumura. Dissecting Tumour Pathophysiology using Intravital Microscopy. *Nat. Rev. Cancer* **2002**, *2*, 266–276.
52. R. A. Gatenby and R. J. Gillies. Why Do Cancers Have High Aerobic Glycolysis? *Nat. Rev. Cancer* **2004**, *4*, 891–899.
53. P. Caro, A. U. Kishan, E. Norberg, I. A. Stanley, B. Chapuy, S. B. Ficarro, K. Polak, D. Tondera, J. Gounarides, H. Yin, F. Zhou, M. R. Green, L. Chen, S. Monti, J. A. Marto, M. A. Shipp and N. N. Danial. Metabolic Signatures Uncover Distinct Targets in Molecular Subsets of Diffuse Large B cell Lymphoma. *Cancer Cell* **2012**, *22*, 547–560.
54. J. A Engelman, L. Chen, X. Tan, K. Crosby, A. R. Guimaraes, R. Upadhyay, M. Maira, K. McNamara, S. A. Perera, Y. Song, L. R. Chirieac, R. Kaur, A. Lightbown, J. Simendinger, T. Li, R. F. Padera, C. Garcı´a-Echeverrı´a, R. Weissleder, U. Mahmood, L. C. Cantley and K. Wong. Effective use of PI3K and MEK Inhibitors to Treat Mutant Kras G12D and PIK3CA H1047R Murine Lung Cancers. *Nat. Med.* **2008***, 14*, 1351–1356.
55. C. T. Hensley, A. T. Wasti and R. J. DeBerardinis. Glutamine and Cancer: Cell Biology, Physiology, and Clinical Opportunities. *J. Clin. Invest.* **2013**, *123*, 3678–3684.
56. D. R. Wise, R. J. DeBerardinis, A. Mancuso, N. Sayed, X. Zhang, H. K. Pfeiffer, I. Nissim, E. Daikhin, M. Yudkoff, S. B. McMahon and C. B. Thompson. Myc Regulates a Transcriptional Program That Stimulates Mitochondrial Glutaminolysis and Leads to Glutamine Addiction. *Proc. Natl. Acad. Sci. USA* **2008**, *105*, 18782–18787.
57. P. Gao, I. Tchernyshyov, T. Chang, Y. Lee, K. Kita, T. Ochi, K. I. Zeller, A. M. De Marzo, J. E. V. Eyk, J. T. Mendell and C. V. Dang. c-Myc Suppression of Mir-23a/B Enhances Mitochondrial Glutaminase Expression and Glutamine Metabolism. *Nature* **2009**, *458*, 762–765.
58. D. Gaglio, C. M. Metallo, P. A. Gameiro, K. Hiller, L. S. Danna, C. Balestrieri, L. Alberghina, G. Stephanopoulos and F. Chiaradonna. Oncogenic K-Ras Decouples Glucose and Glutamine Metabolism to Support Cancer Cell Growth. *Mol. Syst. Biol.* **2011**, *7*, 523.
59. J. Y. Guo1, H. Chen, R. Mathew, J. Fan, A. M. Strohecker, G. Karsli-Uzunbas, J. J. Kamphorst, G. Chen, J. M. S. Lemons, V. Karantza, H. A. Coller, R. S. DiPaola, C. Gelinas, J. D. Rabinowitz and E. White. Activated Ras Requires Autophagy to Maintain Oxidative Metabolism and Tumorigenesis. *Genes Dev*. **2011**, *25*, 460–470.

60. G. Bjelakovic, G. and C. Gluud. Surviving Antioxidant Supplements. *J. Natl. Cancer Inst.* **2007**, *99*, 742–743.
61. B. J. Snow, F. L. Rolfe, M. M. Lockhart, C. M. Frampton, J. D. O'Sullivan, V. Fung, R. A. J. Smith, M. P. Murphy and K. M. Taylor. A Double-Blind, Placebo-Controlled Study to Assess The Mitochondria-targeted Antioxidant MitoQ as a Disease-Modifying Therapy in Parkinson's disease. *Mov. Disord.* **2010,** *25*, 1670–1674.
62. G. M. DeNicola, F. A. Karreth, T. J. Humpton, A. Gopinathan, C. Wei, K. Frese, D. Mangal, K. H. Yu, C. J. Yeo, E. S. Calhoun, F. Scrimieri, J. M. Winter, R. H. Hruban, C. Iacobuzio Donahue, S. E. Kern, I. A. Blair and D. A. Tuveson. Oncogene-Induced Nrf2 Transcription Promotes ROS Detoxification and Tumorigenesis. *Nature* **2011**, *475*, 106–109.
63. J. W. Locasale. Serine, Glycine and One-carbon Units: Cancer Metabolism in Full Circle. *Nat. Rev. Cancer* **2013**, *13*, 572–583.
64. A. T. Hoye, J. E. Davoren and P. Wipf, Targeting Mitochondria. *Acc. Chem. Res.* **2008**, *41*, 87 97.
65. J. Zielonka, J. Joseph, A. Sikora, M. Hardy, O. Ouari, J. Vasquez-Vivar, G. Cheng, M. Lopez, and B. Kalyanaraman. Mitochondria-Targeted Triphenylphosphonium-Based Compounds: Syntheses, Mechanisms of Action, and Therapeutic and Diagnostic Applications. *Chem. Rev.* **2017**, *117*, 10043−10120.
66. M. P.Murphy. Selective Targeting of Bioactive Compounds to Mitochondria. *Trends Biotechnol.* **1997**, *15*, 326-330.

# Chapter 2

# Impairing Powerhouse in Colon Cancer Cells by Hydrazide-Hydrazone-based Small Molecule

*ACS Omega*, **2018**, *3*, 1470-1481

## 2.1 Introduction:

Colon cancer is the 3rd most devastating disease claiming nearly 0.7 million deaths per year globally.[1,2] Numerous FDA approved small molecule drugs (5-fluorouracil, oxaliplatin and irinotecan) are already in clinics for the treatment of colon cancer patients under chemotherapy regimen.[3-5] However, small molecule anti-cancer drugs kill healthy cells along with targeted cancer cells as collateral damage to induce severe toxic side effects to the patients. Moreover, most of the cancer cells emerge resistance mechanisms (intrinsic or extrinsic) to overcome the effect of the drugs.[6-9] Hence, there is an urgent need to develop novel small molecules to perturb unconventional sub-cellular targets as next-generation cancer therapeutics. In recent years, the understanding of biological function beyond ATP (energy currency) generation prompted mitochondrion as an alternative target for anti-cancer therapy.

Mitochondrion, the powerhouse of the cells, is one of the most important sub-cellular organelles which contains genomic materials and plays a central role in innumerable cellular processes including bioenergetics, metabolism, biosynthesis, signal transduction and apoptosis.[10-15] Subsequently, mitochondrial functions have been high-jacked in different types of cancers[16-19] directed mitochondrion as one of the unorthodox targets for cancer chemotherapy.[20-23] As a result, several conventional anti-cancer drugs were routed into mitochondria for improved efficacy, evade drug resistance and reduce off-target toxicity.[24-**28**] Recently, mitochondrion was found to play a crucial role in colon cancer development and progression.[29,30] Although, natural products and synthetic small molecules have evolved as powerful tools to perturb and understand biological phenomena,[31-34] development of novel small molecules to impair mitochondrial functions selectively in cancer cells especially in colon cancer remained a daunting task,[35-37] hence mostly underexplored.

In recent years, hydrazine, hydrazone and hydrazide-based compounds having nitrogen-nitrogen (N-N) bond emerged as interesting natural and non-natural products.[38, 39] Similarly, hydrazide-hydrazone (-CO-NH-N=CH-) derivatives (a fusion of hydrazide and hydrazone moieties) demonstrated significant diverse biological effects including anti-inflammatory, anti-bacterial, anti-malarial and anti-cancer activities (Scheme 1a).[40-46] Despite showing immense

potential as future anti-cancer drug candidates, the effect of hydrazide-hydrazone derivatives on mitochondrion (intrinsic program cell death mediator) in cancer cells is completely unexplored.

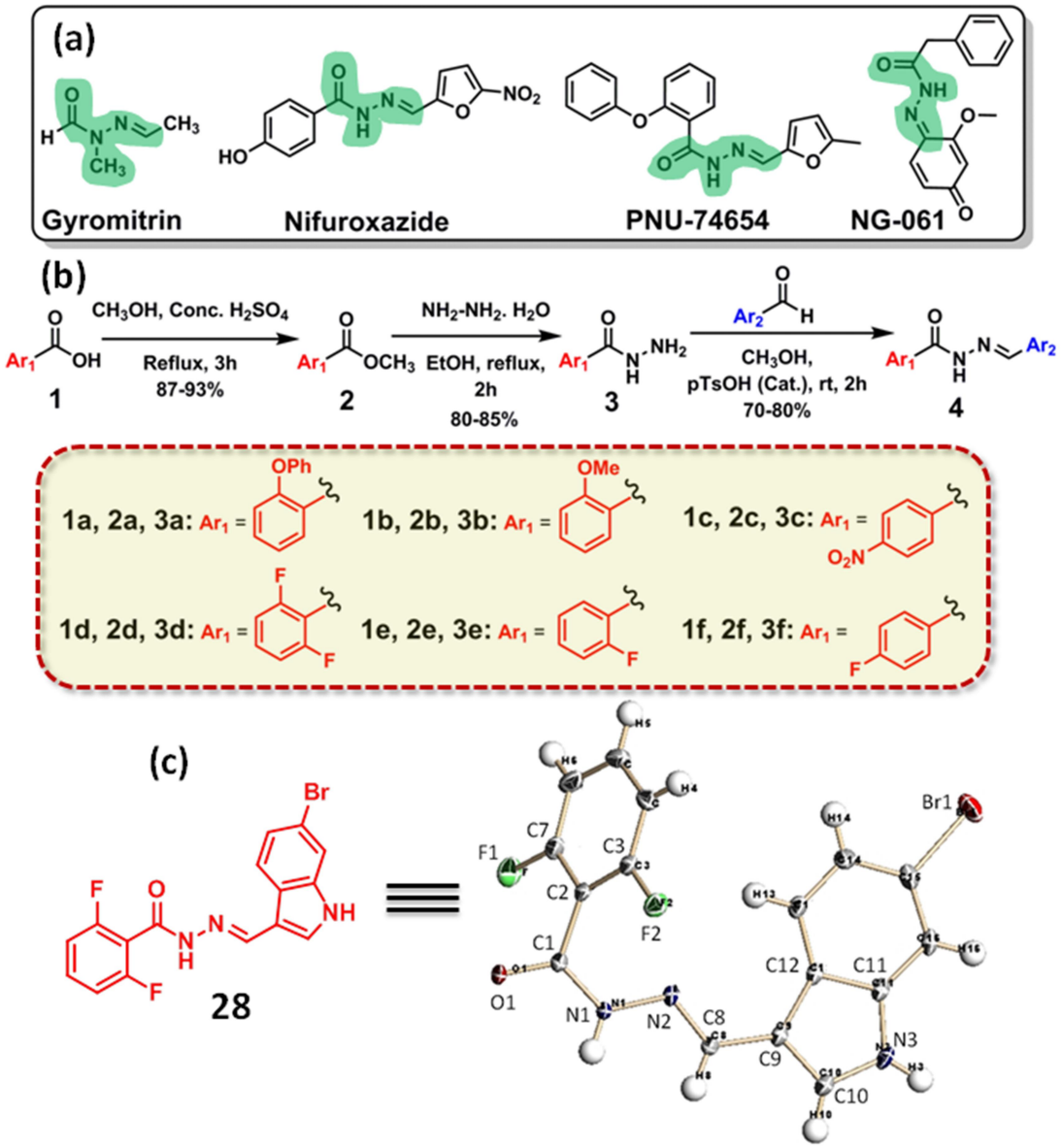


**Scheme 2.1**: (a) Chemical structures of hydrazide-hydrazone containing biologically active natural products. (b) A synthetic scheme of hydrazide-hydrazone based small molecule library. (c) Chemical structure and ORTEP diagram of compound **28** with 50% thermal ellipsoid

To address this, herein, we illustrate a short and easy synthesis of hydrazide-hydrazone based library. Screening of library members in colon cancer cell lines (HCT-116, DLD-1 and SW-620) yielded a novel small molecule which can damage mitochondria through Bcl-2 inhibition-mediated outer membrane permeabilization (MOMP). This mitochondrial impairment

released cytochrome c, generated reactive oxygen species (ROS) and finally induced apoptosis through cell cycle arrest and caspase-9/3 cleavage.

## 2.2 Results and Discussion:

### 2.2.1 Synthesis of hydrazide-hydrazone library and characterization

The synthesis of hydrazide-hydrazone library is described in Scheme 1b. First, benzoic acid derivatives (**1a-1f**) were reacted with methanol in presence of concentrated sulphuric acid in refluxing condition to obtain the methyl esters (**2a-2f**) in 87-93 % yield. The methyl-benzoate derivatives (**2a-2f**) were further reacted with hydrazine monohydrate in ethanol in refluxing condition to afford benzoic acid based hydrazides (**3a-3f**) in 80-85 % yield (Figure 2.1). Finally, aromatic hydrazides (**3a-3f**) were reacted with aromatic aldehydes in the presence of catalytic *p*-toluenesulfonic acid to generate hydrazide-hydrazone derivatives (**4**) in 70-80 % isolated yield. A library of 30 hydrazide-hydrazone compounds (**5-34**, Figure 2.2) was synthesized by this strategy. Chemical structures of the all the library members were confirmed by $^{1}H$, $^{13}C$ NMR and high-resolution mass spectroscopy (HR-MS) (Appendix-A; Figure A1-90).

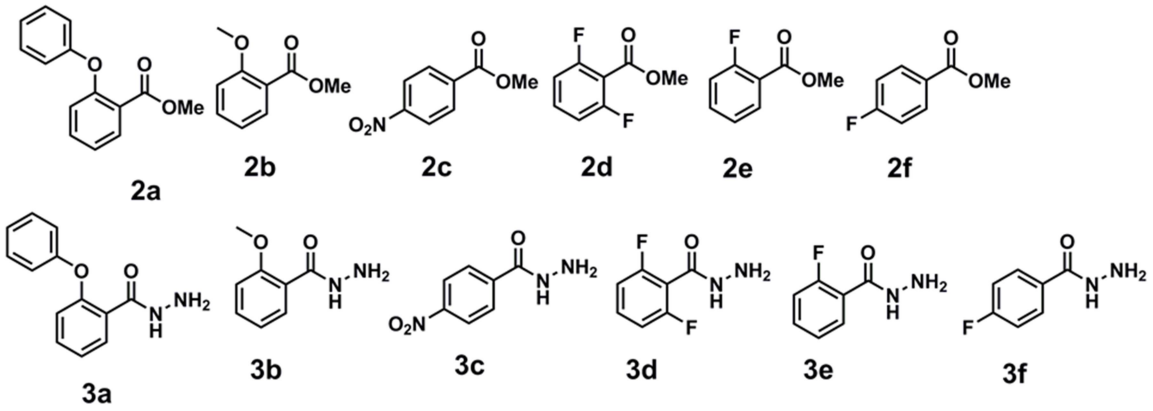


**Figure 2.1:** Chemical structures of the methyl benzoates and aromatic hydrazide intermediates

### 2.2.2 Screening of hydrazide-hydrazones in colon cancer cells

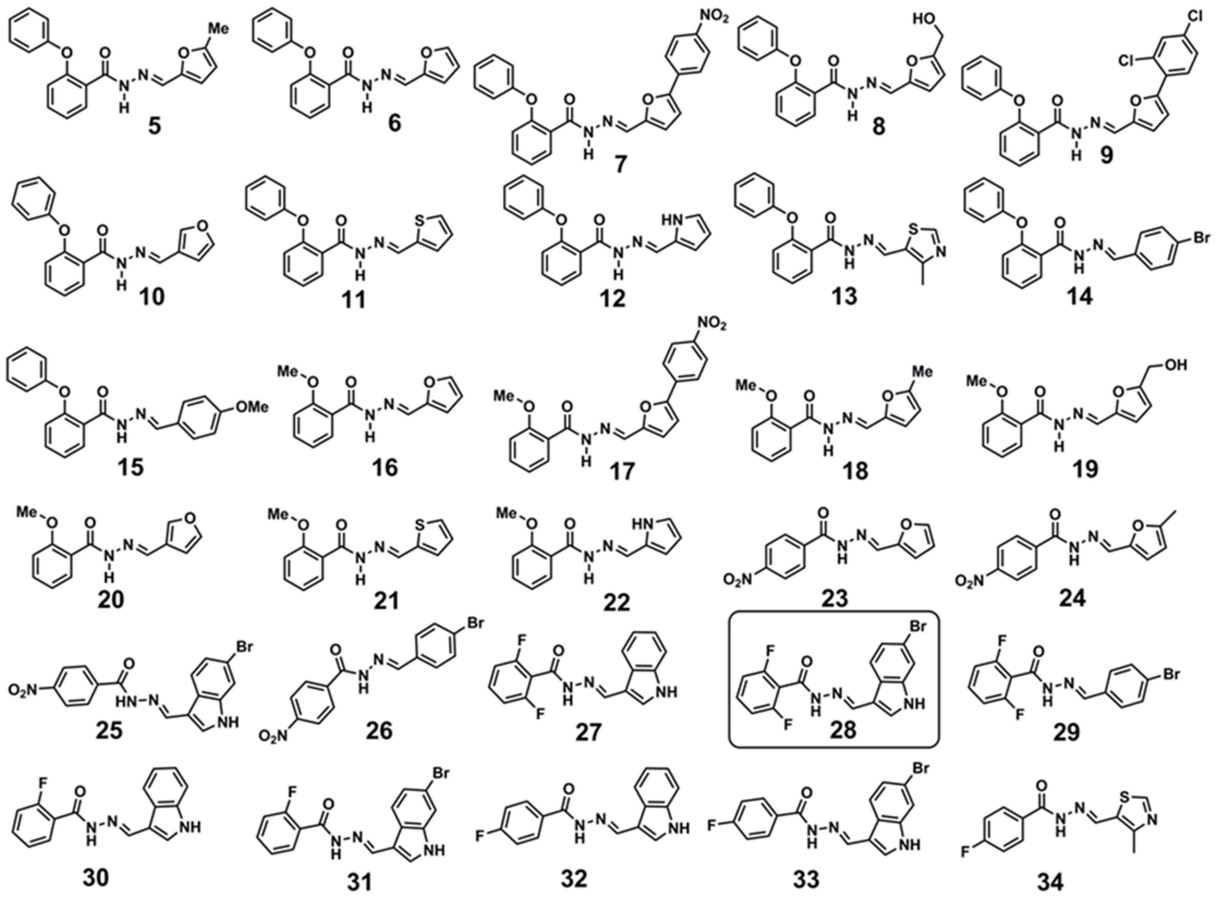

**Figure 2.2:** Chemical structures of the hydrazide-hydrazone library members

First, the hydrazide-hydrazones were screened to check their ability to induce cell death in colon cancer cells. As there is no previous study of hydrazide-hydrazone derivatives in colon cancer cells, we intended to generate single point data using one concentration for each compounds in high-throughput screening (HTS) method.[47,48] We chose high initial concentration (30 μM) to avoid false negative and false positive hits at lower concentration. Moreover, the non-toxic molecules in high concentration should be easily eliminated for further studies. Hence, HCT-116, DLD-1 and SW-620 colon cancer cells were treated with hydrazide-hydrazone derivatives at 30 μM concentration and cell viability was assessed by MTT assay at 24 h post incubation. Interestingly, it was found that, only compound **28** (Scheme 1c; Figure 2.2) induced 31.7 ± 1.7, 41.7 ± 3 and 35.4 ± 3.4 % cell viability in HCT-116, DLD-1 and SW-620 cells respectively at 30 μM concentrations (Figure 1a-c). The rest of the library members showed negligible cell death even at 30 μM after 24 h.

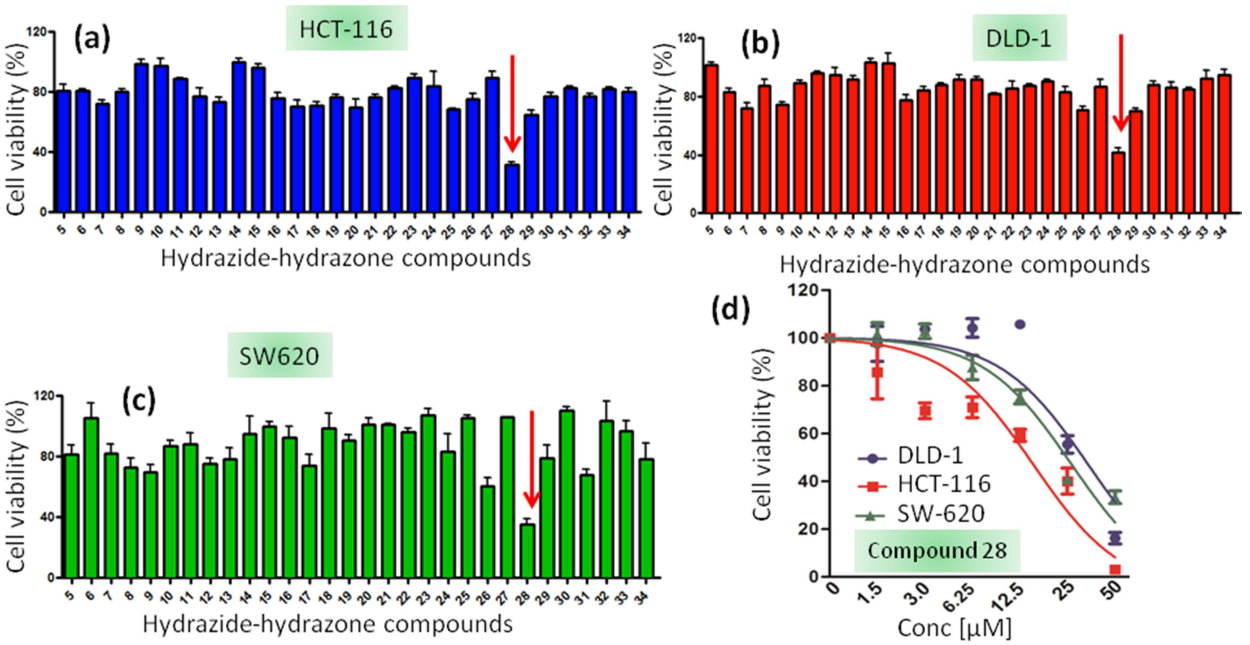


**Figure 2.3:** MTT assay of hydrazide-hydrazone derivatives in (a) HCT-116, (b) DLD-1 and (c) SW-620 cells at 30 µM concentrations at 24 h post-incubation. (d) Dose-dependent cell viability assay of compound **28** in HCT-116, DLD-1 and SW-620 cells at 24 h post-incubation.

The dose-dependent cytotoxicity of compound **28** was estimated further in HCT-116, DLD-1 and SW-620 cells by MTT assay at 24 h post-incubation. Compound **28** demonstrated $IC_{50}$ = 20.0 ± 2.7, 27.7 ± 1.8 and 20.5 ± 0.5 µM (with cell viability = 3.15 ± 0.9, 16.2 ± 2.4 and 33.3 ± 2.6 % at 50 µM) in HCT-116, DLD-1 and SW-620 cells respectively (Figure 1d). To compare the potential of compound **28** in inducing cell death in colon cancer cells with other traditional chemotherapeutic drugs used in clinics, we treated HCT-116 cells with 5-fluorouracil (5-FU), camptothecin and cisplatin in a dose-dependent manner for 24 h and evaluated cell viability by MTT assay. Interestingly, it was observed that 5-FU, camptothecin and cisplatin showed much higher $IC_{50}$ = 57.3 ± 3.6 µM (cell viability = 57.3 ± 3.6 % at 50 µM), 44.5 ± 2.9 µM (cell viability = 44.5 ± 2.9 % at 50 µM) and 24.6 ± 0.5 µM (cell viability = 33.9 ± 1.8 % at 50 µM) respectively (Figure 2.4). Furthermore, we wanted to check if the dissociation components of compound **28** in the acidic medium can induce cellular toxicity. Hence, HCT-116 cells were treated with 2, 6-Difluorobenzohydrazide (**3d** in Figure 2.5) and 6-Bromo-1H-indole-3-carbaldehyde in a dose dependent manner for 24 h and the cell viability was measured by MTT

assay. It was observed that both the compounds showed negligible toxicity (Figure 2.5) towards HCT-116 cells.

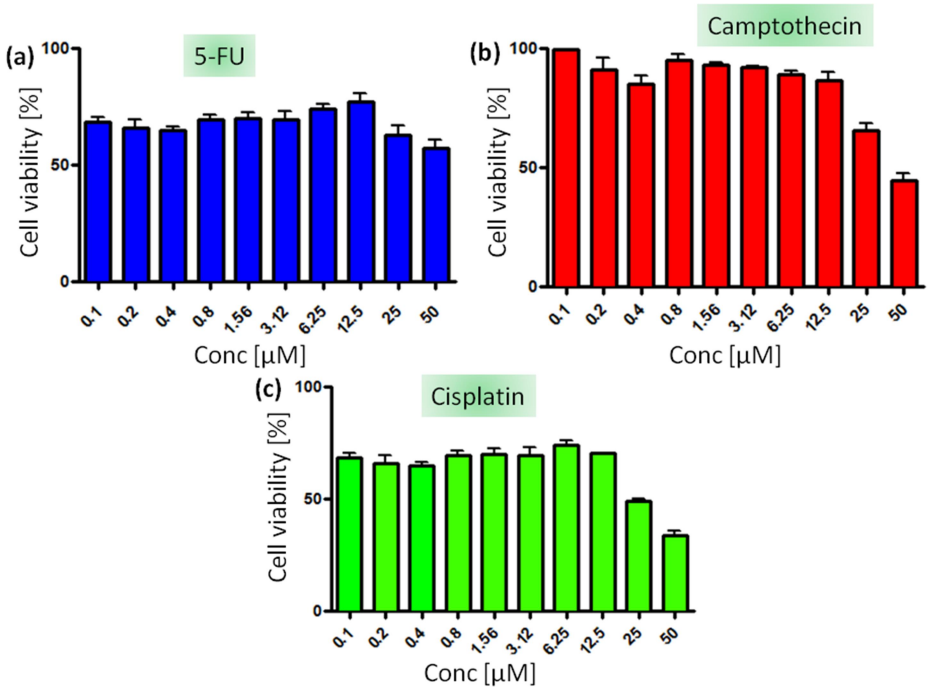


**Figure 2.4**: Concentration dependent cell viability assay of (a) 5-FU, (b) Camptothecin and (c) Cisplatin in HCT-116 cells after 24 h post incubation

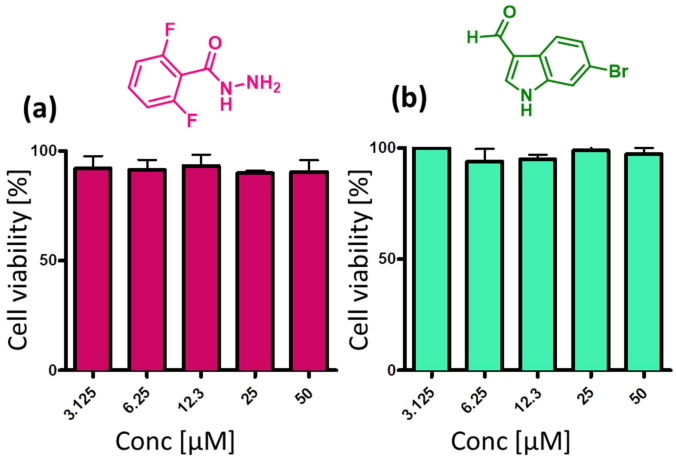


**Figure 2.5**: Concentration dependent cell viability assay of (a) 2, 6-difluorobenzohydrazide and (b) 6-bromo-1H-indole-3-carbaldehyde in HCT-116 cells at 24 h post-incubation

One of the major challenges in current cancer therapy is to target cancer cells selectively, keeping normal healthy cells unperturbed. To evaluate the effect in healthy cells, we treated L929 fibroblast cells with compound **28** in a dose dependent manner at 24 h post-incubation.

Cell viability was measure by MTT assay. Interestingly, compound **28** showed almost no toxicity (cell viability = 96.67 ± 6.3 %, n = 3, mean ± SEM) to L929 cells even at a higher concentration of 100 µM (Figure 2.6a). On the other hand, cisplatin, camptothecin and 5-FU showed dose-dependent toxicity in L929 with 78.3%, 63.5 % and 72.0 % cell viability respectively at 100 µM concentration at 24 h post-incubation (Figure 2.6b). These MTT assays provided convincing evidence that compound **28** can kill colon cancer cells much efficiently compared to clinically approved traditional cytotoxic drugs and at the same time keep healthy cells unharmed. The selectivity of any cytotoxic drugs over healthy cells can be explain by unique properties of cancer cells such as diverse chemical, structural, metabolic and biophysical characteristics.

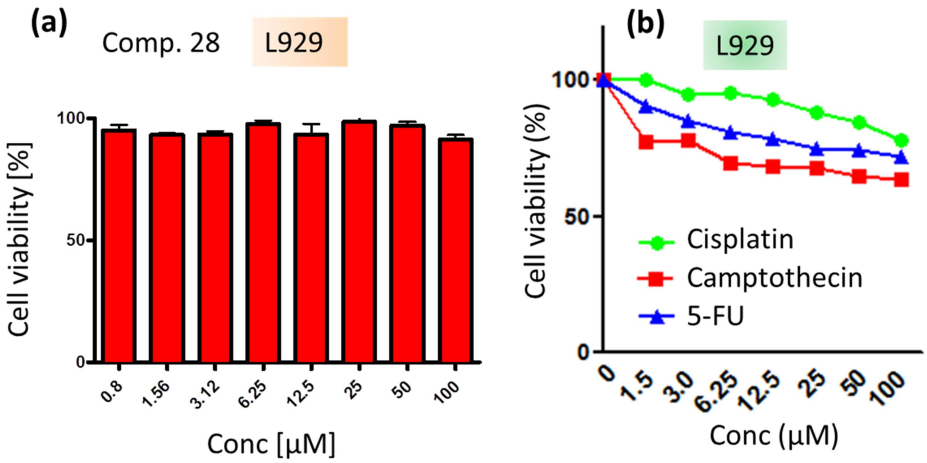


**Figure 2.6**: Concentration dependent cell viability assay of (a) compound 28 and (b) cisplatin, camptothecin, and 5-FU in L929 cells at 24 h post-incubation.

### 2.2.3 Stability of compound 28

We further characterized the structure of the lead compound **28** by X-ray crystallography (Scheme 1c; Appendix-A table A1). The purity of compound **28** was also evaluated to be 98.6 % by High-Performance Liquid Chromatography (HPLC) (Appendix-A; Figure A91). The hydrazone and hydrazide functionality are known to be labile in acidic medium.[49] Hence, to be successful in targeting sub-cellular organelles in colon cancer, compound **28** should be stable in acidic tumor environment. The stability of compound **28** in acidic medium was further evaluated. Compound **28** was incubated in pH = 5.5 buffer for short (24 h) and longer (72 h) time and the

integrity of compound **28** was confirmed by MALDI-TOF and LC-HRMS. From the MALDI-TOF spectroscopy and LC-HRMS (**Appendix-A Figures A92-A94)** it was evident that compound **28** remained stable in acidic milieu even after 72 h which indicated its potential for therapeutic application in cancer.

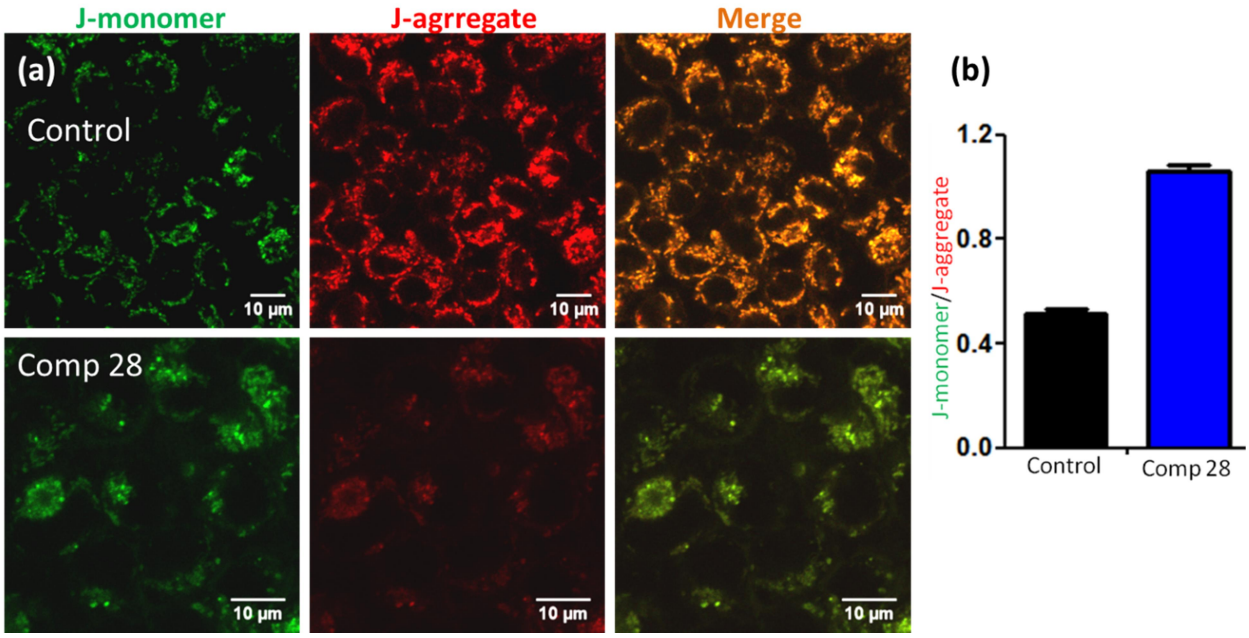


**Figure 2.7: (**a) Confocal microscopy images of HCT-116 cells treated with compound 28 followed by JC1 staining to observe mitochondrial outer membrane permeabilization (MOMP) (b) Quantification of J-monomer/J-aggregate. Scale bar = 10 µm.

### 2.2.4 Mitochondrial outer membrane permeabilization (MOMP)

One of the hallmarks of cancer cells is to resist cellular death.[50,51] Mitochondria play a crucial role in controlling cancer cell death by inducing mitochondrial outer membrane permeabilization (MOMP).[15,52-54] To evaluate the effect of compound **28** on mitochondria in colon cancer cells, mitochondrial membrane potential (Δψm) was investigated by JC1 assay. 5,5′,6,6′-tetrachloro-1,1′,3,3′-tetraethylbenzimidazolocarbocyanine iodide (JC1), a cationic carbocyanine dye, shows membrane potential-dependent homing into mitochondria with a switch from green (~ 525 nm) to red (~ 590 nm) in fluorescence emission by forming J-aggregates (red fluorescence) in higher concentration. We estimated the mitochondrial membrane permeabilization by the increase of green: red fluorescent intensity ratio.[55] HCT-116 cells were

treated with compound **28** at 15 µM (sub $IC_{50}$ concentration to avoid cell death, stress response and morphology change) for 24 h and stained the cells with JC1 dye. Confocal laser scanning microscopy (CLSM) was performed to visualize the live stained cells (Figure 2.7a). It evidently showed that compound **28** treated cells induced significant increase in green: red ratio (green: red = 1.06 ± 0.2) compared to control non-treated cells (green: red = 0.51 ± 0.2) (Figure 2.7b). This confocal microscopy of JC1 assay confirmed that compound **28** induced mitochondrial membrane permeabilization.

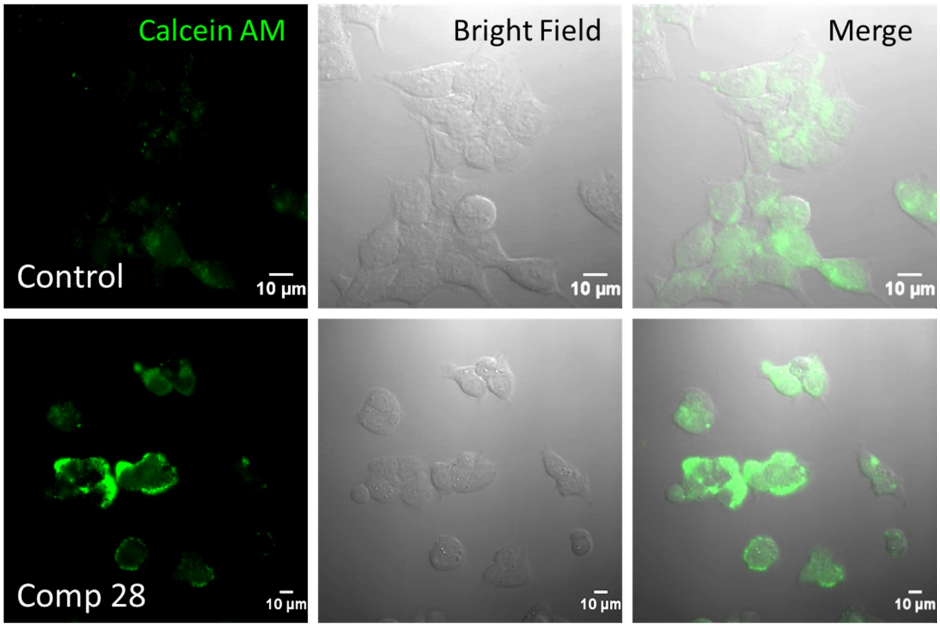


**Figure 2.8**: Confocal microscopy images of HCT-116 cells treated with compound 28 followed Calcein AM staining to observe mitochondrial transition pore opening (MTPs). Scale bar = 10 µm.

### 2.2.5 Mitochondrial transition pore (MTP) formation

Mitochondrial outer membrane permeabilization leads to the opening of mitochondrial transition pores (MTPs). Further opening of MTPs was assessed by Calcein acetoxymethyl ester (Calcein AM) assay, where Calcein AM penetrates into the cells and homes into cytosol and mitochondria.[56] Sub-cellular esterases cleave acetoxymethyl esters into acid functionality to release green fluorescent Calcein which is quenched with externally added $CoCl_2$, keeping mitochondrial Calcein AM unperturbed. However, upon opening MTPs, mitochondrial Calcein

AM will be sequestered into cytosol, leading to the production of green fluorescent Calcein. To evaluate MTP formation, HCT-116 cells were treated with compound **28** for 24 h and stained with Calcein AM and CoCl2. As control, HCT-116 cells were treated with only Calcein AM and $CoCl_2$ without compound **28**. Live cells were further imaged with CLSM (Figure 2.8). It confirmed that compound **28** significantly increased the sequestration of green fluorescent Calcein in cytosol compared to the control cells. This Calcein AM assay evidently validated that compound **28** damaged mitochondria and opened up MTPs in HCT-116 colon cancer cells.

### 2.2.6 Induction of mitochondrial damage

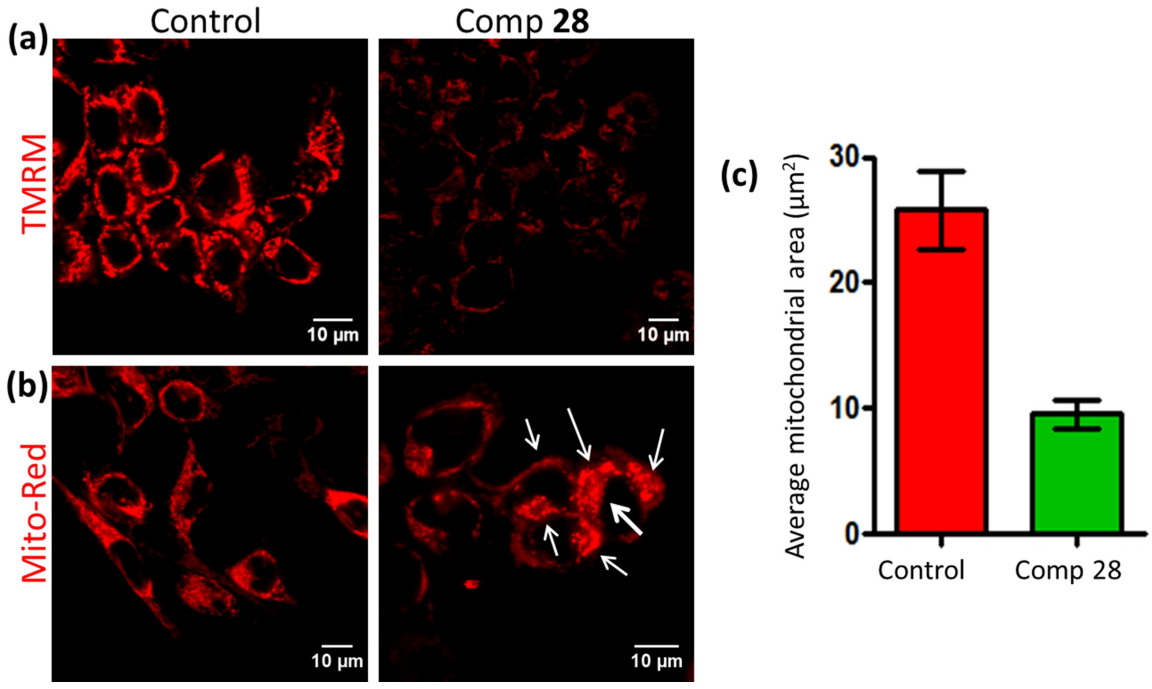


**Figure 2.9:** Confocal microscopy images of HCT-116 cells treated with compound 28 followed by (a) stained with red fluorescent TMRM to evaluate mitochondrial depolarization after treatment with compound 28 and (b) MitoTracker Red CMXROS to observe damaged mitochondrial morphology. Scale bar = 10 µm (c) Quantification of mitochondrial area after treatment with compound 28 determined from CLSM using Mito-Morphology macro and ImageJ analysis software.

Mitochondrial outer membrane polarization and transition pore formation diminish mitochondrial hyperpolarization. To evaluate whether compound **28** can reinstate the hyperpolarization of HCT-116 cells, we performed tetramethyl rhodamine methyl ester (TMRM)

assay.[57] Ideally cancer cells acquire significantly higher hyperpolarized Δψm leading to accumulation of red fluorescent TMRM in control cells. However, compound **28** (15 μM) treatment for 24 h reversed the mitochondrial hyperpolarization leading to efflux of TMRM from HCT-116 cells. As a result, a significant reduction of red fluorescent intensity was observed by CLSM (Figure 2.9a). Mitochondrial outer membrane permeabilization (MOMP)-mediated transition pore opening and reduction of Δψm leads to mitochondrial structural damage.

We further estimated the damage of mitochondrial morphology induced by compound **28**. HCT-116 cells were treated with compound **28** (15 μM) for 24 h and mitochondria were stained with MitoTracker Red CMXROS. Confocal microscopy images in Figure 2.9b exhibited that elongated healthy mitochondrial morphology was visibly disrupted into punctate structure (shown by white arrows), leading to mitochondrial damage by compound **28** treatments. Further quantification of the average mitochondrial area was performed by Mito-Morphology macro which measures mitochondrial elongation and morphology from confocal images through ImageJ analysis software.[58] Mitochondrial average area for compound **28** treated HCT-116 cells were found significantly less (9.54 ± 0.6 μm2, n = 3, mean ± SEM) compared to the average mitochondrial area in control cells (25.8 ± 1.8 μm2, n = 3, mean ± SEM) (Figure 2.9c). These confocal microscopy images clearly demonstrated that compound **28** damaged mitochondrial through inducing MOMP.

### 2.2.7 Bcl-2 inhibition

MOMP is tightly controlled by the Bcl-2 (B-cell CLL/Lymphoma 2) family proteins.[53] As a result, small molecules inhibiting Bcl-2 proteins have emerged as potent anti-cancer drugs.[59] To evaluate the effect on Bcl-2, we treated HCT-116 cells with compound **28** for 24 h and Bcl-2 protein was stained with green fluorescent Alexa Fluor 488 labelled antibody. The CLSM images in Figure 2.10a confirmed that compound **28** inhibited the expression of Bcl-2 proteins compared to non-treated control cells. Furthermore, we estimated the expression of the Bcl-2 by western blot analysis. HCT-116 cells were treated with compound **28** and expression of the Bcl-2 protein was visualized by gel electrophoresis. Figure 2.10b showed that compound **28** reduced the expression of Bcl-2 protein significantly compared to non-treated control cells. We also quantified the expression of Bcl-2 from gel electrophoresis by normalizing the respective GAPDH expression. It was observed that compound **28** reduced the expression of Bcl-2 1.2 folds

compared to control cells (Figure 2.10c). These confocal microscopy and protein expression from western blotting experiments confirmed that compound **28** induced mitochondrial damage by inhibiting Bcl-2 proteins on the mitochondrial outer membrane.

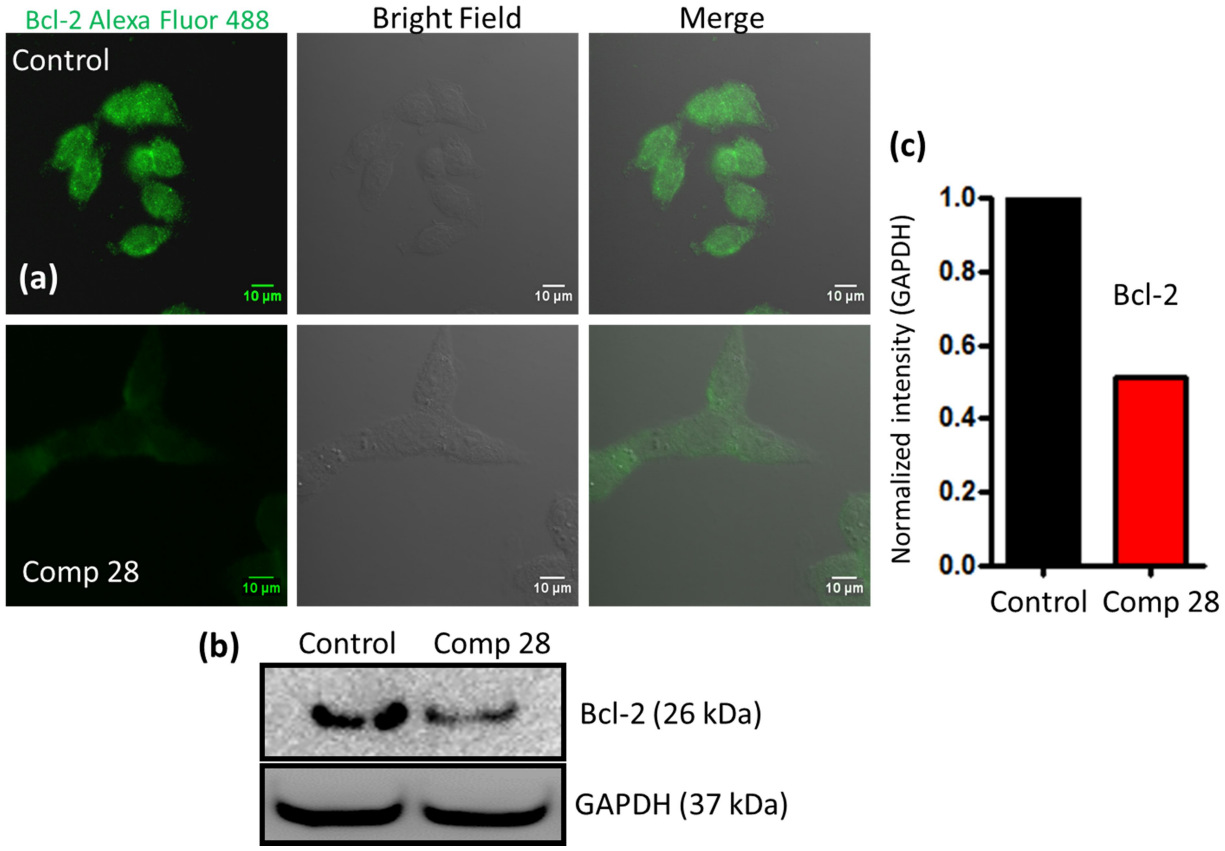


**Figure 2.10**: (a) Confocal microscopy images of HCT-116 cells treated with compound 28 followed by stained with green fluorescent Alexa Fluor 488 labelled Bcl-2 antibody Scale bar = 10 µm (b) Western blot analysis to evaluate cytochrome c expression in HCT-116 cells after treated with compound 28 for 24 h (c) Quantification of Bcl-2 expression from western blot analysis.

### 2.2.8 Cytochrome c release

Mitochondrial damage directs translocation of pro-apoptotic cytochrome c from mitochondria into the cytosol to trigger programmed cell death.[15,60] To visualize the expression of cytochrome c, HCT-116 cells were treated with compound **28** (15 µM) for 24 h and cytochrome c was stained with antibody tagged with green fluorescent Alexa Fluor 488. The confocal images (Figure 2.11a) evidently confirmed that compound **28** induced significantly

increased cytochrome c in cytosol compared to non-treated control cells. Further, expression of cytochrome c was determined by western blot analysis after treatment of HCT-116 cells with compound **28** (15 μM) for 24 h. Gel electrophoresis images (Figure 2.11b) demonstrated a significant increase in the expression of cytochrome c in compound **28** treated cells compared to control cells. We also quantified the expression of cytochrome c from the western blot. It was found that compound **28** treatment increased cytochrome c expression by 2.2 folds compared to the control cells (Figure 2.11c). These confocal images and gel electrophoresis assays demonstrated that compound **28** induced the release of pro-apoptotic cytochrome c after mitochondrial damage.

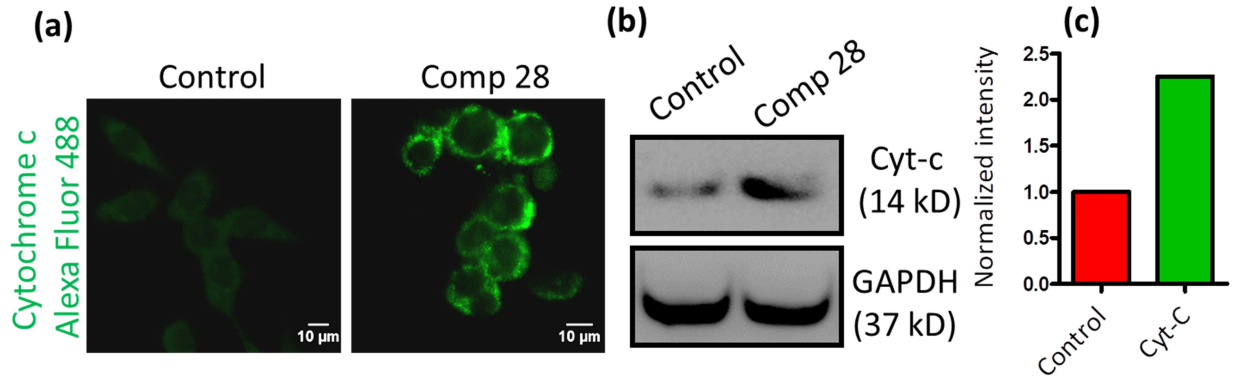


**Figure 2.11**: (a) Confocal images of HCT-116 cells treated with compound 28 for 24 h. Cells were stained with green fluorescent Alexa Fluor 488 labelled Cytochrome c antibody. (b) Western blot analysis to evaluate cytochrome c expression in HCT-116 cells after treated with compound 28 for 24h. (c) Quantification of cytochrome c expression from Western Blot analysis as a measure of mitochondrial damage after treatment with compound 28 at 24 h post-incubation

### 2.2.9 Reactive oxygen species (ROS) generation

One of the hallmarks of mitochondrial damage through MOMP is the production of reactive oxygen species (ROS).[15] We evaluated the MOMP-mediated ROS generation by cell-permeable 2',7'-dichlorodihydrofluorescein diacetate (H2DCFDA) assay.[61] H2DCFDA is a non-fluorescent probe which upon cellular internalization gets hydrolyzed by esterases followed by oxidation by reactive oxygen species (ROS) to generate green fluorescent 2', 7'-dichlorofluorescein (DCF). To evaluate the ROS generation, HCT-116 cells were incubated with compound **28** (15 μM) for 24 h followed by staining the cells with H2DCFDA. The live cells

were visualized by confocal microscopy. Figure 2.12 unmistakably demonstrated that cells treated with compound **28** generated significantly increased ROS, leading to the production of much improved green fluorescent DCF compared to control cells. These CLSM images indicated that compound **28** generated ROS through mitochondrial damage.

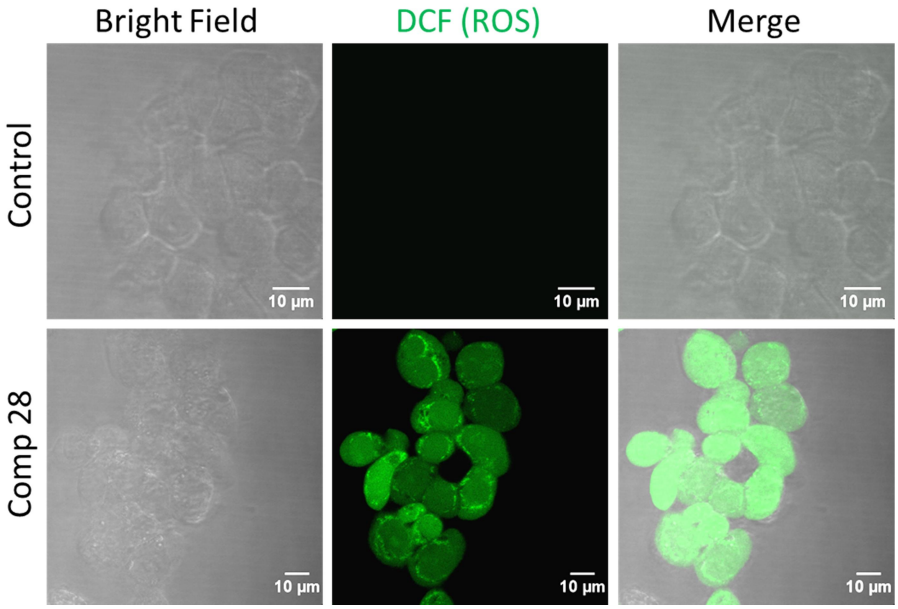


**Figure 2.12:** Confocal images of HCT-116 cells stained with H2DCFDA to observe reactive oxygen species (ROS) generated by compound 28 at 24 h post-incubation. Scale bar = 10 µm.

### 2.2.10 Cell cycle arrest and apoptosis induction

Mitochondrial damage followed by production of pro-apoptotic cytochrome c and ROS instigate cell cycle arrest prior to apoptosis.62 We measured cell cycle arrest induced by compound **28** by fluorescence activated cell sorting (FACS) analysis. HCT-116 cells were incubated with compound **28** (15 µM) for 24 h and cell cycle arrest was analyzed by propidium iodide (PI)-labelled DNA. Flow cytometric analysis revealed that, compound **28** treatment lead to 24.3 %, 11.6 % and 65.4 % cells into G0/G1, S1 and G2/M phase respectively (Figure 2.13). In contrast, 57.6%, 25.4 % and only 17.1 % cells were found in G0/G1, S1 and G2/M phase respectively in non-treated control cells. These FACS analyses showed evidently that compound **28** arrested HCT-116 cells into G2/M phase.

Subsequently, cell cycle arrest pushes the cells into programmed cell death or apoptosis.[62] We further evaluated the induction of apoptosis by FACS analysis. HCT-116 cells were treated with compound **28** (15 µM) for 24 h and 48 h followed by staining apoptotic and necrotic cells by green fluorescent FITC-labelled Annexin V (staining the flipped phosphatidylserine at the outer surface of apoptotic cells) and red fluorescent PI (staining the DNA of the late apoptotic and necrotic cells) respectively. At 24 h post-incubation with compound **28**, significantly increased 78.4 % and 13.4 % cells were found in early and late apoptotic stages respectively (Figure 2.14; upper panel). In comparison, only 0.2 % and 0 % cells were found in early and late apoptotic stages respectively in control cells. Similarly, at 48 h post-incubation, 38.7 % and 31.8% cells were observed in early and late apoptotic stages in compound **28** treatments (Figure 2.14; lower panel). We anticipated that prolonged exposure of colon cancer cells with mitochondria damaging compound **28** shifts the programmed cell death from early to late stages of apoptosis. These FACS analyses demonstrated that compound **28** induced apoptosis in colon cancer cells through mitochondrial damage.

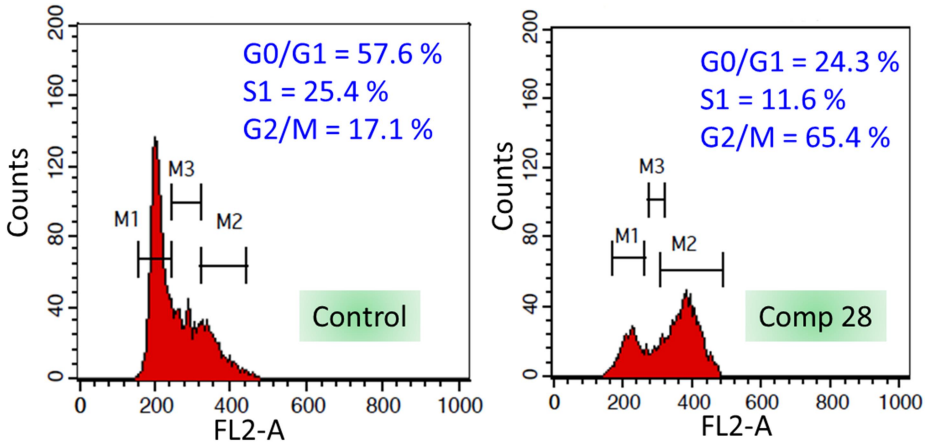


**Figure 2.13**: Cell cycle analysis by staining the DNA in HCT-116 cells with PI at 24 h post-incubation with compound 28

### 2.2.11 Caspase-9/3 and p53 expression

Induction of apoptosis in cancer cells activates initiator caspase-9, which further activates activator caspase-3 after cleavage.[63,64] We estimated the expression of caspase-9 and caspase-3 by western blot analysis in HCT-116 cells at 24 h post-incubation with compound **28** (15 µM).

Gel electrophoresis revealed that compound **28** triggered the cleavage of caspase-9 and caspase-3 compared to control cells (Figure 2.15a). Further quantification from western blot showed that compound **28** reduced the expression of caspase-3 and caspase-9 by 1.6 folds and 2.5 folds respectively (Figure 2.15b). These gel electrophoresis studies undoubtedly exhibited that compound **28** induced apoptosis in HCT-116 cells through cleavage of caspase-9 and caspase-3.

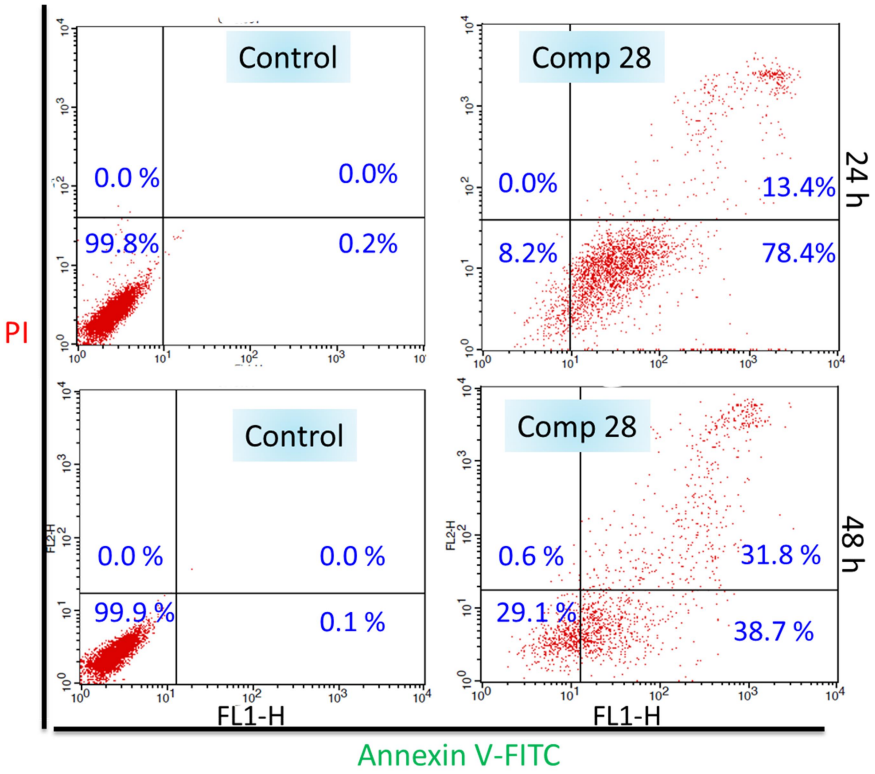


**Figure 2.14**: FACS analysis of HCT-116 cells after treatment with compound 28 for 24 h and 48 h to observe apoptosis (lower left, lower right, upper left and upper right quadrants represent healthy, early apoptotic, necrotic and late apoptotic cells respectively).

Mitochondria-mediated apoptosis is highly dependent on p53 protein which is one of the most important tumor suppressors.[65] Moreover, Bcl-2 inhibition on mitochondria in colon cancer triggers the cells into p53 driven apoptosis.[66] Hence, we further evaluated the expression of p53 in compound **28**-mediated mitochondrial damage followed by apoptosis. We treated HCT-116 cells with compound **28** (15 μM) for 24 h and assessed the expressions of p53 by western blot analysis. The gel electrophoresis image in Figure 2.15c confirmed that compound **28** remarkably increased the expression of p53 compared to control cells. Further quantification from gel

electrophoresis showed that compound **28** increased the expression of p53 in HCT-116 cells 14.7 folds compared to control cells (Figure 2.15d).

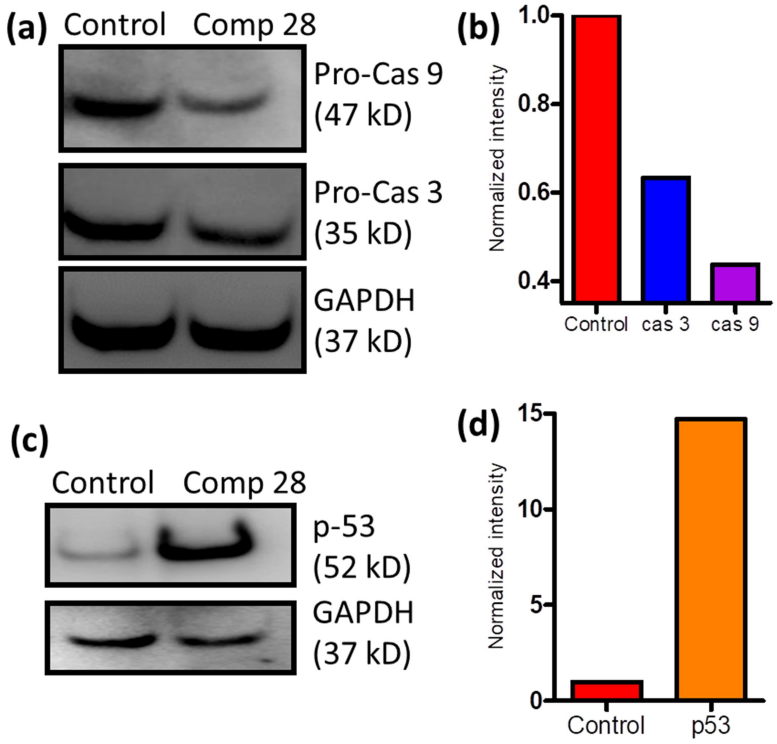


Figure 2.15: Western blot analysis and quantification in HCT-116 cells after treatment with compound 28 for 24 h; (a) the expression of pro-caspase-9 and pro-caspase-3 (b) quantification of pro-caspase-9 and pro-caspase-3 (c) the expression of p-53 (d) quantification of p53.

## 2.3 Conclusion

In conclusion, this report describes a straightforward and concise synthesis of natural product-guided hydrazide-hydrazone based small molecule library. One of the library members was discovered to impair mitochondria by disrupting outer membrane through inhibition of Bcl-2 protein followed by producing reactive oxygen species. This small molecule blocked the cell cycle in G2/M phase, cleaved caspase-9/3 and increased p53 to stimulate programmed cell death in colon cancer cells. This hydrazide-hydrazone based small molecule showed remarkable efficacy in a panel of colon cancer cell lines, without collateral toxicity in healthy cells. We anticipate this novel small molecule has the potential to become a tool to illuminate

mitochondrial biology and further optimization studies need to be performed for translating it successfully into clinics as an anti-cancer agent.

## 2.4 Materials and Methods

### 2.4.1 Materials

Commercially available chemicals and solvents were used without further purification and distillation. Chemical reactions were carried out without any inert gas condition. Pre-coated silica gel aluminium sheets 60F254 for analytical thin layer chromatography (TLC) were obtained from EMD Millipore Laboratories. Cell culture media (DMEM) and 3-(4, 5-dimethylthiazol-2-yl)-2, 5-diphenyltetrazolium bromide (MTT) were purchased from HiMedia. Sodium dodecyl sulfate (SDS), Hanks' Balanced Salts [HBSS], HEPES sodium salt, propidium iodide, calcein AM, Annexin-V-FITC Staining Kit and 2',7'-dichlorofluorescein-diacetate (DCFH-DA) were obtained from Sigma-Aldrich. MitoTracker® Red CMXRos and tetramethylrhodamine methyl ester perchlorate (TMRM) were purchased from Thermo Fisher Scientific. All primary and secondary antibodies were obtained from Cell Signaling Technology, Biolegend and Abcam. Confocal laser scanning microscopy was performed by Zeiss LSM 710 machine. Flow cytometry analysis was performed using BD FACS Calibur flow cytometer. Each sample was done in triplicate.

### 2.4.2 General procedure for the synthesis of benzoic acid methyl esters (2a-2f)

Substituted benzoic acids (0.5 g) were dissolved in absolute methanol (8 mL) followed by addition of concentrated sulfuric acid (0.3 mL). The reaction mixture was refluxed and the progress of the reaction was monitored by thin layer chromatography (TLC). After completion of the reaction, methanol was evaporated under reduced pressure. To the residue aqueous 10 % sodium bicarbonate ($NaHCO_3$ ) (15 mL) was added, extracted with ethyl acetate (3 X 20 mL) and washed with saturated NaCl solution (2 X 10 mL). The organic layer was dried over anhydrous $Na_2SO_4$ and the organic solvent was evaporated to get methyl esters of substituted benzoic acid in 87-93% yield as a light yellow viscous liquid.

### 2.4.3 General procedure for the synthesis of benzoic acid hydrazides (3a-3f)

Substituted benzoic acid methyl esters (**2a-2f**) (0.4 g, 1 equiv) were dissolved in absolute ethanol (3 mL) and hydrazine monohydrate (1.183 mL, 10 equiv) was added into it. The reaction was refluxed and monitored by TLC. After the completion of the reaction, ethanol was evaporated. To the residue, ice-cold water (10 mL) was added and the organic layer was extracted with dichloromethane (DCM) (3 X 20 mL). The organic layer was further washed with saturated NaCl solution (2 X 10 mL). The organic layer was dried over anhydrous $Na_2SO_4$ and the solvent was evaporated. Finally, the crude product was re-crystallized (ethanol-water) to obtain desired hydrazides in 80-85% yield.

### 2.4.4 General procedure for the synthesis of hydrazide-hydrazone derivatives (5-34)

To the solution of substituted benzoic acid hydrazides (3) (0.1 g, 1 equiv) in absolute methanol (1.5 mL) different aromatic aldehydes (1 equiv) were added followed by addition of catalytic amount of *p*-toluenesulfonic acid (*p*TsOH). After stirring for 2 h at room temperature, methanol was evaporated under reduced pressure. To the residue, aqueous 10 % $NaHCO_3$ (10 mL) was added and the organic layer was extracted with ethyl acetate (3 X 10 mL) followed by washing with saturated NaCl solution (2 X 10 mL). The organic layer was dried over anhydrous $Na_2SO_4$ and the solvent was evaporated. Final compounds were purified by using column chromatography on basic aluminium oxide ($Al_2O_3$) (ethyl acetate/hexane = 20 %) to give hydrazide-hydrazone derivatives in 70-80 % yield.

### 2.4.5 HPLC analysis

The purity of compound **28** was determined by Reverse Phase High Performance Liquid Chromatography (RP-HPLC) using 4.6 X 250 mm 5 micron C18 column using acetonitrile: water with gradient for 10 minutes. 20 µL of sample was injected (concentration = 1 mg/mL) into the column with 1 mL/min flow rate.

### 2.4.6 Cell viability assay

Five thousand colorectal cancer cells (DLD1, HCT-116 and SW-620) were seeded per well in 96-well plate for attachment. To screen all compounds, 3 mM stock solutions of all compounds were prepared in DMSO. Cells were then treated with all compounds (30 µM) for 24 h. For calculation of IC50, cells were treated with compound **28** in different concentration (0.1,

0.2, 0.4, 0.8, 1.6, 3.2, 6.4, 12.5, 25, 50 μM). Cell viability was determined by adopting the previously described procedure.[67]

For fibroblast cells, 10,000 L929 (murine lung fibroblast) cells were plated in each well of a 96 well plate and incubated in 5% CO2 at 37 °C for overnight. Drug dilutions were made in complete 10% FBS containing DMEM media. 100 μL of each drug solutions (diluted in DMSO) was added in each well of the 96 well plates (in triplicates). Untreated cells (without any drug) were considered as control. After adding drugs, cells were incubated for 24 h. After 24 h, media was aspirated and 100 μL MTT reagent (10 μL of 5mg/mL solution and 90 μL sterile media) was added in each well. It was incubated for 3h. Finally, all the media was aspirated, Formazan crystals were dissolved in100 μL DMSO and read in a plate reader having 550 nm cut off filter. Percent cell death calculation data was normalized with untreated cells. Each data represents an average of 3 data points. Error calculated as standard error following (STDEV/(SQRT(3))) using Microsoft excel.

### 2.4.7 Confocal laser scanning microscopy (CLSM)

1.5 × 104 HCT-116 cells were seeded in each well in 8 well Lab-Tek chamber slides for attachment. Compound **28** (15 μM) was incubated with the cells for 24 h. Control cells were not treated with any compound.

#### *2.4.7.1 JC1 Assay*

Cells were washed thoroughly with PBS followed by addition of JC1 dye to incubate for 20 min. The green and red fluorescently labeled cells were seen and quantified by confocal microscopy.[68]

#### *2.4.7.2 Calcein AM assay.*

After 24 h, Calcein AM (1 μM) and 1 mM CoCl2 were added into cells followed by imaging through confocal microscopy.[68]

#### *2.4.7.3 Mitochondrial morphology assay*

After 24 h of incubation with compound **28**, cells were washed thoroughly with PBS and stained with MitoTracker Red CMXROS for 20 min. Cells were then fixed with paraformaldehyde for 10 min and visualized an d quantified by CLSM.[67]

#### *2.4.7.4 ROS generation by DCFH-DA assay*

After treatment with compound **28**, cells were then washed with PBS (pH 7.4) and treated with DCFH-DA for 15 minutes. Finally cells were washed thrice with PBS (pH 7.4) and visualized by CLSM.

#### *2.4.7.5 TMRM assay*

Cells were washed with cold PBS 3 times and treated with TMRM (10 μM mL-1) for 30 minutes. Cells were then washed with PBS (pH 7.4) and imaged by CLSM to visualize mitochondrial damage.

#### *2.4.7.6 Immuno-staining to visualize cytochrome c*

5 X 104 HCT-116 cells were attached on cover slip in 6-well plate followed by incubation with compound **28** for 24 h. Cells were thoroughly rinsed with PBS and fixed with paraformaldehyde for 10 min. Cells were then further washed and permeabilized by blocking buffer. Cells were then treated with cytochrome c primary antibody solution (1: 100 dilution) for 3 h. After further washing with blocking buffer, cells were treated with Alexa Fluor 488 labeled secondary antibody solution (1: 500 dilutions) for 30 min in dark. Fluorescently labeled cells were visualized further by CLSM.[67]

#### *2.4.7.7 Immuno-staining to visualize Bcl-2*

After treatment with compound **28**, cells were washed once with PBS and fixed with 3.7 % paraformaldehyde at 37 °C for 15 min. Cells were further washed twice with PBS (pH = 7.4) and were permeabilized by incubating in blocking buffer (PBS containing 0.3 % Tween and 5 % FBS) at room temperature. Cells were then incubated in Bcl-2 primary antibody (Santa Cruz Biotechnology, Inc.) in 1:100 dilution at 37 °C for 3 h. Cells are washed thrice with blocking buffer followed by incubation in Alexa Fluor 488 anti-mouse IgG secondary antibody solution (1:500 dilutions) at 37 °C for 40 min in the dark. Cells were washed thrice with PBS and mounted on a glass slide using SlowFade Gold antifade reagent. The slides were subjected to fluorescence imaging using CLSM.

#### *2.4.7.8 General procedure for western blot analysis*

1 X 105 HCT-116 cells were treated with compound **28** for 24 h followed by cell lysis. SDS-PAGE was used to separate respective proteins and transferred them onto the membrane by electroblotting. The protein containing membranes were blocked and incubated with primary antibodies for 24 h at 4 °C. Further, the membrane was washed and incubated with secondary antibody for 1 h at 25 °C. Preoteins were then detected and quantified by ImageQuant LAS 4000 and ImageJ software.[67, 68]

#### *2.4.7.9 Fluorescence activated cell sorting (FACS) assay*

HCT-116 cells (2 × 106 cell per well) were attached in 6-well plates and then treated with compounds **28** for 24 h at 15 µM.

2.4.7.9.1 *Apoptosis detection;* cells were detached by using trypsin and washed with PBS. Suspended cells were then incubated with Annexin V-FITC Staining Kit using the manufacturer's protocol. The apoptotic and necrotic cells were quantified by using BD Accuri c6 flow cytometer.[67]

2.4.7.9.2 *Cell cycle analysis;* after treatment with compound **28**, cells were then harvested and washed with 1 mL PBS (pH = 7.4) and centrifuged at 850 rpm for 4 min. After discarding the supernatant, cells was fixed with cold 70 % EtOH for 0.5 h. Cells were washed thoroughly with PBS followed by addition of 500 µL staining solution. BD Accuri C6 flow cytometer was used for cell cycle analysis.[67]

## 2.5 Compounds Characterization data

### 2.5.1 Characterization of Intermediates:

Characterization of intermediate compounds **2a-2f** and **3a-3f (figure 2.1)** are previously reported.[69-74]

### 2.5.2 Characterization of hydrazide-hydrazone derivatives:

All hydrzide-hydrazone derivatives were characterized by $^{1}$H-NMR, $^{13}$C-NMR, HRMS as follows:

***N'-((5-methylfuran-2-yl) methylene)-2-phenoxybenzohydrazide* (5):**

**$^1$H NMR (400 MHz, Chloroform-d):** δ= 10.62 (s, 1H), 8.46 (s, 1H), 8.32 (dd, *J* = 7.9 Hz, 1.8, 1H), 7.46 – 7.37 (m, 3H), 7.26 – 7.20 (m, 2H), 7.10 (dt, *J* = 9.3 Hz, 2.2 Hz, 2H), 6.84 – 6.81 (m, 1H), 6.67 (d, *J* = 3.3 Hz, 1H), 6.09 – 6.07 (m, 1H), 2.35 (s, 3H).

**$^{13}$C NMR (101 MHz, Chloroform-d)**: δ= 161.86, 155.69, 155.04, 147.93, 139.38, 133.37, 132.78, 130.46, 125.33, 123.91, 122.65, 120.15, 117.94, 115.91, 108.52, 14.03.

**HRMS (ESI-TOF):** *m/z*: [M + H] calculated for $C_{19}H_{16}N_2O_3$ = 321.1239; found= 321.1357.

***N'-(furan-2-ylmethylene)-2 phenoxybenzohydrazide* (6):**

**$^1$H NMR (400 MHz, Chloroform-d):** δ= 10.68 (s, 1H), 8.47 (s, 1H), 8.34-8.32 (dd, *J* = 8.3 Hz, 1H), 7.51 (d, 1H), 7.45-7.39 (m, 3H), 7.24-7.22 (m, 2H), 7.11-7.10 (d, *J* = 7 Hz, 2H), 6.84-6.82 (d, *J* = 7 Hz, 2H), 6.49-6.47(dd, *J* = 6.48 Hz, 1H).

**$^{13}$C NMR (101 MHz, Chloroform-d):** δ= 161.9, 155.6, 155.0, 149.6, 144.7, 139.1, 133.5, 132.8, 130.5, 125.4, 123.9, 122.5, 120.1, 117.9, 113.6, 112.1.

**HRMS (ESI-TOF):** *m/z*: [M + H] calculated for $C_{18}H_{14}N_2O_3$= 307.1082; Found= 307.1083.

***N'-((5-(4-nitrophenyl) furan-2-yl) methylene)-2-phenoxybenzohydrazide* (7):**

**$^1$H NMR (400 MHz, Chloroform-d):** δ = 10.81 (s, 1H), 8.49 (s, 1H), 8.36-8.34 (dd, *J* = 8.3 Hz, 1H), 8.27-8.23(m, 2H), 7.89-7.86 (m, 2H), 7.48-7.41(m, 2H), 7.29-7.24 (q, 2H), 7.15-7.13 (d, 2H), 6.98-6.95 (q, *J* = 7 Hz, 2H), 6.85-6.83 (d, 1H).

**$^{13}$C NMR (101 MHz, Chloroform-d)**: δ = 162.1, 155.8, 154.9, 153.5, 151.0, 147.0, 138.3, 135.6, 133.7, 132.9, 130.57, 125.5, 124.7, 124.5, 124.0, 122.3, 120.3, 117.9, 115.7, 111.1.

**HRMS (ESI-TOF):** *m/z*: [M + H] calculated for $C_{24}H_{17}N_3O_5$ = 428.1246; found = 428.1288.

***N'-((5-(hydroxymethyl)furan-2-yl)methylene)-2-phenoxybenzohydrazide* (8):**

**$^1$H NMR (400 MHz, Chloroform-d)**: δ = 10.73 (s, 1H), 8.37 (s, 1H), 8.30 (dd, *J* = 7.9 Hz, 1.8 Hz, 1H), 7.45 – 7.37 (m, 3H), 7.25 – 7.20 (m, 2H), 7.12 – 7.07 (m, 2H), 6.82 (dd, *J* = 8.3 Hz, 1H), 6.71 (d, *J* = 3.4 Hz, 1H), 6.37 (d, *J* = 3.4 Hz, 1H), 4.65 (s, 2H), 2.42 (bs, 1H).

**$^{13}$C NMR (101 MHz, Chloroform-d):** δ = 162.02, 157.02, 155.67, 155.02, 149.07, 138.66, 133.50, 132.77, 130.48, 125.35, 123.92, 122.50, 120.12, 117.96, 115.13, 109.76, 57.65.

**HRMS (ESI-TOF):** *m/z*: [M + Na] calculated for $C_{19}H_{16}N_2O_4$ = 359.1007; found = 359.1110.

***N'-((5-(2,4-dichlorophenyl)furan-2-yl)methylene)-2-phenoxybenzohydrazide* (9):**

**$^{1}$H NMR (400 MHz, Chloroform-d):** δ = 10.75 (s, 1H), 8.44 (s, 1H), 8.35 (dd, *J* = 7.9, 1.8 Hz, 1H), 7.95 (d, *J* = 8.6 Hz, 1H), 7.49 – 7.39 (m, 4H), 7.32 – 7.26 (m, 2H), 7.26 – 7.22 (m, 2H), 7.15 – 7.11 (m, 2H), 6.94 (d, *J* = 3.7 Hz, 1H), 6.84 (d, *J* = 8.2 Hz, 1H).

**$^{13}$C NMR (101 MHz, Chloroform-d):** δ = 161.95, 155.77, 154.97, 151.36, 149.04, 138.54, 134.03, 133.62, 132.91, 131.06, 130.55, 129.38, 127.53, 127.03, 125.49, 123.99, 122.35, 120.28, 117.90, 115.79, 113.56.

**HRMS (ESI-TOF):** *m/z*: [M + H] calculated for $C_{24}H_{16}C_{l2}N_2O_3$ = 451.0616; found = 451.0621.

***N'-(furan-3-ylmethylene)-2-phenoxybenzohydrazide* (10):**

**$^{1}$H NMR (400 MHz, Chloroform-d):** δ = 10.61 (s, 1H), 8.35 (dd, *J* = 7.9, 1.8 Hz, 1H), 8.16 (s, 1H), 7.69 (s, 1H), 7.46 – 7.39 (m, 4H), 7.26 – 7.21 (m, 2H), 7.14 – 7.09 (m, 2H), 6.94 (d, *J* = 1.8 Hz, 1H), 6.83 (d, *J* = 8.5, 1H).

**$^{13}$C NMR (101 MHz, Chloroform-d):** δ = 161.59, 155.64, 155.09, 144.73, 144.31, 141.13, 133.44, 132.93, 130.51, 125.36, 124.00, 122.55, 120.12, 117.98, 108.06.

**HRMS (ESI-TOF):** *m/z*: [M + Na] calculated for $C_{18}H_{14}N_2O_3$ = 329.001; found = 329.0901.

***2-phenoxy-N'-(thiophen-2-ylmethylene) benzohydrazide* (11):**

**$^{1}$H NMR (400 MHz, Chloroform-d):** δ = 10.63 (s, 1H), 8.70 (s, 1H), 8.33 (dd, *J* = 7.9, 1.8 Hz, 1H), 7.47 – 7.38 (m, 4H), 7.31 – 7.27 (m, 1H), 7.26 – 7.21 (m, 2H), 7.15 – 7.10 (m, 2H), 7.05 (dd, *J* = 5.0, 3.7 Hz, 1H), 6.82 (dd, *J* = 8.3, 0.8 Hz, 1H).

**$^{13}$C NMR (101 MHz, Chloroform-d):** δ = 161.80, 155.72, 155.01, 144.22, 139.15, 133.46, 132.86, 130.51, 128.98, 127.53, 125.43, 123.93, 122.52, 120.29, 117.87.

**HRMS (ESI-TOF):** *m/z*: [M + H] calculated for $C_{18}H_{14}N_2O_2S$ = 323.0854; found = 323.053.

***N'-((1H-pyrrol-2-yl) methylene)-2-phenoxybenzohydrazide* (12):**

**$^{1}$H NMR (400 MHz, Chloroform-d):** δ = 10.56 (s, 1H), 9.63 (bs, 1H), 8.35 (dd, *J* = 7.9, 1.8 Hz, 1H), 7.89 (s, 1H), 7.47 – 7.39 (m, 3H), 7.26 – 7.22 (m, 2H), 7.14 – 7.10 (m, 2H), 6.93 (q, *J* = 2.6 Hz, 1H), 6.84 (dd, *J* = 8.3 Hz, 1H), 6.45-6.44 (m, 1H), 6.25 – 6.20 (m, 1H).

**$^{13}$C NMR (101 MHz, Chloroform-d):** δ = 161.52, 155.67, 155.06, 139.63, 133.39, 132.82, 130.54, 127.08, 125.39, 124.01, 122.60, 122.39, 120.08, 118.02, 114.82, 110.05.

**HRMS (ESI-TOF):** *m/z*: [M + H] calculated for $C_{18}H_{15}N_3O_2$ = 306.1242; found = 306.1238.

***N'-((4-methylthiazol-5-yl) methylene)-2-phenoxybenzohydrazide* (13):**

**$^{1}$H NMR (400 MHz, Acetone-d6):** δ = 10.94 (s, 1H), 8.91 (s, 1H), 8.84 (s, 1H), 7.97 (dd, *J* = 7.7, 1.6 Hz, 1H), 7.53 – 7.49 (m, 1H), 7.44 (t, *J* = 7.9 Hz, 2H), 7.29 – 7.219 (m, 2H), 7.13 (d, *J* = 7.8 Hz, 1H), 7.08-7.01 (m,1H), 6.91 (d, *J* = 8.2 Hz, 1H), 2.48 (s, 3H).

**$^{13}$C NMR (101 MHz, Acetone-d6):** δ = 162.37, 157.12, 156.07, 155.49, 154.92, 141.72, 133.77, 132.37, 131.14, 130.66, 129.02, 126.09, 125.43, 124.62, 120.55, 119.42, 15.79.

**HRMS (ESI-TOF):** *m/z*: [M + H] calculated for $C_{18}H_{15}N_3O_2S$ = 338.0963; found = 338.0970.

***N'-(4-bromobenzylidene)-2-phenoxybenzohydrazide* (14):**

**$^{1}$H NMR (400 MHz, Chloroform-d):** δ = 10.71 (s, 1H), 8.35 (dd, *J* = 7.9, 1.8 Hz, 1H), 8.11 (s, 1H), 7.64 – 7.61 (m, 2H), 7.52 – 7.49 (m, 2H), 7.46 – 7.39 (m, 3H), 7.27-7.21 (m, 2H), 7.13 – 7.11(m, 2H), 6.82 (d, *J* = 8.2 Hz, 1H).

**$^{13}$C NMR (101 MHz, Chloroform-d):** δ = 161.74, 155.75, 155.06, 147.21, 133.61, 133.01, 132.90, 132.04, 130.56, 129.23, 125.45, 124.86, 124.04, 122.43, 120.18, 117.99.

**HRMS (ESI-TOF):** *m/z*: [M + Na] calculated for $C_{20}H_{15}BrN_2O_2$ = 417.0214; found = 417.0216.

***N'-(4-methoxybenzylidene)-2-phenoxybenzohydrazide* (15):**

**$^{1}$H NMR (400 MHz, DMSO-d6):** δ = 11.61 (bs, 1H), 8.23 (s, 1H), 7.66 – 7.63 (m, 2H), 7.50 – 7.36 (m, 3H), 7.29 – 7.21 (m, 2H), 7.15 (t, *J* = 7.4 Hz, 1H), 7.06 – 7.00 (m, 3H), 6.96 – 6.93 (m, 2H), 3.80 (s, 3H).

**$^{13}$C NMR (101 MHz, DMSO-d6):** δ = 161.78, 160.81, 156.45, 153.79, 153.00, 147.20, 143.23, 131.78, 129.94, 129.62, 128.64, 128.08, 127.46, 126.70, 123.64, 123.54, 123.03, 118.69, 118.09, 114.28, 55.25.

**HRMS (ESI-TOF):** *m/z*: [M + H] calculated for $C_{21}H_{18}N_2O_3$ = 347.1428; found = 347.1402.

***N'-(furan-2-ylmethylene)-2-methoxybenzohydrazide* (16):**

**$^{1}$H NMR (400 MHz, Chloroform-d):** δ = 10.82 (s, 1H), 8.62 (s, 1H), 8.28-8.26 (dd, *J* = 8.3 Hz, 1H), 7.53-7.47(m, 2H), 7.14-7.11 (t, *J* = 7 Hz, 1H), 7.02-7.00 (d, *J* = 7 Hz, 1H), 6.84-6.83 (d, *J* = 7 Hz, 1H), 6.50-6.49 (q, 1H), 4.02 (s, 3H).

**$^{13}$C NMR (101 MHz, Chloroform-d):** δ = 162.56, 157.19, 149.83, 144.68, 139.05, 133.65, 132.86, 121.89, 120.52, 113.41, 112.11, 111.54, 56.26.

**HRMS (ESI-TOF):** *m/z*: [M + H] calculated for $C_{13}H_{12}N_2O_3$ = 245.0926; found = 245.1017.

***2-methoxy-N'-((5-(4-nitrophenyl) furan-2-yl)methylene)benzohydrazide* (17):**

**$^{1}$H NMR (400 MHz, Chloroform-d):** δ = 10.94 (s, 1H), 8.63 (s, 1H), 8.30 – 8.25 (m, 3H), 7.89 (d, *J* = 9.0 Hz, 2H), 7.54 – 7.50 (m, 1H), 7.15 (t, *J* = 7.2 Hz, 1H), 7.03 (d, *J* = 8.4 Hz, 1H), 6.98 (q, *J* = 3.7 Hz, 2H), 4.05 (s, 3H).

**$^{13}$C NMR (100 MHz, Chloroform-d):** δ = 162.66, 157.24, 153.36, 151.23, 146.98, 138.18, 135.61, 133.88, 132.93, 124.71, 124.49, 121.99, 120.29, 115.60, 111.59, 111.24, 56.32.

**HRMS (ESI-TOF):** *m/z*: [M + H] calculated for $C_{19}H_{15}N_3O_5$ = 366.1090; found = 366.1151.

***2-methoxy-N'-((5-methylfuran-2-yl)methylene)benzohydrazide* (18):**

**$^{1}$H NMR (400 MHz, Chloroform-d):** δ = 10.76 (s, 1H), 8.64 (s, 1H), 8.27 (dd, *J* = 7.9, 1.9 Hz, 1H), 7.49 (m, 1H), 7.15 – 7.10 (m, 1H), 7.01 (d, *J* = 8.1 Hz, 1H), 6.68 (d, *J* = 3.3 Hz, 1H), 6.10 (dd, *J* = 3.2, 1H), 4.01 (s, 3H), 2.38 (s, 3H).

**$^{13}$C NMR (100 MHz, Chloroform-d):** δ = 162.50, 157.15, 155.54, 148.19, 139.44, 133.51, 132.80, 121.86, 120.69, 115.70, 111.52, 108.50, 56.23, 14.06.

**HRMS (ESI-TOF):** *m/z*: [M + Na] calculated for $C_{14}H_{14}N_2O_3$ = 281.0901; found = 281.1031.

***N'-((5-(hydroxymethyl)furan-2-yl)methylene)-2-methoxybenzohydrazide* (19):**

**$^1$H NMR (400 MHz, Chloroform-d):** δ = 10.84 (s, 1H), 8.52 (s, 1H), 8.25 (dd, *J* = 7.8, 1.8 Hz, 1H), 7.52 – 7.46 (m, 1H), 7.15 – 7.09 (m, 1H), 7.00 (d, *J* = 8.1 Hz, 1H), 6.73 (d, *J* = 3.3 Hz, 1H), 6.39 (d, *J* = 3.4 Hz, 1H), 4.68 (s, 2H), 4.01 (s, 3H), 2.48 (bs, 1H).

**$^{13}$C NMR (101 MHz, Chloroform-d):** δ = 162.60, 157.23, 156.89, 149.30, 133.69, 133.16, 132.80, 131.12, 121.87, 120.42, 116.54, 114.90, 112.44, 111.54, 110.19, 109.79, 57.67, 56.25.

**HRMS (ESI-TOF):** *m/z*: [M + Na] calculated for $C_{14}H_{14}N_2O_4$ = 297.0850; found = 297.0851.

***N'-(furan-3-ylmethylene)-2-methoxybenzohydrazide* (20):**

**$^1$H NMR (400 MHz, Chloroform-d):** δ = 10.74 (s, 1H), 8.31 – 8.28 (m, 2H), 7.73 (s, 1H), 7.50 (ddd, *J* = 8.4, 7.4, 1.8 Hz, 1H), 7.44 (t, *J* = 1.7 Hz, 1H), 7.16 – 7.11 (m, 1H), 7.01 (d, *J* = 8.4 Hz, 1H), 6.97 (d, *J* = 1.8 Hz, 1H), 4.03 (s, 4H).

**$^{13}$C NMR (101 MHz, Chloroform-d):** δ = 162.19, 157.22, 144.58, 144.31, 140.98, 133.57, 132.98, 122.88, 121.94, 120.54, 111.53, 108.09, 56.27.

**HRMS (ESI-TOF):** *m/z*: [M + Na] calculated for $C_{13}H_{12}N_2O_3$ = 267.0745; found = 267.0751.

***2-methoxy-N'-(thiophen-2-ylmethylene)benzohydrazide* (21):**

**$^1$H NMR (400 MHz, Chloroform-d):** δ = 10.76 (s, 1H), 8.85 (s, 1H), 8.27 (dd, *J* = 7.8, 1.8 Hz, 1H), 7.49 (ddd, *J* = 8.3, 7.4, 1.8 Hz, 1H), 7.40 (dd, *J* = 5.0, 0.9 Hz, 1H), 7.32 (dd, *J* = 3.6 , 0.8 Hz, 1H), 7.15 – 7.10 (m, 1H), 7.06 (dd, *J* = 5.0, 3.7 Hz, 1H), 7.01 (d, *J* = 8.2 Hz, 1H), 4.03 (s, 3H).

**$^{13}$C NMR (101 MHz, Chloroform-d):** δ = 162.43, 157.19, 144.23, 139.51, 133.59, 132.85, 130.29, 128.76, 127.54, 121.89, 120.60, 111.54, 56.28.

**HRMS (ESI-TOF):** *m/z*: [M + Na] calculated for $C_{13}H_{12}N_2O_2S$ = 283.0516; found = 283.0515.

***N'-((1H-pyrrol-2-yl)methylene)-2-methoxybenzohydrazide* (22):**

**$^1$H NMR (400 MHz, Chloroform-d):** δ = 10.70 (s, 1H), 9.62 (s, 1H), 8.30 (dd, *J* = 7.8, 1.8 Hz, 1H), 8.00 (s, 1H), 7.49 (ddd, *J* = 8.3, 7.4, 1.8, 1H), 6.27 – 6.22 (m, 1H), 7.16 –

7.09 (m, 1H), 7.01 (d, *J* = 8.2 Hz, 1H), 6.94 (q, *J* = 2.5 Hz, 1H), 6.49-6.48 (m, 1H), 4.03 (s, 3H).

**$^{13}$C NMR (101 MHz, Chloroform-d):** δ = 162.07, 157.25, 139.40, 133.50, 132.83, 127.27, 122.51, 121.88, 120.35, 114.54, 111.51, 109.98, 56.26.

**HRMS (ESI-TOF):** *m/z*: [M + H] calculated for $C_{13}H_{13}N_3O_2$ = 244.1086; found = 244.1086.

***N'-(furan-2-ylmethylene)-4-nitrobenzohydrazide* (23):**

**$^{1}$H NMR (400 MHz, DMSO-d6):** δ = 12.12 (s, 1H), 8.73 (s, 1H), 8.44 – 8.30 (m, 3H), 7.88-7.82 (m, 3H), 6.99 (s, 1H), 6.66 (s, 1H).

**$^{13}$C NMR (101 MHz, DMSO-d6):** δ = 160.89, 149.21, 147.79, 145.53, 138.46, 134.69, 134.12, 130.35, 126.39, 122.27, 114.25, 112.31.

**HRMS (ESI-TOF):** *m/z*: [M + H] calculated for $C_{12}H_9N_3O_4$ = 260.0678; found = 260.0685.

***N'-((5-methylfuran-2-yl)methylene)-4-nitrobenzohydrazide* (24):**

**$^{1}$H NMR (400 MHz, DMSO-d6):** δ = 12.04 (s, 1H), 8.73 (s, 1H), 8.44 (d, *J* = 8.1 Hz, 1H), 8.35 (d, *J* = 7.7 Hz, 1H), 8.26 (s, 1H), 7.84 (t, *J* = 7.9 Hz, 1H), 6.87 (s, 1H), 6.29 (s, 1H), 2.37 (s, 3H).

**$^{13}$C NMR (101 MHz, DMSO-d6):** δ = 160.76, 154.96, 147.68, 138.31, 134.77, 134.08, 130.33, 126.32, 122.24, 116.15, 108.71, 13.53.

**HRMS (ESI-TOF):** *m/z*: [M + H] calculated for $C_{13}H_{11}N_3O_4$ = 274.0778; found = 274.0836.

***N'-((6-bromo-1H-indol-3-yl)methylene)-4-nitrobenzohydrazide* (25):**

**$^{1}$H NMR (400 MHz, DMSO-d6):** δ = 11.92 (s, 1H), 11.76 (s, 1H), 8.76 (s, 1H), 8.63 (s, 1H), 8.43 (d, *J* = 8.2 Hz, 1H), 8.37 (d, *J* = 7.8 Hz, 1H), 8.24 (d, *J* = 8.5 Hz, 1H), 7.92 (s, 1H), 7.84 (t, *J* = 8.0 Hz, 1H), 7.65 (d, *J* = 1.7 Hz, 1H), 7.33 (dd, *J* = 8.4, 1.7 Hz, 1H).

**$^{13}$C NMR (101 MHz, DMSO-d6):** δ = 160.38, 147.80, 145.37, 137.96, 135.33, 134.05, 131.73, 130.27, 126.06, 123.46, 122.19, 115.41, 114.57, 111.72.

**HRMS (ESI-TOF):** *m/z*: [M + H] calculated for $C_{16}H_{11}BrN_4O_3$ = 387.0078; found = 387.0097.

***N'-((4-methylthiazol-5-yl)methylene)-4-nitrobenzohydrazide* (26):**

**$^{1}$H NMR (400 MHz, DMSO-d6):** δ = 12.24 (s, 1H), 8.76 (s, 1H), 8.46 (s, 2H), 8.37 (d, *J* = 7.7 Hz, 1H), 7.85 (t, *J* = 7.9 Hz, 1H), 7.71 (t, *J* = 6.7 Hz, 4H).

**$^{13}$C NMR (100 MHz, DMSO-d6):** δ = 161.02, 147.77, 147.55, 134.65, 134.16, 133.36, 131.89, 130.33, 129.09, 126.42, 123.60, 122.32.

**HRMS (ESI-TOF):** *m/z*: [M + H] calculated for $C_{14}H_{10}BrN_3O_3$ = 347.9984; found = 347.9988.

***N'-((1H-indol-3-yl)methylene)-2,6-difluorobenzohydrazide* (27):**

**$^{1}$H NMR (400 MHz, DMSO-d6):** δ = 11.88 (d, *J* = 44.8 Hz, 1H), 11.58 (d, *J* = 61.5 Hz, 1H), 8.44 – 8.21 (m, 1H), 7.80 (d, *J* = 41.4 Hz, 1H), 7.67 – 7.54 (m, 1H), 7.40 (dd, *J* = 40.6, 8.0 Hz, 1H), 7.28 – 7.05 (m, 4H), 6.81 – 6.73 (m, 1H).

**$^{13}$C NMR (101 MHz, DMSO-d6):** δ = 162.06, 158.30 (dd, *J* = 247.1, 8.5 Hz), 155.06, 145.54, 141.81, 137.00 (d, *J* = 15.6 Hz), 131.33-131.19 (m), 130.59, 124.08 (d, *J* = 40.4 Hz), 122.77-120.07 (m), 112.23, 111.76, 111.21.

**HRMS (ESI-TOF):** *m/z*: [M + H] calculated for $C_{16}H_{11}F_2N_3O$ = 300.0948; found = 300.0950.

***N'-((6-bromo-1H-indol-3-yl)methylene)-2,6-difluorobenzohydrazide* (28):**

**$^{1}$H NMR (400 MHz, DMSO-d6):** δ = 11.95 (d, *J* = 47.0 Hz, 1H), 11.69 (bs 1H), 8.30 (d, *J* = 70.9 Hz, 1H), 7.84 (d, *J* = 40.9 Hz, 1H), 7.67 – 7.54 (m, 2H), 7.35 – 7.21 (m, 3H), 7.00 – 6.86 (m, 1H).

**$^{13}$C NMR (101 MHz, DMSO-d6):** δ = 162.16, 159.21 (d, *J* = 240.7 Hz), 158.28 (d, *J* = 247.0 Hz), 155.16, 145.03, 141.16, 137.86 (d, J = 18.5 Hz), 132.10 (d, J = 15.4 Hz), 131.41 (d, J = 18.4 Hz), 123.56 (d, J = 10.4 Hz), 123.28, 122.80 (d, J = 21.5 Hz), 115.27 (d, J = 32.6 Hz), 114.53 (d, J = 14.4 Hz), 112.12 (d, J = 24.4 Hz), 111.74 (d, J = 23.7 Hz).

**HRMS (ESI-TOF):** *m/z*: [M + H] calculated for $C_{16}H_{10}BrF_2N_3O$ = 378.0078; found = 378.0054.

***N'-(4-bromobenzylidene)-2,6-difluorobenzohydrazide* (29):**

**$^{1}$H NMR (400 MHz, Chloroform-d)** δ 10.72 (bs, 1H), 7.92 (s, 1H), 7.66 – 7.53 (m, 1H), 7.46 – 7.43 (m, 2H), 7.32 (d, *J* = 8.5 Hz, 2H), 7.00 (dd, *J* = 8.1, 3.0 Hz, 2H).

**$^{13}$C NMR (101 MHz, Chloroform-d)** δ 164.74, 160.89, 159.67 (d, *J* = 244.8 Hz), 144.77, 132.34 (d, *J* = 32.5 Hz), 132.08, 129.39, 128.84, 124.78, 111.63 (d, *J* = 25.0 Hz).

**HRMS (ESI-TOF):** *m/z*: [M + H] calculated for $C_{14}H_9BrF_2N_2O$ 338.994; found 338.9949.

***N'-((1H-indol-3-yl)methylene)-2-fluorobenzohydrazide* (30):**

**$^{1}$H NMR (400 MHz, DMSO-d6):** δ = 11.64 (d, *J* = 19.9 Hz, 1H), 11.49 (d, *J* = 20.7 Hz, 1H), 8.50 (d, *J* = 13.1 Hz, 1H), 8.30 – 8.22 (m, 1H), 7.83 (d, *J* = 2.7 Hz, 1H), 7.73 – 7.43 (m, 3H), 7.33 (q, *J* = 7.8 Hz, 2H), 7.23 – 7.15 (m, 1H), 7.10 – 6.77 (m, 1H).

**$^{13}$C NMR (101 MHz, DMSO-d6):** δ = 166.67, 159.78, 159.13 (d, *J* = 248.5 Hz), 158.24(d, *J* = 246.5Hz), 145.10, 141.04, 137.00 (d, *J* = 15.8 Hz), 131.83 (dd, *J* = 111.8, 8.1 Hz), 130.71, 130.18, 129.20, 125.03 (d, *J* = 17.6 Hz), 124.49-123.85 (m), 122.71-120.03 (m) , 115.72 (dd, *J* = 85.8, 21.7 Hz), 111.78 (d, *J* = 20.2 Hz), 111.53.

**HRMS (ESI-TOF):** *m/z*: [M + H] calculated for $C_{16}H_{12}FN_3O$ = 282.1042; found = 282.1047.

***N'-((6-bromo-1H-indol-3-yl)methylene)-2-fluorobenzohydrazide* (31):**

**$^{1}$H NMR (400 MHz, DMSO-d6):** δ = 11.73 (s, 1H), 11.57 (s, 1H), 8.46 (s, 1H), 8.25 – 8.14 (m, 1H), 7.81 (d, *J* = 41.4 Hz, 1H), 7.69 – 7.45 (m, 3H), 7.40 – 7.26 (m, 2H), 7.19 – 6.73 (m, 1H).

**$^{13}$C NMR (101 MHz, DMSO-d6):** δ = 167.72, 160.32, 159.08 (d *J* = 248.6 Hz), 144.48, 139.10 (d, *J* = 240.9 Hz), 137.73, 131.98 (d, *J* = 8.5 Hz), 131.39(t, *J* = 18.4 Hz), 130.12 (d, *J* = 3.0 Hz), 129.08(d, *J* = 4.3 Hz), 125.59 (d, *J* = 3.4 Hz), 124.18-124.19 (m), 116.12 (d, *J* = 21.9 Hz), 115.19(d, *J* = 30.0 Hz), 114.41 (d, *J* = 18.2 Hz), 111.66.

**HRMS (ESI-TOF):** *m/z*: [M + H] calculated for $C_{16}H_{11}BrFN_3O$ = 360.0148; found = 360.0151.

***N'-((1H-indol-3-yl)methylene)-4-fluorobenzohydrazide* (32):**

**$^{1}$H NMR (400 MHz, DMSO-d6):** δ = 11.60 (s, 1H), 11.55 (s, 1H), 8.61 (s, 1H), 8.30 (d, *J* = 7.6 Hz, 1H), 8.00 (dd, *J* = 8.8, 5.5 Hz, 2H), 7.84 (d, *J* = 2.7 Hz, 1H), 7.45 – 7.33 (m, 3H), 7.23-7.14 (m, 2H).

**$^{13}$C NMR (101 MHz, DMSO-d6):** δ = 162.67 (d, *J* = 125.9 Hz), 161.42, 145.05, 137.04, 130.39 (d, *J* = 23.7 Hz), 130.07, 124.34, 122.63, 122.02 (d, *J* = 61.1 Hz), 120.39, 115.46 (d, *J* = 21.8 Hz), 115.24 (d, *J* = 13.5 Hz), 111.82 111.68 (d, *J* = 13.5 Hz).

**HRMS (ESI-TOF):** *m/z*: [M + H] calculated for $C_{16}H_{12}FN_3O$ = 282.1043; found = 282.1049.

***N'-((6-bromo-1H-indol-3-yl)methylene)-4-fluorobenzohydrazide* (33):**

**$^{1}$H NMR (400 MHz, DMSO-d6):** δ = 11.65 (bs, 2H), 8.59 (s, 1H), 8.24 (d, *J* = 8.5 Hz, 1H), 7.99 (dd, *J* = 8.8, 5.5 Hz, 2H), 7.87 (s, 1H), 7.64 (s, 1H), 7.40 – 7.29 (m, 3H).

**$^{13}$C NMR (101 MHz, DMSO-d6):** δ = 165.17, 162.70, 161.49, 144.45, 137.94, 131.26, 130.40 (d, *J* = 3.1 Hz), 130.13 (d, *J* = 9.0 Hz), 123.66, 123.32 (d, *J* = 6.5 Hz), 115.36 (d, *J* = 21.8 Hz), 114.50, 111.84.

**HRMS (ESI-TOF):** *m/z*: [M + H + 2] calculated for $C_{16}H_{11}BrFN_3O$ = 362.0148; found = 362.0128.

***4-fluoro-N'-((4-methylthiazol-5-yl)methylene)benzohydrazide* (34):**

**$^{1}$H NMR (400 MHz, DMSO-d6):** δ = 11.87 (bs, 1H), 9.05 (s, 1H), 8.72 (s, 1H), 7.95 (dd, *J* = 8.5, 5.6 Hz, 2H), 7.35 (t, *J* = 8.8 Hz, 2H), 2.47 (s, 3H).

**$^{13}$C NMR (101 MHz, DMSO-d6):** δ = 164.19 (d, *J* = 249.4 Hz), 161.75, 154.97, 154.21, 140.90, 130.24 (d, *J* = 9.1 Hz), 129.63 (d, *J* = 2.8 Hz), 127.59, 115.54 (d, *J* = 21.9 Hz), 15.33.

**HRMS (ESI-TOF):** *m/z*: [M + H] calculated for $C_{12}H_{10}FN_3OS$ = 264.0577; found = 264.0604.

## 2.6 References


1. American Cancer Society. Colorectal Cancer Facts & Figures 2011-2013. Atlanta: American Cancer Society, **2011**.
2. Ferlay, J.; Soerjomataram, I.; Ervik, M.; Dikshit, R.; Eser, S.; Mathers, C.; Rebelo, M.; Parkin, D. M.; Forman, D.; Bray, F. GLOBOCAN 2012 v1.0, Cancer Incidence and Mortality Worldwide: IARC CancerBase No. 11. http://globocan.iarc.fr, accessed on day/month/year
3. Rubbia-Brandt, L.; Audard, V.; Sartoretti, P.; Roth, A. D.; Brezault, C.; Le Charpentier, M.; Dousset, B.; Morel, P.; Soubrane, O.; Chaussade, S.; Mentha, G.; Terris, B. Severe hepatic

sinusoidal obstruction associated with oxaliplatin-based chemotherapy in patients with metastatic colorectal cancer. *Ann. Oncol.* **2004**, *15*, 460-466.

4. André, T.; Boni, C.; Mounedji-Boudiaf, L.; Navarro, M.; Tabernero, J.; Hickish, T.; Topham, C.; Zaninelli, M.; Clingan, P.; Bridgewater, J.; Tabah-Fisch, I.; de Gramont, A. Oxaliplatin, Fluorouracil, and Leucovorin as Adjuvant Treatment for Colon Cancer. *N. Engl. J. Med*. **2004**, *350*, 2343-2351.
5. Klotz, H. P.; Weder, W.; Largiadèr, F. Local and systemic toxicity of intra-hepatic-arterial 5-FU and high-dose or low-dose leucovorin for liver metastases of colorectal cancer. *Surg. Oncol.* **1994**, *3*, 11-16.
6. Knight, Z. A.; Lin, H.; Shokat, K. M. Targeting the cancer kinome through polypharmacology. *Nat. Rev. Cancer* **2010**, *10*, 130-137.
7. Wilson, T. R.; Fridlyand, J.; Yan, Y.; Penuel, E.; Burton, L.; Chan, E.; Peng, J.; Lin, E.; Wang, Y.; Sosman, J.; Ribas, A.; Li, J.; Moffat, J.; Sutherlin, D. P.; Koeppen, H.; Merchant, M.; Neve, R.; Settleman, J. Widespread potential for growth-factor-driven resistance to anticancer kinase inhibitors. *Nature* **2012**, *487*, 505-509.
8. Gottesman, M. M.; Fojo, T.; Bates, S. E. Multidrug resistance in cancer: role of ATP-dependent transporters. *Nat. Rev. Cancer* **2002**, *2*, 48-58.
9. Holohan, C.; Van Schaeybroeck, S.; Longley, D. B.; Johnston, P. G. Cancer drug resistance: an evolving paradigm. *Nat. Rev. Cancer* **2013**, *13*, 714-726.
10. Trifunovic, A.; Wredenberg, A.; Falkenberg, M.; Spelbrink, J. N.; Rovio, A.T.; Bruder, C. E.; Bohlooly, M.; Gidlöf, S.; Oldfors, A.; Wibom, R.; Törnell, J.; Jacobs, H. T.; Larsson, N. Premature ageing in mice expressing defective mitochondrial DNA polymerase. *Nature* **2004**, *429*, 417-423.
11. Smith, R. A. J.; Hartley, R. C.; Cochemé, H. M.; Murphy, M. P. Mitochondrial pharmacology. *Trends Pharmacol. Sci.* **2012**, *33*, 341-352.
12. Ward, S.; Thompson, C. B. Metabolic reprogramming: a cancer hallmark even warburg did not anticipate. *Cancer Cell* **2012**, *21*, 297-308.
13. Navdeep, C. S. Mitochondria as signaling organelles. *BMC Biol.* **2014**, *12*, 34-40.
14. Galluzzi, L.; Oliver, K.; Guido, K. Mitochondria: master regulators of danger signalling. *Nat. Rev. Mol. Cell Biol.* **2012**, *13*, 780-788.
15. Tait, S.W.G.; Douglas, R. G. Mitochondria and cell death: outer membrane permeabilization and beyond. *Nat. Rev. Mol. Cell Biol.* **2010**, *11*, 621-632.
16. Calvo, S. E.; Mootha, V. K. The mitochondrial proteome and human disease. *Annu. Rev. Genomics Hum. Genet.* **2010**, *11*, 25-44.

17. Nunnari, J.; Suomalainen, A. Mitochondria: in sickness and in health. *Cell* **2012**, *148*, 1145-1159.
18. Gogvadze, V.; Orrenius, S.; Zhivotovsky, B. Mitochondria in cancer cells: what is so special about them? *Trends Cell Biol.* **2008**, *18*, 165-173.
19. Boroughs, L. K.; DeBerardinis, R. J. Metabolic pathways promoting cancer cell survival and growth. *Nat. Cell Biol.* **2015**, *17*, 351-359.
20. Fulda, S.; Galluzzi, L.; Kroemer, G. Targeting mitochondria for cancer therapy. *Nat. Rev. Drug Discovery* **2010**, *9*, 447-464.
21. Weinberg, S. E.; Chandel, N. S. Targeting mitochondria metabolism for cancer therapy. *Nat. Chem. Biol.* **2015**, *11*, 9-15.
22. Wallace, D. C. Mitochondria and cancer. *Nat. Rev. Cance*r **2012**, *12*, 685-698.
23. Vyas, V.; Zaganjor, E.; Haigis, M .C. Mitochondria and Cancer. *Cell* **2016**, *166*, 555-566.
24. Marrache, S.; Pathaka, R. K.; Dhar, S. Detouring of cisplatin to access mitochondrial genome for overcoming resistance. *Proc. Natl. Acad. Sci. U.S.A.* **2014**, *111*, 10444-10449.
25. Marrache S.; Dhar, S. Engineering of blended nanoparticle platform for delivery of mitochondria-acting therapeutics. *Proc. Natl. Acad. Sci. U.S.A.* **2012**, *109*, 16288-16293.
26. Jean, S. R.; Ahmed, M.; Lei, E. K.; Wisnovsky, S. P.; Kelley, S.O. Peptide-Mediated Delivery of Chemical Probes and Therapeutics to Mitochondria. *Acc*. *Chem*. *Res*. **2016**, *49*, 1893-1902.
27. Wisnovsky, S.; Lei, E. K.; Jean, S. R.; Kelley, S. O. Mitochondrial Chemical Biology: New Probes Elucidate the Secrets of the Powerhouse of the Cell. *Cell Chem. Biol*. **2016**, *23*, 917-927.
28. Jean, S. R.; Tulumello, D. V.; Wisnovsky, S. P.; Lei, E. K.; Pereira, M. P.; Kelley, S. O. Molecular vehicles for mitochondrial chemical biology and drug delivery. *ACS Chem. Biol*. **2014**, *9*, 323-333.
29. Chatterjee, A.; Mambo, E.; Sidransky, D. Mitochondrial DNA mutations in human cancer. *Oncogene* **2006**, *25*, 4663-4674.
30. Sánchez-Aragó, M.; Chamorro, M.; Cuezva, J. M. Selection of cancer cells with repressed mitochondria triggers colon cancer progression. *Carcinogenesis*, **2010**, *31*, 567-576.
31. Hübel, K.; Lessmann T.; Waldmann H. Chemical biology--identification of small molecule modulators of cellular activity by natural product inspired synthesis. *Chem. Soc. Rev.* **2008**, *37*, 1361-1374.
32. Schreiber, S. L. Target-oriented and diversity-oriented organic synthesis in drug discovery. *Science* **2000**, *287*, 1964-1969.
33. DeVita, V. T. Jr.; Chu, E. A. History of cancer chemotherapy. *Cancer Res.* **2008**, *68*, 8643-8653.
34. Ziegler, S.; Pries, V.; Hedberg, C.; Waldmann, H. Target identification for small bioactive molecules: finding the needle in the haystack. *Angew. Chem. Int. Ed.* **2013**, *52*, 2744-2792.

35. Škrtić, M.; Sriskanthadevan, S.; Jhas, B.; Gebbia, M.; Wang, X.; Wang, Z.; Hurren, R.; Jitkova, Y.; Gronda, M.; Maclean, N.; Lai, C. K. Eberhard, Y.; Bartoszko, J.; Spagnuolo, P.; Rutledge, A. C.; Datti, A.; Ketela, T.; Moffat, J.; Robinson, B. H.; Cameron, J. H.; Wrana, J.; Eaves, C. J.; Minden, M. D.; Wang, J. C.; Dick, J. E.; Humphries, K.; Nislow,C.; Giaever, G.; Schimmer, A. D. Inhibition of mitochondrial translation as a therapeutic strategy for human acute myeloid leukemia. *Cancer Cell* **2011**, *20*, 674-688.
36. Wang, D.; Wang, J.; Bonamy, G. M. C.; Meeusen, S.; Brusch, R.G.; Turk, C.; Yang, P.; Schultz, P.G. A small molecule promotes mitochondrial fusion in mammalian cells. *Angew. Chem. Int. Ed.* **2012**, *51*, 9302-9305.
37. Leanza, L.; Romio, M.; Becker, K. A.; Azzolini, M.; Trentin, L.; Managò, A.; Venturini, E.; Zaccagnino, A.; Mattarei, A.; Carraretto, L.; Urbani, A.; Kadow, S.; Biasutto, L.; Martini, V.; Severin, F.; Peruzzo, R.; Trimarco, V.; Egberts, J. H.; Hauser, C.; Visentin, A.; Semenzato, G.; Kalthoff, H.; Zoratti, M.; Gulbins, E.; Paradisi, C.; Szabo, I. Direct pharmacological targeting of a mitochondrial ion channel selectively kills tumor cells in vivo. *Cancer Cell* **2017**, *31*, 516-531.
38. Goff, G. L.; Ouazzani, J. Natural hydrazine-containing compounds: biosynthesis, isolation, biological activities and synthesis. *Bioorg. Med. Chem.* **2014**, *22*, 6529-6544.
39. Blair, L. M.; Sperry, J. Natural products containing a nitrogen-nitrogen bond. *J. Nat. Prod.* **2013**, *76*, 794-812.
40. Trosset, J.Y.; Dalvit, C.; Knapp, S.; Fasolini, M.; Veronesi, M.; Mantegani, S.; Gianellini, L. M.; Catana, C.; Sundström, M.; Stouten, P. F.; Moll, J. K. Inhibition of protein-protein interactions: the discovery of druglike beta-catenin inhibitors by combining virtual and biophysical screening. *Proteins* **2006**, *64*, 60-67.
41. Das Mukherjee, D.; Kumar, N. M.; Tantak, M. P.; Das, A.; Ganguli, A.; Datta, S.; Kumar, D.; Chakrabarti, G. Development of novel bis(indolyl)-hydrazide-hydrazone derivatives as potent microtubule-targeting cytotoxic agents against A549 lung cancer cells. *Biochemistry*, **2016**, *55*, 3020-3035.
42. Nasr, T.; Bondock, S.; Youns, M. Anticancer activity of new coumarin substituted hydrazide-hydrazone derivatives. *Eur. J. Med. Chem.* **2014**, *76*, 539-548.
43. Vogel, S.; Kaufmann, D.; Pojarová, M.; Müller, C.; Pfaller, T.; Kühne, S.; Bednarski, P. J.; von Angerer, E. Aroyl hydrazones of 2-phenylindole-3-carbaldehydes as novel antimitotic agents. *Bioorg. Med. Chem.* **2008**, *16*, 6436-6447.
44. Liu, T.; Sun, C.; Xing, X.; Jing, L.; Tan, R.; Luo, Y.; Huang, W.; Song, H.; Li, Z.; Zhao, Y. Synthesis and evaluation of 2-[2-(phenylthiomethyl)-1H-benzo[d] imidazol-1-yl)acetohydrazide derivatives as antitumor agents. *Bioorg. Med. Chem. Lett.* **2012**, *22*, 3122-3125.

45. Cui, Z.; Li, Y.; Ling, Y.; Huang, J.; Cui, J.; Wang, R.; Yang, X. New class of potent antitumor acylhydrazone derivatives containing furan. *Euro. J. Med. Chem.* **2010**, *45*, 5576-5584.
46. Popiołek, Ł. Hydrazide-hydrazones as potential antimicrobial agents: overview of the literature since 2010. *Med. Chem. Res.* **2017**, *26*, 287-301.
47. Hughes, J. P.; Rees, S.; Kalindjian, S. B.; Philpott, K. L. Principles of early drug discovery. *Br. J. Pharm.* **2011**, *162*, 1239-1249.
48. Vrijens, K.; Lin, W.; Cui, J.; Farmer, D.; Low, J.; Pronier, E.; Zeng, F. Y.; Shelat, A. A.; Guy, K.; Taylor, M. R.; Chen, T.; Roussel, M. F. Identification of small molecule activators of BMP signalling. *PloS One*, **2013**, *8*, e59045.
49. Kalia, J.; Raines, R. T. Hydrolytic stability of hydrazones and oximes. *Angew. Chem. Int. Ed.* **2008**, *47*, 7523-7526.
50. Hanahan, D.; Weinberg, R. A. The hallmarks of cancer. *Cell* **2000**, *100*, 57-70.
51. Hanahan, D.; Weinberg, R. A. Hallmarks of cancer: the next generation. *Cell* **2011**, *144*, 646-674.
52. Green, D. R.; Kroeme, G. The pathophysiology of mitochondrial cell death. *Science* **2004**, *305*, 626-629.
53. Chipuk, J. E.; Green, D. R. How do BCL-2 proteins induce mitochondrial outer membrane permeabilization? *Trends Cell Biol.* **2008**, *18*, 157-164.
54. Chipuk, J. E.; Bouchier-Hayes, L.; Green.D. R. Mitochondrial outer membrane permeabilization during apoptosis: the innocent bystander scenario. *Cell Death Differ.* **2006**, *13*, 1396-1402.
55. Cossarizza, A.; Baccaranicontri. M. A new method for the cytofluorimetric analysis of mitochondrial membrane potential using the J-aggregate forming lipophilic cation 5,5',6,6'-tetrachloro-1,1',3,3'-tetraethylbenzimidazolcarbocyanine iodide (JC-1). *Biochem. Biophys. Res. Commun*. **1993**, *197*, 40-45.
56. Petronilli, V.; Miotto, G.; Canton, M.; Brini, M.; Colonna, R.; Bernardi, P.; Lisa, F.D. Transient and long-lasting openings of the mitochondrial permeability transition pore can be monitored directly in intact cells by changes in mitochondrial calcein fluorescence. *Biophys. J*. **1999**, *76*, 725-734.
57. Floryk, D.; Houštěk, J. Tetramethyl rhodamine methyl ester (TMRM) is suitable for cytofluorometric measurements of mitochondrial membrane potential in cells treated with digitonin. *Biosci. Rep*. **1999**, *19*, 27-34.
58. Dagda, R. K.; Cherra, S. J.; Kulich, S. M.; Tandon, A.; Park, D.; Chu, C. T. Loss of PINK1 function promotes mitophagy through effects on oxidative stress and mitochondrial fission. *J. Biol. Chem*. **2009**, *284*, 13843-13855.

59. Ashkenazi, A.; Fairbrother, W. J.; Leverson, J. D.; Souers, A. J. From basic apoptosis discoveries to advanced selective BCL-2 family inhibitors. Nat. Rev. Drug Discov. **2017**, *16*, 273-284.
60. Jiang,X.; Wang, X. Cytochrome C-mediated apoptosis. *Annu. Rev. Biochem*. **2004**, *73*, 87-106.
61. Wu, D.; Yotnda, P. Production and detection of reactive oxygen species (ROS) in cancers. *J. Vis. Exp*. **2011**, (57), 3357-3360.
62. Koczor, C. A.; Shokolenko, I. N.; Boyd, A. K.; Balk, S. P.; Wilson, G. L.; LeDoux, S. P. Mitochondrial DNA damage initiates a cell cycle arrest by a Chk2-associated mechanism in mammalian cells. *J. Biol. Chem*. **2009**, *284*, 36191-36201.
63. Mariño, G.; Niso-Santano, M.; Baehrecke, E. H.; Kroemer, G. Self-consumption: the interplay of autophagy and apoptosis. *Nat. Rev. Mol. Cell Biol*. **2014**, *15*, 81-94.
64. Li, P.; Nijhawan, D.; Budihardjo, I.; Srinivasula, S. M.; Ahmad, M.; Alnemri, E. S. X. Wang, X. Cytochrome c and dATP-dependent formation of Apaf-1/caspase-9 complex initiates an apoptotic protease cascade. *Cell* **1997**, *91*, 479-489.
65. Vaseva, A. V.; Moll, U. M. The mitochondrial p53 pathway. *Biochim. Biophys. Acta.* **2009**, *1787*, 414-420.
66. Jiang, M.; Milner, J. Bcl-2 constitutively suppresses p53-dependent apoptosis in colorectal cancer cells. *Genes Dev.* **2003**, *17*, 832-837.
67. Mallick, A.; More, P.; Ghosh, S.; Chippalkatti, R.; Chopade, B. A.; Lahiri, M.; Basu, S. Dual drug conjugated nanoparticle for simultaneous targeting of mitochondria and nucleus in cancer cells. *ACS Appl. Mater. Interfaces.* **2015**, *7 (14)*, 7584-7598.
68. Mallick, A.; More, P.; Syed, M. M.; Basu, S. Nanoparticle-mediated mitochondrial damage induces apoptosis in cancer. *ACS Appl. Mater. Interfaces.* **2016**, *8*, 13218-13231.
69. Kini, S. D; Bhat, A. R.; Bryant, B.; Williamson, J. S.; Dayan, F. E. Synthesis, antitubercular activity and docking study of novel cyclic azole substituted diphenyl ether derivatives. *Eur. J. Med. Chem.* **2009**, *44*, 492-500.
70. Cui, Z. N.; Li, Y. S.; Hu, D. K.; Tian, H.; Jiang, Y. Z.; Wang, Y.; Yan, X. J. Synthesis and fungicidal activity of novel 2,5-disubstituted-1,3,4- thiadiazole derivatives containing 5-phenyl-2-furan. *Sci. Rep.* **2016**, *6*, 20204.
71. Mehr-un-Nisa.; Munawar, M. A.; Chattha, F. A.; Kousar, S.; Munir, J.; Ismail, T.; Ashraf, M.; Khan, M. A. Synthesis of novel triazoles and a tetrazole of escitalopram as cholinesterase inhibitors. *Bioorg. Med. Chem.* **2015**, *23*, 6014-6024.
72. Johnson, A. M.; Wiley, C. A.; Young, M. C.; Zhang, X.; Lyon, Y.; Julian, R. R.; Hooley, R. J. Narcissistic self-sorting in self-assembled cages of rare Earth metals and rigid ligands. *Angew. Chem. Int. Ed.* **2015**, *54*, 5641-5645.

73. Murty, M. S. R.; Penthala, R.; Polepalli, S.; Jain, N. Synthesis and biological evaluation of novel resveratrol-oxadiazole hybrid heterocycles as potential antiproliferative agents. *Med. Chem. Res.* **2016**, *4*, 627-643
74. He, H.; Wang, W.; Zhou, Y.; Xia, Q.; Ren, Y.; Feng, J.; Peng, H.; He, H.; Feng. L. Rational design, synthesis and biological evaluation of 1, 3, 4-oxadiazole pyrimidine derivatives as novel pyruvate dehydrogenase complex E1 inhibitors. *Bioorg. Med. Chem.* **2016,** *24*, 1879-1888.

## 2.7 Appendix-A:

### Characterization of the compounds

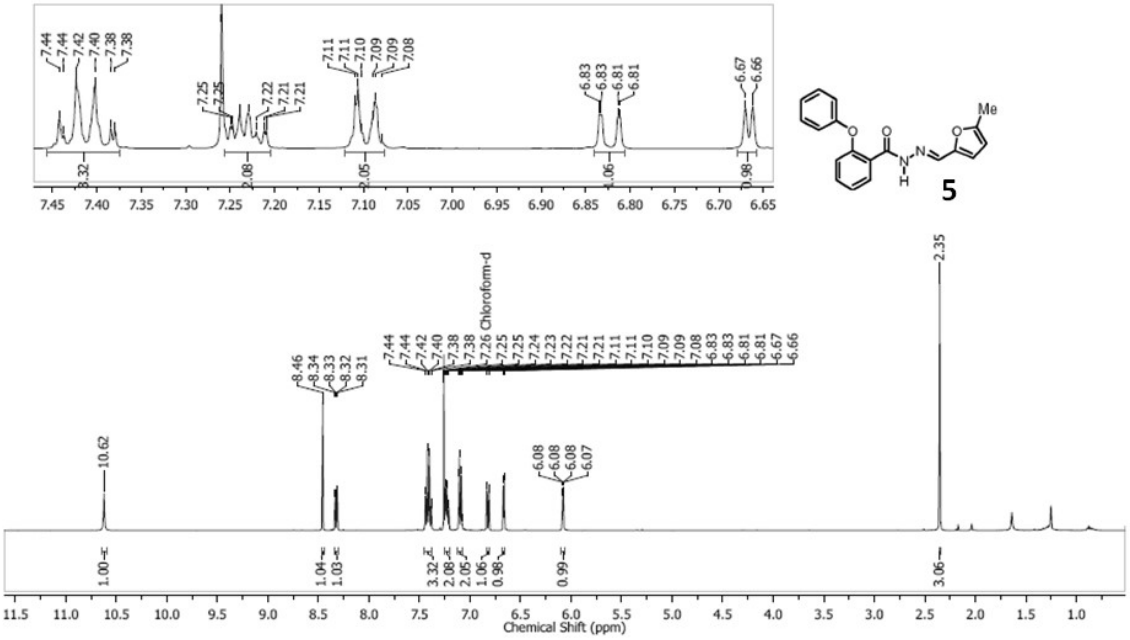


**Figure A1:** $^{1}$H NMR spectra of compound **5**.

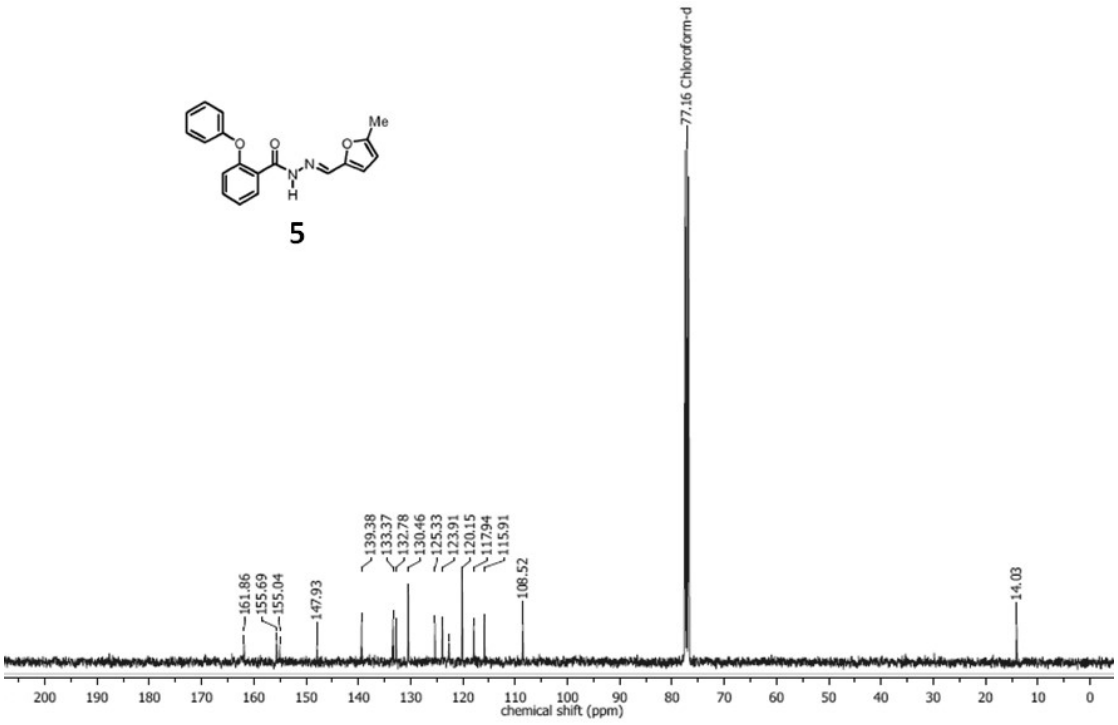


**Figure A2:** $^{13}$C NMR spectra of compound **5**

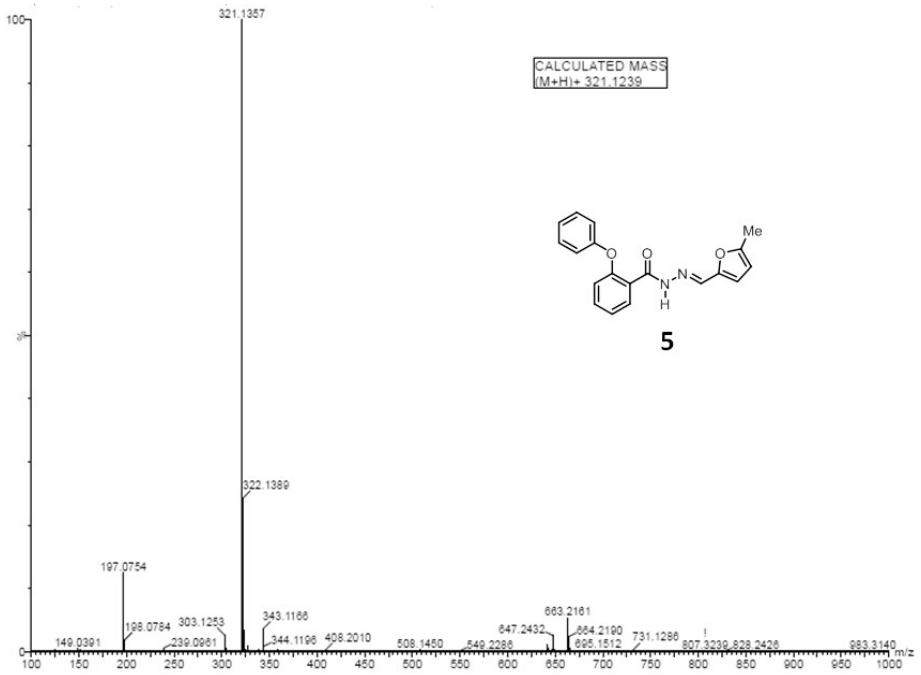


**Figure A3:** HR-MS spectra of compound **5.**

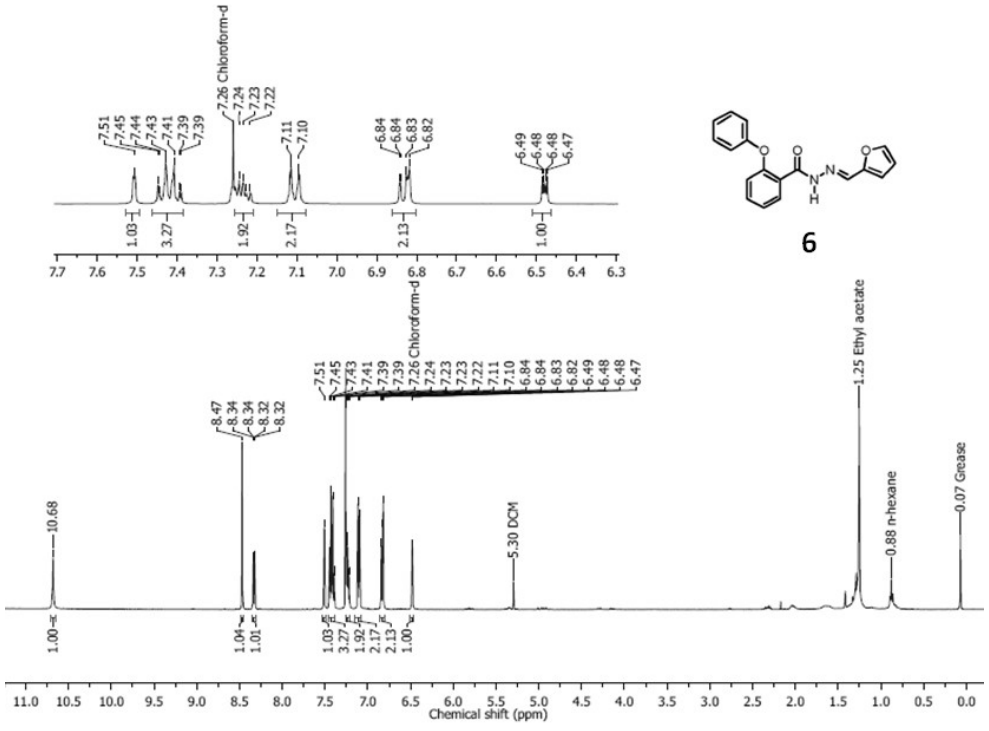


**Figure A4:** $^{1}$H NMR spectra of compound **6**

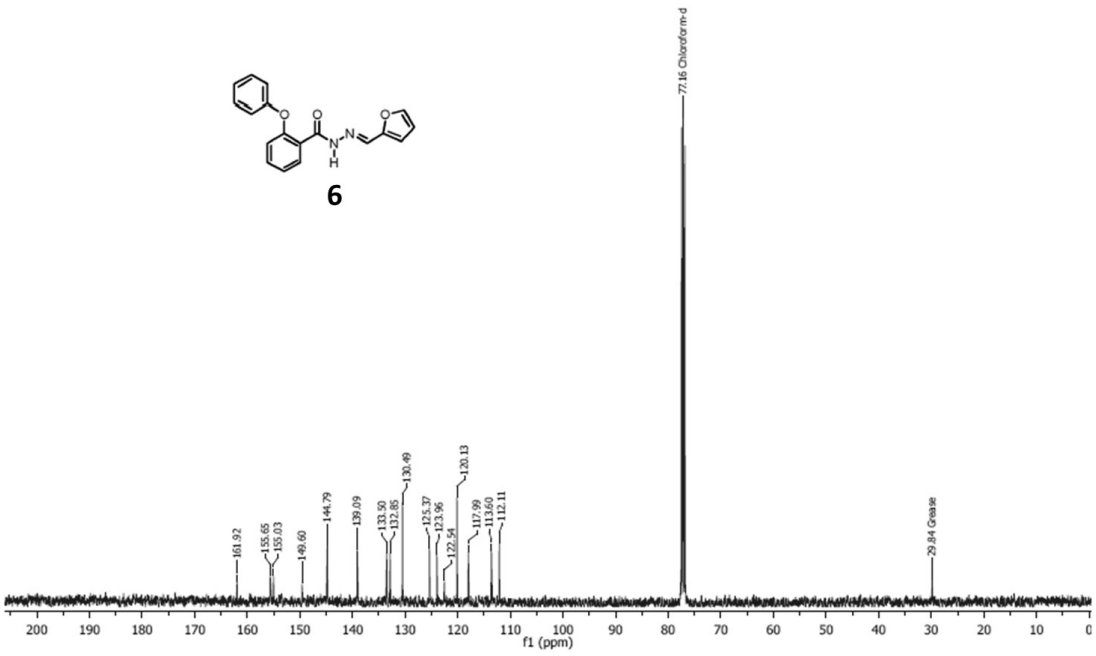


**Figure A5:** $^{13}$C NMR spectra of compound **6**

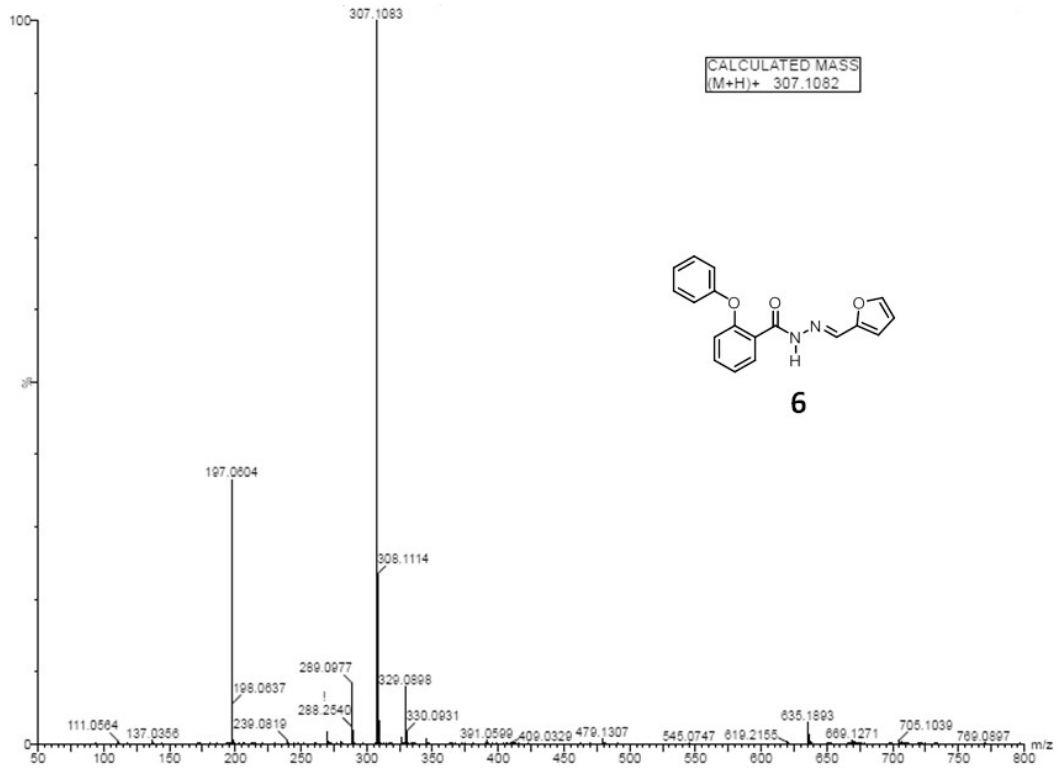


**Figure A6:** HR-MS spectra of compound **6**

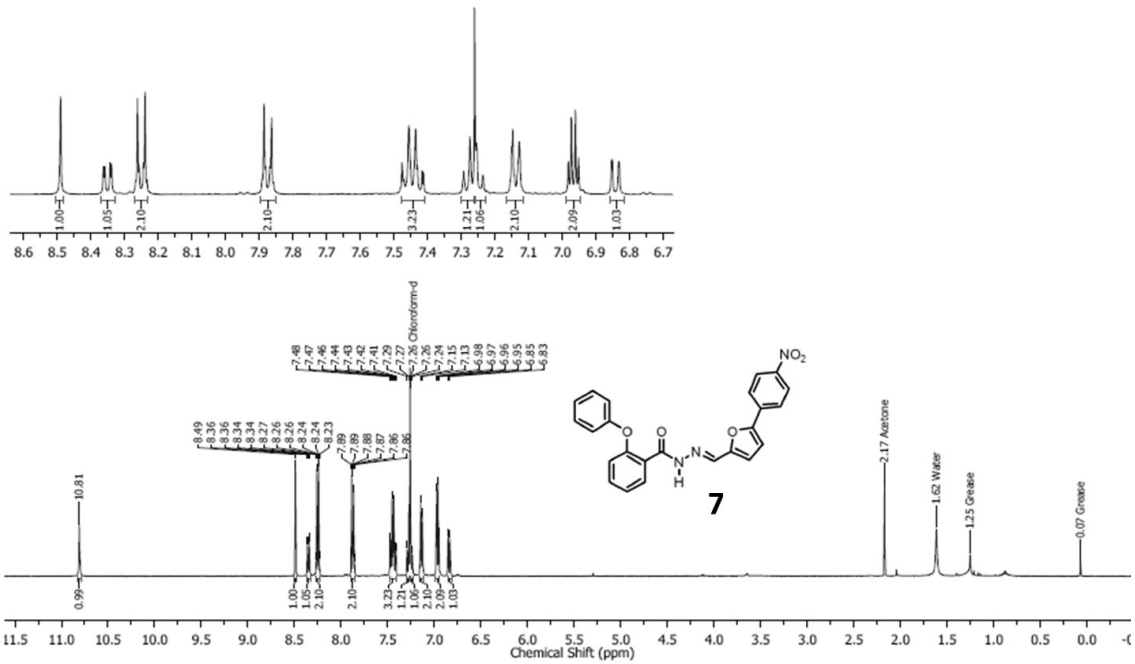


**Figure A7**: $^{1}$H NMR spectra of compound **7**

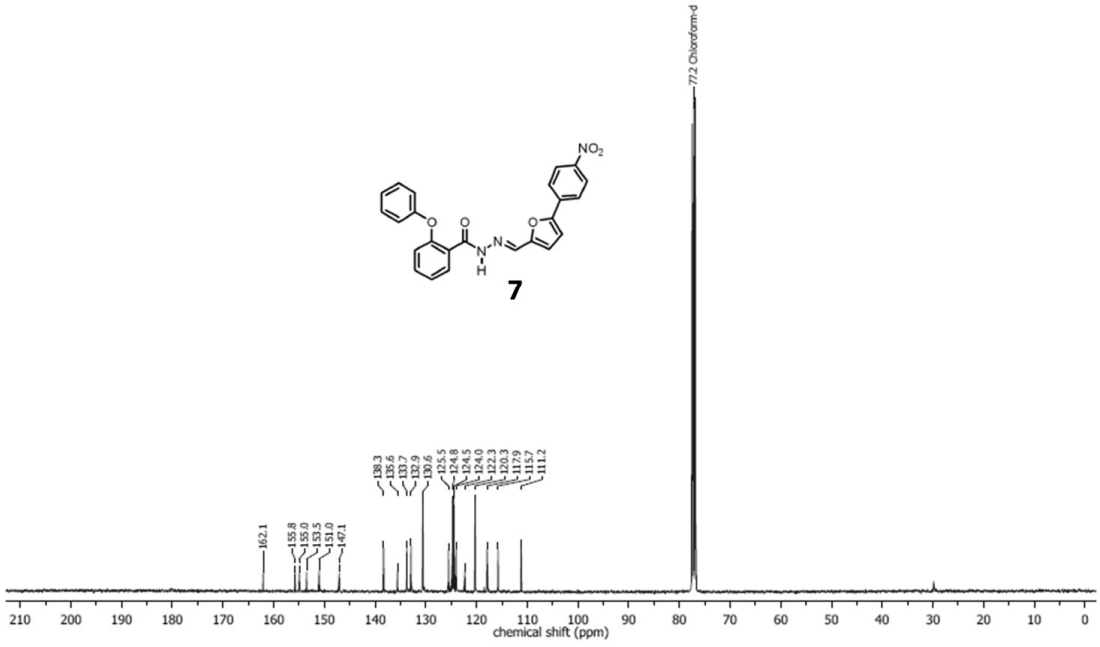


**Figure A8:** $^{13}$C NMR spectra of compound **7**

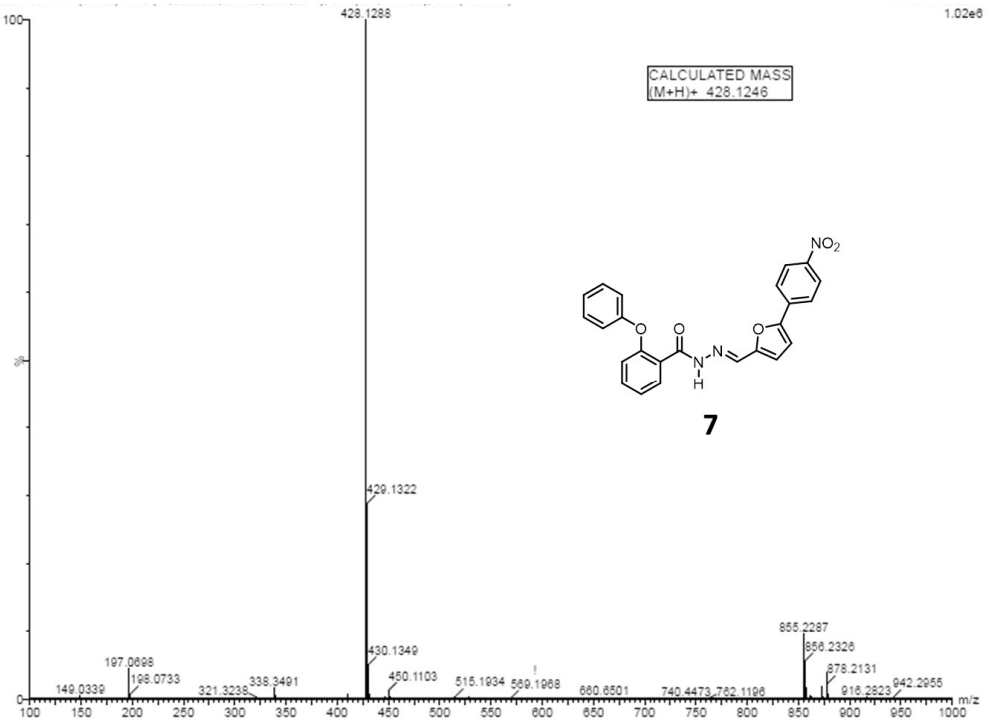


**Figure A19:** HR-MS spectra of compound **7**

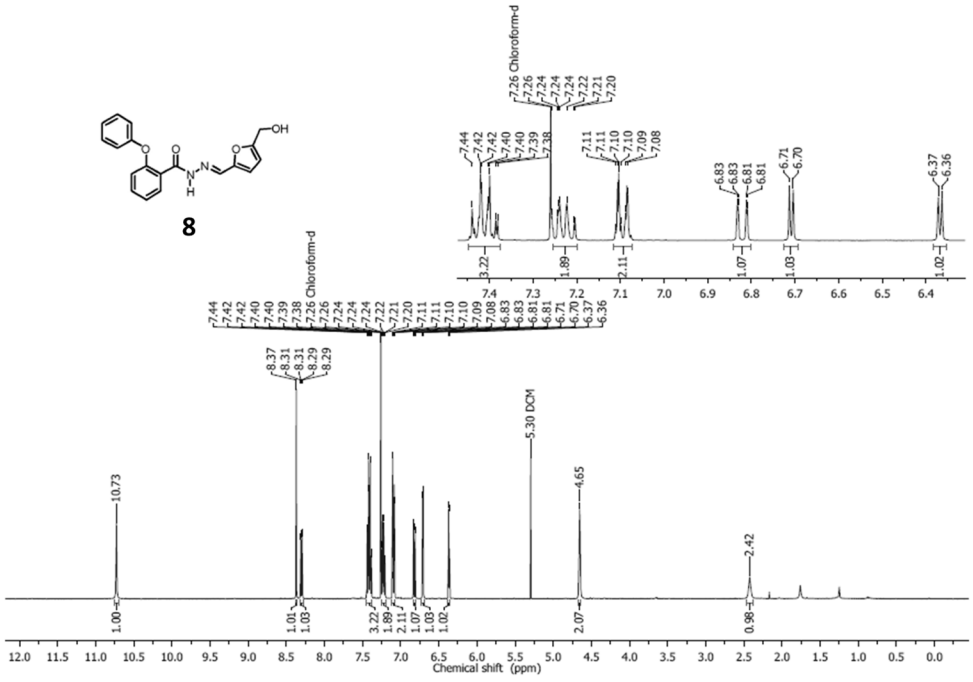


**Figure A10:** $^{1}$H NMR spectra of compound **8**

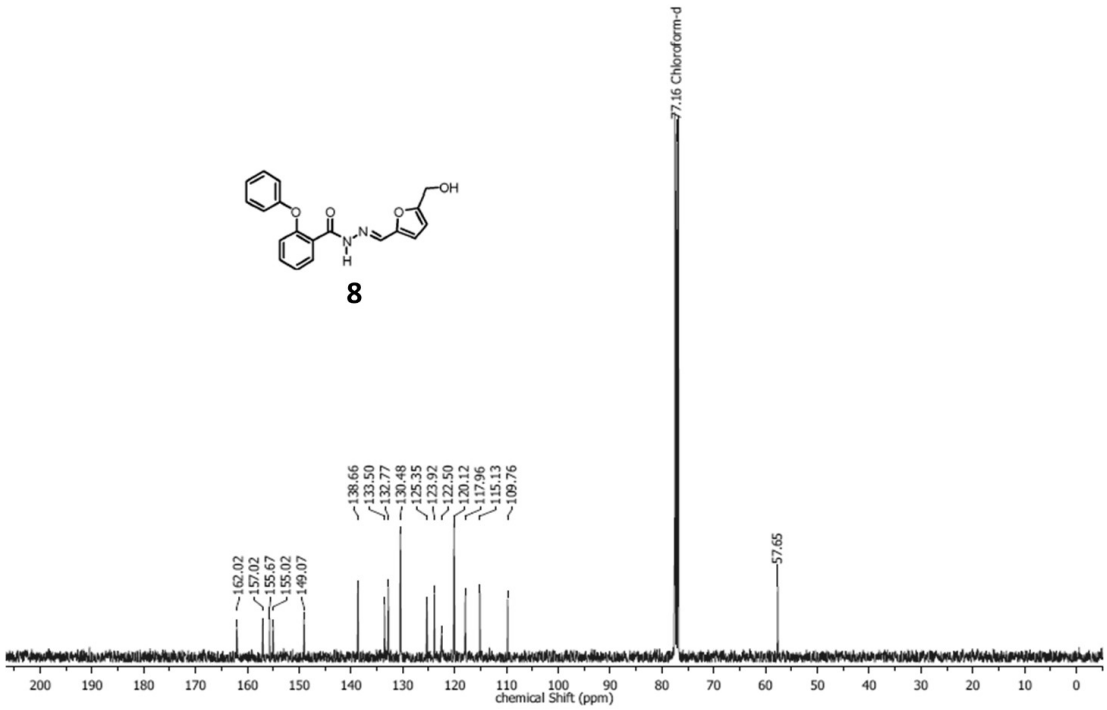


**Figure A11:** $^{13}$C NMR spectra of compound **8.**

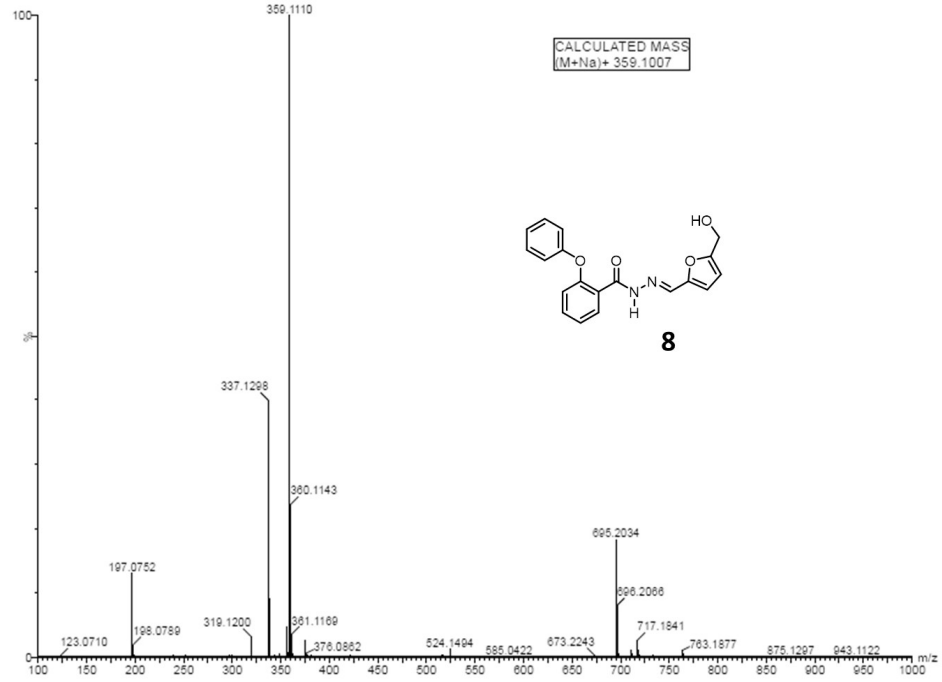


**Figure A12:** HR-MS spectra of compound **8.**

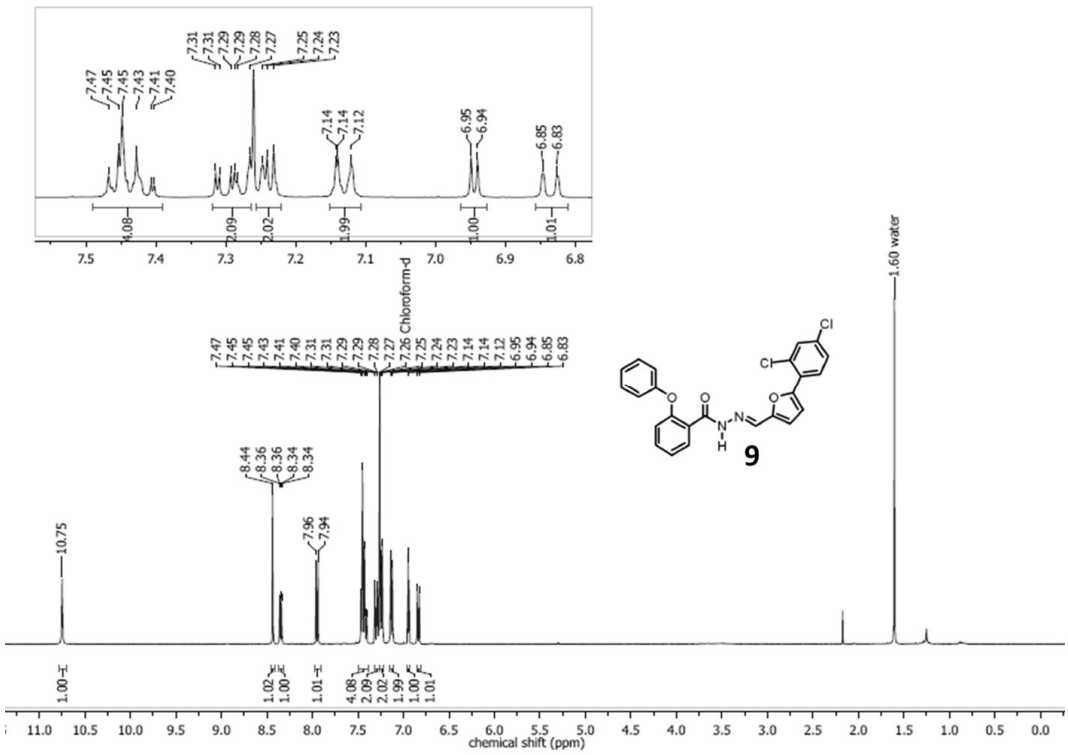


**Figure A13:** $^{1}$H NMR spectra of compound **9**

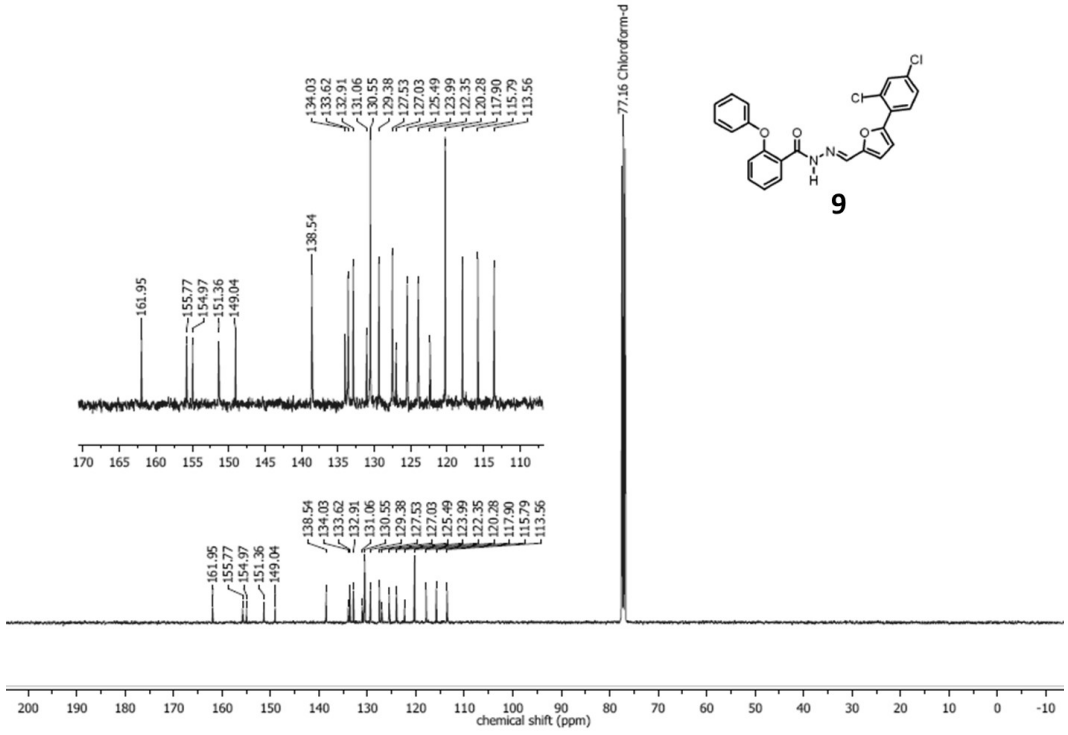


**Figure A14:** $^{13}$C NMR spectra of compound **9**

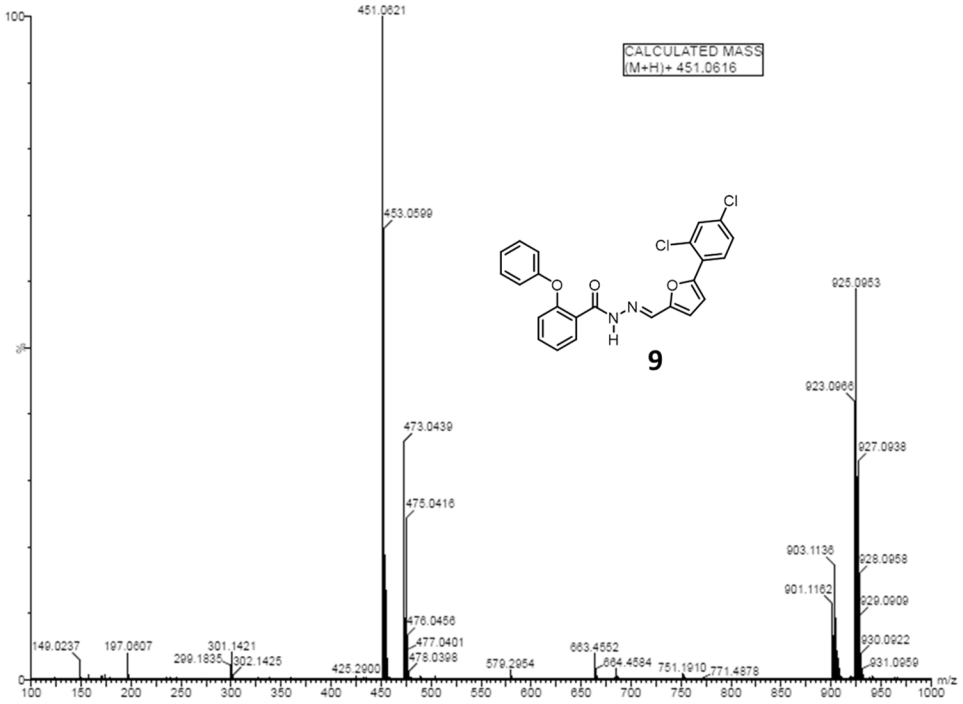


**FigureA15:** HR-MS spectra of compound **9**

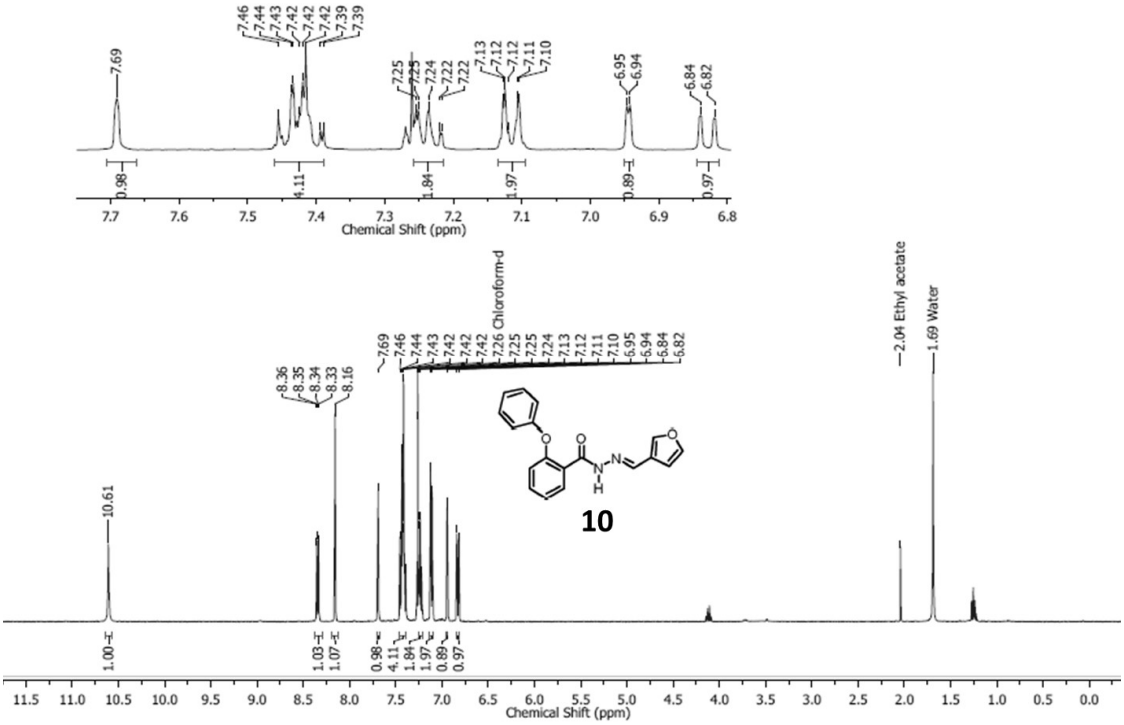


**Figure A16:** $^{1}$H NMR spectra of compound **10**

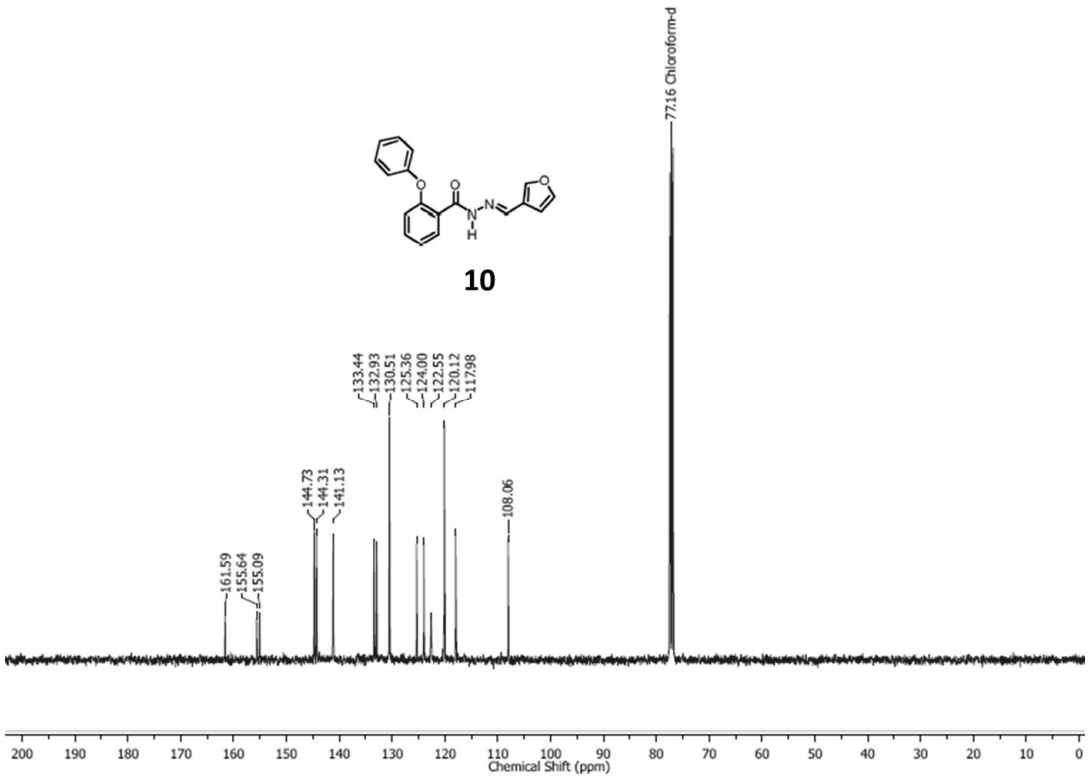


**Figure A17**: $^{13}$C NMR spectra of compound **10**

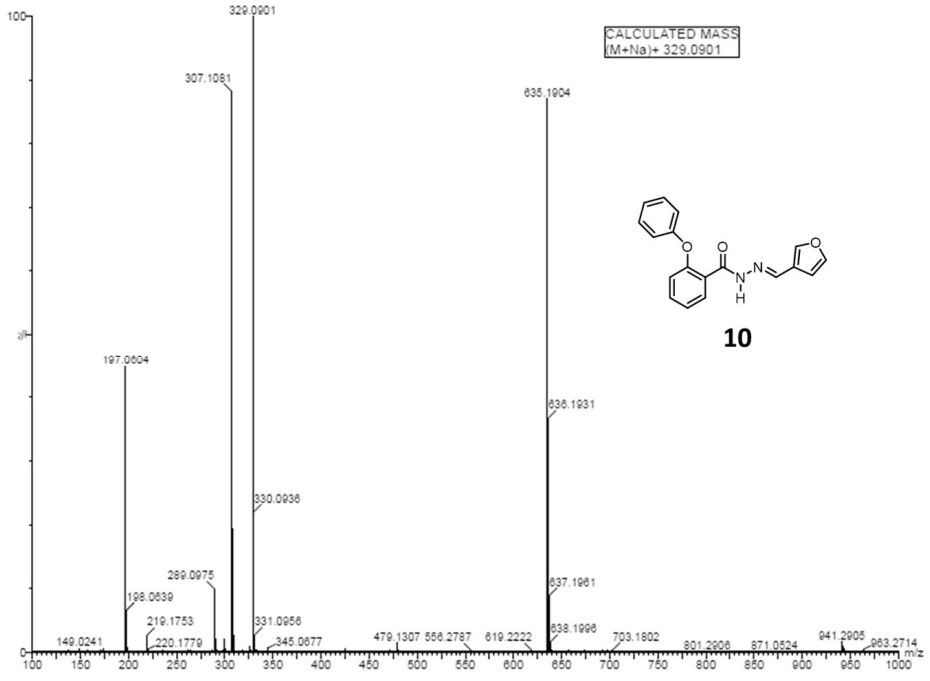


**Figure A18:** HR-MS spectra of compound **10**

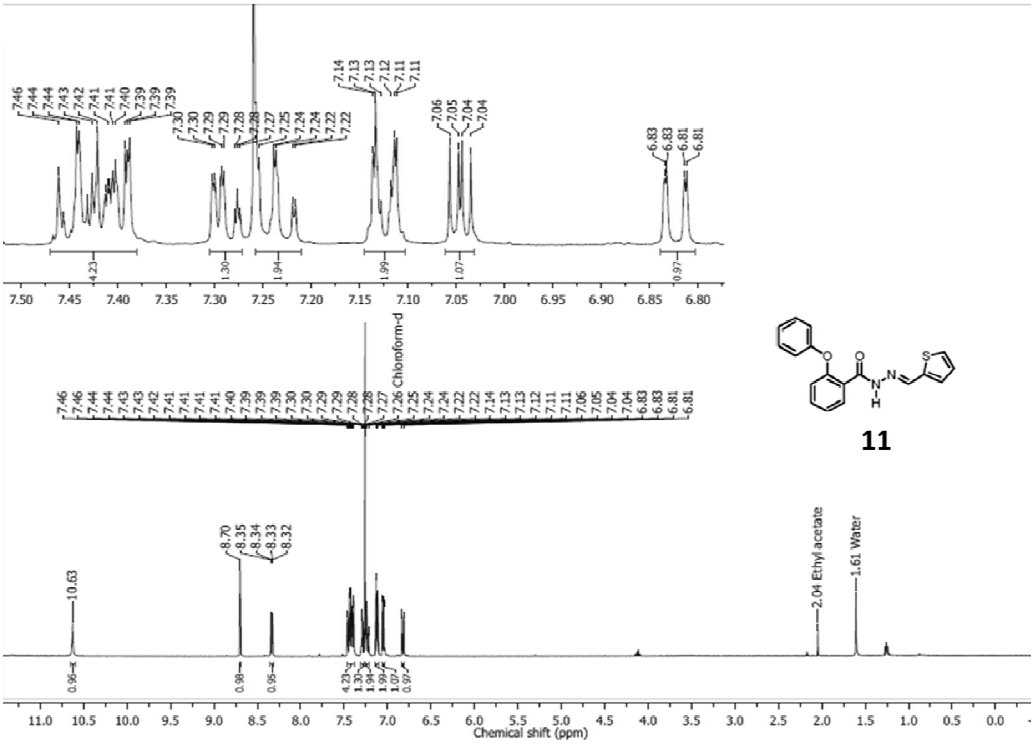


**Figure A19:** $^{1}$H NMR spectra of compound **11**

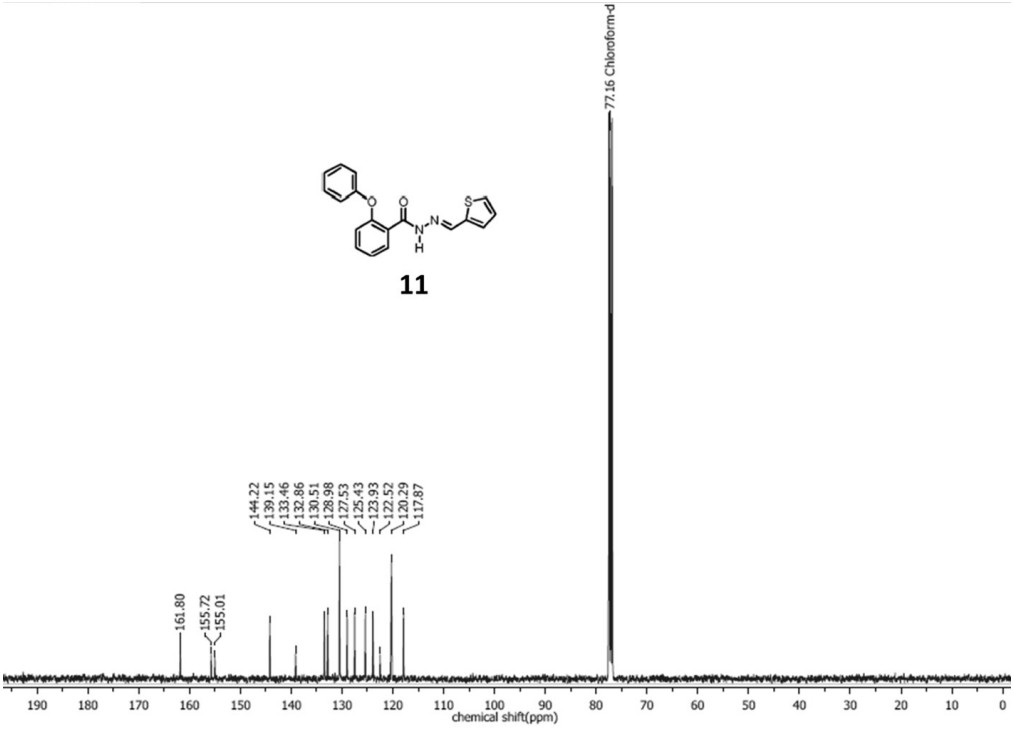


**Figure A20**: $^{13}$C NMR spectra of compound **11**

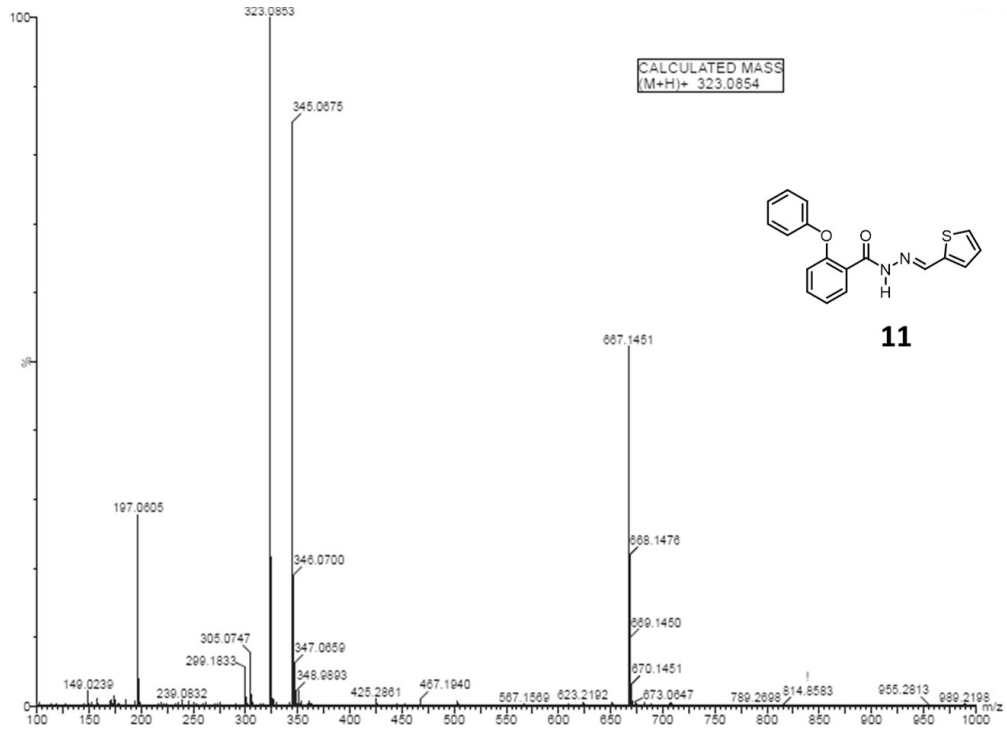


**Figure A21:** HR-MS spectra of compound **11**

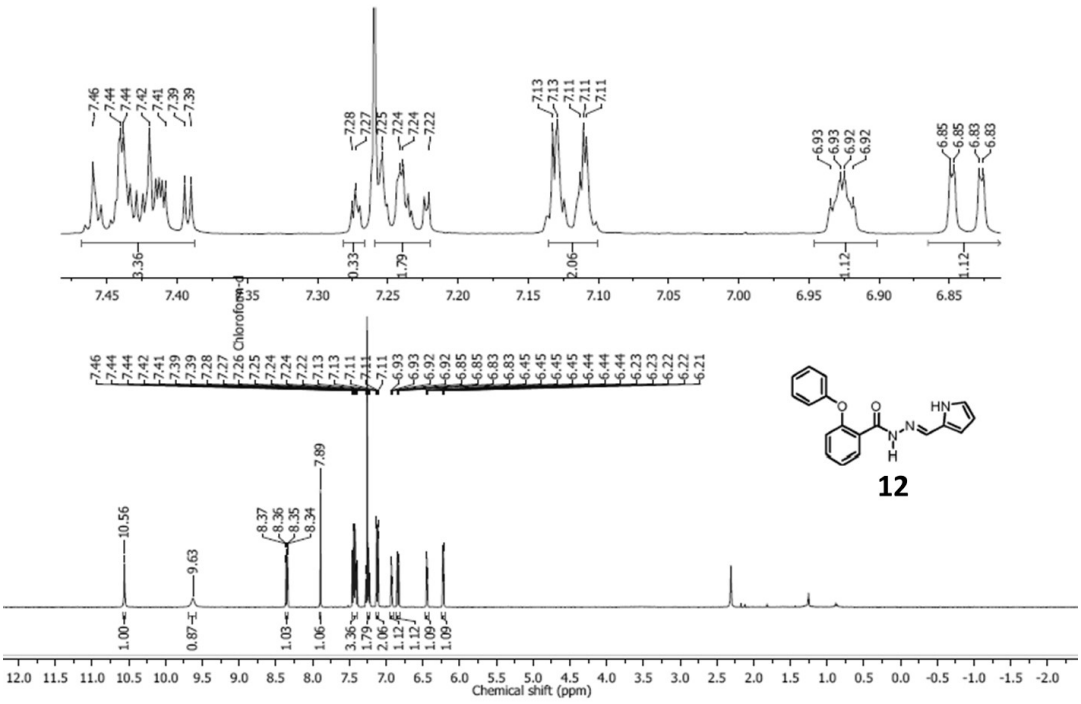


**FigureA22:** $^{1}$H NMR spectra of compound **12**

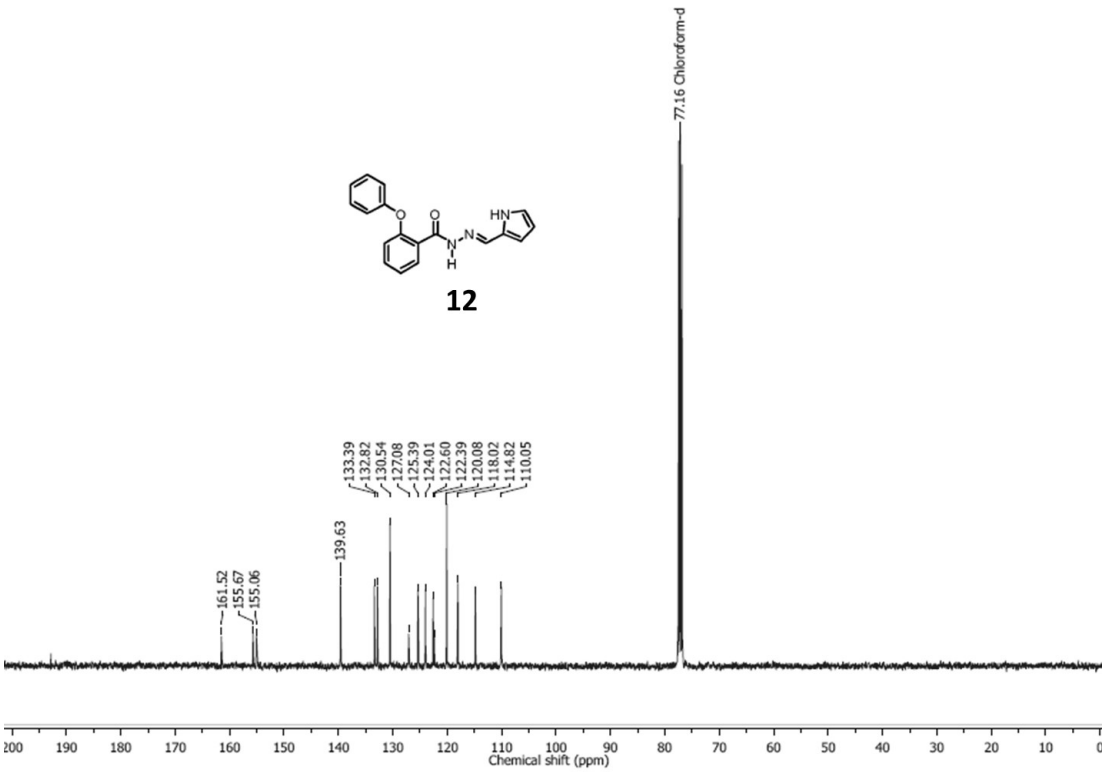


**Figure A23:** $^{13}$C NMR spectra of compound **12**

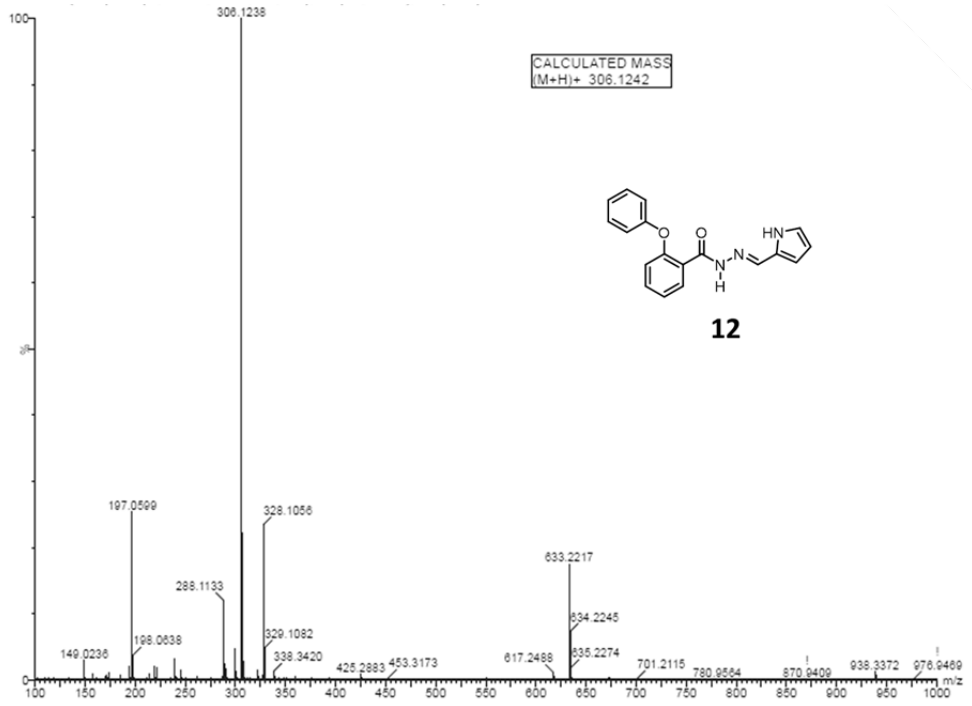


**Figure A24:** HR-MS spectra of compound **12**

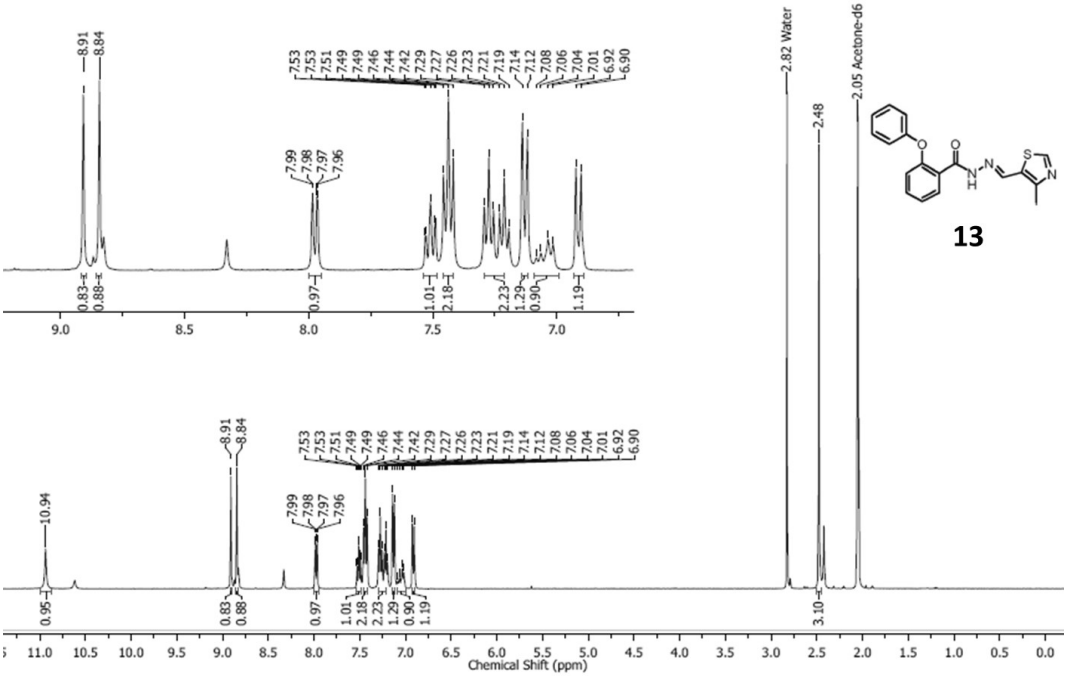


**Figure A25:** $^{1}$H NMR spectra of compound **13**

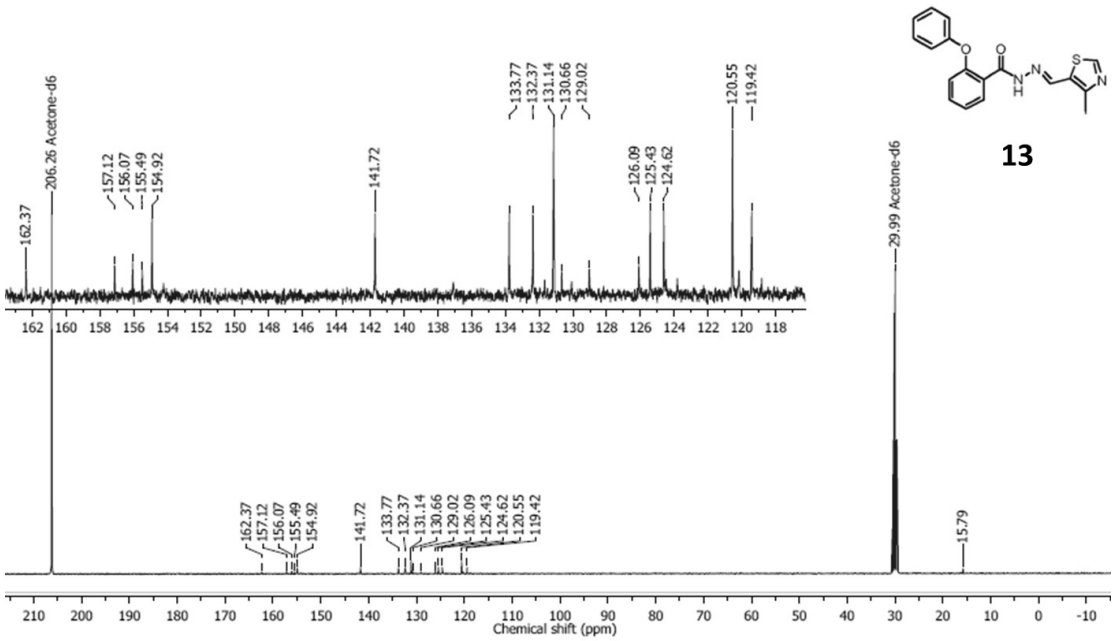


**Figure A26:** $^{13}$C NMR spectra of compound **13**

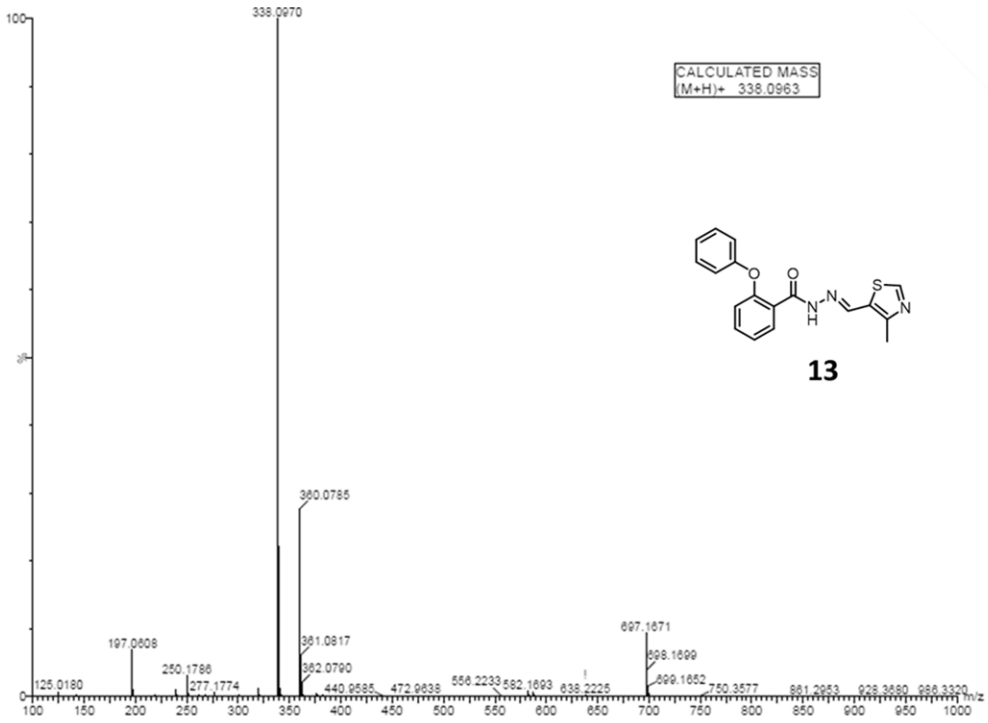


**Figure A27:** HR-MS spectra of compound **13**

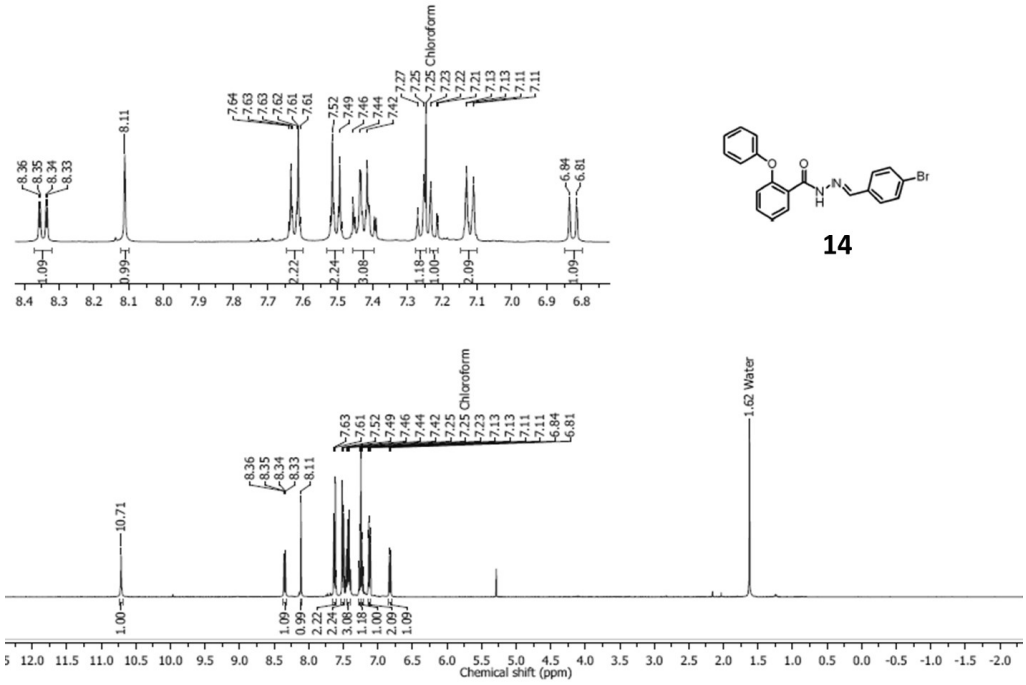


**Figure A28:** $^{1}$H NMR spectra of compound **14**

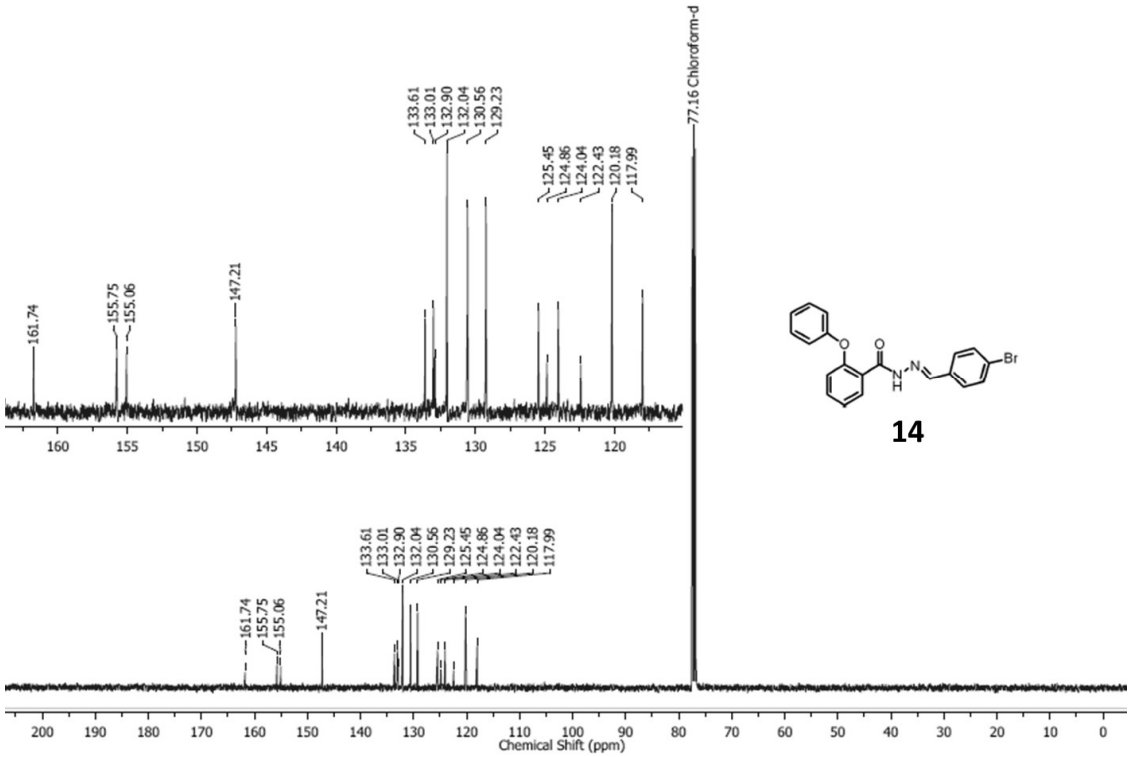


**Figure A29:** $^{13}$C NMR spectra of compound **14**

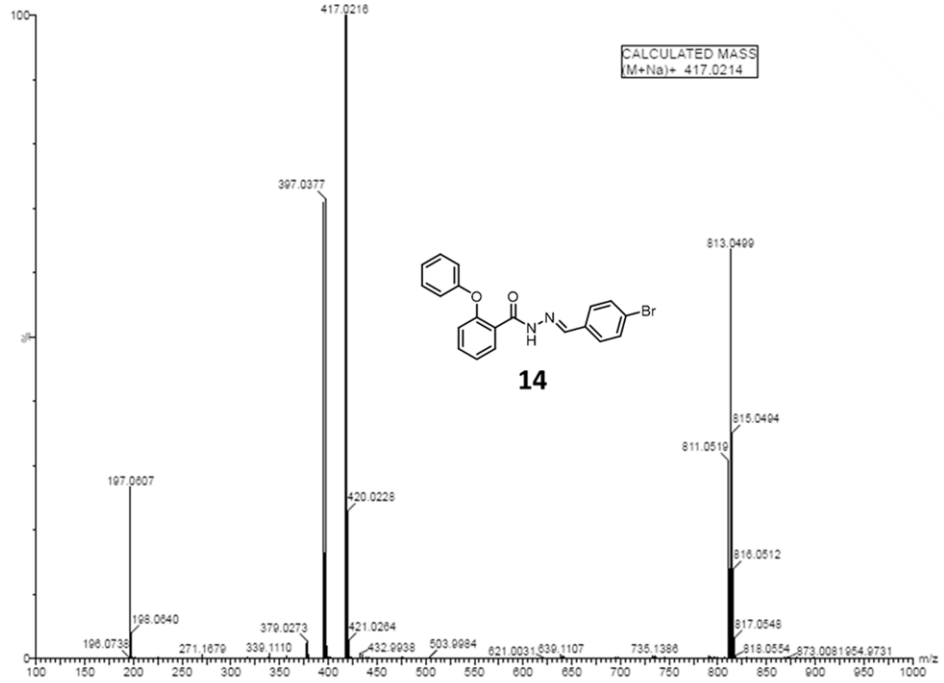


**Figure A30:** HR-MS spectra of compound **14**

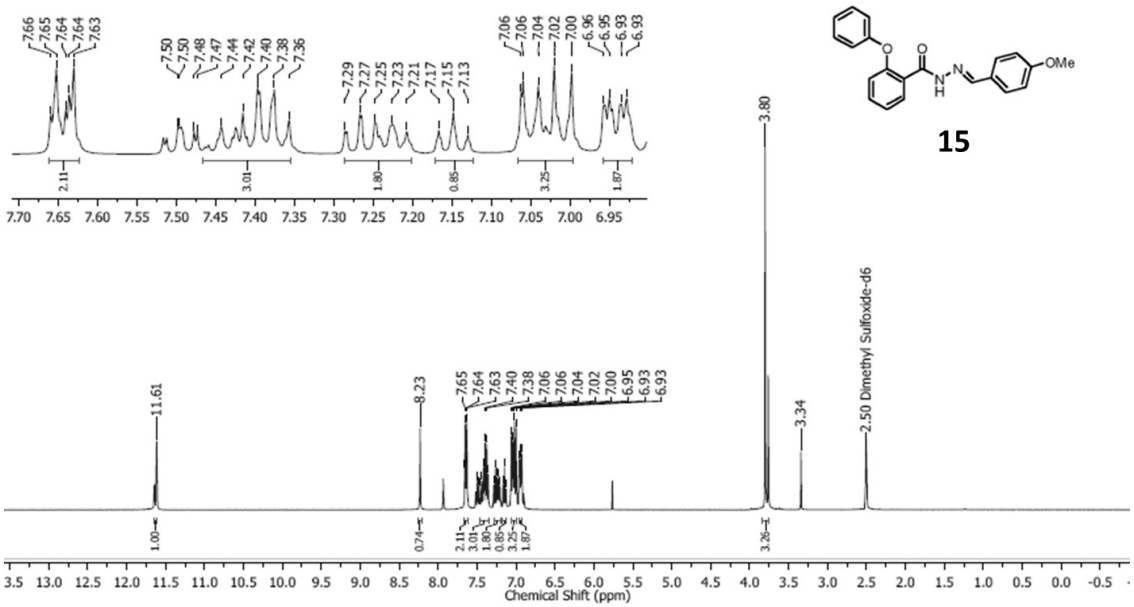


**Figure A31:** $^{1}$H NMR spectra of compound **15**

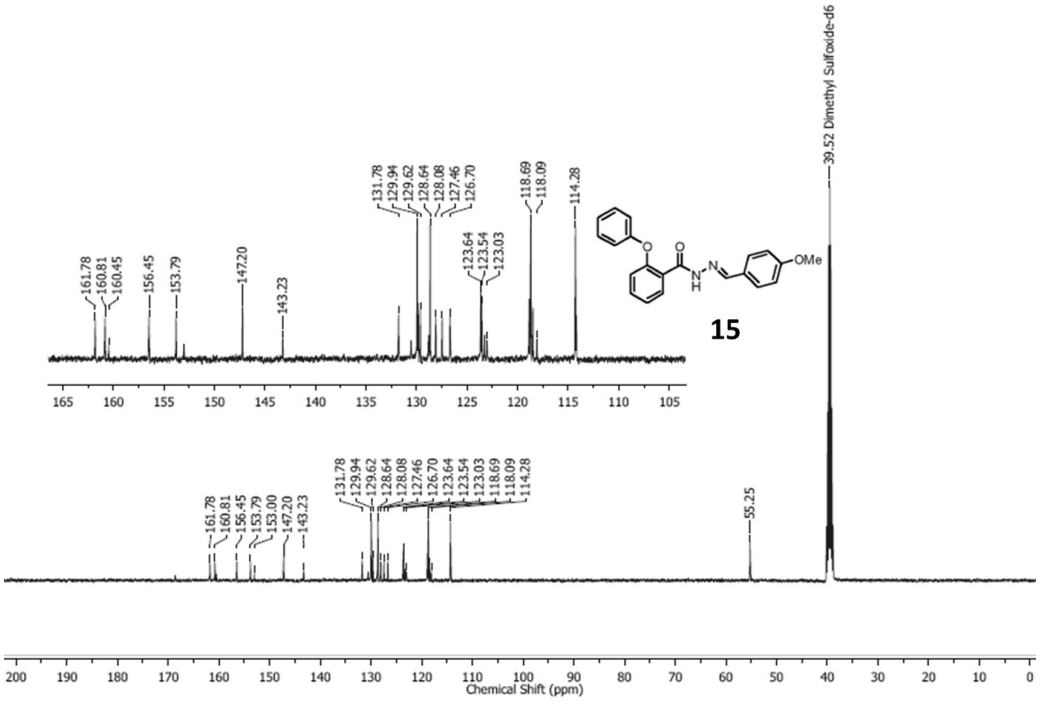


**Figure A32:** $^{13}$C NMR spectra of compound **15**

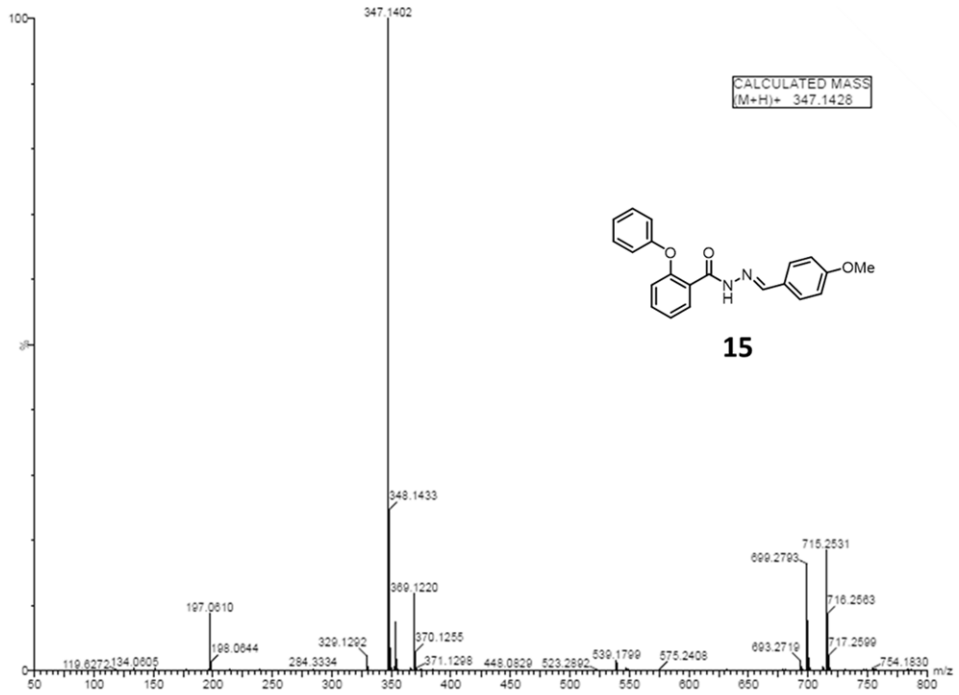


**Figure A33:** HR-MS spectra of compound **15**

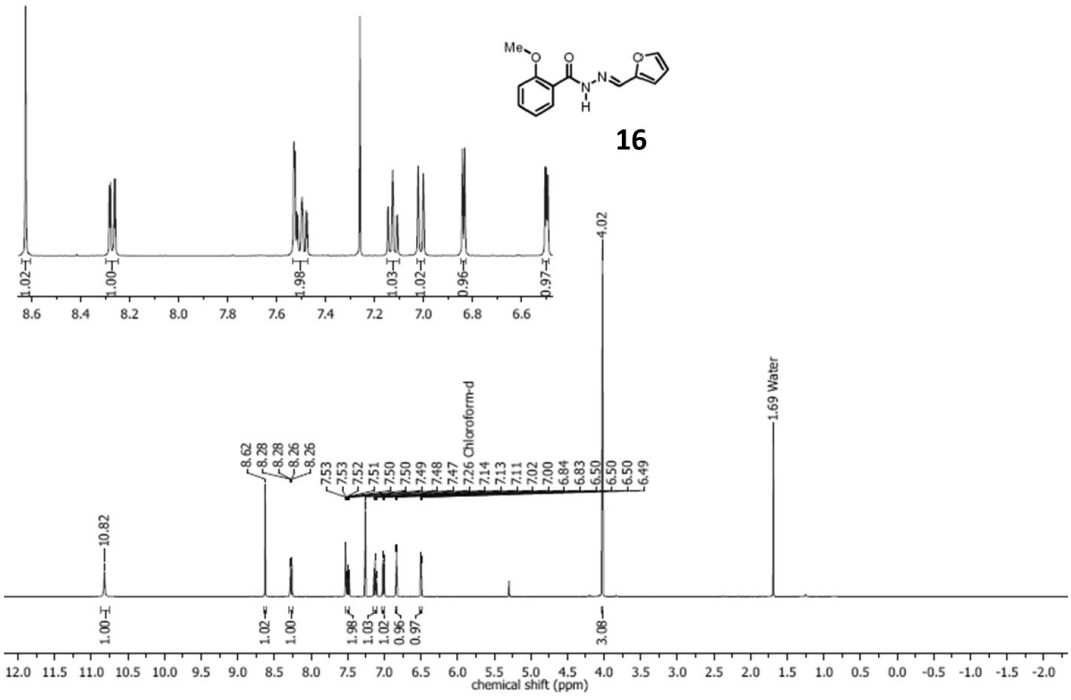


**Figure A34:** $^{1}$H NMR spectra of compound **16**

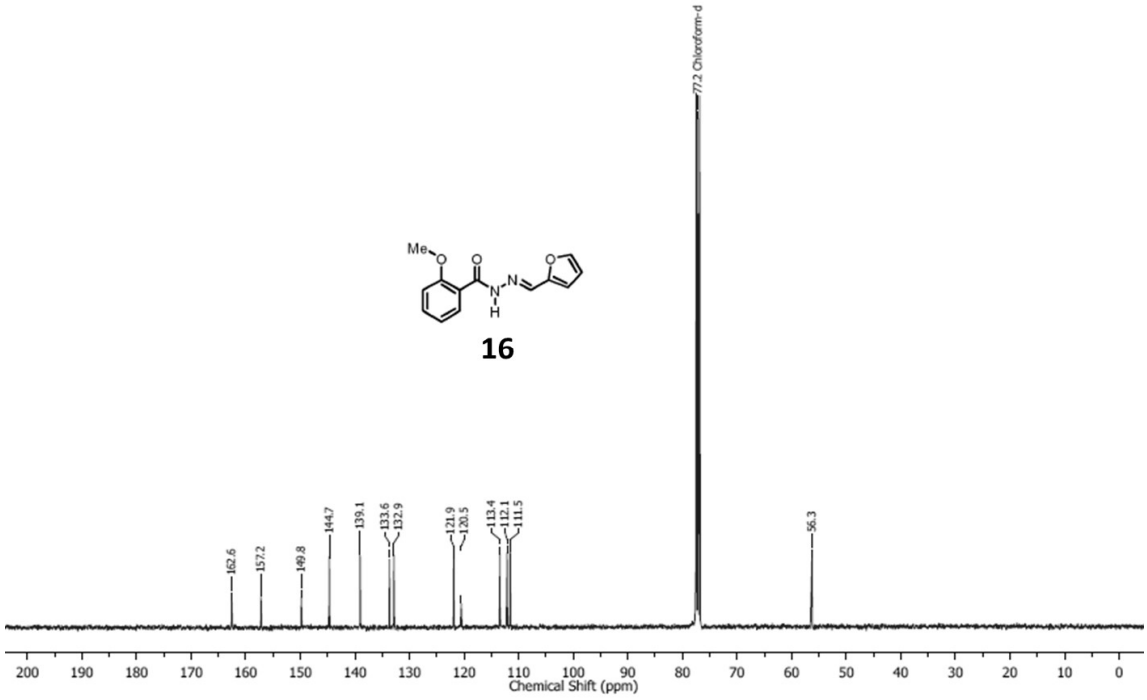


**Figure A35:** $^{13}$C NMR spectra of compound **16**

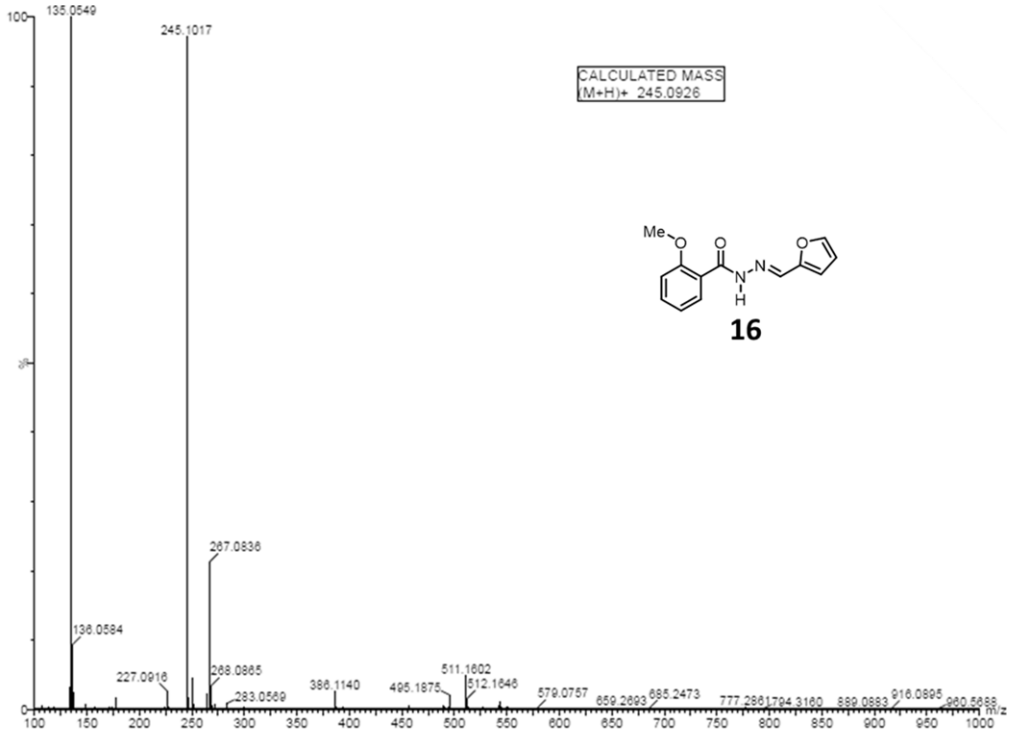


**Figure A36:** HR-MS spectra of compound **16**

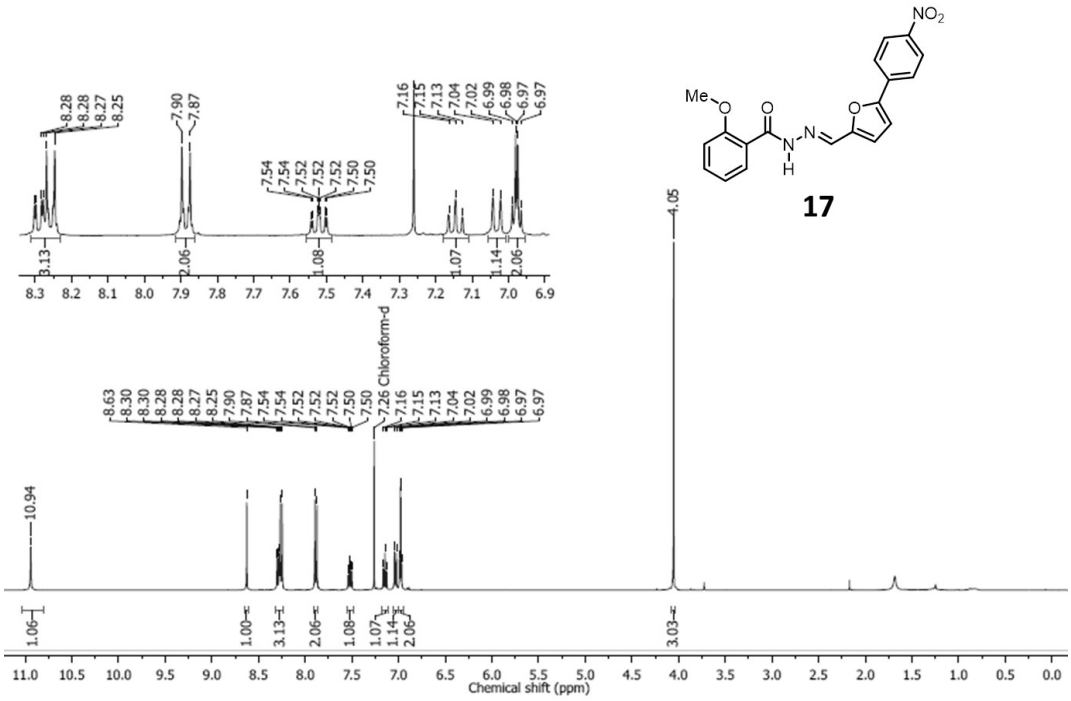


**Figure A37:** $^{1}$H NMR spectra of compound **17**

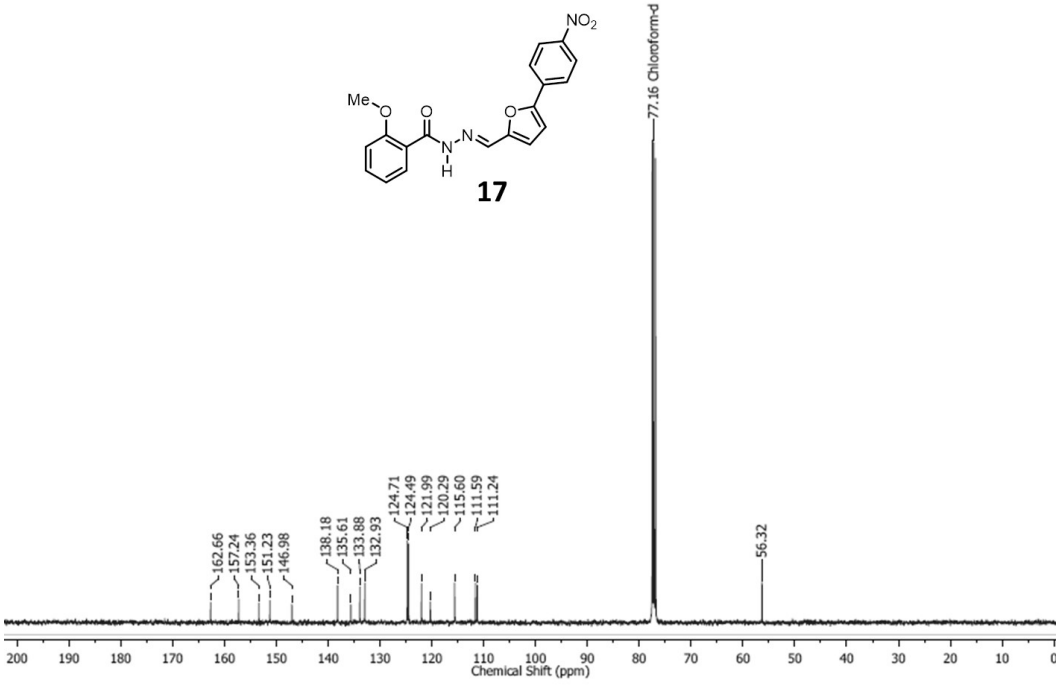


**Figure A38:** $^{13}$C NMR spectra of compound **17**

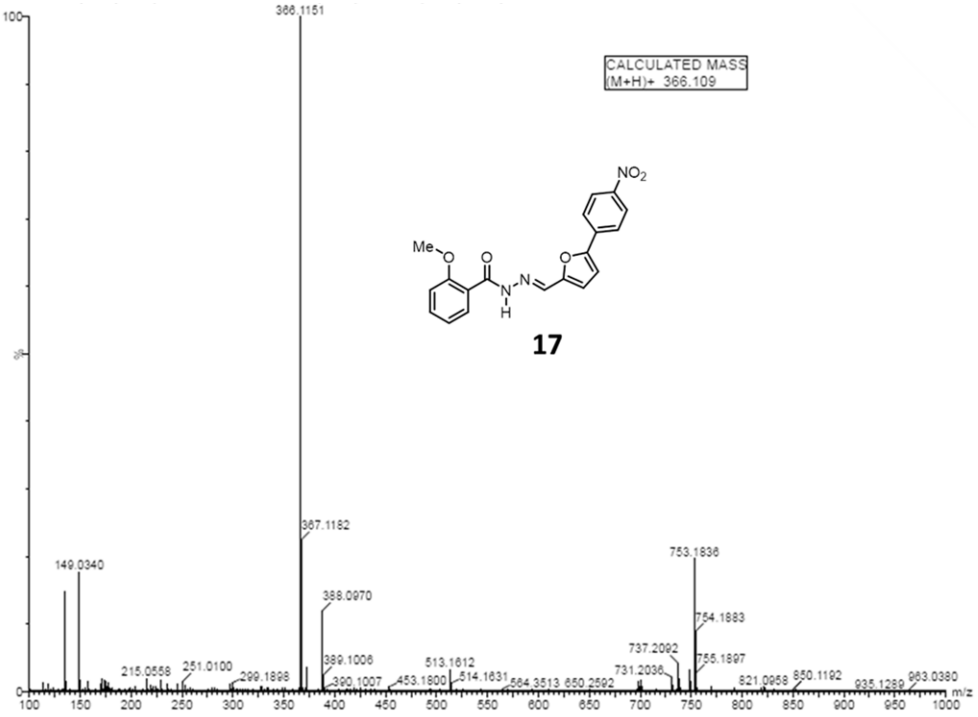


**Figure A39:** HR-MS spectra of compound **17**

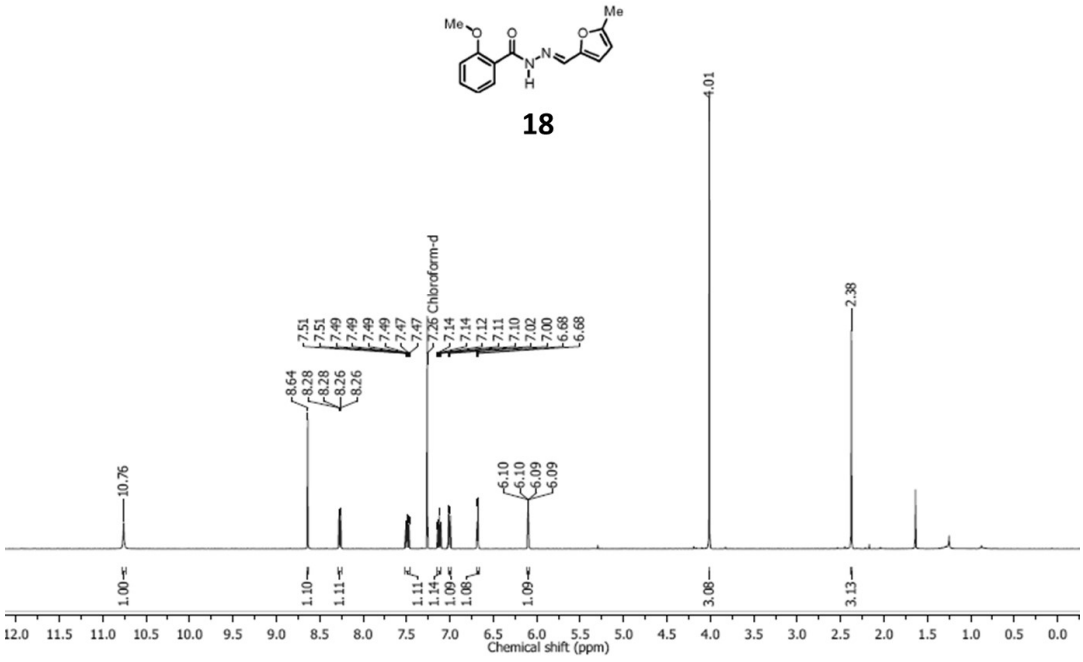


**Figure A40:** $^{1}$H NMR spectra of compound **18**

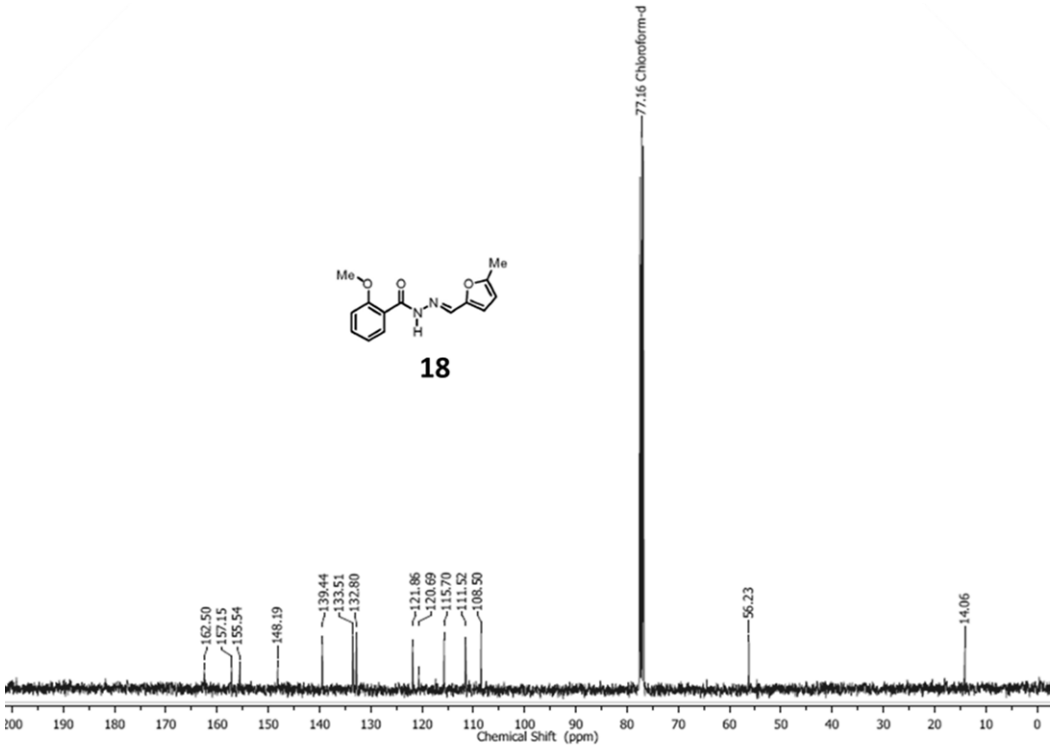


**Figure A41:** $^{13}$C NMR spectra of compound **18**

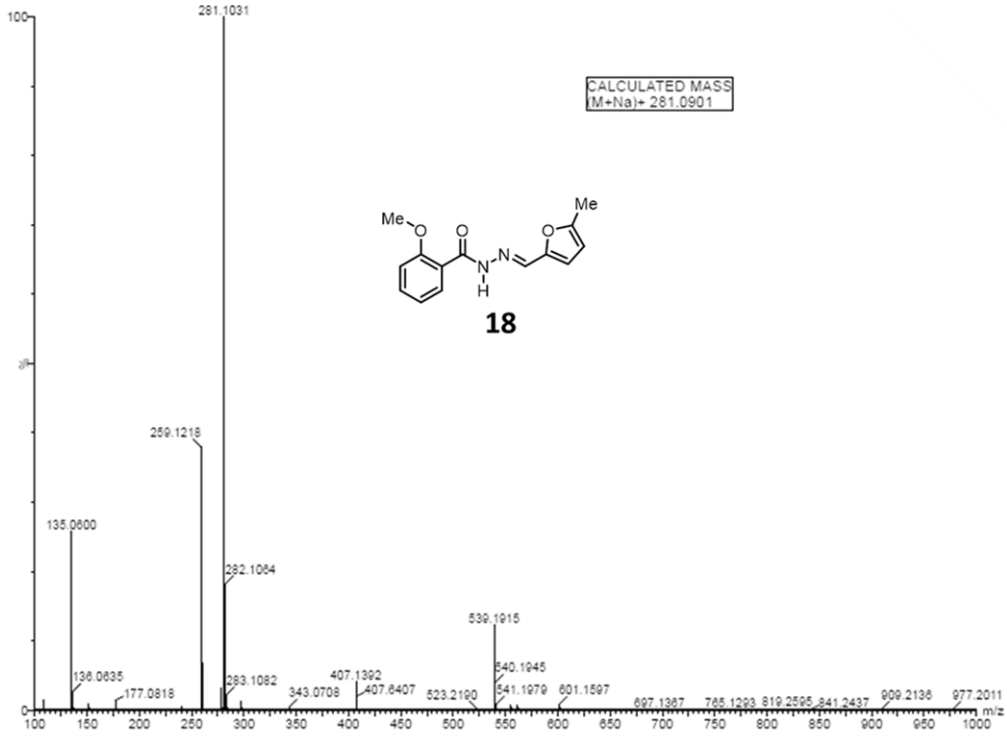


**Figure A42**: HR-MS spectra of compound **18**

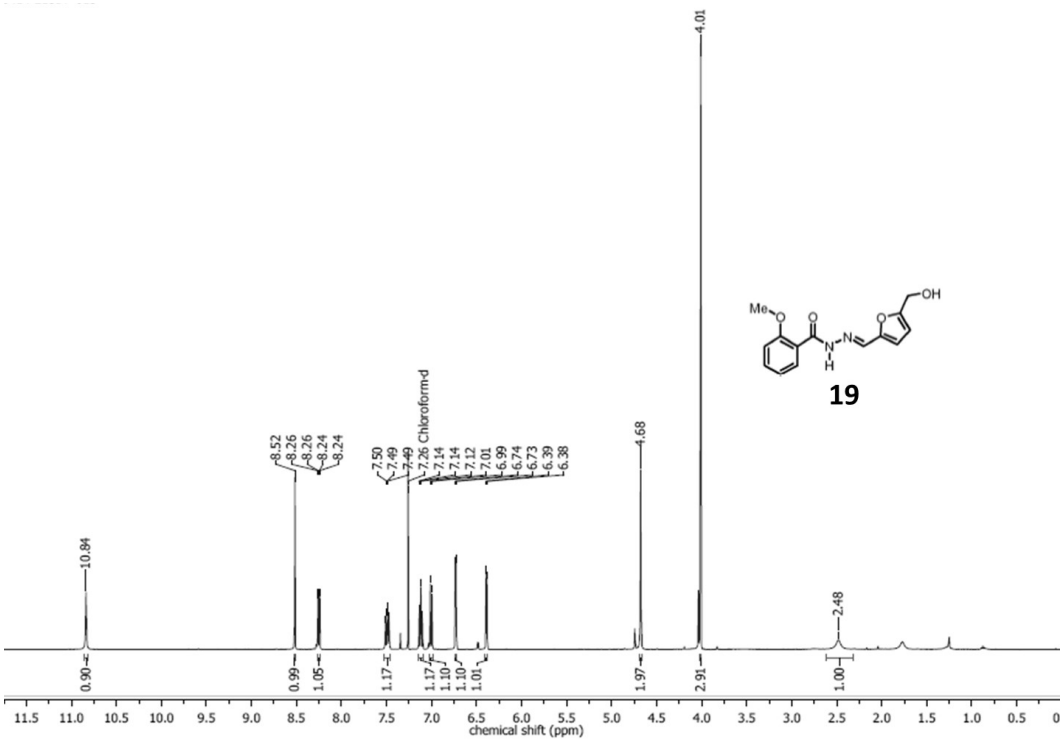


**Figure A43:** $^{1}$H NMR spectra of compound **19**

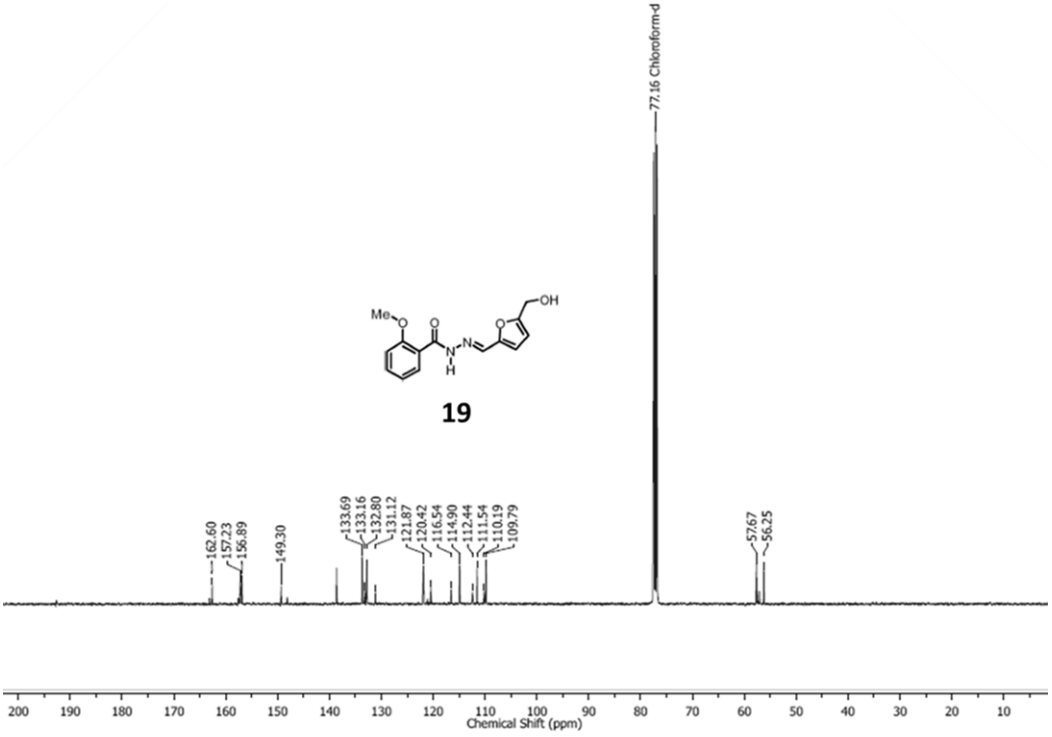


**Figure A44:** $^{13}$C NMR spectra of compound **19**

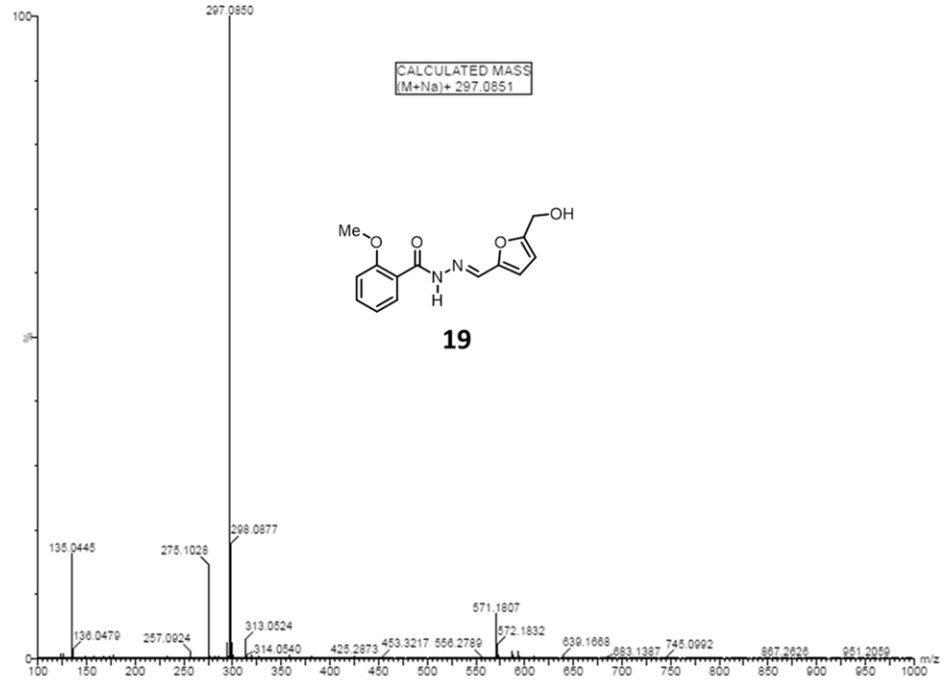


**Figure A45:** HR-MS spectra of compound **19**

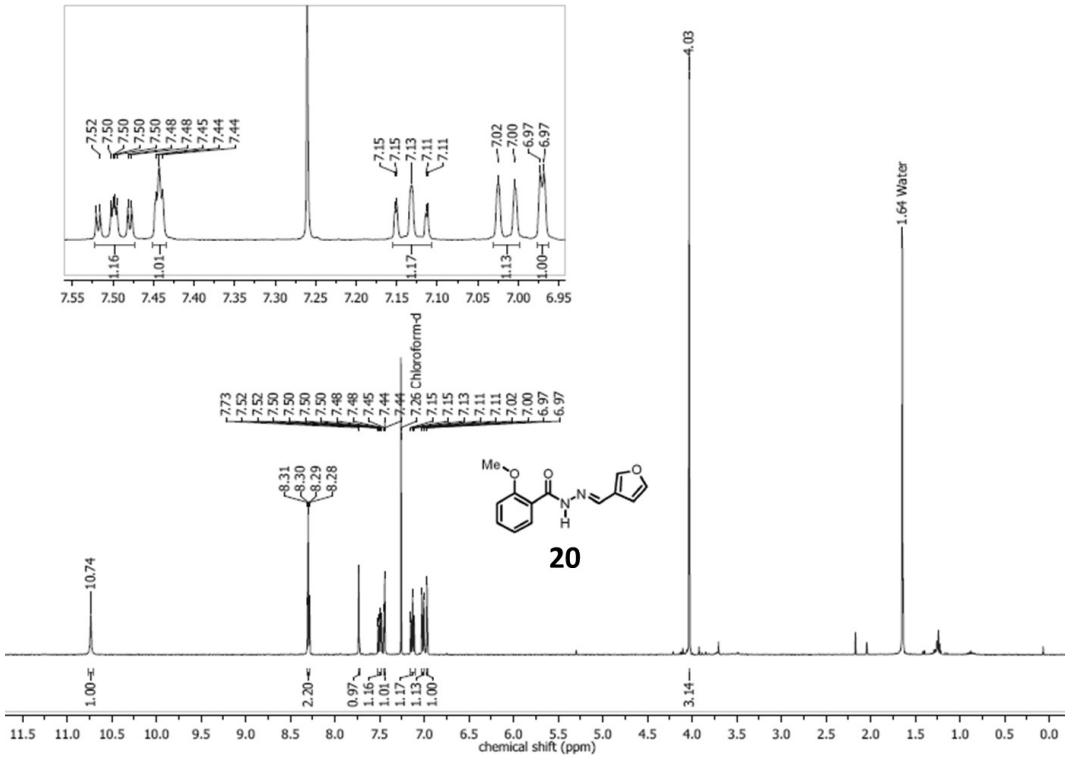


**Figure A46:** $^{1}$H NMR spectra of compound **20**

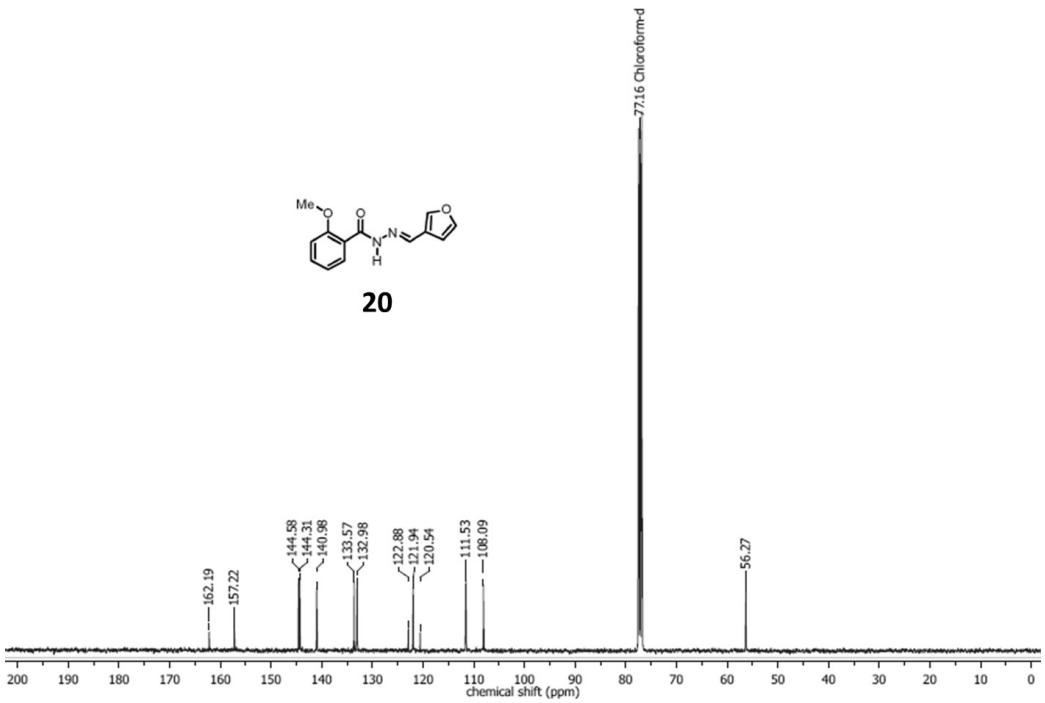


**Figure A47:** $^{13}$C NMR spectra of compound **20**

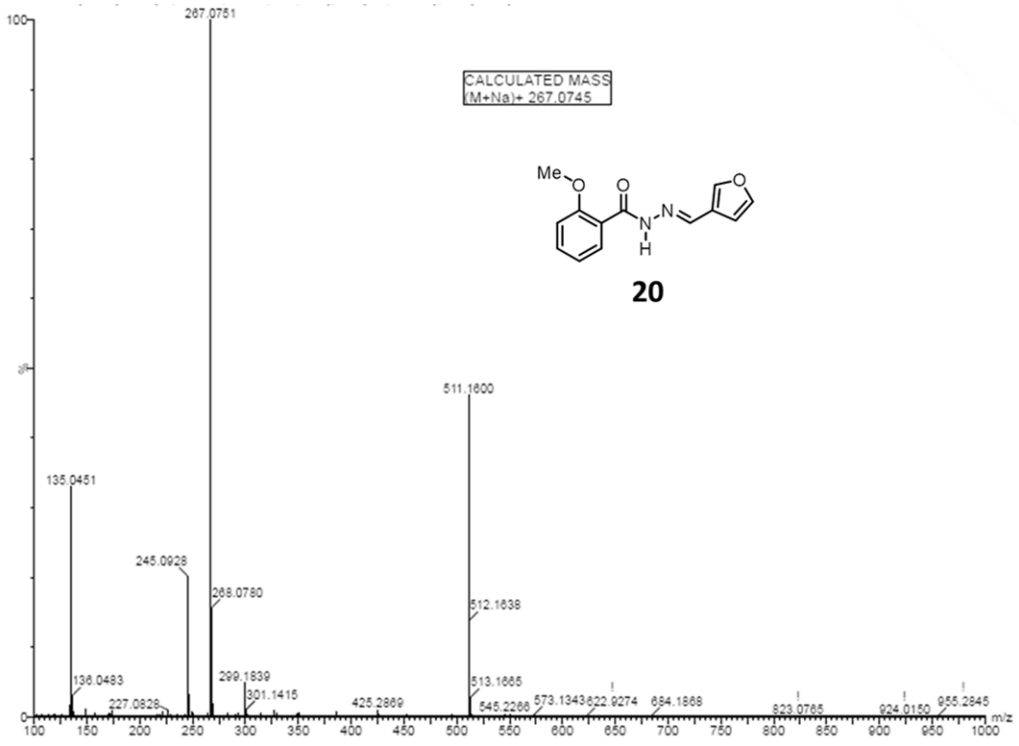


**Figure A48:** HR-MS spectra of compound **20**

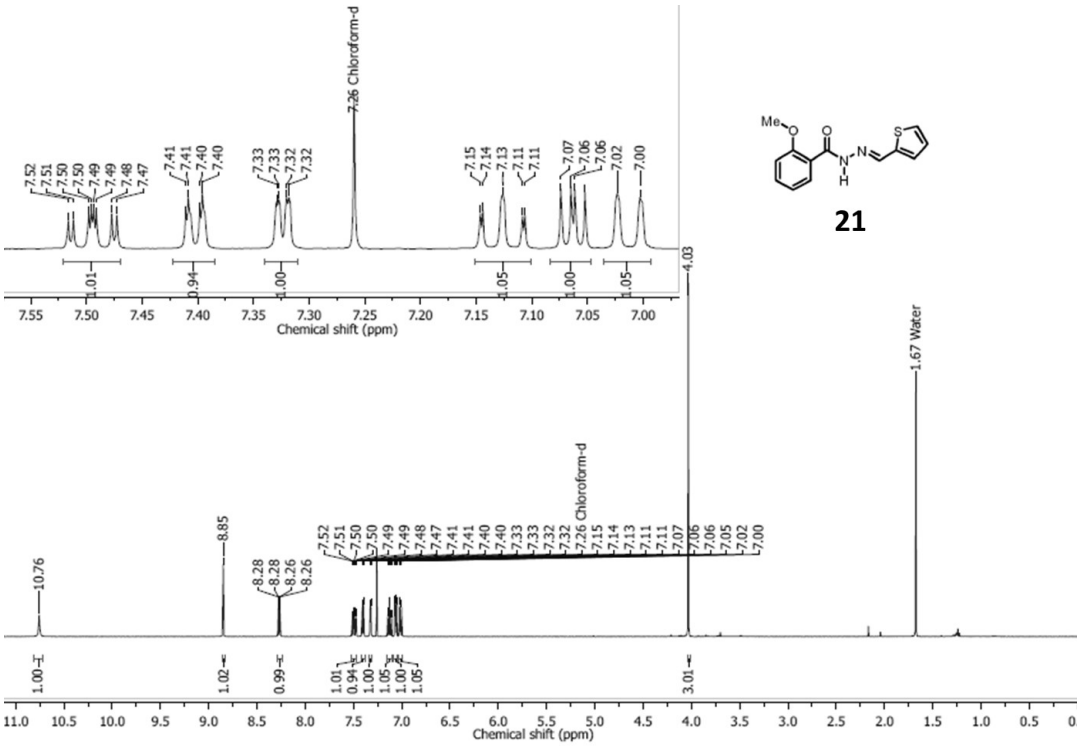


**Figure A49:** $^{1}$H NMR spectra of compound **21**

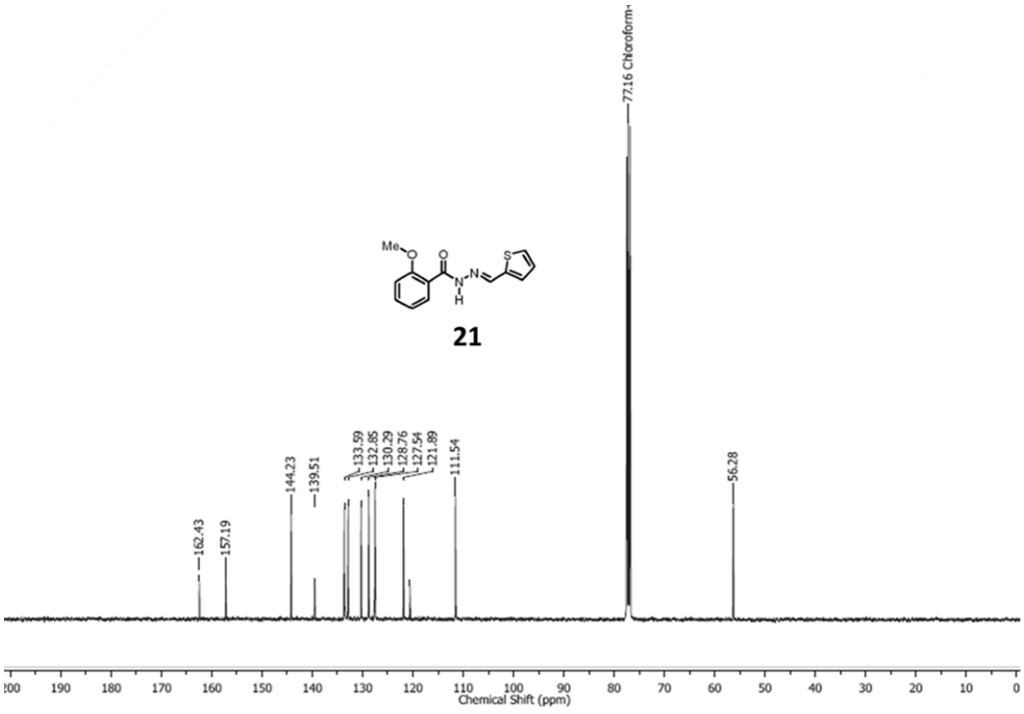


**Figure A50:** $^{13}$C NMR spectra of compound **21**

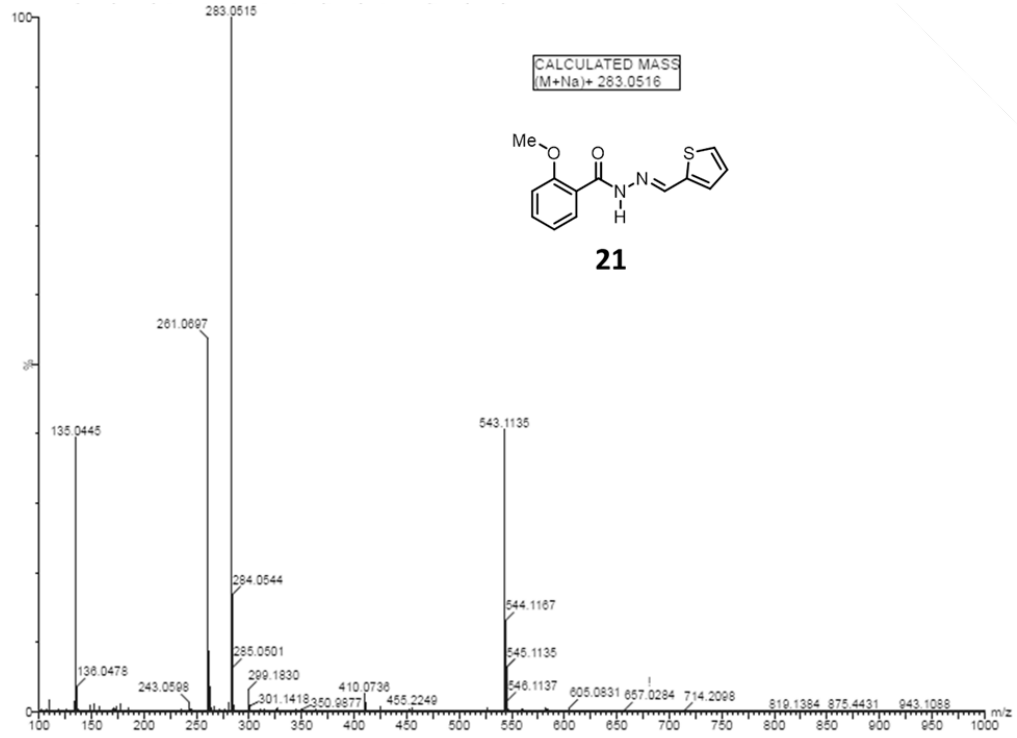


**Figure A51:** HR-MS spectra of compound **21**

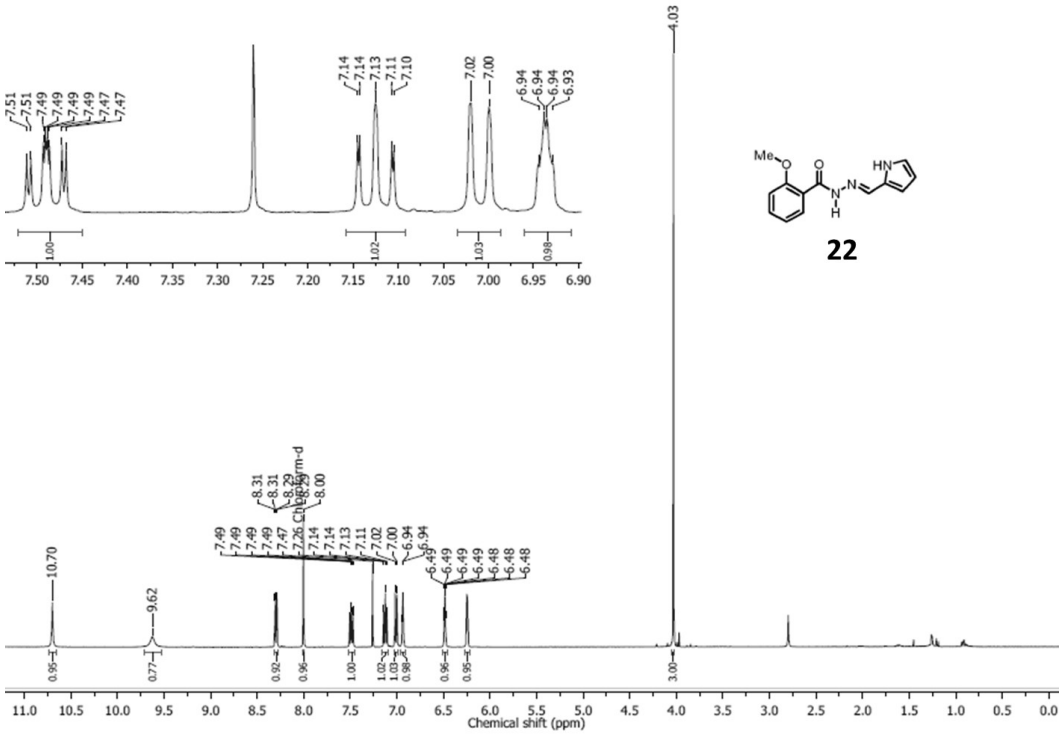


**Figure A52:** $^{1}$H NMR spectra of compound **22**

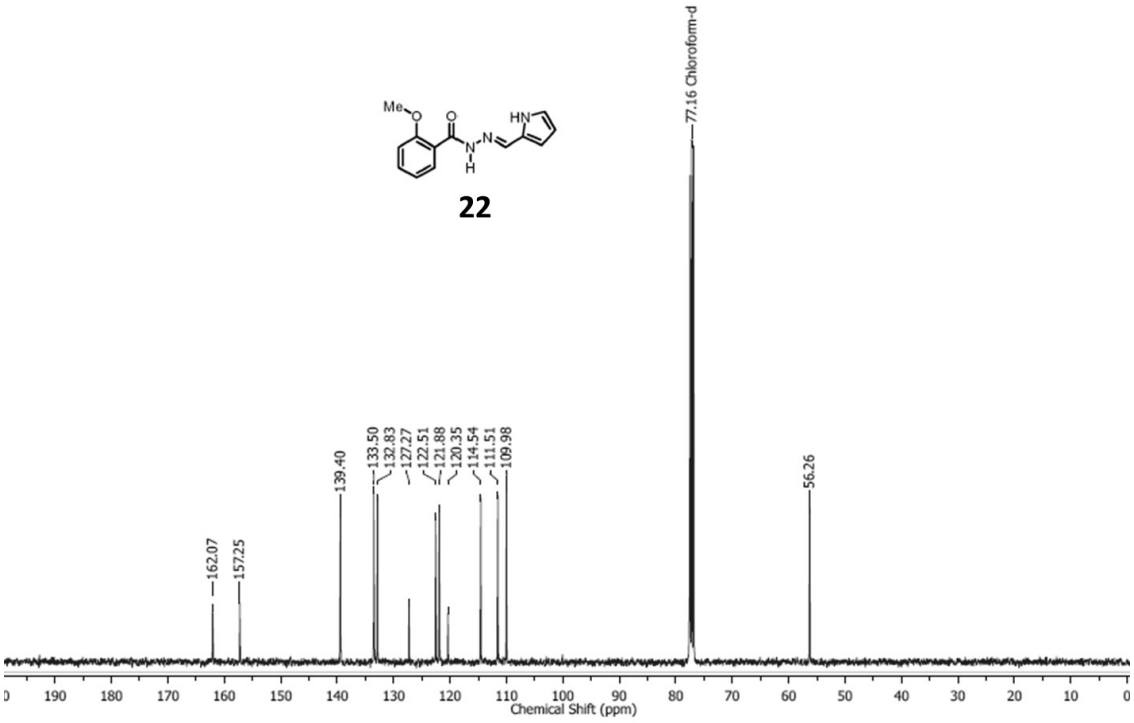


**Figure A53:** $^{13}$C NMR spectra of compound **22**

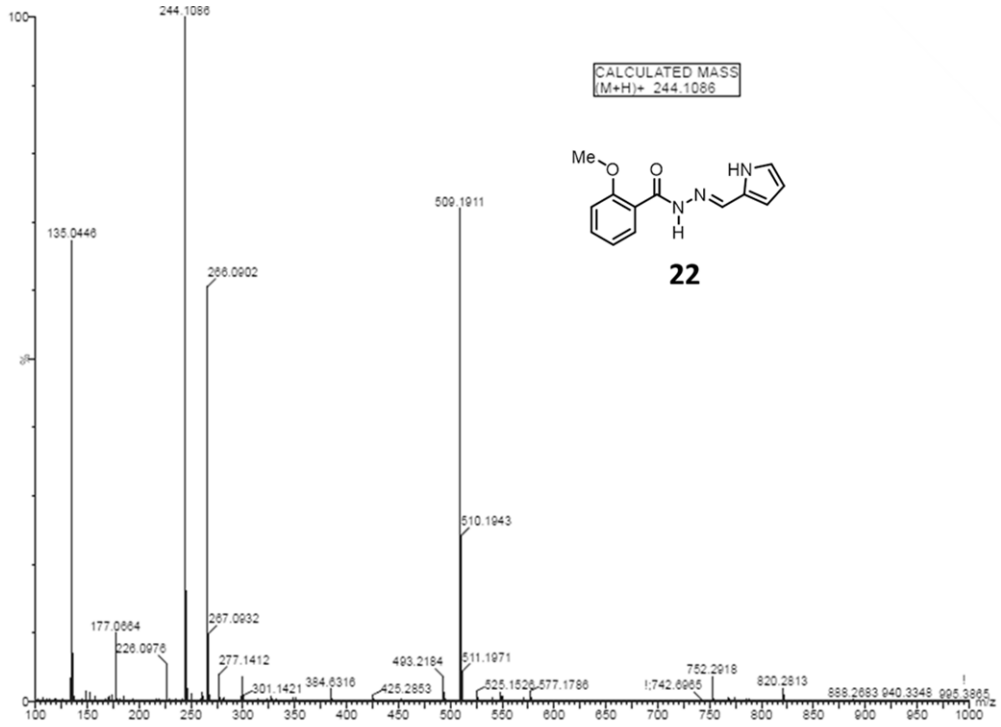


**Figure A54:** HR-MS spectra of compound **22**

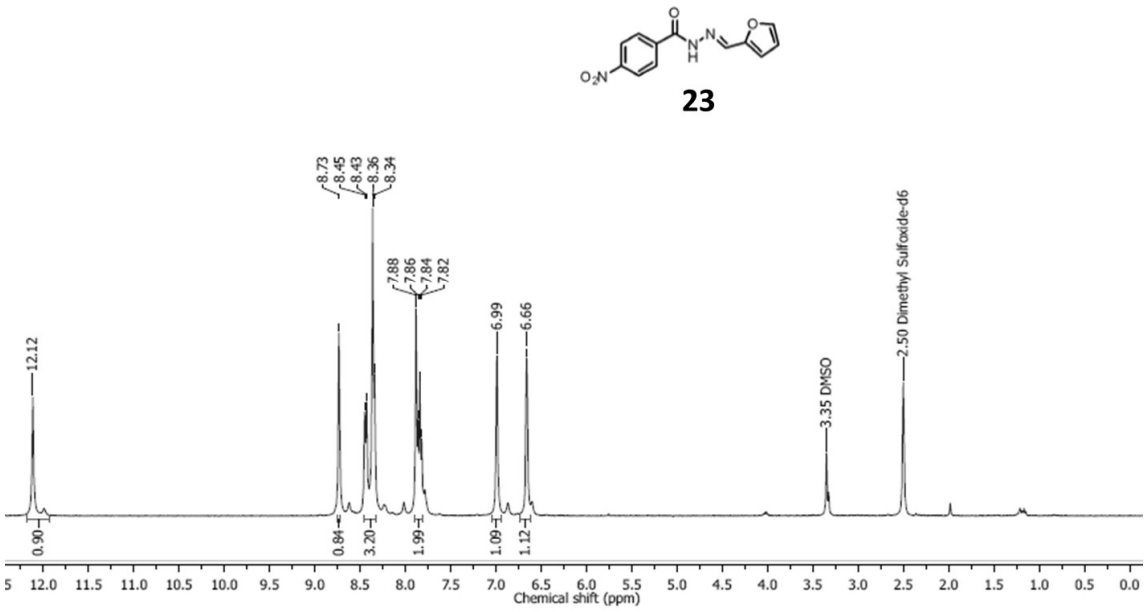


**Figure A55:** $^{1}$H NMR spectra of compound **23**

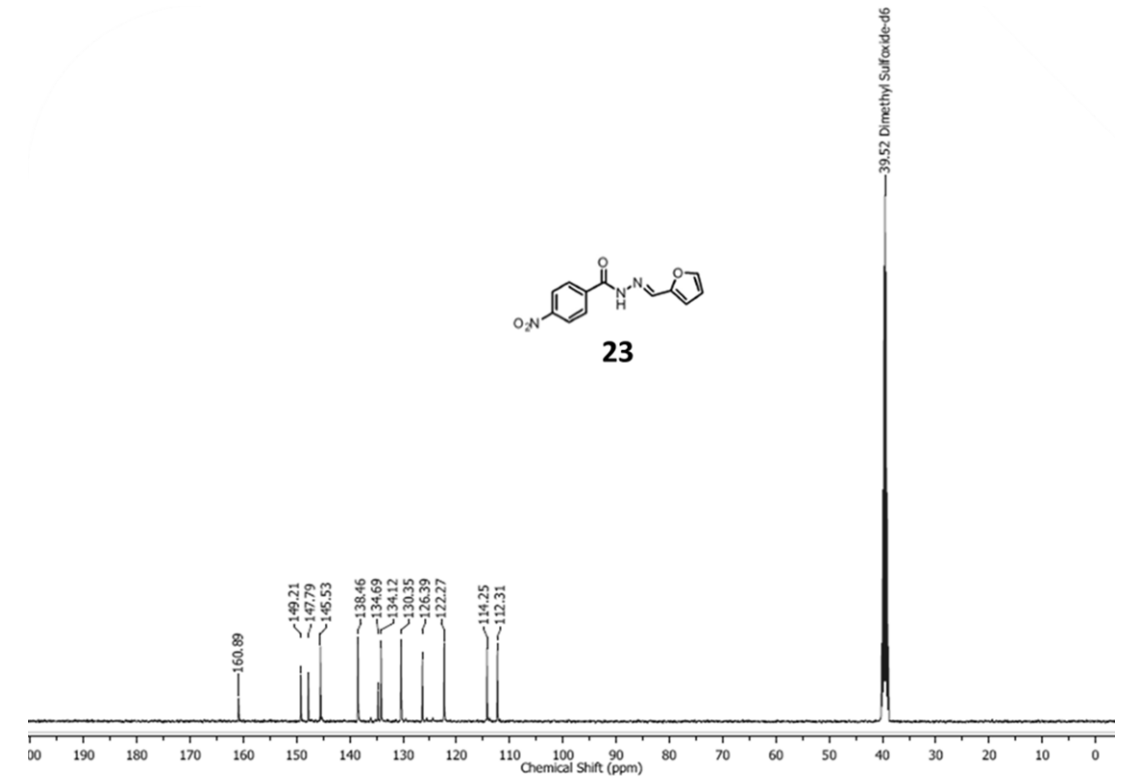


**Figure A56:** $^{13}$C NMR spectra of compound **23**

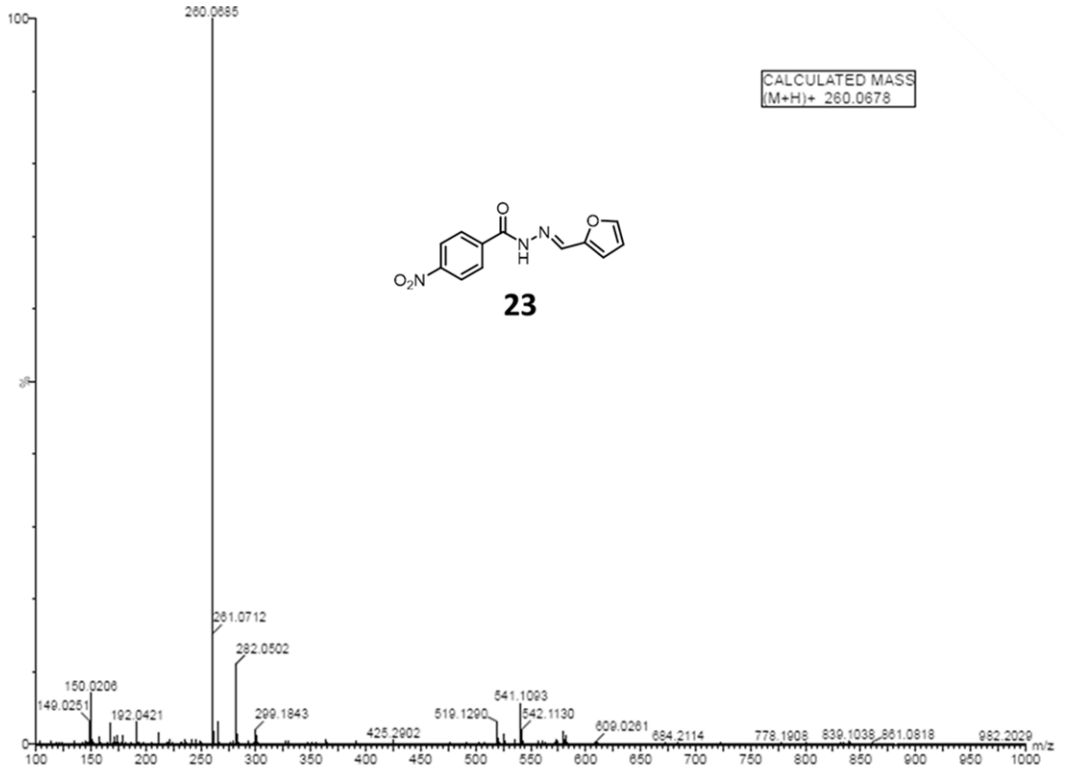


**Figure A57:** HR-MS spectra of compound **23**

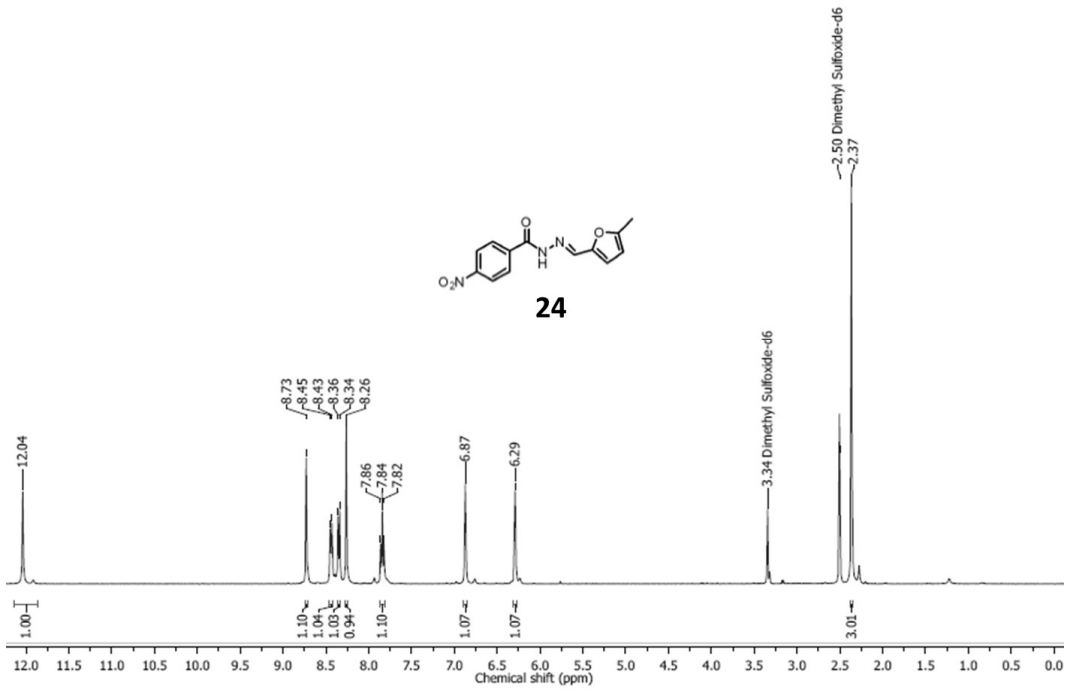


**Figure A58:** $^{1}$H NMR spectra of compound **24**

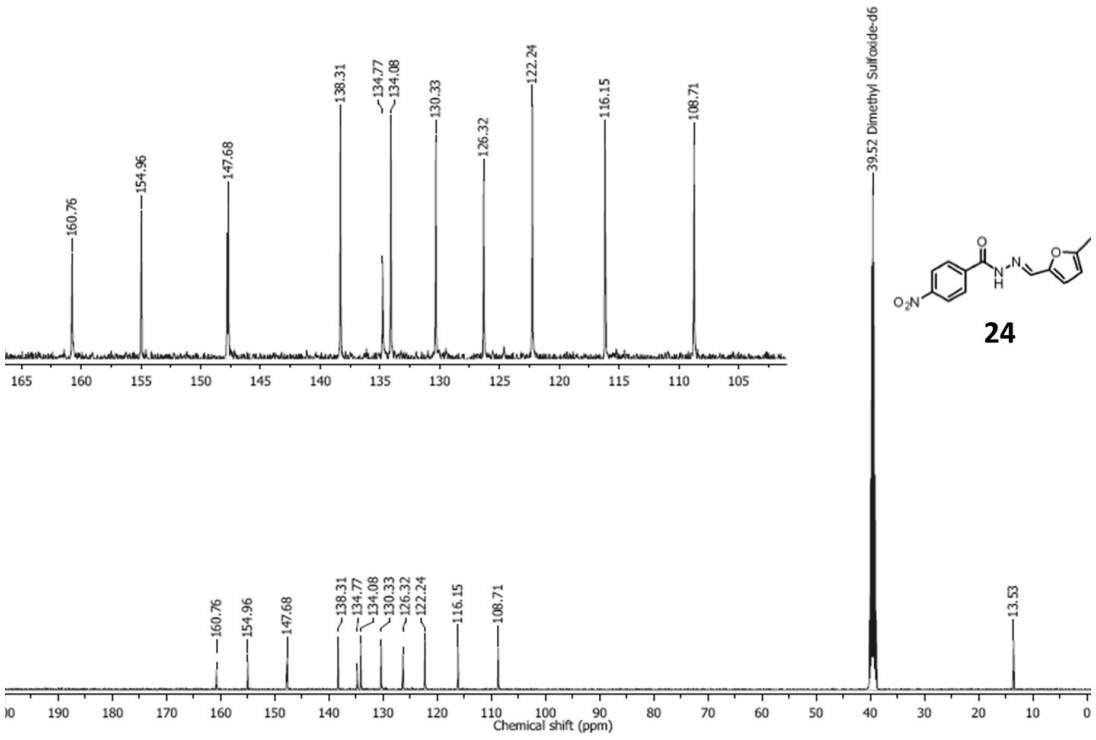


**Figure A59:** $^{13}$C NMR spectra of compound **24**

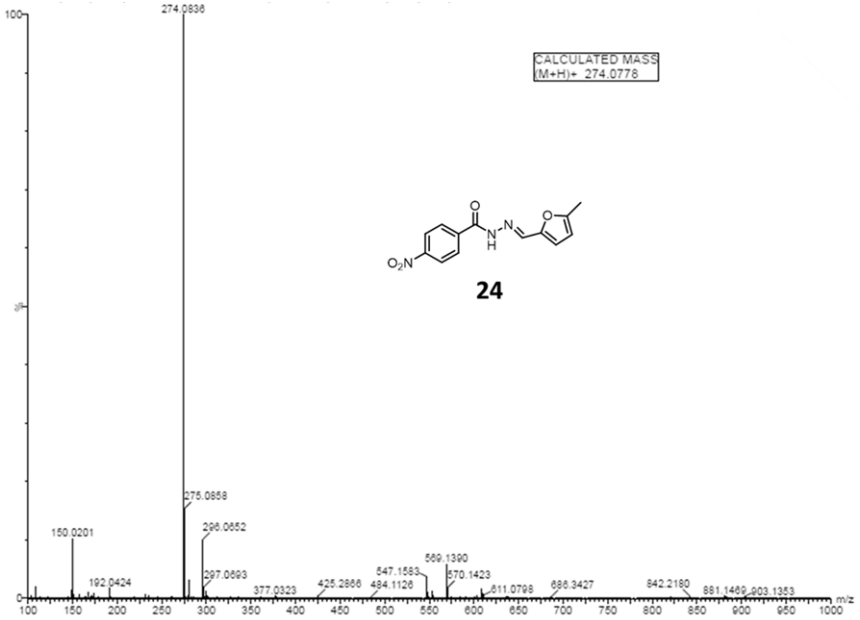


**Figure A60:** HR-MS spectra of compound **24**

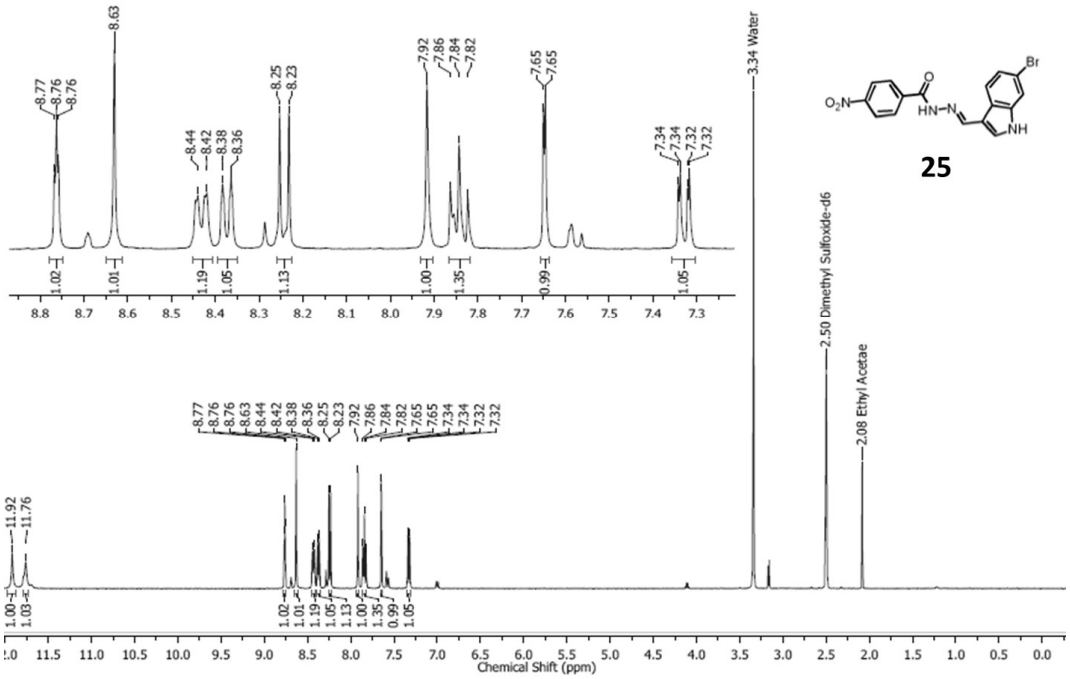


**Figure A61:** $^{1}$H NMR spectra of compound **25**

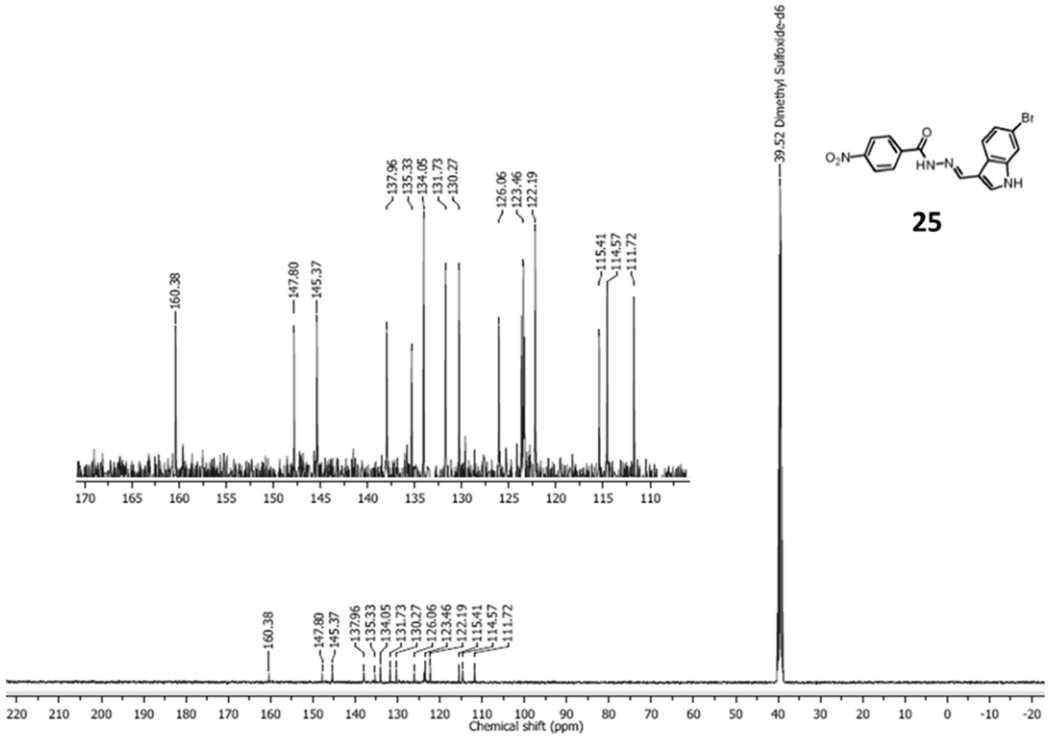


**Figure A62:** $^{13}$C NMR spectra of compound **25**

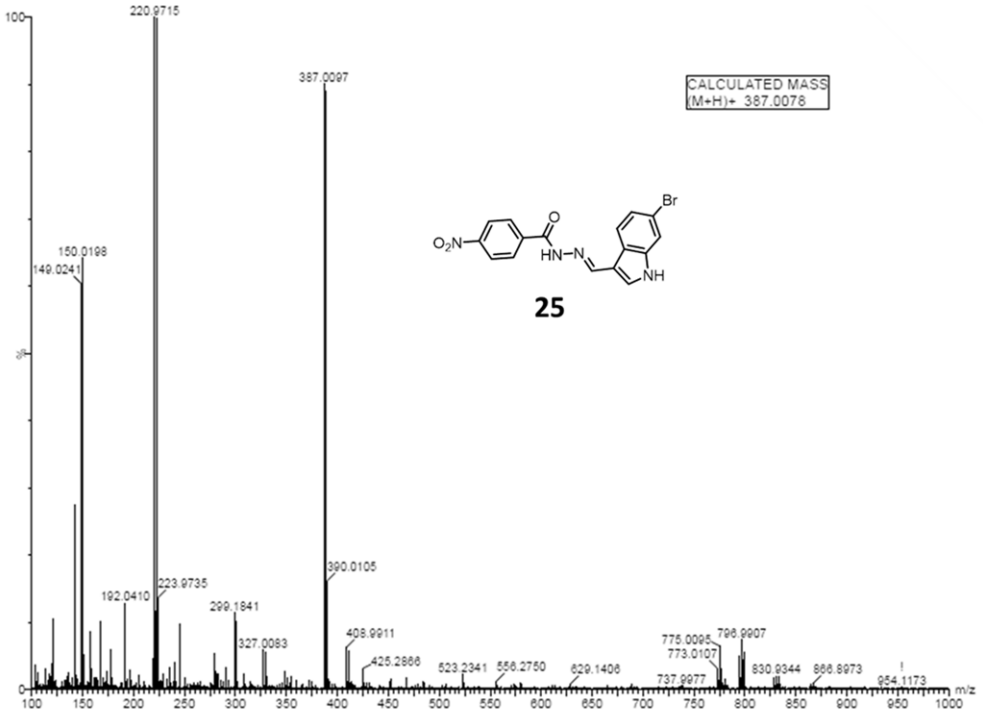


**Figure A63:** HR-MS spectra of compound **25**

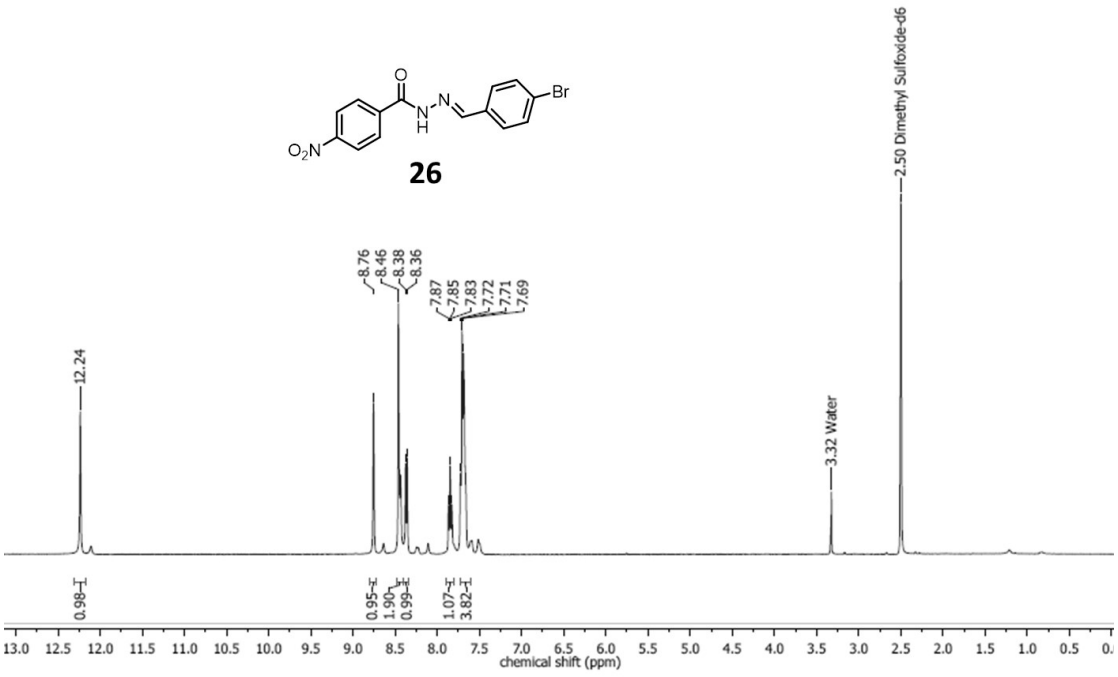


**Figure A64:** $^{1}$H NMR spectra of compound **26**

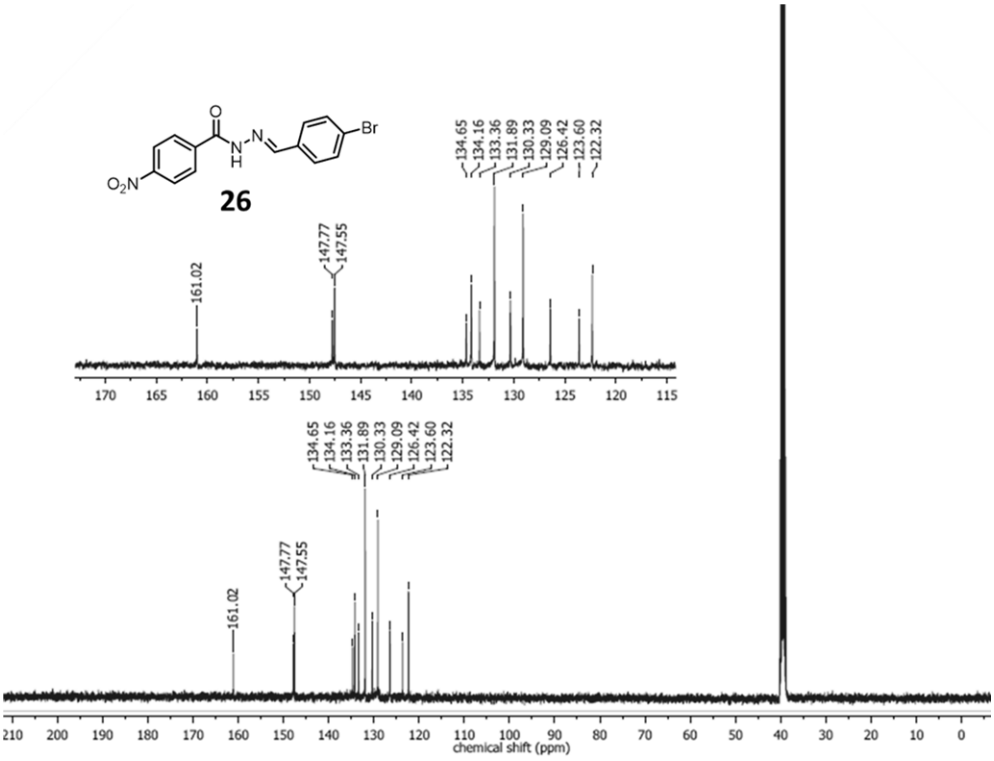


**Figure A65:** $^{13}$C NMR spectra of compound **26**

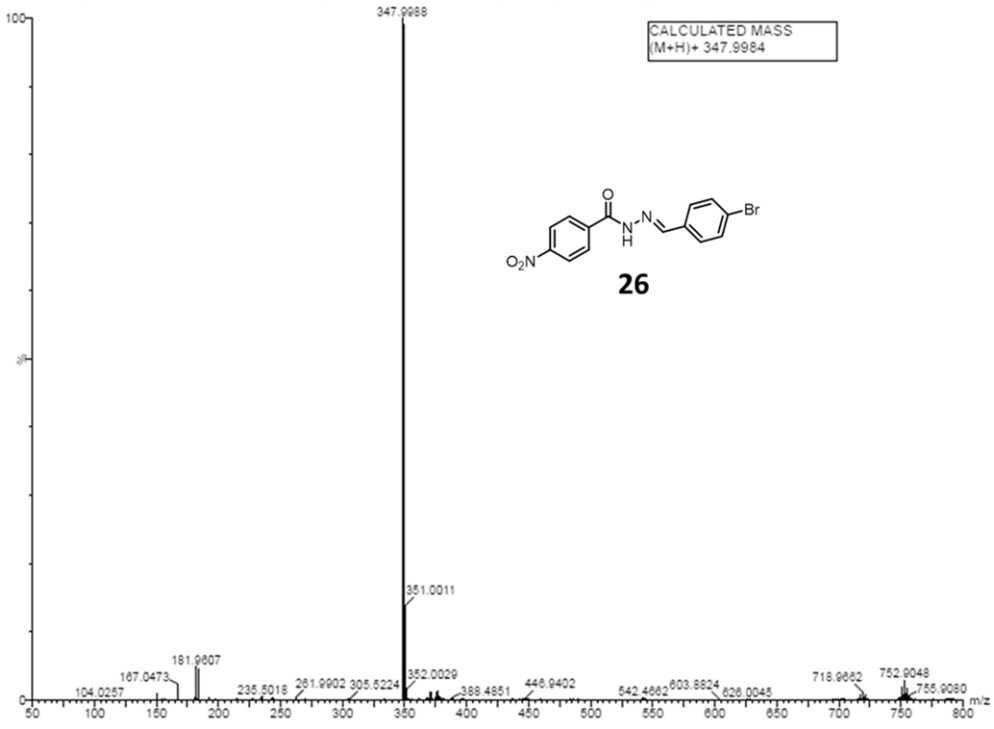


**Figure A66:** HR-MS spectra of compound **26**

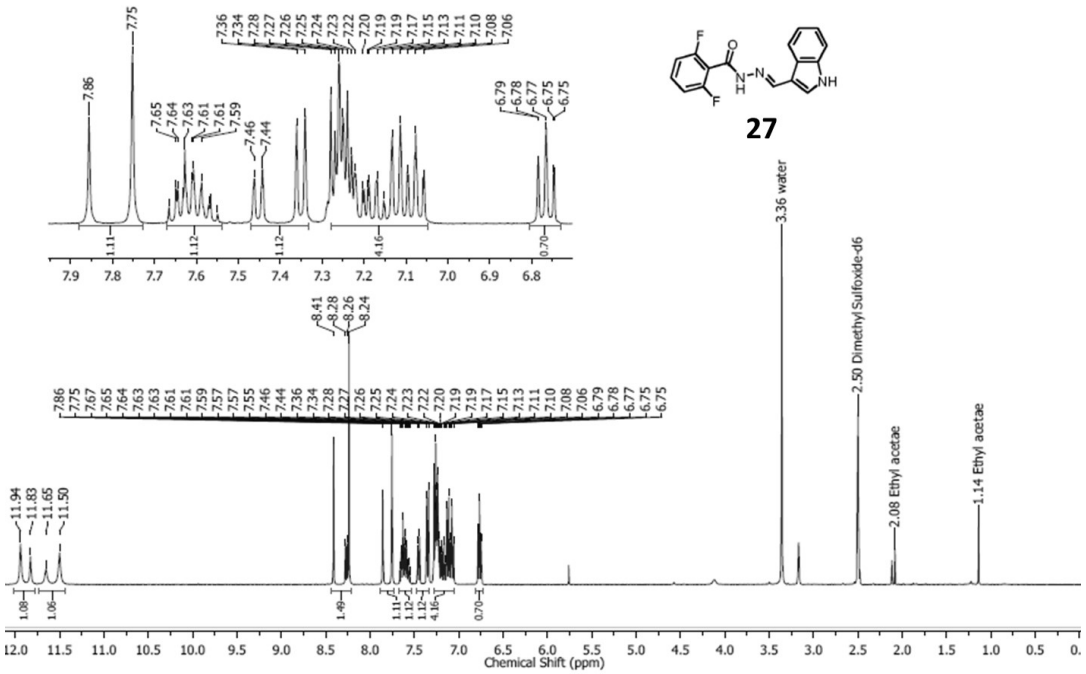


**Figure A67:** $^{1}$H NMR spectra of compound **27**

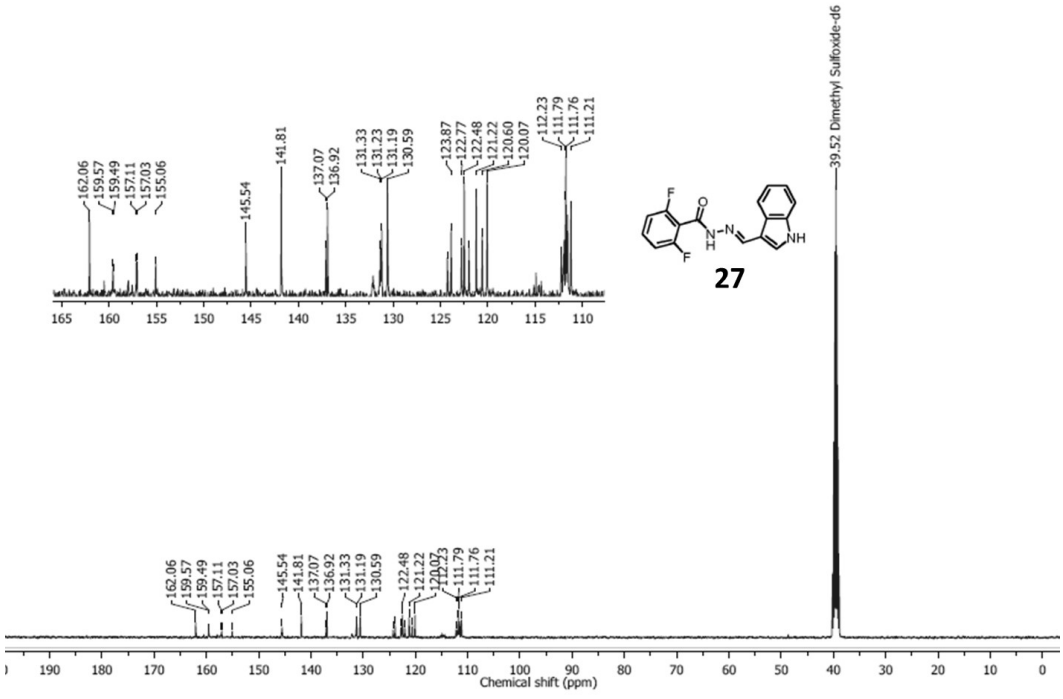


**Figure A68:** $^{13}$C NMR spectra of compound **27**

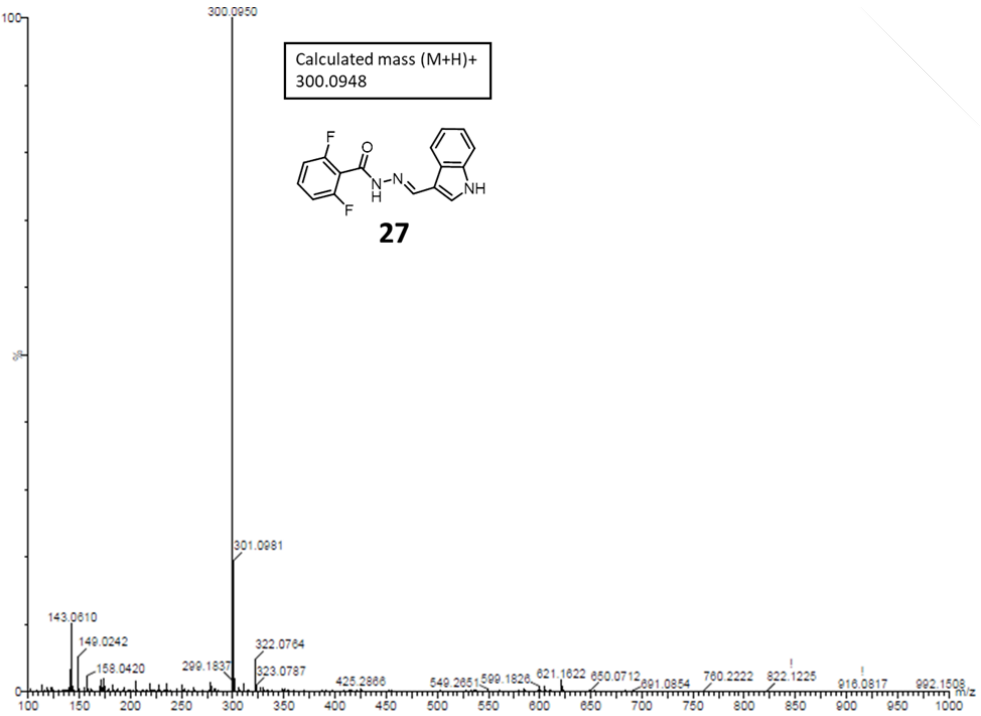


**Figure A69:** HR-MS spectra of compound **27**

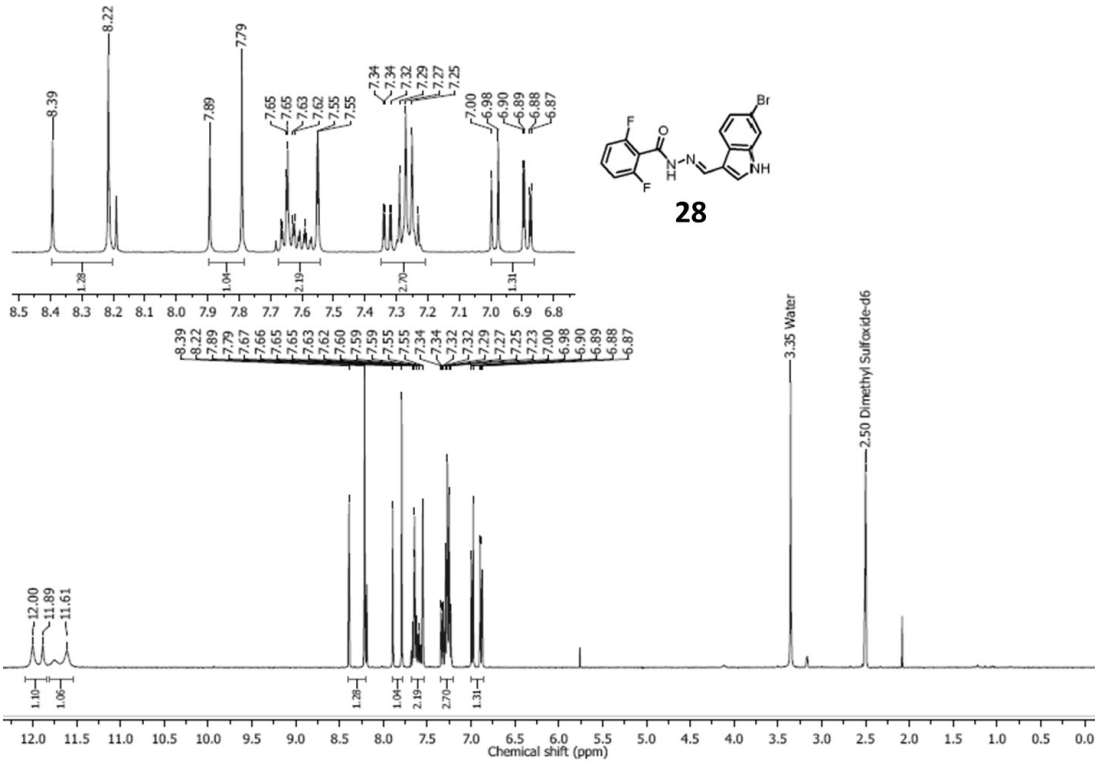


**Figure A70:** $^{1}$H NMR spectra of compound **28**

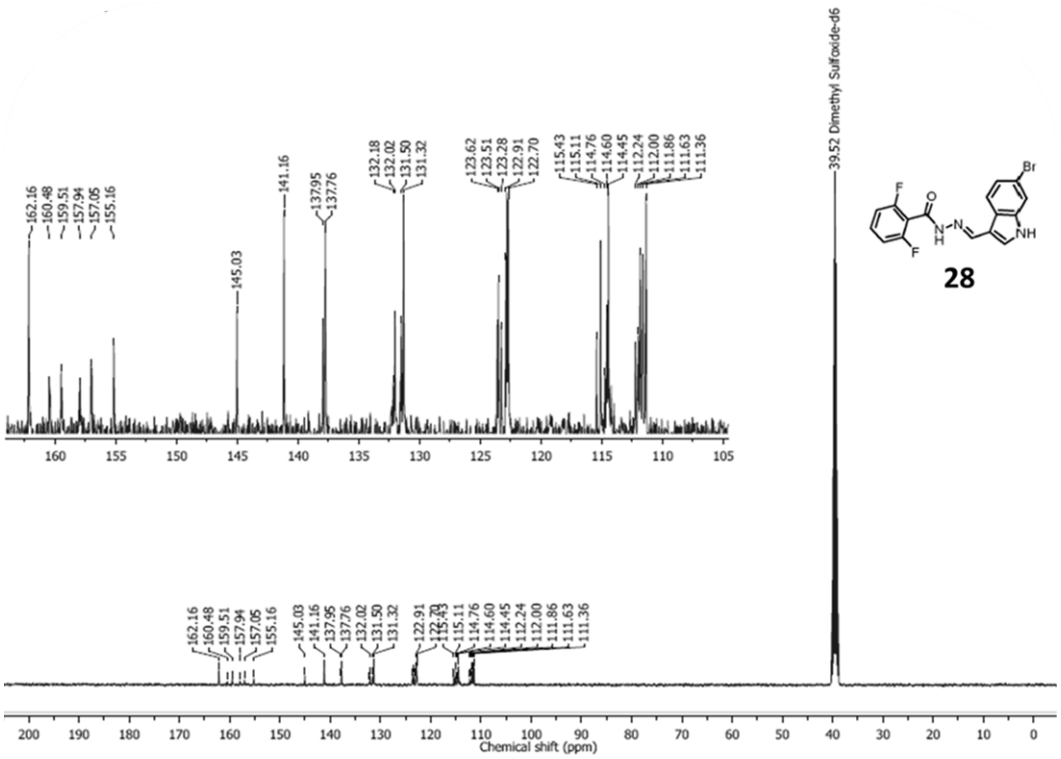


**Figure A71:** $^{13}$C NMR spectra of compound **28**

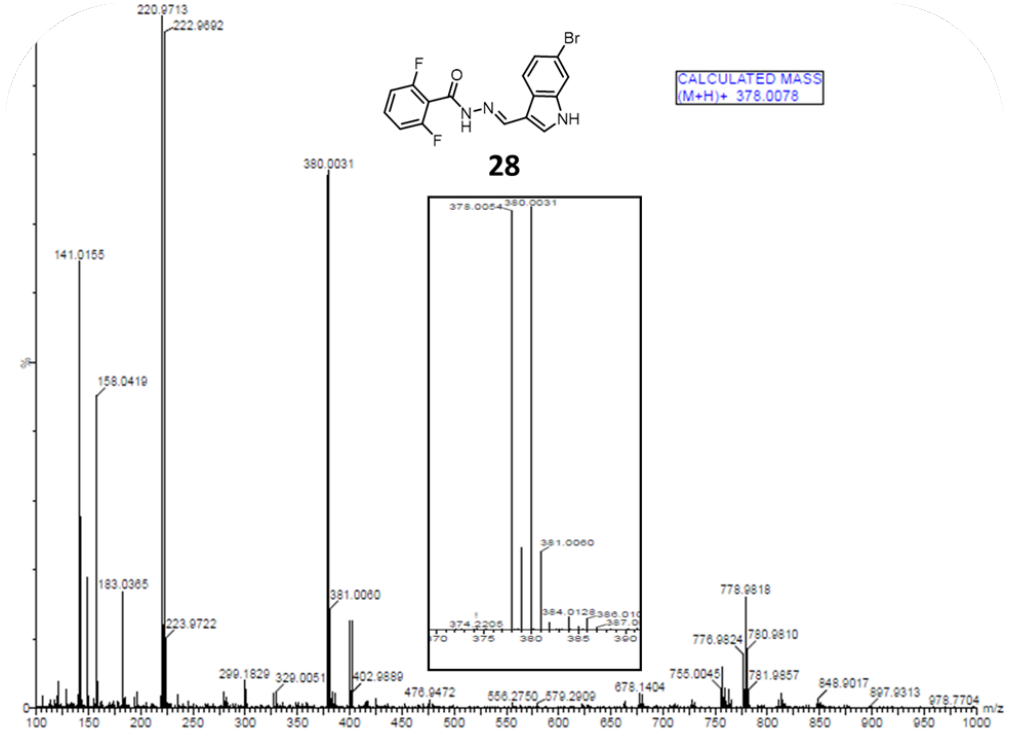


**Figure A72:** HR-MS spectra of compound **28**

**Table A1:** Crystal data and structure refinement of compound **28**

| | | |
|---|---|---|
| CCDC number | 1559783 | |
| Empirical formula | C16 H10 Br F2 N3 O | |
| Formula weight | 378.17 | |
| Temperature | 100(2) K | |
| Wavelength | 0.71073 Å | |
| Crystal system | Monoclinic | |
| Space group | P 21/n | |
| Unit cell dimensions | a = 11.218(2) Å | α= 90° |
| | b = 9.7135(17) Å | β= 108.759(4)° |
| | c = 14.594(3) Å | γ = 90° |
| Volume | 1505.8(5) $Å^3$ | |
| Z | 8 | |
| Density (calculated) | 1.668 $Mg/m^3$ | |
| Absorption coefficient | 2.758 $mm^{-1}$ | |
| F(000) | 752 | |
| Crystal size | 0.17 x 0.12 x 0.09 $mm^3$ | |
| Theta range for data collection | 2.008 to 28.402° | |
| Index ranges | -15<=h<=15, -12<=k<=8, -19<=l<=17 | |
| Reflections collected | 7259 | |
| Independent reflections | 3760 [R(int) = 0.0273] | |
| Completeness to theta = 25.242° | 99.8 % | |
| Absorption correction | Multi-scan | |
| Max. and min. transmission | 0.679 and 0.780 | |
| Refinement method | Full-matrix least-squares on $F^2$ | |
| Data / restraints / parameters | 3760 / 0 / 208 | |
| Goodness-of-fit on F2 | 1.0449 | |
| Final R indices [I>2sigma(I)] | R1 = 0.0273, wR2 = 0.0675 | |
| indices (all data) | R1 = 0.0369, wR2 = 0.0639 | |
| Largest diff. peak and hole | 0.370 and -0.455 e.$Å^{-3}$ | |

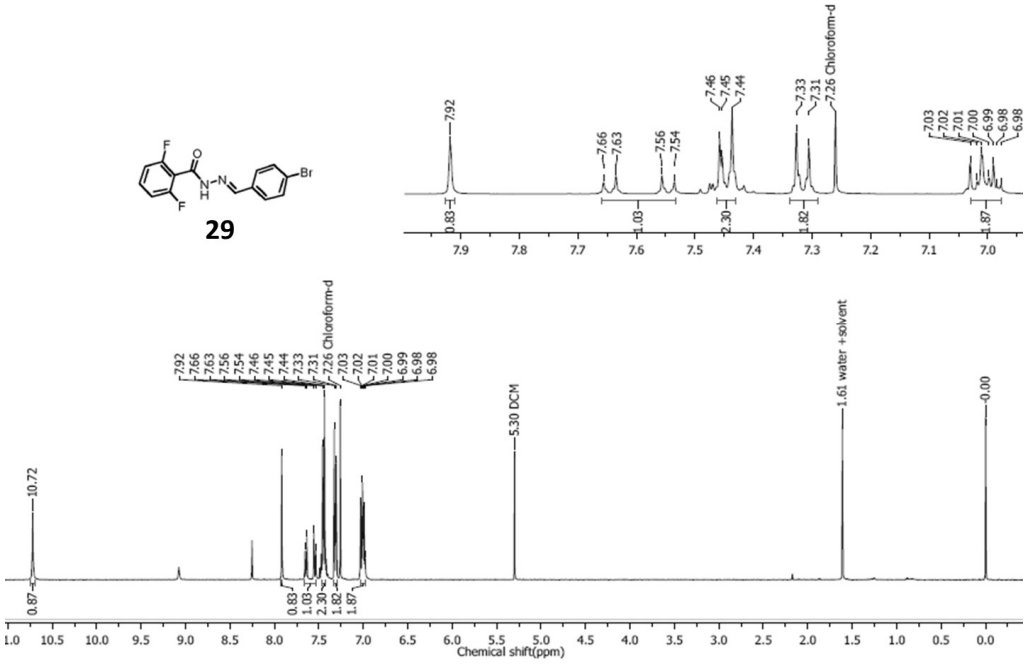


**Figure A73:** $^{1}$H NMR spectra of compound **29**

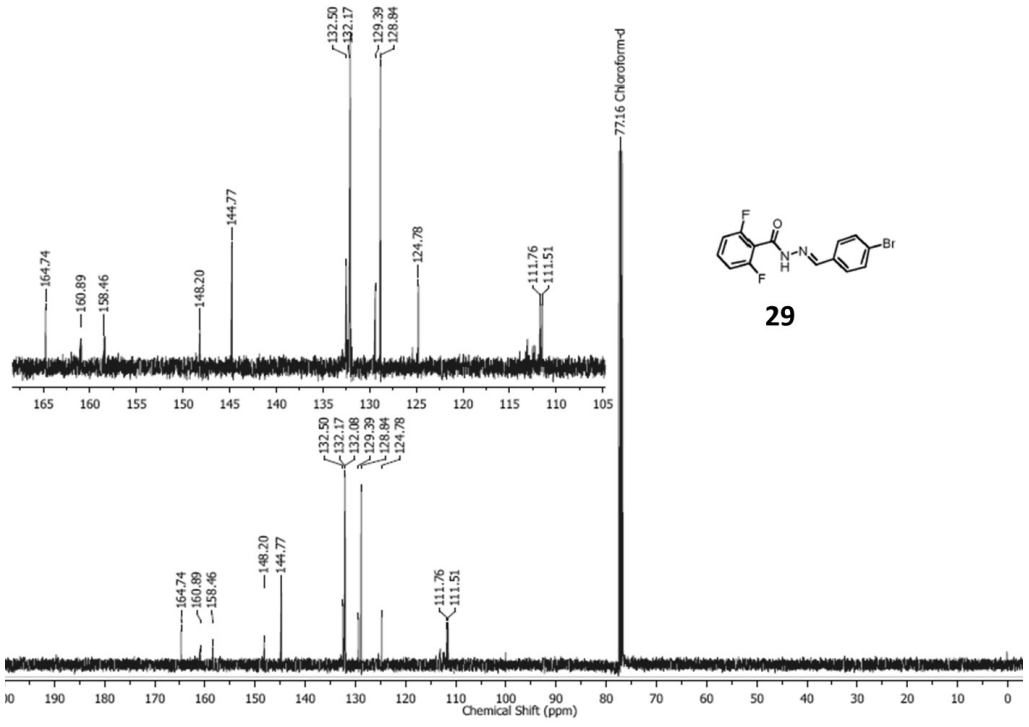


**Figure A74:** $^{13}$C NMR spectra of compound **29**

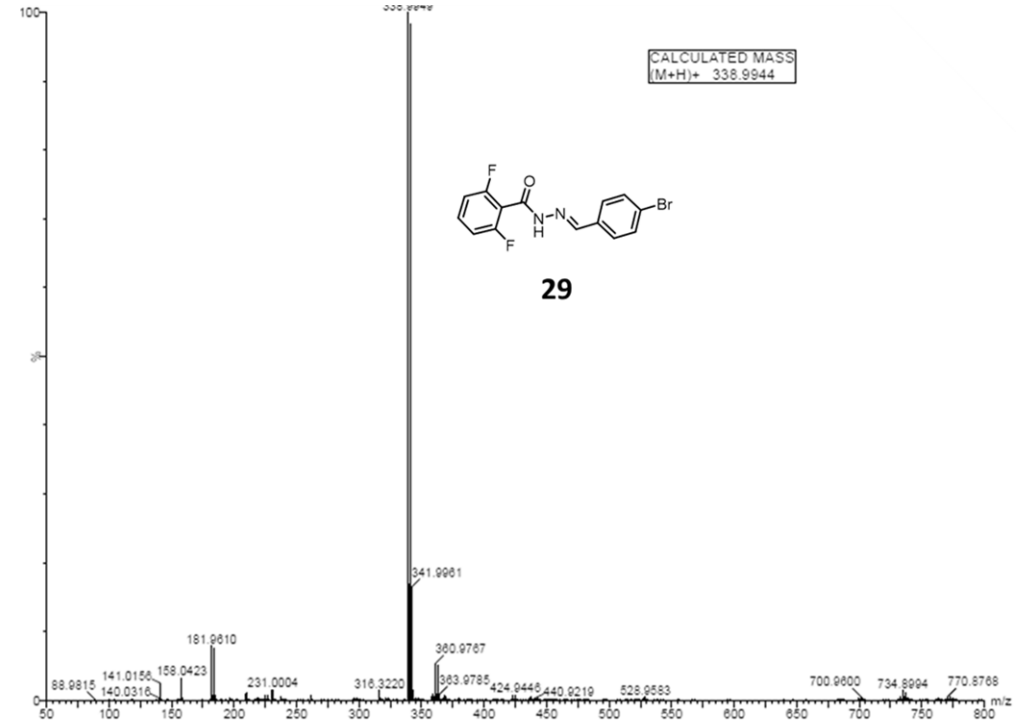


**Figure A75:** HR-MS spectra of compound **29**

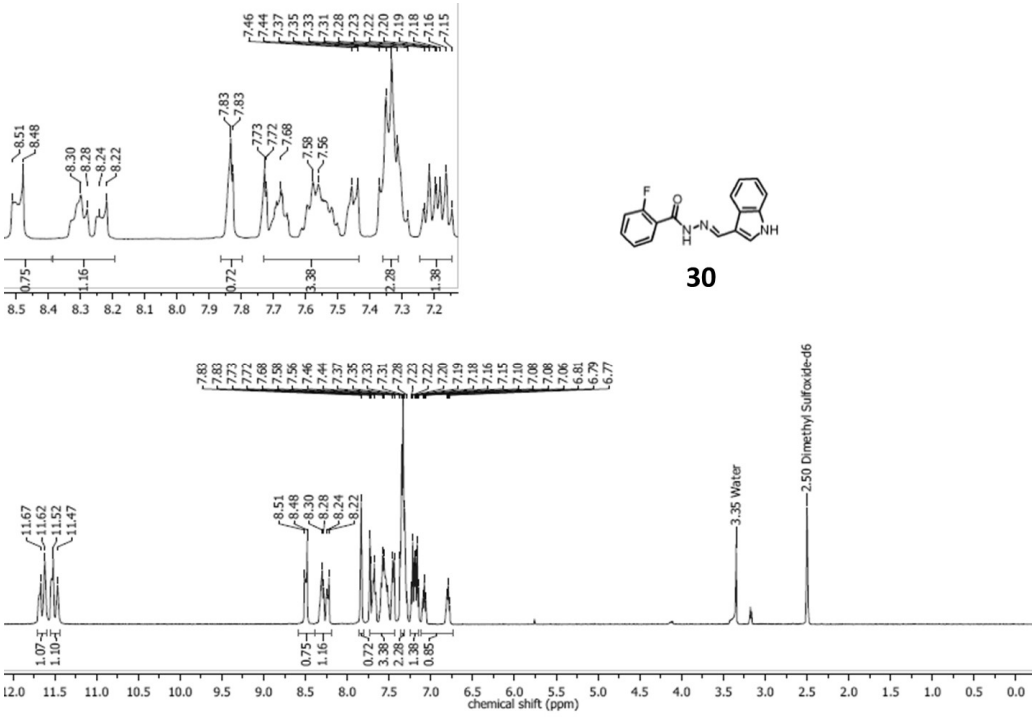


**Figure A76:** $^{1}$H NMR spectra of compound **30**

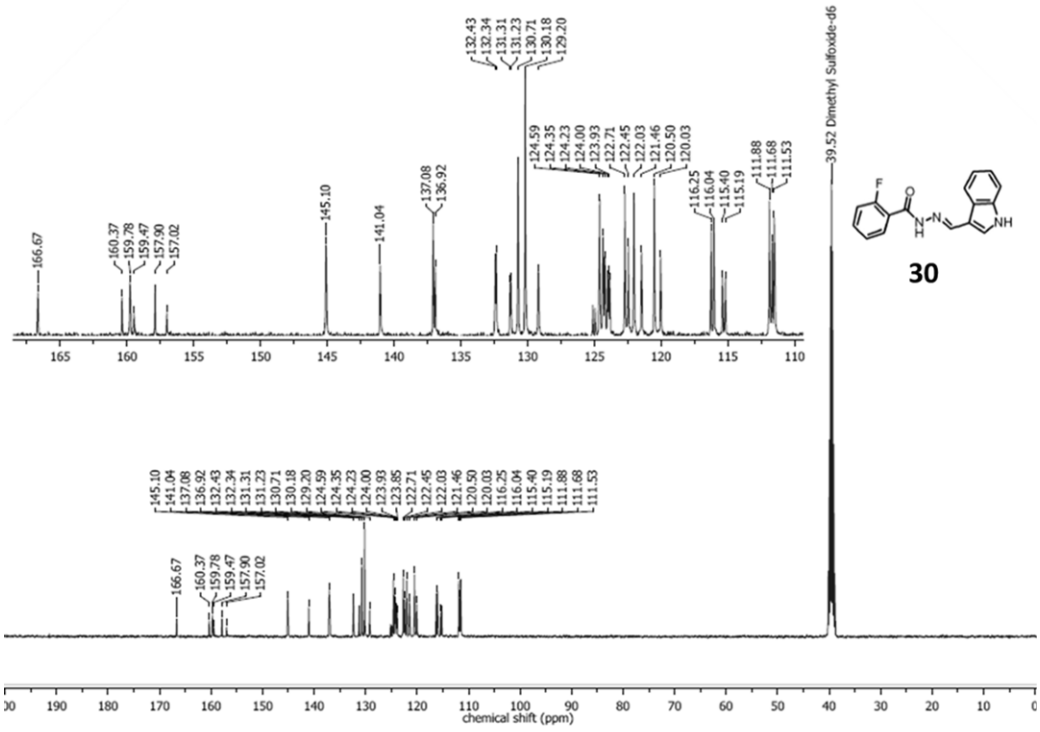


**Figure A77:** $^{13}$C NMR spectra of compound **30**

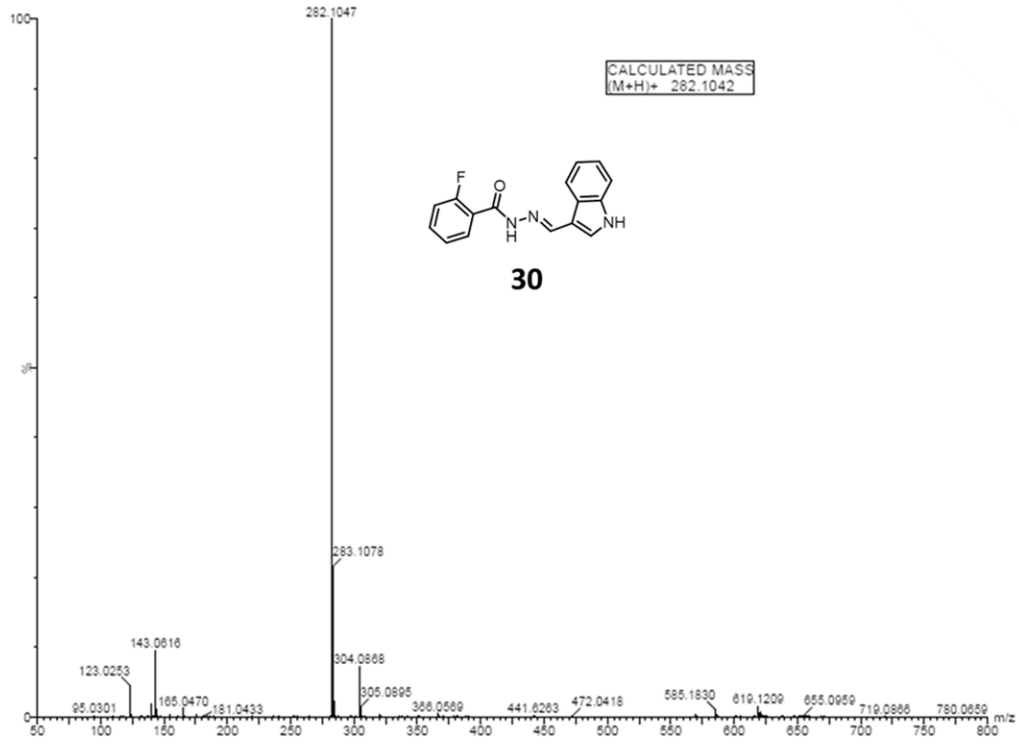


**Figure A78:** HR-MS spectra of compound **30**

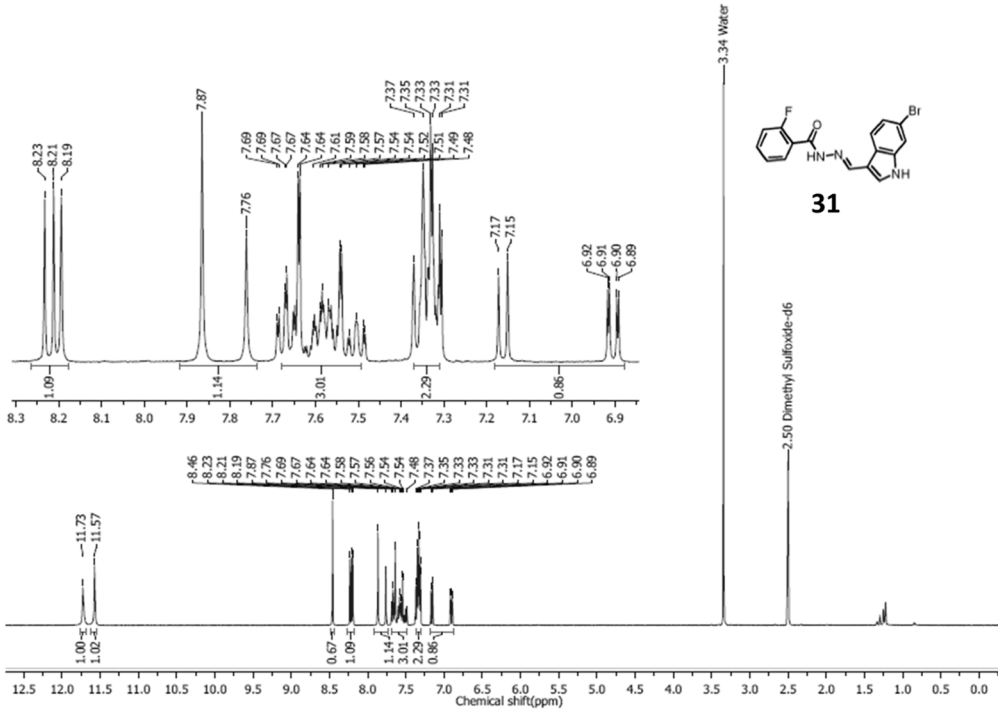


**Figure A79:** $^{1}$H NMR spectra of compound **31**

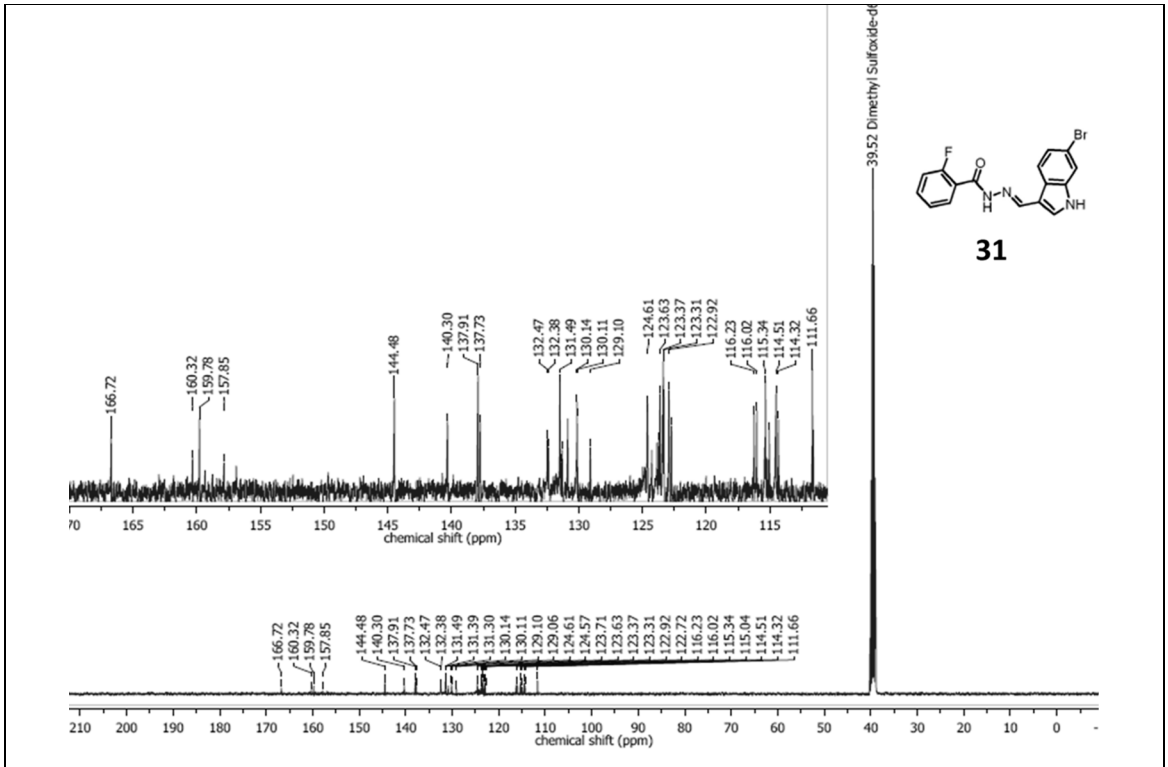


**Figure A80:** $^{13}$C NMR spectra of compound **31**

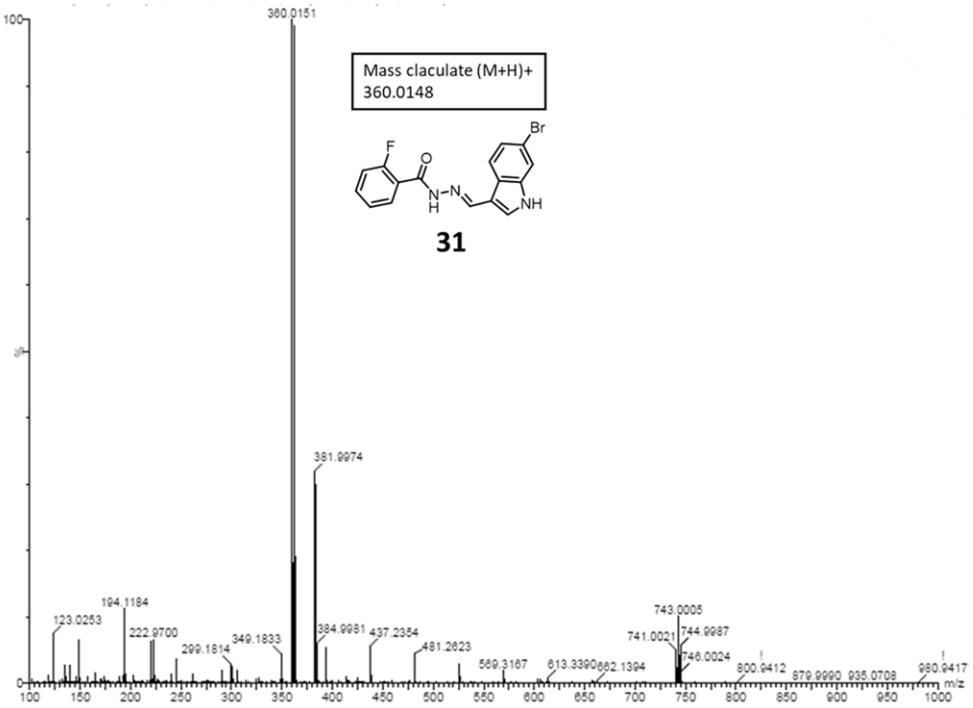


**Figure A81:** HR-MS spectra of compound **31**

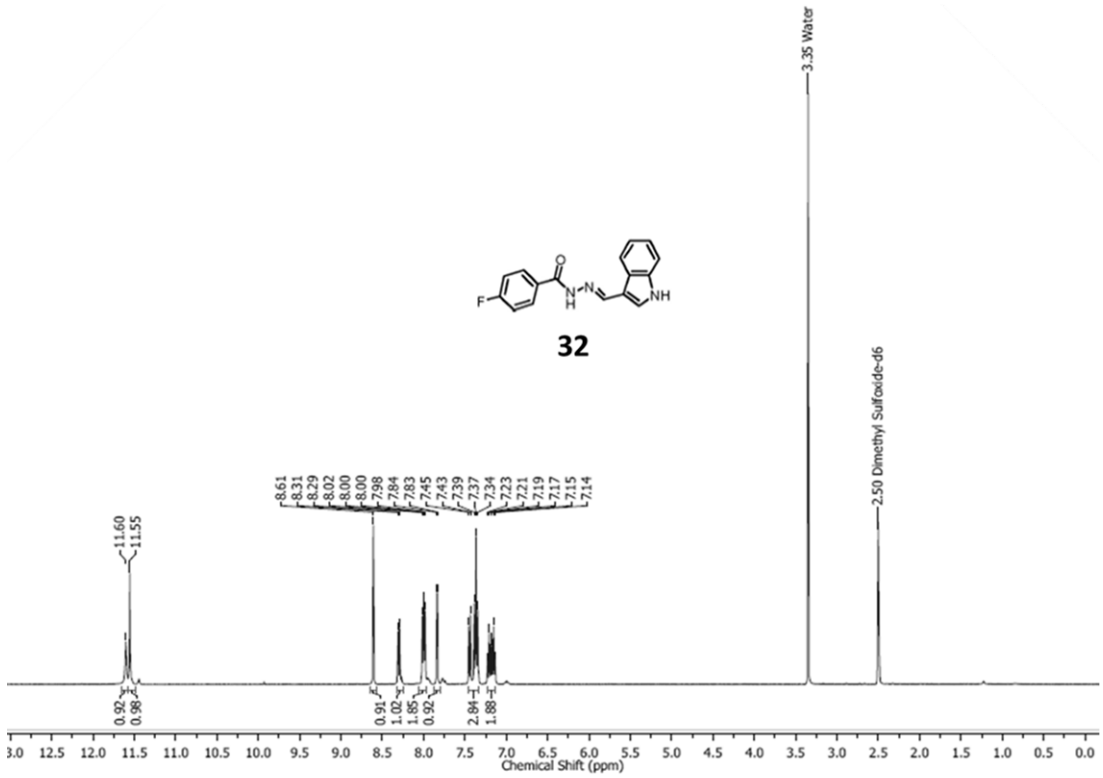


**Figure A82:** $^{1}$H NMR spectra of compound **32**

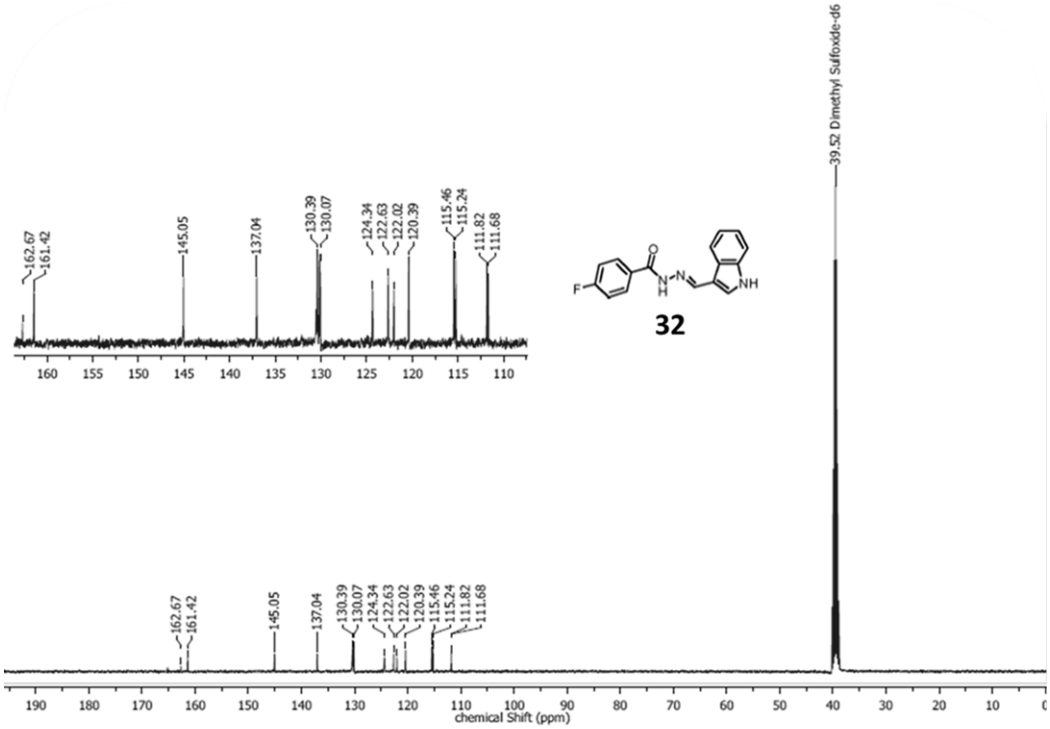


**Figure A83:** $^{13}$C NMR spectra of compound **32**

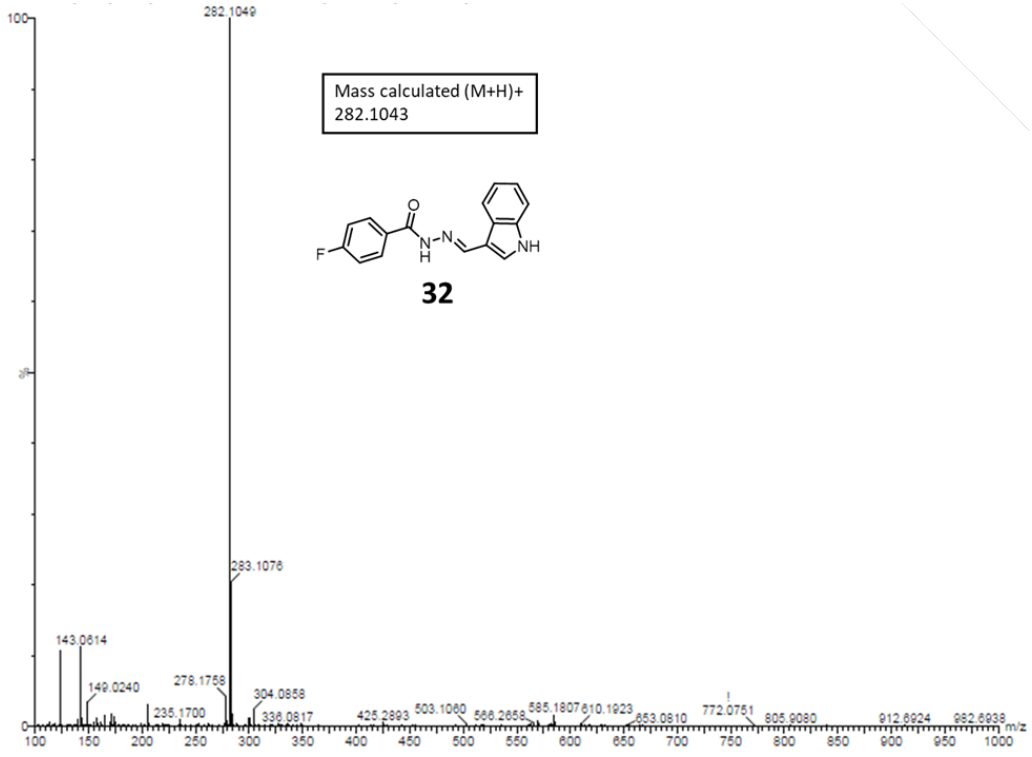


**Figure A84:** HR-MS spectra of compound **32**

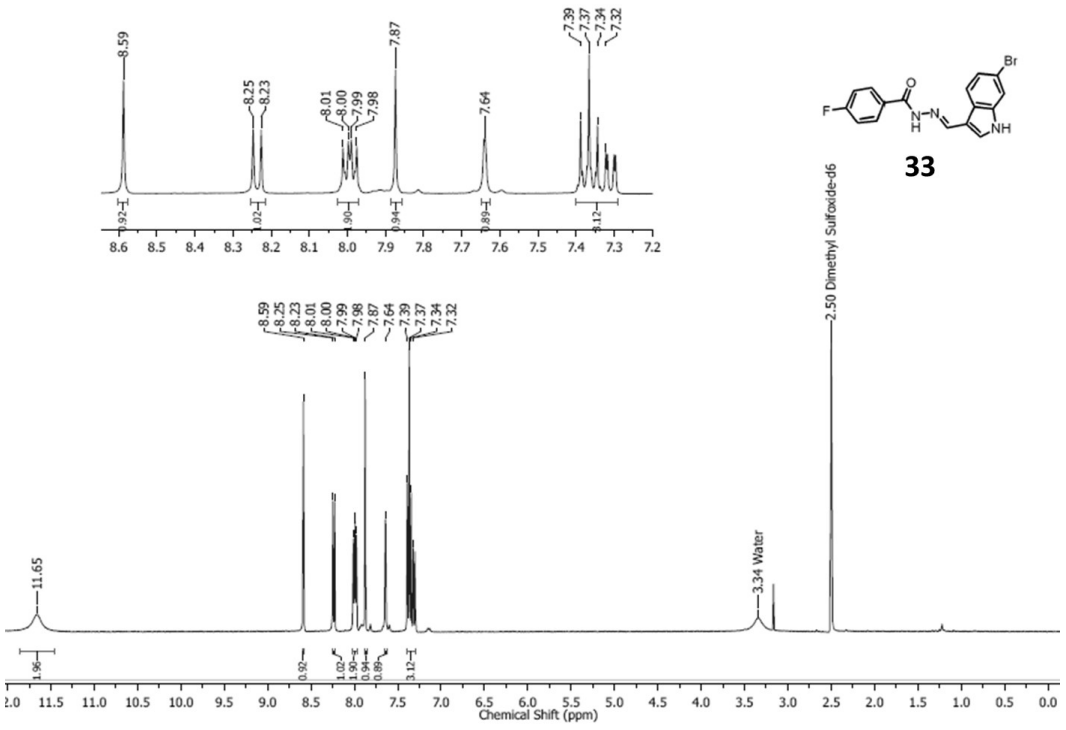


**Figure A85:** $^{1}$H NMR spectra of compound **33**

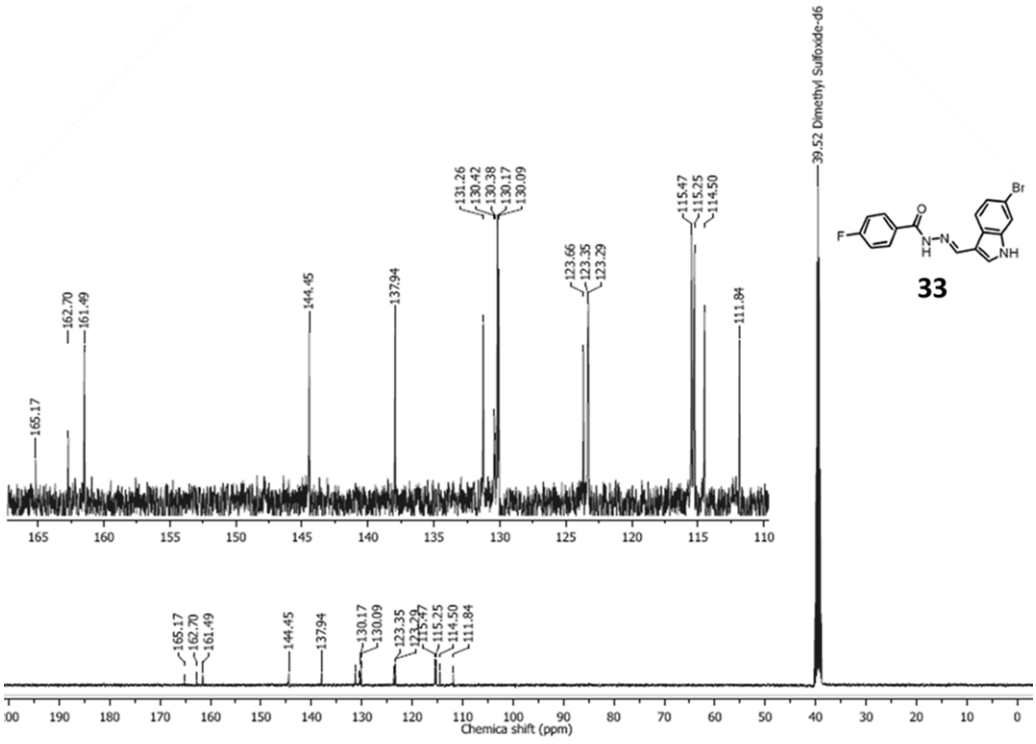


**Figure A86:** $^{13}$C NMR spectra of compound **33**

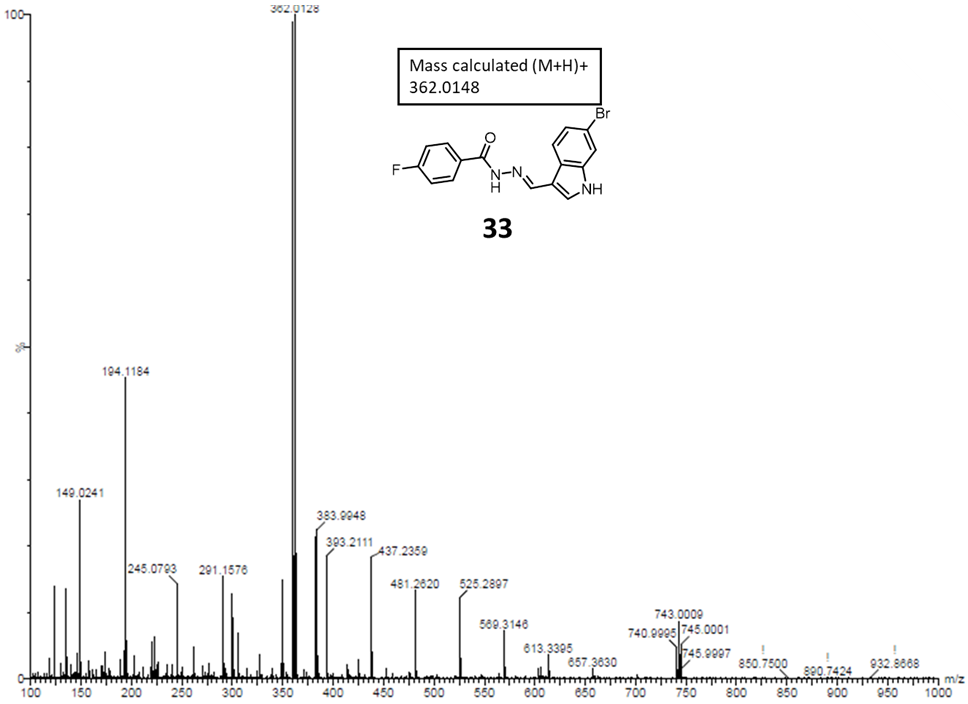


**Figure A87: HR-MS spectra of compound 33**

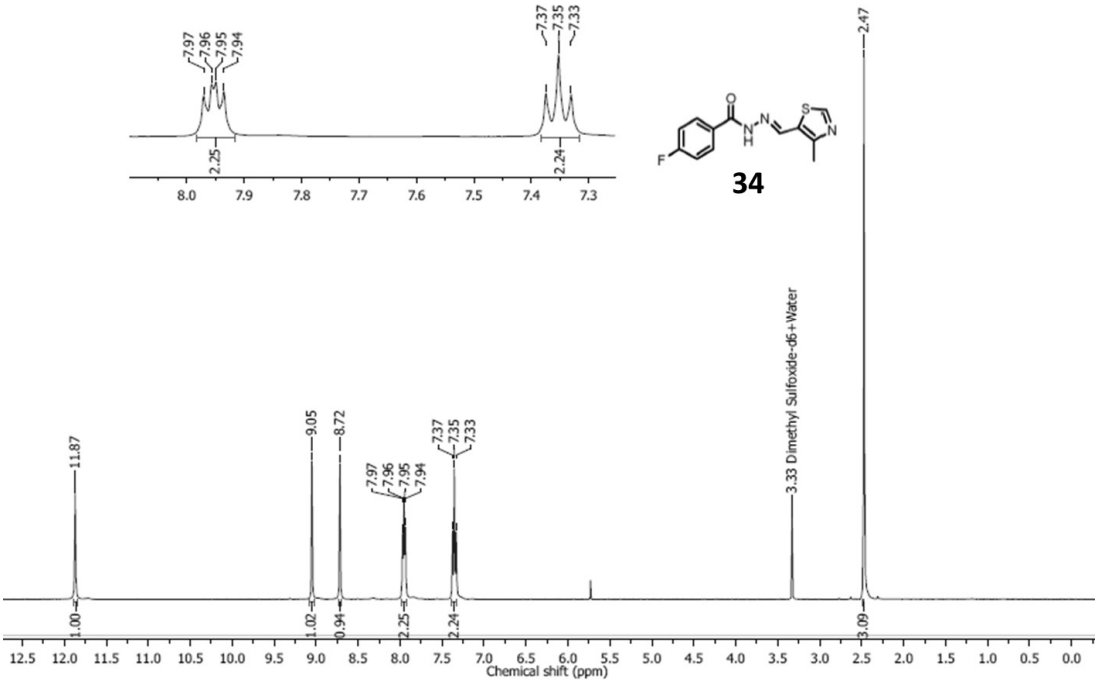


**Figure A88:** $^{1}$H NMR spectra of compound **34**

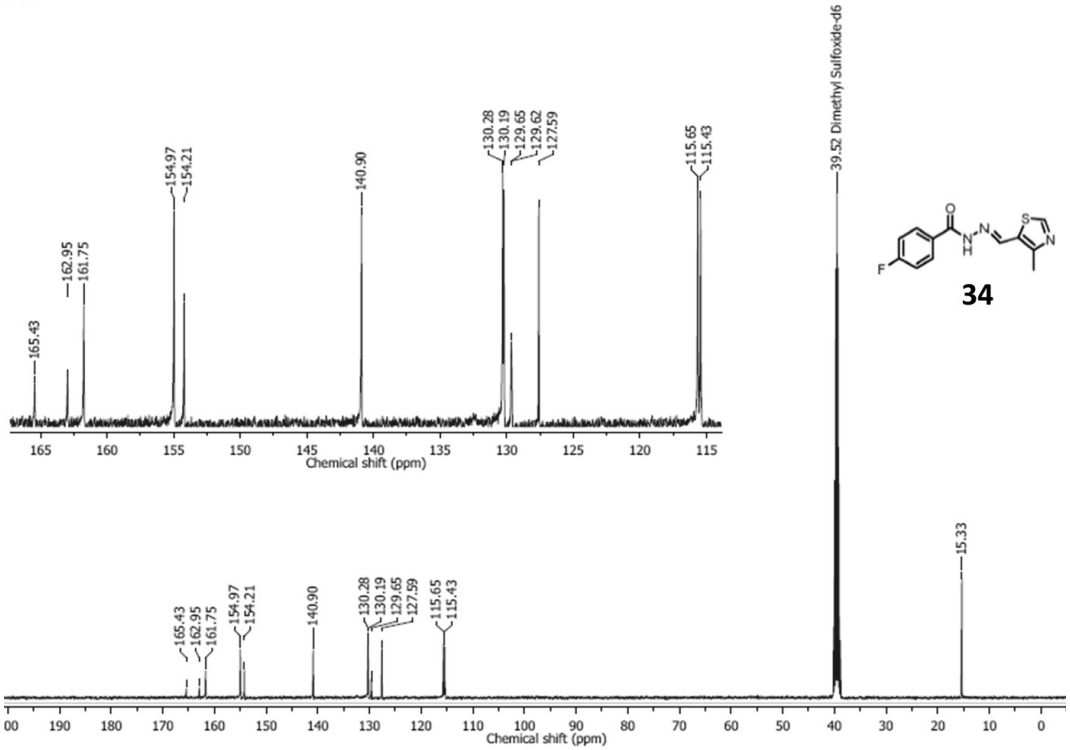


**Figure A89:** $^{13}$C NMR spectra of compound **34**

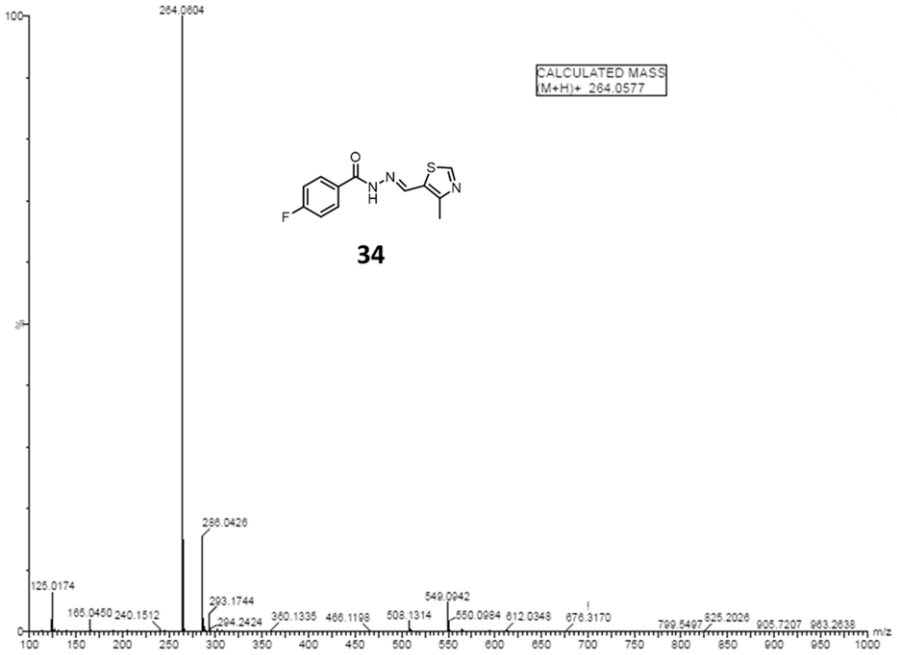


**Figure A90:** HR-MS spectra of compound **34**

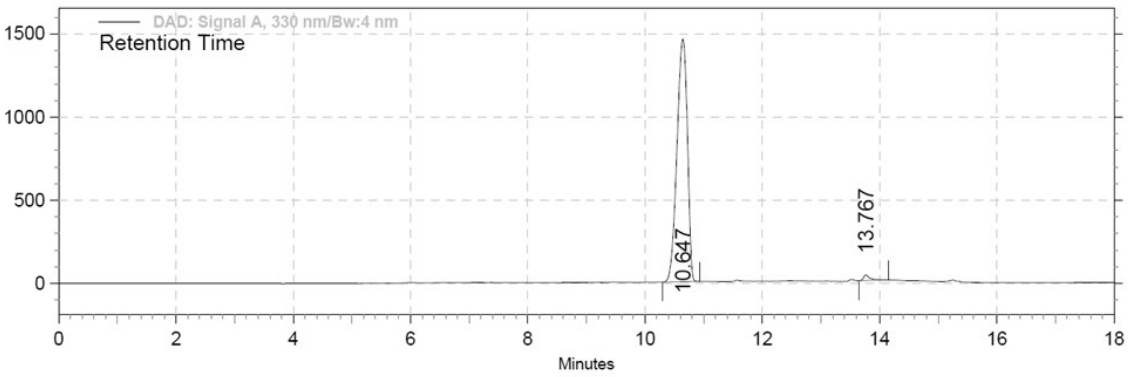


| Pk # | Area | Area % |
|---|---|---|
| 1 | 37778053 | 98.59 |
| 2 | 540136 | 1.41 |
| Totals | 38318189 | 100.00 |

**Figure A91:** RP-HPLC traces of compound **28** after purification showing 98.6 % purity

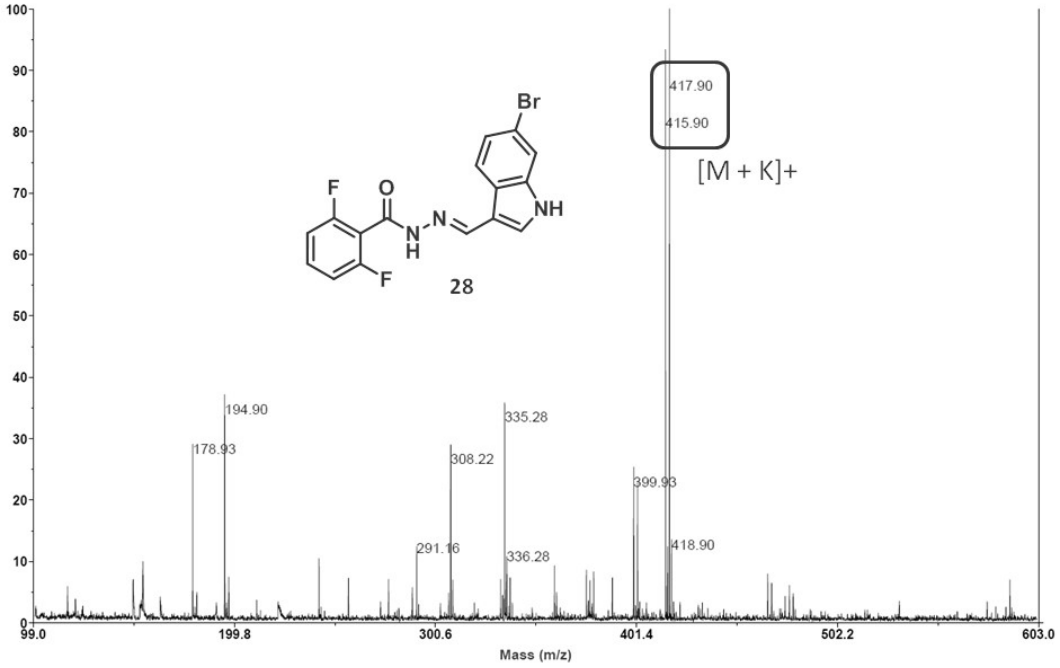


**Figure A92:** MALDI-TOF spectra of compound **28** after incubation at pH = 5.5 for 24 h

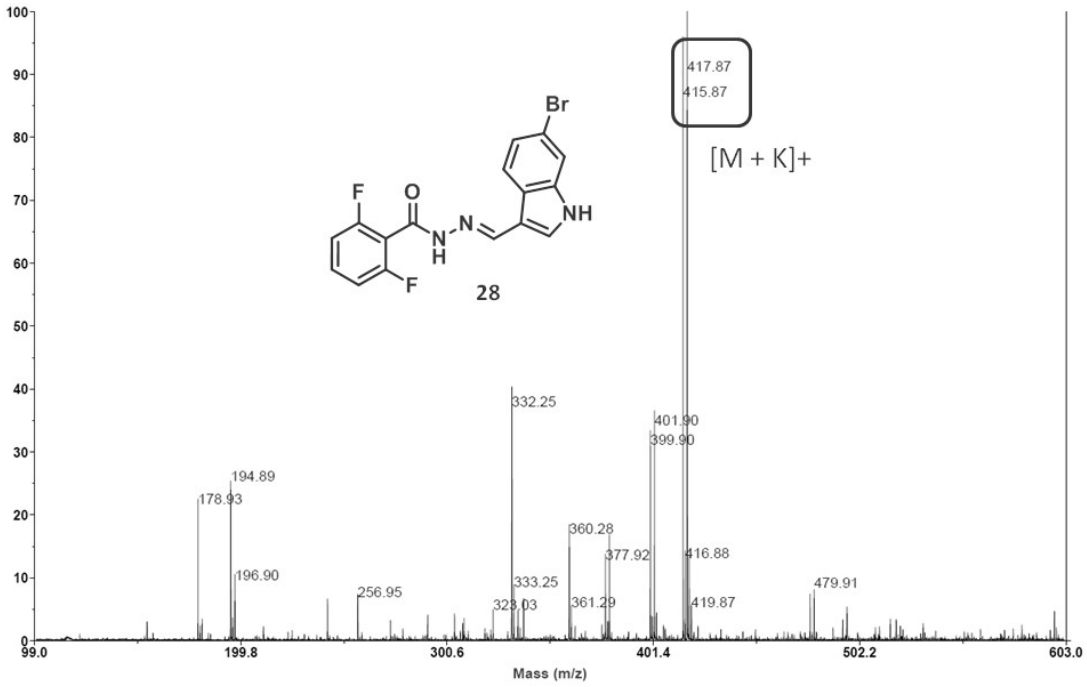


**Figure A93:** MALDI-TOF spectra of compound 28 after incubation at pH = 5.5 for 72 h

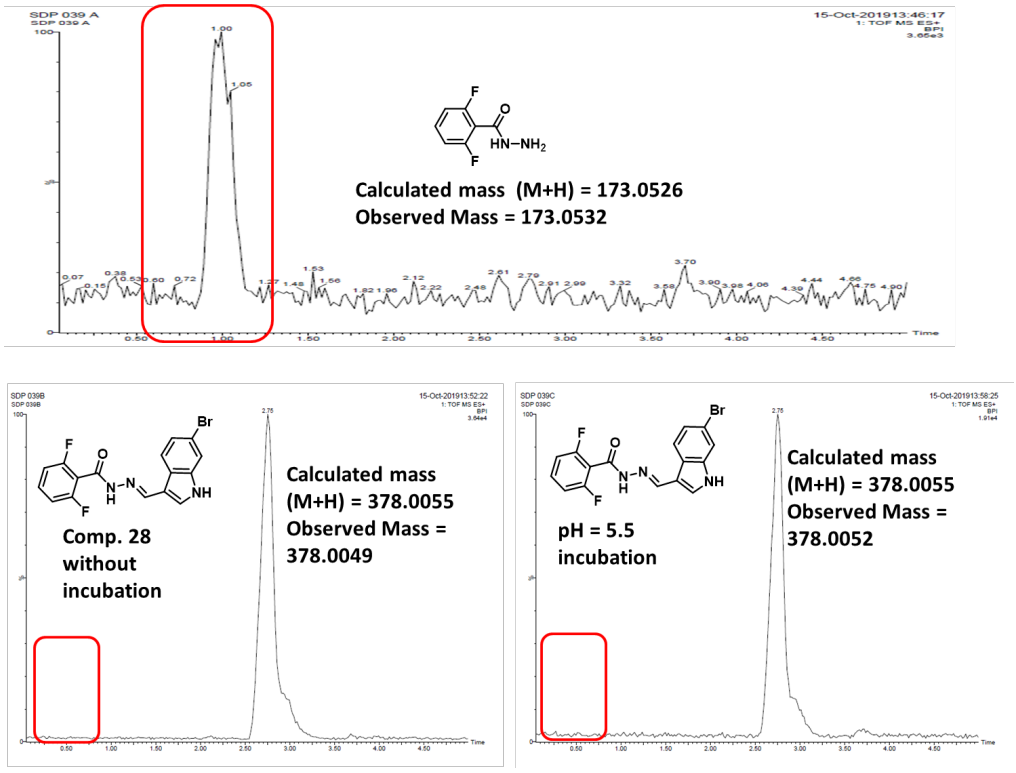


**Figure A94**: LC-HRMS anaysis of compound 28 to check stability at pH = 5.5 for 48 h

# Chapter 3

# Hydrazide-Hydrazone Small Molecules as AIEgens: Illuminating Mitochondria in Cancer Cells

*Chemistry: A European Journal*, **2019**, *25*, 8229-8235

(**Hot Paper**)

## 3.1 Introduction:

In 2001, Tang and his co-workers first time discovered a new phenomenon of luminescence called aggregation-induced emission (AIE), which was described by the mechanism of restricted intramolecular rotations (RIR).[1] AIE is a photophysical phenomenon of luminescent materials which are non-emissive in good solvents as molecules, but highly luminesce when they dissolve in poor solvents or in the solid state as aggregates.[1] This phenomenon is exalt apposite to the aggregation-induced quenching (ACQ), is a group of fluorogens show good fluorescence in dilute solutions, but low and no fluorescence in concentrated solutions, or solid state due to the self-quenching effect of adjacent molecules.

In last decade, aggregation-induced emission luminogens (AIEgens) have emerged as powerful tools to develop chemical sensors, optoelectronic devices and theranostic probes for biomedical applications due to their brightness and excellent photo-stability.[1-6] However, till date, tetraphenylethylene (TPE) and hexaphenylsilole (HPS) moieties are extensively explored as effective AIEgens despite their tedious synthetic steps and highly hydrophobic nature leading to incompatibility for biological applications.[7-10] To introduce biocompatibility for imaging and therapy, majority of the AIEgens was tagged with hydrophilic moieties to decorate hydrophobic AIE core through multiple synthetic steps.[11-15] Recently, numerous biocompatible AIEgens have been developed for *in vitro* cellular imaging, especially to visualize intra-cellular organelles.[16-21] Mitochondrion is one of the most important organelles which orchestrate several cellular functions, hence implicated in different disease states including cancer.[22-24] As a result, visualizing mitochondria inside the cancer cells is of utmost importance to understand their form and function in cancer progression and management. Despite several TPE and HPS-based AIEgens have been explored lately,[25-30] there is still a serious lack of biocompatible small molecule based AIEgens for visualization of mitochondria in cancer cells.

In this work, for the first time, we have developed hydrazide-hydrazone based small molecules through simple and concise synthetic steps, which showed remarkable aggregation-induced emission (AIE) properties in water as well as in solid state by dual intra-molecular H-bonding. This dual H-bonding mediated restriction in intra-molecular motions (RIM) for AIE

properties was confirmed by temperature and pH-dependent fluorescence quenching studies, $^{1}H$ NMR spectroscopy and theoretical calculations as well as X-ray crystallography. One of the hydrazide-hydrazone based AIEgens was decorated with positively charged triphenylphosphine (TPP) to illuminate mitochondria in HeLa cervical cancer cells compared to L929 non-cancerous fibroblast cells. These hydrazide-hydrazone small molecule AIEgens showed remarkable biocompatibility by demonstrating negligible cell killing even at significantly high concentrations. These novel biocompatible AIEgens can act as platform probes to further illuminate several intra-cellular organelles and bio-targets.

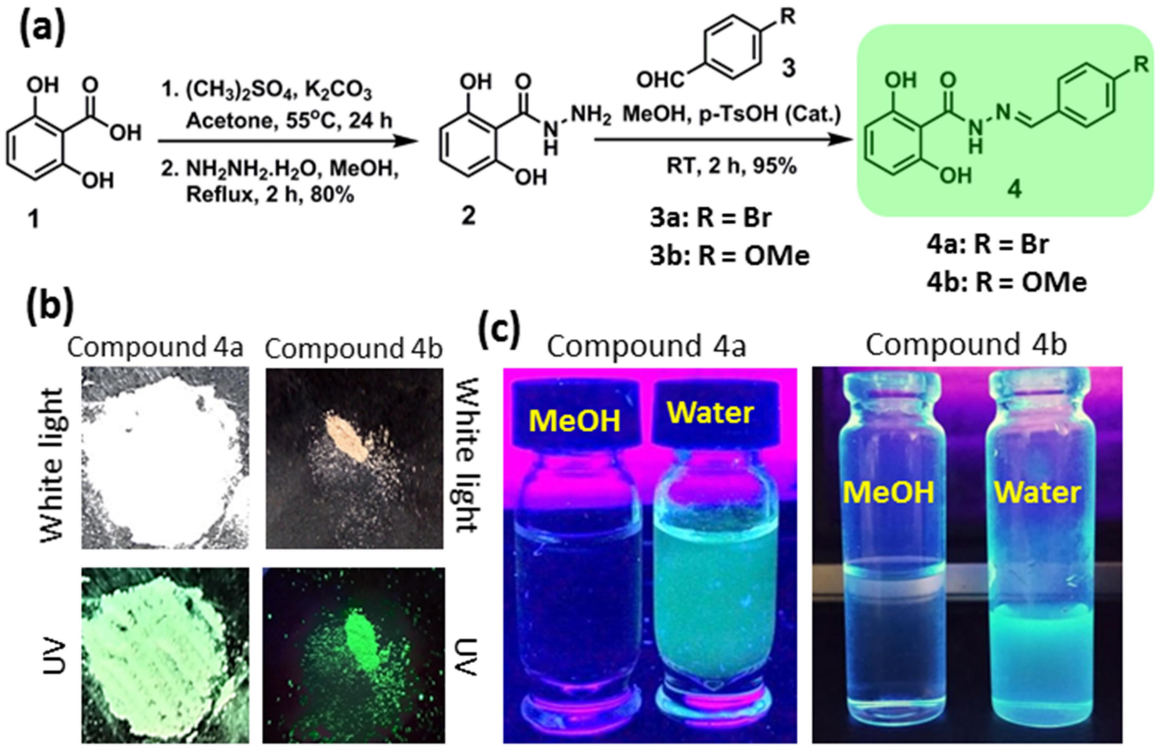


**Figure 3.1**: (a) Synthetic scheme of hydrazide-hydrazone molecules. (b) Fluorescence emission images of compound **4a** and **4b** under UV lights and white light in solid state. (c) Images of AIE property of compound **4a** and **4b** in water and in methanol

## 3.2 Result and Discussion:

### 3.2.1 Synthesis of hydrazide-hydrazone 4 and characterization

The synthetic scheme of hydrazide-hydrazone derivatives (**4**) is shown in Figure 3.1a. 2,6-dihydroxybenzoic acid was reacted with dimethyl sulfate in presence of potassium carbonate as base at 55 °C in acetone for 24 h to obtain 2,6-dihydroxy benzoic acid methyl ester which was

subsequently reacted with hydrazine monohydrate in methanol at refluxing condition to afford 2,6-dihydroxy benzohydrazide (**2**) in 80% overall yield. Finally, different 4-substituted benzaldehydes (**3a, b**) were reacted with compound **2** in presence of catalytic *p*-toluenesulfonic acid (*p*-TsOH) to afford hydrazide-hydrazone derivatives (**4a, b**) in 95% yield. All the intermediates and final compounds were characterized by NMR ($^{1}$H and $^{13}$C) and mass spectroscopy (HR- MS) (Annexin-B; Figure B1-9).

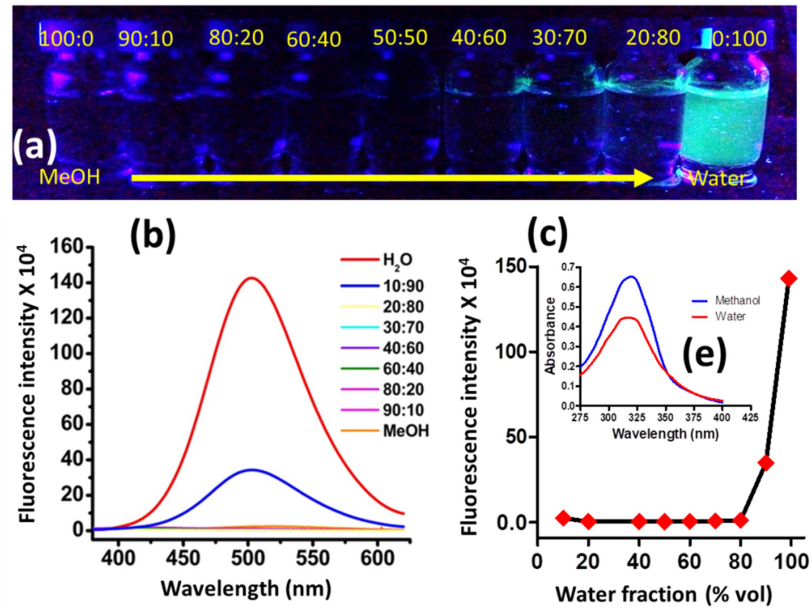


**Figure 3.2**: (a) Change in fluorescence emission of compound **4a** in different methanol/water mixture. (b) Fluorescence emission spectra of compound 4a in different methanol: water ratios. (c) Fluorescence emission intensity (λmax = 502 nm) versus water fraction graph of compound 4a in different methanol: water mixture. (e) UV-Vis spectra of compound 4a in methanol and water

### 3.2.2 Indication of AIE

Interestingly, all the hydrazidhydrazone derivatives (**4a, b**) showed remarkable fluorescence emission under long range of UV light in solid state (Figure 3.1b). However, no fluorescence emission was observed under white visible light. Similarly, compounds **4a, b** showed no fluorescence emission in methanol. On the other hand, both the hydrazide-hydrazone derivatives (**4a, b**) showed remarkable fluorescence emission in water (Figure 3.1c). This observation clearly indicated the aggregation-induced emission (AIE) properties of compound **4**.

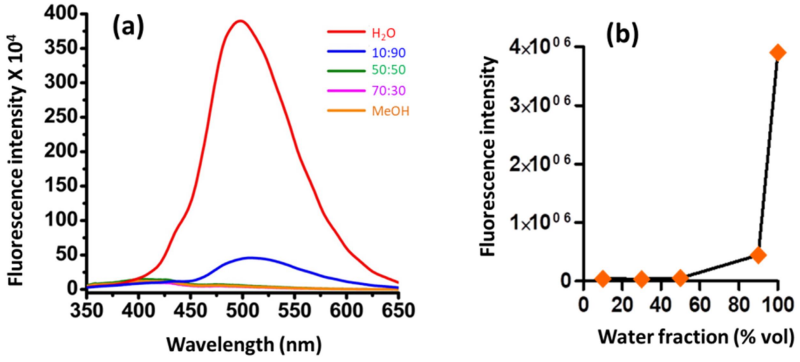


**Figure 3.3**: (a) Change in fluorescence intensity of compound **4b** at λmax = 492 nm in different methanol/water mixture. (b) Graph of fluorescence intensity versus water fraction in methanol for compound **4b**.

### 3.2.3 AIE confirmation studies

#### *3.2.3.1 Photophysical studies*

To evaluate the exact solvent ratio of aggregation induction, we dissolved compound **4a** in methanol and gradually titrated with increased amount of water. There was no fluorescence signal observed till methanol: water = 20:80 (v/v). However, compound **4a** showed an increase in fluorescence emission intensity at methanol: water = 10:90 (v/v) at $\lambda_{max}$ = 502 nm, which increased significantly at 100 % water (Figure 3.2a-e). The UV-Vis spectra of compound **4a** showed absorption maxima at $\lambda_{max}$ = 322 nm in methanol and water (Figure 3.2e), indicative of a large Stokes shift of 180 nm with negligible overlap between absorption and emission spectra, which is highly suited for fluorescence imaging. Similarly, compound **4b** showed remarkable fluorescence emission intensity increment ($\lambda_{max}$ = 492 nm) in water compared to methanol due to aggregation (Figure 3.3a, b). To confirm the remarkable enhancement in the fluorescence emission intensity of compound **4a** and **4b** due to the effect of aggregation, we assessed the fluorescence emission in a concentration dependent manner. As expected, the fluorescence emission intensity of compound **4a** and **4b** were increased continuously after increasing the concentration of the compounds in water (Figure 3.4a, b). We also performed fluorescence life time experiment which revealed that compound **4a** and **4b** had 1.97 and 1.50 ns of fluorescence life time respectively which is little less compared to Rhodamine 123, a traditionally used commercial mitochondria imaging agent (Figure 3.4c).[31] The fluorescence quantum yield of compound **4a** and **4b** were found to be 12.2% and 5.4 % respectively which are comparable with

the structurally similar imine compounds as well as much higher to Rhodamine 123 (~ 0.9%).[31,32]

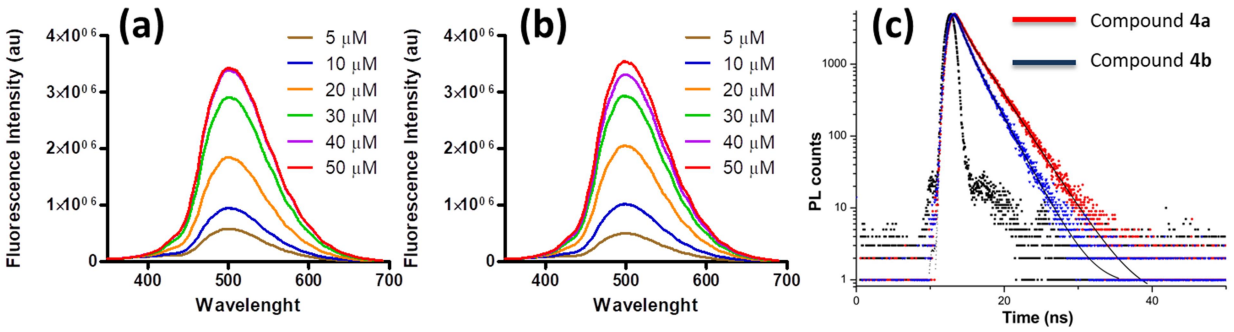


**Figure 3.4**: Change of fluorescence emission intensity of (a) compound **4a** and (b) **4b** in different concentrations in water. (c) Fluorescence lifetime decay of compound **4a** and **4b.**

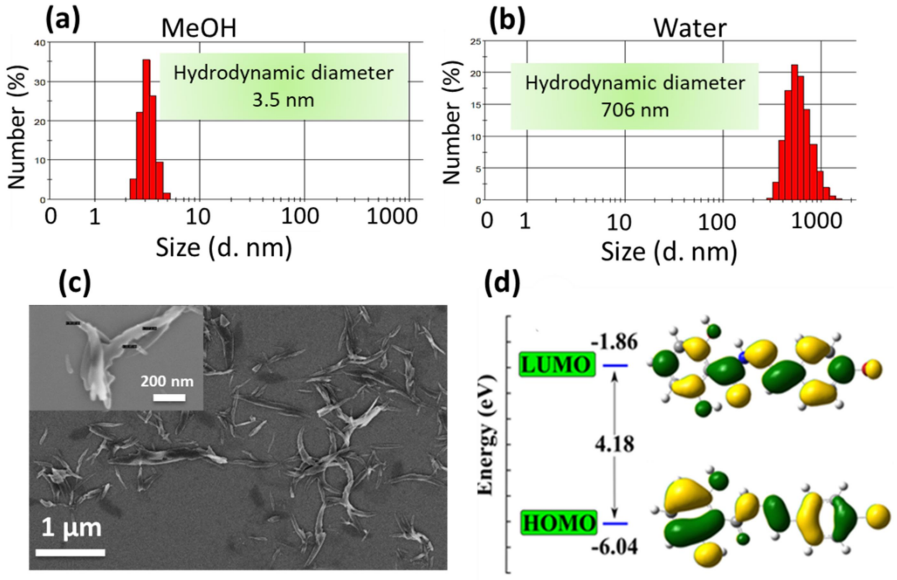


**Figure 3.4**: (a, b) Hydrodynamic diameter of compound **4a** in methanol and water respectively by dynamic light scattering (DLS). (c) FESEM images of compound 4a in water. (d) Schematic diagram of the energy level difference between the HOMOs and LUMOs of compound **4a**, estimated from DFT computation and the isodensity surface plots of the frontier molecular orbitals (FMOs) with isovalue of 0.02 au

### *3.2.3.2 Aggregation of the compounds in water*

The aggregation of compound **4a** in water was further validated by dynamic light scattering (DLS), which demonstrated that the mean hydrodynamic diameter of the aggregated

structure in water to be 706 nm (Figure 3.4a, b). In contrast, compound **4a** showed very small hydrodynamic diameter (~ 3.5 nm) in methanol indicating negligible aggregation (Figure 3.4a, b). We also visualized the aggregation of compound **4a** by scanning electron microscopy. The FESEM images evidently showed that compound **4a** aggregated into 2D-sheet like structures in water, whereas no such significant aggregation was found in methanol (Figure 3.4c).

#### *3.2.3.3 Theoretical energy calculation*

Subsequently the Frontier molecular orbitals and the energy gap between HOMOs and LUMOs of compound **4a** was calculated by Density functional theory (DFT), which revealed the energy gap was ~ 4.18 eV (~ 300 nm) correlating with the wavelength of UV-Vis absorbance (Figure 3.4d).

### 3.2.4 AIE mechanism

We hypothesize dual intra-molecular H-bonding as the guiding factor for this hitherto unobserved AIE property for these novel hydrazide-hydrazone small molecules leading to restriction in intra-molecular motion (RIM) (Figure 3.5a).

#### *3.2.4.1 Theoretical calculation*

To confirm our hypothesis, we performed theoretical calculation using Gaussian 09 program on compound **4a**.[33] 3D coordinates of compound **4a** were generated from the crystal structure of 4-N, N-dimethylaminoaniline salicylaldehyde reported by Feng et. al.[27] with a few modifications. The geometries were then additionally optimized by the B3LYP[34] hybrid density functional with 6-31G* Gaussian basis set. The presence of water was mimicked with polarizable continuum model using the integral equation formalism variant.[35] The geometry of the optimized molecular structure of compound **4a** showed that all the atoms were in the same plane (Figure 3.5b) and confirmed the proposed dual intra-molecular H-bonding.

#### *3.2.4.2 Effect of temperature on the AIE property:*

Inter- or intra-molecular H-bonding are weak supramolecular forces which can be disrupted by increasing the temperature of the medium.[36] Moreover, $^{1}$H NMR spectroscopy has emerged as one of the tools to probe the presence of inter- and intra-molecular H-bonding.[37] Hence, we performed temperature dependent $^{1}$H NMR spectroscopy of compound **4a** from 25°C to 80°C and monitored the H-bonded proton peaks at 12.07 (-OH) and 11.81 ppm (-NH). Remarkably, we observed the gradual broadening of both these peaks while increasing the

temperature from 25°C to 80°C (Figure 3.5c). This observation is in complete agreement with our previous study.[38] To validate our hypothesis further, we performed temperature dependent fluorescence spectroscopy on compound **4a** in water. It was observed that, with gradual increase in temperature from 25°C to 80°C, the intensity of fluorescence emission was gradually decreased by 3.5 folds (Figure 3.5d) due to the destruction of H-bonding in structure **4a'**. Interestingly, this fluorescence quenching phenomenon was found to be reversible.

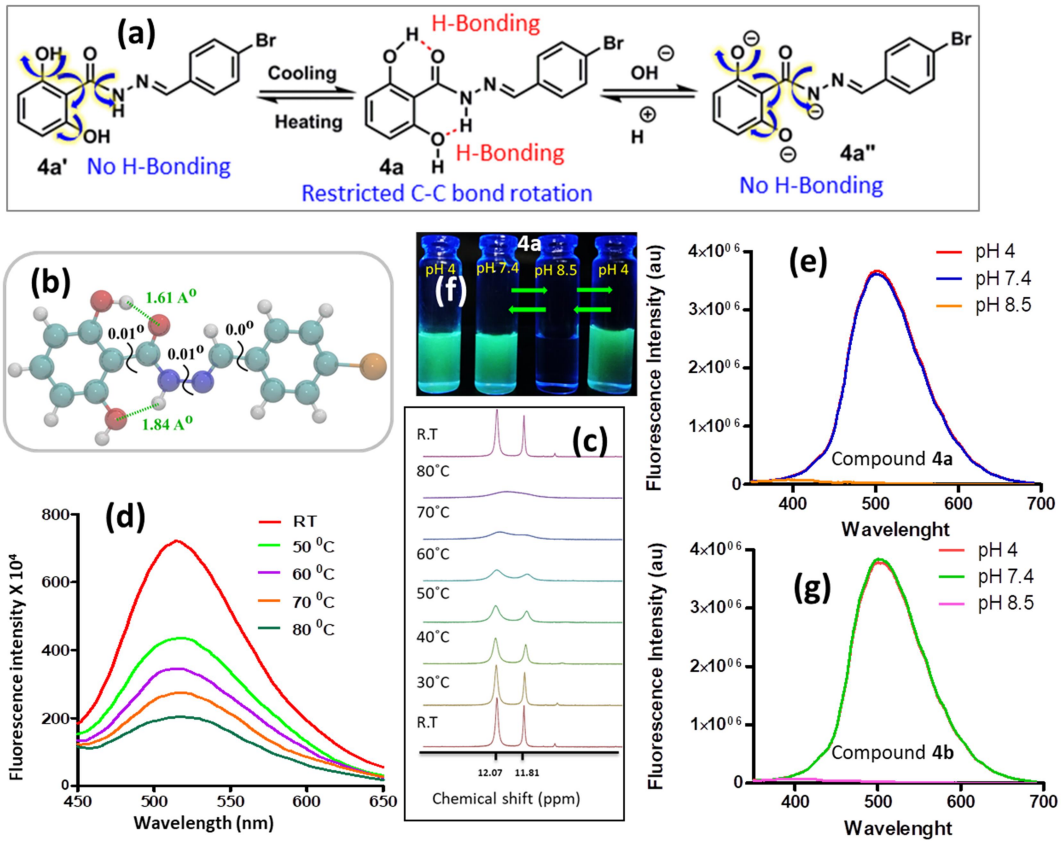


**Figure 3.5** (a) Scheme of H-bonding disruption of compound **4a** in temperature and pH change. (b) Optimized geometry of compound **4a** obtained from B3LYP/6-31G* computation. Black zig-zag lines showing values for the respective dihedral angles (in degree) whereas hydrogen bonding is shown in green dotted lines. Atoms of C, O, N, Br and H are shown in cyan, red, blue, orange and white colors, respectively. (c) Temperature dependent $^{1}$H NMR spectra of compound **4a**. (d) Temperature dependent change in fluorescence emission spectra of compound **4a** in water. (e, f) Images and fluorescence emission spectra of compound **4a** in different pH (g) Fluorescence emission spectra of compound **4b** in different pH

### *3.2.4.3 Effect of pH on the AIE property:*

Inter- and intra-molecular H-bonding leading to AIE property is highly sensitive to the pH of the medium.[39] Hence, we perturbed intra-molecular H-bonding by increasing the pH of the medium from 7.4 to 8.5. Interestingly, it was observed that compound **4a** lost its fluorescence property completely (Figure 3.5e, f) leading to the destruction of H-bonding in structure **4a"**. On the other hand, decreasing the pH from 8.5 to 7.4 resumed the fluorescence property into compound **4a** which even retained at much lower pH = 4 (Figure 3.5e, f). As expected, compound **4b** also showed similar pH dependent fluorescence property (Figure 3.5g). For future mitochondrial imaging, the AIE probe should be fluorescent at pH 7.8-8.0 which mimics the mitochondria matrix. Hence, we assessed the AIE property of compound **4a** at pH = 7.8 and 8.0. It was observed that the fluorescence intensity of compound **4a** was marginally reduced at pH = 7.8 and 8.0 compared to pH = 7.4 (Figure 3.6a, b). Also 9.3% quantum yield was calculated for compound **4a** at pH = 7.8 which indicated that compound **4a** is suitable for mitochondrial bio-imaging.

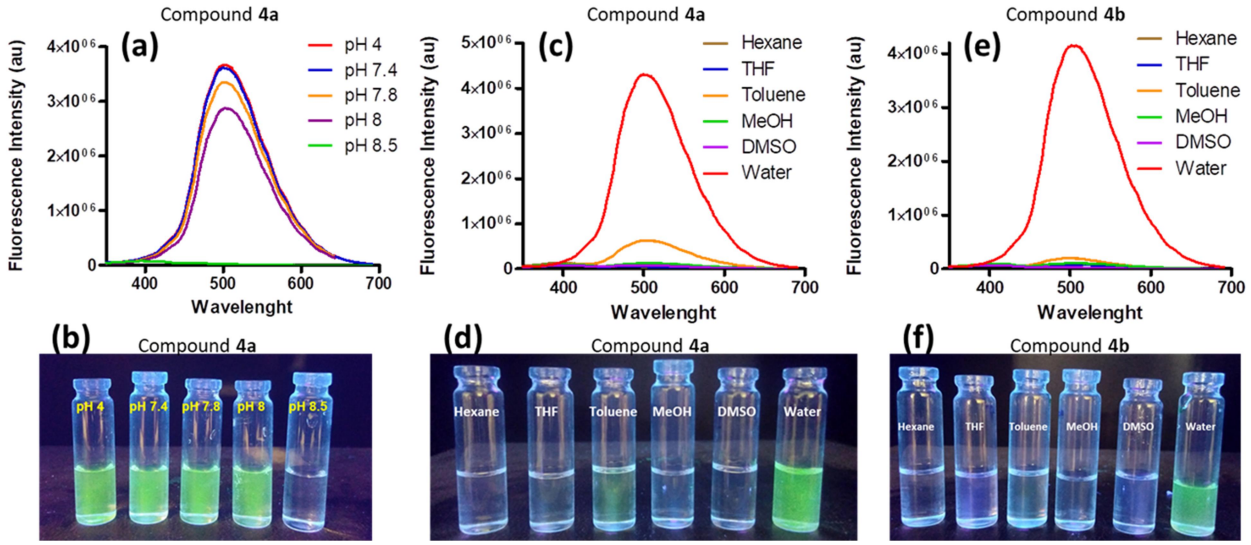


**Figure 3.6:** (a) pH dependent change in fluorescence emission spectra of compound **4a** (b) Fluorescent emission images of compound **4a** in different pH under UV light. (c, e) Fluorescence emission spectra of compound **4a** and **4b** in different solvents. (d, f) Fluorescence emission images of compound **4a** and **4b** in different solvents under UV light.

#### *3.2.4.4 Effect of solvents on the AIE property:*

We further evaluated the effect of solvents on the AIE property of compound **4a** and **4b**. To our surprise, compound **4a** showed high and marginal AIE property in water and toluene respectively

(Figure 3.6c, d). However, compound **4a** showed no AIE property in other solvents like hexane, THF and DMSO. Similarly, compound **4b** also demonstrated AIE property in water only (Figure 3.6e, f). This theoretical calculation along with temperature and pH dependent reversible fluorescence quenching-regaining clearly confirmed the role of intra-molecular H-bonding in inducing AIE property in compound **4a**. However, we anticipate that the amphiphilicity of compound **4a** and **4b** also played a crucial role in inducing AIE property, which needs to be explored carefully in future to understand the exact mechanism.

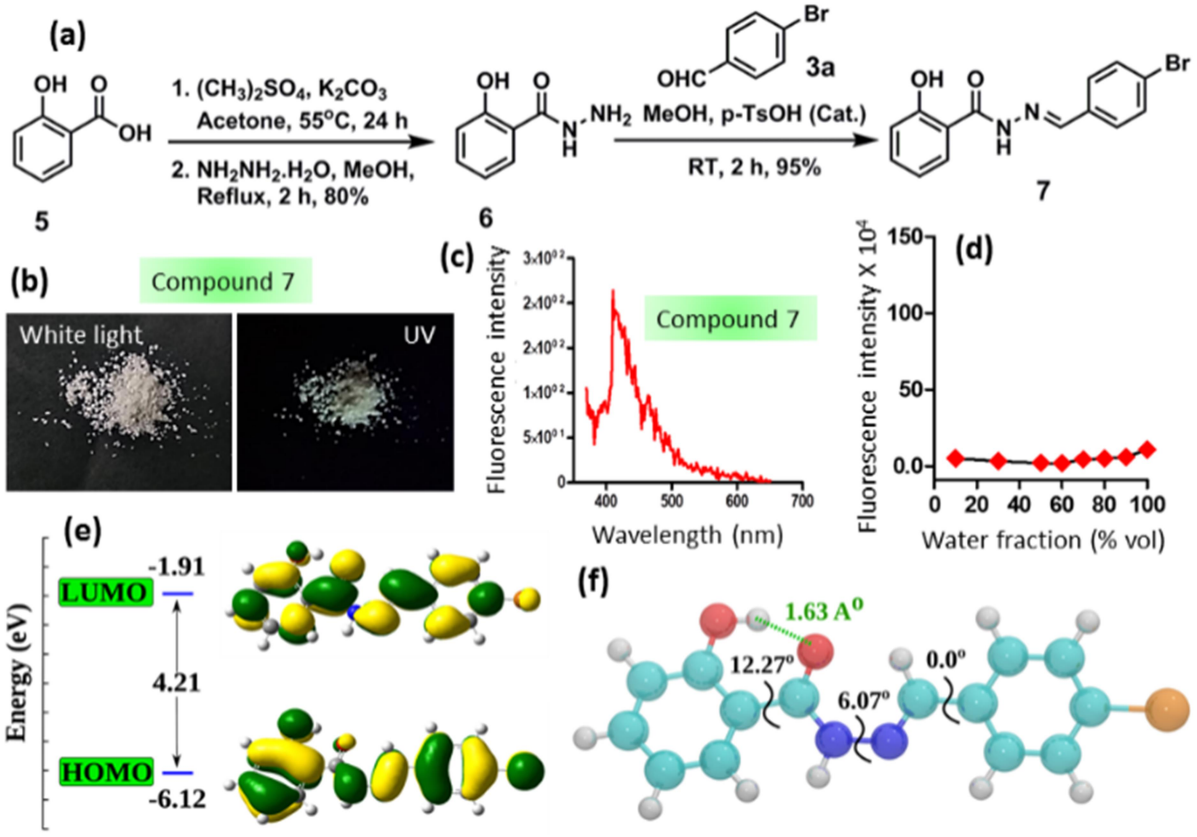


**Figure 3.7:** (a) Scheme for the synthesis of compound 7. (b) Solid state fluorescence images of compound 7 under white light and UV. (c) Fluorescence spectra of compound 7 in water. (d) Fluorescence emission intensity versus water fraction graph of compound 7 in different methanol: water mixture.(e) Schematic diagram of the energy level difference between the HOMOs and LUMOs of compound 7, estimated from DFT computation and the isodensity surface plots of the frontier molecular orbitals (FMOs) with isovalue of 0.02 au. (f) Optimized geometry of compound 7 obtained from B3LYP/6-31G* computation. Black zig-zag lines showing values for the respective dihedral angles (in degree) whereas hydrogen bonding is shown in green dotted lines. The atoms of C, O, N, Br and H are shown in cyan, red, blue, orange and white colors, respectively.

### 3.2.5 Validation of hydrogen bond guided AIE property:

One of the plausible mechanisms of this photophysical property of compound **4a, b** could be exited state intramolecular proton transfer (ESIPT).[40,41] To validate the involvement of ESIPT as well as the role of dual intra-molecular H-bonding in triggering AIE property in compound **4a**, we have synthesized mono-hydroxy hydrazide-hydrazone compound **7** starting from 2-hydroxybenzoic acid (**5**) by the same synthetic strategy via 2-hydroxy benzohydrazide (**6**) (Figure 3.7a). All the compounds were chemically characterized by NMR ($^{1}$H and $^{13}$C) and HR-MS spectroscopy (Annexin-B; Figure B10-15). Interestingly, compound **7** showed negligible fluorescence property in solid state as well as in water (Figure 3.7b, c). We further evaluated the change in fluorescence property in methanol/water mixture. Negligible increase in fluorescence intensity of compound **7** was observed in 100% methanol to 100% water (Figure 3.7d). The Frontier molecular orbitals and the energy gap between HOMOs and LUMOs of compound **7** were calculated by DFT which showed the energy gap was ~ 4.21 eV (~ 295 nm) (Figure 3.7e) comparable to the energy gap in compound **4a**. Finally, we executed theoretical calculations using Gaussian 09 program on compound **7**. Most interestingly, the optimized molecular geometry of compound **7** showed the dihedral angle of the mono-intramolecular H-bonded moiety was increased to ~12.3º (Figure 3.7f) compared to nearly 0º dihedral angle found in compound **4a**. This clearly indicated that single intra-molecular H-bonding is not sufficient to maintain coplanarity along the largest molecular axis in compound **7** leading to lack of aggregated structure with negligible AIE property. Moreover, in chapter 2, we synthesized O-phenyl-hydrazide–hydrazone analogue of compound 7, which showed no AIE in the solid state as well as in solution. These solid state fluorescence, water titration studies and theoretical structure optimization clearly confirmed that (i) *ESIPT is not the mechanism involved* and (ii) *dual intra-molecular H-bonding is critical to maintain the planarity in compound **4a, b** to induce aggregation to show AIE property*. However, at this point, the exact mechanism of this photophysical phenomena in these novel hydrazide-hydrazone based small molecules is elusive and we are exploring this area currently.

### 3.2.6 Biocompatibility studies

To be successful in bio-imaging, the hydrazide-hydrazone AIE probes should be biocompatible. Hence, we evaluated the *in vitro* cytotoxicity of compound **4a** and **4b** in HeLa cervical cancer

cells at 48 h post-incubation in a dose dependent manner. The cell viability was measured by MTT assay which showed compound **4a** induced only 94.2 ± 4.5 %, 97.4 ± 2.2 % and 91.8 ± 5.6 % cell viability at 12.5, 25 and 50 µM concentrations respectively (Figure 3.8a). Similarly, compound **4b** also demonstrated 99.5 ± 0.4 %, 95.3 ± 2.7 % and 94.1 ± 2.2 % cell viabilities at 12.5, 25 and 50 µM concentrations (Figure 3.8a). To evaluate the biocompatibility in non-cancerous cells, we incubated fibroblast L929 cells with compound **4a** and **4b** in a concentration dependent manner for 24 h. The MTT assay revealed that compound **4a** induced only 97.6 ± 1.4%, 94.3 ± 1.7% and 86.3 ± 1.8% cell viability at 12.5, 25 and 50 µM concentrations respectively (Figure 3.8b). Similarly, compound **4b** also showed only 94.6 ± 4.8%, 91.3 ±5.6% and 83.2 ± 2.3% cell viability at 12.5, 25 and 50 µM concentrations respectively. This cell viability assay confirmed that compound **4a** and **4b** were not at all toxic to the cancer cells as well as non-cancerous fibroblast cells, hence can be used for bio-imaging.

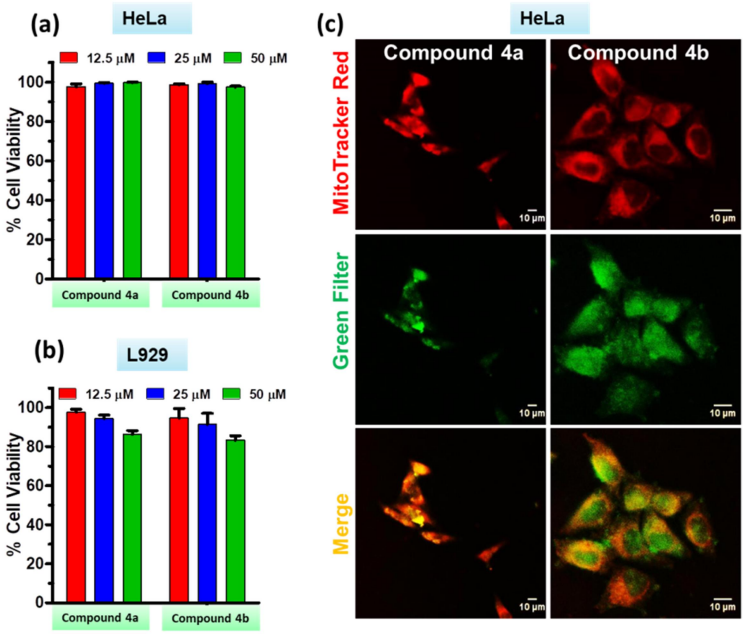


**Figure 3.8:** (a, b) Viability of HeLa and L929 cells after treatment with compound **4a** and **4b** for 48 h and 24h respectively in a concentration dependent manner by MTT assay. (c) Confocal laser scanning microscopy (CLSM) images of HeLa cells after treatment with compound **4a** and **4b** for 12 h. Mitochondria were stained with MitoTraker Red dye. Scale bar = 10 µm.

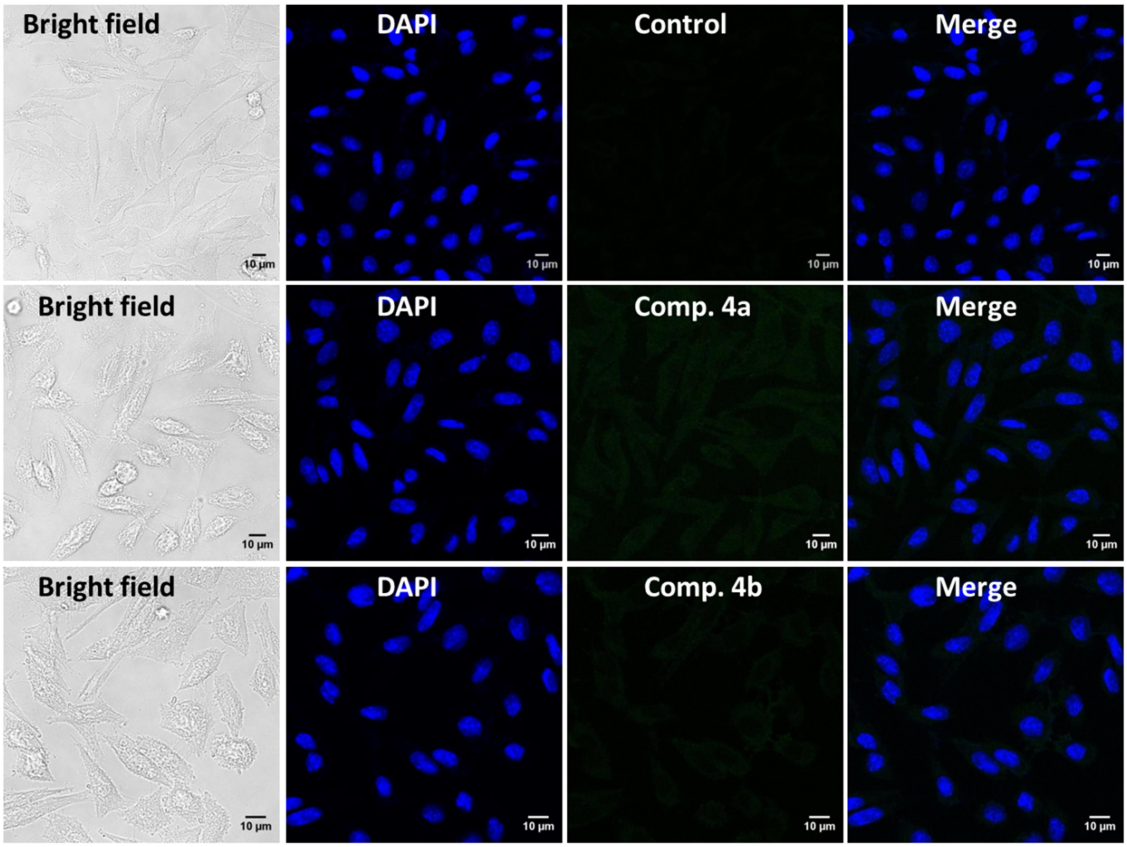


**Figure 3.9:** Confocal laser scanning microscopy images of non-cancerous L929 fibroblast cells at 12 h incubation with compound 4a and 4b. Nuclei of the cells were stained by DAPI (blue). Scale bar = 10 µm.

### *3.2.7* Mitochondrial colocalization of compound 4a and 4b

To evaluate the effectiveness of compound **4a** and **4b** in sub-cellular mitochondria imaging in cancer cells, we treated HeLa cells with both the compounds at 10 µM concentrations for 12 h. Mitochondria were co-stained by MitoTracker Red dye and the live cells were visualized by fluorescence confocal microscopy. Confocal images in Figure 3.8c evidently showed that both compounds **4a** and **4b** were internalized into the cells successfully and localized into mitochondria leading to the generation of yellow regions by overlapping green and red fluorescence signals. However, both the compounds were also localized into the nucleus of the cells significantly. In fact, compound **4a** and **4b** showed non-specific sub-cellular localization which was non-effective in specific mitochondria labeling. Furthermore, to estimate the cancer cell specificity over non-cancerous cells, we incubated fibroblast L929 cells with compound **4a**

and **4b** at 20 μM concentrations for 12 h. The nuclei of the cells were counter stained with blue fluorescence DAPI. The cells were then fixed and visualized by confocal microscopy. Surprisingly, the fluorescence microscopy images (Figure 3.9) hardly showed any sub-cellular green fluorescence signals, indicating that compound **4a** and **4b** barely internalized into L929 cells even after 12h. These confocal images confirmed that the novel AIE active hydrazide-hydrazone derivatives specifically internalized into HeLa cancer cells over L929 non-cancerous cells.

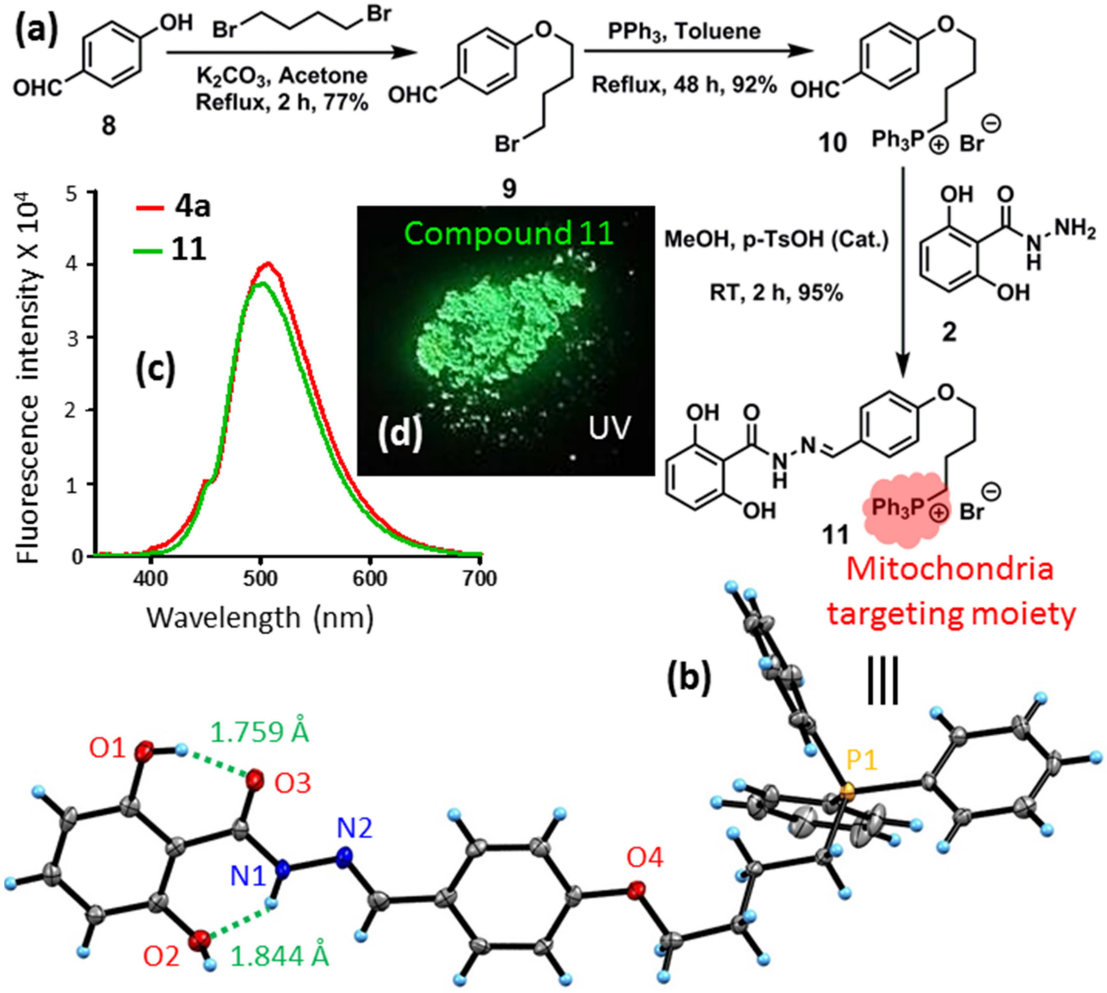


**Figure 3.10:** (a) Synthetic scheme of mitochondria targeted hydrazide-hydrazone molecule (11). (b) ORTEP diagram of compound 11 with 50% thermal ellipsoids. Solvent and counter ion removed for clarity. (c) Fluorescence emission spectra of compound 11 in water. (d) Fluorescence emission image of compound 11 in solid state under UV light

### 3.2.8 Selectively illuminate mitochondria in HeLa cells:

#### *3.2.8.1 Synthesis of compound 11 and characterization*

To overcome this challenge, we have synthesized hydrazide-hydrazone based molecule tagged with positively charged triphenylphosphonium (TPP) moiety for mitochondria targeting. 4-hydroxybenzaldehyde (**8**) was first reacted with excess 1,4-dibromobutane in the presence of potassium carbonate as base in acetone in refluxing condition to obtain compound **9** in 77 % yield (Figure 3.10a). The bromine moiety was further replaced by triphenylphosphine in refluxing condition to obtain compound **10** in 92% yield. Finally, compound **10** was coupled with 2,6-dihydroxy benzohydrazide (**2**) in presence of *p*-TsOH as catalyst to obtain positively charged triphenylphosphonium tagged hydrazide-hydrazone (**11**) in 95% yield. NMR ($^{1}$H, $^{13}$C and $^{31}$P) and HR-MS were used to characterize all the compounds (Annexin-B; Figure B16-26). We also characterized the structure of compound **11** by X-ray crystallography (Figure 3.10b; Annexin-B Table B1) which clearly confirmed the presence of proposed dual intra-molecular H-bonding correlating with the theoretical electronic structure in Figure 3b.We further assessed the photo-physical properties of compound **11** which showed fluorescence emission at $\lambda_{max}$ = 500 nm in water as well as AIE in solid state under UV light (Figure 3.10c, d).

#### *3.2.8.2 Biocompatibility and mitochondria visualization*

The viability of HeLa cells in presence of compound **11** after 48 h was determined by MTT assay in a dose dependent manner. This cell viability assay showed that compound **11** induced only 5.5± 1.8, 15.9±3.7 and 23.8±3.6 % cell death at 12.5, 25 and 50 μM concentrations respectively (Figure 3.11a). We also evaluated the biocompatibility of compound **11** in non-cancerous fibroblast L929 cells at 24 h post-incubation. The MTT assay revealed that compound **11** induced 92.0± 3.5%, 87.6 ± 1.4% and 76.1 ±1.9% cell viability at 12.5, 25 and 50 μM concentrations respectively (Figure 3.11b). These cell viability assays indicated that compound **11** is biocompatible for cervical cancer cells as well as non-cancerous fibroblast cells for imaging. Furthermore, compound **11** showed much better biocompatibility compared to the traditionally used Rhodamine 123 as mitochondria staining red fluorescent dye.[42,43]

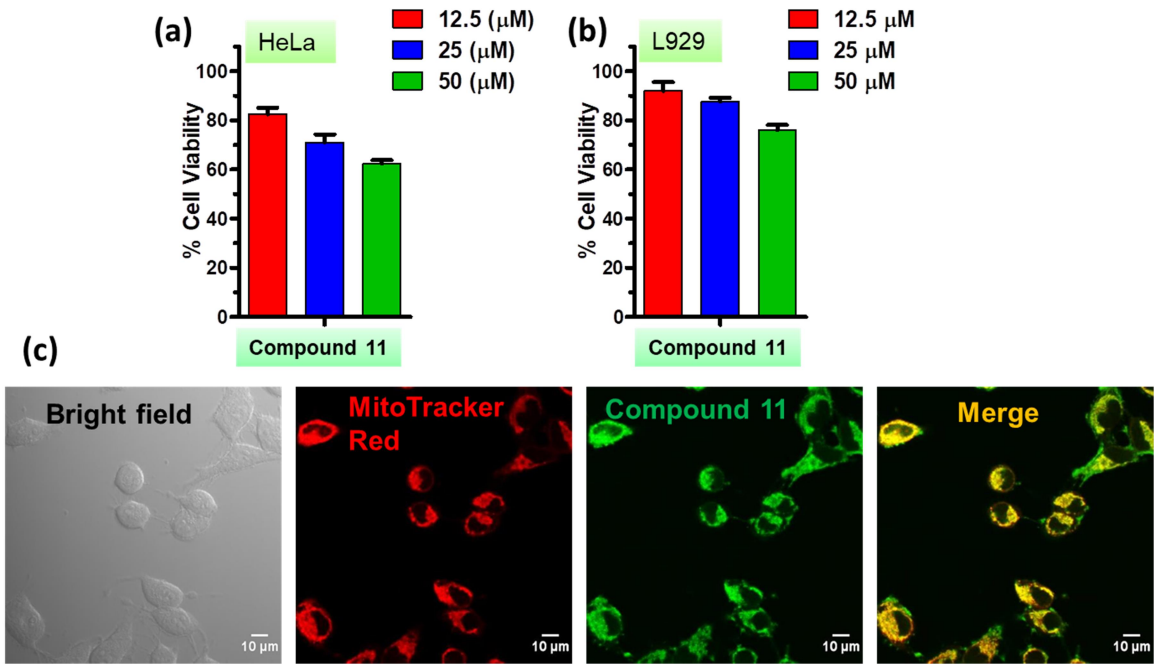


**Figure 3.11:** (a) Viability of HeLa cells after treatment with compound **11** in a dose dependent manner for 48 h by MTT assay. (b) Cell viability assay of compound **11** in L929 cells at 24 h post-incubation (c) CLSM images of HeLa cells after treatment with compound **11** for 12 h. Mitochondria were stained by MitoTracker Red. Scale bar = 10 μm

To estimate its potential in mitochondria imaging, we treated HeLa cells with compound **11** at 10 μM concentration for 12 h, followed by staining mitochondria by MitoTracker Red. The confocal images of the live cells (Figure 3.11c) evidently showed that compound **11** homed into mitochondria of HeLa cells leading to yellow overlapping regions. Interestingly, hardly any green fluorescence signal was observed into nucleus of the HeLa cells, which confirmed the specific mitochondria imaging by compound **11**. We also visualized the specificity of compound **11** to illuminate mitochondria in cancer cells over non-cancerous cells by confocal microscopy. Non-cancerous fibroblast L929 cells were treated with compound **11** at 20 μM concentration followed by staining nuclei and mitochondria by DAPI (blue) and MitoTracker Red (red). The confocal microscopy images (Figure 3.12) barely showed any green or yellow fluorescence signal inside the cells or in mitochondria respectively. This microscopy experiment established that compound **11** is highly specific for mitochondria in HeLa cancer cells compared to non-cancerous L929 cells at much lower concentration compared to Rhodamine 123.[44]

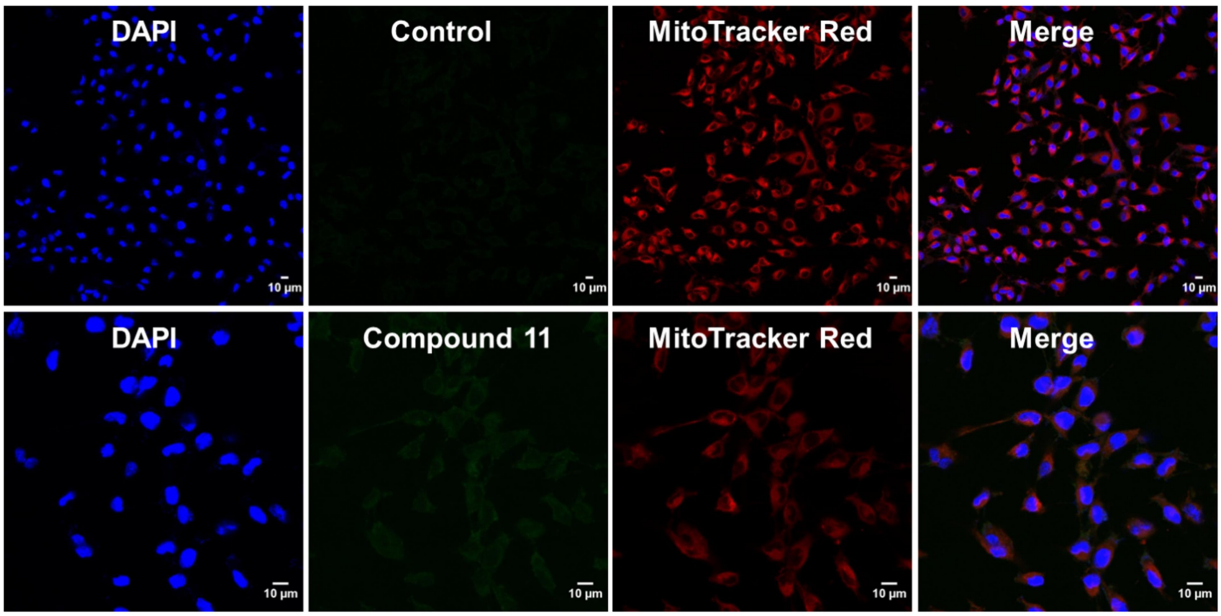


**Figure 3.12:** CLSM images of non-cancerous L929 fibroblast cells after incubation with compound 11 for 12 h. Nuclei and mitochondria were stained by DAPI (blue) and MitoTracker Red (red) dye. Scale bar = 10 µm

## 3.3 Conclusion

We have synthesized hydrazide-hydrazone based small molecules in concise and easy steps in high yield, which demonstrated for the first time remarkable aggregation-induced emission (AIE) property in water as well as in solid state. Theoretical calculation, crystal structure, proton-NMR spectroscopy along with reversible temperature and pH dependent studies confirmed that dual intra-molecular H-bonding was responsible for restricting the intra-molecular motion to show this hitherto unobserved AIE property. A triphenylphosphonium labeled hydrazide-hydrazone AIEgen was synthesized to illuminate mitochondria in HeLa cells selectively. These novel biocompatible hydrazide-hydrazone small molecules can be used as platform to develop innovative AIEgens to image different sub-cellular organelles and targets in cancer cells as future theranostic strategies by incorporating photothermal and photo-dynamic probes.

## 3.4 Material and methods

### 3.4.1 Materials

Materials were purchased from commercial suppliers or vendors and used without further purification unless noted otherwise. All reactions were performed in the oven-dried glassware with or without inert gas. Analytical thin-layer chromatography (TLC) was performed using pre-coated silica gel aluminium sheets 60 F254 bought from EMD Millipore Laboratories. The compounds were purified by column chromatography by using silica gel 100-200 mesh as the stationary phase. $^{1}H$, $^{13}C$, $^{31}P$ spectra were recorded on a Bruker Avance III HD Ascend 9.4 Tesla/400 MHz with autosampler and/or Jeol 9.4 Tesla/400 MHz with autosampler spectrometer. The chemical shifts are mention in parts per million (ppm) and referred to residual protons on the corresponding deuterated solvent. DMEM media and 3-(4, 5-dimethylthiazol-2-yl)-2, 5-diphenyltetrazolium bromide (MTT) was purchased from HiMedia. Nunc® Lab-Tek® II chambered coverglass, and Sodium dodecyl sulfate (SDS) was purchased from Sigma-Aldrich. MitoTracker® Red CMXRos was purchased from Thermo Fisher Scientific.

### 3.4.2 Synthesis of AIEgen

#### *3.4.2.1 Synthesis of 2, 6-dihydroxybenzohydrazide (2):*

To an oven-dried 100 mL round-bottom flask with a magnetic stirrer, 2,6-dihydroxybenzoic acid (1 g, 6.5 mmol, 1 equiv), dimethyl sulphate (0.55 mL, 5.8 mmol, 0.9 equiv) potassium carbonate (0.9 g, 6.5 mmol, 1 equiv) were dissolved in 20 mL of acetone. The reaction mixture was stirred at 55°C for 24 h. Acetone was evaporated with the help of a rotary evaporator. After neutralization to pH = 7 using 1 M HCl, the reaction mixture was extracted with ethyl acetate (3 × 50 mL). The combined organic layer was washed with saturated $Na_2HCO_3$ solution (3 × 50 mL) followed by brine, dried over anhydrous $Na_2SO_4$, filtered and concentrated with the help of a rotary evaporator. The product, methyl ether of 2,6-dihydroxybenzoic acid (1 g, 5.95 mmol, 1 equiv) was taken in the oven-dried 100 mL flask with a magnetic stirrer and dissolved in methanol (20 mL). Hydrazine monohydrate (3 mL, 59.5 mmol, 10 equiv) was added drop-wise and kept stirring at room temperature for 2 h. After 2 h, methanol was evaporated on a rotary evaporator. The crude product was purified by silica gel column chromatography using MeOH (5%) in DCM solvent system. White color solid product (**2**) was separated with 80 % overall yield.

**Characterization**

**$^{1}$H NMR** (400 MHz, Methanol-d4): $\delta$= 7.13 (t, $J$ = 8.2 Hz, 1H), 6.36 (d, $J$ = 8.2 Hz, 2H).

**$^{13}$C NMR** (100 MHz, Methanol-d4): δ= 171.29, 161.33, 134.44, 108.38, 103.07.

**HRMS (ESI-TOF):** m/z: [M + H] calculated for $C_7H_9N_2O_3$ 169.0613; found 169.0617.

#### *3.4.2.2 Synthesis of N'-(4-bromobenzylidene)-2, 6-dihydroxybenzohydrazide (4a)*

In a clean and oven-dried 25 mL round-bottom flask with magnetic stirrer, solution of compound **2** (50 mg, 0.29 mmol, 1 equiv) in absolute methanol (1.5 mL) were added 4-bromobenzaldehyde (55 mg, 0.29 mmol, 1 equiv) and catalytic amount of *p*-toluenesulfonic acid. After stirring for 2 h at room temperature, methanol was evaporated using rotary evaporator. The crude product was purified by silica gel column chromatography using MeOH (2 %) in DCM solvent system. White color solid product (**4a**) was purified with 95 % yield.

**Characterization**

**$^{1}$H NMR** (400 MHz, DMSO-D6): *δ*= 12.07 (s, 2H), 11.81 (s 1H), 8.40 (s, 1H), 7.91-7.51 (m, 4H), 7.21 (t, *J* = 8.2 Hz, 1H), 6.43 (d, *J* = 8.2 Hz, 2H).

**$^{13}$C NMR** (100 MHz, DMSO-D6): *δ*= 166.08, 159.65, 148.06, 133.71, 133.35, 131.94, 129.18, 123.66, 107.25, 103.47.

**HRMS (ESI-TOF):** m/z: [M + H] calculated for $C_{14}H_{12}BrN_2O_3$ 335.0031; found 335.0029.

#### *3.4.2.3 Synthesis of 2, 6-dihydroxy-N'-(4-hydroxybenzylidene) benzohydrazide (4b)*

In a clean and oven-dried 25 mL round-bottom flask with magnetic stirrer, solution of compound **2** (50 mg, 0.29 mmol, 1 equiv) in absolute methanol (1.5 mL) were added 4-metoxybenzaldehyde (36.17 µL, 0.29 mmol, 1 equiv) and catalytic amount of *p*-toluenesulfonic acid. After stirring for 2 h at room temperature, the methanol was evaporated using rotary evaporator. The crude product was purified by silica gel column chromatography using MeOH (3 %) in DCM solvent system. White color solid product was purified with 90 % yield.

**Characterization:**

**$^{1}$H NMR** (400 MHz, DMSO-d6): *δ*= 12.22 (s, 2H), 11.67 (s, 1H), 8.35 (s, 1H), 7.70 (d, *J* = 8.8 Hz, 2H), 7.20 (t, *J* = 8.2 Hz, 1H), 7.04 (d, *J* = 8.8 Hz, 2H), 6.42 (d, *J* = 8.2 Hz, 2H), 3.82 (s, 3H).

**$^{13}$C NMR** (100 MHz, DMSO-d6): *δ*= 165.94, 161.09, 159.76, 149.25, 133.62, 129.03, 126.53, 114.40, 107.26, 103.09, 55.35, 39.52.

**HRMS (ESI-TOF)**: m/z: [M + H] calculated for $C_{15}H_{15}N_2O_4$ 287.1032; found 287.1039.

#### *3.4.2.4 Synthesis of N'-(4-bromobenzylidene)-2-hydroxybenzohydrazide (7)*

Compound **7** was synthesized by using the same protocol of compound **4a** starting from 2-hydroxybenzoic acid (**5**) in 95 % yield.

**Characterization of 2-hydroxybenzohydrazide 6:**

**$^1$H NMR** (400 MHz, DMSO-D6): $\delta$= 12.50 (s, 1H), 10.05 (s, 1H), 7.79 (dd, $J$ = 7.9, 1.4 Hz, 1H), 7.37 (ddd, $J$ = 8.5, 7.3, 1.6 Hz, 1H), 6.91 – 6.82 (m, 2H), 4.63 (s, 2H).

**$^{13}$C NMR** (100 MHz, DMSO-D6): $\delta$= 167.95, 159.64, 133.42, 127.08, 118.65, 117.32, 114.36.

**HRMS (ESI-TOF)**: m/z: [M + H] calculated for $C_7H_8N_2O_2$ 153.0664; found 153.0663.

**Characterization of N'-(4-bromobenzylidene)-2-hydroxybenzohydrazide 7:**

**$^1$H NMR** (400 MHz, DMSO-d6): $\delta$= 11.89 (s, 1H), 11.78 (s, 1H), 8.44 (s, 1H), 7.88 (dd, $J$ = 7.9, 1.2 Hz, 1H), 7.72-7.65 (m, 4H), 7.47-7.42 (m, 1H), 6.97 (dd, $J$ = 12.5, 7.8 Hz, 2H).

**$^{13}$C NMR** (100 MHz, DMSO-d6): $\delta$= 164.71, 158.86, 147.38, 133.86, 133.43, 131.90, 129.09, 128.68, 123.54, 119.01, 117.26, 116.04.

**HRMS (ESI-TOF):** m/z: [M + H] calculated for $C_{14}H_{11}BrN_2O_2$ 319.0082; found 319.0087.

#### *3.4.2.5 Synthesis of 4-(4-bromobutoxy) benzaldehyde (9)*

To an oven-dried 50 mL two-neck round-bottom flask with a magnetic stirrer under nitrogen, 4-hydroxybenzaldehyde (**8**) (0.5 g, 4.1 mmol, 1 equiv), 1,4-dibromobutane (3.54 mL, 16.1 mmol, 4 equiv) potassium carbonate (1.42 g 20.5mmol, 5 equiv) were dissolved in 20 mL of dry acetone. The reaction mixture was refluxed for 5 h. After complete consumption of 4-hydroxybenzaldehyde (checked by TLC), the reaction mixture was then cooled to room temperature. The reaction mixture was filtered through celite and acetone was evaporated. Aqueous NaOH was added and the reaction mixture was extracted with ethyl acetate (3 × 20 mL). The combined organic layer was washed with brine, dried over anhydrous $Na_2SO_4$, filtered and concentrated with the help of a rotary evaporator. The crude product was purified by silica gel column chromatography using ethyl acetate (5%) in the pet-ether solvent system. Yellow color oily product was purified in 77 % yield.

**Characterization:**

**$^1$H NMR** (400 MHz, $CDCl_3$): $\delta$= 9.86 (s, 1H), 7.81 (d, $J$ = 8.7 Hz, 2H), 6.97 (d, $J$ = 8.6 Hz, 2H), 4.07 (t, $J$ = 5.9 Hz, 2H), 3.48 (t, $J$ = 6.4 Hz, 2H), 2.11-2.03 (m, 2H), 2.01-1.94 (m, 2H).

**$^{13}$C NMR** (100 MHz, $CDCl_3$): $\delta$= 190.89, 163.98, 132.09, 130.02, 114.80, 67.34, 33.35, 29.37, 27.77.

**HRMS (ESI-TOF):** m/z: [M + H] calculated for $C_{11}H_{14}BrO_2$ 259.0157; found 259.0159.

#### *3.4.2.6 Synthesis of (4-(4-formylphenoxy)butyl) triphenylphosphonium bromide (10):*

To a 25 mL oven-dried round-bottom flask with a magnetic stirrer under $N_2$ atmosphere, triphenylphosphine (0.1 g, 0.39 mmol, 1 equiv), (**9**) (0.1g, 0.39 mmol, 1 equiv) was dissolved in dry toluene (2 mL) and reflux for 48 h. Progress of the reaction was monitored by TLC. After 48 h, the solidified reaction mixture was cooled to room temperature and washed with pentane (3 × 5 mL) followed by ethyl acetate (3 × 5 mL). Residual solvent was removed by high vacuum pump and collected yellow crystalline solid in 92 % yield.

**Characterization:**

**$^1$H NMR** (400 MHz, $CDCl_3$): $\delta$= 9.81 (s, 1H), 7.84-7.72 (m, 12H), 7.67-762 (m, 5H), 6.92 (d, $J$ = 8.7 Hz, 2H), 4.18 (t, $J$ = 5.8 Hz, 2H), 3.95-3.84 (m, 2H), 2.26-2.19 (m, 2H), 1.89-1.79 (m, 2H).

**$^{13}$C NMR** (100 MHz, $CDCl_3$): $\delta$= 190.92, 163.88, 135.13, 135.10, 133.77, 133.67, 132.07, 130.61, 130.49, 129.91, 118.67, 117.81, 114.94, 67.08, 29.29, 21.89, 19.27.

**$^{31}$P NMR** (162 MHz, $CDCl_3$): $\delta$= 24.45.

**HRMS (ESI-TOF)** m/z: [$M^+$] calculated for $C_{29}H_{28}O_2P^+$ 439.1821; found 439.1829.

#### *3.4.2.7 Synthesis of (4-(4-((2-(2,6-dihydroxybenzoyl) hydrazineylidene) methyl) phenoxy) butyl) triphenylphosphonium bromide (11):*

In a clean and dried 25 mL round-bottom flask with magnetic stirrer, solution of **2** (25 mg, 0.15 mmol, 1 equiv) in absolute methanol (1.5 mL) was added into compound **11** (77 mg, 0.15 mmol, 1 equiv) and catalytic amount of *p*-toluenesulfonic acid. After stirring for 2 h at room temperature, methanol was evaporated using rotary evaporator. The resulting crude reaction mixture was washed with acetone (3 × 5 mL) followed by diethyl ether (3 × 5 mL) and yellow color solid product (**11**) was collected in 95 % yield.

**Characterization:**

**$^{1}$H NMR** (400 MHz, $CD_3OD$): $\delta$= 8.20 (s, 1H), 7.92-7.85 (m, 4H), 7.84-7.71 (m, 13H), 7.22 (td, *J* = 8.3, 2.3 Hz, 1H), 6.94-6.87 (m, 2H), 6.44 (dd, *J* = 8.5, 1.1 Hz, 2H), 4.09 (q, *J* = 6.2 Hz, 2H), 3.58-3.44 (m, 2H), 2.08-1.99 (m, 2H), 1.91-1.85 (m, 2H).

**$^{13}$C NMR** (100 MHz, $CD_3OD$): $\delta$= 168.71, 168.69, 162.30, 161.73, 151.25, 136.29, 136.26, 135.38, 134.83, 134.73, 131.65, 131.59, 131.57, 131.47, 131.40, 131.38, 130.75, 127.92, 120.19, 120.17, 119.33, 115.80, 108.71, 103.01, 79.48, 67.55, 30.75, 20.22.

**$^{31}$P NMR** (162 MHz, $CD_3OD$): $\delta$= 24.47.

**HRMS (ESI-TOF):** m/z: [$M^+$] calculated for $C_{36}H_{34}N_2O_4P^+$ 589.2251; found 589.2258.

### 3.4.3 Dynamic Light Scattering (DLS):

DLS was recorded using Zetasizer Nano2590 (Malvern, UK). A 20 μM solution of compound **4** was diluted in methanol and deionized water. DLS was recorded in triplicate.

### 3.4.4 Field-Emission Scanning Electron Microscopy (FE-SEM):

FE-SEM was recorded using Carl Zeiss, Ultra plus, scanning electron microscope. 10 μL microliters of a diluted solution of compound **4a** in water and methanol were placed on a silicon chip without any dopant, and it was allowed to dry at room temperature under vacuum desiccators for 2 h. The silicon chips were then gold coated (30-40 nm thickness) using Quorum, Q150T-E5 and then images were taken.

### 3.4.5 General protocols for photo-physical studies:

A 5 mM stock solution of compounds **4a** and **4b** was prepared in methanol or dimethyl sulphoxide. A 10 μM concentration of **4a** and **4b** was made from a stock solution to record ultra-violate spectra in methanol and water. The UV spectra were recorded on a Shimadzu UV-2600 spectrophotometer. From a stock solution of methanol, a series of dilution of **4a** and **4b** in methanol and water (v/v) were prepared. A 10 μM uniform concentration was kept through the experiment. The fluorescence of solution was recorded on a Fluoromax-4 spectrofluorometer (Horibha Scientific) using slit width 4/4.5 Solid state fluorescence was recorded using FLS 980, Edinburg Instrument. For temperature dependent fluorescence measurements, a 20 μM stock of **4a** in DMSO was used for the preparation of 99% aqueous solution. A magnetic stir bar was kept

in the cuvette to ensure a uniform temperature throughout the sample. Sample excited at 322 nm, and the PL spectra were recorded at 450 nm. The temperature was increased by 10 degree Celsius each time the fluorescence was recorded. (Slit width: excitation/emission = 4/5) using PerkinElmer EnSight multimode plate reader. Three different solutions of compound **4a** of 10 μM each were maintained at three different pH (8.5, 7.4 and 4). 1 M aq. HCl was then added drop-wise to solution with pH 8.5 till it reduced to pH 7.4 and further to pH 4. The solutions were visualized under UV light.

Quantum yields were calculated with reference to Quinine Sulphate in 0.1M $H_2SO_4$.

### 3.4.6 Cell viability assay:

100 μL of four thousand HeLa cells in DMEM media were seeded per well in 96-well microtiter plate and incubated for 16 h in a 5% $CO_2$ incubator at 37 °C for attachment. Cells were treated with compounds **4a, 4b** and **11** at different concentrations for 48 h. After 48 h, DMEM media with compounds were removed, and 100 μL MTT solutions in DMEM (0.5 mg/ ml) was added to each well and incubated for 4 h at 37 °C. Formazan crystals were then solubilized in 50 μL of the solubilization buffer (10% SDS in 0.01 M HCl) and incubated overnight. Absorbance was measured using a PerkinElmer EnSight multimode plate reader at 570 nm. The percent cell viability was calculated considering the untreated cells as 100% viability.

### 3.4.7 General protocols for CLSM imaging:

A quantity of $1.5 \times 10^4$ cells were seeded in a Lab-Tek chamber slide 8 well (per well) for attachment. Cells were incubated with compound **4a, 4b** and **11** (10 μM) for 12 h. Control was kept without adding any compounds. Cells were then washed thrice with cold PBS (pH 7.4) and treated with MitoTracker™ Red CMXRos (200 nM in PBS (pH 7.4)) for 25 minutes. Cells were then washed three times with PBS (pH 7.4) and imaged immediately by confocal laser scanning microscope (CLSM, Zeiss LSM 710). Compound **11** was excited at 405 nm and 497-584 nm emission filter was used; for MitoTracker™ Red CMXRos as prescribe manual.

## 3.5 References:

1. J. Mei, N. L. C. Leung, R. T. K. Kwok, J. W. Y. Lam, B. Z. Tang. Aggregation-Induced Emission: Together We Shine, United We Soar! *Chem. Rev.* **2015**, *115*, 11718-11940.

2. B. Liu, R. Zhang. Aggregation Induced Emission: Concluding Remarks. *Faraday Discussion* **2017**, *196*, 461-472.
3. X. Jiang, H. Gao, X. Zhang, J. Pang, Y. Li, K. Li, Y. Wu, S. Li, J. Zhu, Y. Wei, L. Jiang. Highly-Sensitive Optical Organic Vapor Sensor through Polymeric Swelling Induced Variation of Fluorescent Intensity. *Nat. Commun*. **2018**, *9*, 3799.
4. Y. Chen, X. Min, X. Zhang, F. Zhang, S. Lu. L. Xu, X. Lou, F. Xia, X. Zhang, S. Wang. AIE-based Superwettable Microchips for Evaporation and Aggregation Induced Fluorescence Enhancement Biosensing. *Biosens. Bioelectron*. **2018**, *111*, 124-130.
5. J. Qi, C. Chen, D. Ding, B. Z. Tang. Aggregation-Induced Emission Luminogens: Union Is Strength, Gathering Illuminates Healthcare. *Adv. Healthc. Mater.* **2018**, *7*, e1800477.
6. C. Zhu, R. T. K. Kwok, J. W. Y. Lam, B. Z. Tang. Aggregation-Induced Emission: A Trailblazing Journey to the Field of Biomedicine. *ACS Appl. Bio. Mater.* **2018**, *1*, 1768-1786.
7. Y. Hong, J. W. Y. Lam, B. Z. Tang. Aggregation-Induced Emission: Phenomenon, Mechanism and Applications. *Chem. Commun*. **2009**, *0*, 4332-4353.
8. Y. Hong, J. W. Y. Lam, B. Z. Tang. Aggregation-induced Emission. *Chem. Soc. Rev*. **2011**, *40*, 5361-5388.
9. D. Ding, K. Li, B. Liu, B. Z. Tang. Bioprobes Based on AIE Fluorogens. *Acc. Chem. Res*. **2013**, *46*, 2441-2453.
10. J. Mei, Y. Hong, J. W. Y. Lam, A. Qin, Y. Tang, B. Z. Tang. Aggregation-Induced Emission: The Whole Is More Brilliant than the Parts. *Adv. Mater.* **2014**, *26*, 5429-5479.
11. Y. Chen, W. Zhang, Z. Zhao, Y. Cai, J. Gong, R. T. K. Kwok, J. W. Y. Lam, H. H. Y. Sung, I. D. Williams, B. Z. Tang. An Easily Accessible Ionic Aggregation-Induced Emission Luminogen with Hydrogen-Bonding-Switchable Emission and Wash-Free Imaging Ability. *Angew Chem. Int. Ed.* **2018**, *57*, 5011-5015.
12. Y. Hong, S. Chen, C. Wai, T. Leung, J. Wing, Y. Lam, B. Z. Tang. Water-Soluble Tetraphenylethene Derivatives as Fluorescent "Light-Up" Probes for Nucleic Acid Detection and Their Applications in Cell Imaging. *Chem. Asian J.* **2013**, *8*, 1806-1812.
13. H. Shi, R. T. K. Kwok, J. Liu, B. Xing, B. Z. Tang, B. Liu. Real-Time Monitoring of Cell Apoptosis and Drug Screening Using Fluorescent Light-Up Probe with Aggregation-Induced Emission Characteristics. *J. Am. Chem. Soc.* **2012**, *134*, 17972-17981.
14. G. Jiang, G. Zeng, W. Zhu, Y. Li, X. Dong, G. Zhang, X. Fan, J. Wang, Y. Wu, B. Z. Tang. A Selective and Light-Up Fluorescent Probe for B-Galactosidase Activity Detection and Imaging in Living Cells Based on an AIE Tetraphenylethylene Derivative. *Chem. Commun.* **2017**, *53*, 4505-4508.

15. F. Hu, D. Mao, Kenry, X. Cai, W. Wu, D. Kong, B. Liu. A Light-Up Probe with Aggregation-Induced Emission for Real-Time Bio-orthogonal Tumor Labeling and Image-Guided Photodynamic Therapy. *Angew Chem. Int. Ed*. **2018**, *57*, 10182-10186.
16. F. Hu, B. Liu. Organelle-Specific Bioprobes Based on Fluorogens with Aggregation-Induced Emission (AIE) Characteristics. *Org. Biomol. Chem*. **2016**, *14*, 9931-9944.
17. J. Qian, B. Z. Tang AIE Luminogens for Bioimaging and Theranostics: From Organelles to Animals. *Chem* **2017**, *3*, 56-91.
18. G. Niu, R. Zhang, J. P. C. Kwong, J. W. Y. Lam, C. Chen, J. Wang, Y. Chen, X. Feng, R. T. K. Kwok, H. H.-Y. Sung, I. D. Williams, M. R. J. Elsegood, J. Qu, C. Ma, K. S. Wong, X. Yu, B. Z. Tang. Specific Two-Photon Imaging of Live Cellular and Deep-Tissue Lipid Droplets by Lipophilic AIEgens at Ultralow Concentration. *Chem. Mater*. **2018**, *30*, 4778–4787.
19. Y. Cai, C. Gui, K. Samedov, H. Su, X. Gu, S. Li, W. Luo, H. H. Y. Sung, J. W. Y. Lam, R. T. K. Kwok, I. D. Williams, A. Qin, B. Z. Tang. An Acidic pH Independent Piperazine–TPE Aiegen as A Unique Bioprobe for Lysosome Tracing. *Chem. Sci.* **2017**, *8*, 7593-7603.
20. Y. Li, Y. Wu, J. Chang, M. Chen, R. Liu, F. Li. A Bioprobe Based on Aggregation Induced Emission (AIE) for Cell Membrane Tracking. *Chem. Commun*. **2013**, *49*, 11335-11337.
21. C. Y. Y. Yu, W. Zhang, R. T. K. Kwok, C. W. T. Leung, J. W. Y. Lam, B. Z. Tang. A Photostable AIEgen for Nucleolus and Mitochondria Imaging with Organelle-Specific Emission. *J. Mater. Chem. B* **2016**, *4*, 2614-2619.
22. D. C. Wallace. Mitochondria and Cancer. *Nat. Rev. Cancer* **2012**, *12*, 685-698.
23. S. Fulda, L. Galluzzi, G. Kroemer. Targeting Mitochondria for Cancer Therapy. *Nat. Rev. Drug Discovery* **2010**, *9*, 447- 464.
24. J. Nunnari, A. Suomalainen. Mitochondria: In Sickness and in Health. *Cell* **2012**, *148*, 1145-1159.
25. N. Zhao, M. Li, Y. Yan, J. W. Y. Lam, Y. L. Zhang, Y. S. Zhao, K. S. Wong, B. Z. Tang. A Tetraphenylethene-Substituted Pyridinium Salt with Multiple Functionalities: Synthesis, Stimuli-Responsive Emission, Optical Waveguide and Specific Mitochondrion Imaging. *J. Mater. Chem. C* **2013**, *1*, 4640-4646.
26. C. W. T. Leung, Y. Hong, S. Chen, E. Zhao, J. W. Y. Lam, B. Z. Tang. A Photostable AIE Luminogen for Specific Mitochondrial Imaging and Tracking. *J. Am. Chem. Soc.* **2013**, *135*, 62-65.
27. M. Gao, C. K. Sim, C. W. T. Leung, Q. Hu, G. Feng, F. Xu, B. Z. Tang, B. Liu. A Fluorescent Light-Up Probe with AIE Characteristics for Specific Mitochondrial Imaging to Identify Differentiating Brown Adipose Cells. *Chem. Commun.* **2014**, *50*, 8312-8315.

28. W. Zhang, R. T. K. Kwok, Y. Chen, S. Chen, E. Zhao, C. Y. Y. Yu, J. W. Y. Lam, Q. Zheng, B. Z. Tang. Real-Time Monitoring of the Mitophagy Process by a Photostable Fluorescent Mitochondrion-Specific Bioprobe with AIE Characteristics. *Chem. Commun.* **2015**, *51*, 9022-9025.
29. Q. Hu, M. Gao, G. Feng, B. Liu. Mitochondria-Targeted Cancer Therapy using a Light-Up Probe with Aggregation-Induced-Emission Characteristics. *Angew. Chem. Int. Ed.* **2014**, *53*, 14225-14229.
30. G. Yu, D. Wu, Y. Li, Z. Zhang, L. Shao, J. Zhou, Q. Hu, G. Tang, F. Huang. A Pillar[5]arene-based [2]rotaxane Lights Up Mitochondria. *Chem. Sci.* **2016**, *7*, 3017-3024.
31. M. Savarese, A. Aliberti, I. D. Santo, E. Battista, F. Causa, P. A. Netti, N. Rega., Fluorescence Lifetimes and Quantum Yields of Rhodamine Derivatives: New Insights from Theory and Experiment. *J. Phys. Chem. A.* **2012**, *116*, 7491-7497.
32. Q. Feng, Y. Li, L. Wang, C. Li, J. Wang, Y. Liu, K. Li, H. Hou. Multiple-color Aggregation-Induced Emission (AIE) Molecules as Chemodosimeters for pH Sensing. *Chem. Commun*. **2016**, *52*, 3123-3126.
33. M. J. Frisch, G. W. Trucks, H. B. Schlegel, G. E. Scuseria, M. A. Robb, J. R. Cheeseman, G. Scalmani, V. Barone, B. Mennucci, G. A. Petersson, Gaussain 09, Revision D. 01; Gaussian. *Inc.: Wallingford, CT, USA*, **2013**.
34. P. J. Stephens, F. J. Devlin, C. F. N. Chabalowski, M. J. Frisch. Ab Initio Calculation of Vibrational Absorption and Circular Dichroism Spectra Using Density Functional Force Fields. *J. Phys. Chem.* **1994**, *98*, 11623-11627.
35. S. Miertuš, E. Scrocco, J. Tomasi. Electrostatic Interaction of a Solute with a Continuum. A Direct Utilizaion of AB Initio Molecular Potentials for the Prevision of Solvent Effects. *Chem. Phys.* **1981**, *55*, 117-129.
36. Q. Yuan, T. Zhou, L. Li, J. Zhang, X. Liu, X. Ke, A. Zhang. Hydrogen Bond Breaking of TPU upon Heating: Understanding from the Viewpoints of Molecular Movements and Enthalpy. *RSC Adv.* **2015**, *5*, 31153-31165.
37. N. Avakyan, A. A. Greschner, F. Aldaye, C. J. Serpell, V. Toader, A. Petitjean, H. F. Sleiman. Reprogramming the Assembly of Unmodified DNA with a Small Molecule. *Nat. Chem.* **2016**, *8*, 368-376
38. C. Ghosh, A. Nandi, S. Basu. Supramolecular Self-assembly of Triazine-based Small Molecules: Targeting the Endoplasmic Reticulum in Cancer Cells. *Nanoscale* **2019**, *11*, 3326-3335.
39. M. S. Mathew, K. Sreenivasan, K. Joseph. Hydrogen-bond Assisted, Aggregation-Induced Emission of Digitonin. *RSC Adv.* **2015**, *5*, 100176.

40. J. Zhao, S. Ji, Y.Chen, H. Guo P.Yang. Excited State Intramolecular Proton Transfer (ESIPT): From Principal Photophysics to the Development of New Chromophores and Applications in Fluorescent Molecular Probes and Luminescent Materials. *Phys. Chem. Chem. Phys*. **2012**, *14*, 8803-8817.
41. A. C. Sedgwick, L. Wu, H-H. Han, S. D. Bull, X-P. He, T. D. James, J. L. Sessler, B. Z. Tang, H. Tian, J. Yoon. Excited-State Intramolecular Proton-Transfer (ESIPT) Based Fluorescence Sensors and Imaging Agents. *Chem. Soc. Rev.* **2018**, *47*, 8842- 8880
42. J. S. Modica-Napolitano, J. R. Aprille. Basis for the Selective Cytotoxicity of Rhodamine. 123, *Cancer Res*. **1987**, *47*, 4361-4365.
43. W. H. Goffney, J. H. Wong, D. H. Kern, D. Chase, D. N. Krag, F. K. Storm. *In Vitro* and *in Vivo* Cytotoxicity of Rhodamine 123 Combined with Hyperthermia. *Cancer Res.* **1990**, 50, 459-463.
44. L. V. Johnson, M. L. Walsh, and L. B. Chen. Localization of Mitochondria in Living Cells with Rhodamine 123. *PNAS*, **1980**, *77*, 990-994.

# Appendix-B:

## Characterization of the compounds

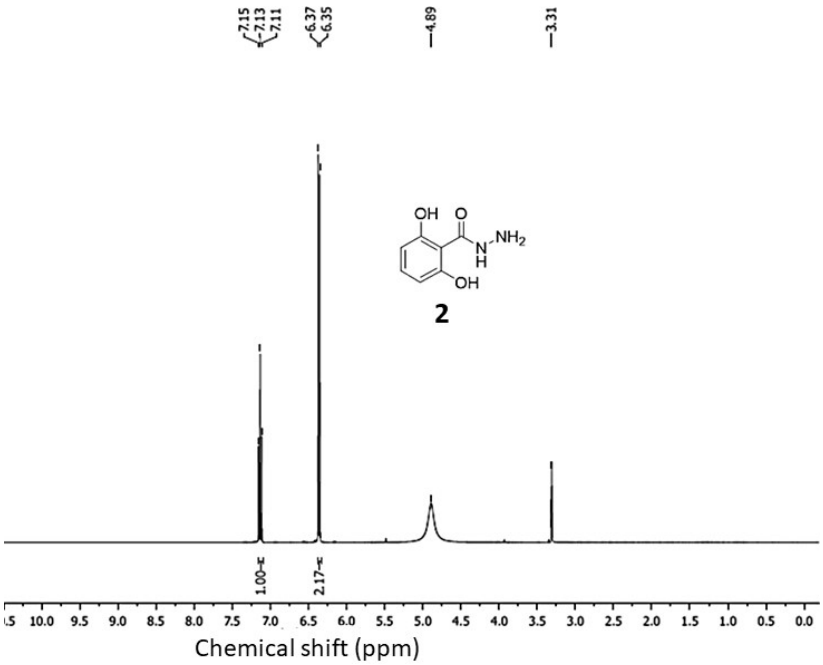


**Figure B1:** $^{1}$H NMR spectra of compound **2**

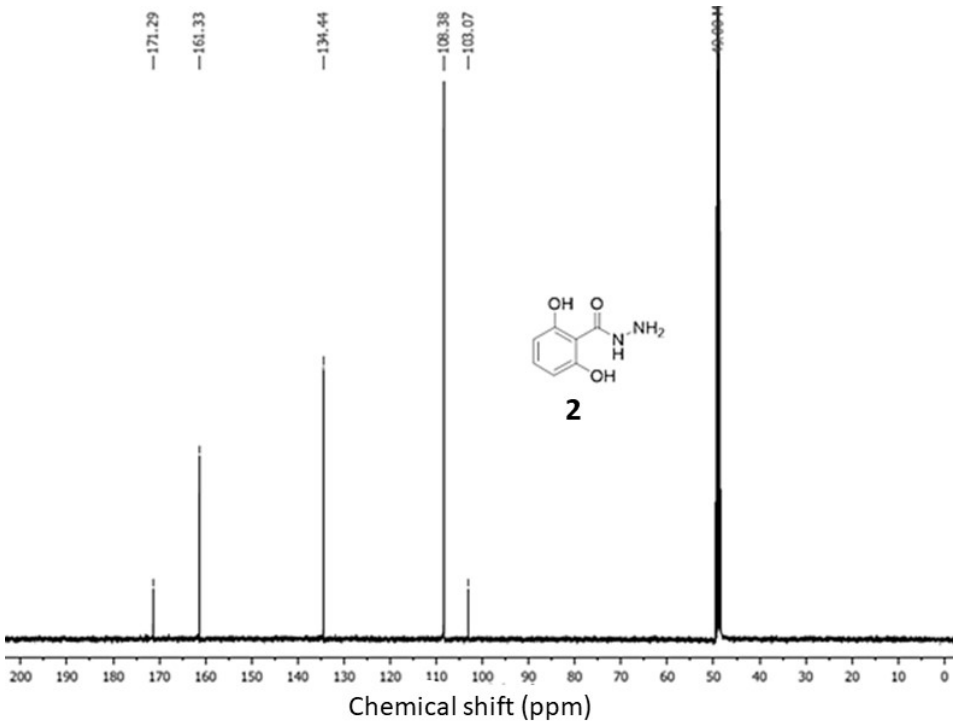


**Figure B2**: $^{13}$C NMR spectra of compound **2**

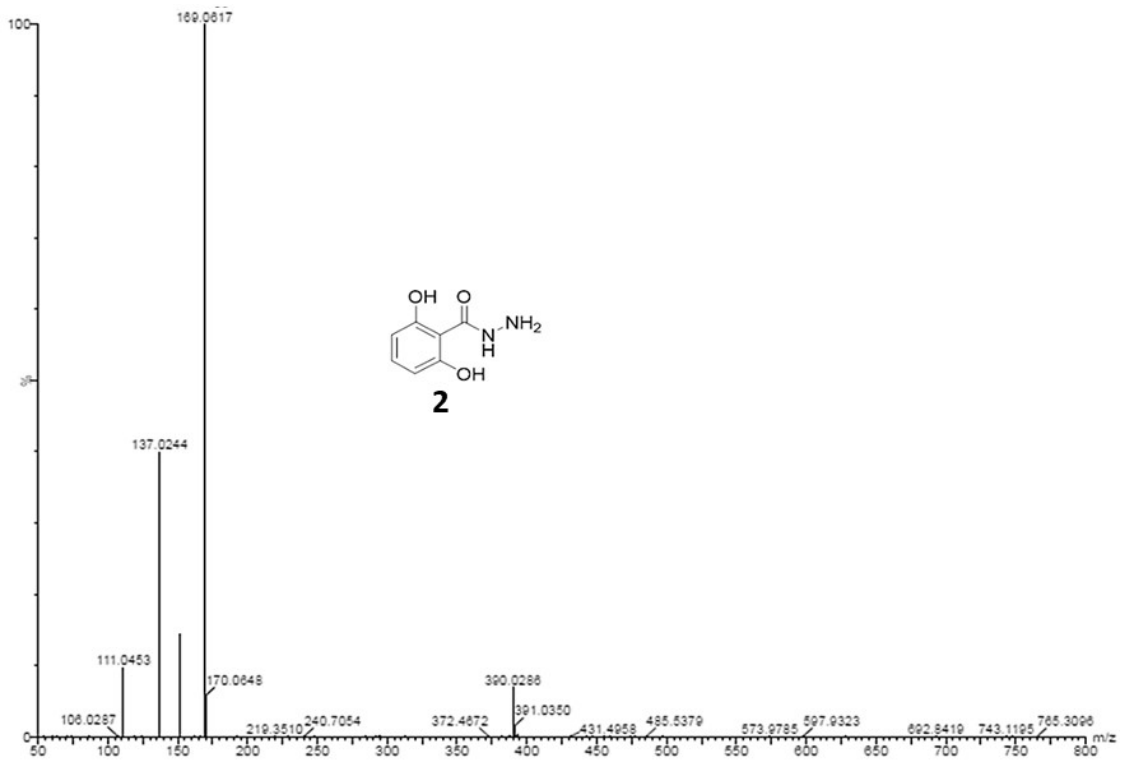


**Figure B3:** HR-MS spectra of compound **2**

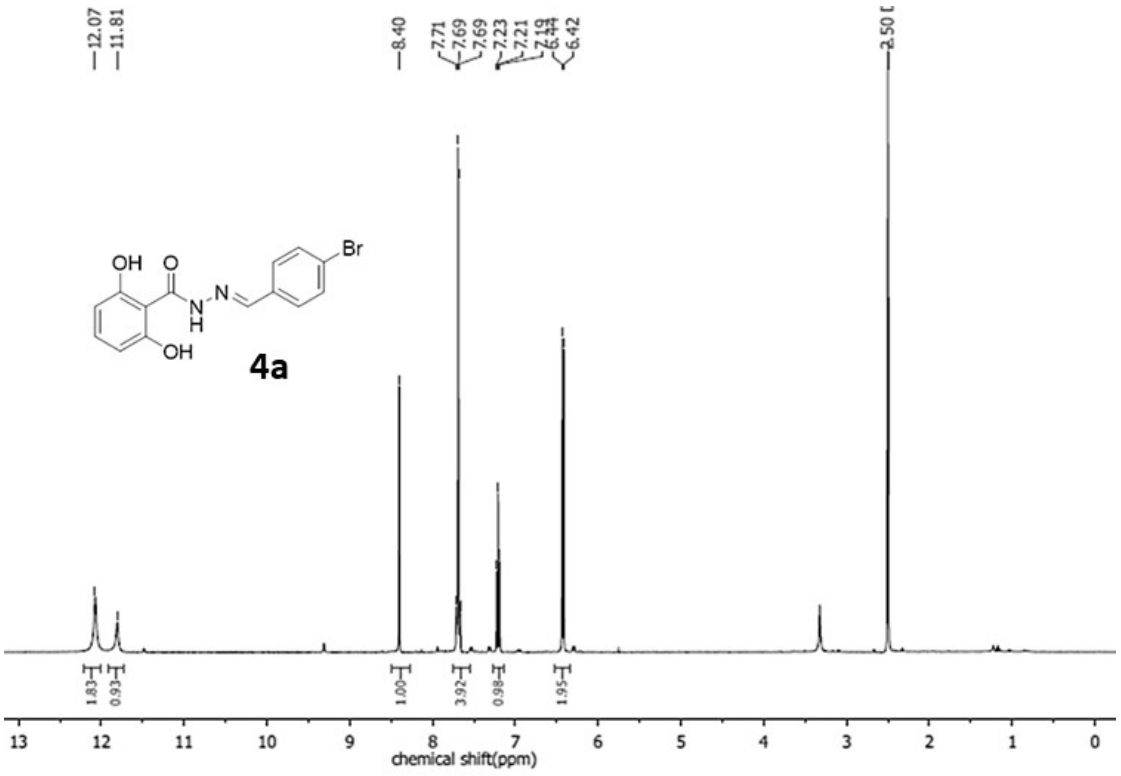


**Figure B4:** $^{1}$H NMR spectra of compound **4a**

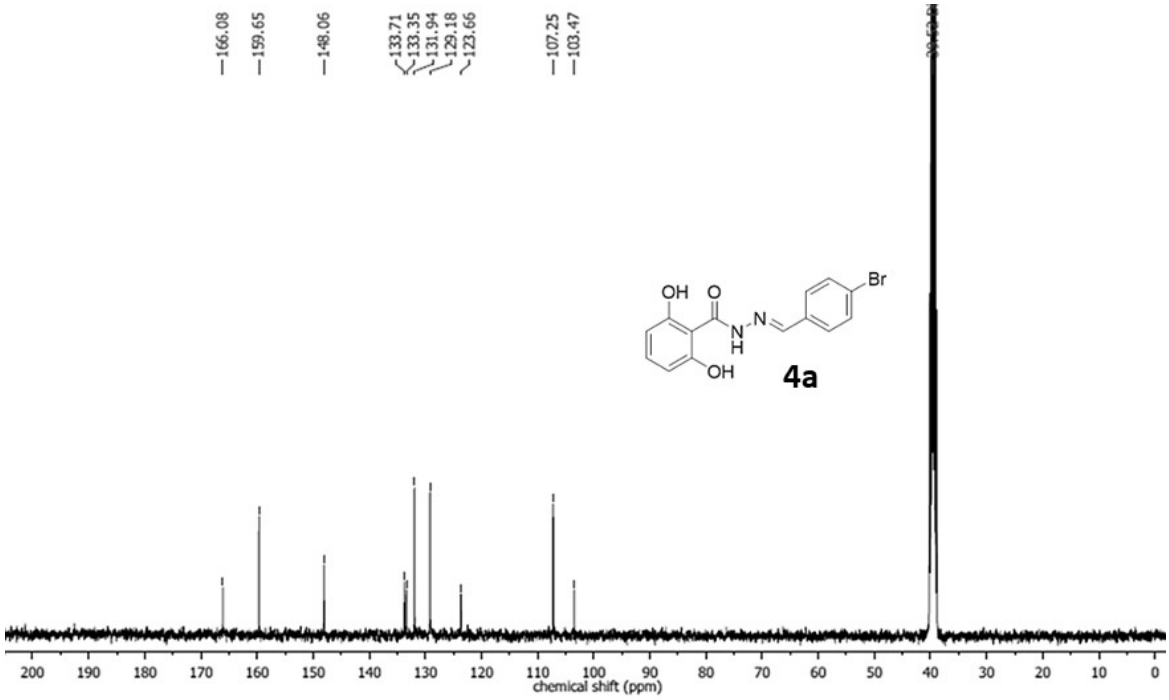


**Figure B5:** $^{13}$C NMR spectra of compound **4a**

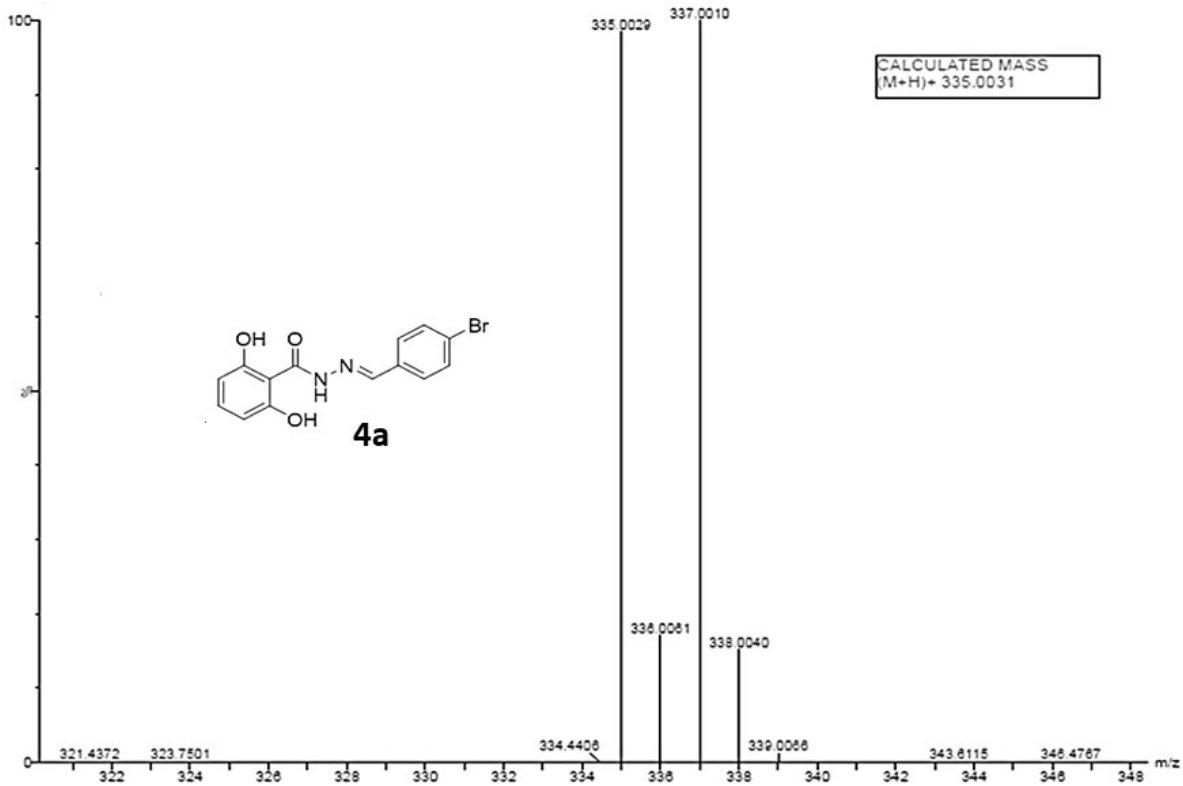


**Figure B6:** HR-MS spectra of compound **4a**

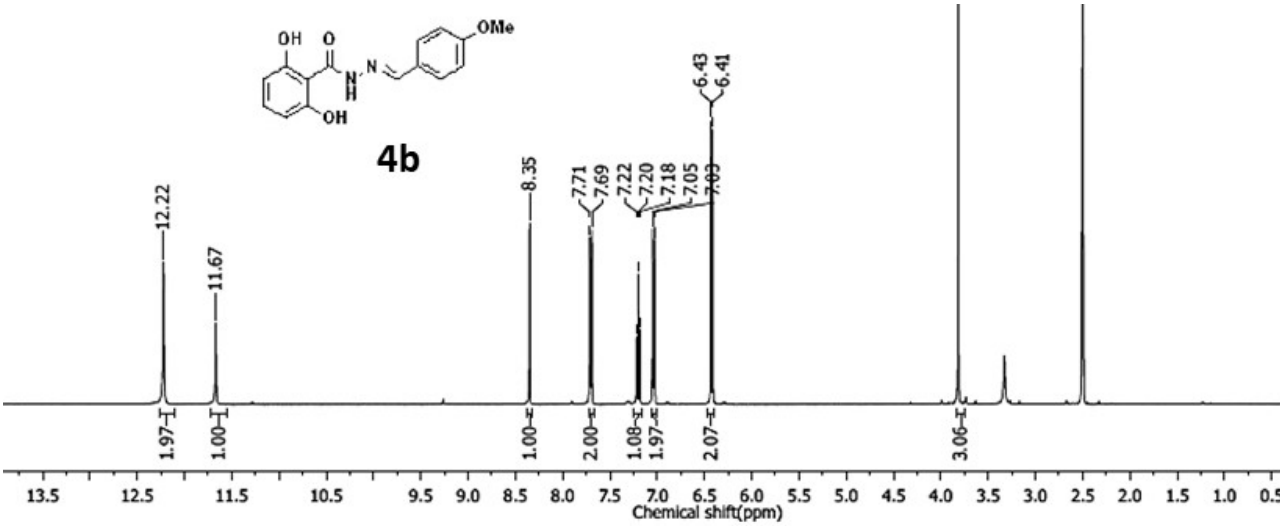


**Figure B7:** $^{1}$H NMR spectra of compound **4b**

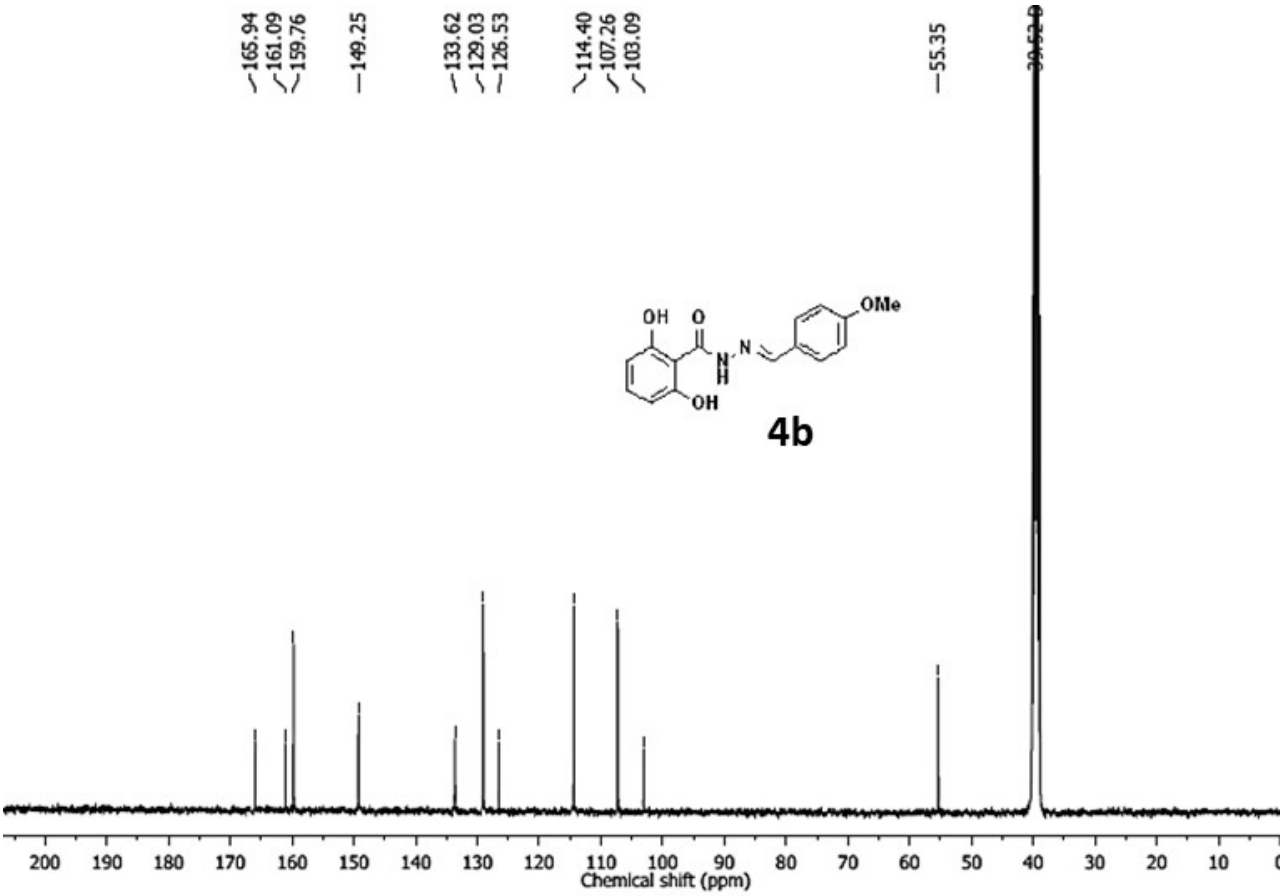


**Figure B8:** $^{13}$C NMR spectra of compound **4b**

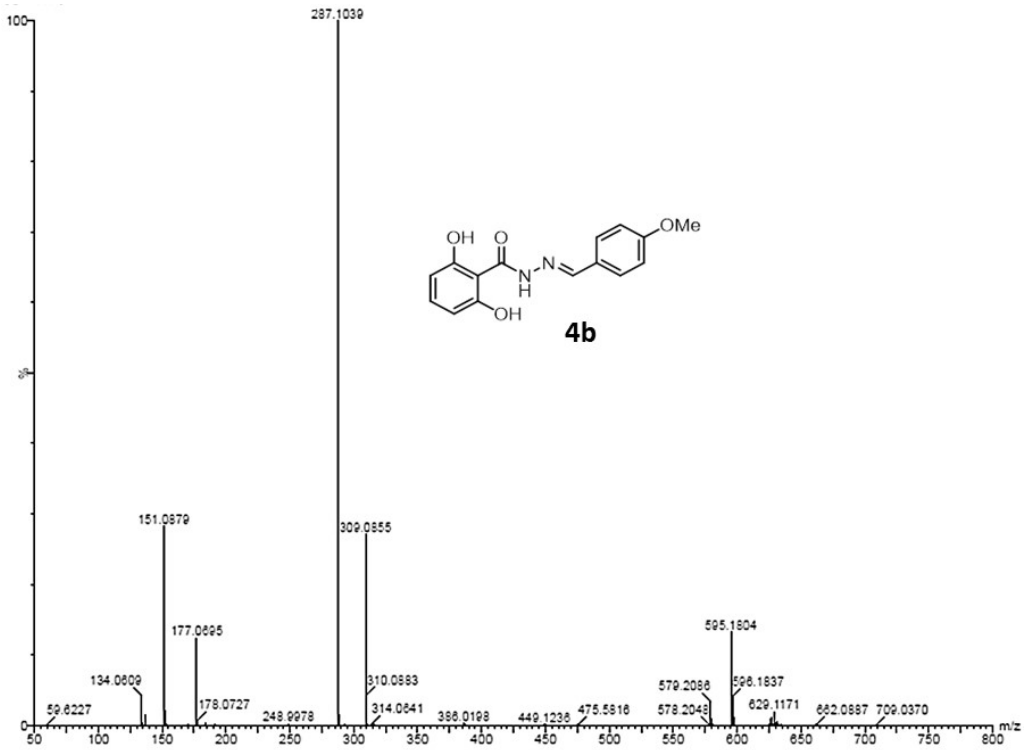


**Figure B9:** HR-MS spectra of compound **4b**

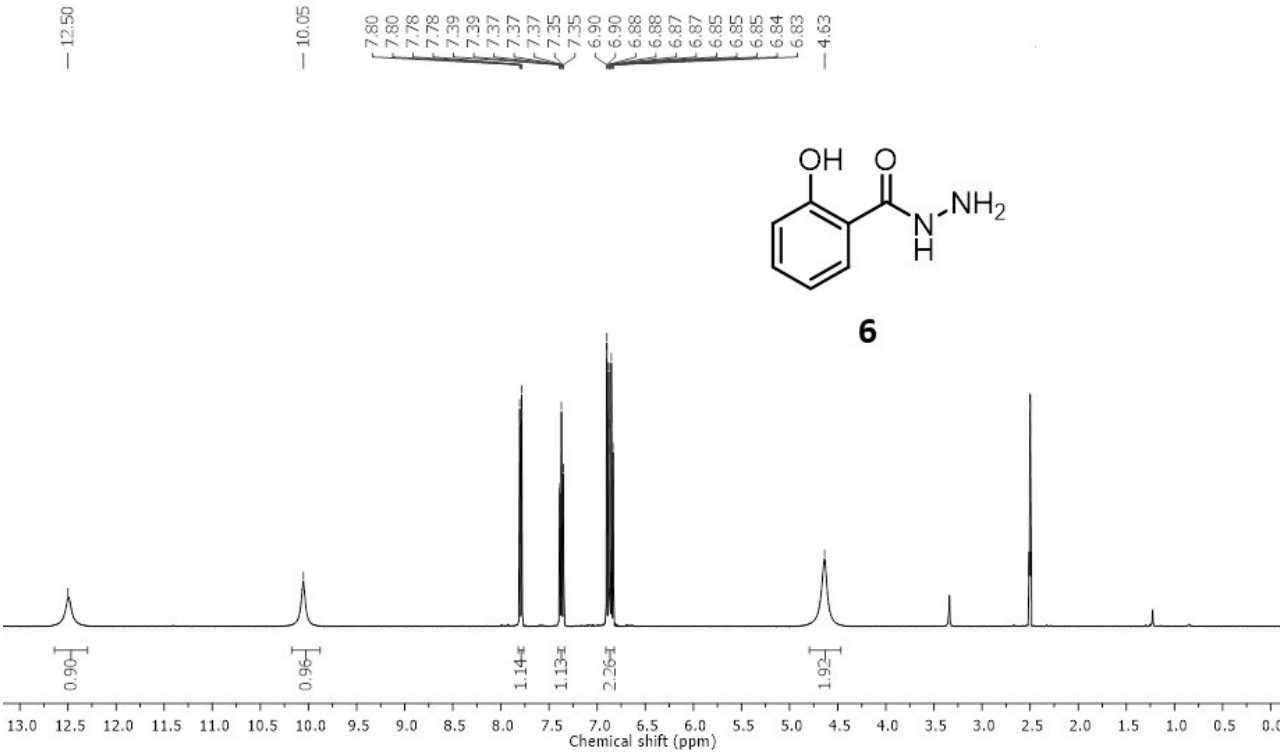


**Figure B10:** $^{1}$H NMR spectra of compound **6**

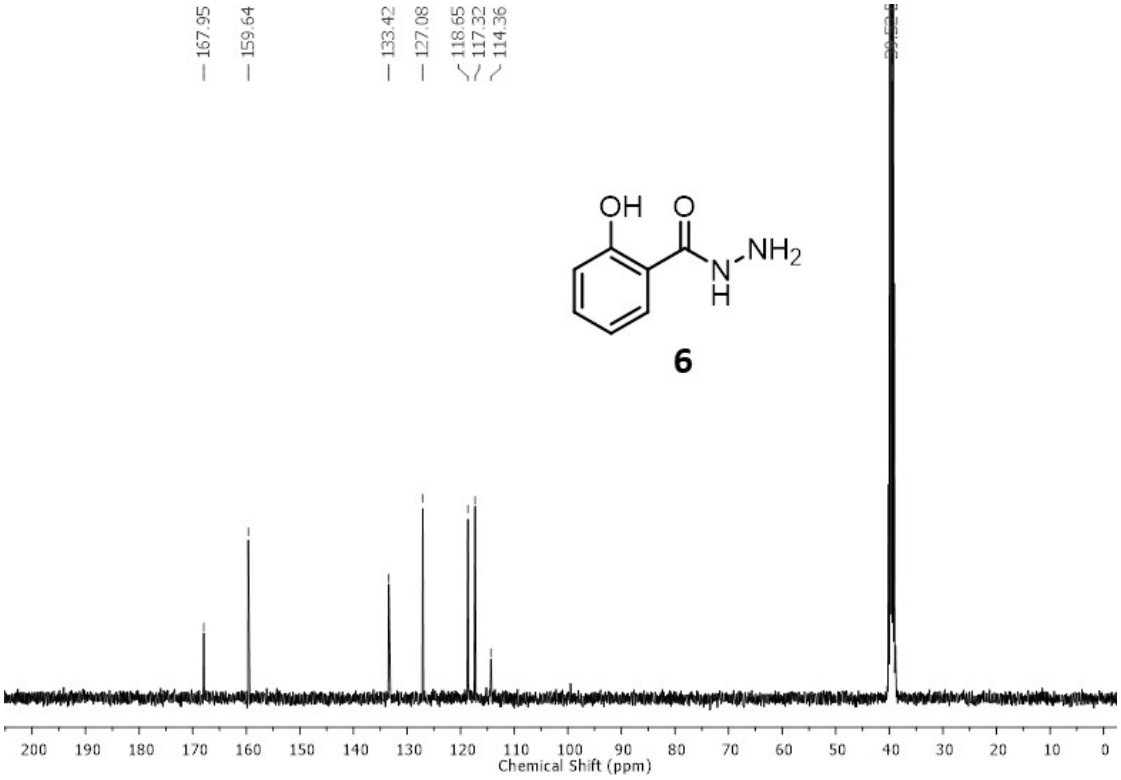


**Figure B11:** $^{13}$C NMR spectra of compound **6**

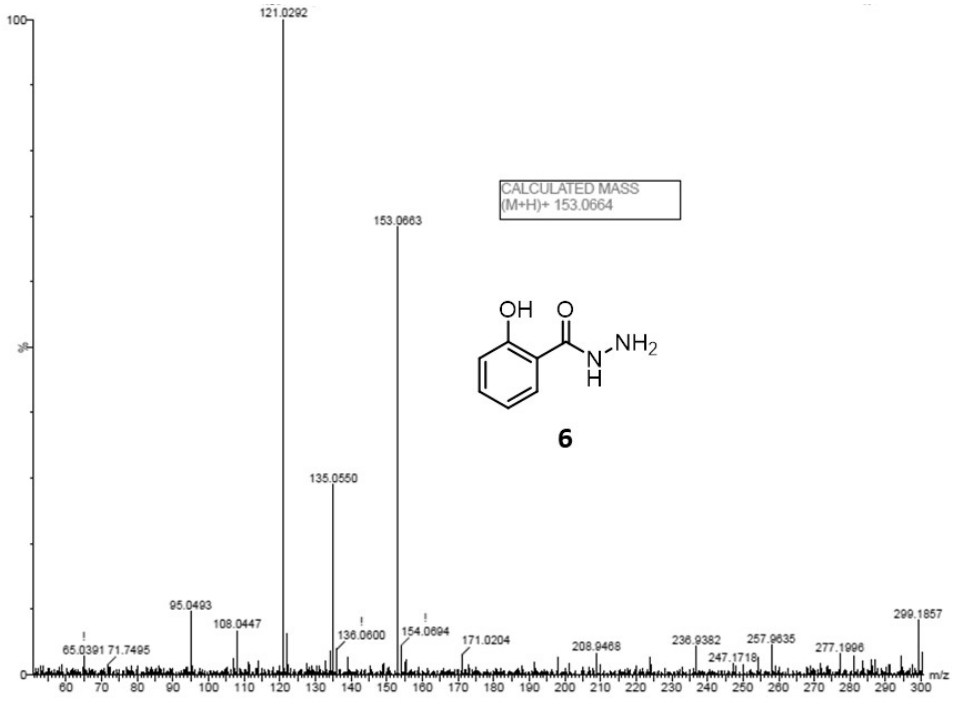


**Figure B12:** HR-MS spectra of compound **6**

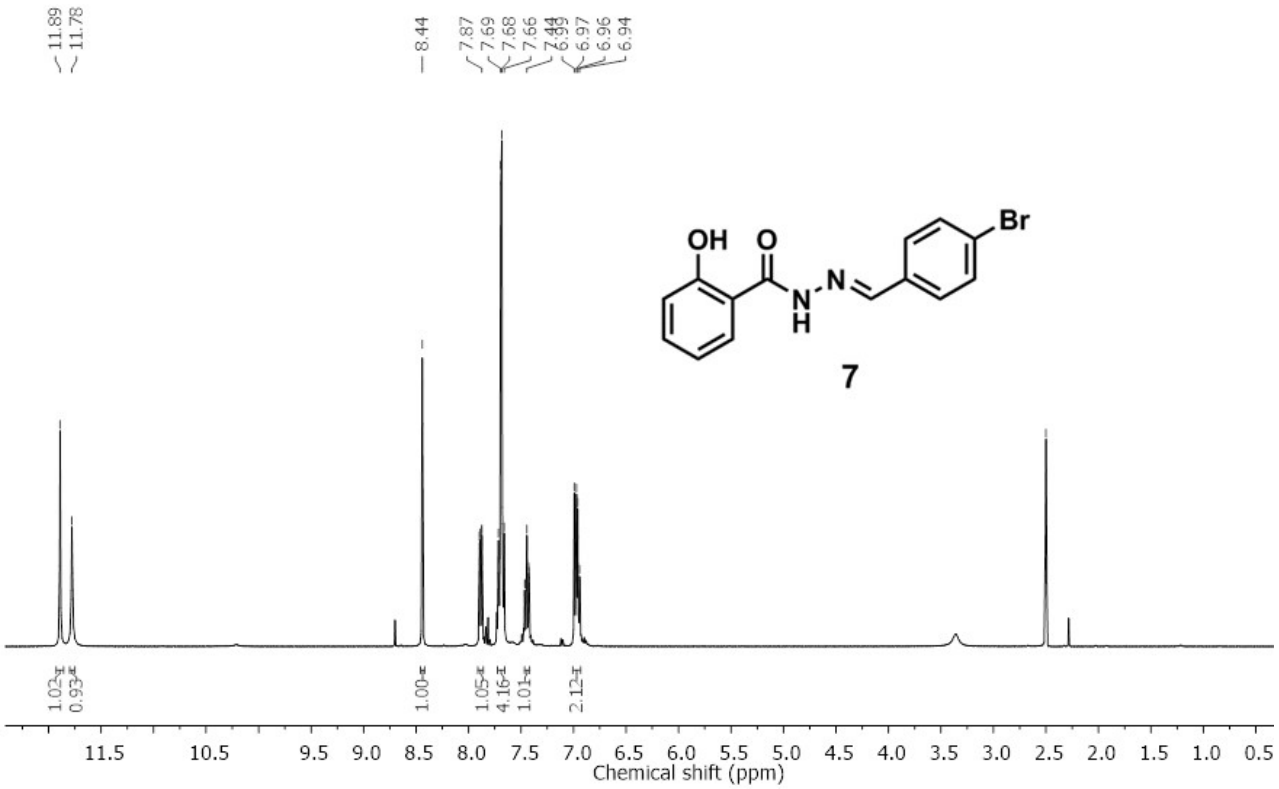


**Figure B13:** $^{1}$H NMR spectra of compound **7**

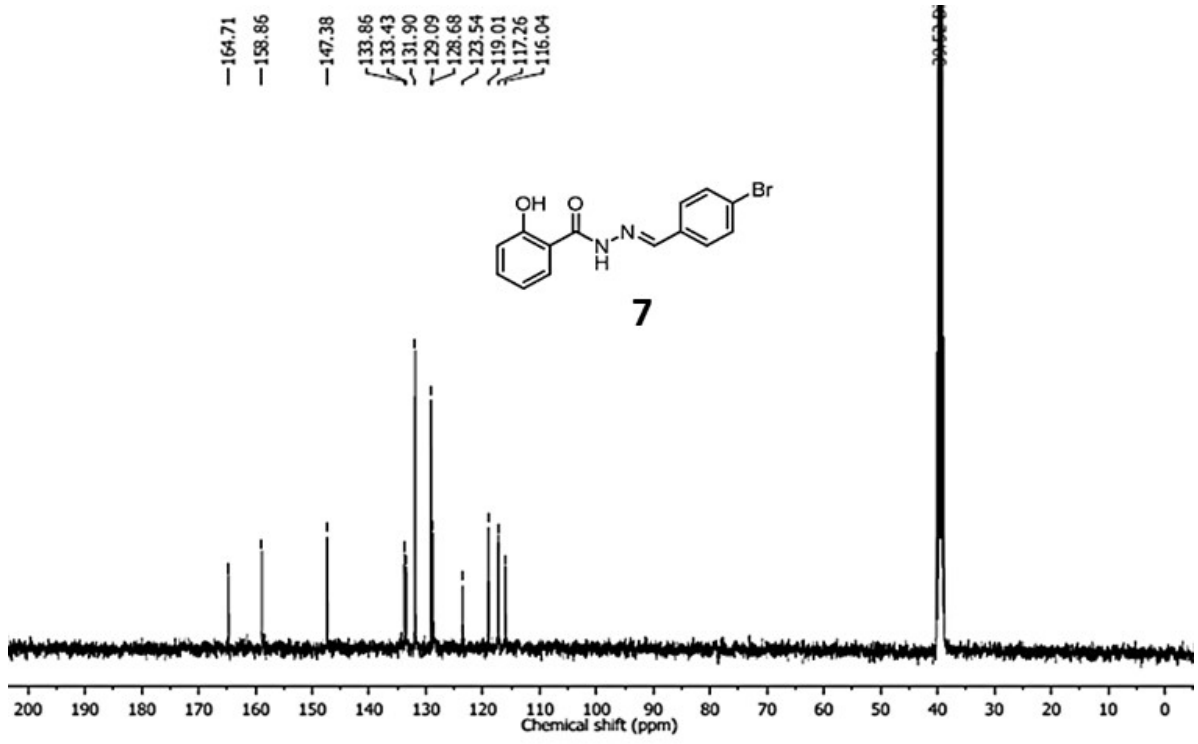


**Figure B14:** $^{13}$C NMR spectra of compound **7**

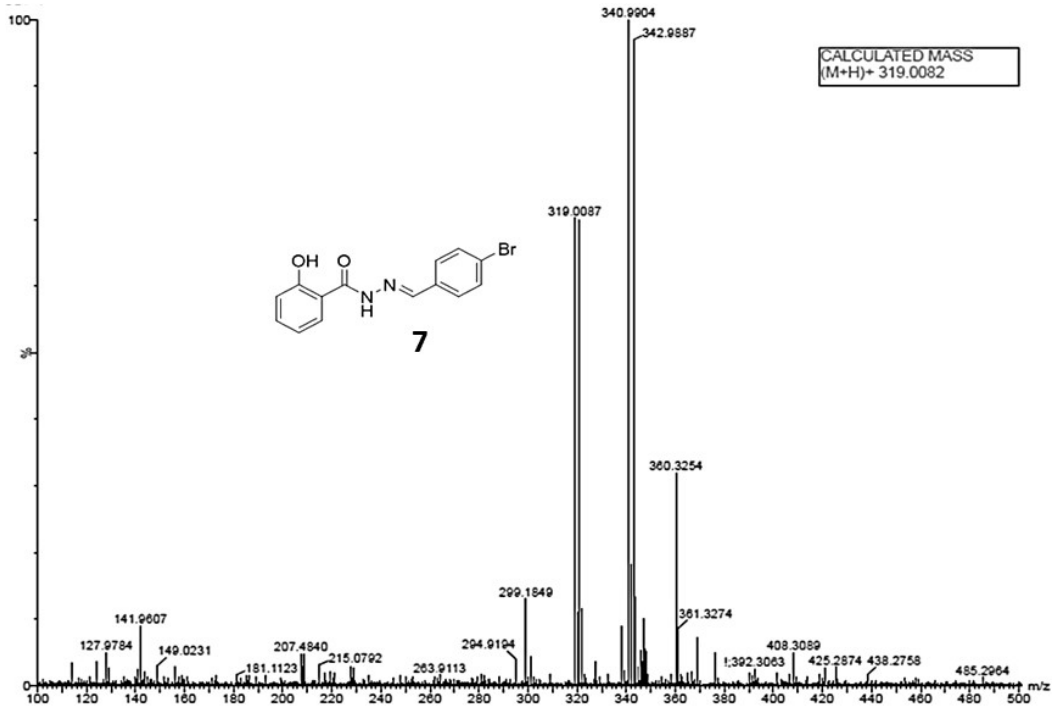


**Figure B15:** HR-MS spectra of compound **7**

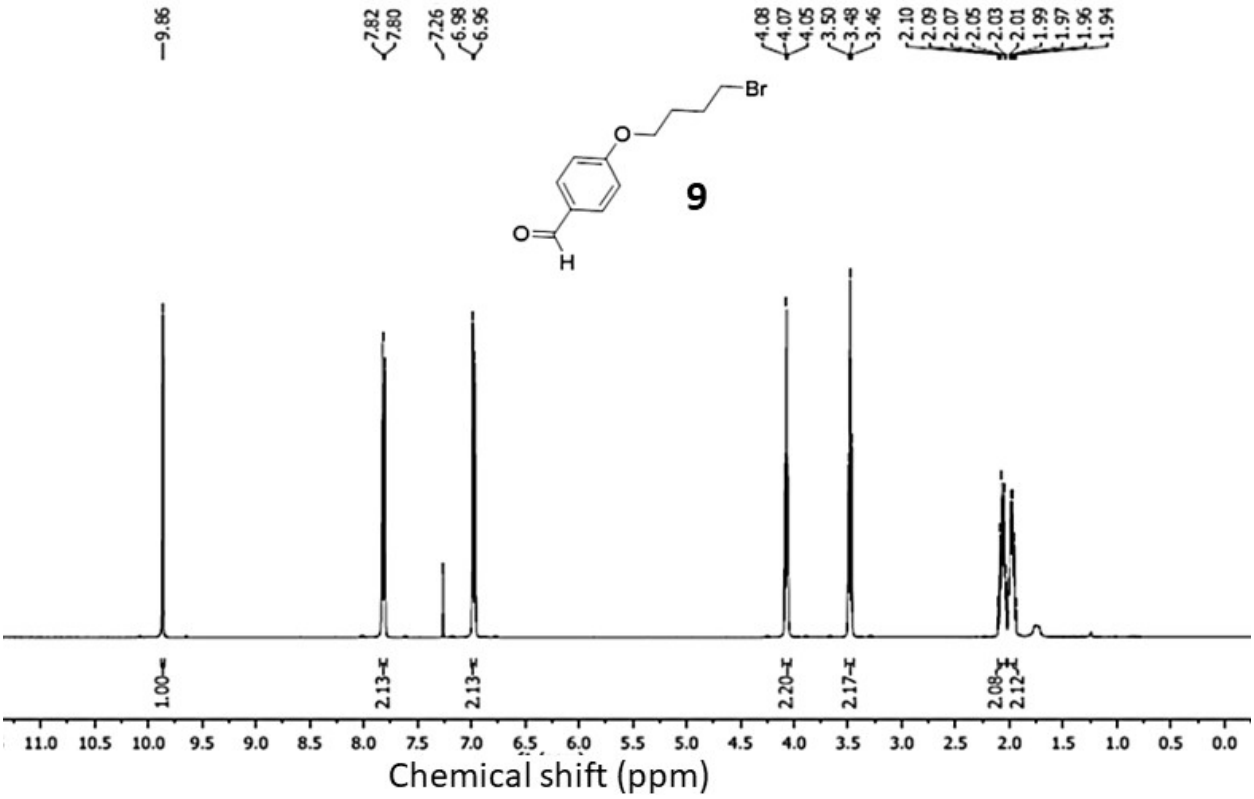


**Figure B16:** $^{1}$H NMR spectra of compound **9**

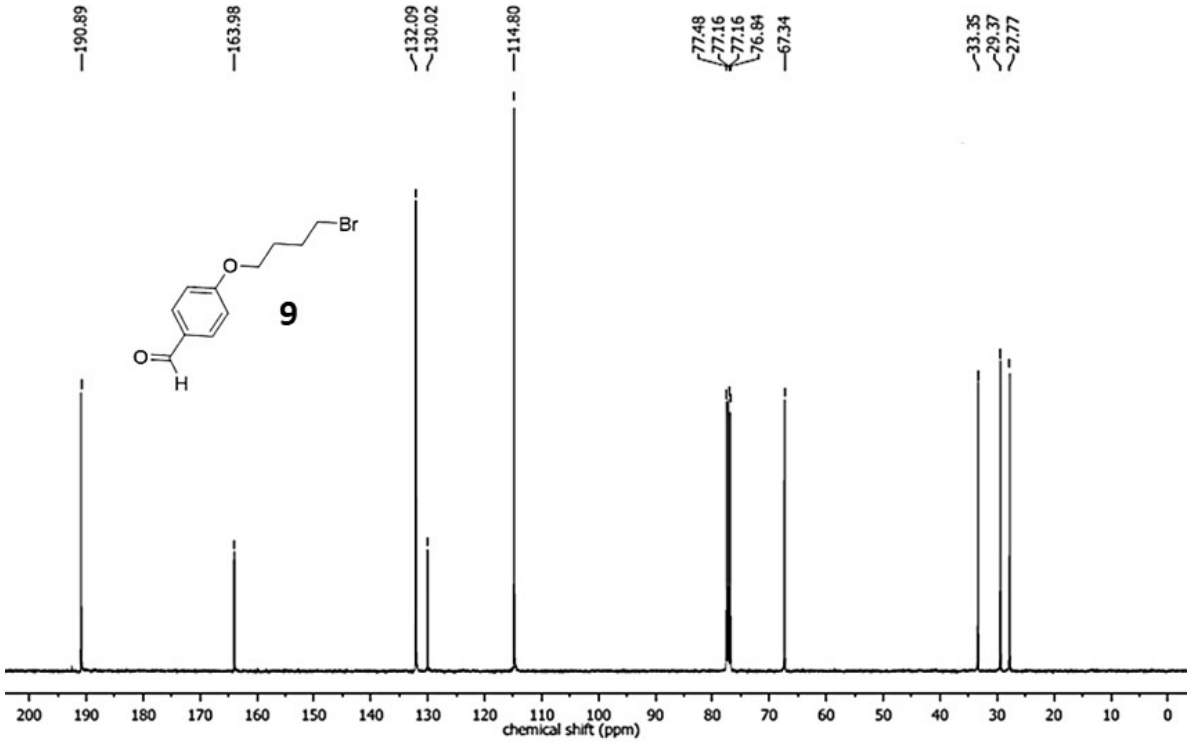


**Figure B17:** $^{13}$C NMR spectra of compound **9**

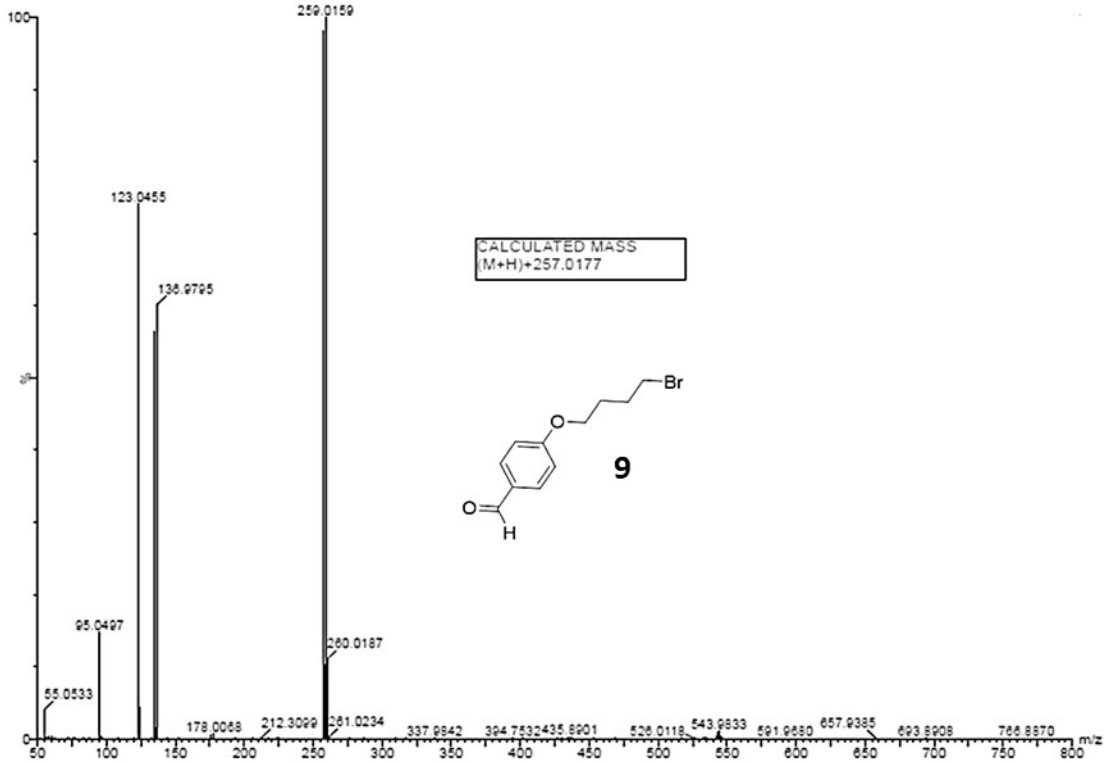


**Figure B18:** HR-MS spectra of compound **9**

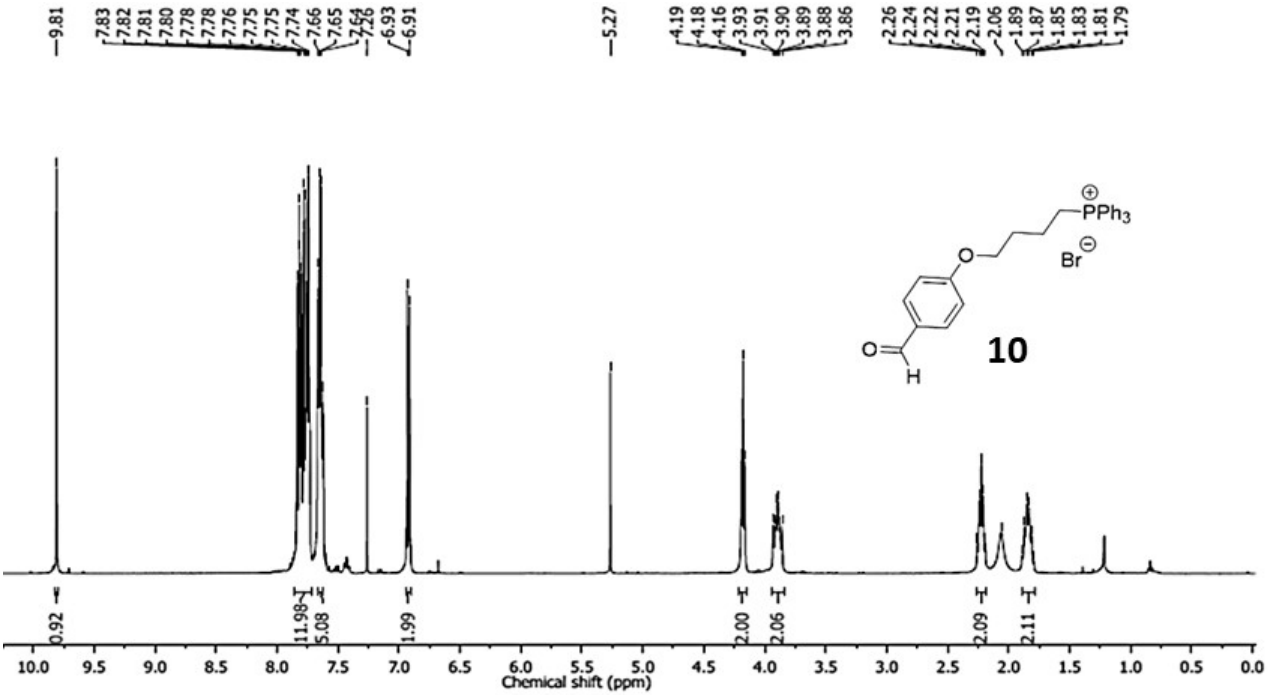


**Figure B19:** $^{1}$H NMR spectra of compound **10**

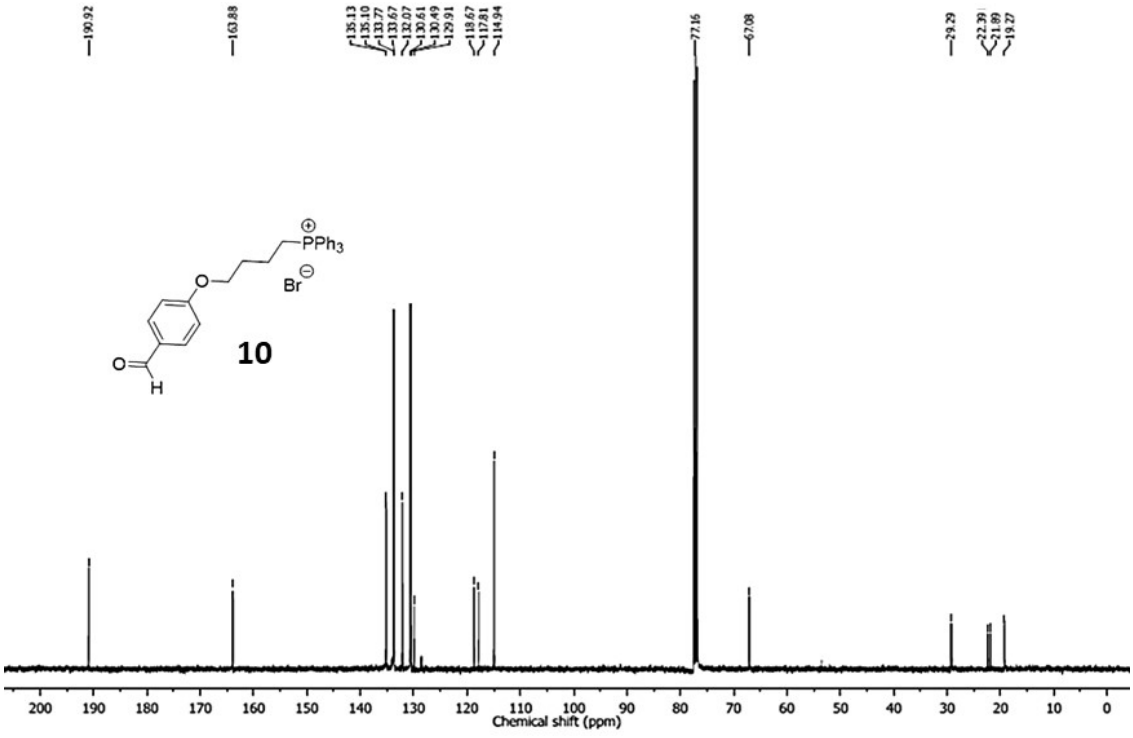


**Figure B20:** $^{13}$C NMR spectra of compound **10**

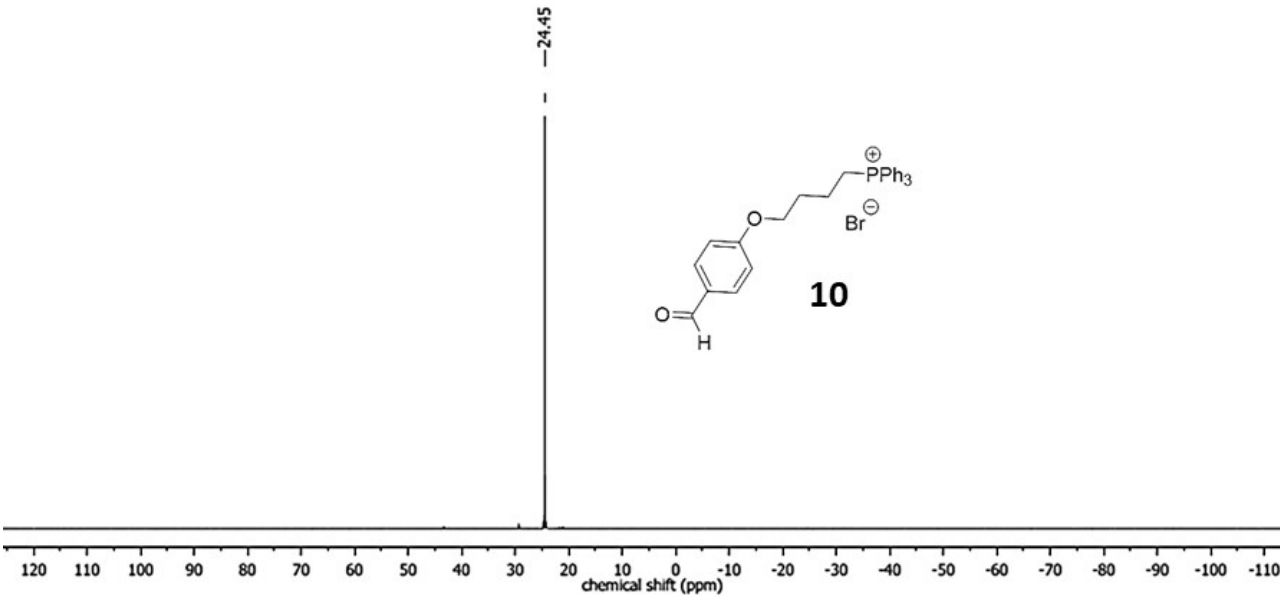


**Figure B21:** $^{31}$P NMR spectra of compound **10**

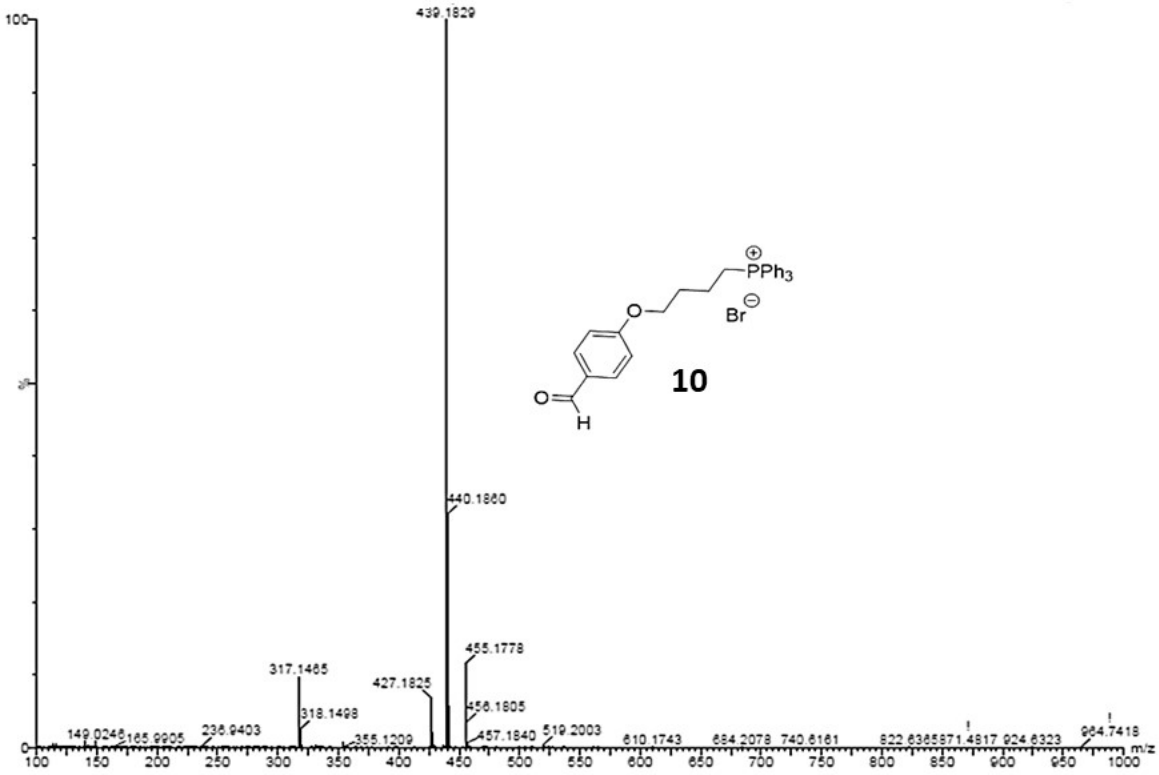


**Figure B22:** HR-MS spectra of compound **10**

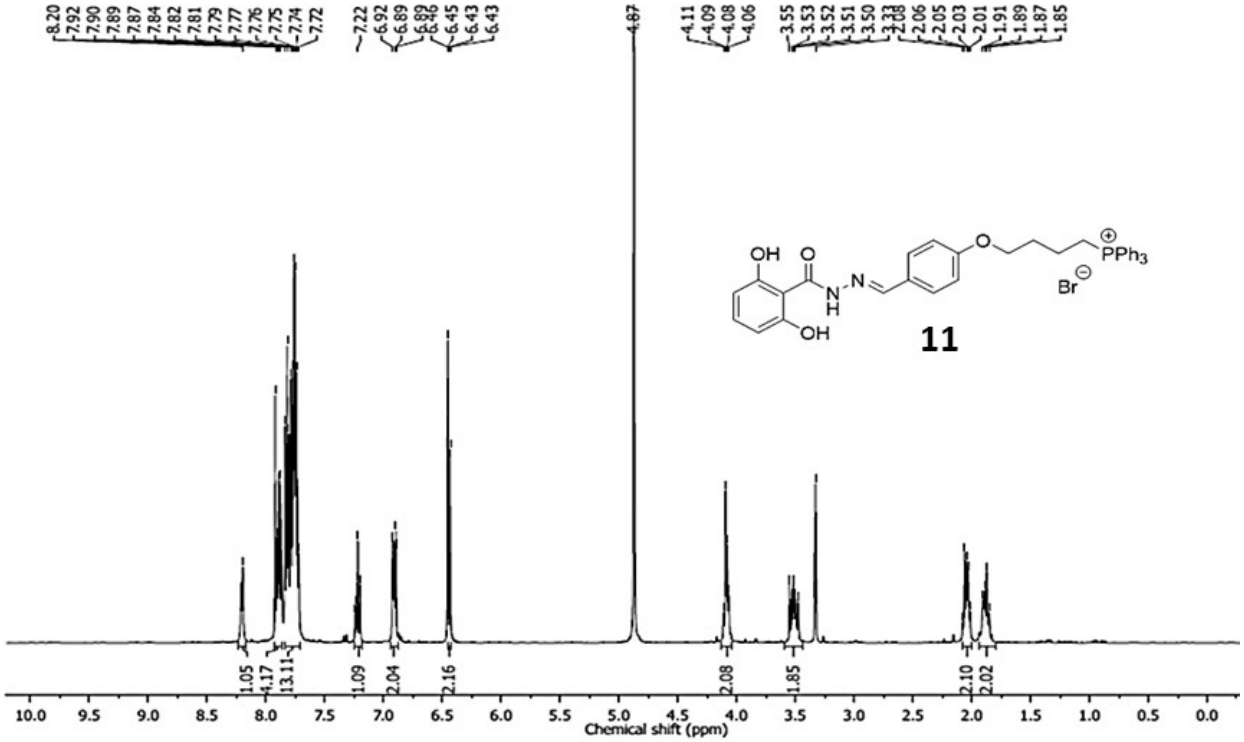


**Figure B23:** $^{1}$H NMR spectra of compound **11**

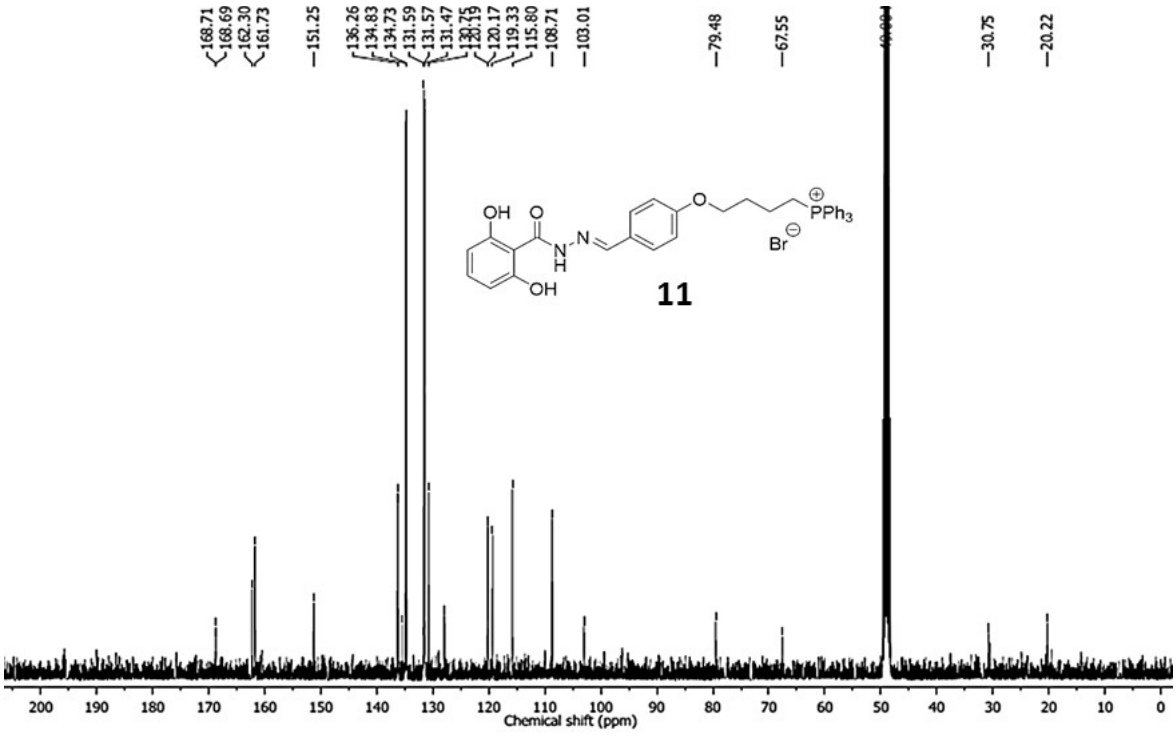


**Figure B24:** $^{13}$C NMR spectra of compound **11**

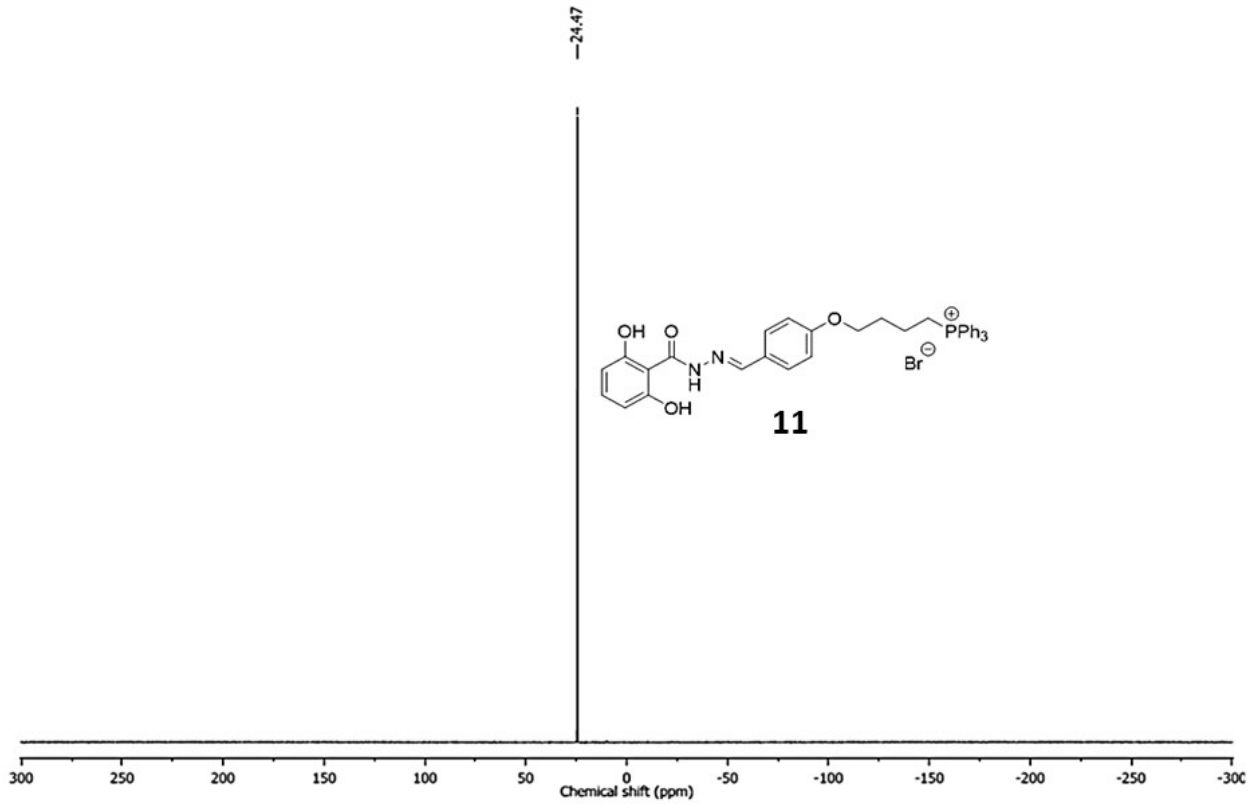


**Figure B25:** $^{31}$P NMR spectra of compound **11**

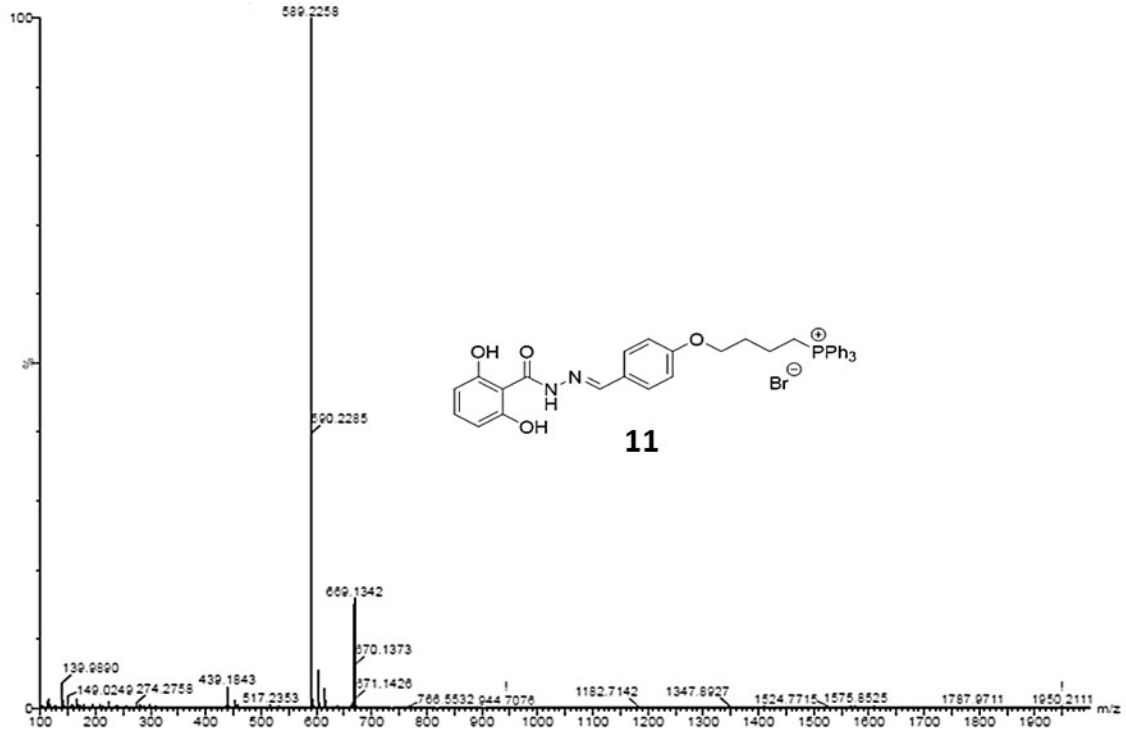


**Figure B26:** HR-MS spectra of compound **11**.

**Table B1:** Crystal data and structure refinement of compound **11 (CCDC 1899210)**

| | |
|---|---|
| Crystal data | |
| Chemical formula | $C_{36}H_{34}ClN_2O_6P$ |
| $M_r$ | 657.07 |
| Crystal system, space group | Triclinic, $P\bar{1}$ |
| Temperature (K) | 296 |
| $a, b, c$ (Å) | 10.8557 (15), 12.7008 (18), 14.0123 (18) |
| α, β, γ (°) | 75.361 (4), 68.049 (4), 66.126 (4) |
| $V$ (Å$^3$) | 1626.8 (4) |
| $Z$ | 2 |
| Radiation type | Mo $K\alpha$ |
| μ (mm$^{-1}$) | 0.22 |
| Crystal size (mm) | 0.06 × 0.05 × 0.04 |
| | |
| Data collection | |
| Diffractometer | Bruker *APEX*-II CCD |
| Absorption correction | Multi-scan |
| No. of measured, independent and observed [$I > 2\sigma(I)$] reflections | 56110, 8066, 3264 |
| $R_{int}$ | 0.363 |
| $(\sin \theta/\lambda)_{max}$ (Å$^{-1}$) | 0.667 |
| | |
| Refinement | |
| $R[F^2 > 2\sigma(F^2)]$, $wR(F^2)$, $S$ | 0.108, 0.281, 1.02 |
| No. of reflections | 8066 |
| No. of parameters | 417 |
| H-atom treatment | H-atom parameters constrained |
| $\Delta\rho_{max}$, $\Delta\rho_{min}$ (e Å$^{-3}$) | 1.19, −0.98 |

# Chapter 4

# Cyanobax: Small Molecules for Mitochondrial Dysfunction upon Inhibiting Bcl-2 Family Proteins in Cancer Cells

## 4.1 Introduction

Cancer is believed to be ranked as the leading cause of death worldwide in the upcoming years.[1] According to GLOBOCAN, in the single year 2018, nearly 18.1 million new cancer cases and 9.6 million cancer deaths were estimated.[1] Over the last couple of decades, numerous efforts have been raised to diagnose and treat cancer.[2,3] Inevitably, the discovery and development of small synthetic molecules in chemotherapy offer great potential.[4,5] A lot of small molecules have been used in chemotherapy as a DNA alkylating agent or kinase inhibitor.[6-8] However, these drugs are initially susceptible to chemotherapy, but over the period, cancer cells can develop drug resistance resulting in cancer cells become tolerant to chemotherapy treatments.[9-11] Hence, immense efforts have been made to explore new cellular targets and biomarkers to overcome this problem. Therefore, the design and development of new small molecules to target alternative cancer subcellular targets is imperative.

One of the targets is mitochondrion, a central metabolic organelle, conventionally known as the powerhouse of the cell which is worthwhile for cancer treatment.[12-15] The mitochondrion is not only involved in biogenesis, biosynthesis, and subcellular signals but also plays a decisive role in triggering programmed cell death by producing reactive oxygen species (ROS) and caspase cascade. Mitochondrial-dependent apoptosis is originated by mitochondrial outer membrane permeabilization (MOMP) via anti-apoptotic and pro-apoptotic proteins. The anti-apoptotic B cell lymphoma-2 (Bcl-2) family proteins are the gatekeeper for the mitochondrion to function normally and prevent from the apoptosis.[16-20] Therefore, to disrupt the function of a mitochondrion as well as inhibit the Bcl-2 family protein in cancer cells remains a challenging arena. Minimal numbers of small molecules that inhibit Bcl-2 family of proteins along with dysfunction of mitochondria have been in developing state.[21-23] One of the experimental small molecules is Obatoclax mesylate, a precursor of natural product Prodigiosin which antagonizes Bcl-2 family of proteins and induces apoptosis in cancer cells (figure 4.1a).[24-26] However, Obatoclax mostly suffers from solubility issues and other problems leading to its discontinuation from a clinical trial.[27,28] Moreover, the Prodiginines show enormous activities such as antimalarial, antifungal, immunosuppressant, and antibiotic, but the exact mechanism of these activities is highly complex and not entirely elucidated.[29,30] inspired from the Prodigiosin and the Obatoclax chemical structure; we hypothesized that we could develop novel small molecules that

will be able to damage mitochondria as well as inhibit the Bcl2- family proteins ultimately leading to apoptosis in cancer cells.

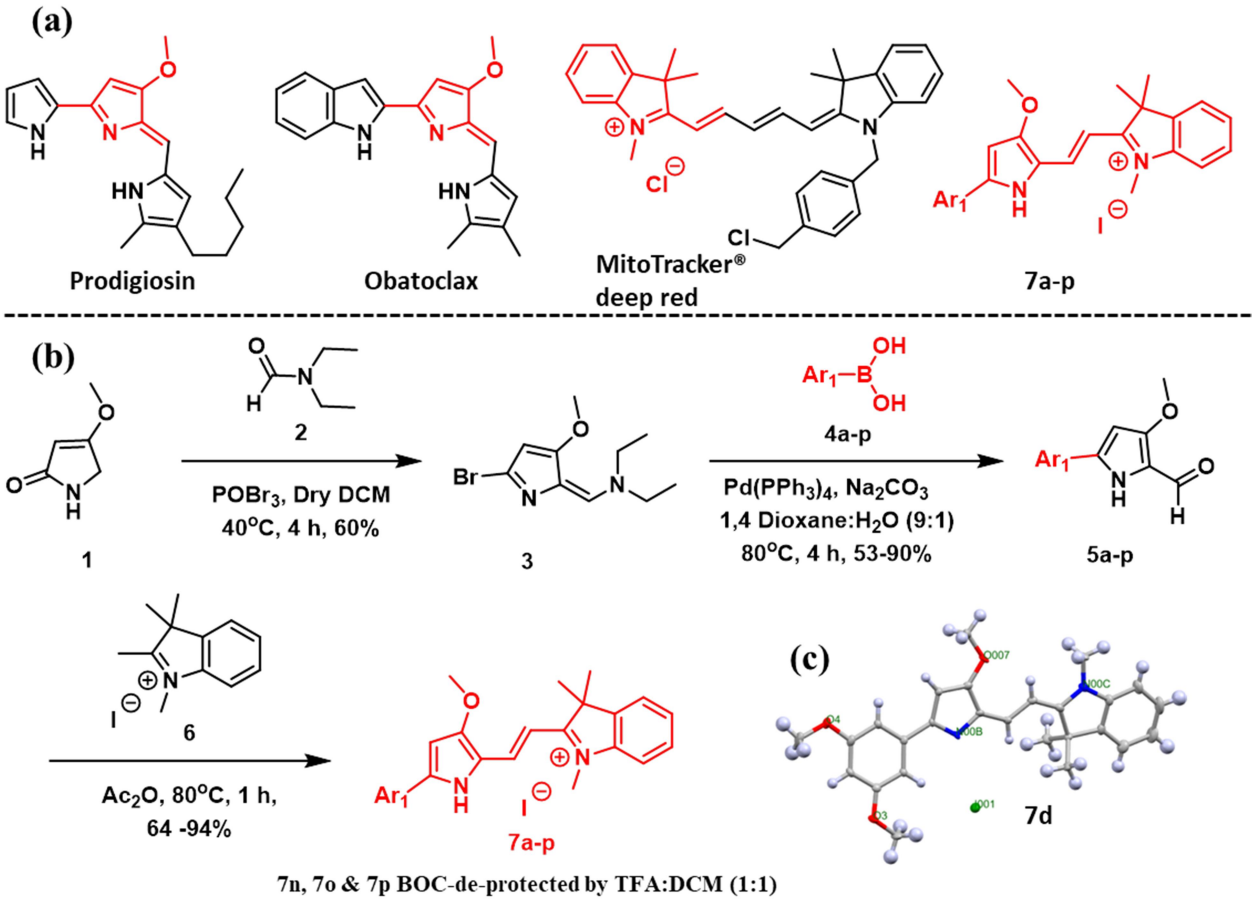


**Figure 4.1:** (a) Chemical Structures of Prodigiosin, Obatoclax, and MitoTracker deep red. (b) A synthetic scheme of a library. (c) ORTEP representation of compound **7d** obtained by X-ray diffraction of a single crystal.

To address this hypothesis, in this chapter, to target mitochondrion organelle selectively, we synthesized a library by modifying the structure of Obatoclax and Prodigiosin into cyanine-based cationic fluorophore (Figure 4.1a).[33-34] Mostly, delocalized cationic molecules accumulate in mitochondria like MitoTracker deep red or rhodamine because mitochondria possess immense negative membrane potential (ΔΨm). Here, one of the pyrrole rings of Prodigiosin is derivatized into positively charge indolium, keeping central ring pyrrole intact, while another part of central pyrrole ring we modified with several aromatic and heterocyclic aromatic groups. We synthesized a library of 16 compounds named as Cyanobax, hybrid of cyanine and Obatoclax.

Upon screening of the cyanobax library in cervical cancer HeLa cells gave two highly potent small molecules that able to localize in mitochondria. Using numerous experiments like cell viability, immunostaining analysis, immunoblot, and flow cytometry, we found that these potent molecules induced the mitochondria-dependent cellular death by inhibiting Bcl-2 family proteins.

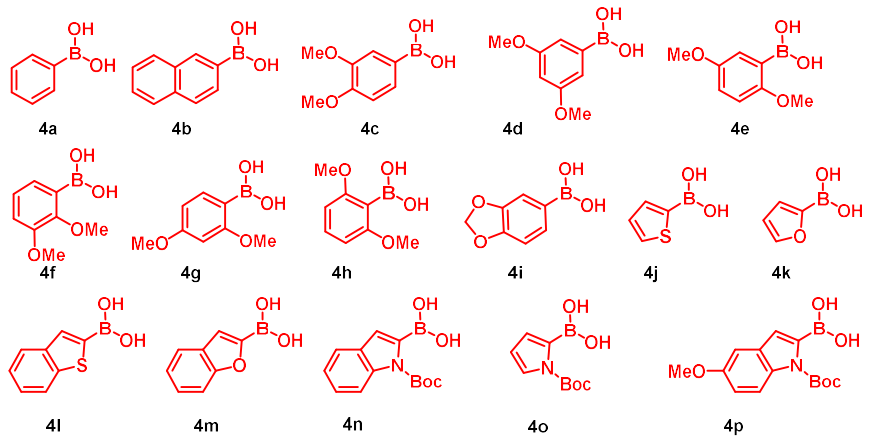


**Figure 4.2:** Chemical structures of boronic acids

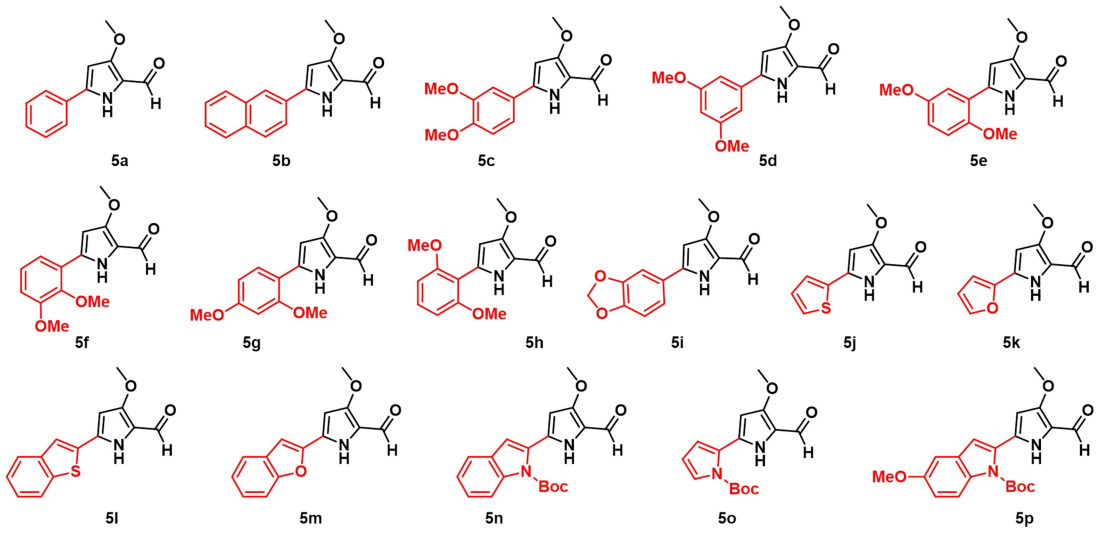


**Figure 4.3:** Chemical structures of intermediate aldehydes (**5a-p**)

## 4.2 Result and discussion

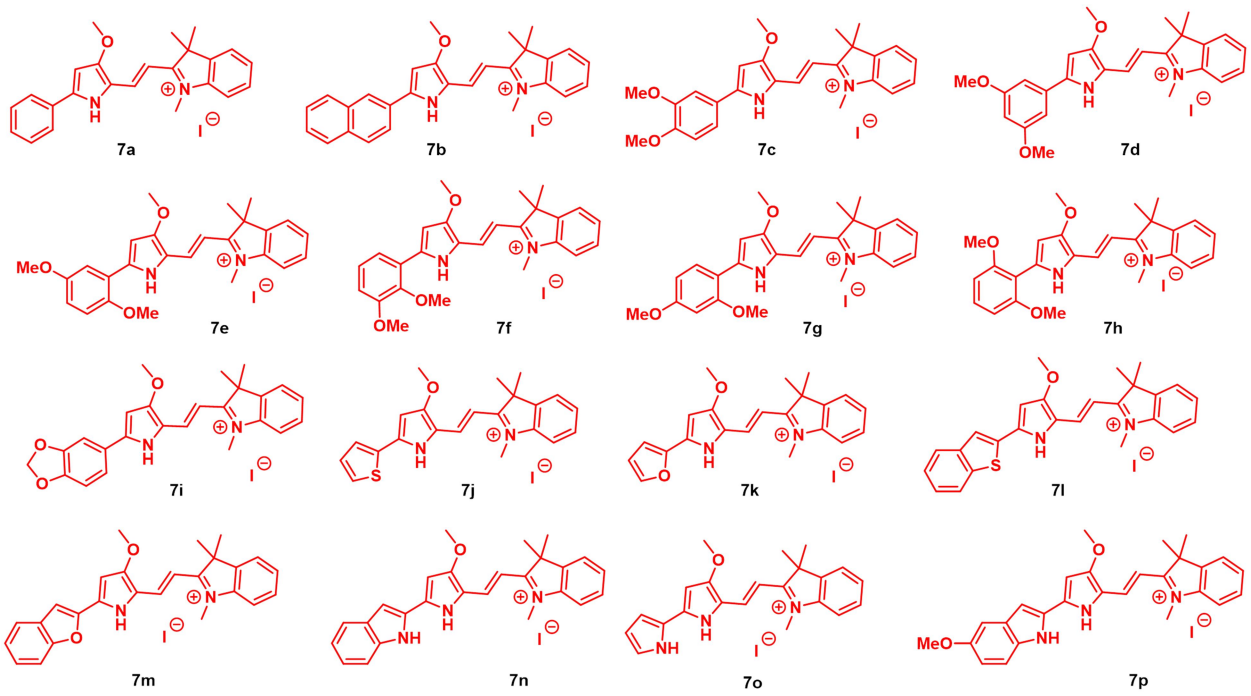


**Figure 4.4:** Chemical structures of the **7a-p** library members

### 4.2.1 Synthesis of library and characterization

The synthesis of the library is described in figure 4.1b. The library of 16 compounds was synthesized. The key intermediates, aromatic substituted 3-methoxy-pyrrole-2-carbaldehydes **5a-p,** were synthesized from commercially available 4-methoxy-3-pyrrolin-2-one **1** (Figure 4.1b).[34] Conversion of the compound **1** into compound **3** achieved using modified Vilsmeier reaction conditions to formylate the ethylethanamine with synchronous putting of a bromine atom in the presence of phosphorous oxybromide to afford 5-bromo-3-methoxy pyrrolidine derivative **3** in 60% yield.[35] Compound **3** then reacted with the commercially available aromatic boronic acids **4a-p** (figure 4.2) under classic Suzuki cross-coupling condition using tetrakis (triphenylphosphine) palladium (0) as catalyst, giving the desired core derivatives **5a-p** (Figure 4.3), along with simultaneous hydrolysis of enamine in moderate to high yield. Finally, compounds **5a-p** were refluxed with 1, 2, 3, 3-tetramethyl-3H-indolium iodide **6** to obtain derivatives **7a-p** (Figure 4.4) in 64-94 % (compounds **7n**, **7o**, **7p** were obtained after deprotection of N-BOC). The accomplished library members were characterized by $^{1}H$ and $^{13}C$, as well as high-resolution mass spectroscopy. (Appendix-C; Figure C1-99) Additionally, the structure of **7d** was confirmed by X-ray diffraction (Figure 4.1d) and showed its one of the

canonical cationic structure with counter-ion iodide. The excitation and emission spectra of the library member were measured in phosphate buffer (Table 4.1). All compounds bear excellent fluorescence with a range of emission 556-593 nm which is well suitable for bio-imaging.

**Table 4.1:** Absorption and emission maxima of the library members

| Compounds | $\lambda_{Abs}$ (nm) | $\lambda_{Em}$ (nm) | Compounds | $\lambda_{Abs}$ (nm) | $\lambda_{Em}$ (nm) |
|---|---|---|---|---|---|
| **7a** | 534 | 552 | **7i** | 546 | 567 |
| **7b** | 544 | 565 | **7j** | 552 | 569 |
| **7c** | 544 | 569 | **7k** | 550 | 565 |
| **7d** | 536 | 556 | **7l** | 554 | 575 |
| **7e** | 540 | 564 | **7m** | 558 | 576 |
| **7f** | 550 | 570 | **7n** | 564 | 591 |
| **7g** | 550 | 570 | **7o** | 560 | 580 |
| **7h** | 524 | 562 | **7p** | 568 | 593 |

### 4.2.2 Screening of library derivatives in cervical cancer (HeLa) cells

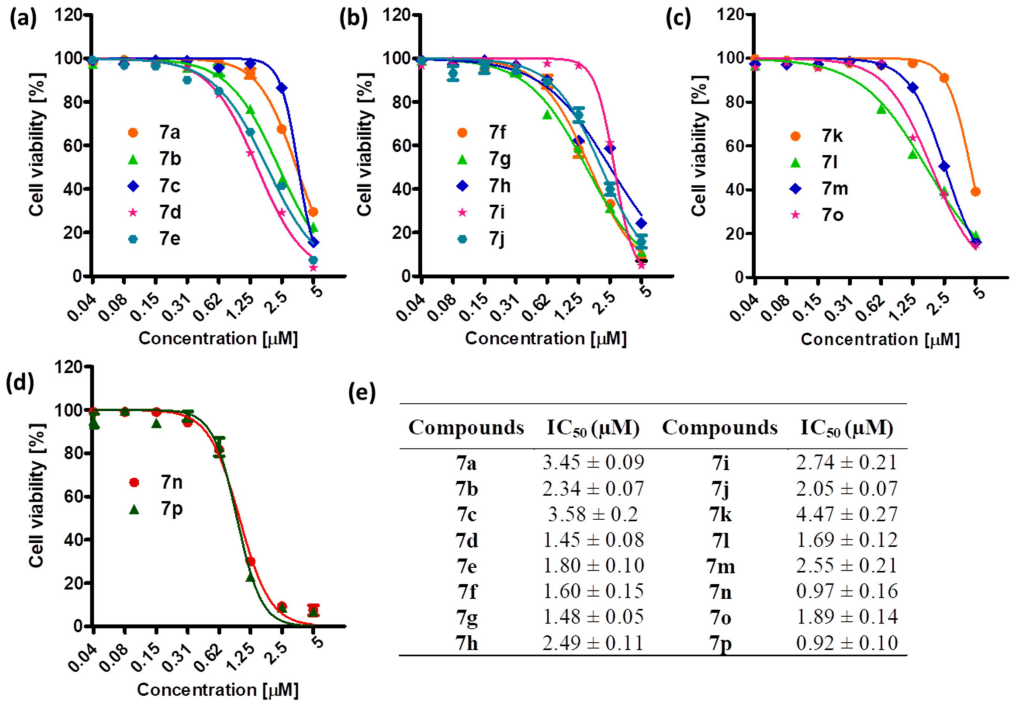


| Compounds | $IC_{50}$ (μM) | Compounds | $IC_{50}$ (μM) |
|---|---|---|---|
| **7a** | 3.45 ± 0.09 | **7i** | 2.74 ± 0.21 |
| **7b** | 2.34 ± 0.07 | **7j** | 2.05 ± 0.07 |
| **7c** | 3.58 ± 0.2 | **7k** | 4.47 ± 0.27 |
| **7d** | 1.45 ± 0.08 | **7l** | 1.69 ± 0.12 |
| **7e** | 1.80 ± 0.10 | **7m** | 2.55 ± 0.21 |
| **7f** | 1.60 ± 0.15 | **7n** | 0.97 ± 0.16 |
| **7g** | 1.48 ± 0.05 | **7o** | 1.89 ± 0.14 |
| **7h** | 2.49 ± 0.11 | **7p** | 0.92 ± 0.10 |

**Figure 4.5:** Cell viability study of library members in cervical cancer HeLa cells. (a), (b), (c), and (d) Dose-dependent cell viability for detection of $IC_{50}$ using MTT assay to all the library members for 24 h post-incubation. (e) $IC_{50}$ values of the library members

The compounds **7a-p** were screened to scrutinize their potential to prompt cell death in HeLa cells assessed by 3-(4,5-dimethylthiazol-2-yl)-2,5-diphenyltetrazolium bromide (MTT) assay at 24h after incubation. Surprisingly, all the compounds were potent to kill all the HeLa cells at 10 µm concentration. Furthermore, all the compounds of the library were screened at 5, 2.5, and 1.25 µM concentration for 24 h post-incubation. At 5 and 2.5 µM concentration, most of the compounds were found highly active. Finally, the dose-dependent cytotoxicity of all the compounds was calculated in HeLa by MTT assay 24 h post-incubation (Figure 4.5a-e). Interestingly, it was found that compounds **7n** and **7p** were extremely active with $IC_{50}$ 0.97 ± 0.16 µM (cell viability 7.45 ± 2.2% at 5 µM) and 0.92 ± 0.10 µM (cell viability 6.80 ± 1.3% at 5 µM) respectively.

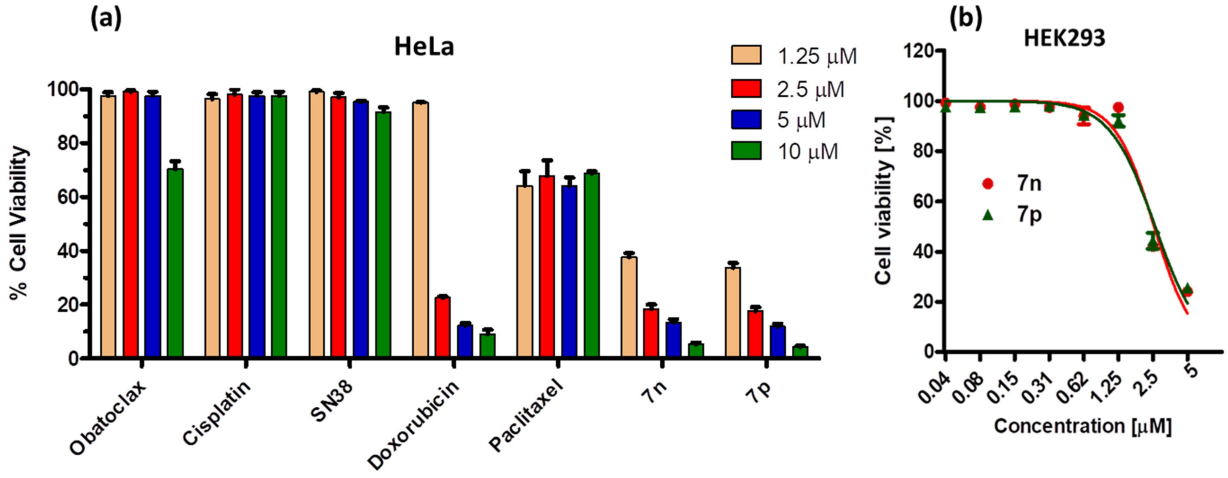


**Figure 4.6:** (a) Cytotoxic efficiency of potent compound **7n** and **7p** with other cytotoxic drugs in HeLa cells for 24 h at different concentrations. (b) Dose-dependent Cytotoxicity of compounds **7n** (IC50 2.56 ± 0.51) and **7p** (IC50 2.61 ± 0.48) in HEK293 for 24 h.

To compare the potential of compound **7n** and **7p** to induce cell death with other cytotoxic chemotherapeutic drugs, Obatoclax, Cisplatin, SN38, Doxorubicin, and Paclitaxel were used at 10, 5, 2.5 and 1.25 µM concentrations for 24 h and evaluate the cell viability by MTT assay (Figure 4.6a). It was observed that Cisplatin (cell viability 97.66 ± 2.1% at 10 µM) and SN38 (cell viability 91.66 ± 4.5% at 10 µM) here not active at 10 µM concentration whereas Obatoclax (cell viability 70.35 ± 5.0% at 10 µM) and paclitaxel (cell viability 68.74 ± 3.2% at 10 µM) showed moderate activity. Also, doxorubicin (cell viability 9.06 ± 3.5% at 10 µM) showed

comparable activity with $IC_{50}$ 2.02 ± 0.3 µM. Interestingly, both the compounds **7n** and **7p** were found more potent than these chemotherapeutics drugs; hence, we decided to use for further experiments. Adding in, we evaluated the cytotoxic effect of these compounds on noncancerous human embryonic kidney 293 cells using dose-dependent MTT assay (Figure 4.6b), and it was found that these molecules were less active with compared to the cytotoxic effect in cervical cancer Hela cells.

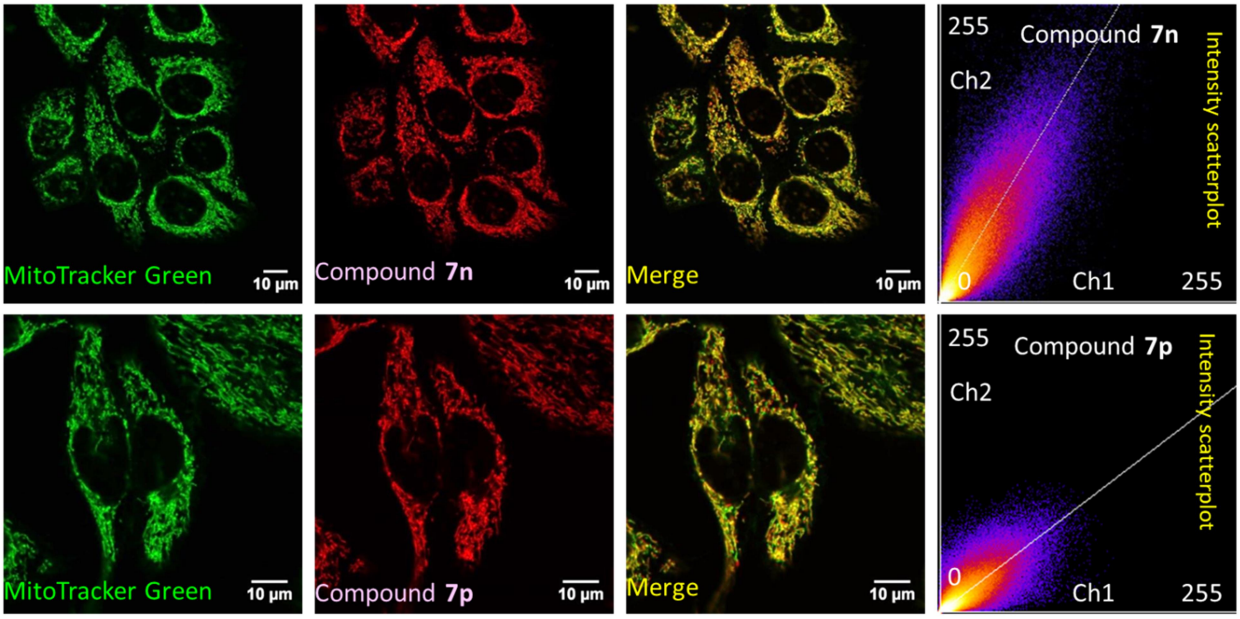


**Figure 4.6:** Laser scanning confocal microscopy images of live HeLa cells incubated with compound **7n** and **7p** for 20 minutes at 150 nM concentration and MitoTracker green FM at 75 nM concentration for 20 minutes to detect the colocalization. Scale bar = 10 µm

### 4.2.3 Mitochondria Localization of compound 7n and 7p

Owing to its positive charge and structural similarity with MitoTracker dye, we speculated that these molecules would localize in mitochondria. The concentrations of the incubation were optimized in live HeLa cells and it was found that the best suitable concentration lies between 100 to 200 nM, similar concentration has been used for MitoTracker red dye. To visualize the localization into mitochondria, 150 nM of the compounds **7n** and **7p** incubated into live HeLa cells for 20 min followed by staining mitochondria with MitoTracker Green FM dye (75 nM) for 20 min. The live HeLa cells were imaged by using confocal laser

scanning microscopy (CLSM) (Figure 4.6). The compounds were excited at 561 nm laser, whereas MitoTracker green FM was excited at 488 nm. Confocal Images exhibited the colocalization of the compounds **7n** and **7p** by merging of red fluorescence and mitochondria tagged green fluorescence led to yellow color. Intensity scatter plots of both the compounds confirmed the colocalization. Quantification of colocalization using Pearson's Correlation Coefficient of compound **7n** and **7p** gives 0.84 and 0.91 respectively, whereas Mander's coefficient showed fractions of red and green fluorescence overlapping to each other were nearly one in both compounds. Finally, to confirm colocalization, we acquired Z-stack images. In this experiment for a compound **7n** image captured as 83 micron 16 slices, whereas for compound **7p** image capture as 73 micron 15 slices with three average acquisitions per slice. The Z-stack maximum projection images (Figure 4.7) undoubtedly showed the colocalization of compound **7n** and **7p** with MitoTracker green. These measurements suggested the successful colocalization of compound **7n** and **7p** into mitochondria.

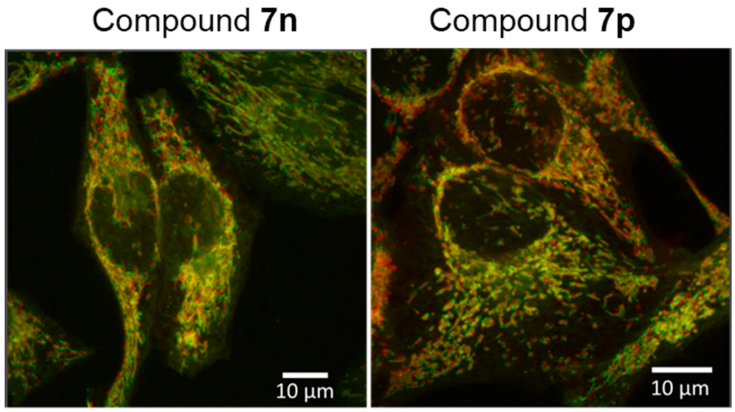


**Figure 4.7:** Z-stack maximum projection laser scanning confocal microscopy images of live HeLa cells incubated with compound **7n** and **7p** at 150 nM for 20 minutes

### 4.2.4 Mitochondrial permeability transition pore (MPTP) formations

Resistance to cell death is a key hallmark of cancer cells.[36] Mitochondria actively partake in controlling cancer death by the opening of MPTP. MPTP is a transitory structure that organizes in the inner mitochondria membrane upon the deprivation of functional mitochondria. The formation of MPTP increases the permeability of the mitochondrial membrane and

decreases transmembrane potential ($\Delta\psi_m$), leading to mitochondria swelling and rupture of the outer mitochondrial membrane.[37] After the confirmation that compound **7n** and **7p** were able to colocalized in mitochondria, further opening of the MPTP was evaluated by Calcein O,O′-diacetate tetrakis(acetoxymethyl) ester (Calcein AM) assay. After cellular uptake of Calcein AM, stays into cytoplasmic matrix and mitochondria.[38] Acetoxymethyl esters groups cleave into acid functionality by subcellular esterase leading to green fluorescent calcein. Externally addition of $CoCl_2$ quenches the green fluorescence without affecting the mitochondrial Calcein AM. Furthermore, after the formation of MPTP, Calcein AM from mitochondria comes out into the cytoplasmic matrix leading to rising green fluorescent calcein molecules.

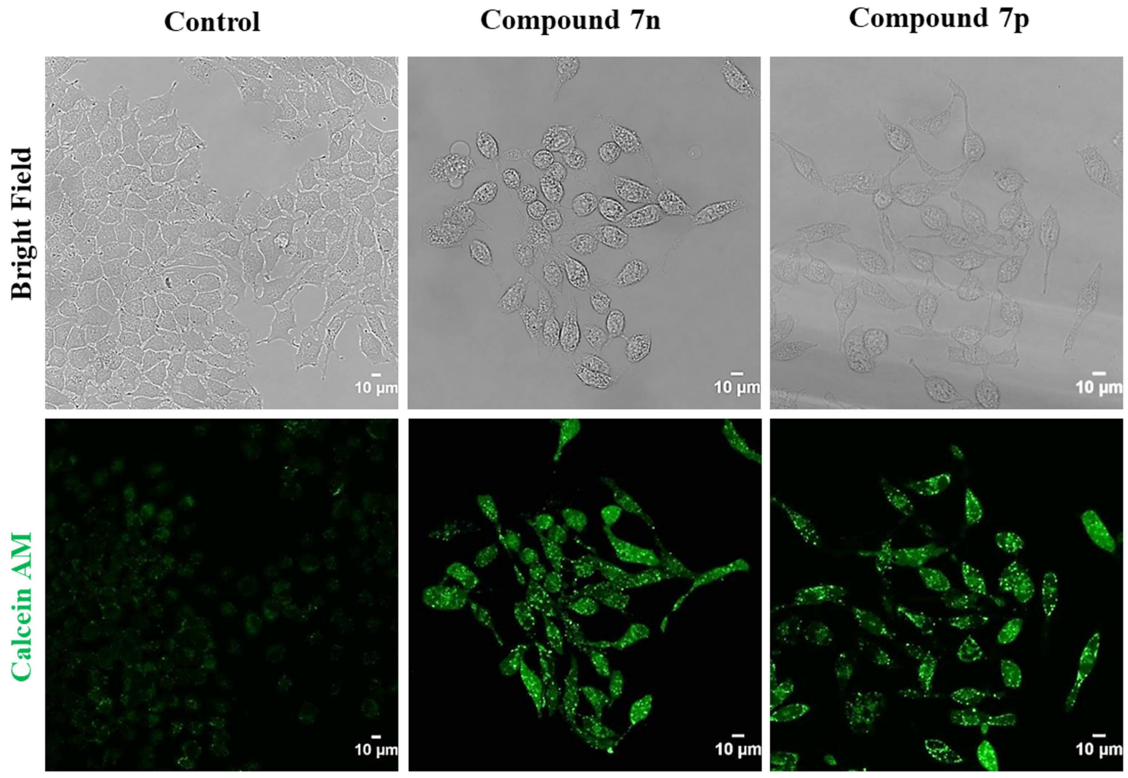


**Figure 4.8:** Laser scanning confocal microscopy images of live HeLa cells to observe Mitochondrial Permeability Transition Pore (MPTP) formations using calcein acetoxymethyl ester (AM) upon treatment of compound 7n and 7p at 800 nM for 24 h. Scale bar = 10 µm

To assess the formation of MPTP, HeLa cells were incubated with compound **7n** and **7p** for 24 h and stained with Calcein AM and $CoCl_2$, whereas control cells were stained only with Calcein AM and $CoCl_2$. The live HeLa cells were then imaged by confocal microscopy with 488

nm laser (Figure 4.8). The figures distinctly confirm the formation of MPTP by both the compounds leading in higher green fluorescence intensity than non-treated control cells. This experiment authenticated that compounds **7n** and **7p** perturb the functions of mitochondria leading to the opening of MPTP in Hela cells.

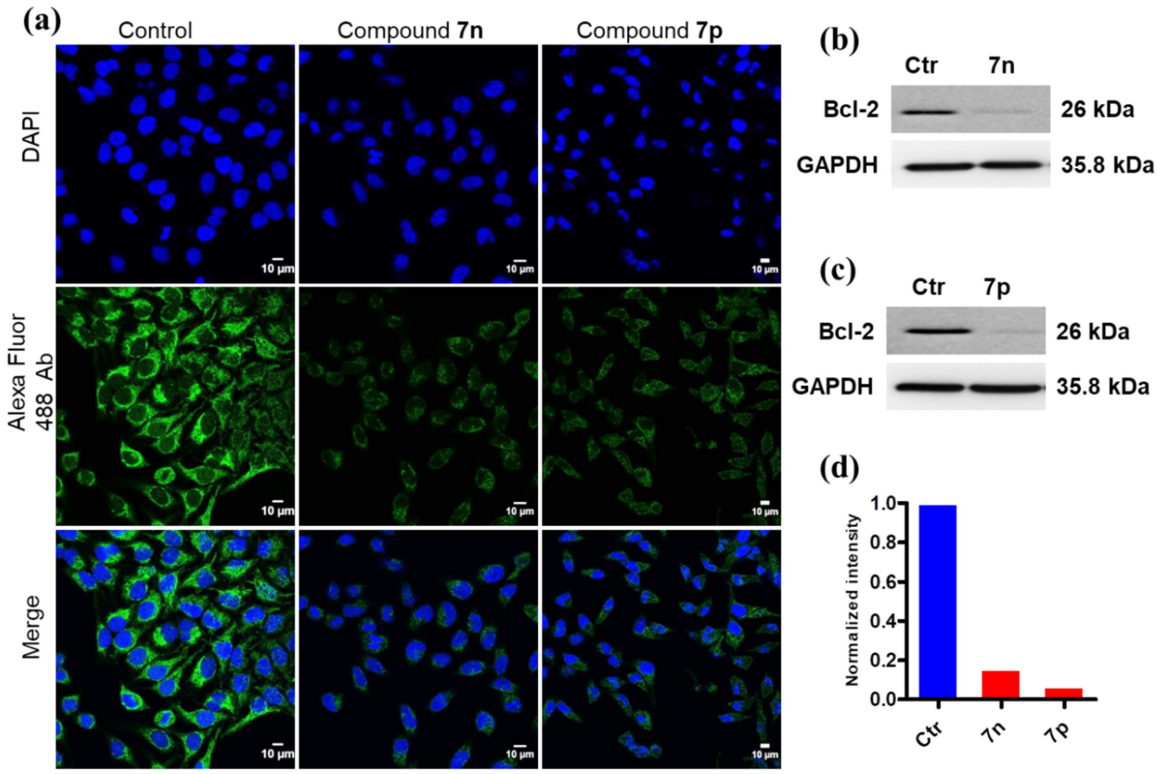


**Figure 4.9:** (a) Bcl-2 protein expression laser scanning confocal microscopy images of HeLa cells incubated with compound **7n** and **7p** at 900 nM for 24 h. Cells stained with Alexa Fluor 488 conjugated secondary antibody (b, c) Immunoblot analysis for Bcl-2 after 24 h incubation of compound **7n** and **7p** at 900 nM. (d) Quantification of Bcl-2 expression from Immunoblot analysis after treatment with compound **7n** and **7p** in HeLa cells for 24 h.

### 4.2.5 Bcl-2, Bcl-xl and Bax protein expression

Anti-apoptotic proteins of Bcl2- family (Bcl2/Bcl-xl) are an essential regulator of apoptosis by suppressing the activity of pro-apoptotic proteins (BAX/BAK).[22] Bcl-2 and Bcl-xl is primarily found on the outer surface of the mitochondrial membrane. They act as a gatekeeper by preventing the release of programmed cell death-promoting molecules such as Cytochrome C and ROS. However, BAX and BAK have a different function to trigger cell death by releasing

cytochrome c and ROS. Given this, small molecules inhibiting Bcl-2 or Bcl-xl to prompt cancer cell death comes with powerful anticancer drugs.[39]

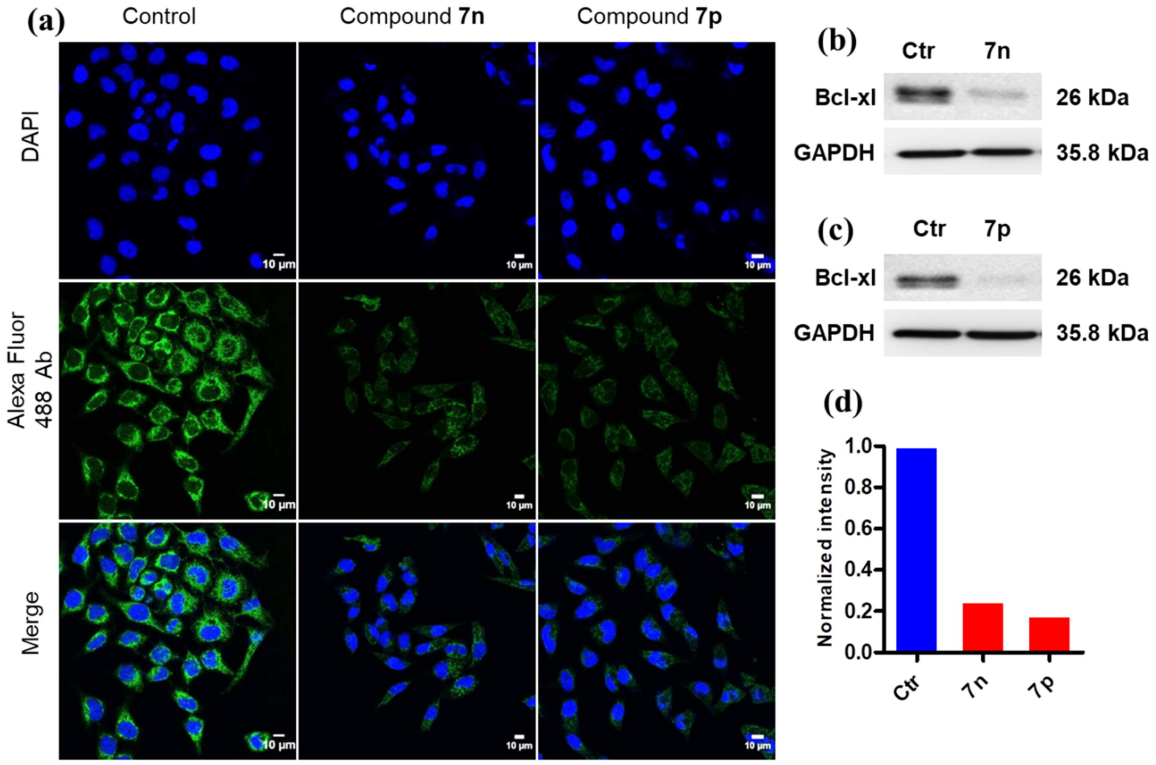


**Figure 4.10:** (a) Bcl-xl protein expression laser scanning confocal microscopy images of HeLa cells incubated with compound **7n** and **7p** at 900 nM for 24 h. Cells stained with Alexa Fluor 488 conjugated secondary antibody (b, c) Immunoblot analysis for Bcl-xl after 24 h incubation of compound **7n** and **7p** at 900 nM. (d) Quantification of Bcl-xl expression from Immunoblot analysis after treatment with compound **7n** and **7p** in HeLa cells for 24 h.

To ascertain, we initially checked the protein expression of anti-apoptotic proteins, Bcl-2, and Bcl-xl using immunostaining and immunoblot analysis. For immunostaining, HeLa cells were treated with compound **7n** and 7**p** and for 24 h and incubated with primary anti-Bcl-2, and anti-Bcl-xl antibodies followed by fluorescence tagged (Alexa Fluor 488) secondary antibodies and visualized the expression for Bcl-2 and Bcl-xl by CLSM (Figure 4.9a: Figure 4.10a). The confocal images evidently showed both the compounds **7n** and **7p** are active enough to lower the expression of Bcl-2 and Bcl-xl as compared to control cells, which were untreated with these compounds. To confirm and quantify the expression of Bcl-2 and Bcl-xl, HeLa cells were treated with both the compounds. The expressions of the proteins were visualized and quantified using

immunoblot assay (Figure 4.9b, c; Figure 4.10b, c). These figures clearly show the significant reduction of protein levels of Bcl-2 and Bcl-xl as compared to untreated control cells. Quantification of the expression of the proteins after normalizing GAPDH observed that compound **7n** reduced 6.4-fold and 4.0-fold Bcl-2 and Bcl-xl respectively, whereas compound **7p** decreased 9.3-fold Bcl-2 and 5.6-fold Bcl-xl compared to control cells (Figure 4.9d; figure 4.10d).

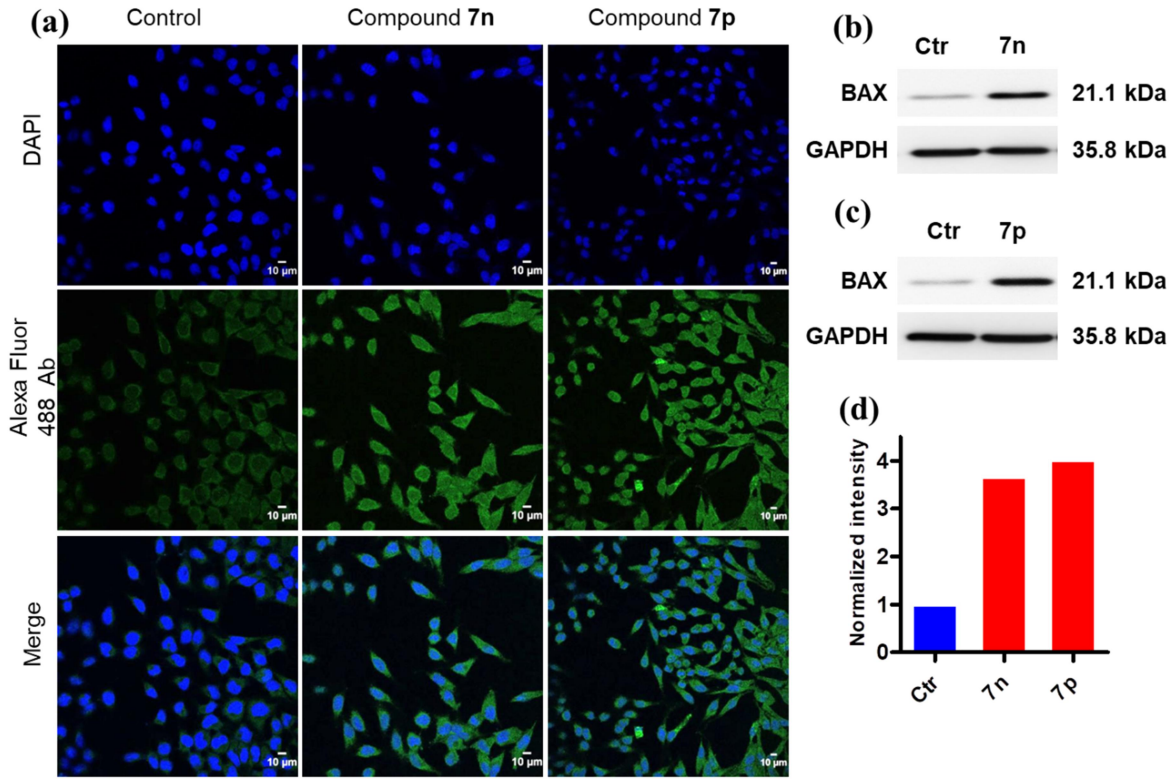


**Figure 4.11:** (a) BAX protein expression laser scanning confocal microscopy images of HeLa cells incubated with compound **7n** and **7p** at 900 nM for 24 h. Cells stained with Alexa Fluor 488 conjugated secondary antibody (b, c) Immunoblot analysis for BAX after 24 h incubation of compound **7n** and **7p** at 900 nM. (d) Quantification of BAX expression from Immunoblot analysis after treatment with compound **7n** and **7p** in HeLa cells for 24 h.

Finally, we checked the pro-apoptotic BAX protein expression using the same protocol. The remarkable increment in the expression of BAX protein was observed in immunostaining (**Figure 4.11a**), and it was confirmed using immunoblot experiment (Figure 4.11b, c). Quantification of Bax protein after treatment of compound **7n** and **7p** showed 3.6-fold and 4.1-

fold enhancement, respectively, as compared with untreated control cells (Figure 4.11d). The immunostaining images and protein expression by immunoblot, experiments confirmed that the compounds **7n** and **7p** triggered the mitochondrial apoptosis pathway by inhibiting anti-apoptotic Bcl-2 and Bcl-xl and activating pro-apoptotic BAX proteins.

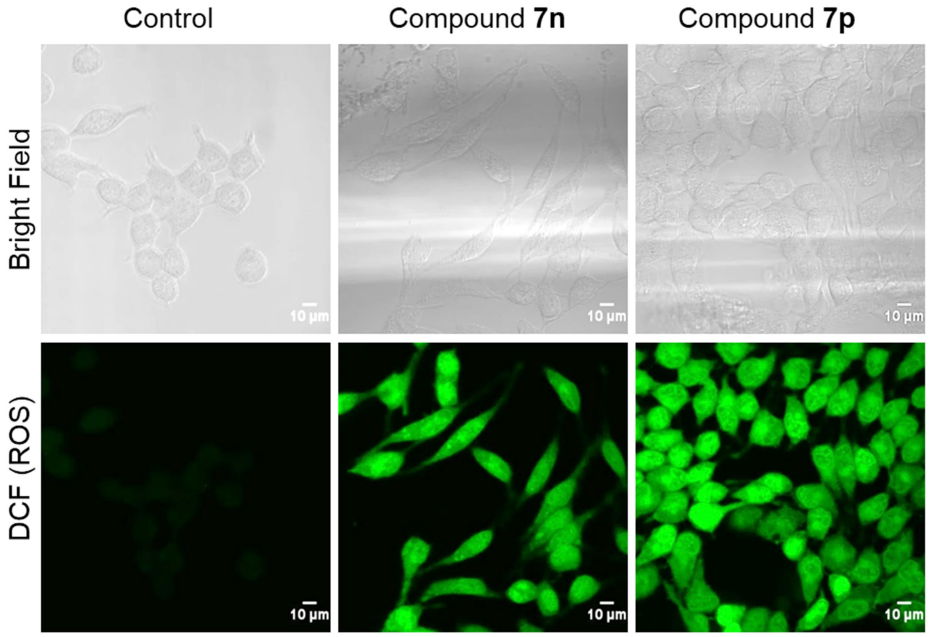


**Figure 4.12:** Laser scanning confocal microscopy images of live HeLa cells stained with 2′,7′-dichlorodihydrofluorescein diacetate ($H_2$DCFDA) to observe reactive oxygen species (ROS) generated by compound **7n** and **7p** at 800 nM for 24 h after incubation. Scale bar = 10 µm

### 4.2.6 Reactive Oxygen Species (ROS) Generation

Inhibition of anti-apoptotic Bcl-2 and Bcl-xl and hyper-activation of pro-apoptotic BAX leads to mitochondrial damage, which triggered reactive oxygen species (ROS) and caspase-dependent apoptotic pathway.[17, 40] To evaluate the ROS production, we performed cell-permeable 2′,7′-dichlorodihydrofluorescein diacetate($H_2$DCFDA) assay.[41] In subcellular environment non-fluorescence, $H_2$DCFDA turns into green fluorescent 2′,7′-dichlorofluorescein (DCF) upon hydrolysis by esterase followed by oxidation due to ROS. To estimate the production of ROS, HeLa cells were treated with compounds **7n** and **7p** for 24 h and stained with $H_2$DCFDA dye. The live cells were then imaged using CLSM using a 488 nm laser (Figure 4.12). The confocal images distinctly illustrated the significant enhancement in the production of

the ROS upon treatment of compound **7n** and **7p**. However, control cells without any treatment showed negligible fluorescence. The increase of the ROS, cells indicate compounds **7n** and **7p** generate ROS through mitochondrial damage.

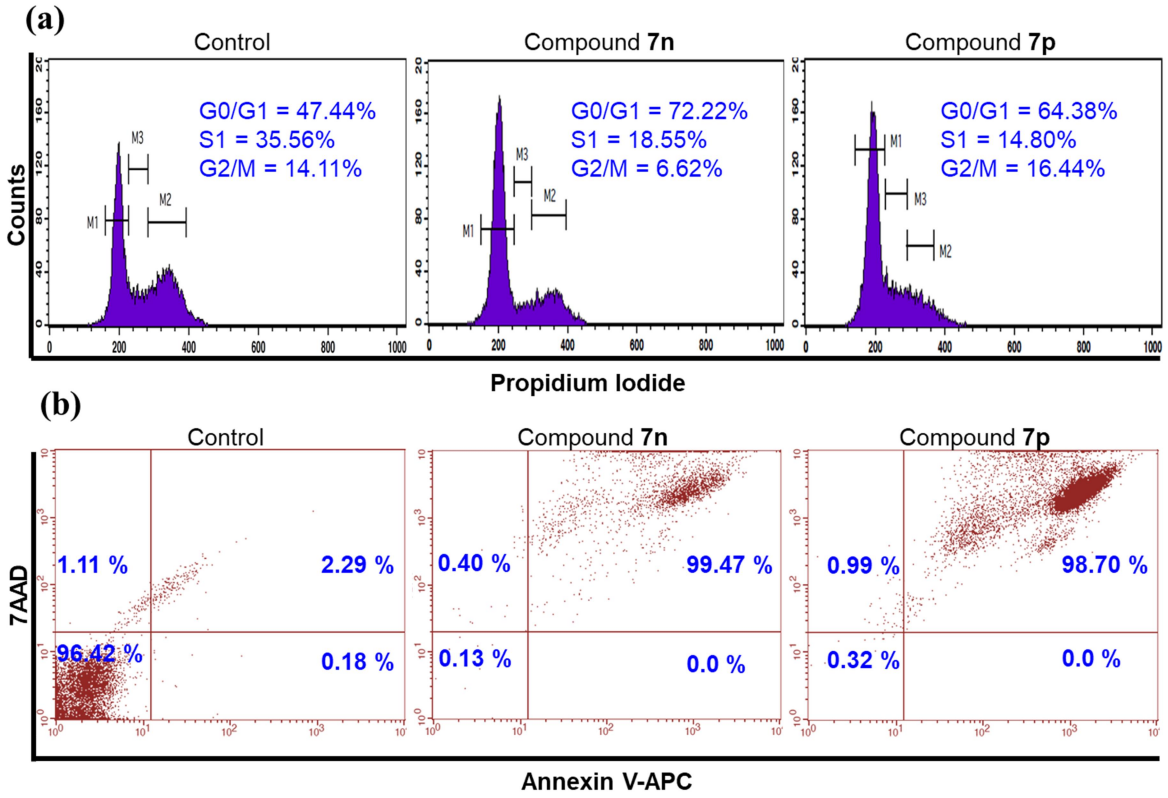


**Figure 4.13:** (a) Flow cytometry analysis for cell cycle in HeLa cells after incubating compound **7n** and **7p** at 900 nM for 24 h using propidium iodide (PI) as DNA staining. (b) Flow cytometry analysis. (b) Flow cytometry analysis for apoptosis in HeLa cell after incubating the compound **7n** and **7p** at 900 nM for 24 h using 7-amino-actinomycin D (7-AAD) with allophycocyanin (APC) bound annexin-V apoptosis kit.

### 4.2.7 Cell Cycle Arrest and Apoptosis Analysis

Inhibition of Bcl-2/Bcl-xl and activation of BAX triggers mitochondrial damage, which activates cell cycle arrest ahead of apoptosis.[44,45] Fluorescence-activated cell-sorting (FACS) method was used to estimate the cell cycle arrest analysis. HeLa cells were treated with compounds **7n** and **7p** for 24h, and cell cycle arrest was analyzed using propidium iodide (PI) labeled DNA (Figure 4.13a). Compound **7n** gave 72.22%, 18.55% and 6.62% cells in G0/G1, S1,

and G2/M phase, respectively. Also compound **7p** gave 64.38%, 14.80% and 16.44%. However, in untreated control cells gave 47.44%, 35.56%, 14.11% cells in G0/G1, S1, and G2/M phase, respectively. These FACS experiments showed that both the compounds arrested HeLa cells into the G0/G1 phase. Cell cycle arrest impels cells into programmed cell death, apoptosis. We then estimated the apoptosis by FACS analysis using 7-amino-actinomycin D (7-AAD) with allophycocyanin (APC) bound annexin-V.[46] Here, APC- annexin-V binds to translocated phosphatidylserine at the outer surface of apoptotic and necrotic cells, whereas & 7AAD selectively binds the DNA of late-stage apoptotic cells. HeLa cells were incubated with compound **7n** and **7p** for 24 h, followed by staining with APC-annexin-V and 7-AAD (Figure 4.13b). It was observed that compound **7n** gave 98.47% cells in late apoptotic stage, and compound **7p** gave 98.70% cells in late apoptotic stage, whereas untreated control cells found only 2.29% late apoptotic cells. This FACS analysis clearly shows that both the compounds are capable of inducing apoptosis through inhibiting Bcl-2 family consequently damaging mitochondria in HeLa cells.

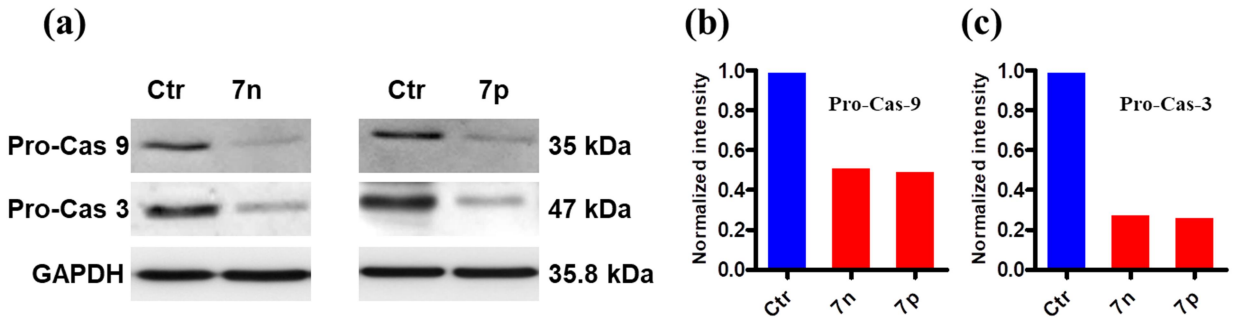


**Figure 4.14:** (a) Immunoblot analysis to check the expression of pro-caspase-9 and pro-caspase-3, in HeLa cells, after 24 h incubation of compound **7n** and **7p** at 900 nM. GAPDH was used to quantify the data. (b, c) Quantification of pro-caspase 9 and pro-caspase 3 expressions from immunoblot analysis after treatment with compound **7n** and **7p** in HeLa cells for 24 h

### 4.2.8 Caspase-9/3 protein expression

Mitochondria-dependent apoptosis in cancer cells activates the initiator caspase-9, which triggers downstream executioner caspase-3 upon cleavage, eventually leading to cell death.[42,43] Hence, we estimate the expression of caspase-9 and caspase-3 using immunoblotting. The

immunoblot analysis after incubation of compound 7n and 7p in HeLa cells for 24 clearly showed that these compounds trigger the cleavage of caspase-9 and caspase-3 compared to control cells (Figure 4.14a). Adding in, quantification of protein expression from western blot showed a 1.9-fold and 3.5-fold reduction in caspase-9 and caspase-3, respectively upon treatment of compound **7n**, whereas compound **7p** showed a 2-fold and 3.6-fold decrease in caspase-9 and caspase-3 respectively (Figure 4.14b, c). These immunoblot studies gave clear evidence that both the compounds induced mitochondria-dependent apoptosis in HeLa cells through inhibiting Bcl-2 family proteins.

## 4.3 Conclusion:

In conclusion, we have designed and synthesized a new small molecule family bearing positively charge analogues inspired by natural product Prodigiosin. All the library members exhibited excellent red fluorescence in λmax = 556-593 nm. Cytotoxicity in cervical cancer HeLa cells showed that all the compounds were active. Two of them were found to be highly potent in HeLa cells as compared to other clinically used cytotoxic drugs.

Further studies found that these two molecules were able to home into mitochondria within 20 minutes. Confocal microscopy, immunostaining, and immunoblot experiments demonstrated that these two molecules were able to damage mitochondria upon inhibiting Bcl-2/Bcl-xl, followed by the production of ROS. These compounds halt the cell cycle in the G0/G1 phase; cleaved caspase-9/3 emerged programmed cell death. This investigation will help understand mitochondrial chemical-biology and imaging, and further molecular biological studies may be encouraging to develop next generational anticancer agents.

## 4.4 Material and methods:

All the chemical reagents were purchased from Sigma Aldrich, and solvents were obtained from local commercial sources and used without purification. All reactions were performed in a round bottom flask or schlenk flask and were monitored by analytical thin-layer chromatography using pre-coated silica gel aluminium sheets 60 $F_{254}$ bought from EMD Millipore Laboratories. Spots on the TLC plates were visualized with UV light and then developed using standard TLC stained. For the purification of all the compounds, column chromatography was carried out using silica gel (100-200 mesh). All the $^{1}H$ NMR (400 MHz) and $^{13}C$ NMR (100 MHz) spectra

were recorded on a Bruker 400 MHz or JEOL 400 MHz spectrometers. The chemical shifts are expressed in parts per million (ppm) using suitable deuterated NMR solvents with residual solvent signal as an internal reference or from internal tetramethylsilane on the δ scale. Water's Synapt G2 was used to record High-Resolution Mass Spectra (HRMS) using electrospray ionization (ESI-TOF).

High Glucose Dulbecco's Modified Eagle Medium (DMEM) media, Dulbecco's phosphate-buffered saline (DPBS), Fetal Bovine Serum (FBS), 2', 7'-dichlorofluorescein-diacetate (H2DCFDA), SlowFade antifade and MitoTracker™ Green FM were purchased from Invitrogen (Thermo Fisher Scientific). The antibiotic solution, trypsin-EDTA, 3-(4, 5-dimethylthiazol-2-yl)-2, 5-diphenyltetrazolium bromide (MTT), 96-well flat bottom, 6-well tissue culture plates and sodium dodecyl sulfate (SDS) were purchased from HiMedia Laboratories. Tissue culture flasks (25 $cm^2$, angled neck, cap; phenolic-style), 15 mL and 50 mL graduated sterile centrifuge tubes, Nunc® Lab-Tek® II chambered coverglass, calcein AM, Hank's Balanced Salt Solution (HBSS) and RNase were purchased from Sigma-Aldrich. APC Annexin V apoptosis detection kit with 7-AAD, procaspase-3/9, and GAPDH antibodies were purchased from Biolegend. Bcl-2 and Bax antibodies were purchased from Santa Cruz Biotechnology. Bcl-xl antibody was purchased from Cell Signaling Technology. The western blot setup was purchased from Bio-Rad Laboratories. The laser scanning confocal microscopy was performed by Zeiss LSM 710 and/or Leica sp8 machine. Each sample was done in triplicate. FACS analysis was performed using BD FACS Calibur flow cytometer.

### 4.4.1 Synthesis of the library:

***N-((5-bromo-3-methoxy-2H-pyrrol-2-ylidene)methyl)-N-ethylethanamine* 3:**

Compound **3** was synthesized by modified reported protocols [47, 48].

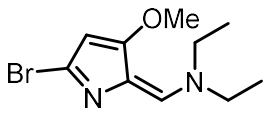


**3**

To an oven-dry two neck, 250 mL round bottom flask with a teflon-coated magnetic stir bar, N, N-diethylformamide **2** (8.05 mL 79.5 mmol) and 20 mL dry DCM was taken under argon. The solution was stirred at 0°C for 10 min. A solution of

phosphorous oxybromide (19.1 g, 66.3 mmol) in dry DCM (20 mL) was added dropwise to the reaction mixture and was kept stirred at 0°C for 30 min. After complete formation of white-colored solid, excess DCM was removed to dryness in a vacuum. Fresh dry DCM (20 mL) was added to the solid and cooled to $0^{o}$C under argon. A solution of the 4-methoxy-3-pyrrolin-2-one **1** (3 g, 26.52 mmol) in dry DCM (30 mL) was added dropwise over 15 min under argon. After addition, the flask was then removed from the ice bath and was warmed to room temperature and efflux at 40°C for 4 hours. To quench the reaction, the reaction mixture was poured onto aqueous sodium bicarbonate-ice-ethyl acetate mixture and was stirred for 10 min. The resulting reaction mixture was filtered through Celite and washed with cold ethyl acetate multiple times. Finally, aqueous layer was extracted with ethyl acetate (3 × 50 mL). The organic layer was washed with brine and dried over anhydrous sodium sulphate, filtered and evaporated under reduced pressure. The resulting residue was dissolved in DCM and adsorbed on silica (100-200 mesh) and was purified using column chromatography (5% ethyl acetate in hexane) gives yellow oil compound **3** (4.12 g, 60%).

**Characterization**

**$^{1}$H NMR** (400 MHz, $CDCl_3$) δ 6.99 (s, 1H), 5.59 (s, 1H), 4.11 (q, *J* = 7.1 Hz, 2H), 3.76 (s, 3H), 3.39 (q, *J* = 7.2 Hz, 2H), 1.29 (td, *J* = 7.2, 4.8 Hz, 6H).

**$^{13}$C NMR** (100 MHz, $CDCl_3$) δ 165.47, 138.71, 133.84, 120.94, 96.61, 58.11, 51.25, 44.69, 14.73, 12.62.

**HRMS (ESI-TOF) *m/z***: [M + H] calculated for $C_{10}H_{15}BrN_2O$ is 259.0446 and found 259.0445.

**The general synthesis procedure of 5a-p using modified reported protocol[49].**

***3-methoxy-5-phenyl-1H-pyrrole-2-carbaldehyde* 5a:**

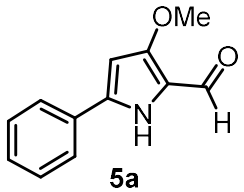


**5a**

1,4-Dioxane and water were degassed by the freeze-pump-thaw method. To an oven-dry schlenk flask, Phenylboronic acid (94 mg, 0.77 mmol) and compound **3** (100 mg, 0.39

mmol) were taken in an argon atmosphere. The degassed 1,4-dioxane (5 mL) and water were added. The mixture purged with argon for 5 min and subsequently Tetrakis(triphenylphosphine)palladium(0) (22.3 mg , 0.01929 mmol) and sodium bicarbonate (122.6 mg, 1.1574 mmol) was added. The schlenk flask was closed and heated to 90°C for 4h. The reaction mixture was cooled to room temperature and poured into ice-cold water (50 mL), and the pH of the mixture was adjusted to pH 7 using 2N aq HCl. Ethyl acetate (60 mL) was added, and the two layers were separated. The aqueous layer was extracted with ethyl acetate (3 x 60 mL), washed with brine and dried over anhydrous sodium sulphate, filtered, and concentrated in reduced pressure. The impure compound was purified using silica gel column chromatography in 10% ethyl acetate in hexane gives compound **5a** as yellow color solid (67 mg, 86%)

**Characterization**

**$^1$H NMR** (400 MHz, $CDCl_3$) δ 9.71 (s, 1H), 9.54 (s, 1H), 7.66 – 7.59 (m, 2H), 7.43 (dd, *J* = 7.3, 5.8 Hz, 2H), 7.39 – 7.34 (m, 1H), 6.19 (d, *J* = 2.7 Hz, 1H), 3.93 (s, 3H).

**$^{13}$C NMR** (100 MHz, $CDCl_3$) δ 174.93, 159.13, 139.13, 130.66, 129.23, 129.05, 125.37, 119.67, 93.35, 58.14.

**HRMS (ESI-TOF)** ***m/z***: [M + Na] calculated for $C_{12}H_{11}NO_2$ is 224.0687 and found 224.0691.

***3-methoxy-5-(naphthalen-2-yl)-1H-pyrrole-2-carbaldehyde*** **5b:**

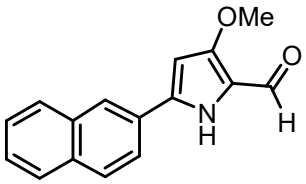


**5b**

The Compound **5b** was purified using silica gel column chromatography using 15% ethyl acetate in hexane gives pale yellow color solid (89.7 mg, 87%)

**Characterization**

**$^1$H NMR** (400 MHz, $CDCl_3$) δ 9.82 (s, 1H), 9.60 (s, 1H), 8.13 (d, *J* = 1.3 Hz, 1H), 7.90 – 7.82 (m, 3H), 7.72 (dd, *J* = 8.6, 1.8 Hz, 1H), 7.55 – 7.48 (m, 2H), 6.32 (d, *J* = 2.7 Hz, 1H), 3.97 (s, 3H).

**$^{13}$C NMR** (100 MHz, $CDCl_3$) δ 174.94, 159.08, 139.02, 133.50, 133.45, 129.07, 128.43, 127.94, 127.04, 126.92, 124.47, 122.98, 119.90, 93.79, 58.19.

**HRMS (ESI-TOF)** ***m/z***: [M + H] calculated for $C_{16}H_{13}NO_2$ is 252.1024 and found 252.1023.

***5-(3,4-dimethoxyphenyl)-3-methoxy-1H-pyrrole-2-carbaldehyde*** **5c:**

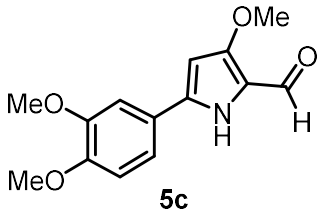


**5c**

The compound **5c** was obtained as a golden color solid (78 mg, 77.3%) after purification using silica gel column chromatography (20% ethyl acetate in hexane).

**Characterization**

**$^{1}$H NMR** (400 MHz, $CDCl_3$) δ 10.18 (s, 1H), 9.47 (s, 1H), 7.35 (d, *J* = 2.0 Hz, 1H), 7.23 (dd, *J* = 8.4, 2.1 Hz, 1H), 6.91 (d, *J* = 8.4 Hz, 1H), 6.11 (d, *J* = 2.7 Hz, 1H), 3.97 (s, 3H), 3.92 (d, *J* = 2.4 Hz, 6H).

**$^{13}$C NMR** (100 MHz, $CDCl_3$) δ 174.11, 159.73, 150.01, 149.56, 140.00, 123.66, 119.40, 118.66, 111.55, 108.57, 92.68, 58.10, 56.23, 56.14.

**HRMS (ESI-TOF)** ***m/z***: [M + Na] calculated for $C_{14}H_{15}NO_4$ is 284.0898 and found 284.0900.

***5-(3,5-dimethoxyphenyl)-3-methoxy-1H-pyrrole-2-carbaldehyde*** **5d:**

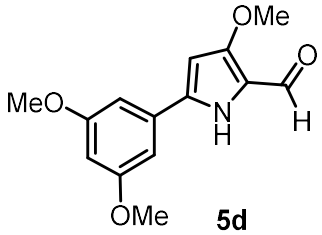


**5d**

The compound **5d** was obtained as a white color solid (84 mg, 83.3%) after purification using silica gel column chromatography (20% ethyl acetate in hexane).

**Characterization**

**$^1$H NMR** (400 MHz, $CDCl_3$) δ 9.83 (s, 1H), 9.53 (s, 1H), 6.83 (d, *J* = 2.2 Hz, 2H), 6.47 (t, *J* = 2.2 Hz, 1H), 6.17 (d, *J* = 2.8 Hz, 1H), 3.92 (s, 3H), 3.85 (s, 6H).

**$^{13}$C NMR** (100 MHz, $CDCl_3$) δ 174.77, 161.43, 159.12, 139.27, 132.49, 119.60, 103.59, 101.50, 93.63, 58.12, 55.69.

**HRMS (ESI-TOF)** ***m/z***: [M + Na] calculated for $C_{14}H_{15}NO_4$ is 284.0898 and found 284.0904.

***5-(2,5-dimethoxyphenyl)-3-methoxy-1H-pyrrole-2-carbaldehyde*** **5e:**

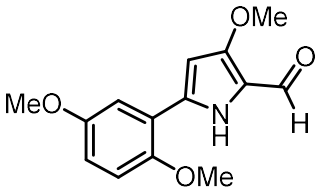


**5e**

The compound **5e** was obtained as a dark green color solid (71 mg, 70.3%) after purification using silica gel column chromatography (30% ethyl acetate in hexane).

**Characterization**

**$^1$H NMR** (400 MHz, $CDCl_3$) δ 10.09 (s, 1H), 9.55 (s, 1H), 7.15 (d, *J* = 3.0 Hz, 1H), 6.93 (d, *J* = 9.0 Hz, 1H), 6.85 (dd, *J* = 9.0, 3.0 Hz, 1H), 6.20 (d, *J* = 2.8 Hz, 1H), 3.95 (s, 3H), 3.92 (s, 3H), 3.82 (s, 3H).

**$^{13}$C NMR** (100 MHz, $CDCl_3$) δ 174.68, 157.99, 154.00, 151.08, 136.22, 119.05, 118.85, 114.68, 113.62, 112.91, 93.06, 58.07, 56.36, 56.01.

**HRMS (ESI-TOF)** ***m/z***: [M + H] calculated for $C_{14}H_{15}NO_4$ is 262.1079 and found 262.1074.

***5-(2,3-dimethoxyphenyl)-3-methoxy-1H-pyrrole-2-carbaldehyde*** **5f:**

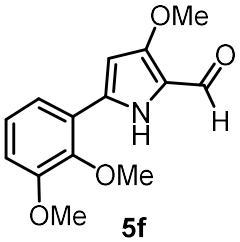


**5f**

The compound **5f** was obtained as a white color solid (79 mg, 78.3%) after purification using silica gel column chromatography (15% ethyl acetate in hexane).

**Characterization**

**$^1$H NMR** (400 MHz, $CDCl_3$) δ 10.05 (s, 1H), 9.57 (s, 1H), 7.19 (dd, *J* = 8.0, 1.5 Hz, 1H), 7.09 (t, *J* = 8.0 Hz, 1H), 6.90 (dd, *J* = 8.1, 1.5 Hz, 1H), 6.23 (d, *J* = 2.8 Hz, 1H), 3.92 (s, 3H), 3.90 (d, *J* = 1.2 Hz, 6H).

**$^{13}$C NMR** (100 MHz, $CDCl_3$) δ 174.87, 157.87, 153.44, 146.59, 135.76, 124.74, 123.36, 119.60, 119.06, 112.69, 93.93, 60.87, 58.08, 56.10.

**HRMS (ESI-TOF)** ***m/z***: [M + Na] calculated for $C_{14}H_{15}NO_4$ is 284.0898 and found 284.0903.

***5-(2,4-dimethoxyphenyl)-3-methoxy-1H-pyrrole-2-carbaldehyde*** **5g:**

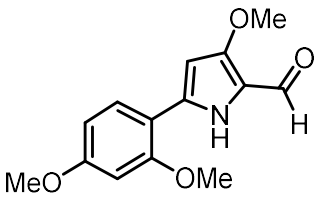


**5g**

The compound **5g** was obtained as a white color solid (91mg, 90.3%) after purification using silica gel column chromatography (45% ethyl acetate in hexane).

**Characterization**

**$^1$H NMR** (400 MHz, $CDCl_3$) δ 9.91 (s, 1H), 9.48 (s, 1H), 7.54 (d, *J* = 8.6 Hz, 1H), 6.56 (dt, *J* = 5.3, 2.3 Hz, 2H), 6.12 (d, *J* = 2.8 Hz, 1H), 3.97 (s, 3H), 3.91 (s, 3H), 3.85 (s, 3H).

**$^{13}$C NMR** (100 MHz, $CDCl_3$) δ 173.94, 161.36, 158.49, 157.99, 137.10, 129.23, 118.30, 111.69, 105.93, 99.15, 92.10, 58.00, 55.97, 55.65.

**HRMS (ESI-TOF)** ***m/z***: [M + H] calculated for $C_{14}H_{15}NO_4$ is 262.1079 and found 262.1079.

***5-(2,6-dimethoxyphenyl)-3-methoxy-1H-pyrrole-2-carbaldehyde*** **5h:**

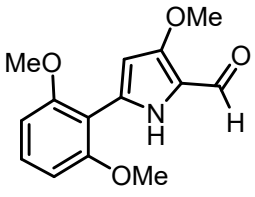


**5h**

The compound **5h** was obtained as a dark peach color solid (60 mg, 59.3%) after purification using silica gel column chromatography (20% ethyl acetate in hexane).

**Characterization**

**$^1$H NMR** (400 MHz, $CDCl_3$) δ 10.06 (s, 1H), 9.54 (s, 1H), 7.29 – 7.24 with reference solvent peak (m, 1H), 6.68 (d, *J* = 8.4 Hz, 2H), 6.56 (d, *J* = 2.8 Hz, 1H), 3.94 (s, 6H), 3.92 (s, 3H).

**$^{13}$C NMR** (100 MHz, $CDCl_3$) δ 174.46, 158.35, 157.59, 132.80, 129.68, 117.70, 108.31, 104.81, 98.36, 57.98, 56.24.

**HRMS (ESI-TOF)** ***m/z***: [M + H] calculated for $C_{14}H_{15}NO_4$ is 262.1079 and found 262.1085.

***5-(benzo[d][1,3]dioxol-5-yl)-3-methoxy-1H-pyrrole-2-carbaldehyde*** **5i:**

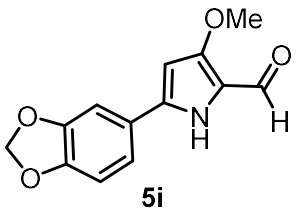


**5i**

The compound **5i** was obtained as a light green color solid (64 mg, 67.7%) after purification using silica gel column chromatography (15% ethyl acetate in hexane).

**Characterization**

**$^1$H NMR** (400 MHz, $CDCl_3$) δ 9.69 (s, 1H), 9.50 (s, 1H), 7.17 – 7.11 (m, 2H), 6.85 (d, *J* = 8.0 Hz, 1H), 6.07 (d, *J* = 2.7 Hz, 1H), 6.01 (s, 2H), 3.91 (s, 3H).

**$^{13}$C NMR** (100 MHz, $CDCl_3$) δ 174.49, 159.27, 148.50, 139.33, 124.98, 119.68, 119.37, 109.01, 105.96, 101.64, 92.93, 58.10.

**HRMS (ESI-TOF)** ***m/z***: [M + H] calculated for $C_{13}H_{11}NO_4$ is 246.0766 and found 246.0770.

***3-methoxy-5-(thiophen-2-yl)-1H-pyrrole-2-carbaldehyde*** **5j:**

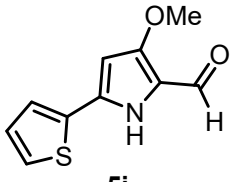


**5j**

The compound **5j** was obtained as a dark green color solid (71 mg, 88.9%) after purification using silica gel column chromatography (2% ethyl acetate in hexane).

**Characterization**

**$^1$H NMR** (400 MHz, $CDCl_3$) δ 9.70 (s, 1H), 9.52 (s, 1H), 7.42 (dd, *J* = 3.7, 1.0 Hz, 1H), 7.32 (d, *J* = 5.0 Hz, 1H), 7.08 (dd, *J* = 5.0, 3.7 Hz, 1H), 6.08 (d, *J* = 1.8 Hz, 1H), 3.91 (s, 3H).

**$^{13}$C NMR** (100 MHz, $CDCl_3$) δ 174.59, 159.15, 134.03, 133.92, 128.42, 126.21, 125.01, 119.22, 93.73, 58.19.

**HRMS (ESI-TOF)** ***m/z***: [M + Na] calculated for $C_{10}H_9NO_2S$ is 230.0251 and found 230.0257

***5-(furan-2-yl)-3-methoxy-1H-pyrrole-2-carbaldehyde*** **5k:**

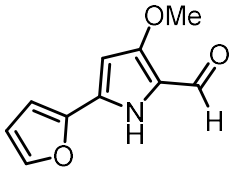


**5k**

The compound **5k** was obtained as a light mustard color solid (56.7 mg, 76.8%) after purification using silica gel column chromatography (15% ethyl acetate in hexane).

**Characterization**

**$^1$H NMR** (400 MHz, $CDCl_3$) δ 9.85 (s, 1H), 9.53 (s, 1H), 7.46 (dd, *J* = 1.8, 0.6 Hz, 1H), 6.86 – 6.78 (m, 1H), 6.49 (dd, *J* = 3.5, 1.8 Hz, 1H), 6.11 (d, *J* = 2.6 Hz, 1H), 3.90 (s, 3H).

**$^{13}$C NMR** (100 MHz, $CDCl_3$) δ 174.65, 158.95, 146.28, 143.08, 130.47, 118.96, 112.20, 108.08, 92.31, 58.16.

**HRMS (ESI-TOF)** ***m/z***: [M + H] calculated for $C_{10}H_9NO_3$ is 192.0660 and found 192.0666.

**5-(benzo[b]thiophen-2-yl)-3-methoxy-1H-pyrrole-2-carbaldehyde 5l:**

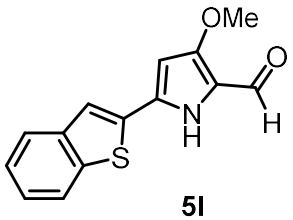


**5l**

The compound **5l** was obtained as a light green color solid (73.3 mg, 73.8%) after purification using silica gel column chromatography (3% ethyl acetate in hexane).

**Characterization**

**$^1$H NMR** (400 MHz, $CDCl_3$) δ 9.94 (s, 1H), 9.59 (s, 1H), 7.84 – 7.76 (m, 2H), 7.67 (s, 1H), 7.40 – 7.33 (m, 2H), 6.19 (d, *J* = 1.8 Hz, 1H), 3.94 (s, 3H).

**$^{13}$C NMR** (100 MHz, $CDCl_3$) δ 175.07, 158.78, 140.17, 139.47, 133.47, 133.42, 125.38, 125.13, 124.22, 122.43, 121.22, 119.81, 94.88, 58.26.

**HRMS (ESI-TOF)** ***m/z***: [M + H] calculated for $C_{14}H_{11}NO_2S$ is 258.0588 and found 258.0591.

***5-(benzofuran-2-yl)-3-methoxy-1H-pyrrole-2-carbaldehyde*** **5m:**

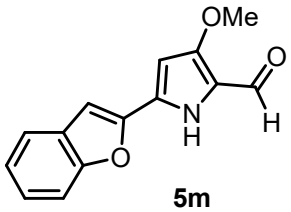


**5m**

The compound **5m** was obtained as a pale yellow color solid (86.3 mg, 92.7%) after purification using silica gel column chromatography (2% ethyl acetate in hexane).

**Characterization**

**$^1$H NMR** (400 MHz, DMSO-D6) δ 12.29 (s, 1H), 9.51 (s, 1H), 7.64 (ddd, *J* = 38.6, 7.9, 0.7 Hz, 2H), 7.53 (s, 1H), 7.31 (dtd, *J* = 27.2, 7.3, 1.1 Hz, 2H), 6.55 (d, *J* = 2.6 Hz, 1H), 3.90 (s, 3H).

**$^{13}$C NMR** (100 MHz, DMSO-D6) δ 174.29, 157.50, 154.09, 148.09, 128.56, 128.32, 125.13, 123.52, 121.52, 119.59, 111.01, 103.37, 94.33, 58.13.

**HRMS (ESI-TOF)** ***m/z***: [M + H] calculated for $C_{14}H_{11}NO_3$ is 242.0817 and found 242.0821.

***Tert-butyl 2-(5-formyl-4-methoxy-1H-pyrrol-2-yl)-1H-indole-1-carboxylate*** **5n:**

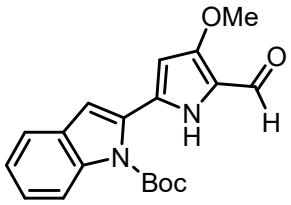


**5n**

The compound **5n** was obtained as a peach color solid (113.3 mg, 82.5%) after purification using silica gel column chromatography (12% ethyl acetate in hexane).

**Characterization**

**$^1$H NMR** (400 MHz, $CDCl_3$) δ 10.01 (s, 1H), 9.58 (s, 1H), 8.10 (d, *J* = 8.7 Hz, 1H), 7.56 (d, *J* = 7.6 Hz, 1H), 7.35 (ddd, *J* = 8.5, 7.2, 1.3 Hz, 1H), 7.26 with reference solvent peak (ddd, *J* = 7.5, 6.8, 0.9 Hz, 1H), 6.91 (s, 1H), 6.15 (d, *J* = 2.7 Hz, 1H), 3.91 (s, 3H), 1.61 (s, 9H).

**$^{13}$C NMR** (100 MHz, $CDCl_3$) δ 175.15, 157.46, 150.60, 137.52, 130.96, 130.74, 128.85, 125.56, 123.61, 121.05, 119.23, 116.04, 112.91, 96.92, 85.46, 58.15, 28.17.

**HRMS (ESI-TOF)** ***m/z***: [M + H] calculated for $C_{19}H_{20}N_2O_4$ is 341.1501 and found 341.1512.

***Tert-butyl 5'-formyl-4'-methoxy-1H,1'H-[2,2'-bipyrrole]-1-carboxylate*** **5o:**

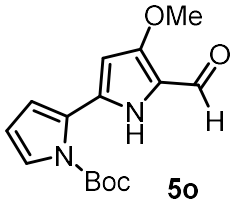


**5o**

The compound **5o** was obtained as a peach color solid (60 mg, 53.6%) after purification using silica gel column chromatography (3% ethyl acetate in hexane).

**Characterization**

**$^1$H NMR** (400 MHz, $CDCl_3$) δ 10.71 (s, 1H), 9.53 (s, 1H), 7.33 (dd, *J* = 3.4, 1.8 Hz, 1H), 6.66 (dd, *J* = 3.6, 1.8 Hz, 1H), 6.24 (t, *J* = 3.5 Hz, 1H), 6.08 (d, *J* = 2.7 Hz, 1H), 3.89 (s, 3H), 1.61 (s, 9H).

**$^{13}$C NMR** (100 MHz, $CDCl_3$) δ 174.51, 157.83, 149.85, 130.40, 126.11, 124.68, 118.39, 117.03, 111.63, 94.89, 85.92, 58.04, 28.05.

**HRMS (ESI-TOF)** ***m/z***: [M + Na] calculated for $C_{15}H_{18}N_2O_4$ is 313.1164 and found 313.1168.

***Tert-butyl-2-(5-formyl-4-methoxy-1H-pyrrol-2-yl)-5-methoxy-1H-indole-1-carboxylate*** **5p:**

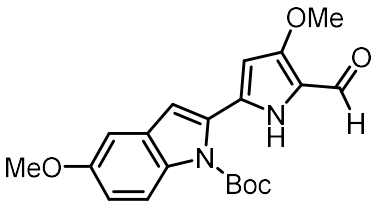


**5p**

The compound **5p** was obtained as a peach color solid (96 mg, 64.42%) after purification using silica gel column chromatography (15% ethyl acetate in hexane).

**Characterization**

**$^{1}$H NMR** (400 MHz, $CDCl_3$) δ 10.05 (s, 1H), 9.58 (s, 1H), 7.97 (d, *J* = 9.1 Hz, 1H), 6.97 (dt, *J* = 9.1, 2.5 Hz, 2H), 6.85 (s, 1H), 6.15 (d, *J* = 2.7 Hz, 1H), 3.91 (s, 3H), 3.86 (s, 3H), 1.62 (s, 9H).

**$^{13}$C NMR** (100 MHz, $CDCl_3$) δ 175.12, 156.40, 132.17, 131.30, 130.46, 129.66, 119.16, 117.01, 114.57, 112.76, 102.95, 96.84, 85.45, 58.14, 55.80, 28.20.

**HRMS (ESI-TOF)** ***m/z***: [M + H] calculated for $C_{20}H_{22}N_2O_5$ is 371.1607 and found 371.1609.

**General procedure for synthesis of 7a-p using modified reported protocol[50].**

***(E)-2-(2-(3-methoxy-5-phenyl-1H-pyrrol-2-yl)vinyl)-1,3,3-trimethyl-3H-indol-1-ium iodide* 7a:**

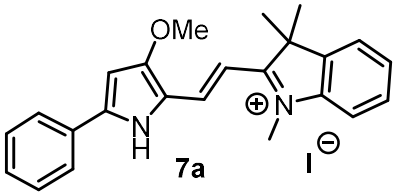


**7a**

To an oven-dry 25 mL round bottom flask compound **5a** (50 mg, 0.2486 mmol), 1, 2, 3, 3-tetramethyl-3H-indolium iodide (82.4 mg, 0.27335 mmol) and sodium acetate (22.4 mg, 0.274 mmol) was dissolved in acetic anhydride (2 mL). The reaction mixture was stirred at 80°C for 1 hour. The mixture was allowed to room temperature, and the solvent was removed under reduced pressure. The residue was dissolved in chloroform (5 mL), and the insoluble sodium acetate was removed by filtration. The resulting solution was concentrated, adsorbed on silica and purified using silica gel column chromatography (1.5% methanol in chloroform) gives **7a** dark golden-green color solid (95 mg, 79%).

The same procedure was used for the **7b-m**, and the **7n-p** one extra step used for N-BOC deprotection.

**Characterization**

**$^1$H NMR** (400 MHz, $CDCl_3$) δ 11.86 (s, 1H), 8.31 (d, *J* = 7.2 Hz, 2H), 8.10 (d, *J* = 7.2 Hz, 1H), 7.86 (d, *J* = 15.1 Hz, 1H), 7.79 (d, *J* = 15.1 Hz, 1H), 7.48 (dd, *J* = 6.0, 1.6 Hz, 2H), 7.38 (dd, *J* = 5.7, 4.6 Hz, 2H), 7.29 (dd, *J* = 7.5, 0.8 Hz, 1H), 7.16 (d, *J* = 7.9 Hz, 1H), 6.26 (s, 1H), 4.06 (s, 3H), 4.02 (s, 3H), 1.72 (s, 6H).

**$^{13}$C NMR** (100 MHz, $CDCl_3$) δ 176.72, 162.38, 150.67, 142.62, 141.52, 132.80, 130.98, 129.36, 129.12, 128.19, 127.11, 125.95, 122.15, 111.27, 101.78, 94.14, 58.69, 49.57, 34.85, 28.36.

**HRMS (ESI-TOF)** ***m/z***: [$M^+$] calculated for $C_{24}H_{25}N_2O^+$ is 357.1961 and found 357.1954.

***(E)-2-(2-(3-methoxy-5-(naphthalen-2-yl)-1H-pyrrol-2-yl)vinyl)-1,3,3-trimethyl-3H-indol-1-ium iodide*** **7b:**

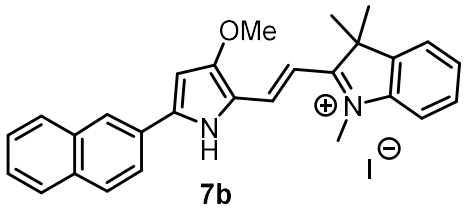


**7b**

Compound **7b** purified using silica gel column chromatography (2% methanol in chloroform) gives dark golden green solid (91 mg 85.6%).

**Characterization**

**$^1$H NMR** (400 MHz, $CDCl_3$) δ 11.94 (s, 1H), 9.20 (s, 1H), 8.21 – 8.16 (m, 2H), 7.92 – 7.85 (m, 2H), 7.82 – 7.78 (m, 2H), 7.50 (dd, *J* = 6.0, 3.5 Hz, 2H), 7.39 (dd, *J* = 7.6, 4.0 Hz, 2H), 7.29 (dd, *J* = 7.4, 0.8 Hz, 1H), 7.16 (d, *J* = 7.9 Hz, 1H), 6.39 (s, 1H), 4.08 (s, 3H), 4.03 (s, 3H), 1.73 (s, 6H).

**$^{13}$C NMR** (100 MHz, $CDCl_3$) δ 176.50, 162.40, 150.62, 142.67, 141.51, 134.49, 133.42, 132.42, 129.77, 128.97, 128.72, 128.59, 127.72, 127.61, 126.85, 125.89, 124.48, 122.16, 111.23, 101.78, 95.09, 94.49, 58.75, 49.55, 34.87, 28.37.

**HRMS (ESI-TOF)** ***m/z***: [$M^+$] calculated for $C_{28}H_{27}N_2O^+$ is 407.2118 and found 407.2118.

***(E)-2-(2-(5-(3,4-dimethoxyphenyl)-3-methoxy-1H-pyrrol-2-yl)vinyl)-1,3,3-trimethyl-3H-indol-1-ium iodide* 7c:**

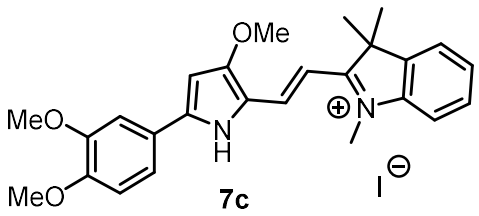


**7c**

Compound **7c** purified using silica gel column chromatography (3% methanol in chloroform) gives dark coffee brown solid (89 mg 85.4%).

**Characterization**

**$^{1}$H NMR** (400 MHz, $CDCl_3$) δ 11.86 (s, 1H), 7.93 (d, *J* = 1.9 Hz, 1H), 7.83 (d, *J* = 15.0 Hz, 1H), 7.77 – 7.70 (m, 2H), 7.39 – 7.34 (m, 2H), 7.24 (d, *J* = 7.5 Hz, 1H), 7.12 (d, *J* = 7.9 Hz, 1H), 6.94 (d, *J* = 8.6 Hz, 1H), 6.21 (s, 1H), 4.17 (s, 3H), 4.02 (s, 6H), 3.93 (s, 3H), 1.71 (s, 6H).

**$^{13}$C NMR** (100 MHz, $CDCl_3$) δ 175.79, 162.70, 151.90, 151.44, 149.71, 142.82, 141.36, 131.62, 128.88, 125.48, 123.10, 122.10, 122.01, 120.68, 111.23, 110.91, 101.14, 94.36, 93.88, 58.69, 58.23, 56.20, 49.29, 34.53, 28.41.

**HRMS (ESI-TOF)** ***m/z***: $[M^+]$ calculated for $C_{26}H_{29}N_2O_3^+$ is 417.2173 and found 417.2179.

***(E)-2-(2-(5-(3,5-dimethoxyphenyl)-3-methoxy-1H-pyrrol-2-yl)vinyl)-1,3,3-trimethyl-3H-indol-1-ium iodide* 7d:**

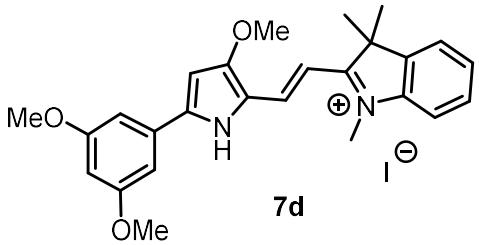


**7d**

Compound **7d** purified using silica gel column chromatography (2% methanol in chloroform) gives burnt sienna solid (96 mg, 92.13%).

**Characterization**

**$^{1}$H NMR** (400 MHz, $CDCl_3$) δ 11.90 (s, 1H), 7.93 (d, *J* = 15.1 Hz, 1H), 7.79 (d, *J* = 15.1 Hz, 1H), 7.39 (dd, *J* = 3.1, 1.3 Hz, 1H), 7.34 (d, *J* = 2.2 Hz, 2H), 7.30 (d, *J* = 6.9 Hz, 1H),

7.22 (d, *J* = 2.2 Hz, 1H), 7.16 (d, *J* = 7.9 Hz, 1H), 6.55 – 6.52 (m, 1H), 6.24 (s, 1H), 4.05 (s, 3H), 4.01 (s, 3H), 3.98 (s, 3H), 3.95 (s, 3H), 1.72 (s, 6H).

**$^{13}$C NMR** (100 MHz, $CDCl_3$) δ 176.86, 162.22, 161.30, 150.55, 142.62, 141.57, 140.08, 132.93, 130.91, 128.98, 125.98, 122.75, 122.17, 111.28, 105.91, 104.84, 104.31, 102.09, 94.64, 58.69, 57.03, 49.60, 34.83, 28.36.

**HRMS (ESI-TOF)** ***m/z***: [$M^+$] calculated for $C_{26}H_{29}N_2O_3^+$ is 417.2173 and found 417.2178.

***(E)-2-(2-(5-(2,5-dimethoxyphenyl)-3-methoxy-1H-pyrrol-2-yl)vinyl)-1,3,3-trimethyl-3H-indol-1-ium iodide*** **7e:**

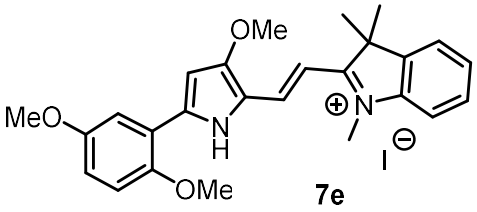


**7e**

Compound **7e** purified using silica gel column chromatography (2.5% methanol in chloroform) gives dark brown solid (93 mg, 89.25%).

**Characterization**

**$^1$H NMR** (400 MHz, $CDCl_3$) δ 11.82 (s, 1H), 7.79 (d, *J* = 2.5 Hz, 2H), 7.58 (d, *J* = 2.4 Hz, 1H), 7.39 (d, *J* = 7.6 Hz, 2H), 7.28 (d, *J* = 7.4 Hz, 1H), 7.13 (d, *J* = 3.4 Hz, 1H), 6.96 – 6.94 (m, 2H), 6.50 (s, 1H), 4.09 (s, 3H), 4.05 (s, 3H), 4.01 (s, 3H), 3.91 (s, 3H), 1.72 (s, 6H).

**$^{13}$C NMR** (100 MHz, $CDCl_3$) δ 175.83, 162.70, 151.87, 151.43, 149.62, 142.75, 141.35, 138.67, 131.57, 128.88, 125.51, 122.94, 122.11, 114.59, 111.18, 110.91, 110.11, 101.26, 93.97, 58.73, 58.35, 56.19, 49.30, 34.81, 28.39.

**HRMS (ESI-TOF)** ***m/z***: [$M^+$] calculated for $C_{26}H_{29}N_2O_3^+$ is 417.2173 and found 417.2181.

**(E)-2-(2-(5-(2,3-dimethoxyphenyl)-3-methoxy-1H-pyrrol-2-yl)vinyl)-1,3,3-trimethyl-3H-indol-1-ium iodide 7f:**

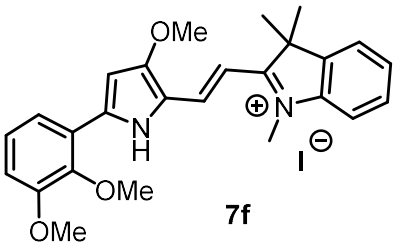


**7f**

Compound **7f** purified using silica gel column chromatography (2% methanol in chloroform) gives dark golden green solid (97 mg, 93.3%).

**Characterization**

**$^1$H NMR** (400 MHz, $CDCl_3$) δ 11.45 (s, 1H), 8.61 (d, *J* = 8.1 Hz, 1H), 7.72 (d, *J* = 14.5 Hz, 1H), 7.61 (d, *J* = 15.3 Hz, 1H), 7.35 (t, *J* = 7.2 Hz, 2H), 7.22 (s, 1H), 7.10 – 7.07 (m, 1H), 6.66 (dd, *J* = 30.5, 7.4 Hz, 1H), 6.47 (d, *J* = 11.2 Hz, 2H), 4.09 (d, *J* = 12.8 Hz, 3H), 4.00 (s, 3H), 3.94 (s, 3H), 3.85 (s, 3H), 1.70 (s, 6H).

**$^{13}$C NMR** (100 MHz, $CDCl_3$) δ 175.17, 163.58, 162.70, 159.51, 149.25, 142.91, 141.24, 138.78, 133.07, 130.87, 128.80, 125.21, 122.61, 122.04, 110.74, 106.11, 105.51, 99.32, 97.26, 58.56, 56.16, 55.81, 49.87, 49.15, 28.41.

**HRMS (ESI-TOF)** ***m/z***: [$M^+$] calculated for $C_{26}H_{29}N_2O_3^+$ is 417.2173 and found 417.2177.

***(E)-2-(2-(5-(2,4-dimethoxyphenyl)-3-methoxy-1H-pyrrol-2-yl)vinyl)-1,3,3-trimethyl-3H-indol-1-ium iodide*** **7g:**

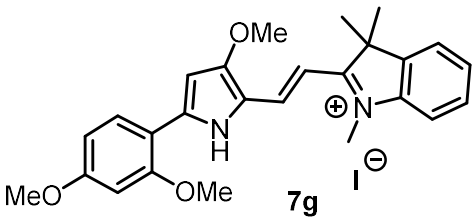


**7g**

Compound **7g** purified using silica gel column chromatography (1% methanol in chloroform) gives dark brown solid (98 mg, 94%).

**Characterization**

**$^1$H NMR** (400 MHz, $CDCl_3$) δ 11.48 (s, 1H), 7.72 (d, *J* = 14.9 Hz, 1H), 7.62 (d, *J* = 14.9 Hz, 1H), 7.38 – 7.32 (m, 3H), 7.23 – 7.19 (m, 1H), 7.09 (d, *J* = 8.0 Hz, 1H), 6.70 (dd, *J* = 8.8, 2.4 Hz, 1H), 6.48 (d, *J* = 2.3 Hz, 1H), 6.46 (s, 1H), 4.00 (s, 3H), 3.98 (s, 3H), 3.94 (s, 3H), 3.85 (d, *J* = 1.0 Hz, 3H), 1.70 (s, 6H).

**$^{13}$C NMR** (101 MHz, $CDCl_3$) δ 175.15, 163.56, 162.69, 159.50, 149.24, 142.90, 141.23, 138.76, 133.04, 130.85, 128.79, 125.20, 122.04, 110.72, 105.50, 100.36, 99.30, 97.26, 58.56, 56.15, 55.80, 49.14, 34.36, 28.40.

**HRMS (ESI-TOF)** ***m/z***: [$M^+$] calculated for $C_{26}H_{29}N_2O_3^+$ is 417.2173 and found 417.2179.

***(E)-2-(2-(5-(2,6-dimethoxyphenyl)-3-methoxy-1H-pyrrol-2-yl)vinyl)-1,3,3-trimethyl-3H-indol-1-ium iodide* 7h:**

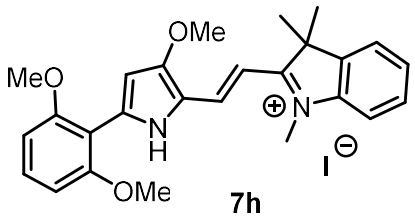


**7h**

Compound **7h** purified using silica gel column chromatography (2% methanol in chloroform) gives dark golden brown solid (92mg, 88.3%).

**Characterization**

**$^1$H NMR** (400 MHz, $CDCl_3$) δ 11.74 (s, 1H), 7.79 (d, *J* = 14.9 Hz, 1H), 7.52 (d, *J* = 14.9 Hz, 1H), 7.38 – 7.32 (m, 3H), 7.24 – 7.22 (m, 1H), 7.11 (t, *J* = 8.2 Hz, 1H), 6.63 (t, *J* = 8.2 Hz, 2H), 6.21 (s, 1H), 4.02 (s, 3H), 3.98 (s, 3H), 3.93 (s, 6H), 1.71 (s, 6H).

**$^{13}$C NMR** (100 MHz, $CDCl_3$) δ 175.82, 161.55, 159.22, 159.03, 145.27, 141.31, 132.32, 132.25, 128.85, 125.48, 122.65, 122.06, 121.88, 110.98, 104.42, 104.27, 100.53, 99.14, 57.08, 56.72, 50.10, 49.32, 34.63, 28.39.

**HRMS (ESI-TOF)** ***m/z***: [$M^+$] calculated for $C_{26}H_{29}N_2O_3^+$ is 417.2173 and found 417.2178.

***(E)-2-(2-(5-(benzo[d][1,3]dioxol-5-yl)-3-methoxy-1H-pyrrol-2-yl)vinyl)-1,3,3-trimethyl-3H-indol-1-ium iodide* 7i:**

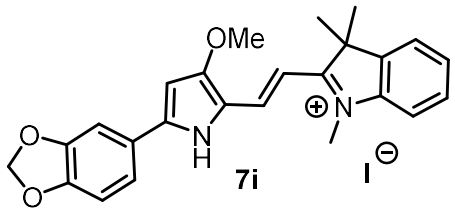


**7i**

Compound **7i** purified using silica gel column chromatography (3% methanol in chloroform) gives dark golden brown solid (79mg, 73%).

**Characterization**

**$^1$H NMR** (400 MHz, $CDCl_3$) δ 7.99 (d, *J* = 8.1 Hz, 1H), 7.84 (d, *J* = 15.0 Hz, 1H), 7.75 (s, 2H), 7.42 – 7.33 (m, 3H), 7.12 (d, *J* = 8.0 Hz, 1H), 6.94 (d, *J* = 8.2 Hz, 1H), 6.13 (s, 1H), 6.02 (d, *J* = 2.2 Hz, 2H), 4.00 (s, 3H), 3.99 (s, 3H), 1.70 (s, 6H).

**$^{13}$C NMR** (100 MHz, $CDCl_3$) δ 175.72, 162.58, 150.30, 148.43, 142.85, 141.35, 131.85, 128.87, 125.48, 123.79, 123.38, 122.08, 110.93, 109.32, 109.10, 108.03, 101.86, 100.99, 93.77, 58.61, 49.28, 34.03, 28.39.

**HRMS (ESI-TOF)** ***m/z***: [$M^+$] calculated for $C_{25}H_{25}N_2O_3^+$ is 401.1860 and found 401.1865.

***(E)-2-(2-(3-methoxy-5-(thiophen-2-yl)-1H-pyrrol-2-yl)vinyl)-1,3,3-trimethyl-3H-indol-1-ium iodide*** **7j:**

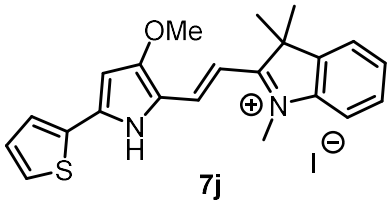


**7j**

Compound **7j** purified using silica gel column chromatography (1% methanol in chloroform) gives dark brown solid (101mg, 85.4%).

**Characterization**

**$^1$H NMR** (400 MHz, $CDCl_3$) δ 11.88 (s, 1H), 8.88 (dd, *J* = 3.9, 1.0 Hz, 1H), 7.78 (d, *J* = 15.0 Hz, 1H), 7.73 (d, *J* = 15.0 Hz, 1H), 7.45 (dd, *J* = 5.0, 1.0 Hz, 1H), 7.41 – 7.35 (m, 2H), 7.28 (dd, *J* = 7.5, 0.8 Hz, 1H), 7.20 (dd, *J* = 5.0, 3.9 Hz, 1H), 7.15 (d, *J* = 7.9 Hz, 1H), 6.10 (d, *J* = 1.4 Hz, 1H), 4.04 (s, 3H), 4.01 (s, 3H), 1.71 (s, 6H).

**$^{13}$C NMR** (100 MHz, $CDCl_3$) δ 176.21, 162.31, 144.55, 142.69, 141.47, 132.23, 131.80, 129.69, 129.26, 128.95, 125.79, 122.69, 122.14, 111.14, 101.62, 94.50, 58.76, 49.46, 34.92, 28.36.

**HRMS (ESI-TOF)** ***m/z***: [$M^+$] calculated for $C_{22}H_{23}N_2OS^+$ is 363.1526 and found 363.1534.

***(E)-2-(2-(5-(furan-2-yl)-3-methoxy-1H-pyrrol-2-yl)vinyl)-1,3,3-trimethyl-3H-indol-1-ium iodide*** **7k:**

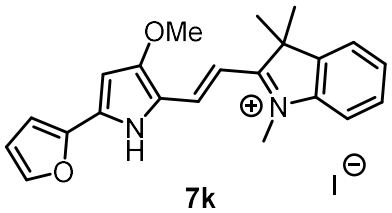


**7k**

Compound **7k** purified using silica gel column chromatography (2% methanol in chloroform) gives dark brown solid (80mg, 64.4%).

**Characterization**

**$^1$H NMR** (400 MHz, $CDCl_3$) δ 12.31 (s, 1H), 8.33 (d, *J* = 3.6 Hz, 1H), 7.74 (s, 2H), 7.55 – 7.53 (m, 1H), 7.42 – 7.35 (m, 2H), 7.30 – 7.26 (m, 1H), 7.14 (d, *J* = 8.0 Hz, 1H), 6.59 (dd, *J* = 3.6, 1.7 Hz, 1H), 6.23 (d, *J* = 2.2 Hz, 1H), 4.00 (d, *J* = 1.3 Hz, 6H), 1.71 (s, 6H).

$^{13}$C NMR (100 MHz, $CDCl_3$) δ 175.88, 162.14, 145.45, 145.08, 142.75, 141.40, 140.60, 131.88, 128.92, 125.69, 122.98, 122.12, 116.40, 113.64, 111.08, 101.28, 93.34, 58.70, 49.39, 34.28, 28.34.

**HRMS (ESI-TOF)** ***m/z***: [$M^+$] calculated for $C_{22}H_{23}N_2O_2^+$ is 347.1754 and found 347.1760.

***(E)-2-(2-(5-(benzo[b]thiophen-2-yl)-3-methoxy-1H-pyrrol-2-yl)vinyl)-1,3,3-trimethyl-3H-indol-1-ium iodide*** **7l:**

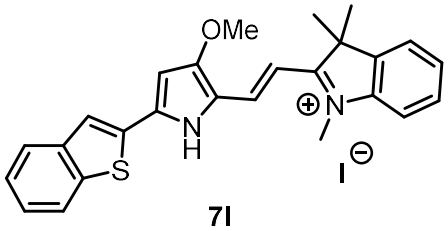


**7l**

Compound **7l** purified using silica gel column chromatography (2.5% methanol in chloroform) gives dark purple solid (88mg, 83.8%).

**Characterization**

**$^1$H NMR** (400 MHz, $CDCl_3$) δ 12.24 (s, 1H), 9.16 (s, 1H), 8.00 (dd, *J* = 6.1, 3.0 Hz, 1H), 7.89 (d, *J* = 15.1 Hz, 1H), 7.79 (d, *J* = 2.0 Hz, 1H), 7.44 – 7.36 (m, 5H), 7.30 (t, *J* = 7.1 Hz, 1H), 7.18 (d, *J* = 7.9 Hz, 1H), 6.18 (s, 1H), 4.08 (s, 3H), 4.02 (s, 3H), 1.73 (s, 6H).

**$^{13}$C NMR** (100 MHz, $CDCl_3$) δ 161.86, 143.85, 142.61, 141.61, 140.66, 140.52, 132.32, 131.41, 129.03, 128.54, 126.26, 126.10, 126.00, 125.16, 122.19, 122.08, 111.38, 102.34, 95.48, 58.79, 49.65, 34.79, 28.32.

**HRMS (ESI-TOF)** ***m/z***: $[M^+]$ calculated for $C_{26}H_{25}N_2OS^+$ is 413.1682 and found 413.1690.

***(E)-2-(2-(5-(benzofuran-2-yl)-3-methoxy-1H-pyrrol-2-yl)vinyl)-1,3,3-trimethyl-3H-indol-1-ium iodide*** **7m:**

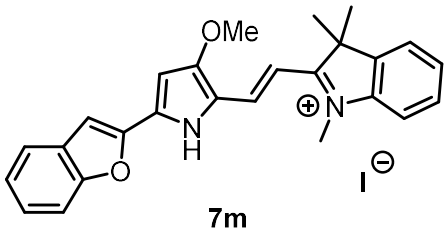


**7m**

Compound **7m** purified using silica gel column chromatography (3% methanol in chloroform) gives dark brown solid (89mg, 82%).

**Characterization**

**$^1$H NMR** (400 MHz, $CDCl_3$) δ 12.46 (s, 1H), 8.66 (s, 1H), 7.83 (q, *J* = 15.1 Hz, 2H), 7.74 (d, *J* = 7.3 Hz, 1H), 7.49 (dd, *J* = 8.2, 0.8 Hz, 1H), 7.44 – 7.27 (m, 5H), 7.19 (d, *J* = 7.9 Hz, 1H), 6.45 (s, 1H), 4.06 (s, 3H), 4.04 (s, 3H), 1.73 (s, 6H).

**$^{13}$C NMR** (100 MHz, $CDCl_3$) δ 161.61, 155.69, 149.33, 146.52, 141.63, 132.54, 129.05, 126.52, 123.76, 123.11, 122.22, 111.45, 111.22, 94.76, 58.78, 49.72, 34.81, 28.30.

**HRMS (ESI-TOF)** ***m/z***: $[M^+]$ calculated for $C_{26}H_{25}N_2O_2^+$ is 397.1911 and found 397.1916

***(E)-2-(2-(5-(1H-indol-2-yl)-3-methoxy-1H-pyrrol-2-yl)vinyl)-1,3,3-trimethyl-3H-indol-1-ium iodide*** **7n:**

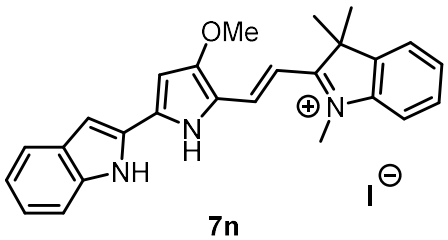


**7n**

In this case, the starting aldehyde compound **5n** was N-BOC derivative. To deprotect, after the reaction (same as **7a**) the solvent was removed under reduced pressure. The reaction mixture was cooled to 0˚C and then trifluoroacetic acid: dichloromethane 1:1 (2 mL) was added dropwise, stirred at room temperature for 20 min. Ice cold dd water (20 mL) was then added. The aqueous layer was extracted with dichloromethane (3 x 20 mL), dried over anhydrous sodium sulphate, filtered, and

concentrated in reduced pressure. The compound **7n** was purified using silica gel column chromatography (2% methanol in chloroform) as a dark purple color solid (55 mg, 71.5%).

The same procedure used for **7o** and **7p**.

**Characterization**

**$^1$H NMR** (400 MHz, $CDCl_3$) δ 12.09 (s, 1H), 7.67 (t, *J* = 11.7 Hz, 2H), 7.60 (d, *J* = 8.0 Hz, 1H), 7.47 – 7.33 (m, 3H), 7.30 – 7.26 (m, 2H), 7.24 (dd, *J* = 5.9, 5.2 Hz, 1H), 7.10 (ddd, *J* = 9.2, 5.8, 1.8 Hz, 3H), 6.29 (d, *J* = 1.8 Hz, 1H), 4.03 (s, 3H), 3.87 (s, 3H), 1.71 (s, 6H).

**$^{13}$C NMR** (101 MHz, $CDCl_3$) δ 174.45, 162.34, 143.67, 142.95, 141.07, 139.08, 130.28, 128.86, 128.11, 127.98, 125.25, 125.16, 123.67, 122.10, 122.03, 121.13, 120.80, 113.09, 110.67, 107.33, 100.91, 94.31, 58.68, 49.11, 32.71, 28.38.

**HRMS (ESI-TOF)** ***m/z***: [$M^+$] calculated for $C_{26}H_{26}N_3O^+$ is 396.2070 and found 396.2077.

***(E)-2-(2-(4-methoxy-1H,1'H-[2,2'-bipyrrol]-5-yl)vinyl)-1,3,3-trimethyl-3H-indol-1-ium iodide* 7o:**

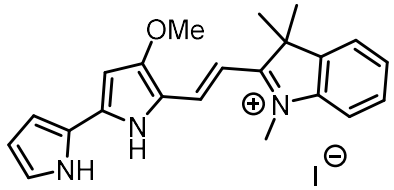


**7o**

The compound **7o** was purified using silica gel column chromatography (1.5% methanol in chloroform) as a dark purple color solid (60 mg, 73.6%).

**Characterization**

**$^1$H NMR** (400 MHz, $CDCl_3$) δ 12.91 (s, 1H), 12.46 (s, 1H), 7.55 (d, *J* = 14.5 Hz, 1H), 7.37 – 7.30 (m, 2H), 7.20 – 7.07 (m, 3H), 7.03 (d, *J* = 7.9 Hz, 1H), 6.83 (ddd, *J* = 3.8, 2.5, 1.4 Hz, 1H), 6.31 (dt, *J* = 3.8, 2.3 Hz, 1H), 6.06 (d, *J* = 2.1 Hz, 1H), 3.99 (s, 3H), 3.76 (s, 3H), 1.68 (s, 6H).

**$^{13}$C NMR** (100 MHz, $CDCl_3$) δ 172.37, 163.05, 145.02, 143.31, 140.69, 128.66, 127.95, 126.01, 124.29, 124.07, 122.95, 121.96, 115.26, 111.19, 109.96, 97.47, 92.98, 58.60, 48.50, 32.00, 28.44.

**HRMS (ESI-TOF)** ***m/z***: [$M^+$] calculated for $C_{22}H_{24}N_3O^+$ is 346.1914 and found 346.1925.

***(E)-2-(2-(3-methoxy-5-(5-methoxy-1H-indol-2-yl)-1H-pyrrol-2-yl)vinyl)-1,3,3-trimethyl-3H-indol-1-ium iodide*** **7p:**

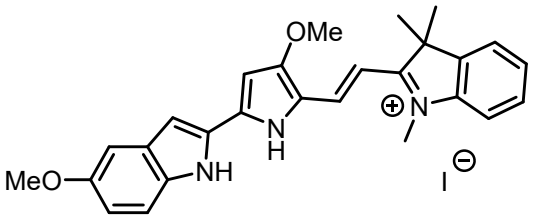


**7p**

The compound **7p** was purified using silica gel column chromatography (1.5% methanol in chloroform) as an aesthetic dark blue color solid (62 mg, 83%).

**Characterization**

**$^1$H NMR** (400 MHz, $CDCl_3$) δ 11.92 (s, 1H), 7.66 (d, *J* = 14.7 Hz, 1H), 7.55 (d, *J* = 8.9 Hz, 1H), 7.42 – 7.34 (m, 3H), 7.26 – 7.20 (m, 2H), 7.11 (d, *J* = 7.9 Hz, 1H), 7.00 – 6.93 (m, 3H), 6.26 (s, 1H), 4.02 (s, 3H), 3.90 (s, 3H), 3.85 (s, 3H), 1.71 (s, 6H).

**$^{13}$C NMR** (100 MHz, $CDCl_3$) δ 174.27, 162.26, 154.85, 143.52, 142.97, 141.08, 134.45, 129.96, 128.85, 128.44, 128.33, 125.17, 123.70, 122.09, 116.65, 113.87, 110.63, 106.71, 101.44, 99.54, 94.12, 58.67, 55.83, 49.04, 33.15, 28.37.

**HRMS (ESI-TOF)** ***m/z***: [$M^+$] calculated for $C_{27}H_{28}N_3O_2^+$ is 426.2176 and found 426.2187.

### 4.4.2 Cell culture protocol

HeLa cells were cultured in DMEM media with high glucose, L-glutamine, phenol red, and sodium pyruvate supplemented with 10% FBS and antibiotic solution (100 units per mL penicillin-streptomycin). The Cells were cultured in the flasks (25 $cm^2$, angled neck, cap; phenolic-style) at 37 °C in humidified 5% $CO_2$ incubator (Eppendorf). Every splitting cells were washed with DPBS and trypsinized by the trypsin-EDTA solution.

Five mM of stock solutions of all the compounds were prepared in the molecular biology grade dimethyl sulfoxide (DMSO) and stored at -20°C.

### 4.4.3 Cell viability and IC50 detection by MTT

Five thousand HeLa cells were seeded in triplicate per well (200 µL) in sterile 96-well flat-bottom tissue culture plates in DMEM media and incubated overnight in a 5% $CO_2$ incubator at 37 °C for attachment. To screen all the compounds, cells were treated by all the compounds with three different concentration 5 µM, 2.5 µM and 1.25 µM from stock solutions by maintaining the maximum amount of DMSO at 1µL for 24 h. For calculation of $IC_{50}$, cells were treated with compounds in different concentration (5, 2.5, 1.25, 0.62, 0.31, 0.16, 0.08, 0.04 µM). After 24 h, DMEM media with compounds in each well were removed, and freshly prepared solution of MTT in DMEM (0.5mg/mL media) 220 µl in each well were added and incubated for 4h in a 5% $CO_2$ incubator at 37 °C. 100 µL SDS (10% SDS in 0.01 M HCl) was then added in each well to dissolve the formazan crystals and incubated overnight. The Absorbance was recorded in the EnSight™ multimode plate reader from PerkinElmer at the wavelength of 570 nm. The percent cell viability was calculated considering the untreated cells as 100% viability. The same protocol was used to study the cytotoxic efficiency with other cytotoxic drugs.

### 4.4.4 Mitochondrial localization; confocal images

Nearly two thousand HeLa cells in DMEM media ( 400 µL per well) were dispersed in each well of 8 well Nunc® Lab-Tek® II chambered coverglass and incubated overnight in a 5% CO2 incubator at 37 °C for attachment. Cells were then treated with compound **7n** and **7p** with a concentration of 150 nM for 20 minutes in media while the control cells were kept without any treatment. Media with compounds were removed, and cells were then washed with cold DPBS (pH 7.4) thrice 2 min each followed by treatment with MitoTracker™ Green FM (75 nM) in DPBS (pH 7.4) including control cells too and incubated in the dark for 20 minutes. After incubation, all cells were washed several times with cold DPBS (pH 7.4). Fluorescence images of live cells were visualized by confocal microscopy.

### 4.4.5 Calcein AM assay

Nearly two thousand HeLa cells in DMEM media ( 400 µL per well) were dispersed in each well of 8 well Nunc® Lab-Tek® II chambered coverglass and incubated overnight in a 5% $CO_2$ incubator at 37 °C for attachment. Cells were then treated with compound **7n** and **7p** with a concentration of 800 nM for 24 h in media while the control cells were kept without any treatment. Media with compounds were removed, and cells were then washed with cold DPBS

(pH 7.4) thrice 2 min each. Cells then treated with 1μM Calcein-AM and 1mM $CoCl_2$ in Hank's Balanced Salt Solution (HBSS) 200 μL each well for 30 minutes at the identical condition. The Cells were then washed several times with DPBS cold (pH 7.4) to removed excess Calcein-AM and $CoCl_2$. Fluorescence images of live cells were visualized by confocal microscopy.

### 4.4.6 Reactive oxygen species (ROS) generation by $H_2$DCFDA

Nearly two thousand HeLa cells in DMEM media ( 400 μL per well) were dispersed in each well of 8 well Nunc® Lab-Tek® II chambered coverglass and incubated overnight in a 5% $CO_2$ incubator at 37 °C for attachment. Cells were then treated with compound **7n** and **7p** with concentrations of 500 nM and 800 nM each for 24 h in media while the control cells were kept without any treatment. Media with compounds were removed, and cells were then washed with cold DPBS (pH 7.4) thrice 2 min each. The cells were then treated with 2μM $H_2$DCFDA for 15 minutes. The Cells were then washed several times with cold PBS (pH 7.4) to remove excess $H_2$DCFDA. Fluorescence images of live cells were visualized by confocal microscopy.

### 4.4.7 Immunostaining analysis

HeLa cells were dispersed at a density of $0.5 \times 10^5$ cells per well in 6-well tissue culture plates on top of glass coverslips and allowed to attach overnight in a 5% $CO_2$ incubator at 37 °C. Cells were then treated with compounds **7n** and **7p** (900 nM) for 24 h while the control cells were kept without any treatment. All cells were washed once with cold PBS and were fixed with 4% paraformaldehyde at 37 °C for 15 minutes. Cells were further washed twice with PBS and were permeabilized by incubating in PBST (0.2% Tween-20 in PBS) for 10 minutes at room temperature and blocked with 1% BSA in PBS for 30 minutes at 37 °C. Cells were then incubated in primary antibody solution diluted in 1% BSA in PBST (0.1% Tween-20) for 3 to 4 hours at 37°C. Cells were washed with PBST and were incubated with fluorophore-conjugated secondary antibody solution diluted in 1% BSA in PBST (0.1% Tween-20) for 1 hour at room temperature in the dark. Cells were washed thrice with PBS, and carefully glass coverslips were mounted on a glass slide using SlowFade Gold antifade with DAPI reagent. Cell images were taken using confocal microscopy.

### 4.4.8 A general protocol for Western blot analysis

HeLa cells were seeded at a density of 3 × $10^5$ cells per well in 6-well tissue culture plates and allowed to attach overnight in a 5% $CO_2$ incubator at 37 °C. The cells were then treated with compounds **7n** and **7p** from the stock solution in DMSO at 900 nM concentration for 24 h. An equivalent volume of DMSO was added to the control cells. Post 24 h, medium containing **7n** and **7p** were removed, and the cells were then washed with cold DPBS. Cells were lysed in lysis buffer (RIPA buffer) supplemented with protease inhibitor (PMSF) and stored at -40°C.

The proteins were resolved using Sodium Dodecyl Sulphate Polyacrylamide Gel Electrophoresis (SDS-PAGE) and transferred to Immobilon-P Polyvinylidene Difluoride (PVDF) membrane. The PVDF membrane was blocked in 5% (w/v) nonfat skimmed milk in Tris-buffered saline containing 0.1% Tween-20 (TBS-T) for 1 hour at room temperature with gentle shaking. The membrane was then washed once with TBST and then incubated with the primary antibody solution (dilutions were made according to their suppliers) overnight at 4°C with gentle shaking (except 3 h for GAPDH antibody). The membrane was then washed with TBST thrice and then incubated in Horseradish Peroxidase (HRP) conjugated secondary antibody solution in 5% (w/v) nonfat skimmed milk in TBST for 1 hour at room temperature with gentle shaking followed by washed thrice with TBST. The blot was then developed using clarity Enhanced Chemiluminescence (ECL) substrate and was visualized using ImageQuant LAS 4000 (GE Healthcare). ImageJ software was used for blots images processing and intensity calculations.

### 4.4.9 Cell cycle Analysis:

HeLa cells were seeded at a density of 3 × $10^5$ cells per well in 6-well tissue culture plates and allowed to attach overnight in a 5% $CO_2$ incubator at 37 °C. The cells were then treated with compounds **7n** and **7p** from the stock solution in DMSO at 900 nM concentration for 24 h. An equivalent volume of DMSO was added to the control cells. Post 24 h, medium containing **7n** and **7p** were removed, and the cells were then washed with cold DPBS. Cells were then trypsinized and again washed with DPBS after centrifugation at 1000 rpm for 5 min. Cells were then again centrifuged at 1000 rpm for 5 min. The supernatant was discarded, and cells were fixed in 70% ice-chilled ethyl alcohol in water for 30 minutes at - 20°C. Fixed cells were centrifuged at 1000 rpm to removed supernatant and again washed with DPBS. The pellets were re-suspended in 250 µL RNase solution (1 mg per mL in PBS) and incubate for 20 minutes at

room temperature. Finally, cells were incubated in 250 µL of propidium iodide (1 mg per mL in PBS). Cells were then analyzed using a BD FACS Caliber to detect cell cycle arrest.

### 4.4.10 Flow cytometry analysis for apoptosis detection:

HeLa cells were seeded at a density of $3 \times 10^5$ cells per well in 6-well tissue culture plates and allowed to attach overnight in a 5% $CO_2$ incubator at 37 °C. The cells were then treated with compounds **7n** and **7p** from the stock solution in DMSO at 900 nM concentration for 24 h. An equivalent volume of DMSO was added to the control cells. Post 24 h, medium containing **7n** and **7p** were removed, and the cells were then washed with cold DPBS. Cells were then trypsinized and again washed with DPBS after centrifugation at 1000 rpm for 5 minutes. Cells were then again centrifuged at 1000 rpm for 5 min; the cell pellets were then re-suspended in 250 µL Annexin V binding buffer containing 7.5 µL of APC-Annexin V and 15 µL of 7AAD and incubated for 15 minutes. Cells were diluted 250 µL with Annexin V binding buffer and passed through a cell strainer to get uniform cell suspension and analyzed using a BD FACS Caliber to detect apoptosis.

## 4.5 References:


1. F. Bray, J. Ferlay, I. Soerjomataram, R. L. Siegel, L. A. Torre and A. Jemal. Global Cancer Statistics 2018: GLOBOCAN Estimates of Incidence and Mortality Worldwide for 36 Cancers in 185 Countries. *CA Cancer J Clin.* **2018**, *68*, 394-424.
2. F. Biemar and M. Foti. Global Progress against Cancer-Challenges and Opportunities. *Cancer Biol Med.* **2013**. *10*, 183–186.
3. American Cancer Society. Cancer Facts & Figures 2018. Atlanta: American Cancer Society; **2018**.
4. S. Hoelder, P. A. Clarke and P. Workman. Discovery of Small Molecule Cancer Drugs: Successes, Challenges and Opportunities. *Mol Oncol.* **2012**, *6*, 155–176.
5. V. T. DeVita Jr. and E. Chu. A History of Cancer Chemotherapy. *Cancer Res.* **2008**, *68*, 8643-8653
6. L. H. Hurley. DNA and Its Associated Processes as Targets for Cancer Therapy. *Nat. Rev. Cancer* **2002**, *2*, 188–200.
7. D. Fu, J. A. Calvo and L. D. Samson. Balancing Repair and Tolerance of DNA Damage Caused by Alkylating Agents. *Nat. Rev. Cancer* **2012**, *12*, 104–120.

8. J. M. Allan and L. B. Travis. Mechanisms of Therapy-related Carcinogenesis. *Nat. Rev. Cancer* **2005**, *5*, 943–955.
9. J. Dancey and E. A. Sausville. Issues and Progress with Protein Kinase Inhibitors for Cancer Treatment. *Nat Rev Drug Discov* **2003**, *2*, 296–313.
10. C. Holohan, S. V. Schaeybroeck, D. B. Longley and P. G. Johnston. Cancer Drug Resistance: An Evolving Paradigm. *Nat. Rev. Cancer* **2013**, *13*, 714–726.
11. T. Fojo and S. Bates. Strategies for Reversing Drug Resistance. *Oncogene*, **2003**, *22*, 7512–7523.
12. S. Fulda, L. Galluzzi and G. Kroemer. Targeting Mitochondria for Cancer Therapy. *Nat. Nat Rev Drug Discov* 2**010**, *9*, 447−464.
13. W. Wang, G. Karamanlidis and R. Tian. Novel Targets for Mitochondrial Medicine. *Sci.Transl. Med.* **2016** *8*, 326rv3.
14. V. Gogvadze, S. Orrenius and B. Zhivotovsky. Mitochondria in Cancer Cells: What is so special about them? *Trends Cell Biol.* **2008**, *18*, 165−173.
15. S. Vyas, E. Zaganjor and M. C. Haigis. Mitochondria and Cancer. *Cell* **2016**, *166*, 555-566.
16. D. R. Green and J. C. Reed. Mitochondria and Apoptosis. *Science* **1998**, *281*, 1309-1312.
17. S. W. G. Tait and D. R. Green. Mitochondria and Cell Death: Outer Membrane Permeabilization and Beyond. *Nat. Rev. Mol. Cell Biol.* **2010**, *11*, 621−632.
18. C. Wang and R. J. Youle. The Role of Mitochondria in Apoptosis. *Annu Rev Genet.* **2009**, *43*, 95–118.
19. N. Badrinath and S. Y. Yoo. Mitochondria in Cancer: In the Aspects of Tumorigenesis and Targeted Therapy. *Carcinogenesis* **2018**, *39*, 1419–1430.
20. R. J. Youle and A. Strasser. The BCL-2 Protein Family: Opposing Activities that Mediate Cell Death. *Nat Rev Mol Cell Biol* **2008**, *9*, 47-59.
21. J. C Reed. Bcl-2 on The Brink of Breakthroughs in Cancer Treatment. *Cell Death Differ.* **2018**, *25*, 3–6.
22. A. N. Hata, J. A. Engelman and A. C. Faber. The BCL-2 Family: Key Mediators of the Apoptotic Response to Targeted Anti-Cancer Therapeutics. *Cancer Discov.* **2015**, *5*, 475–487.
23. M. Vogler, D. Dinsdale, M. J. S. Dyer and G. M. Cohen. Bcl-2 Inhibitors: Small Molecules with a Big Impact on Cancer Therapy. *Cell Death Differ.* **2009**, *16*, 360–367.
24. M. Nguyen, R. C. Marcellus, A. Roulston, M. Watson, L. Serfass, S. R. Murthy Madiraju, *et al.* Small Molecule Obatoclax (GX15-070) Antagonizes MCL-1 and Overcomes MCL-1-mediated Resistance to Apoptosis. *Proc Natl Acad Sci USA*. **2007**, *104*, 19512–7.
25. M. Konopleva, J. Watt, R. Contractor, T. Tsao, D. Harris, Z. Estrov, W. Bornmann, H. Kantarjian, J. Viallet, I. Samudio and M. Andreeff. Mechanisms of Antileukemic Activity of the

Novel Bcl-2 Homology Domain-3 Mimetic GX15-070 (Obatoclax). *Cancer Res.* **2008,** *68*, 3413-20

26. Y. Oki, A. Copeland, F. Hagemeister, L. E. Fayad, M. Fanale, J. Romaguera and A. Younes. Experience with Obatoclax Mesylate (GX15-070), a Small Molecule Pan–Bcl-2 Family Antagonist in Patients with Relapsed or Refractory Classical Hodgkin lymphoma. *Blood* **2012**, *119*, 2171-2172
27. A. D. Schimmer, A. Raza, T. H. Carter, D. Claxton, H. Erba, D. J. DeAngelo, M. S. Tallman, C. Goard and G. Borthakur. A Multicenter Phase I/II Study of Obatoclax Mesylate Administered as a 3- Or 24-hour Infusion in Older Patients with Previously Untreated Acute Myeloid Leukemia. *PLoS One* **2014**, *9*, e108694
28. S. A. Parikh SA, H. Kantarjian, A. Schimmer, W. Walsh, E. Asatiani, K. El-Shami, E. Winton and S. Verstovsek. Phase II Study of Obatoclax Mesylate (GX15-070), A Small-Molecule BCL-2 Family Antagonist, for Patients with Myelofibrosis. *Clin Lymphoma Myeloma Leuk.* **2010,** *10*, 285-9.
29. A. Frstner. Chemistry and Biology of Roseophilin and the Prodigiosin Alkaloids: A Survey of the Last 2500 Years. *Angew. Chem. Int. Ed.* **2003**, *42*, 3582-3603.
30. Nisha, K. Kumar and V. Kumar. Prodigiosin Alkaloids: Recent Advancements in Total Synthesis and their Biological Potential. *RSC Adv.* **2015**, *5*, 10899–10920.
31. W. Xu, Z. Zeng, J. Jiang, Y. Chang and L. Yuan. Discerning the Chemistry in Individual Organelles with Small-Molecule Fluorescent Probes. *Angew. Chem. Int. Ed.* **2016**, *55*, 13658 – 13699.
32. Y. Liu, J. Zhou, L. Wang, X. Hu, X. Liu, M. Liu and Z. Cao. Dihua Shangguan, Weihong Tan. A Cyanine Dye to Probe Mitophagy: Simultaneous Detection of Mitochondria and Autolysosomes in Live Cells. *J. Am. Chem. Soc.* **2016**, *138*, 12368−12374.
33. J. Han, T. H. Lee, C. Tung and D. Y. Lee. Design and Synthesis of a Mitochondria-Targeting Carrier for Small Molecule Drugs. *Org. Biomol. Chem.* **2014**, *12*, 9793–9796
34. L. N. Aldrich, E. S. Dawson and C. W. Lindsley. Evaluation of the Biosynthetic Proposal for the Synthesis of Marineosins A and B. *Org. Lett.* **2010**, *12*, 1048-1051.
35. D. E. Jeffries and C. W. Lindsley. Total Synthesis and Biological Evaluation of Hybrubin A. *J. Org. Chem.* **2017**, *82*, 431–437.
36. D. Hanahan and R. A. Weinberg. Hallmarks of Cancer: The Next Generation. *Cell,* **2011**, *144*, 646-674.
37. J. Q Kwong and J. D Molkentin. Physiological and Pathological Roles of the Mitochondrial Permeability Transition Pore in the Heart. *Cell Metab.* **2015**, *21*, 206–21.

38. V. Petronilli, G. Miotto, M. Canton, M. Brini, R. Colonna, P. Bernardi and F. D. Lisa. Transient and Long-Lasting Openings of the Mitochondrial Permeability Transition Pore Can Be Monitored Directly in Intact Cells by Changes in Mitochondrial Calcein Fluorescence. *Biophys. J.* **1999**, *76*, 725−734.
39. A. Ashkenazi, W. J. Fairbrother, J. D. Leverson and A. J. Souers. From Basic Apoptosis Discoveries to Advanced Selective BCL-2 Family Inhibitors. *Nat Rev Drug Discov* **2017**, *16*, 273−284.
40. H. U. Simon, A. Haj-Yehia, and F. Levi-Schaffer. Role of Reactive Oxygen Species (ROS) in Apoptosis Induction. *Apoptosis* **2000**, *5*, 415–8.
41. D, Wu and P, Yotnda. Production and Detection of Reactive Oxygen Species (ROS) in Cancers. *J. Visualized Exp.* **2011**, No. e3357.
42. G. Mariño, M. Niso-Santano, E. H. Baehrecke and G. Kroemer. Self-Consumption: The Interplay of Autophagy and Apoptosis. *Nat. Rev. Mol. Cell Biol*. **2014**, *15*, 81−94.
43. P. Li, D. Nijhawan, I. Budihardjo, S. M. Srinivasula, M. Ahmad, E. S. X. Alnemri and X. Wang. Cytochrome c and dATP-dependent Formation of Apaf-1/caspase-9 Complex Initiates an Apoptotic Protease Cascade. *Cell* **1997**, *91*, 479−489.
44. X. Gao, L. Han, N. Ding, Y. Mu, P. Guan, C. Hu and X. Huang. Bafilomycin C1 nduces G0/G1 Cell-Cycle Arrest and Mitochondrial-mediated Apoptosis in Human Hepatocellular Cancer SMMC7721 Cells. *The Journal of Antibiotics*, **2018**, *71*, 808–817.
45. T. Finkel and P. M. Hwang. The Krebs Cycle Meets the Cell Cycle: Mitochondria and the G1–S Transition. *PNAS* **2009**, *106,* 11825–11826.
46. W. Wei, Z. Suna, C. Shen, H. Song, X. Zhang, Z. Qiu and Q. Luo. Obatoclax and LY3009120 Efficiently Overcome Vemurafenib Resistance in Differentiated Thyroid Cancer *Theranostic* **2017**, *7*, 987-1001.
47. L. N. Aldrich, E. S. Dawson and C. W. Lindsley. Evaluation of the Biosynthetic Proposal for the Synthesis of Marineosins A and B. *Org. Lett*. **2010**, *12*, 1048-1051.
48. S. R. Chawrai, N. R. Williamson, G. P. C. Salmond, and F. J. Leeper. Chemoenzymatic Synthesis of Prodigiosin Analogues-Exploring the Substrate Specificity of Pigc. *Chem. Commun*. **2008**, *0*, 1862-1864.
49. D. E. Jeffries and C. W. Lindsley. Total Synthesis and Biological Evaluation of Hybrubin A. *J. Org. Chem.* **2017**, *82*, 431–437.
50. J. Han, T. H. Lee, C. Tunga and D. Y. Lee. Design and Synthesis of a Mitochondria-Targeting Carrier for Small Molecule Drugs. *Org. Biomol. Chem*. **2014**, *12*, 9793-9796.

# 4.6 Appendix-C:

## Characterization of the compounds

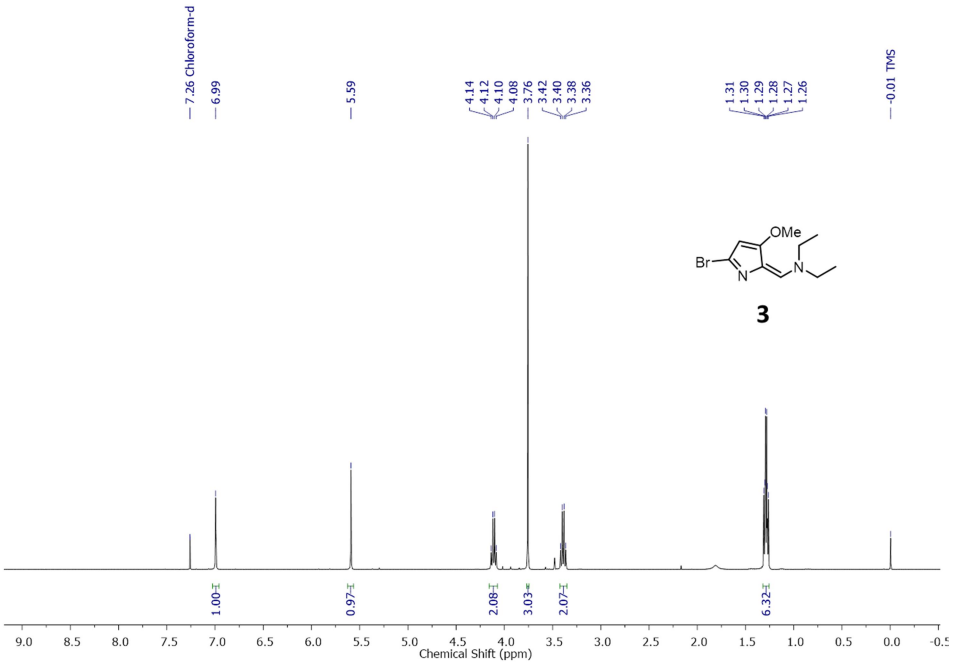


**Figure C1:** $^{1}$H spectrum of compound **3**

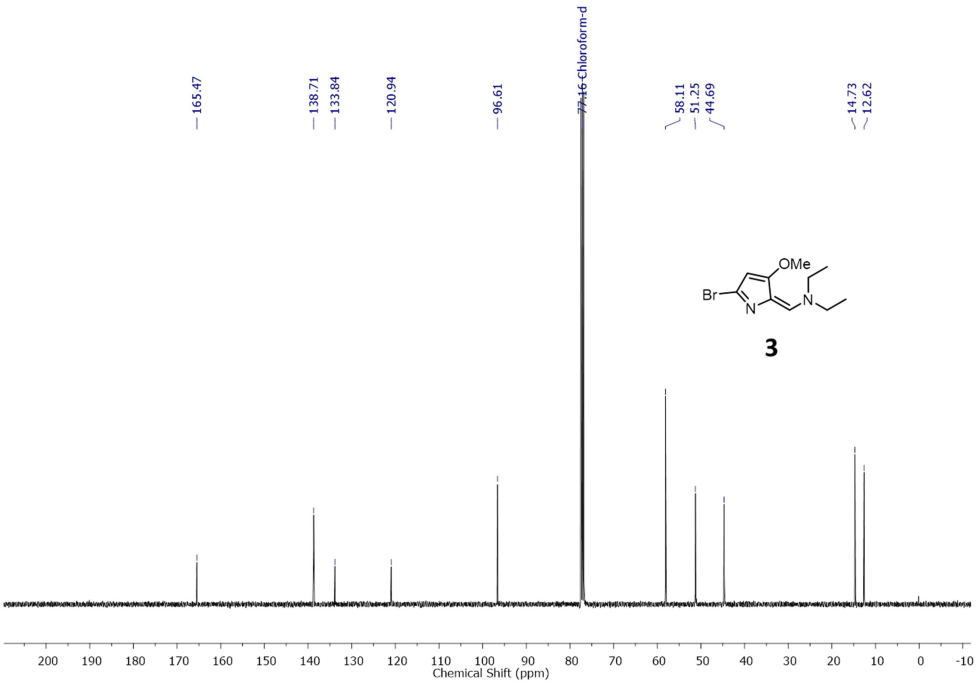


**Figure C2:** 13C spectrum of compound **3**

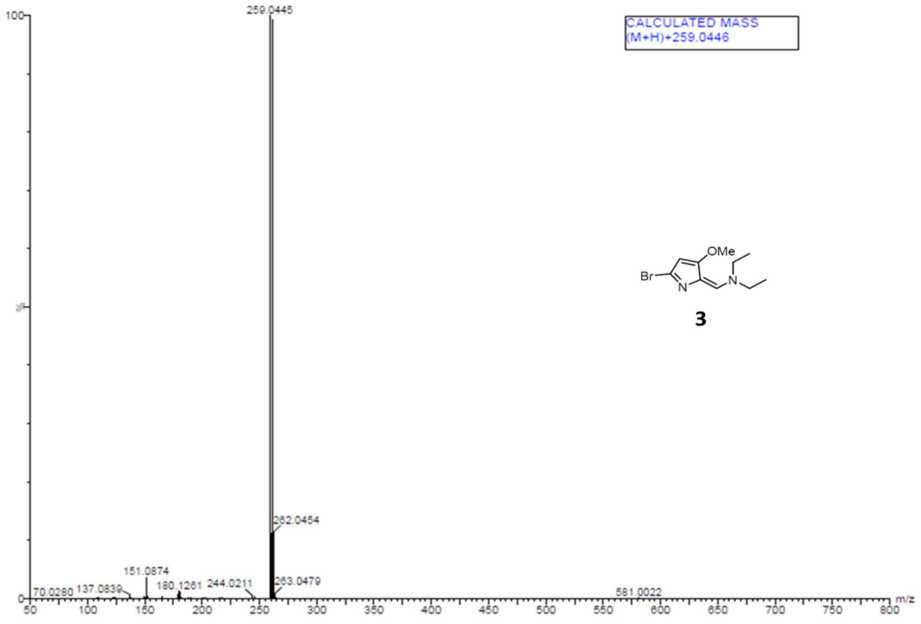


**Figure C3:** HRMS spectrum of compound **3**

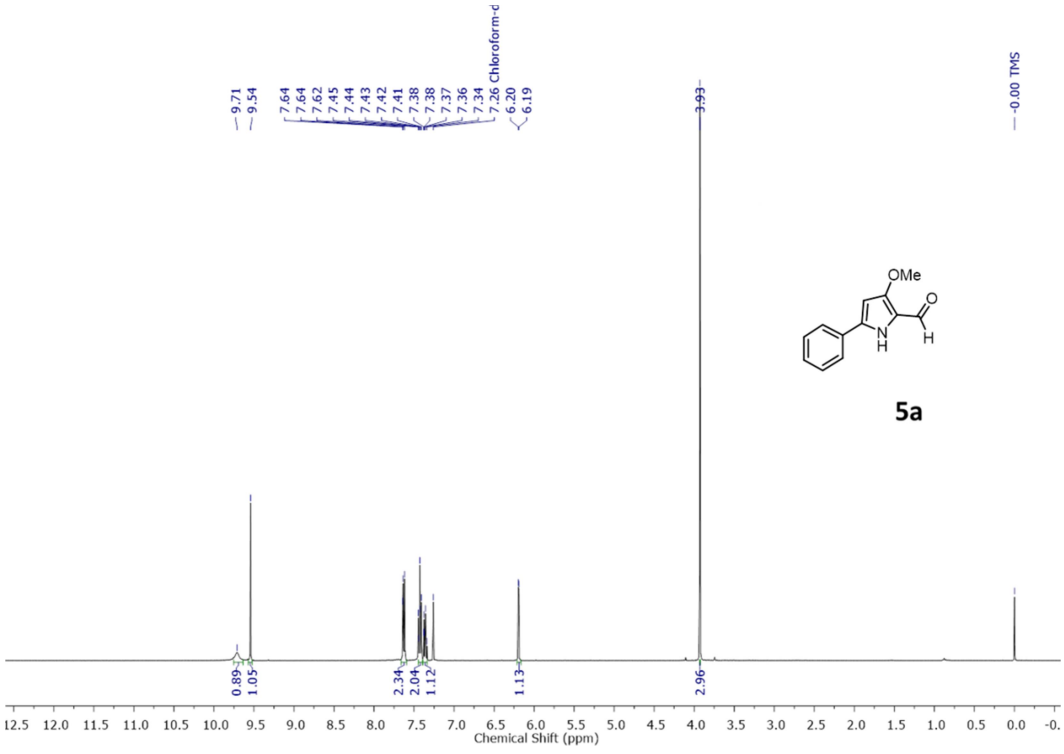


**Figure C4:** $^{1}$H spectrum of compound **5a**

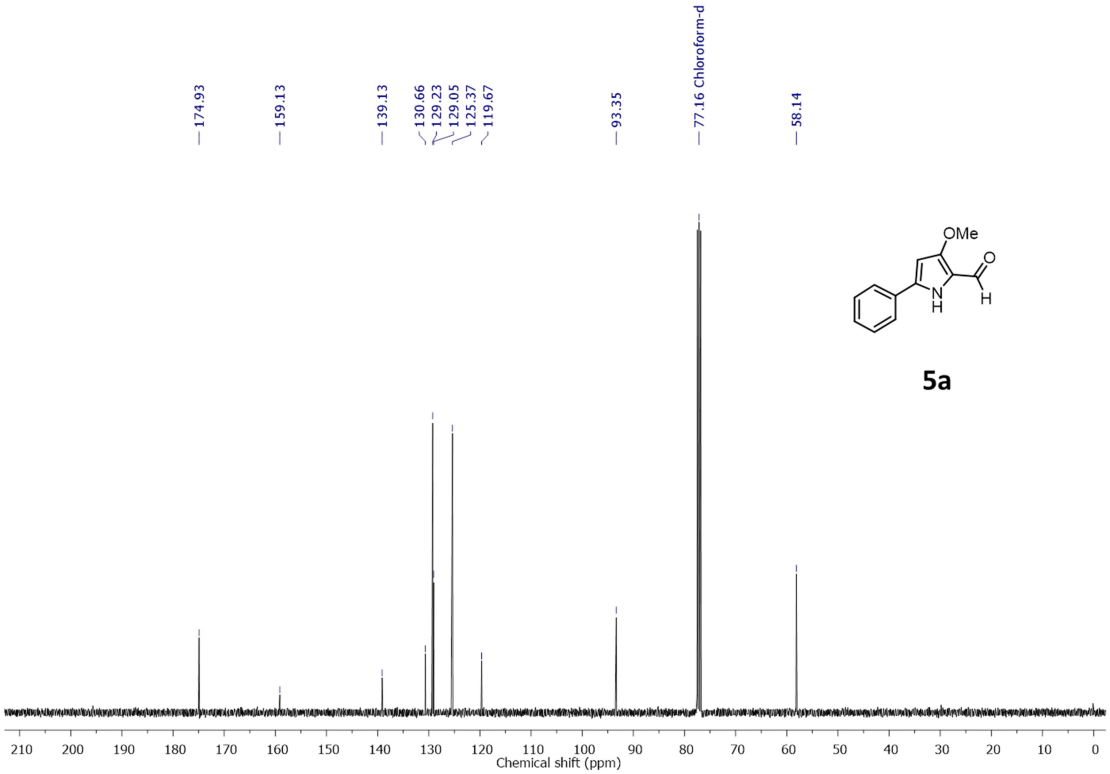


**Figure C5:** $^{13}C$ spectrum of compound **5a**

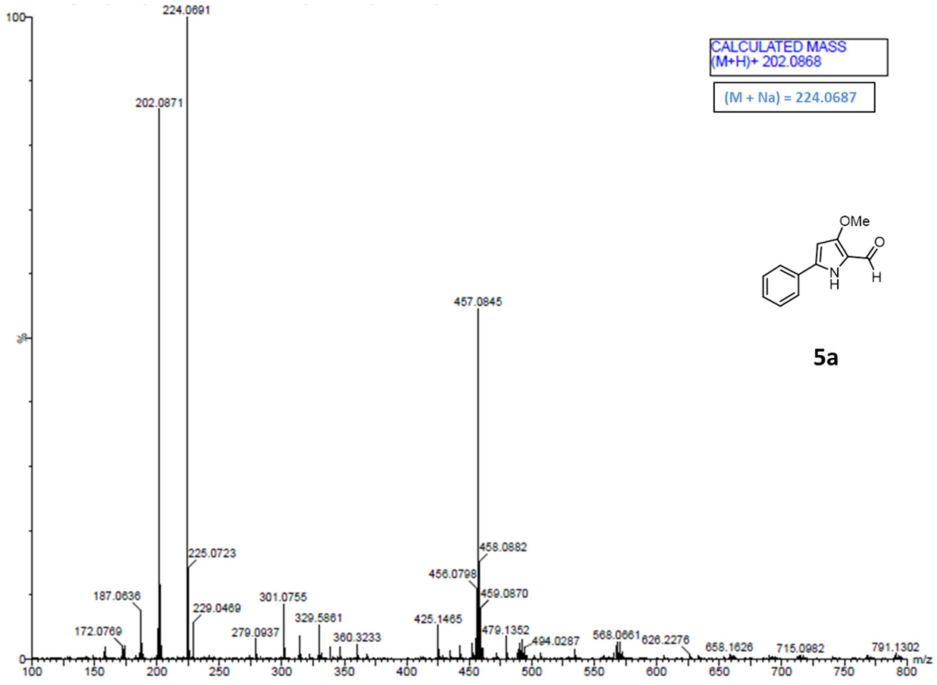


**Figure C6:** HRMS spectrum of compound **5a**

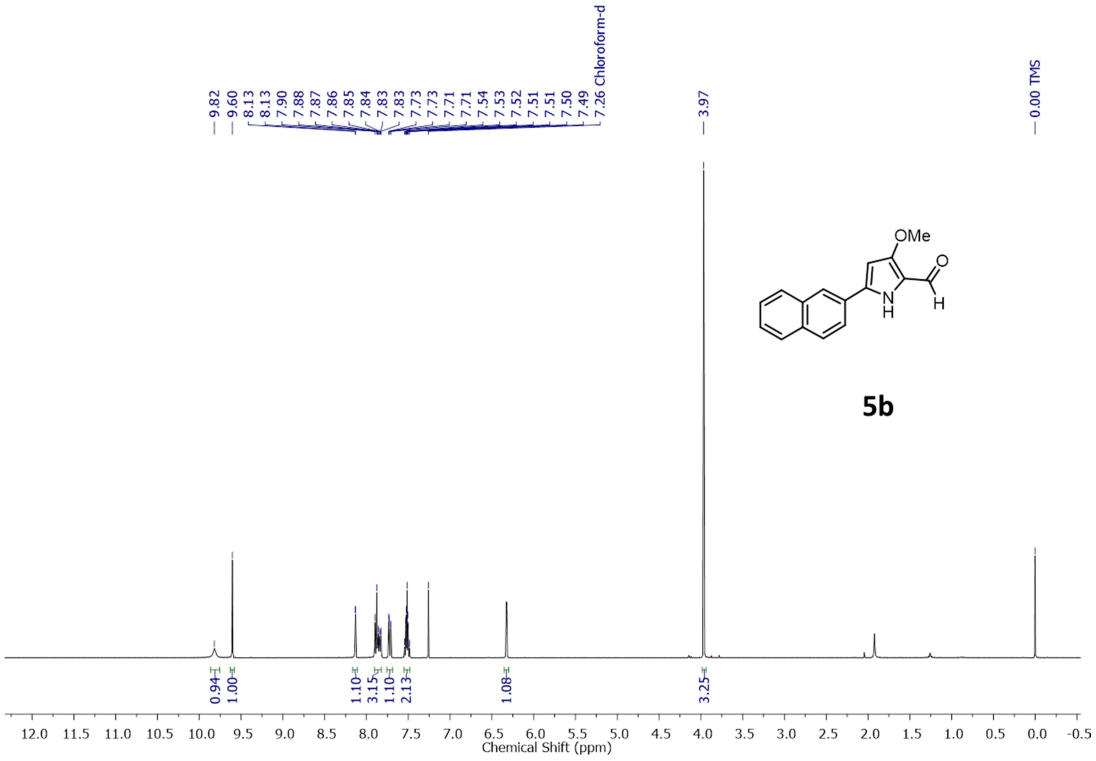


**Figure C7:** $^{1}$H spectrum of compound **5b**

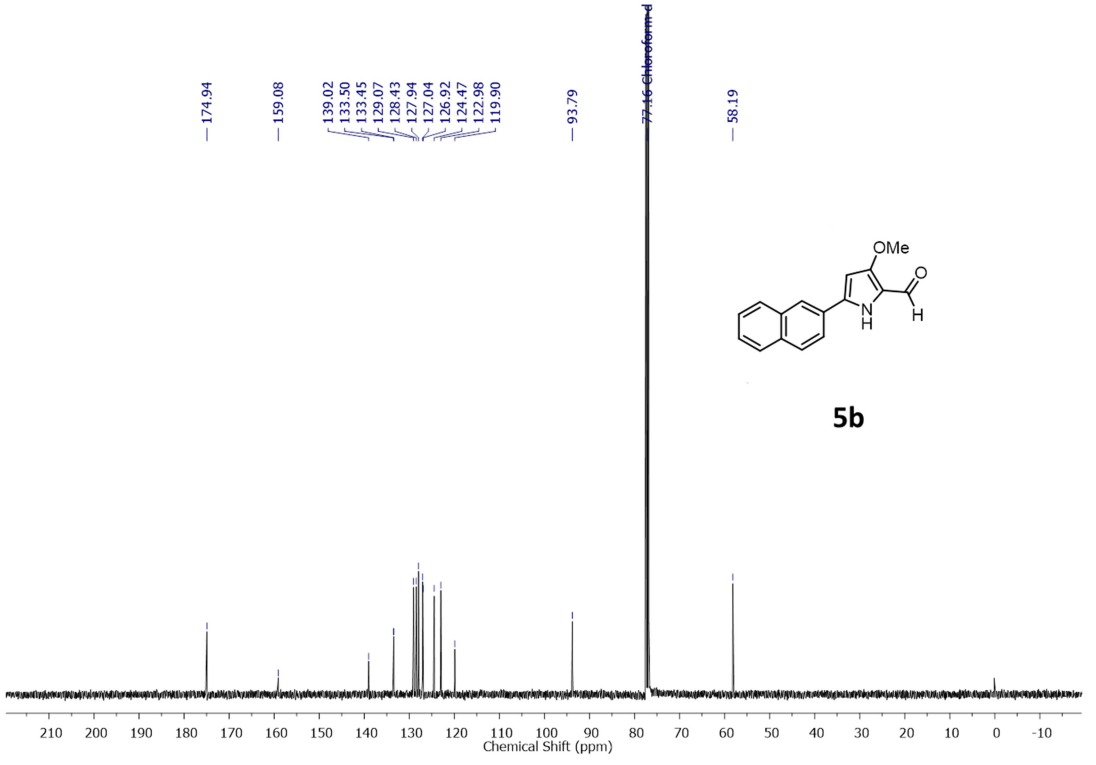


**Figure C8:** $^{13}$C spectrum of compound **5b**

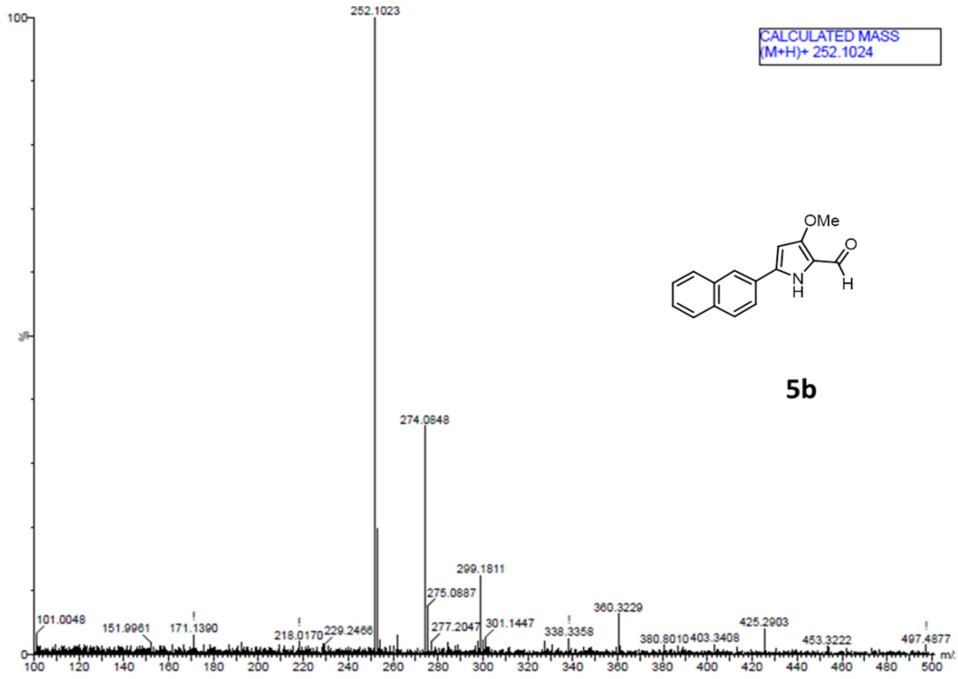


**Figure C9:** HRMS spectrum of compound **5b**

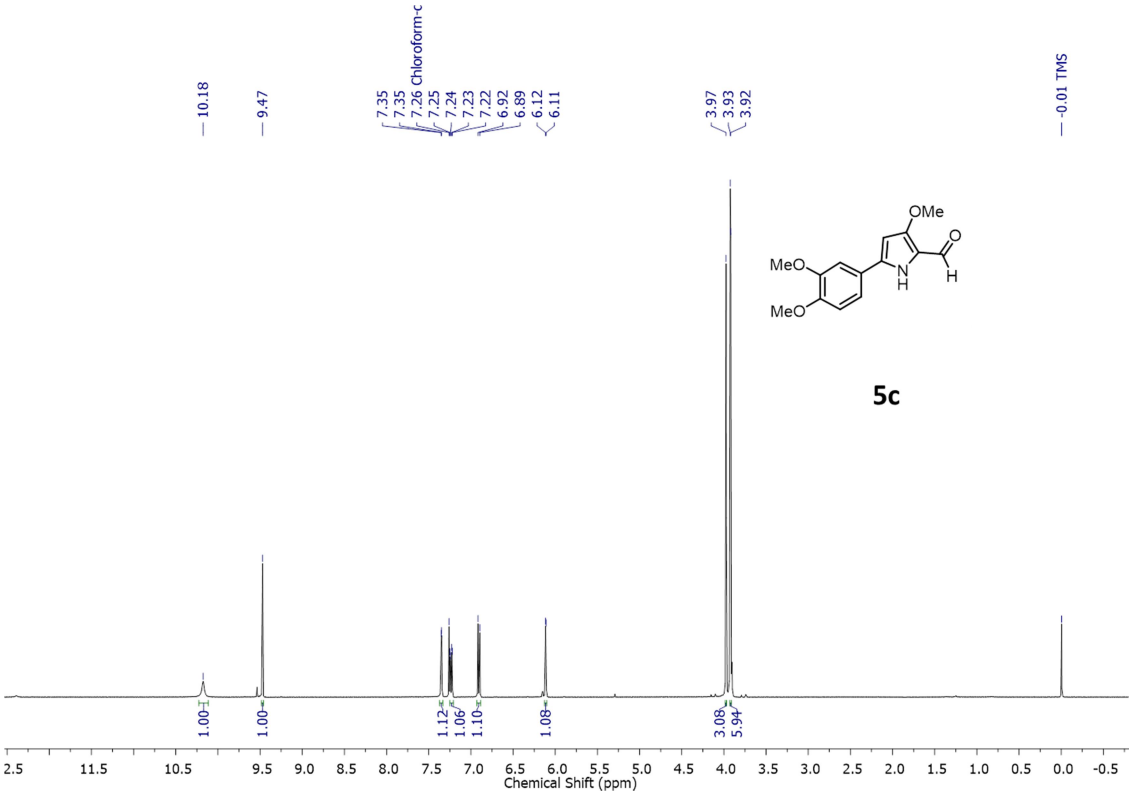


**Figure C10:** $^{1}$H spectrum of compound **5c**

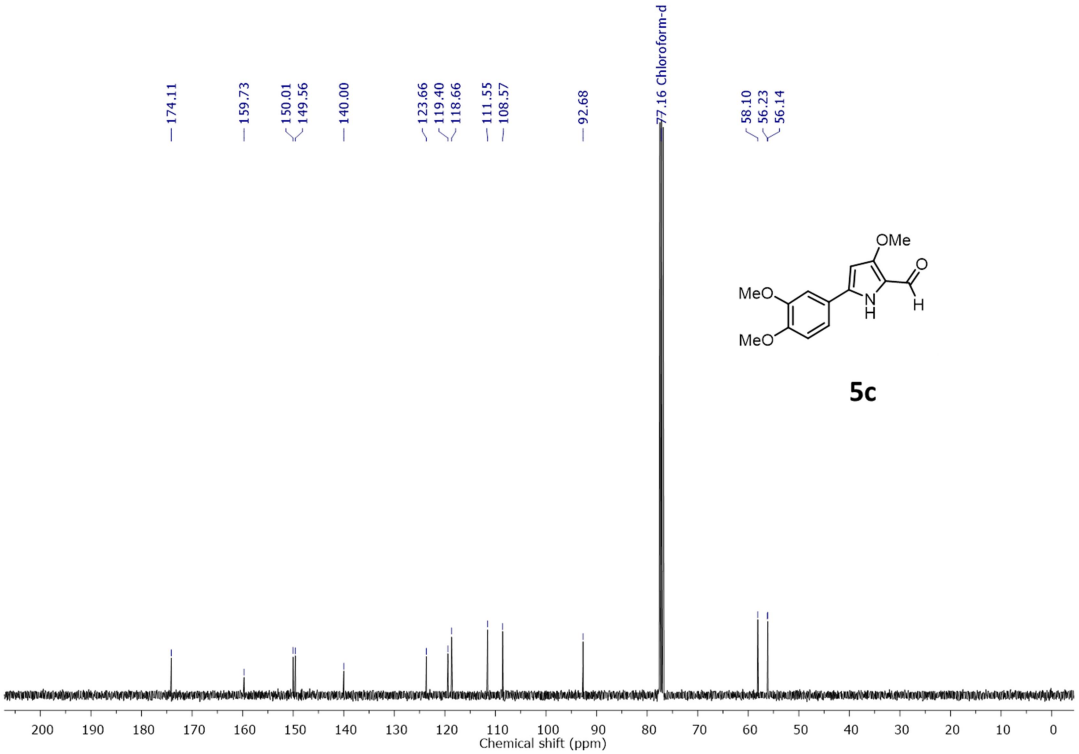


**Figure C11:** $^{13}C$ spectrum of compound **5c**

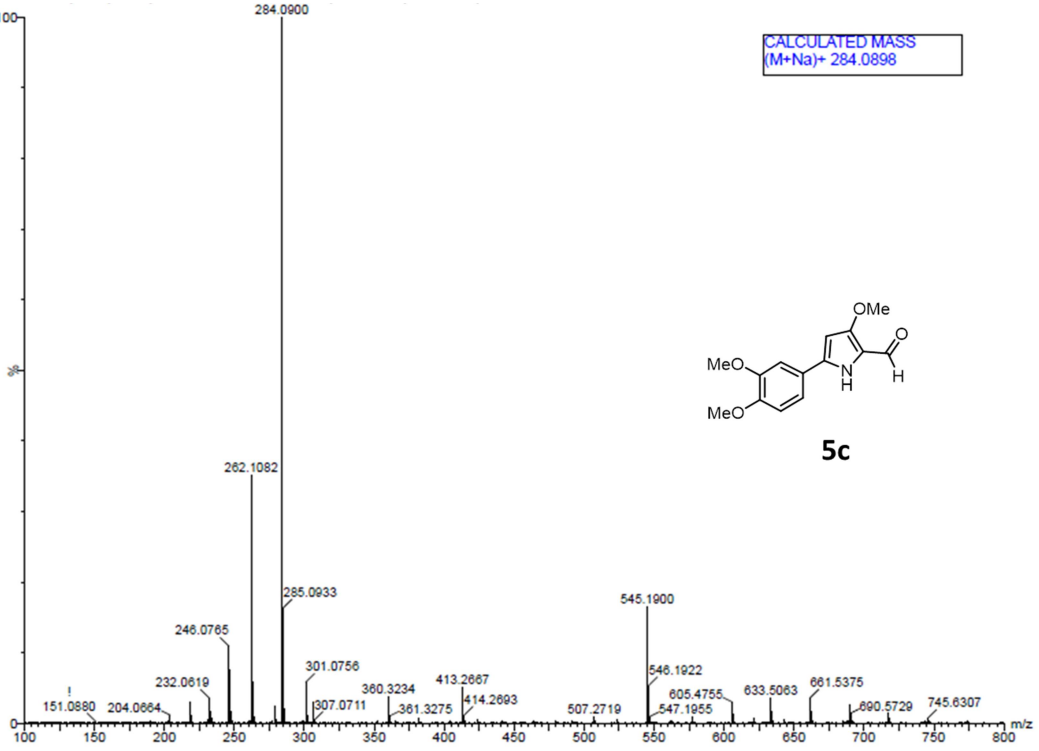


**Figure C12:** HRMS spectrum of compound **5c**

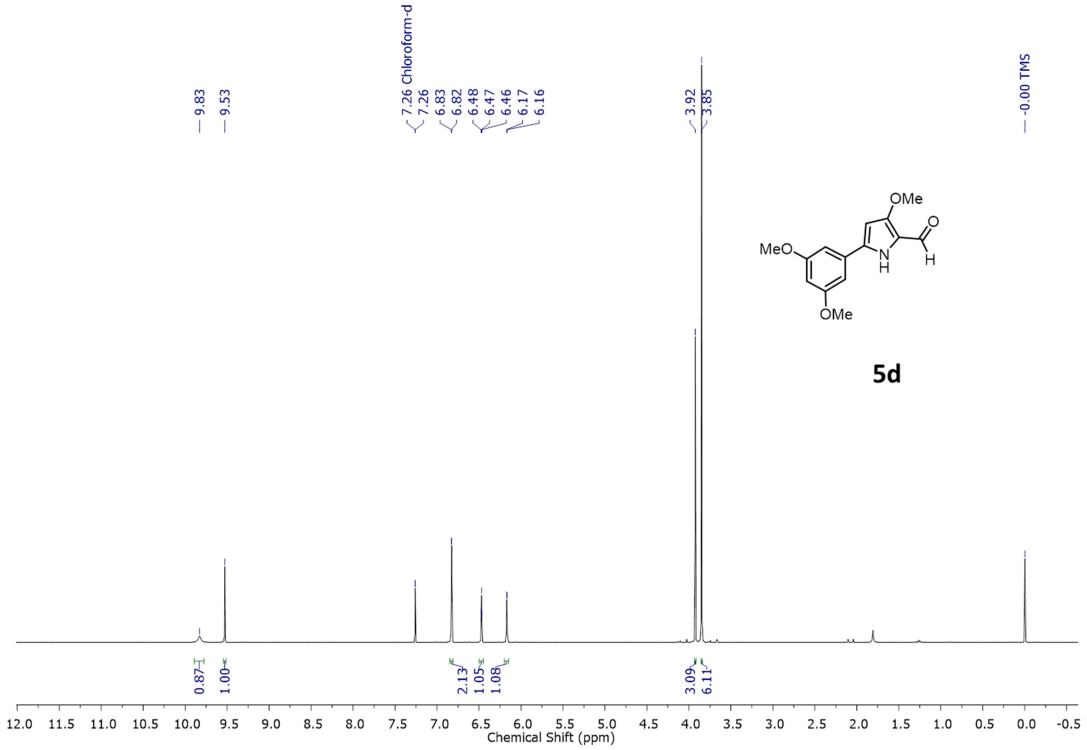


**Figure C13:** $^{1}$H spectrum of compound **5d**

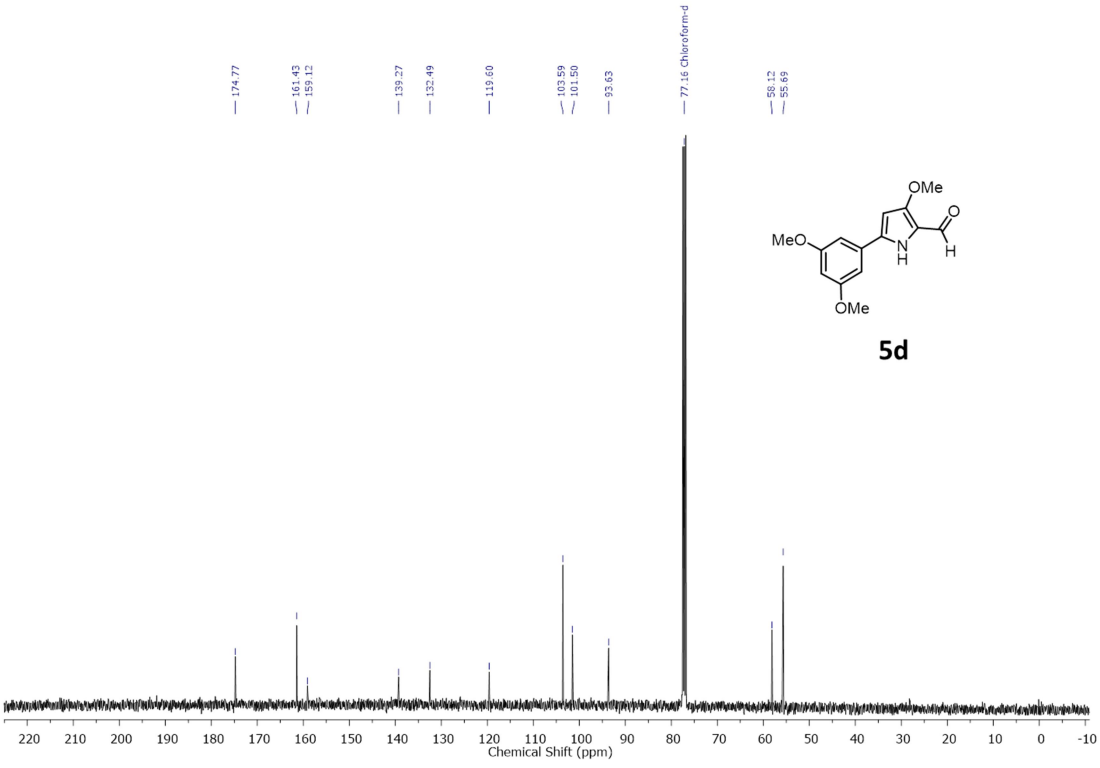


**Figure C14:** $^{13}$H spectrum of compound **5d**

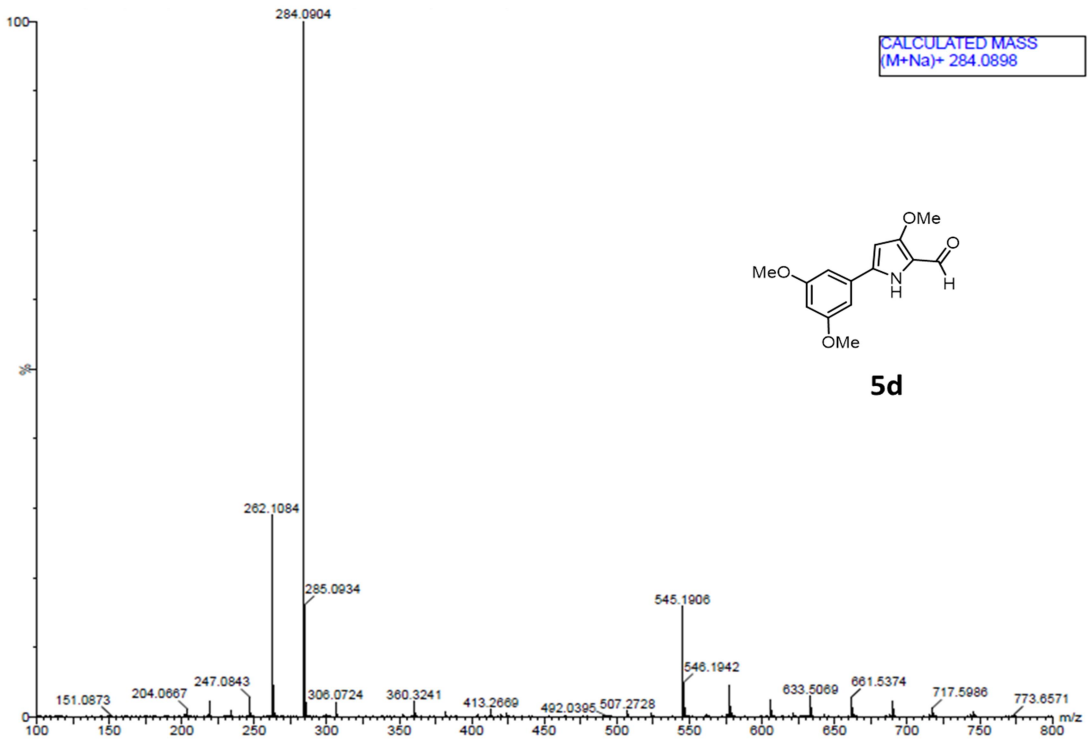


**Figure C15:** HRMS spectrum of compound **5d**

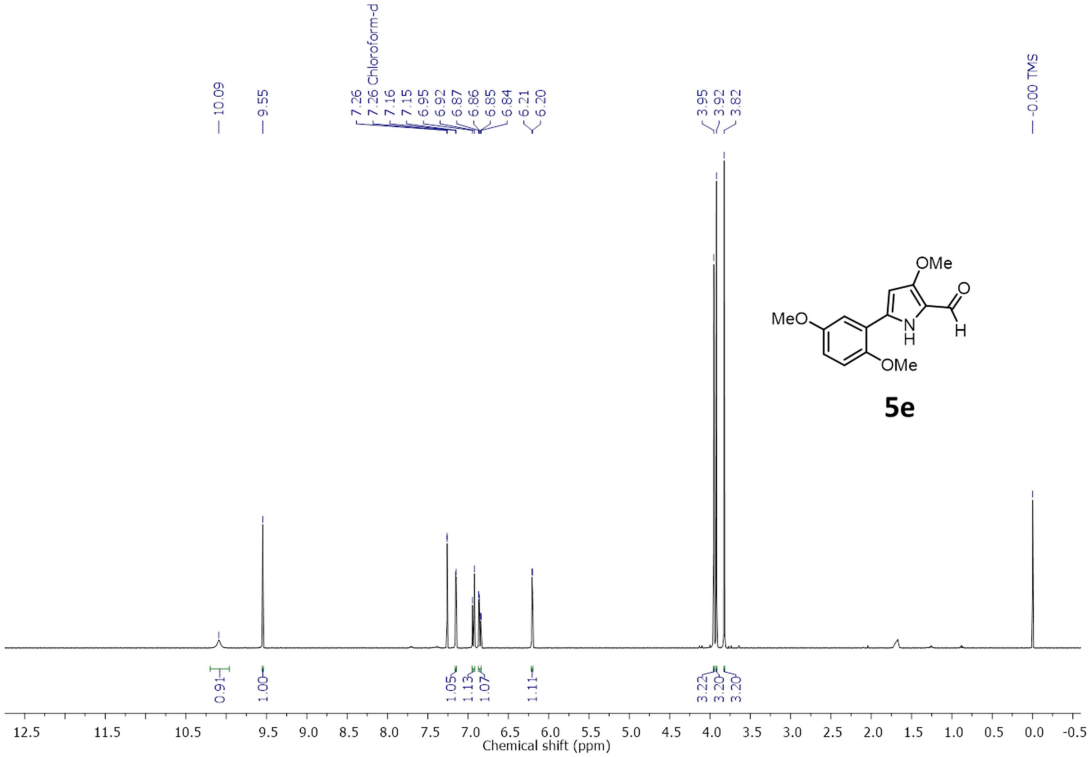


**Figure C16:** $^{1}$H spectrum of compound **5e**

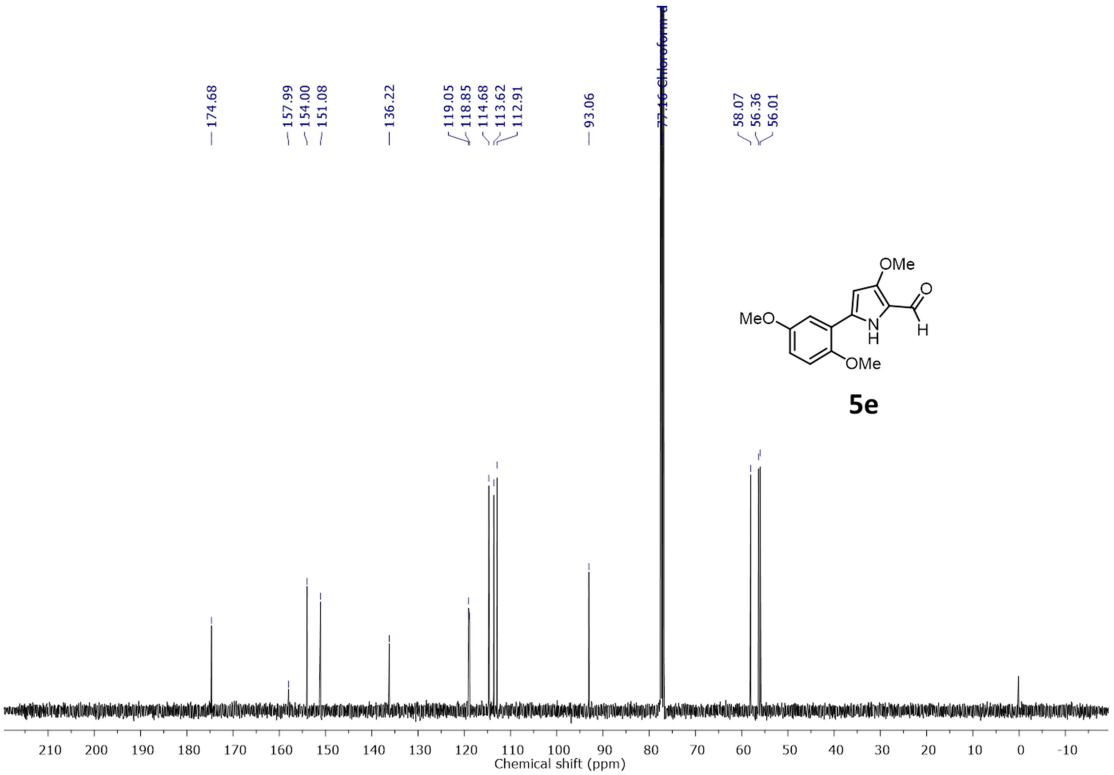


**Figure C17:** $^{13}$C spectrum of compound **5e**

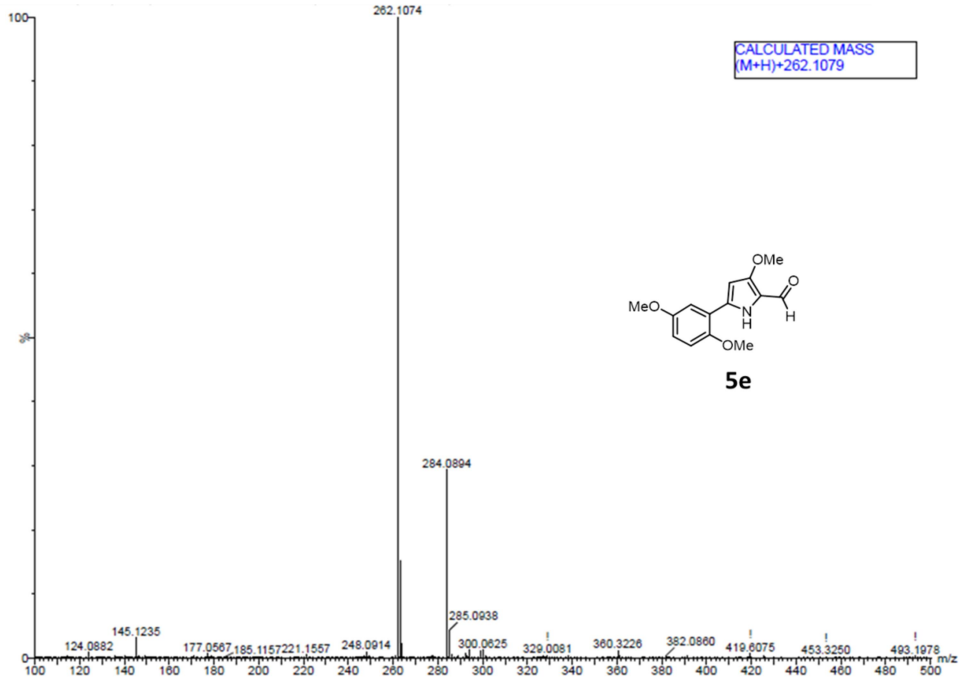


**Figure C18:** HRMS spectrum of compound **5e**

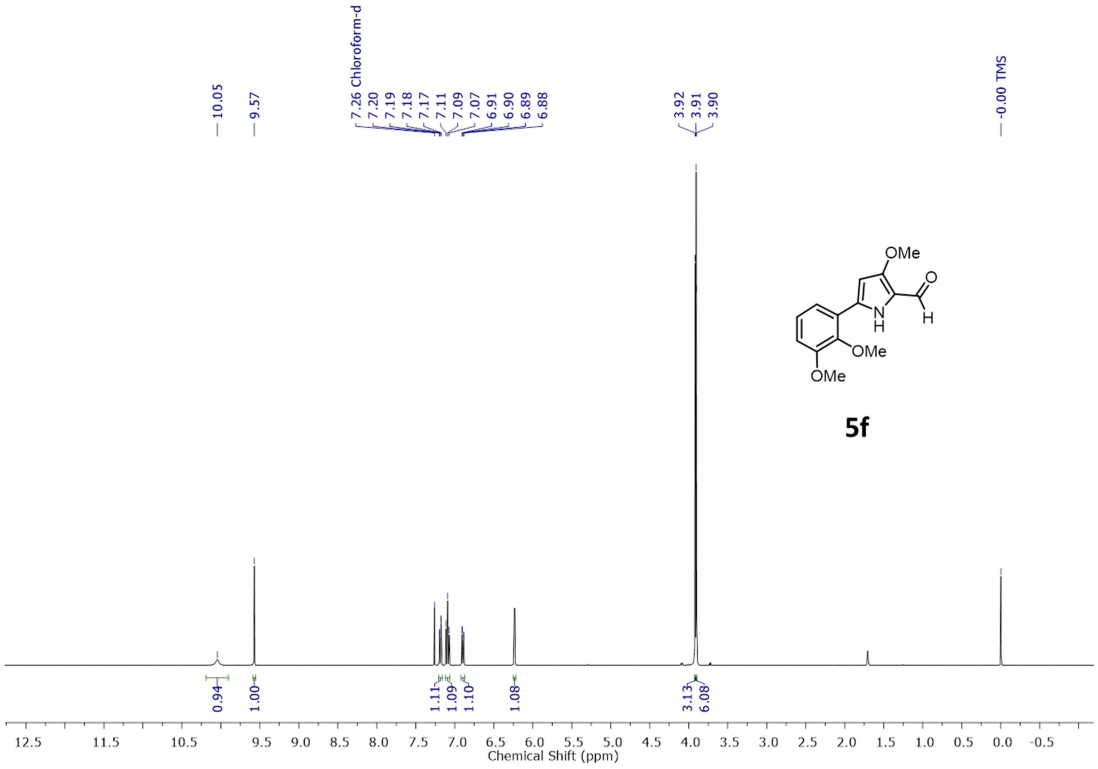


**Figure C19:** $^{1}$H spectrum of compound **5f**

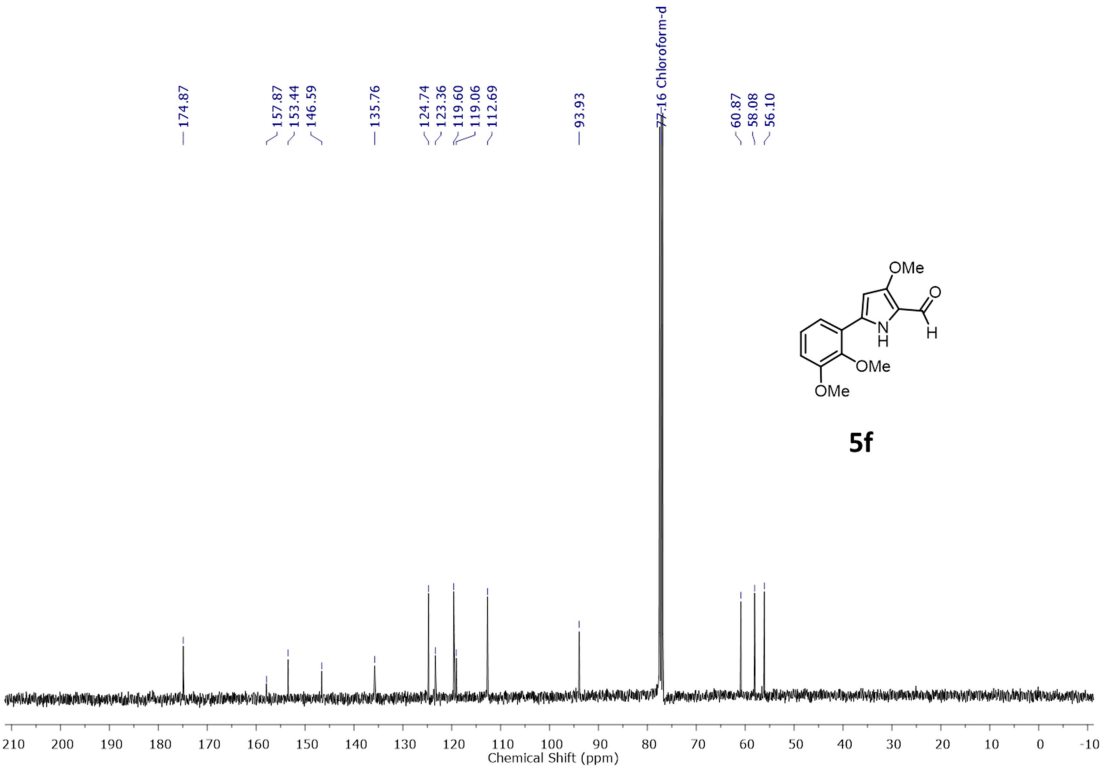


**Figure C20:** $^{13}$C spectrum of compound **5f**

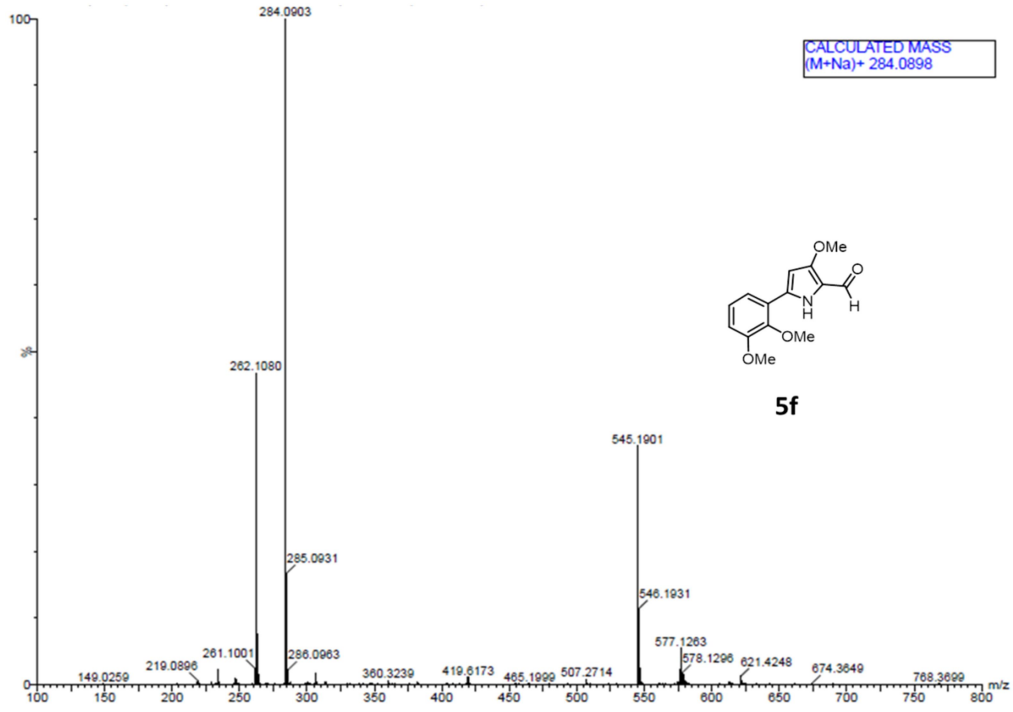


**Figure C21:** HRMS spectrum of compound **5f**

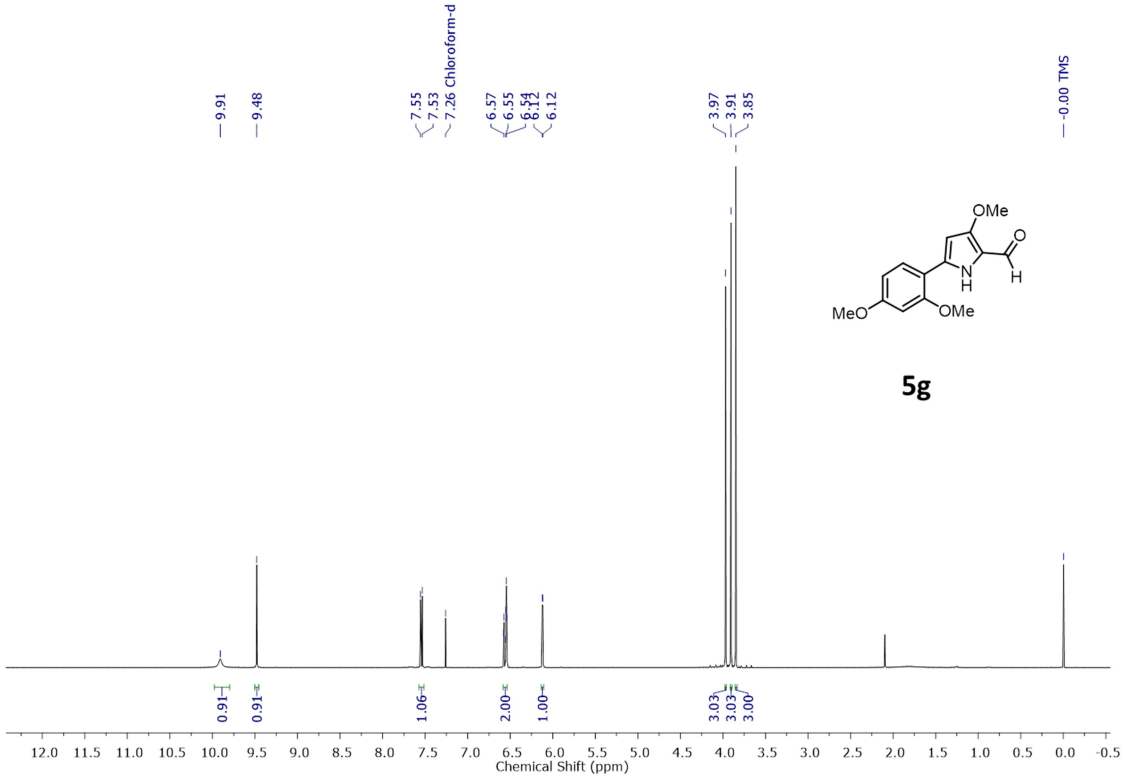


**Figure C22:** $^{1}$H spectrum of compound **5g**

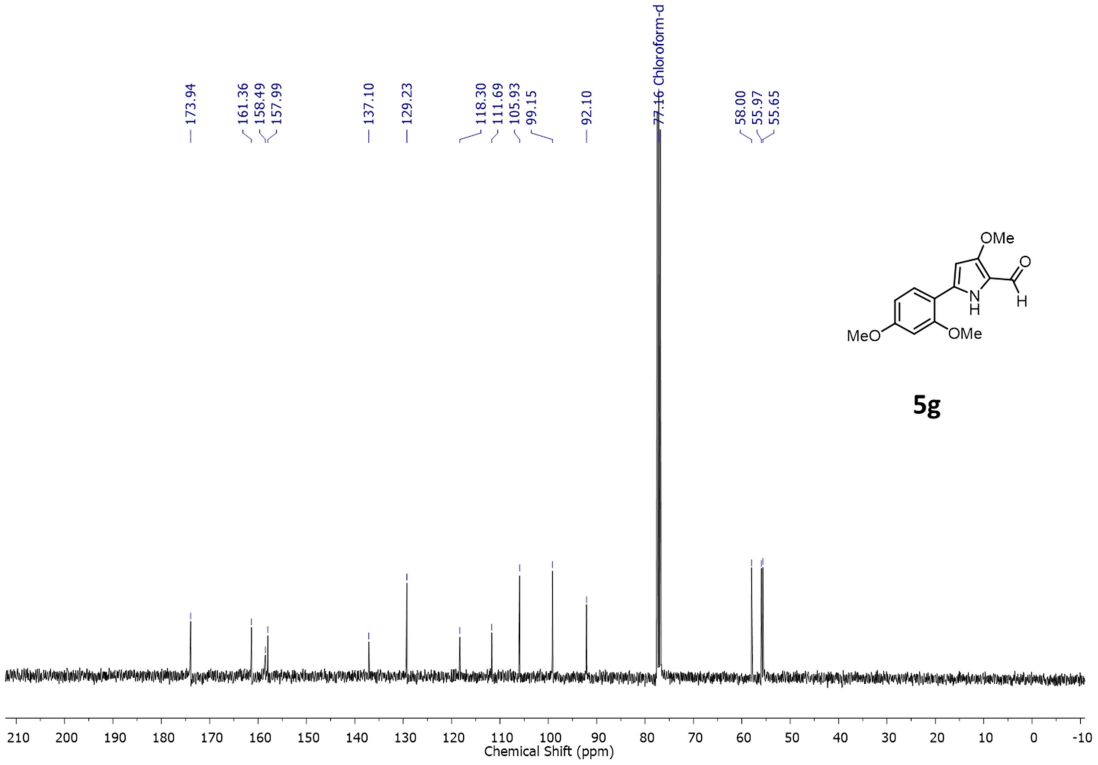


**Figure C23:** $^{13}$Cspectrum of compound **5g**

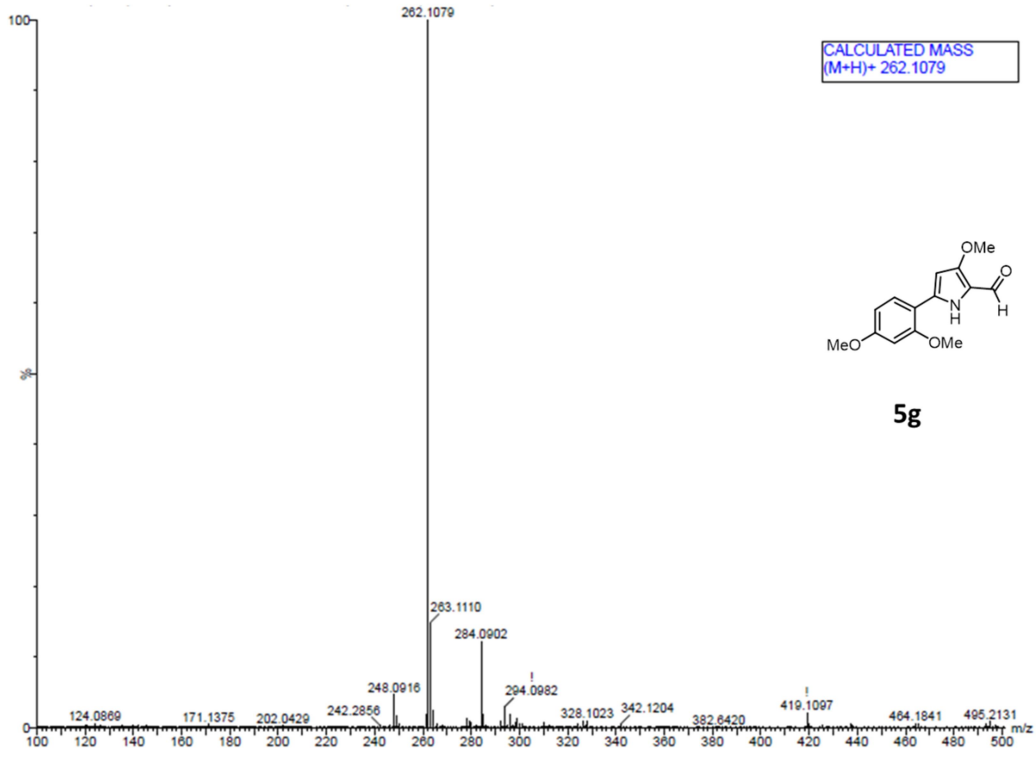


**Figure C24:** HRMS spectrum of compound **5g**

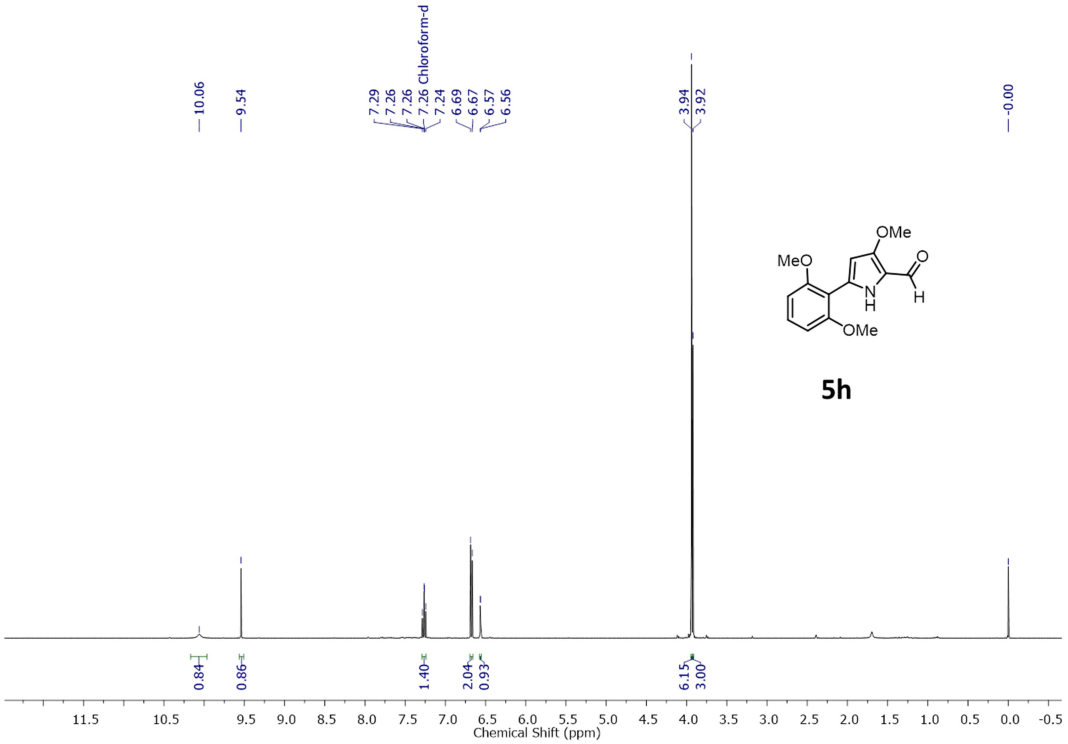


**Figure C25:** $^{1}$H spectrum of compound **5h**

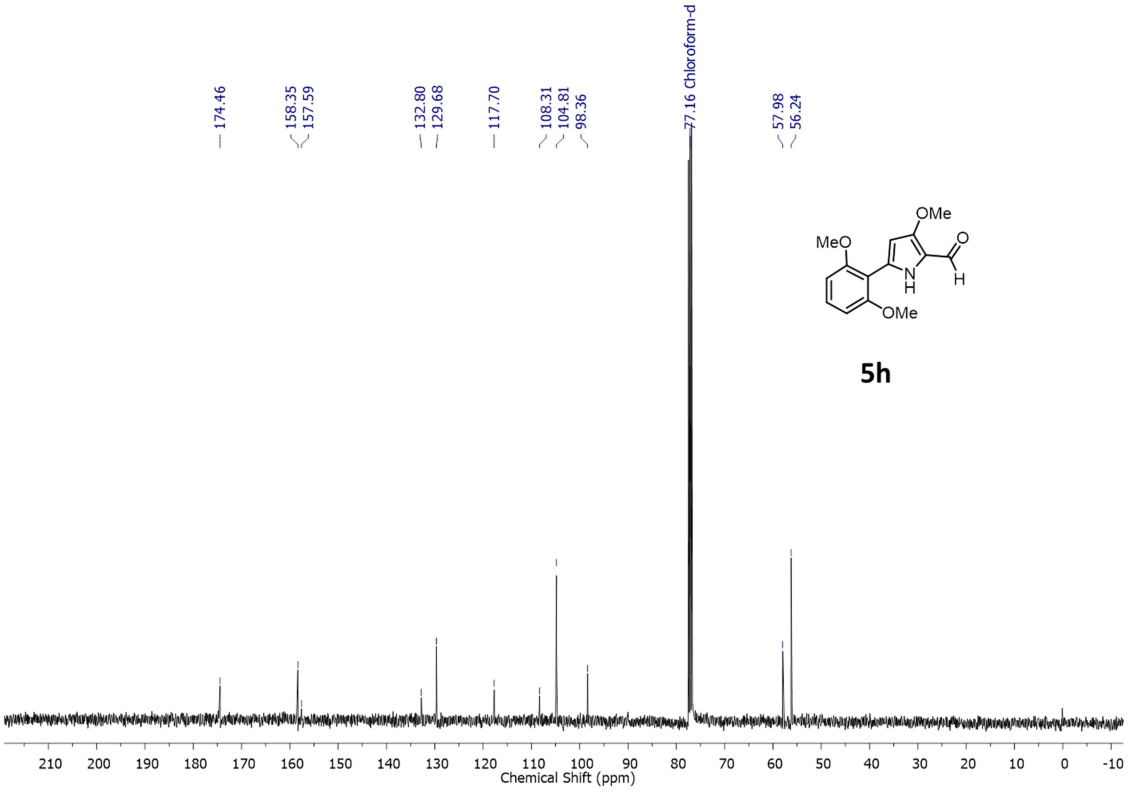


**Figure C26:** $^{13}$C spectrum of compound **5h**

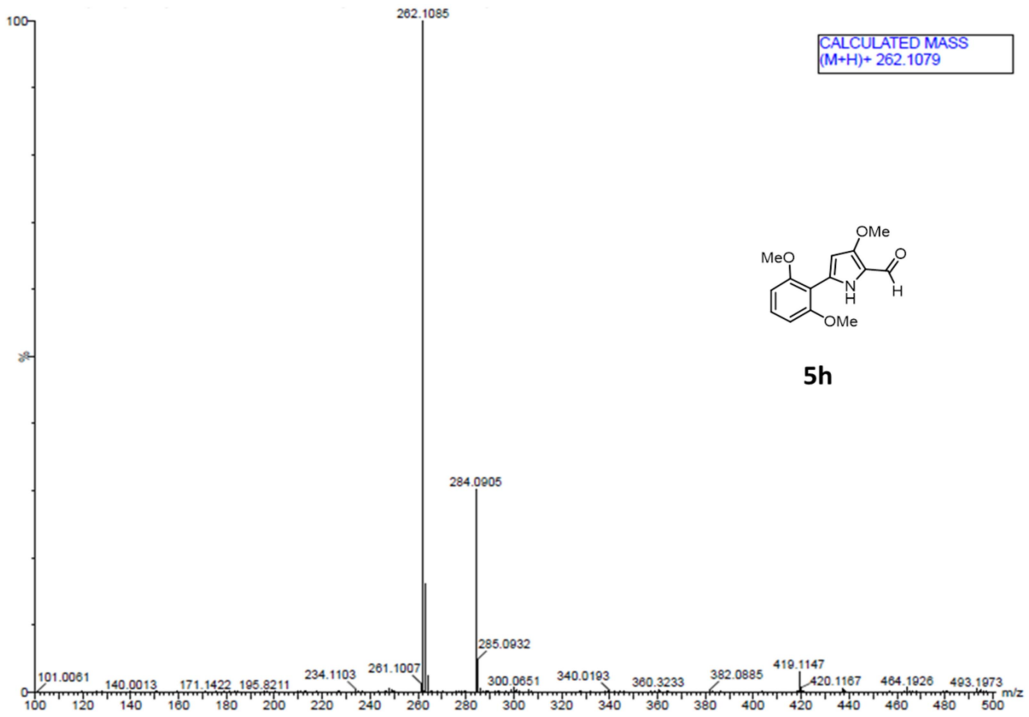


**Figure C27:** HRMS spectrum of compound **5h**

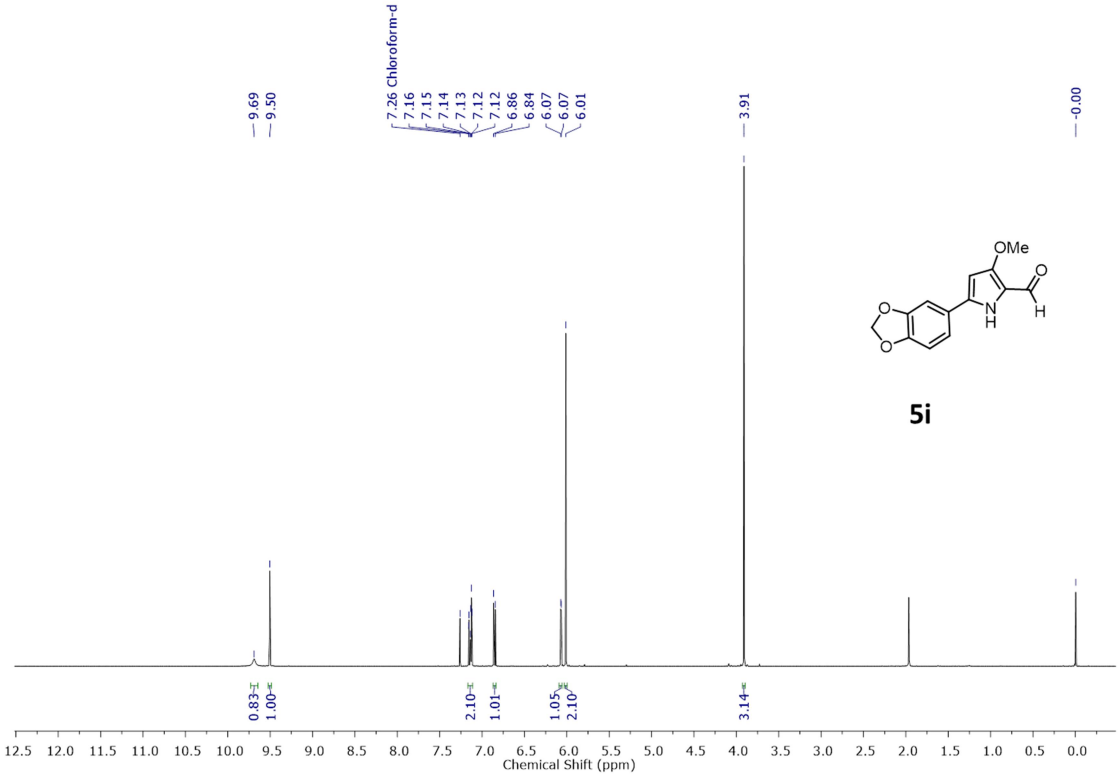


**Figure C28:** $^{1}$H spectrum of compound **5i**

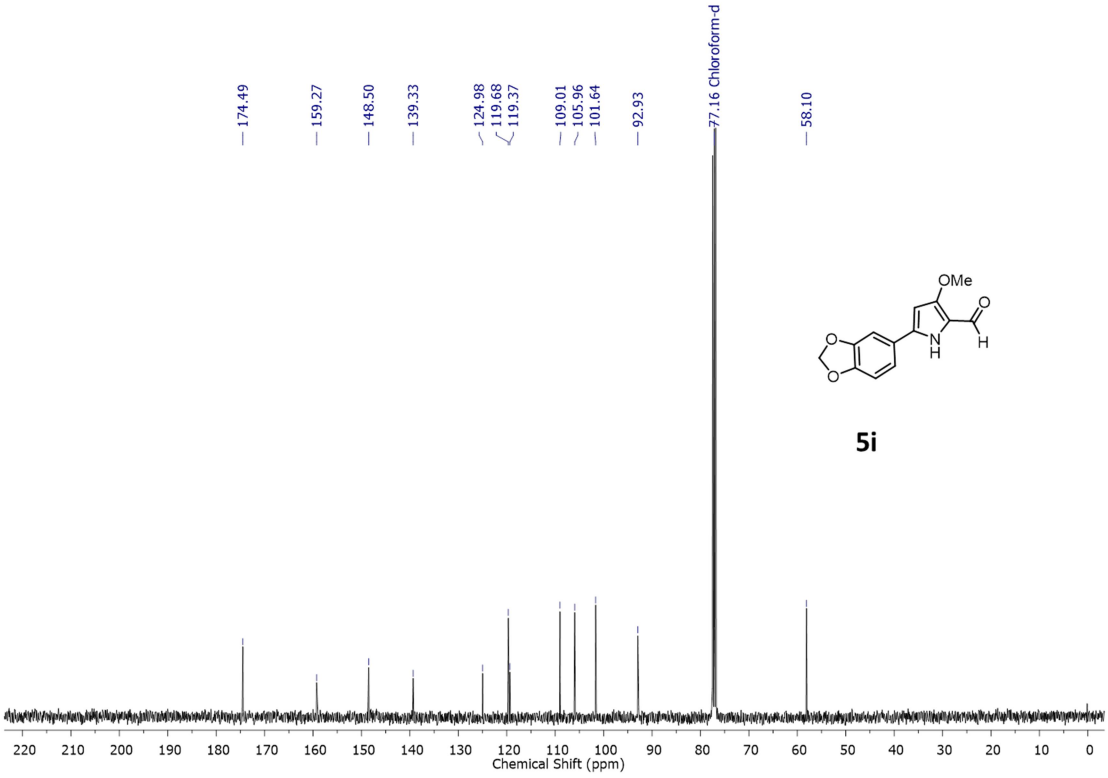


**Figure C29:** $^{13}$C spectrum of compound **5i**

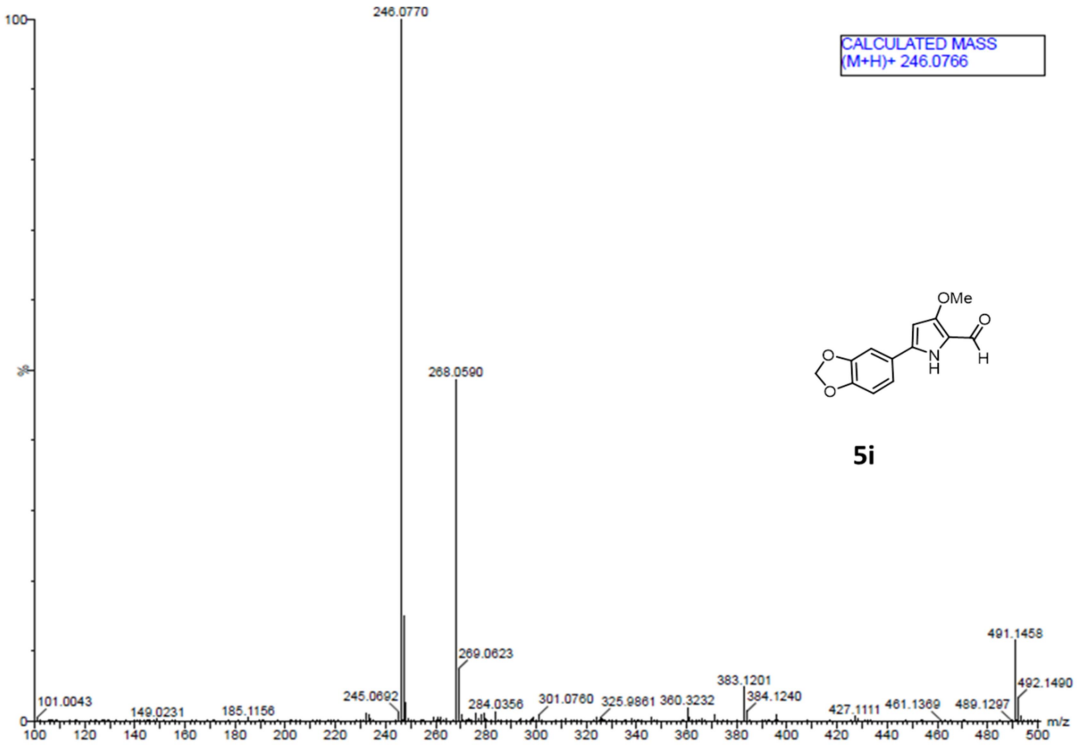


**Figure C30:** HRMS spectrum of compound **5i**

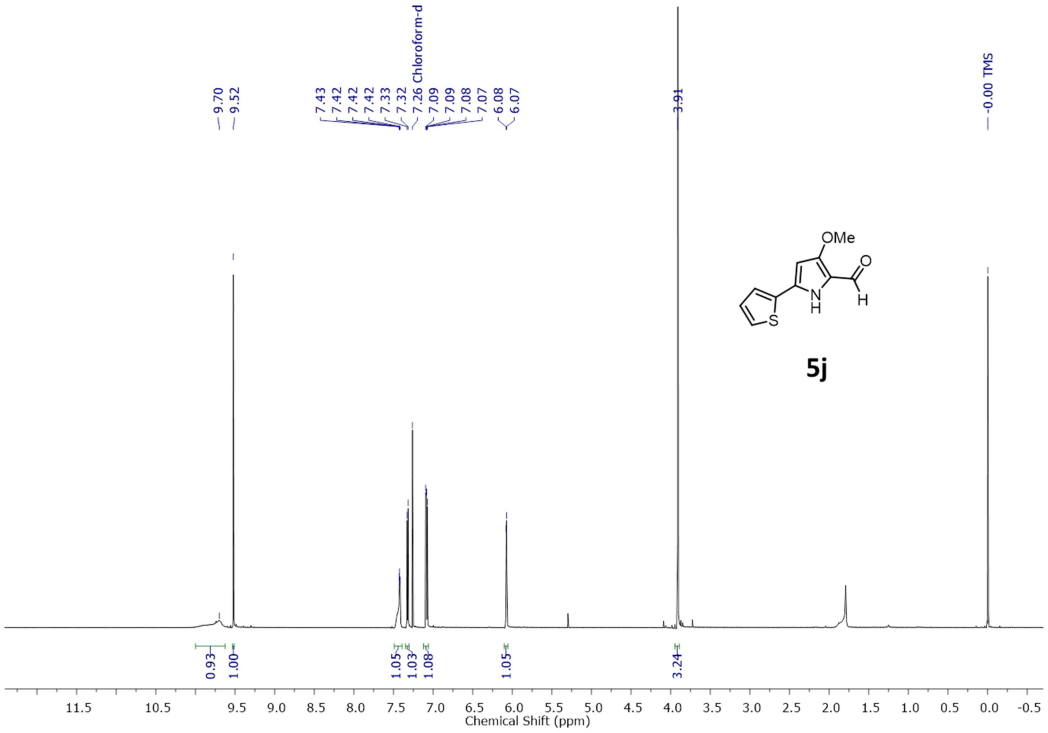


**Figure C31:** $^{1}$H spectrum of compound **5j**

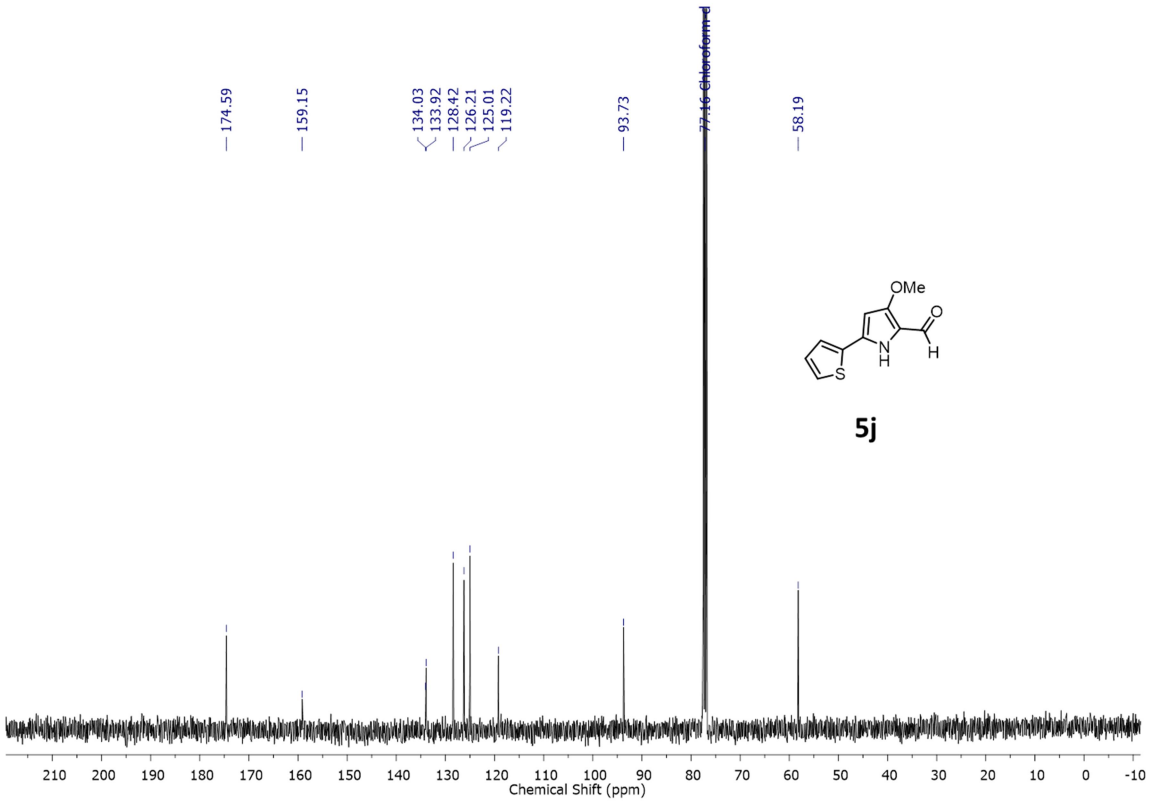


**Figure C32:** $^{13}$C spectrum of compound **5j**

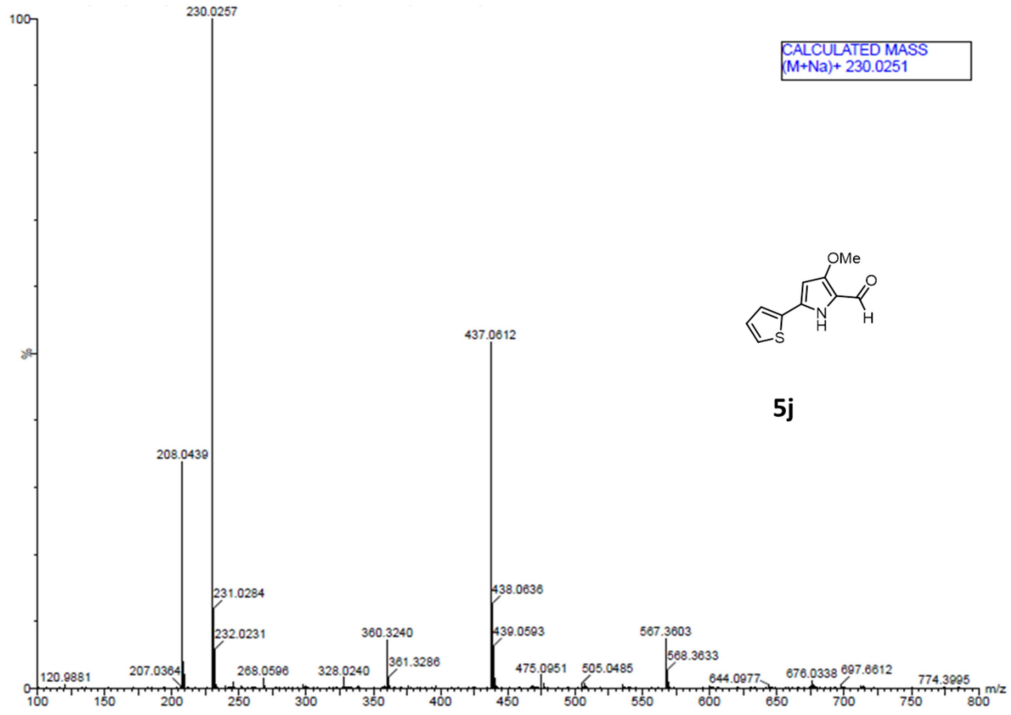


**Figure C33:** HRMS spectrum of compound **5j**

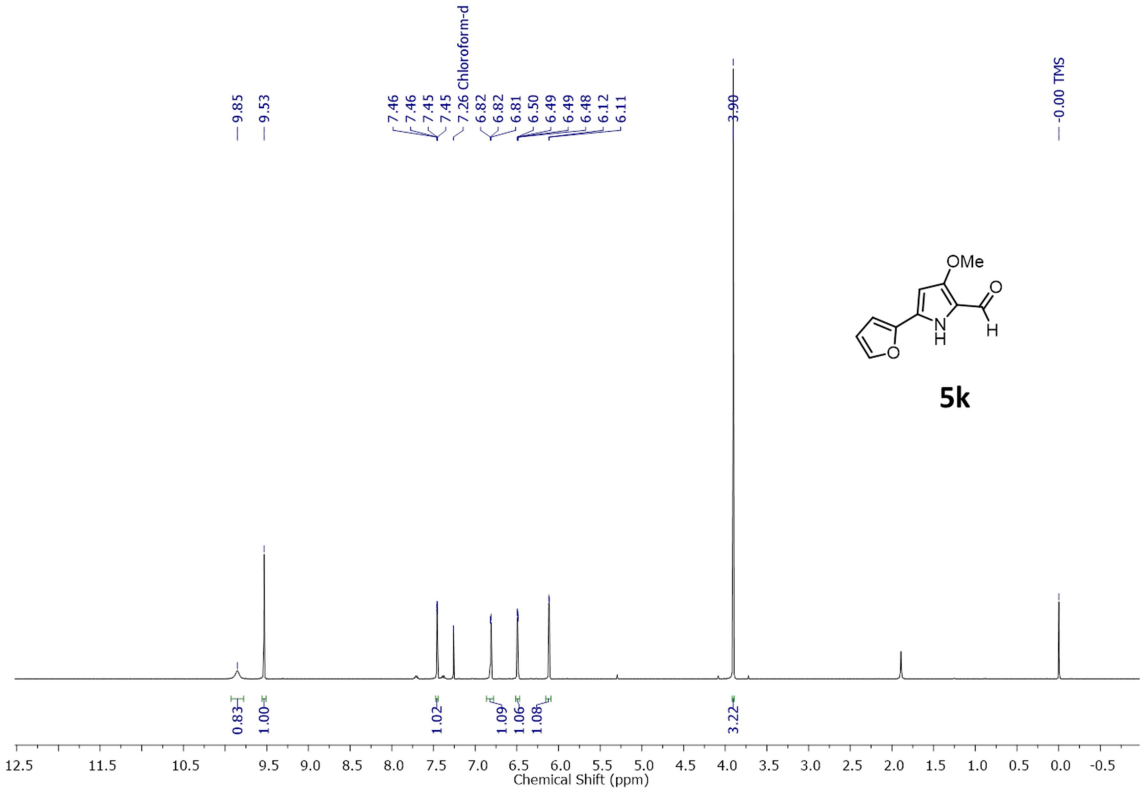


**Figure C34:** $^{1}$H spectrum of compound **5k**

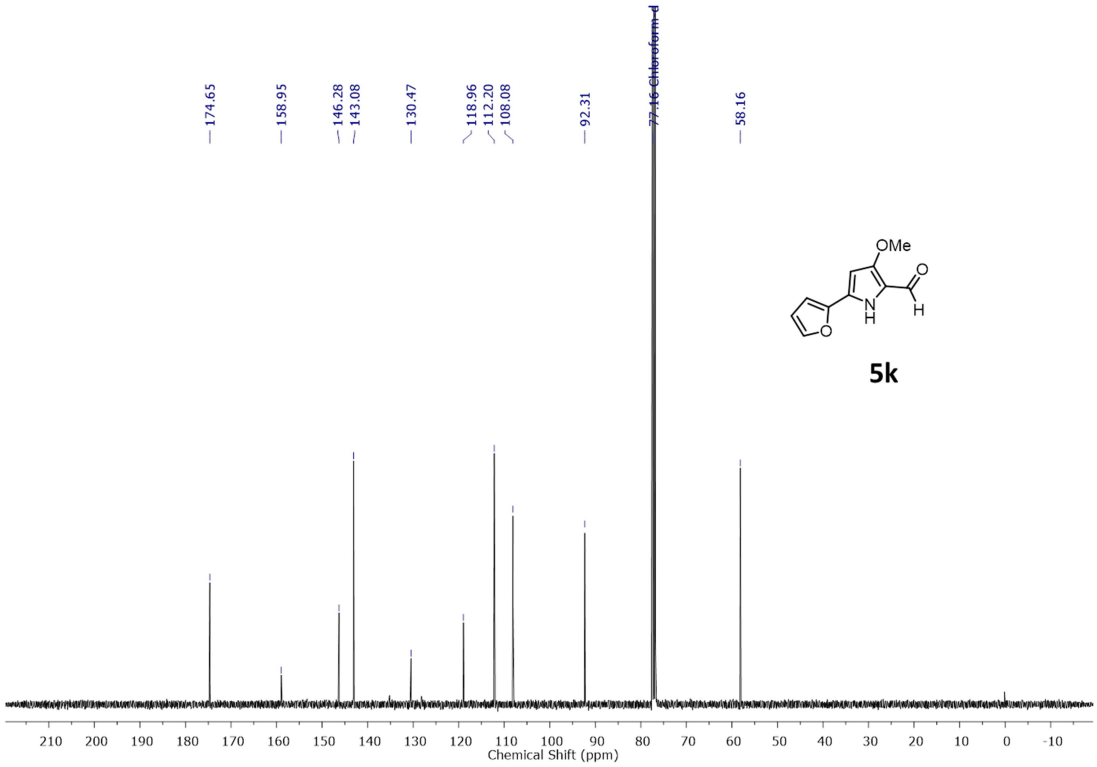


**Figure C35:** $^{13}$C spectrum of compound **5k**

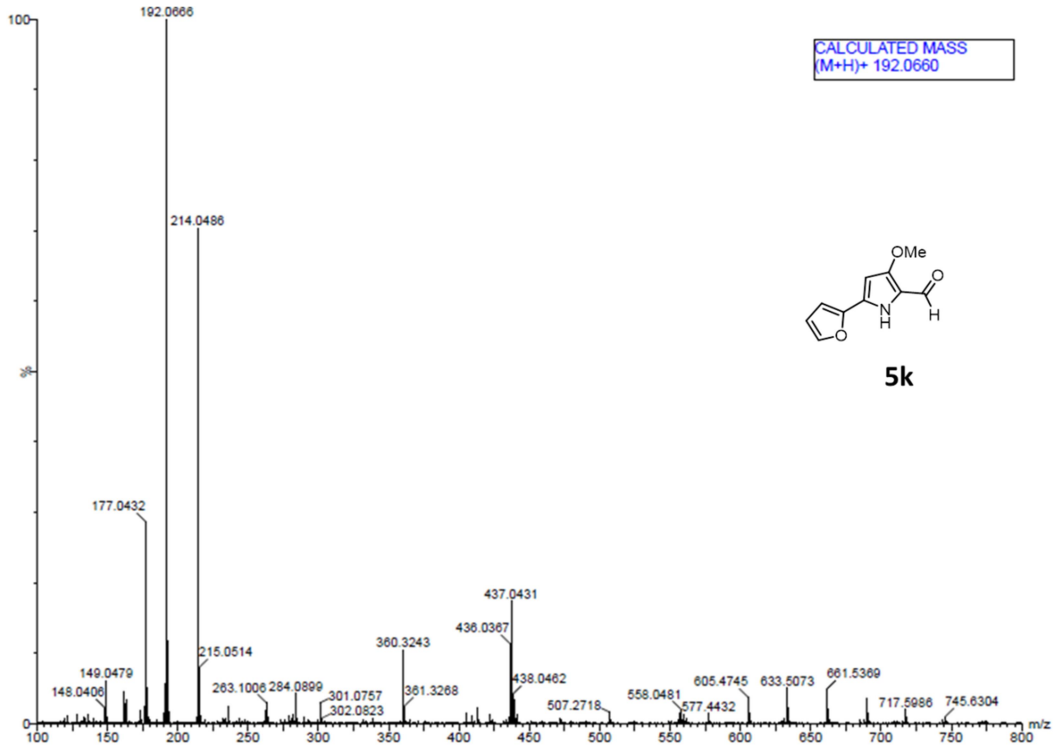


**Figure C36:** HRMS spectrum of compound **5k**

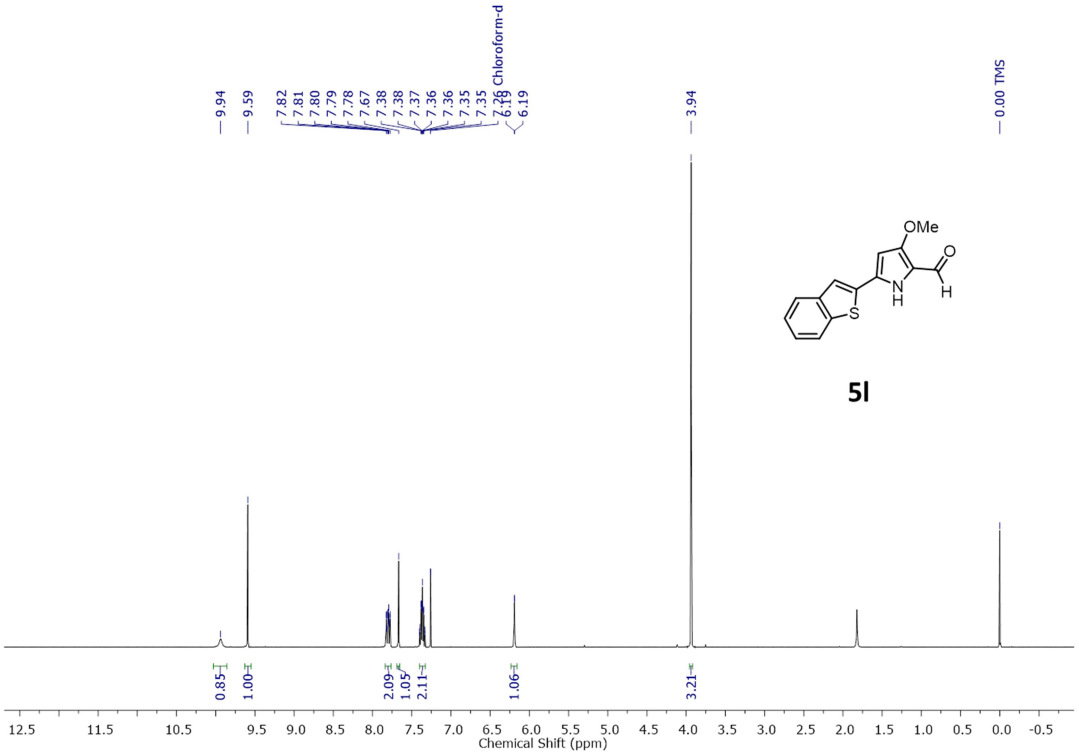


**Figure C37:** $^{1}$H spectrum of compound **5l**

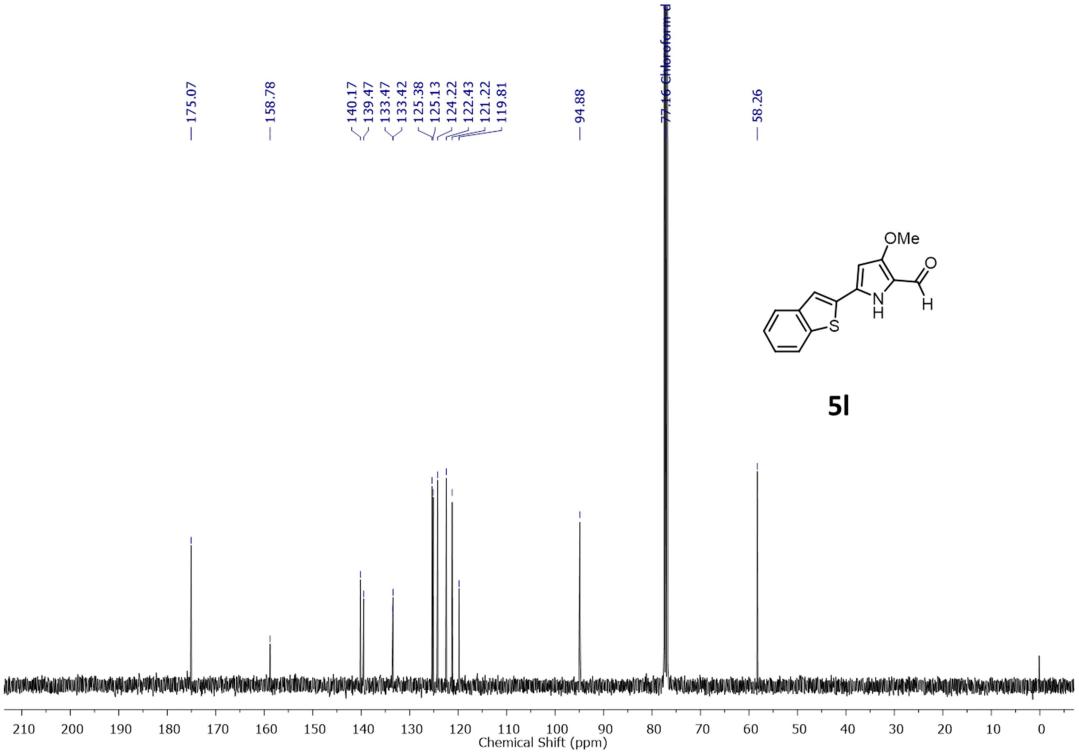


**Figure C38:** $^{13}$Cspectrum of compound **5l**

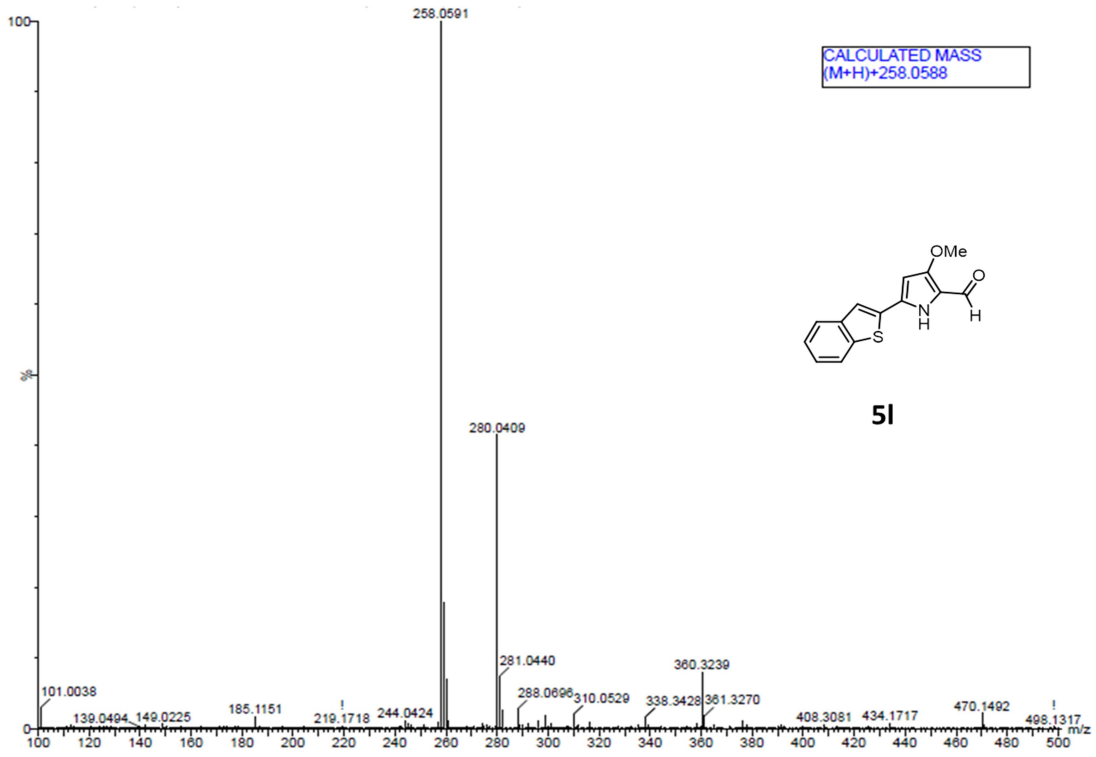


**Figure C39:** HRMS spectrum of compound **5l**

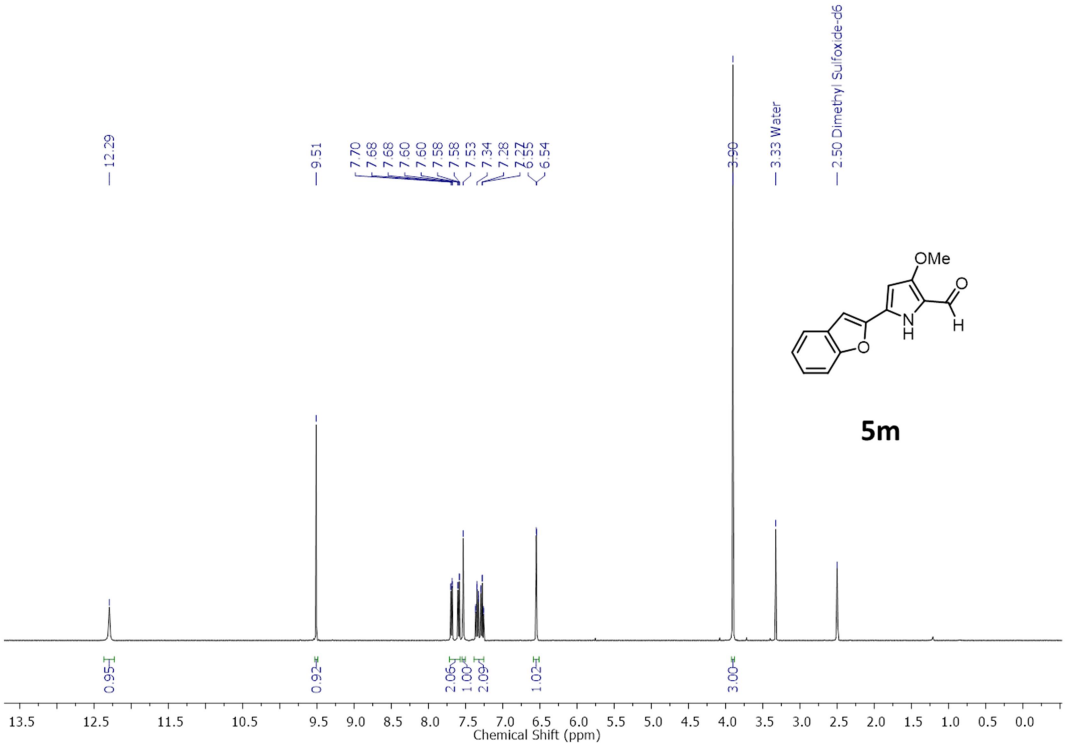


**Figure C40:** $^{1}$H spectrum of compound **5m**

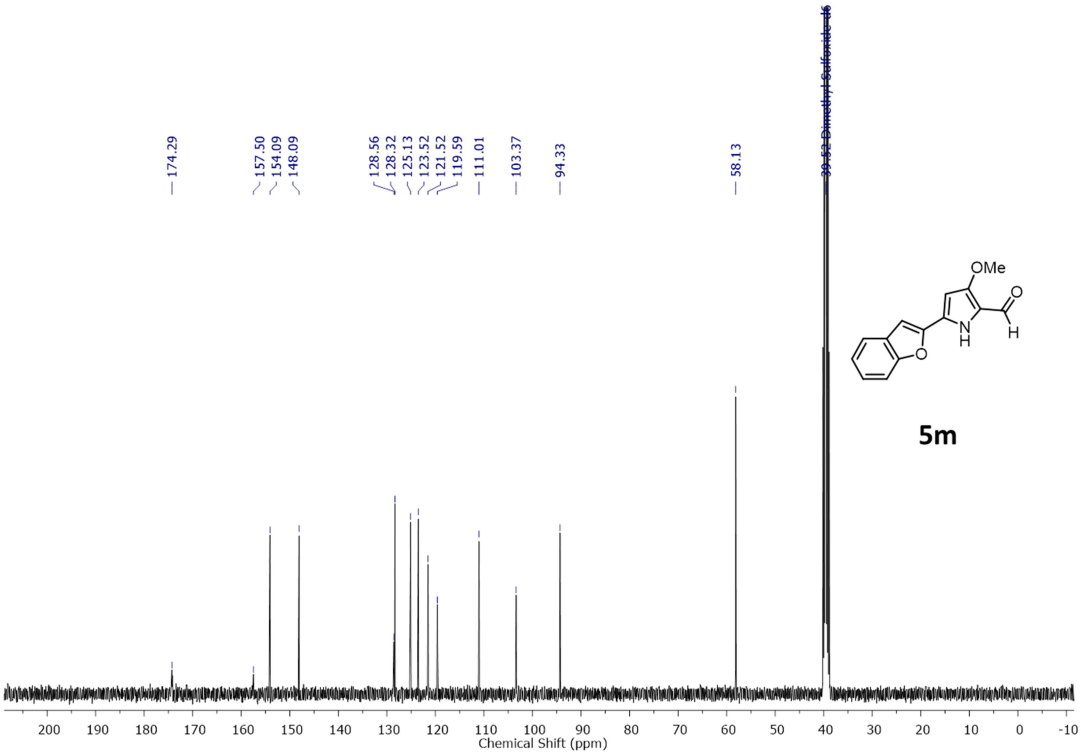


**Figure C41:** $^{13}C$ spectrum of compound **5m**

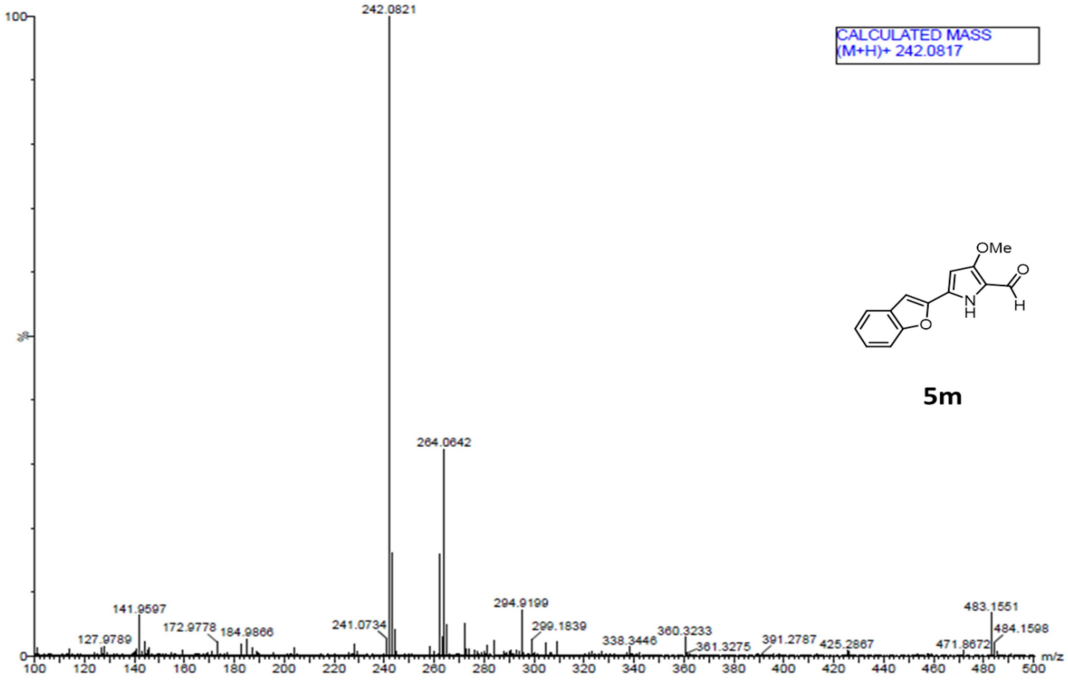


**Figure C42:** HRMS spectrum of compound **5m**

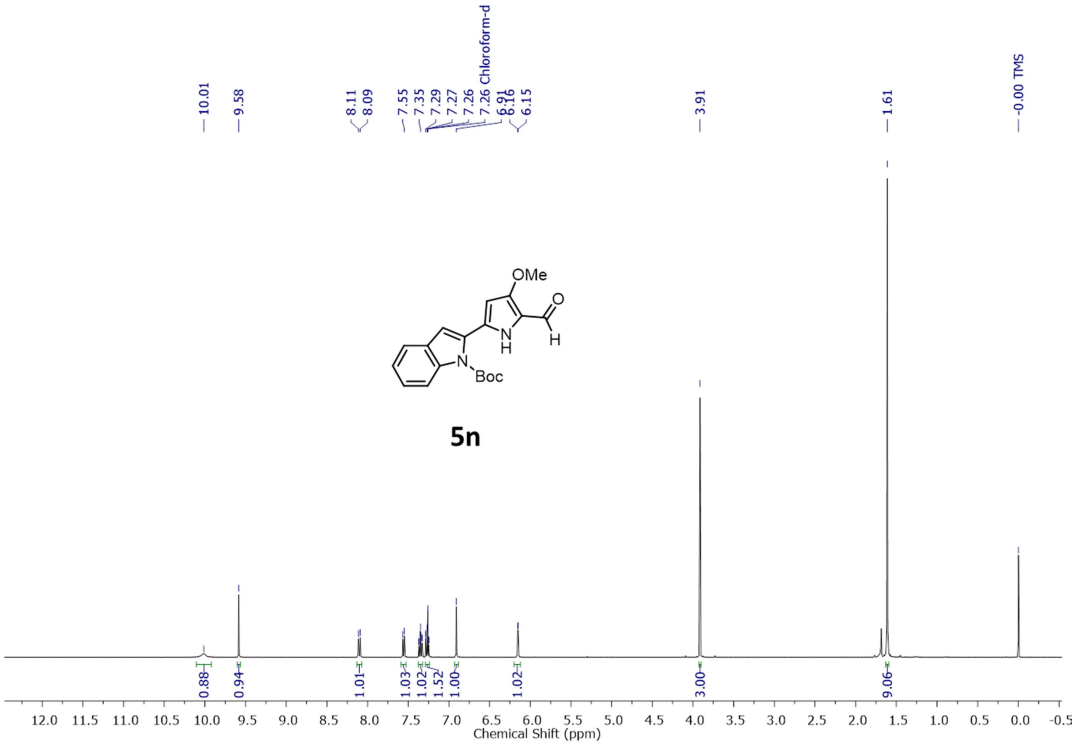


**Figure C43:** $^{1}$H spectrum of compound **5n**

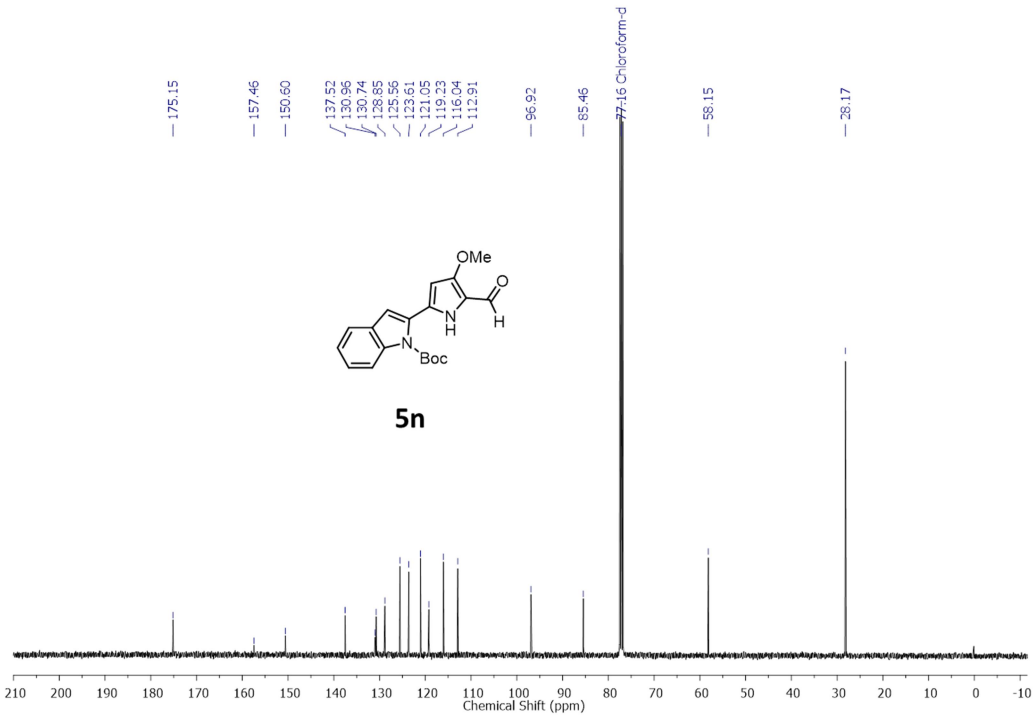


**Figure C44:** $^{13}$C spectrum of compound **5n**

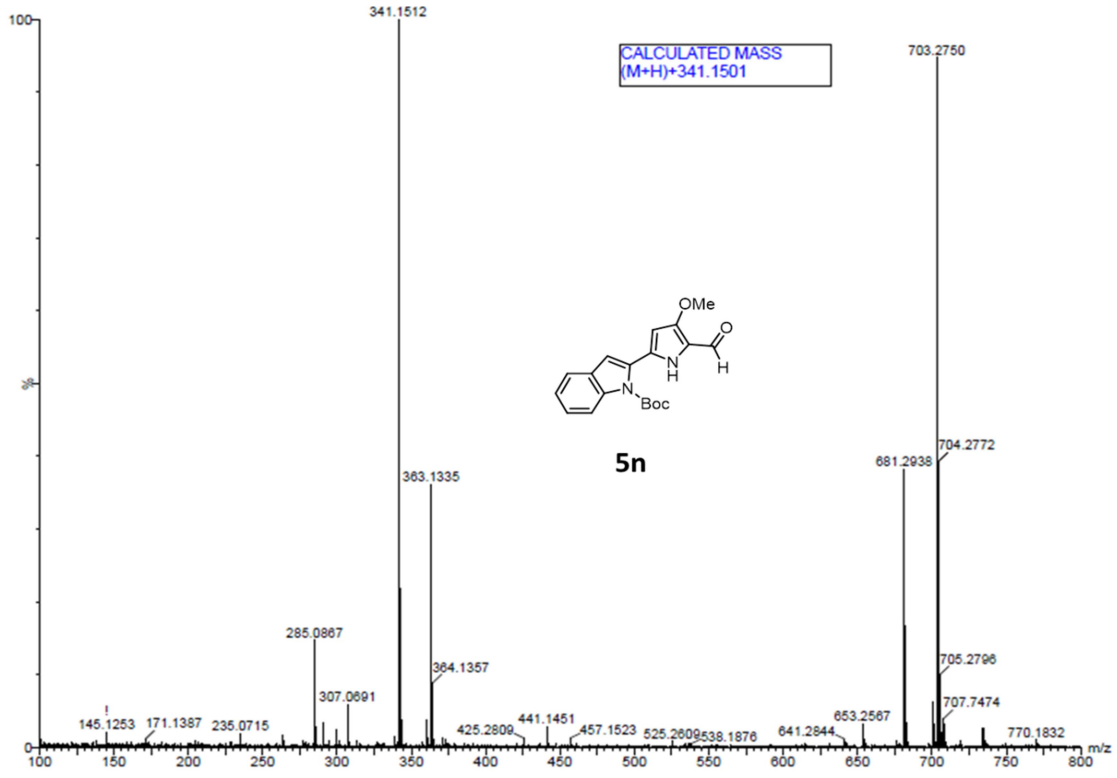


**Figure C45:** HRMS spectrum of compound **5n**

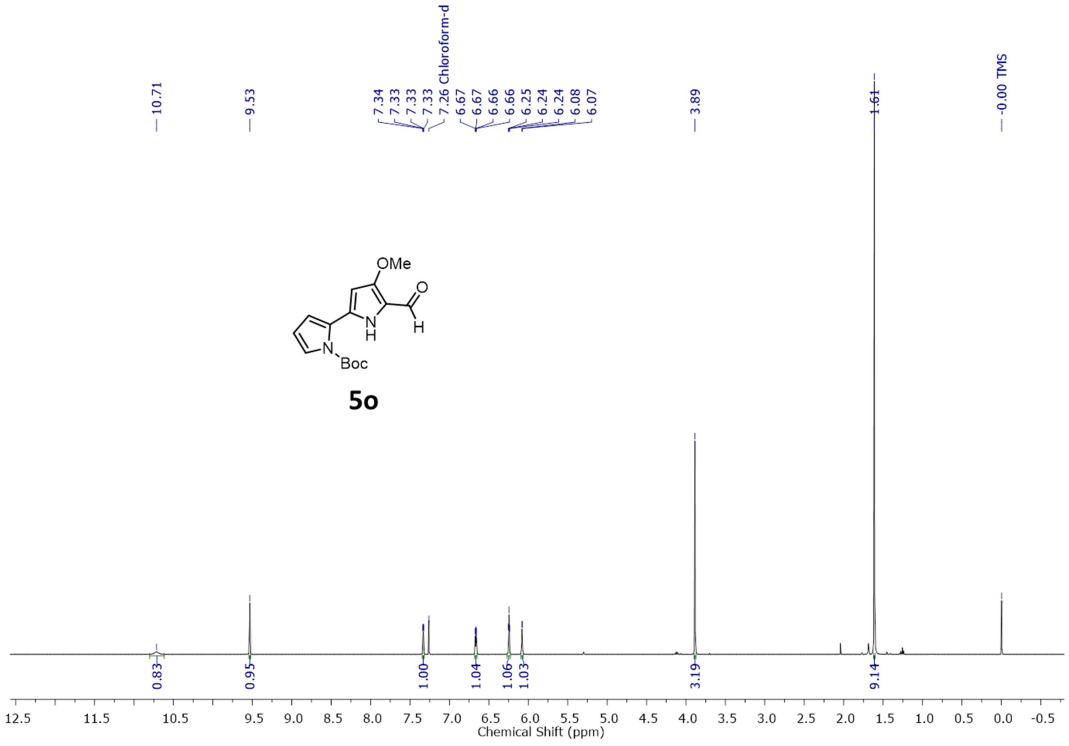


**Figure C46:** $^{1}$H spectrum of compound **5o**

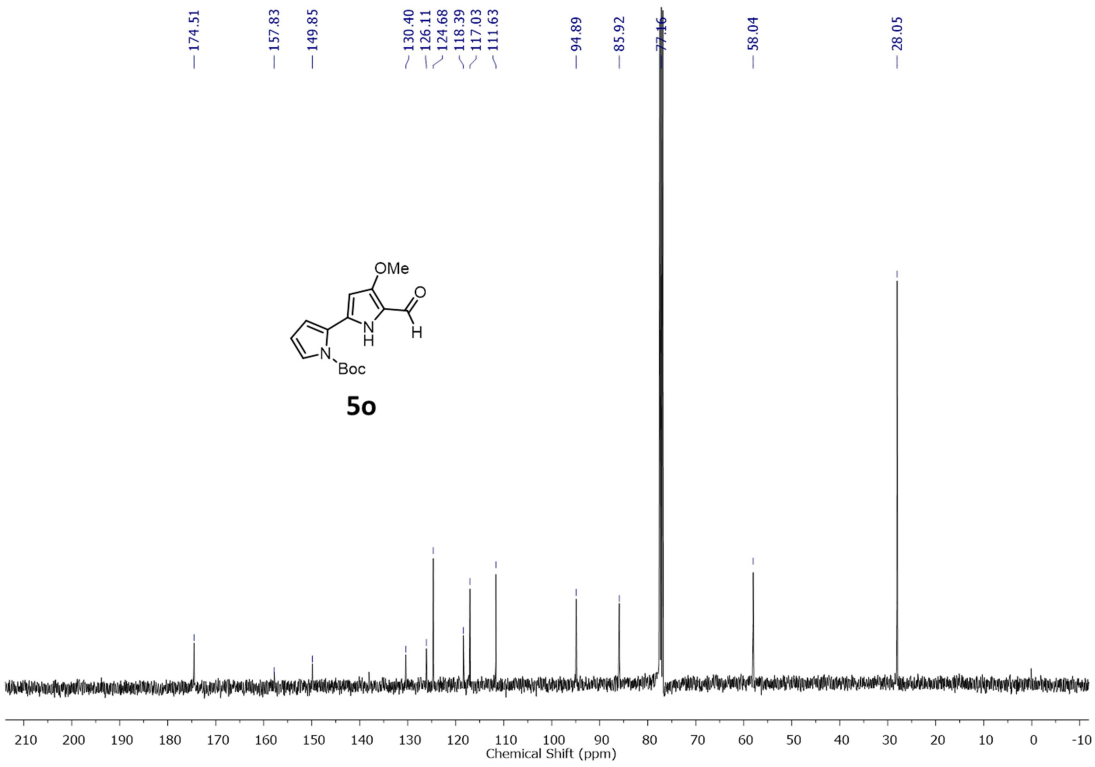


**Figure C47:** $^{13}$C spectrum of compound **5o**

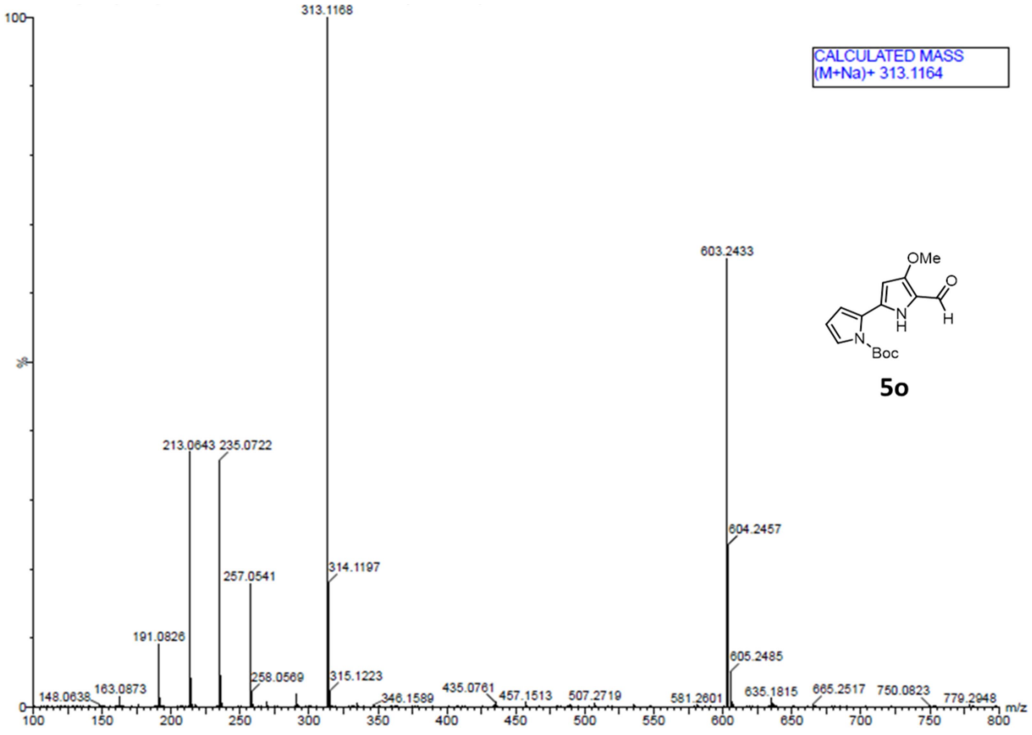


**Figure C48:** HRMS spectrum of compound **5o**

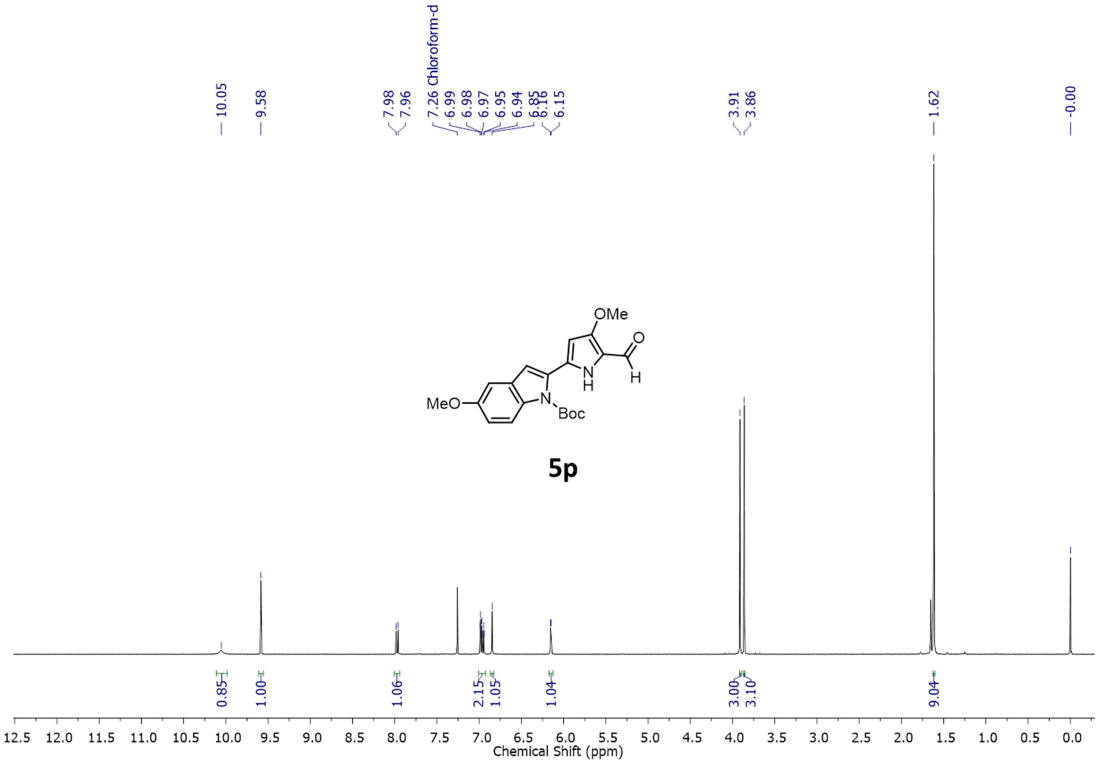


**Figure C49:** $^{1}$H spectrum of compound **5p**

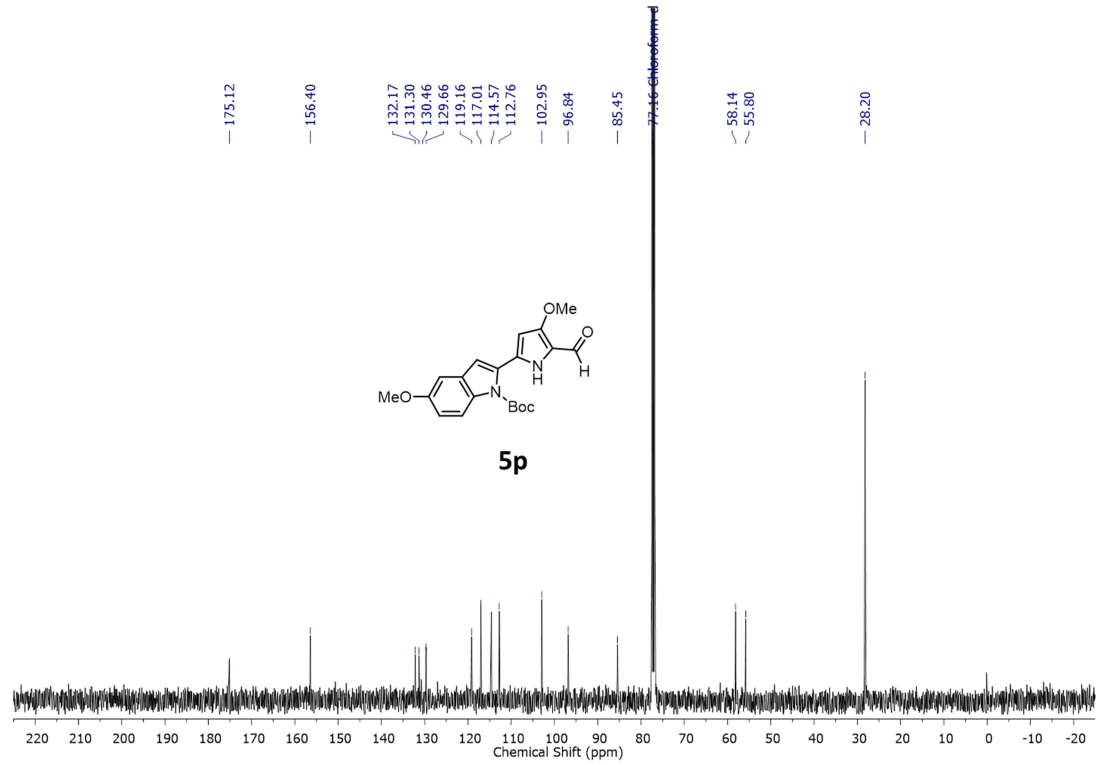


**Figure C50:** $^{13}$C spectrum of compound **5p**

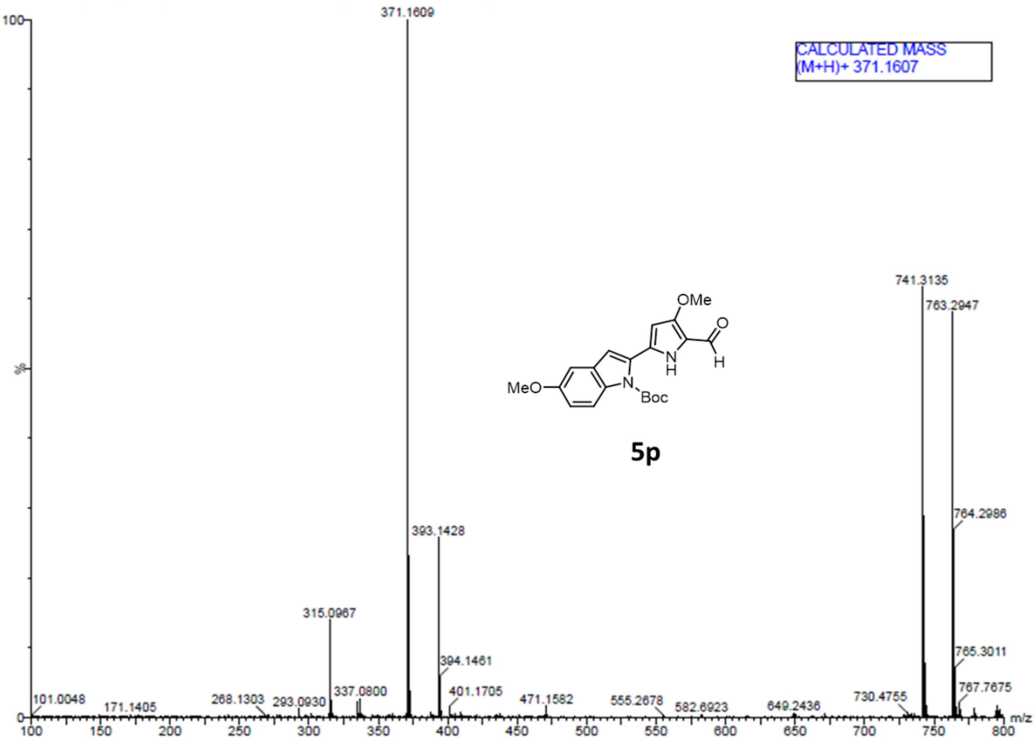


**Figure C51:** HRMS spectrum of compound **5p**

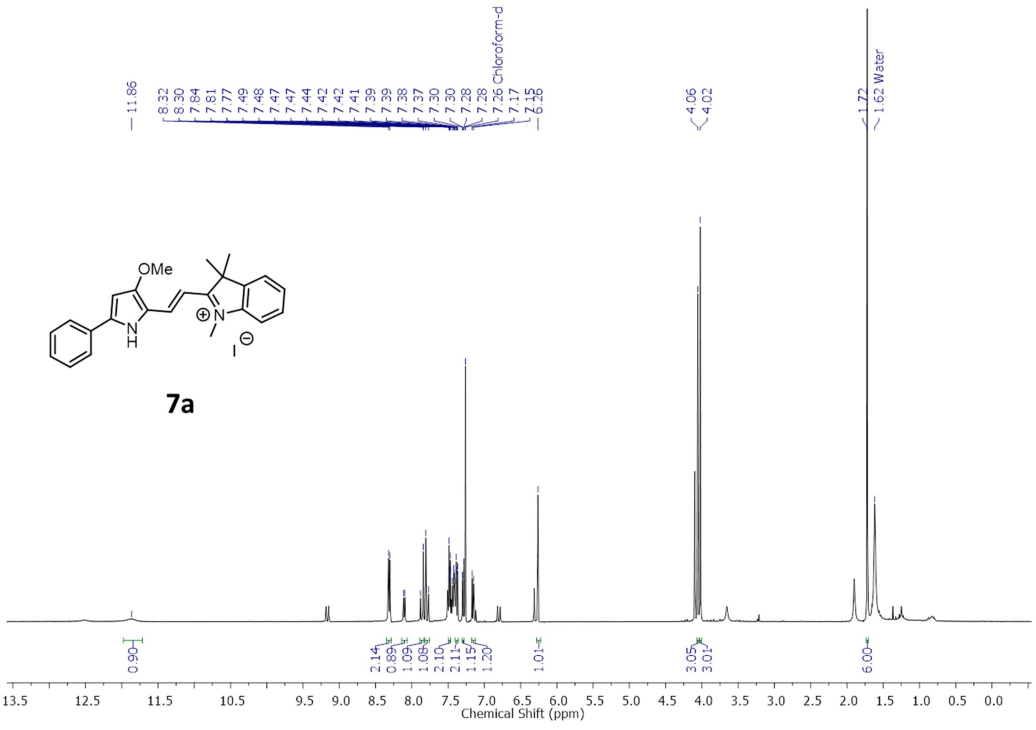


**Figure C52:** $^{1}$H spectrum of compound **7a**

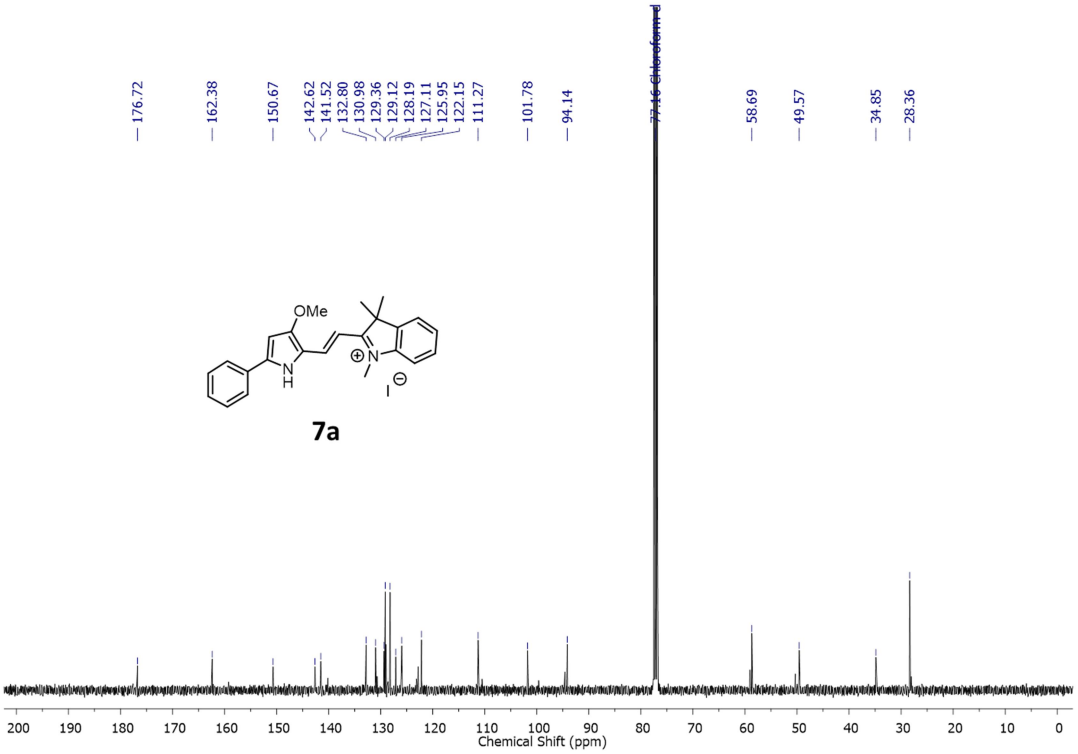


**Figure C53:** $^{13}$C spectrum of compound **7a**

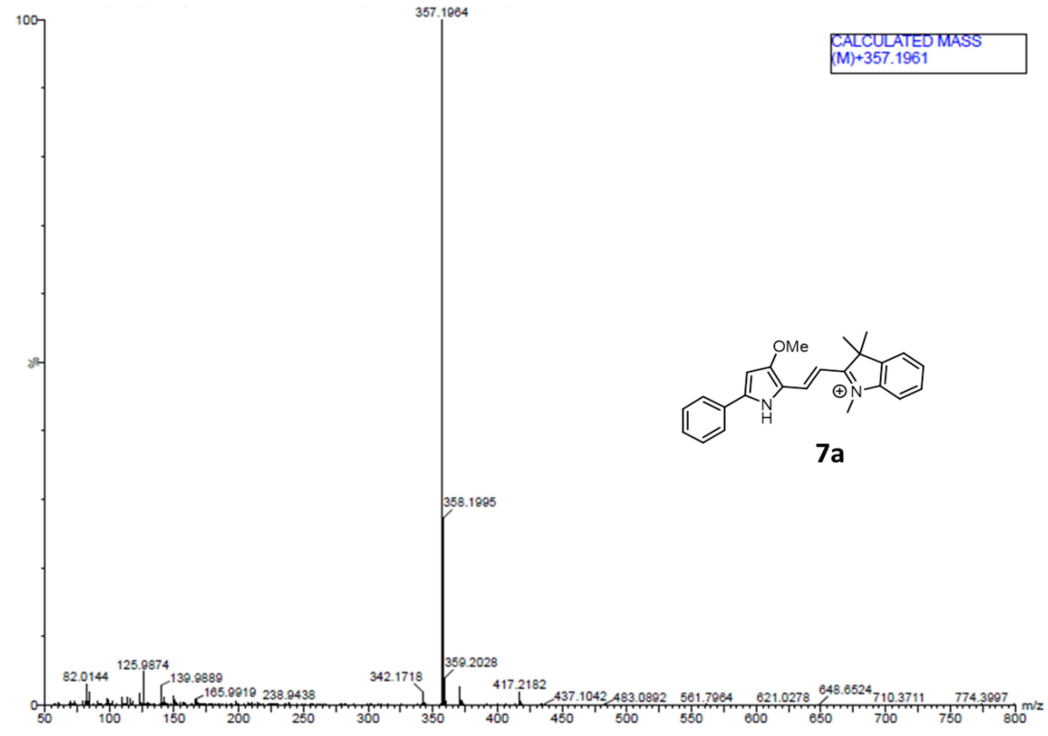


**Figure C54:** HRMS spectrum of compound **7a**

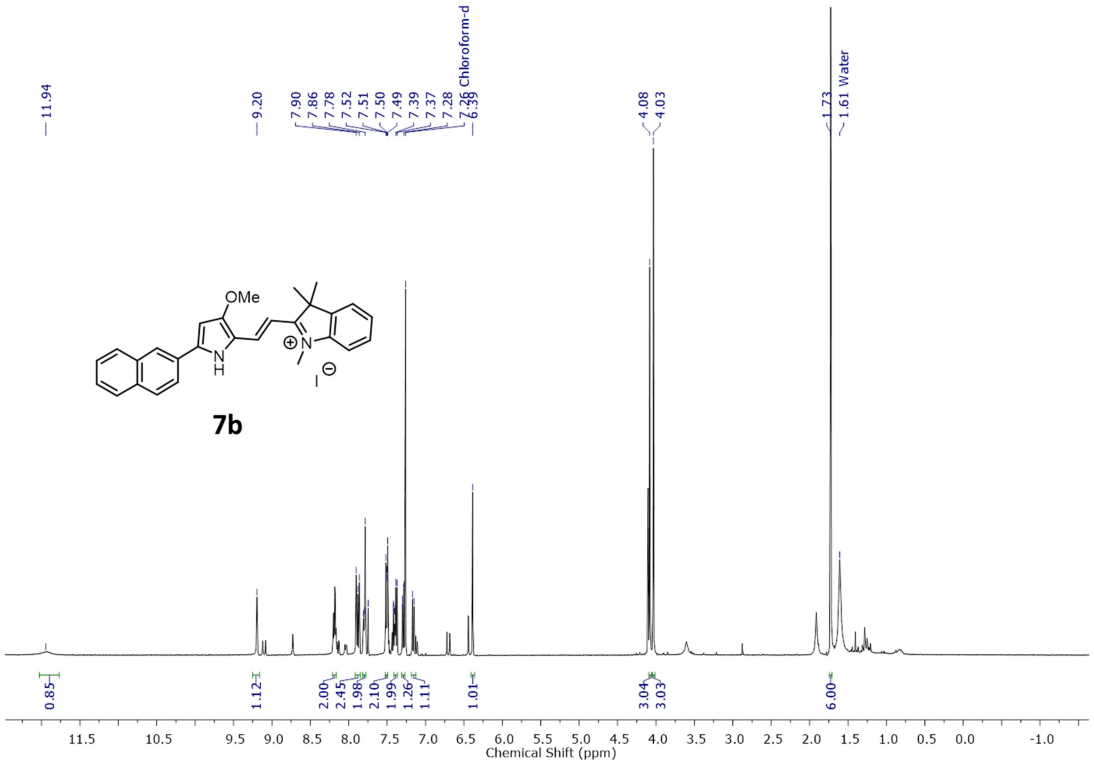


**Figure C55:** $^{1}$H spectrum of compound **7b**

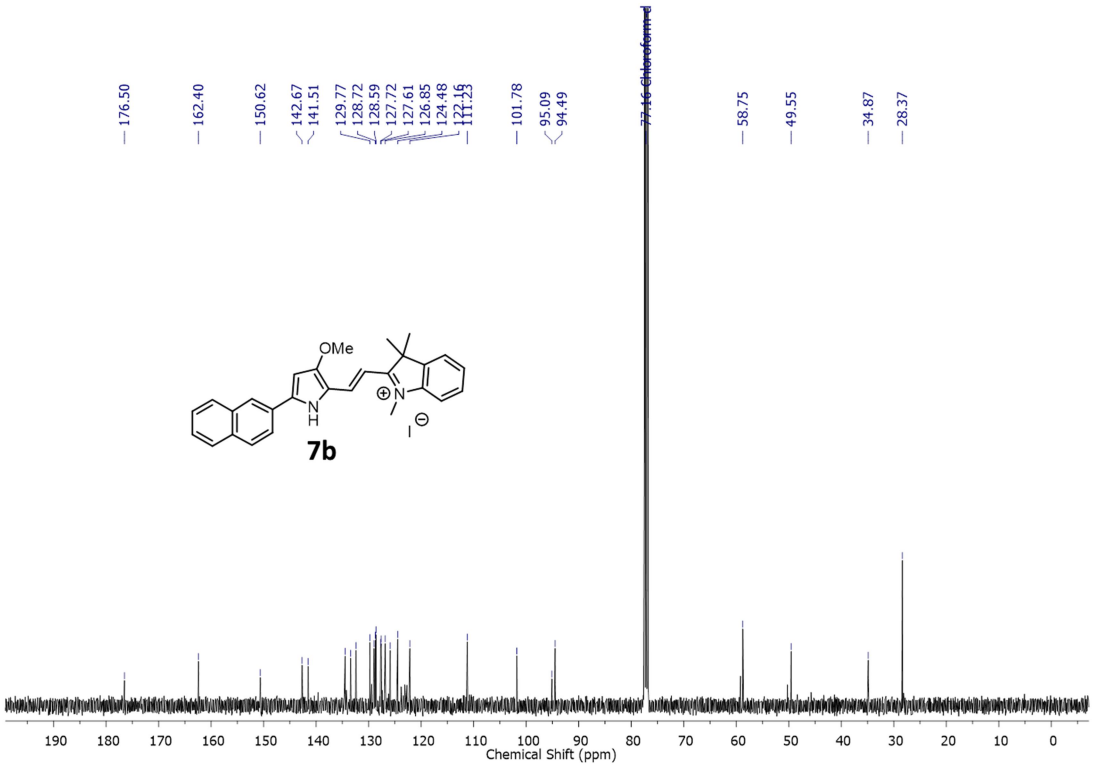


**Figure C56:** $^{13}$C spectrum of compound **7b**

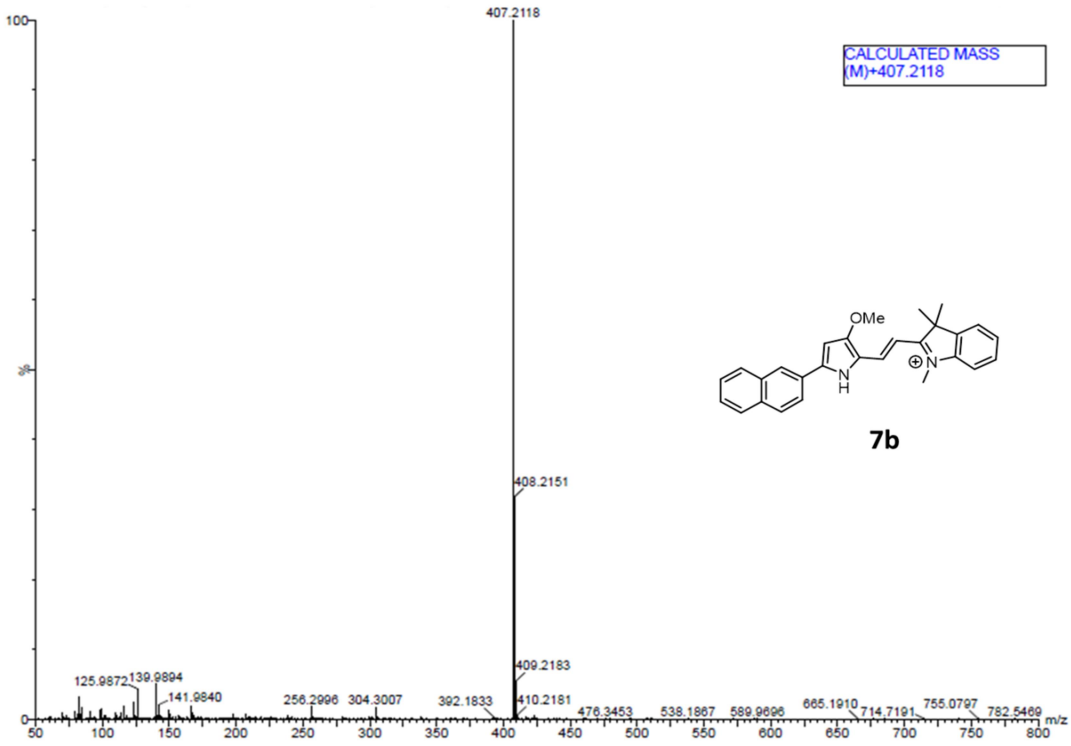


**Figure C57:** HRMS spectrum of compound **7b**

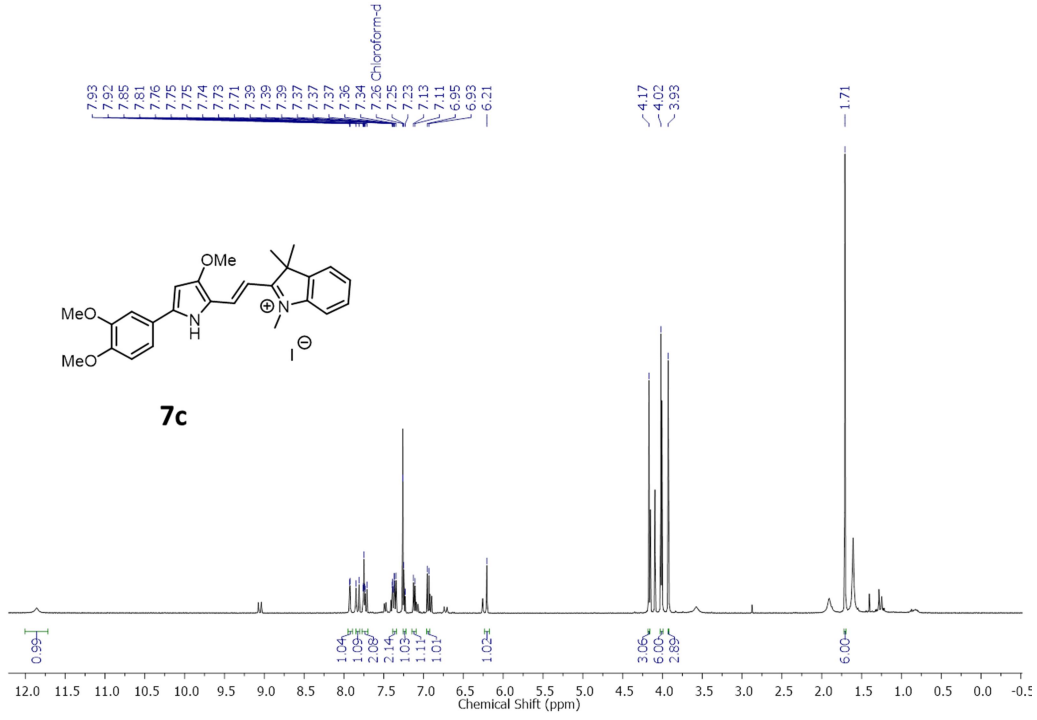


**Figure C58:** $^{1}$H spectrum of compound **7c**

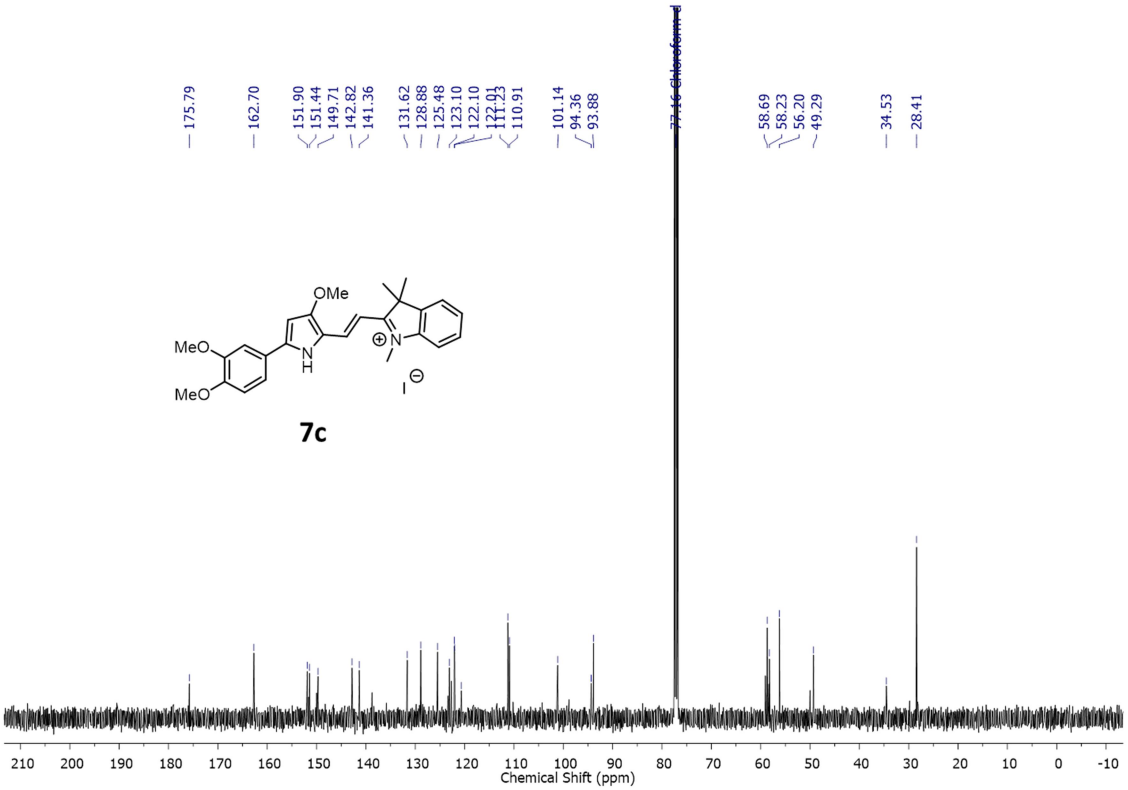


**Figure C59:** $^{13}$C spectrum of compound **7c**

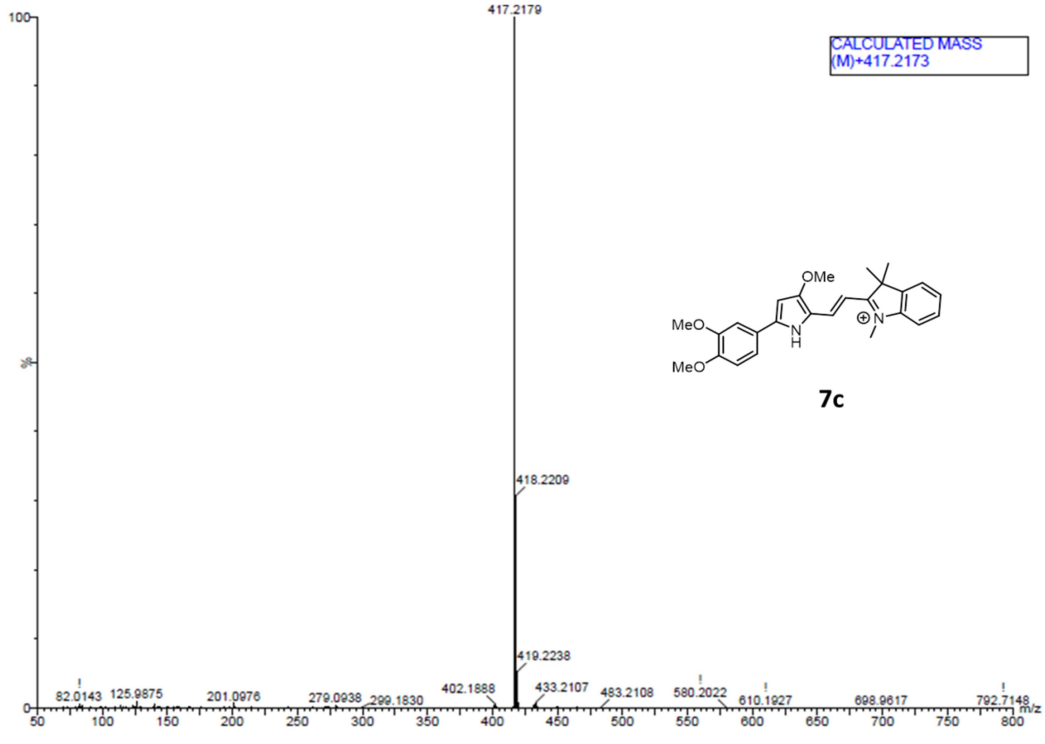


**Figure C60:** HRMS spectrum of compound **7c**

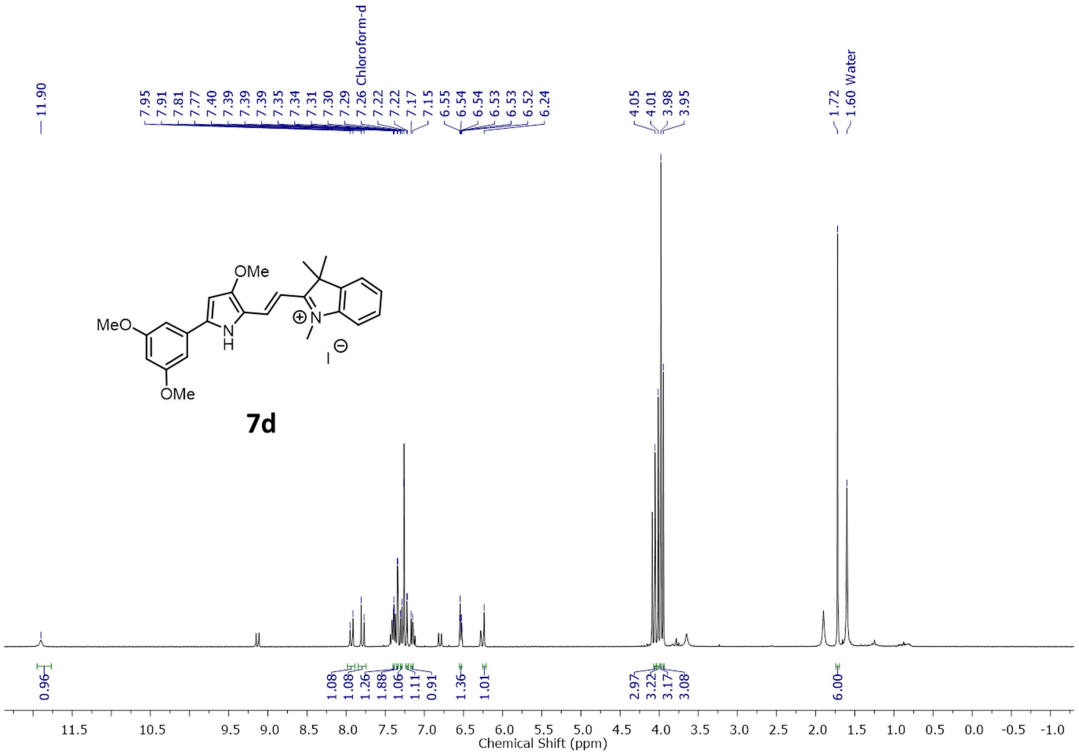


**Figure C61:** $^{1}$H spectrum of compound **7d**

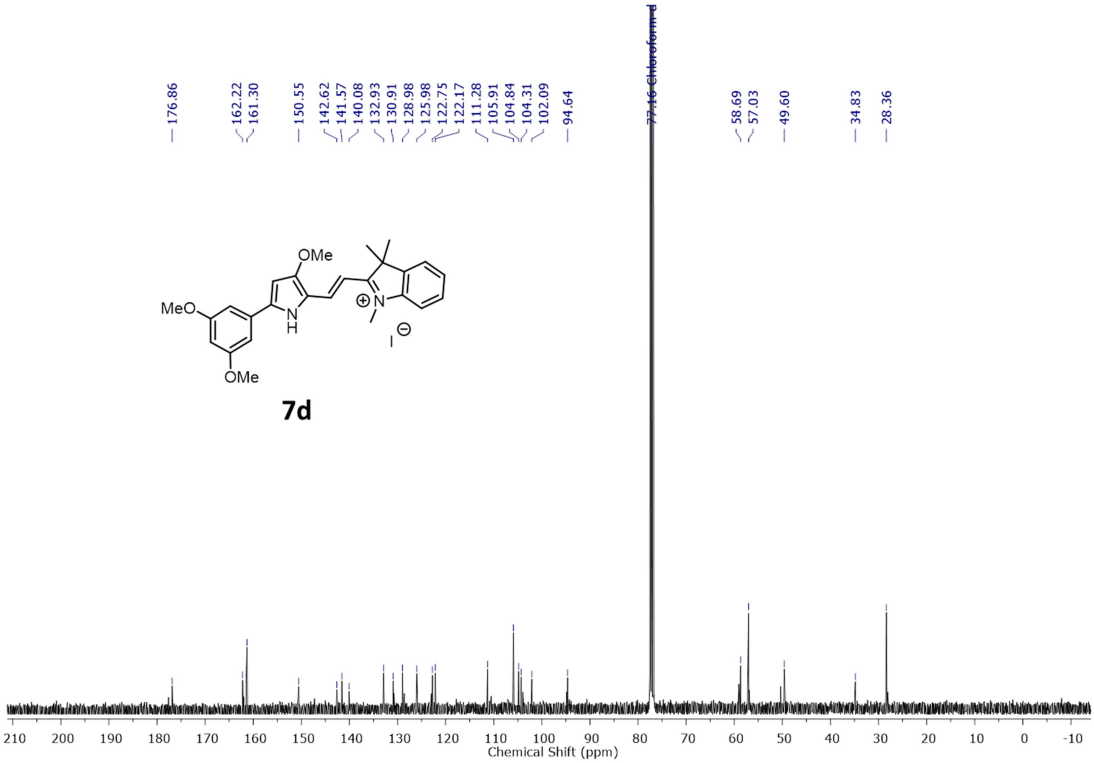


**Figure C62:** $^{13}$C spectrum of compound **7d**

**Table C1:** Crystal data and structure refinement of compound **7d**

| CCDC number | 1902482 |
|---|---|
| Chemical formula | $C_{28}H_{30}Cl_6IN_2O_3$ |
| *M*r | 782.14 |
| Crystal system, space group | Monoclinic, *P*21/*n* |
| Temperature (K) | 296 |
| *a*, *b*, *c* (Å) | 21.713 (6), 7.4052 (17), 23.035 (6) |
| β (°) | 116.924 (7) |
| *V* (Å$^3$) | 3302.3 (14) |
| *Z* | 4 |
| Radiation type | Mo *K*α |
| μ (mm$^{-1}$) | 1.49 |
| Crystal size (mm) | 0.06 × 0.05 × 0.04 |
| Data collection | |
| Diffractometer | Bruker *APEX*-II CCD |
| Absorption correction | none |
| No. of measured, independent and observed [$I > 2\sigma(I)$] reflections | 51781, 5843, 4407 |
| $R_{int}$ | 0.109 |
| $(\sin\theta/\lambda)_{max}$ (Å$^{-1}$) | 0.597 |
| Refinement | |
| $R[F^2 > 2\sigma(F^2)]$, $wR(F^2)$, $S$ | 0.056, 0.112, 1.14 |
| No. of reflections | 5843 |
| No. of parameters | 367 |
| H-atom treatment | H-atom parameters constrained<br>$w = 1/[\sigma^2(F_o^2) + (0.0078P)^2 + 24.8341P]$<br>where $P = (F_o^2 + 2Fc^2)/3$ |
| $\Delta\rho_{max}$, $\Delta\rho_{min}$ (e Å$^{-3}$) | 1.19, −0.92 |

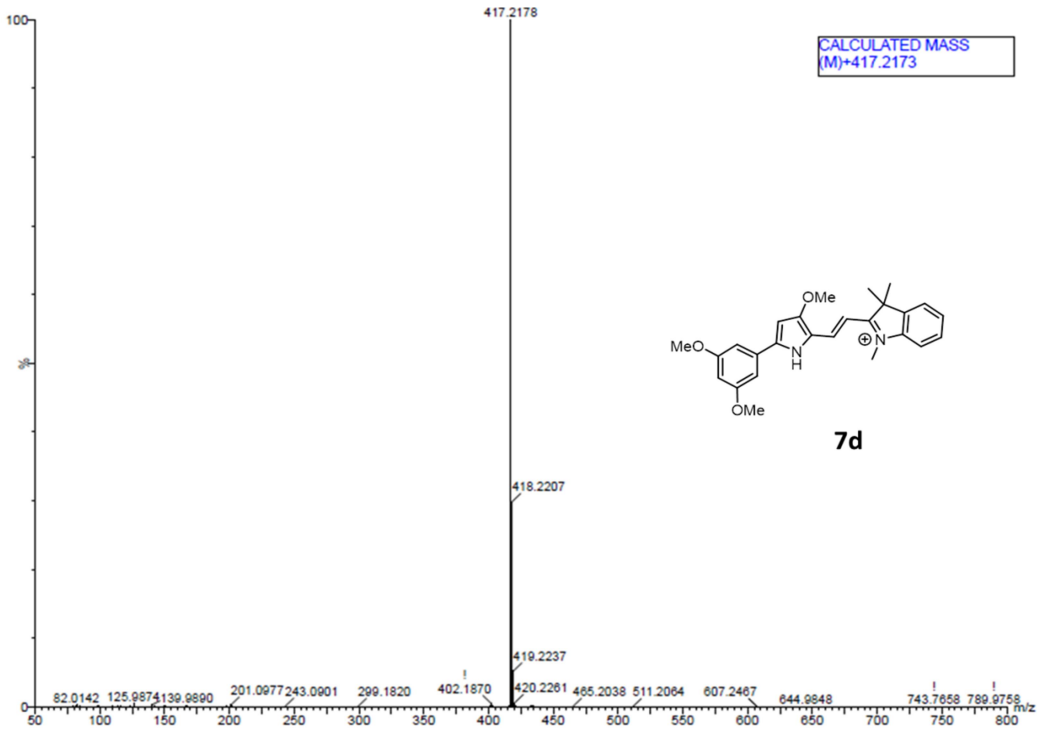


**Figure C63:** HRMS spectrum of compound **7d**

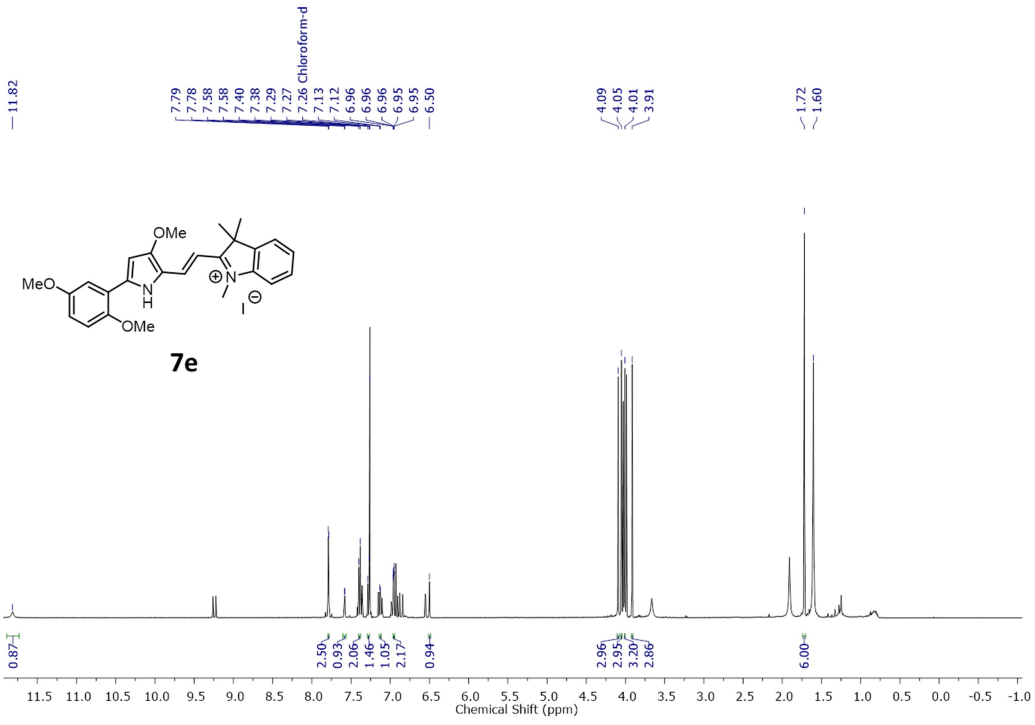


**Figure C64:** $^{1}$H spectrum of compound **7e**

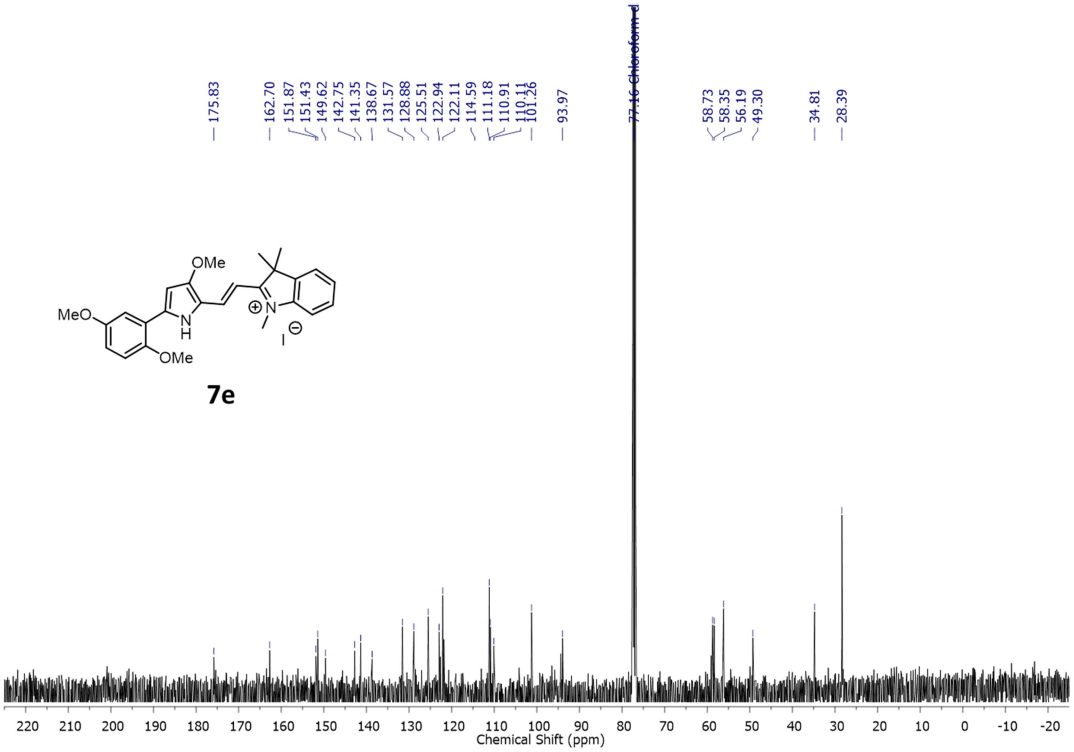


**Figure C65:** $^{13}$C spectrum of compound **7e**

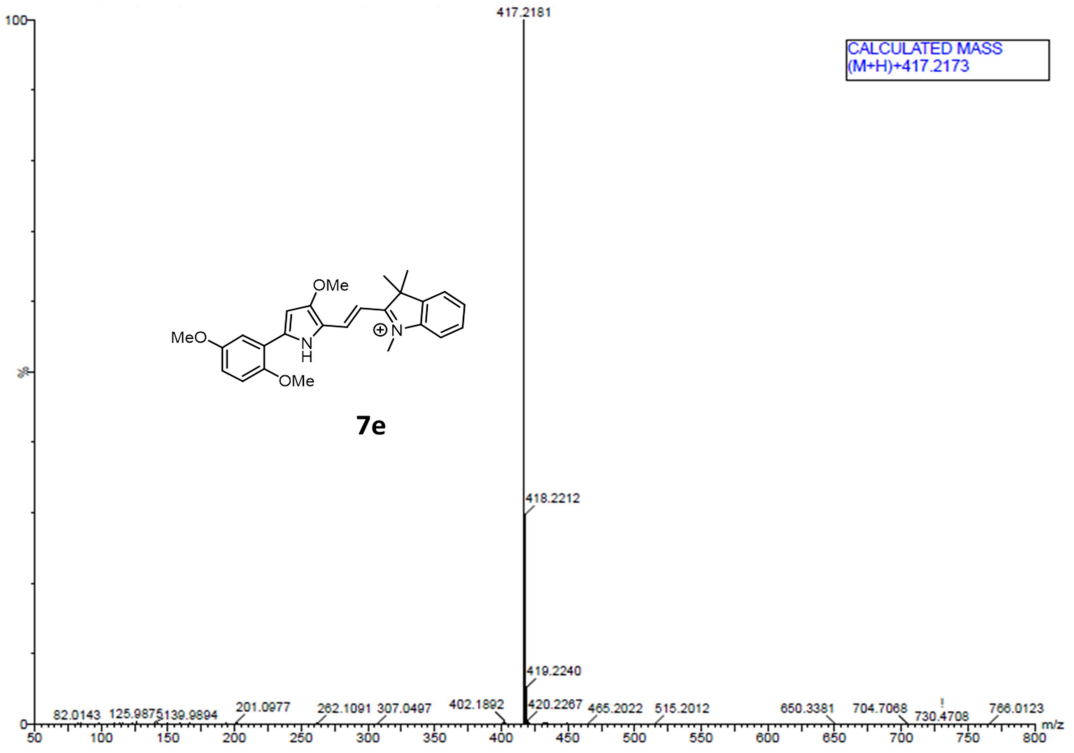


**Figure C66:** HRMS spectrum of compound **7e**

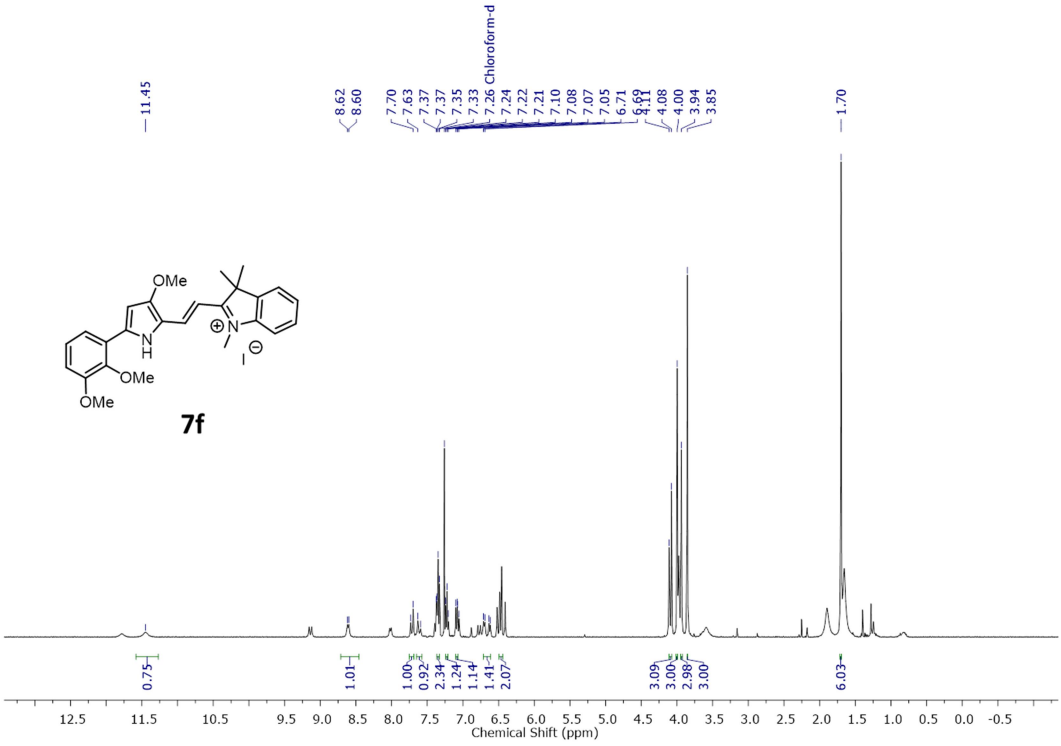


**Figure C67:** $^{1}$H spectrum of compound **7f**

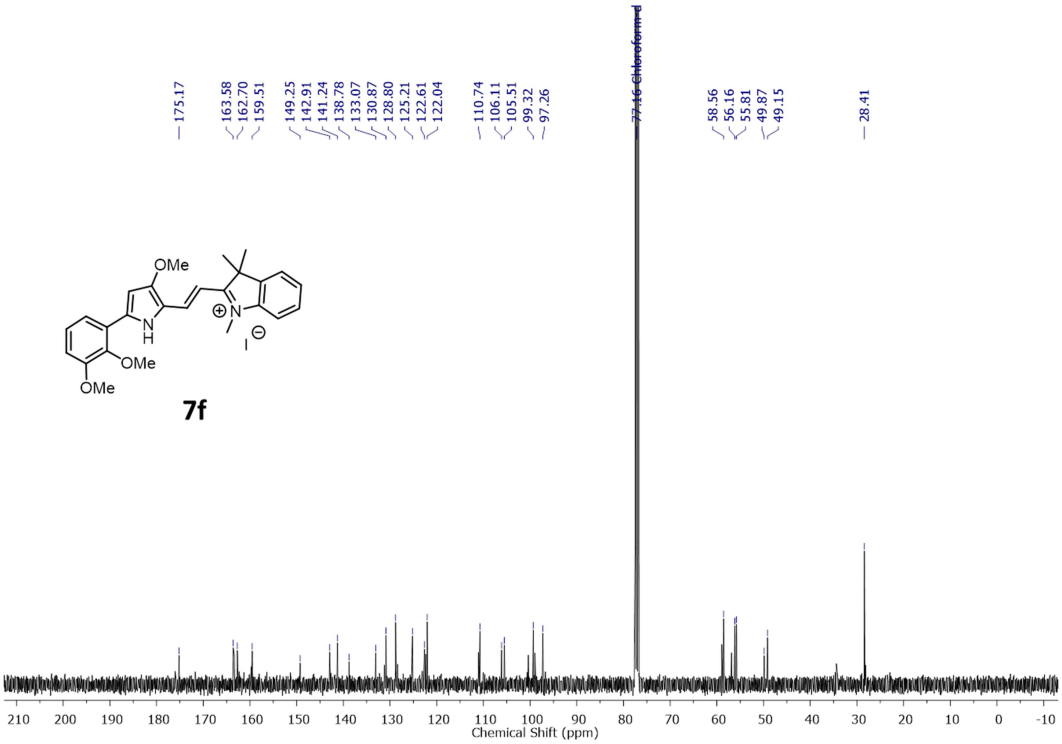


**Figure C68:** $^{13}$C spectrum of compound **7f**

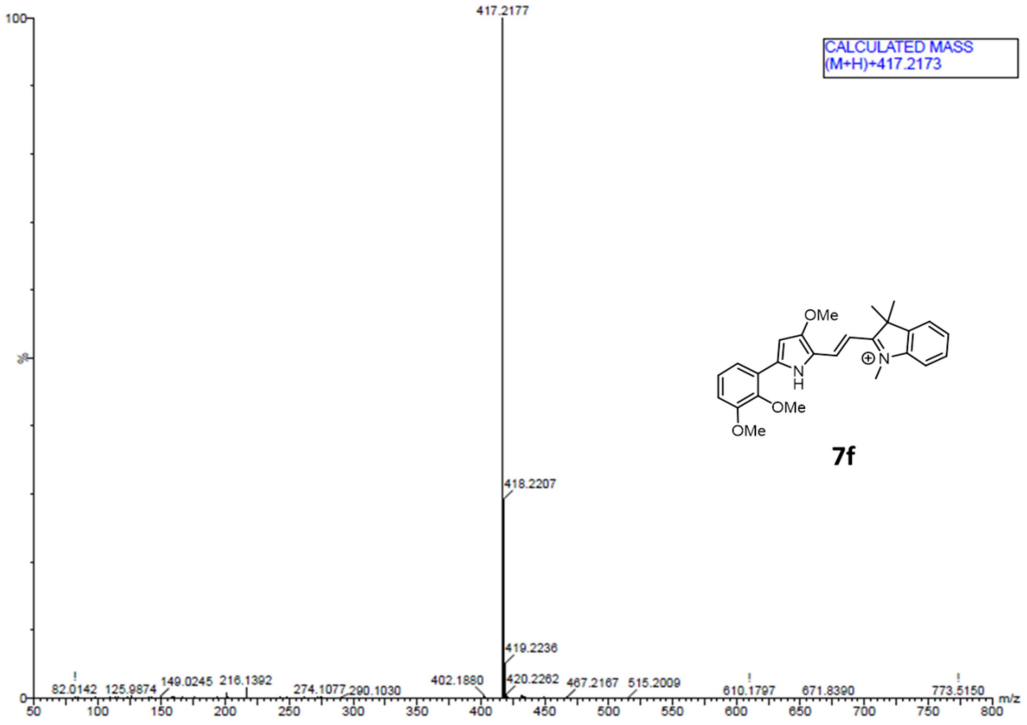


**Figure C69:** HRMS spectrum of compound **7f**

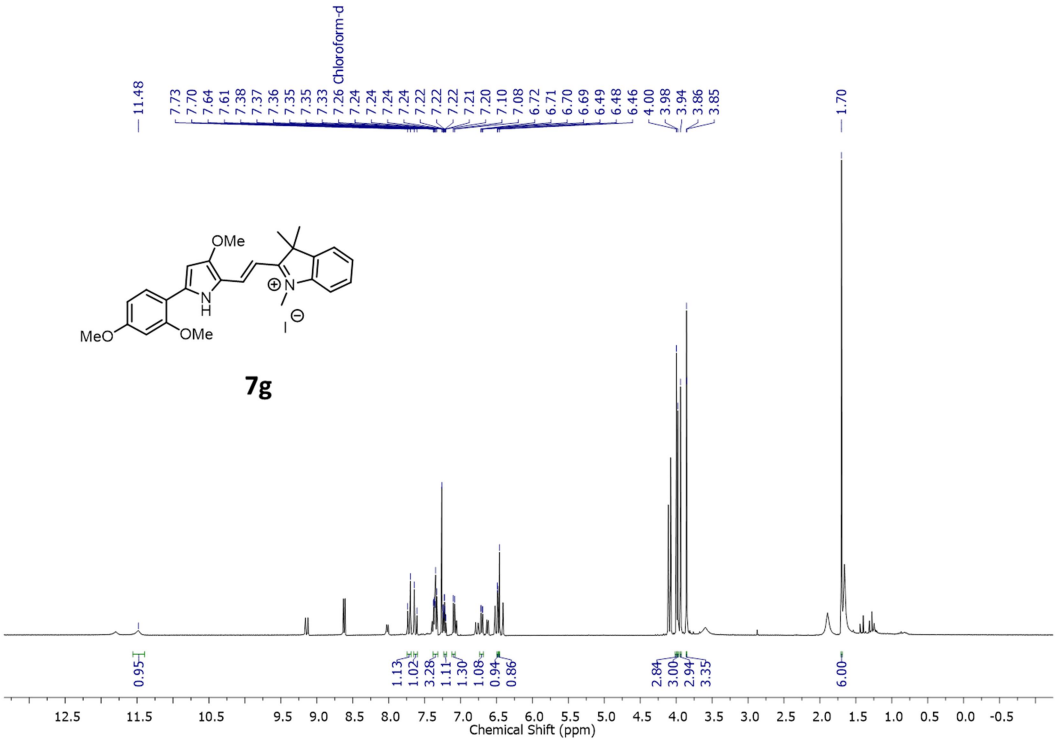


**Figure C70:** $^{1}$H spectrum of compound **7g**

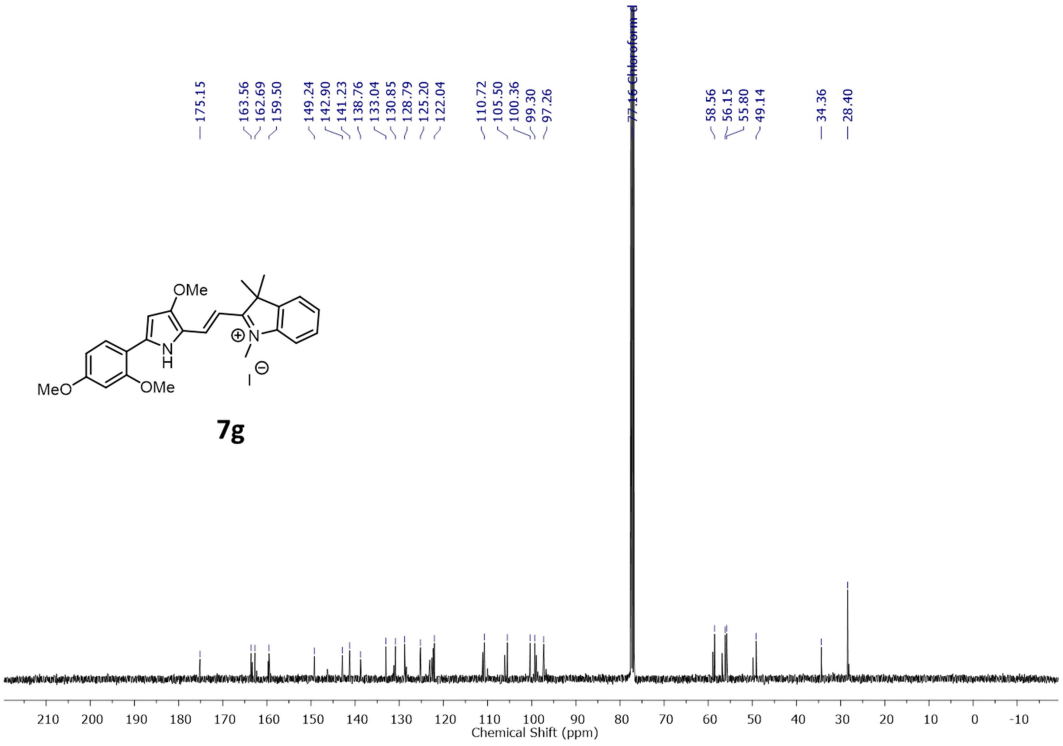


**Figure C71:** $^{13}$C spectrum of compound **7g**

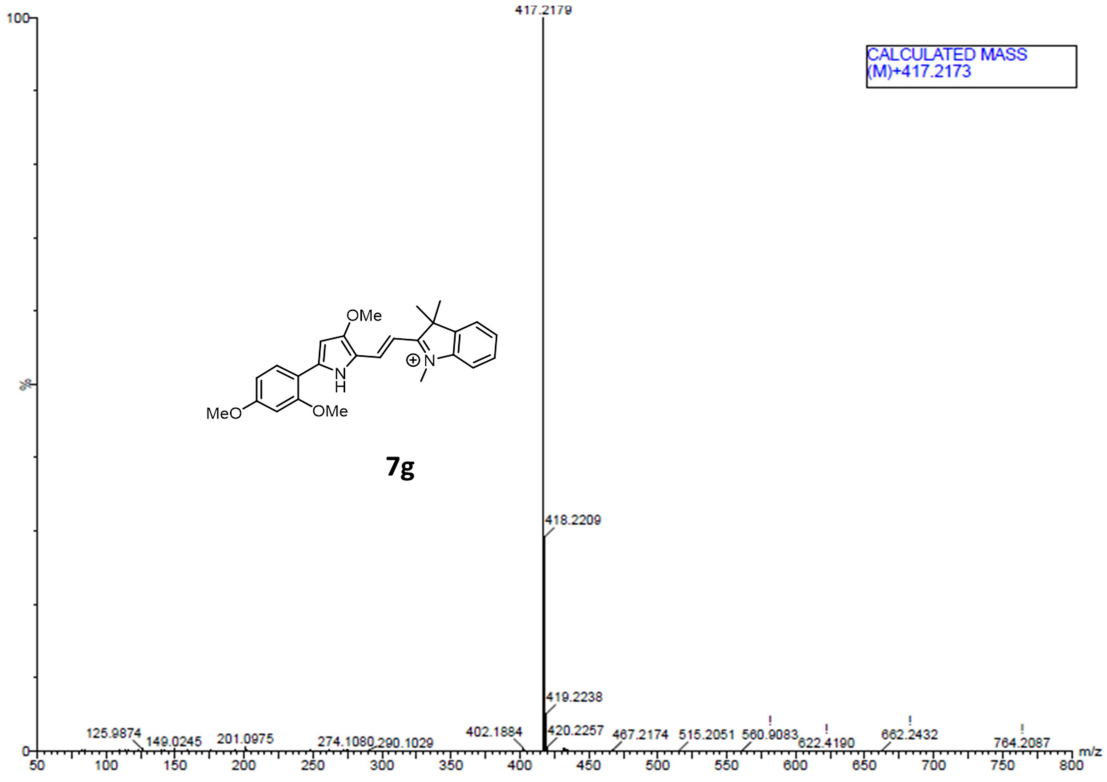


**Figure C72:** HRMS spectrum of compound **7g**

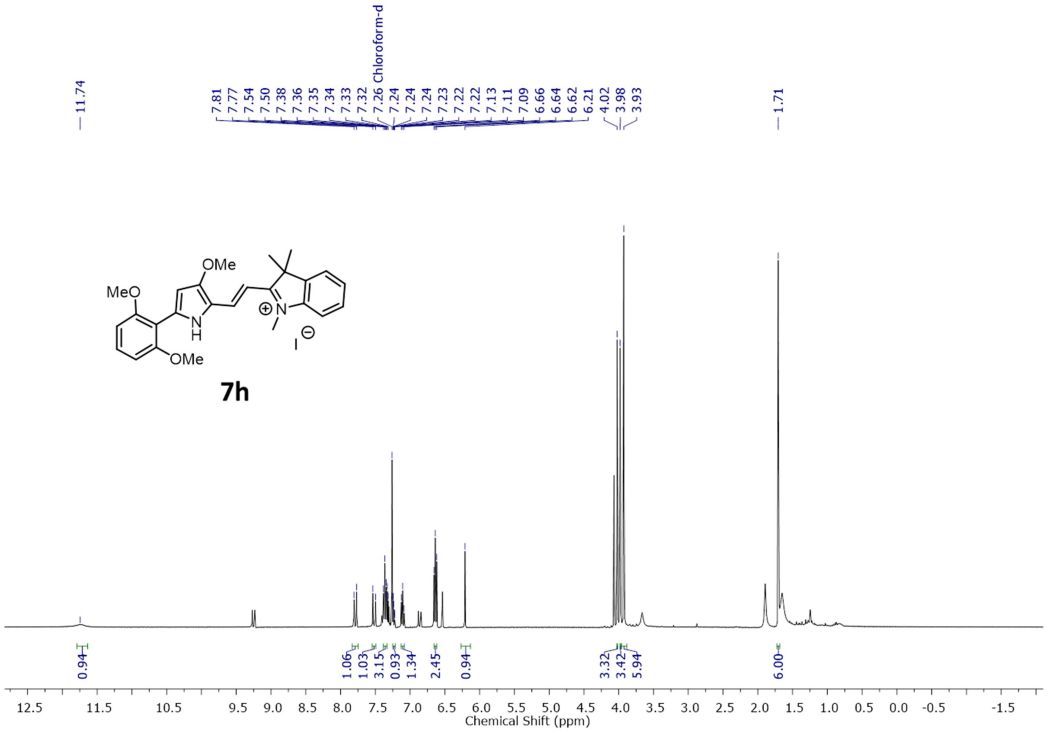


**Figure C73:** $^{1}$H spectrum of compound **7h**

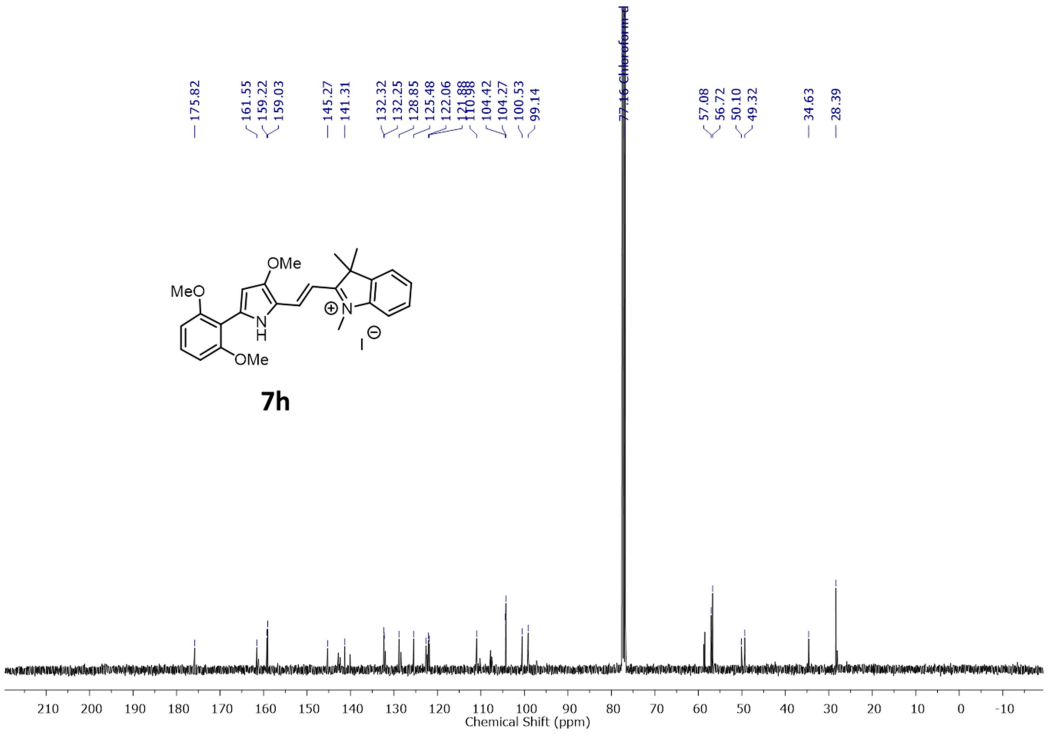


**Figure C74:** $^{13}$C spectrum of compound **7h**

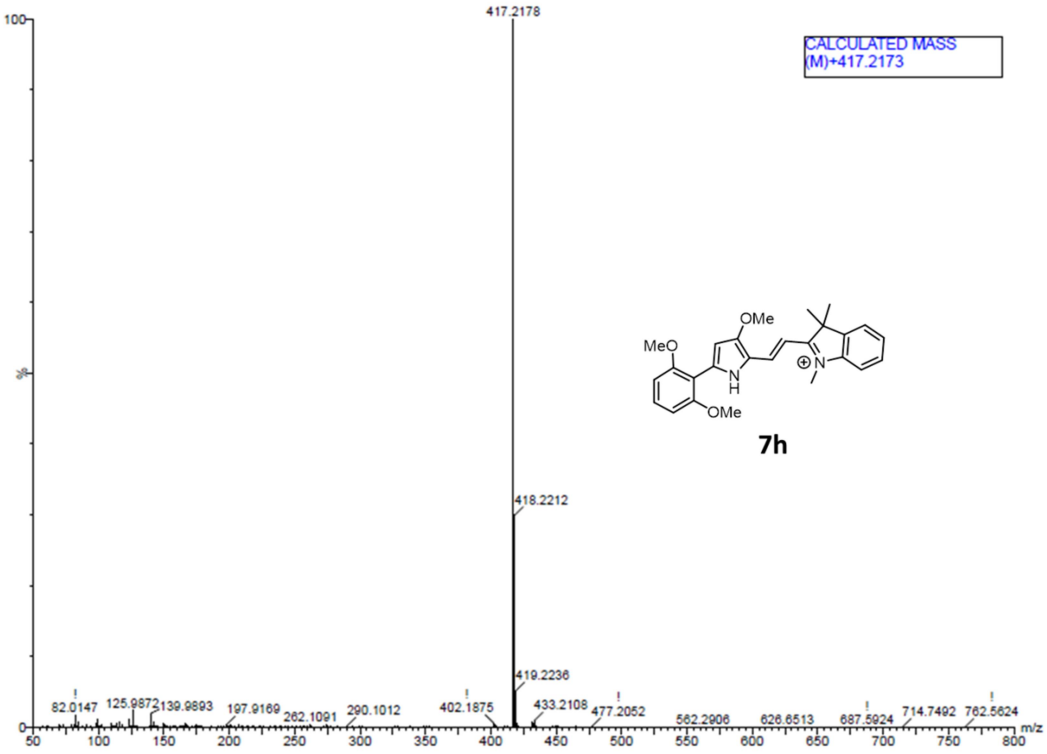


**Figure C75:** HRMS spectrum of compound **7h**

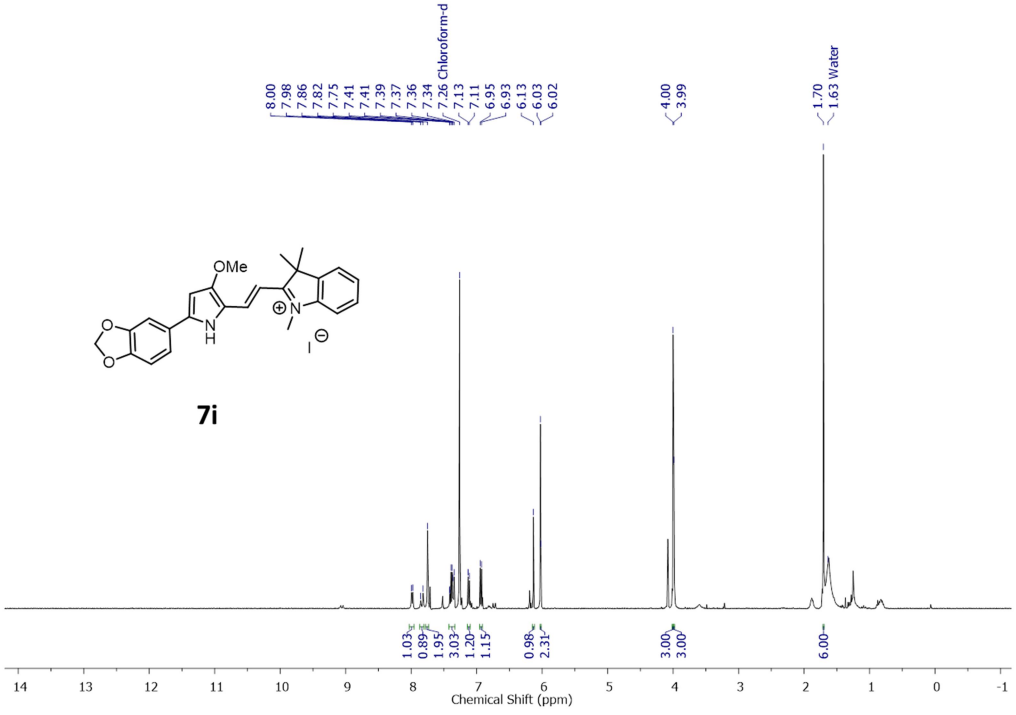


**Figure C76:** $^{1}$H spectrum of compound **7i**

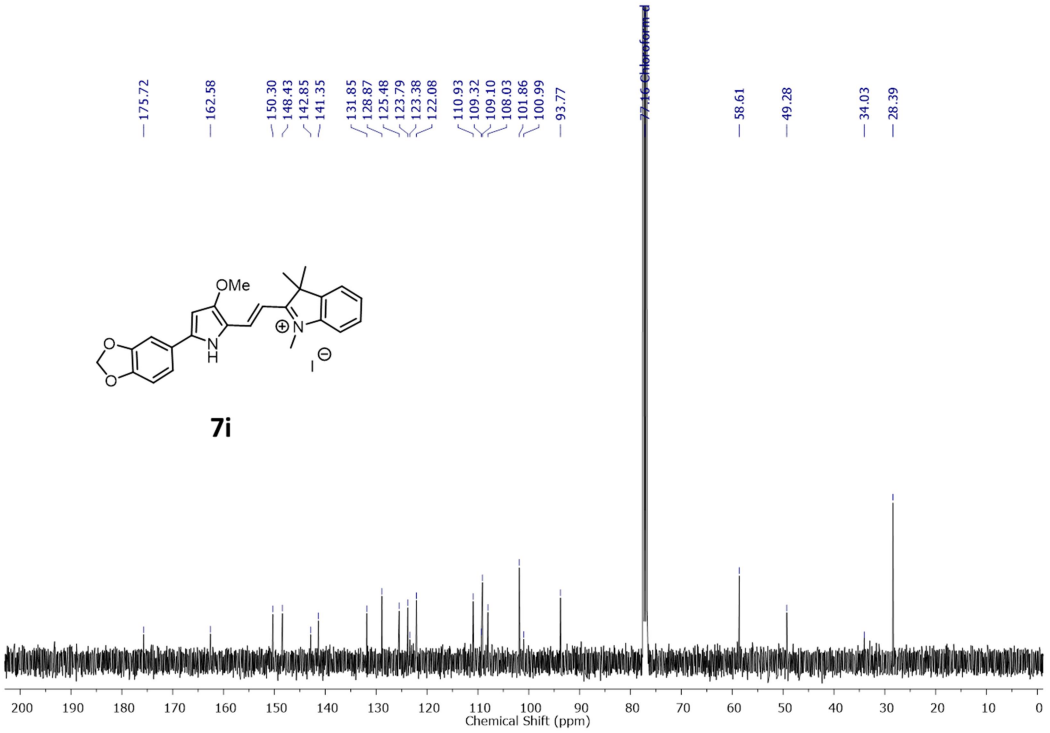


**Figure C77:** $^{13}$C spectrum of compound **7i**

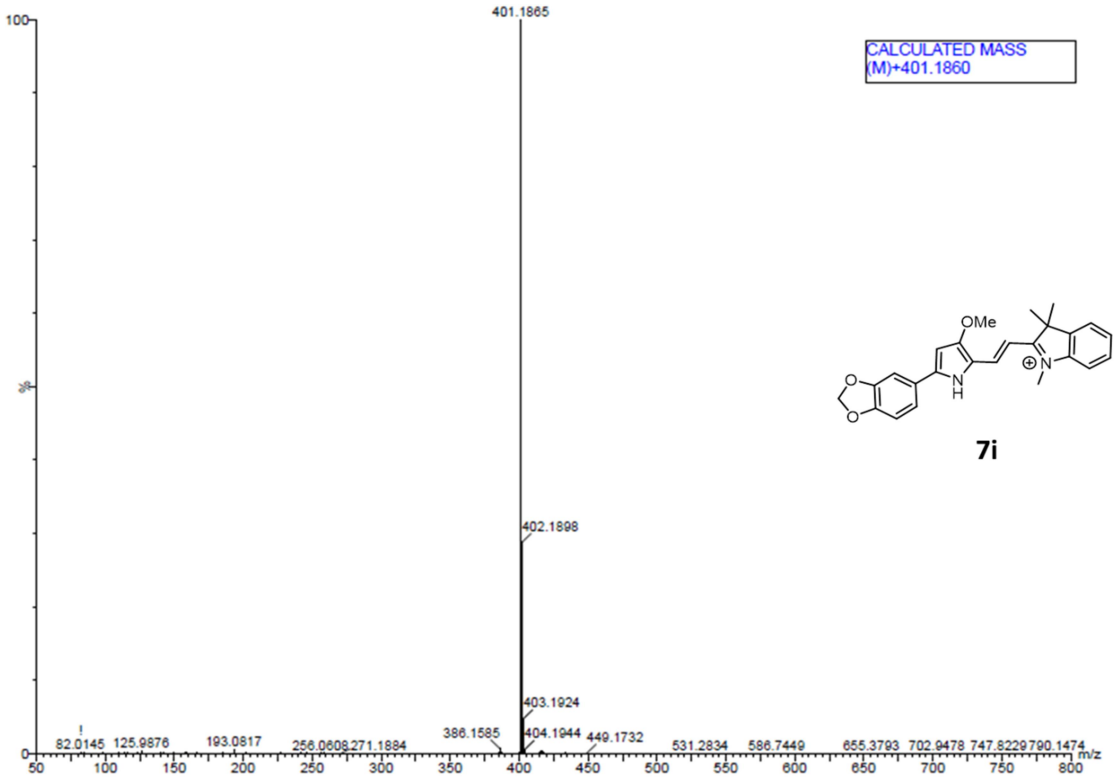


**Figure C78:** HRMS spectrum of compound **7i**

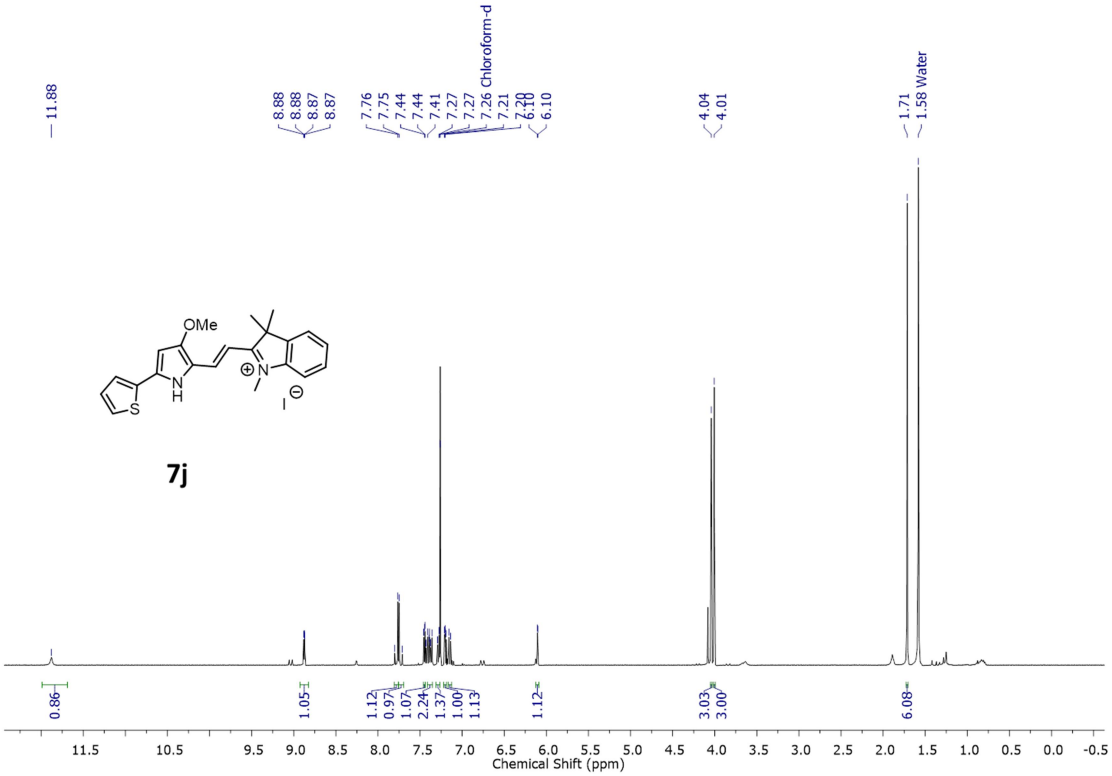


**Figure C79:** $^{1}$H spectrum of compound **7j**

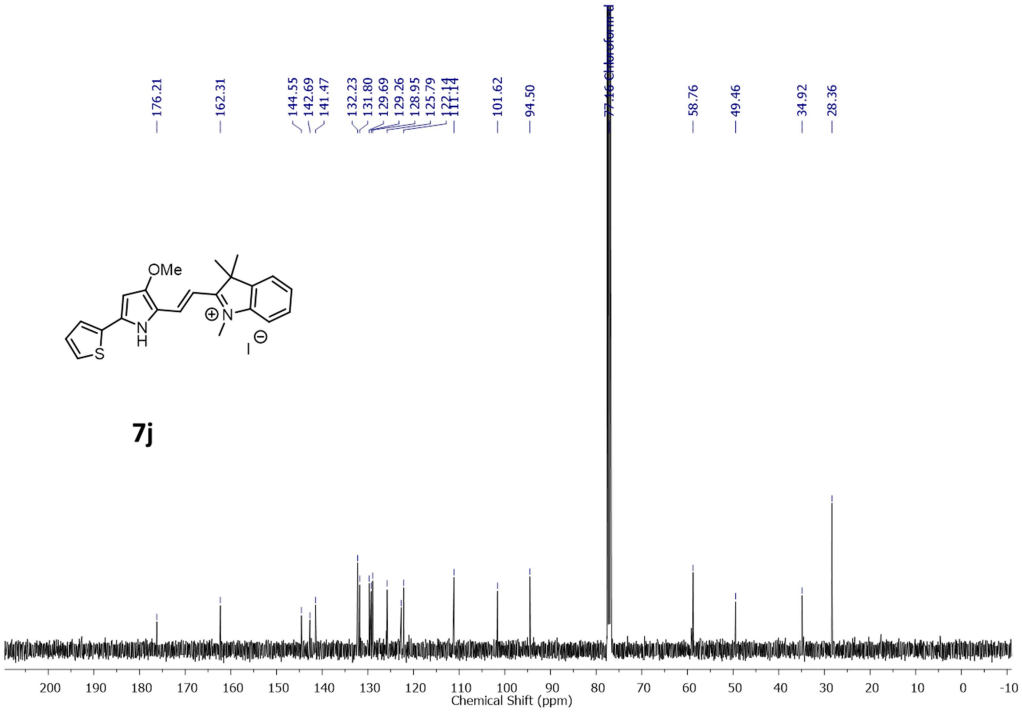


**Figure C80:** $^{13}$Cspectrum of compound **7j**

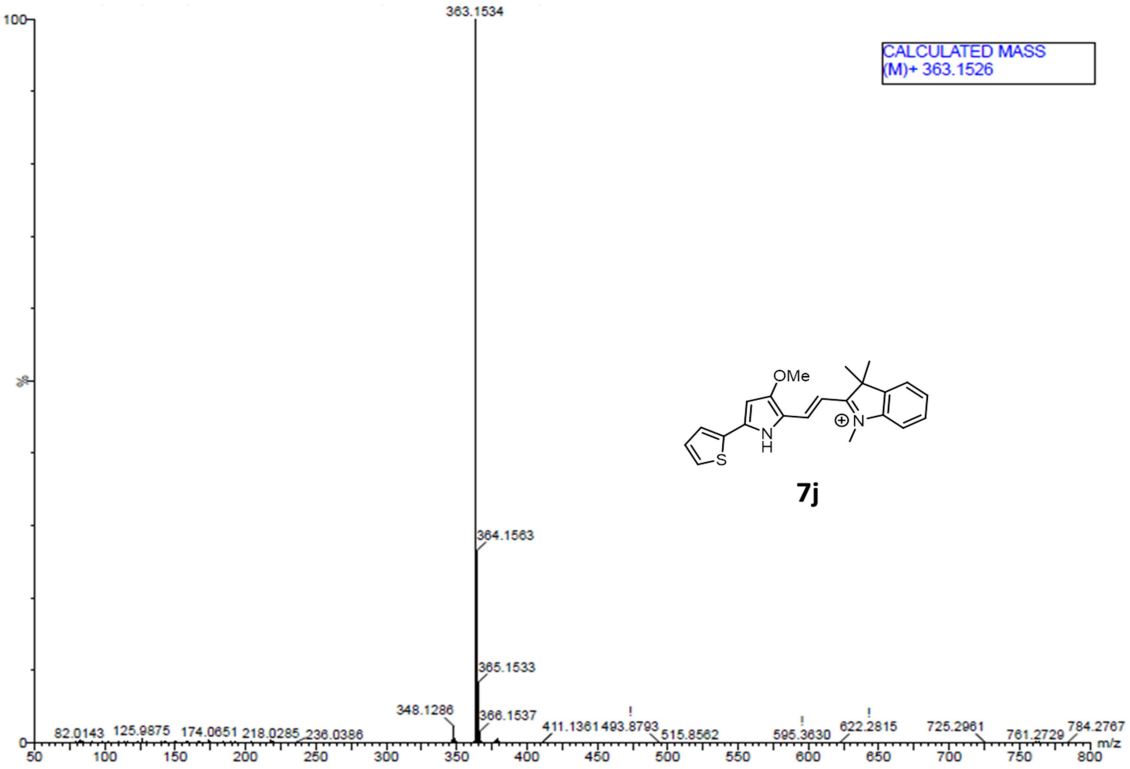


**Figure C81:** HRMS spectrum of compound **7j**

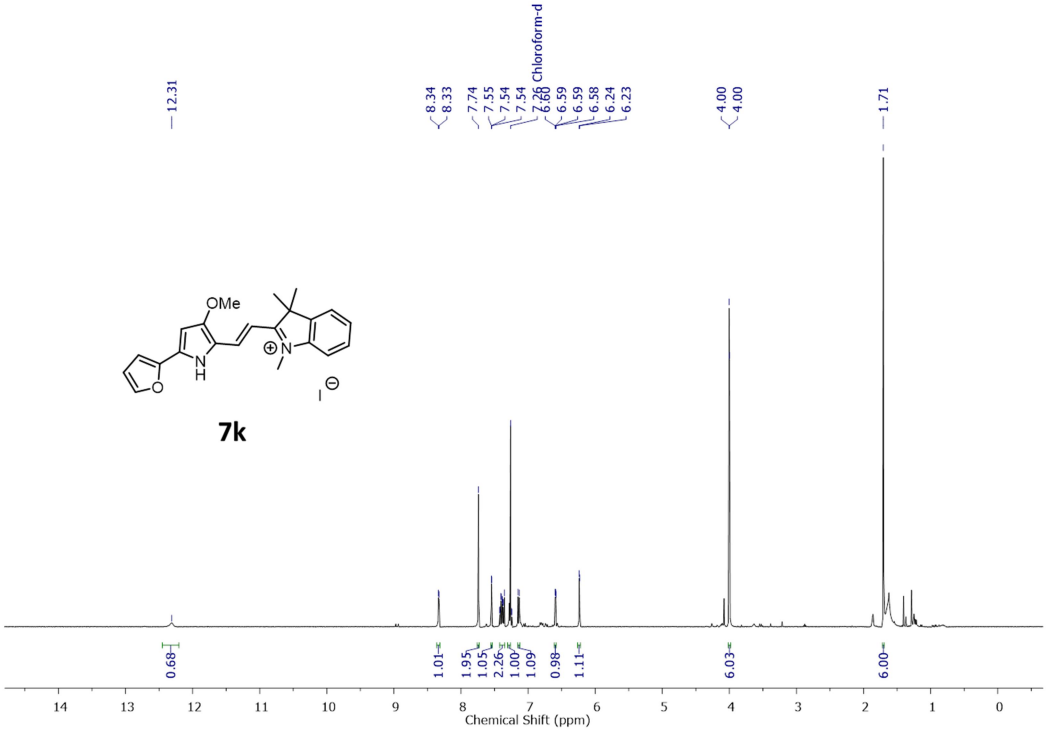


**Figure C82:** $^{1}$H spectrum of compound **7k**

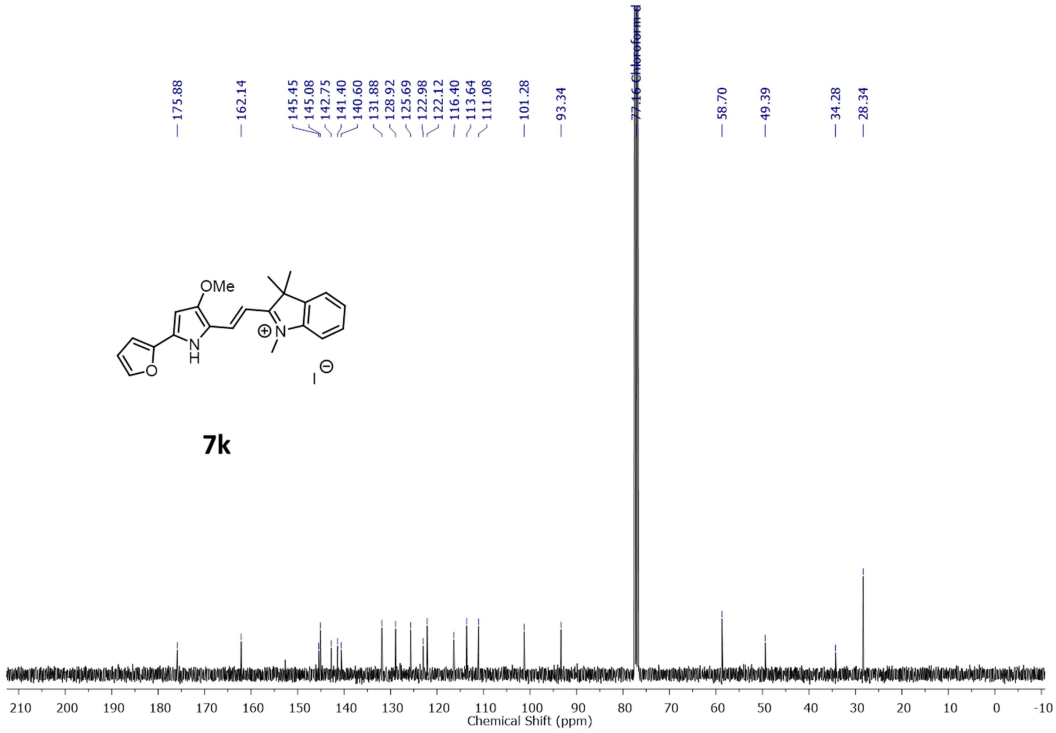


**Figure C83:** $^{13}C$ spectrum of compound **7k**

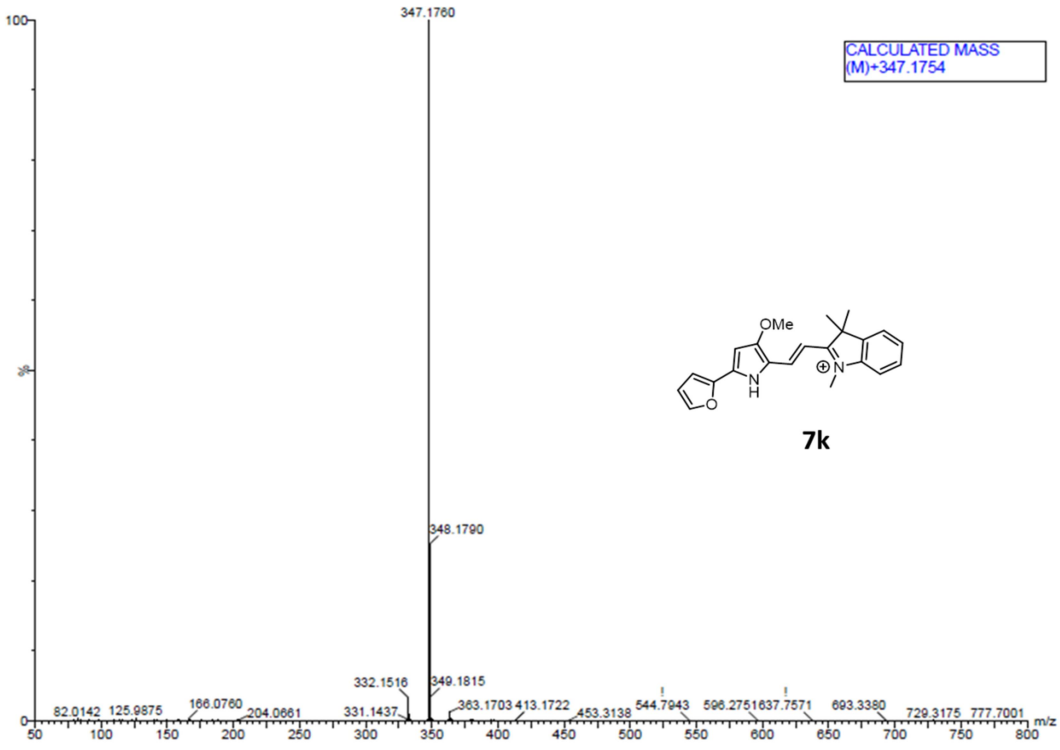


**Figure C84:** HRMS spectrum of compound **7k**

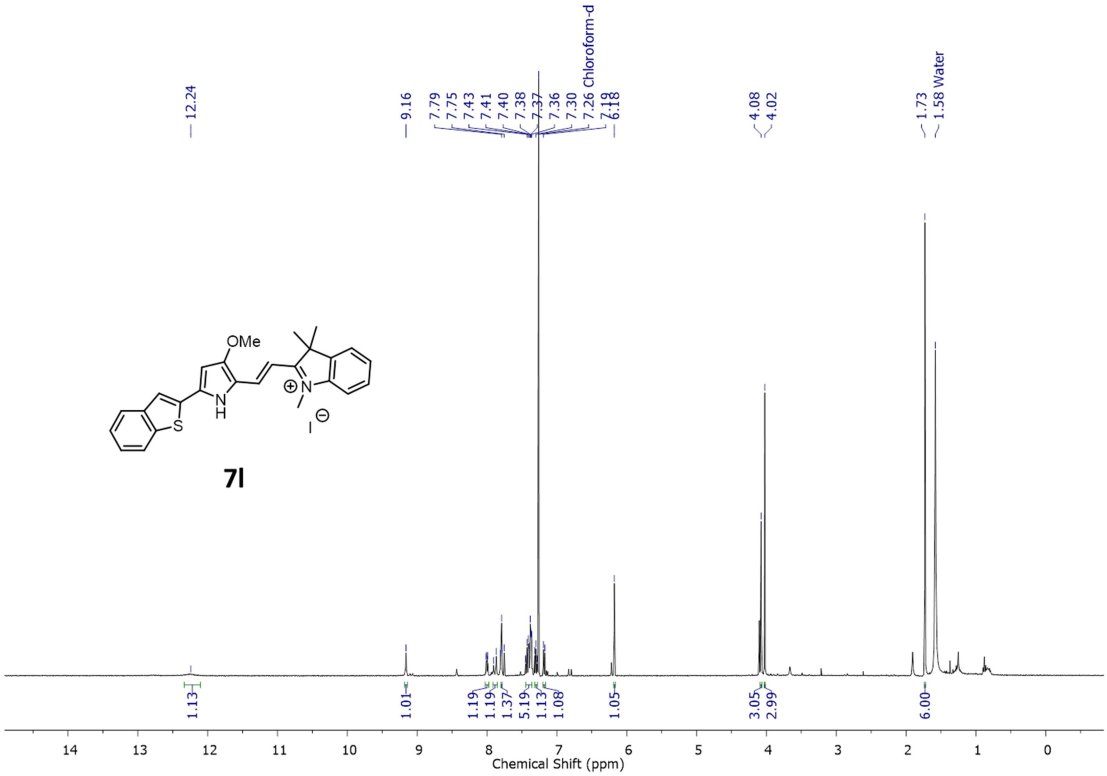


**Figure C85:** $^{1}$H spectrum of compound **7l**

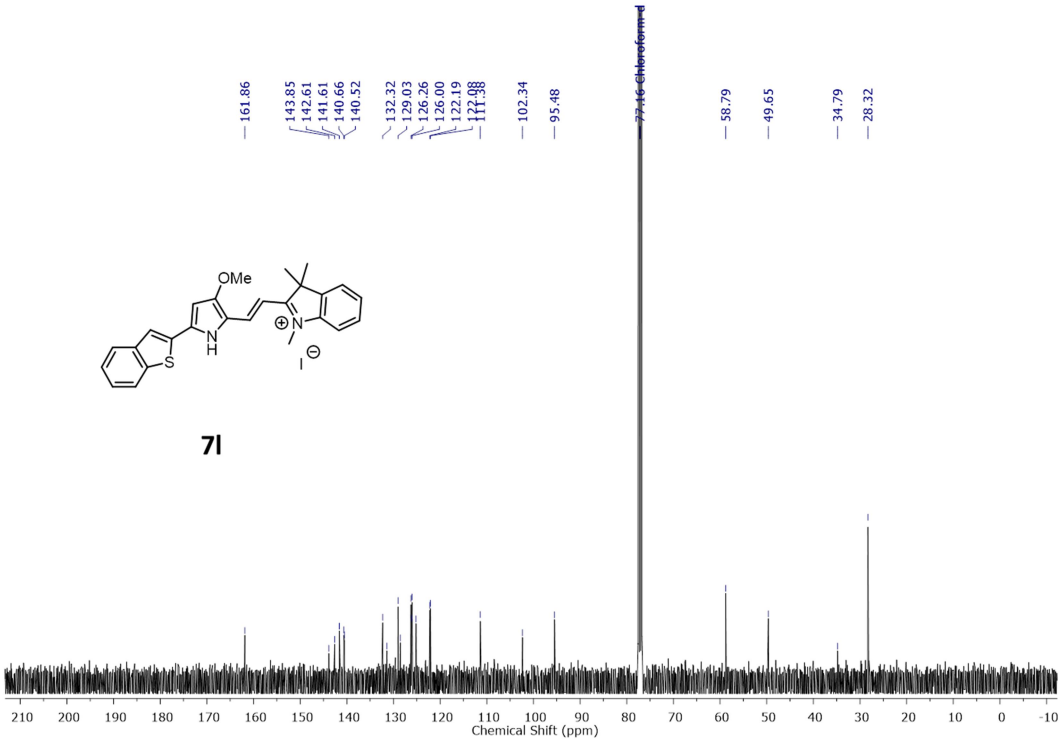


**Figure C86:** $^{13}$C spectrum of compound **7l**

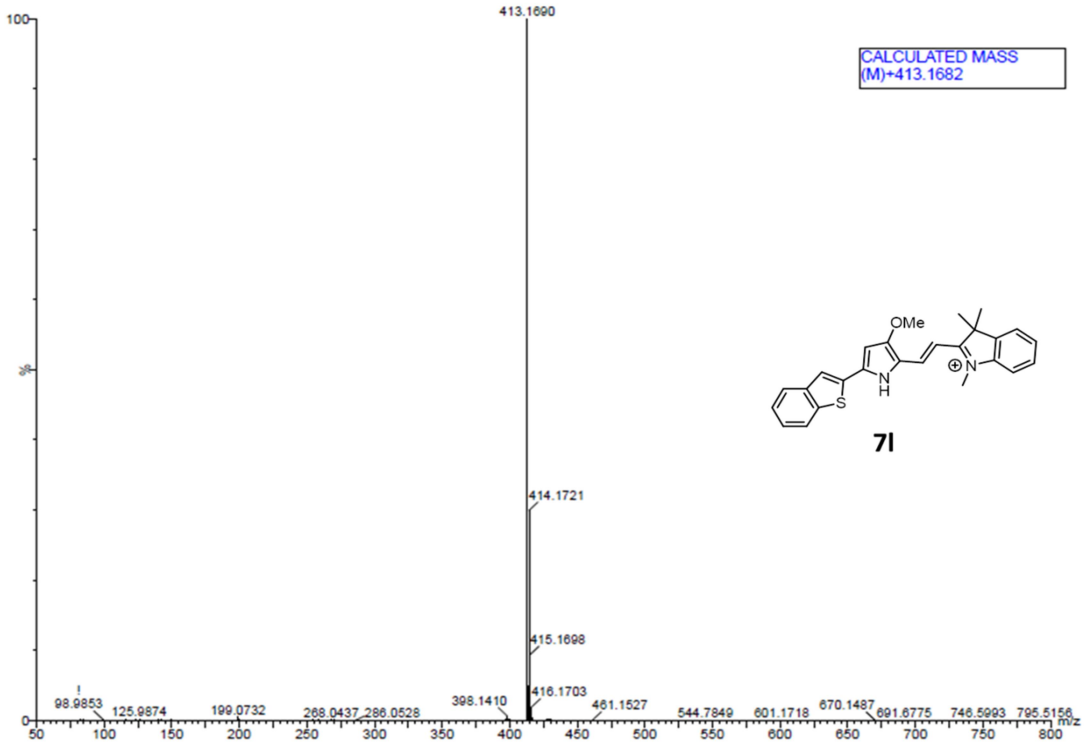


**Figure C87:** HRMS spectrum of compound **7l**

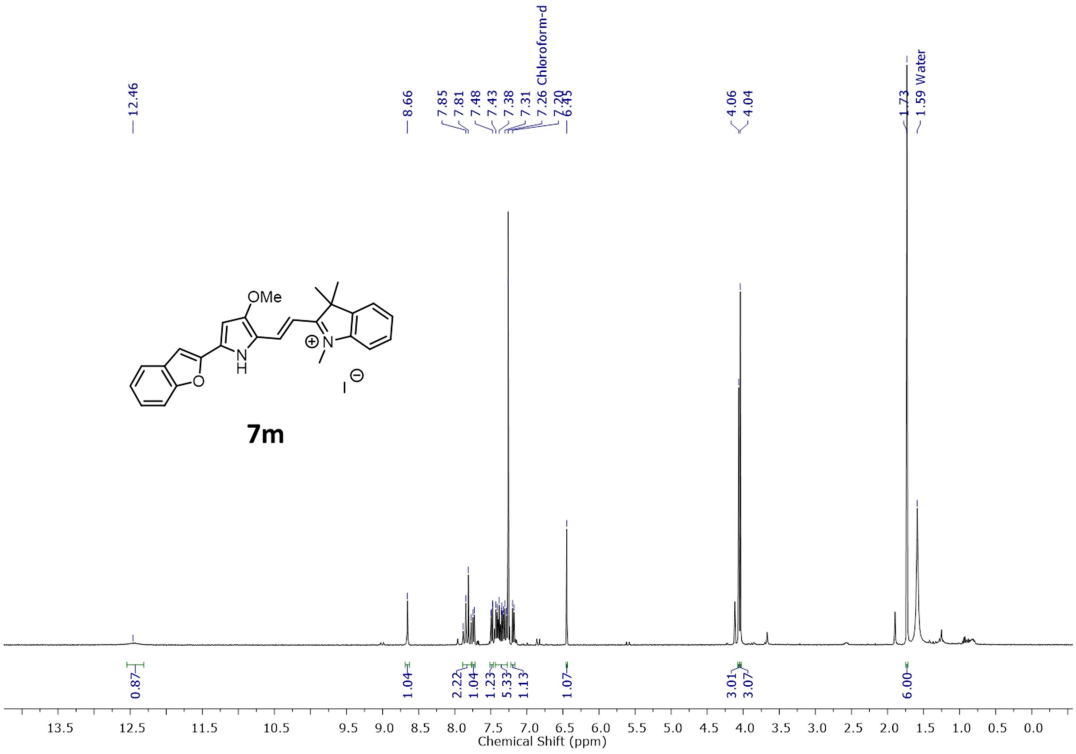


**Figure C88:** $^{1}$H spectrum of compound **7m**

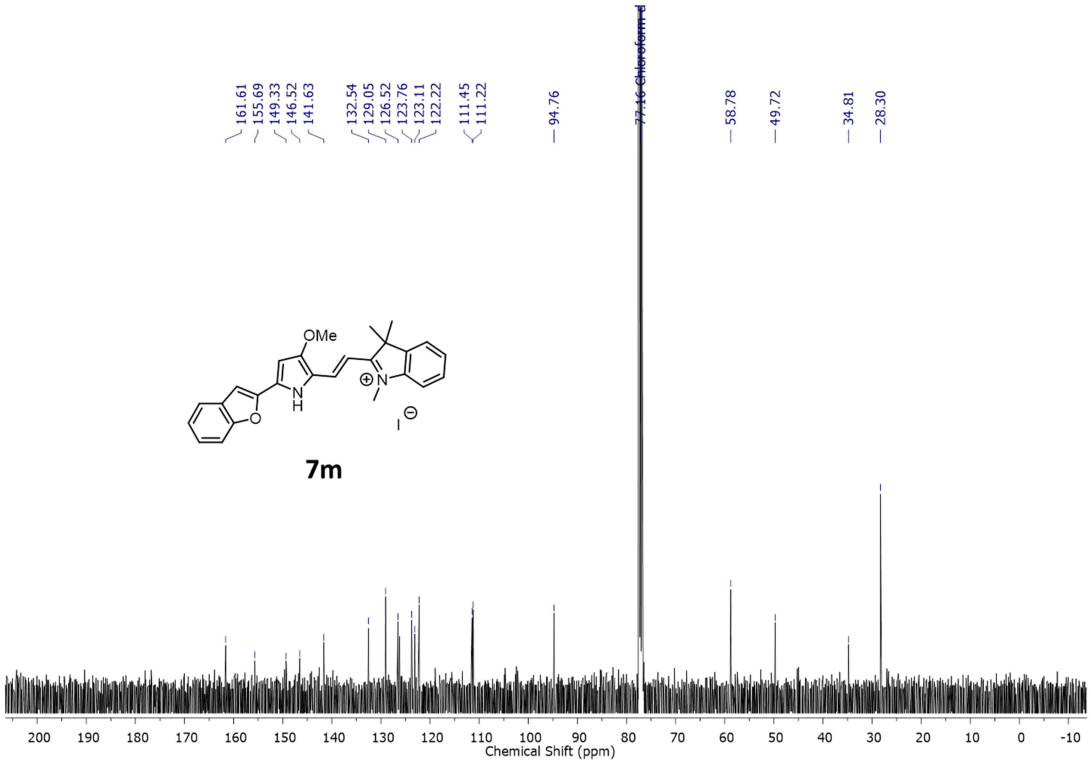


**Figure C89:** $^{13}$C spectrum of compound **7m**

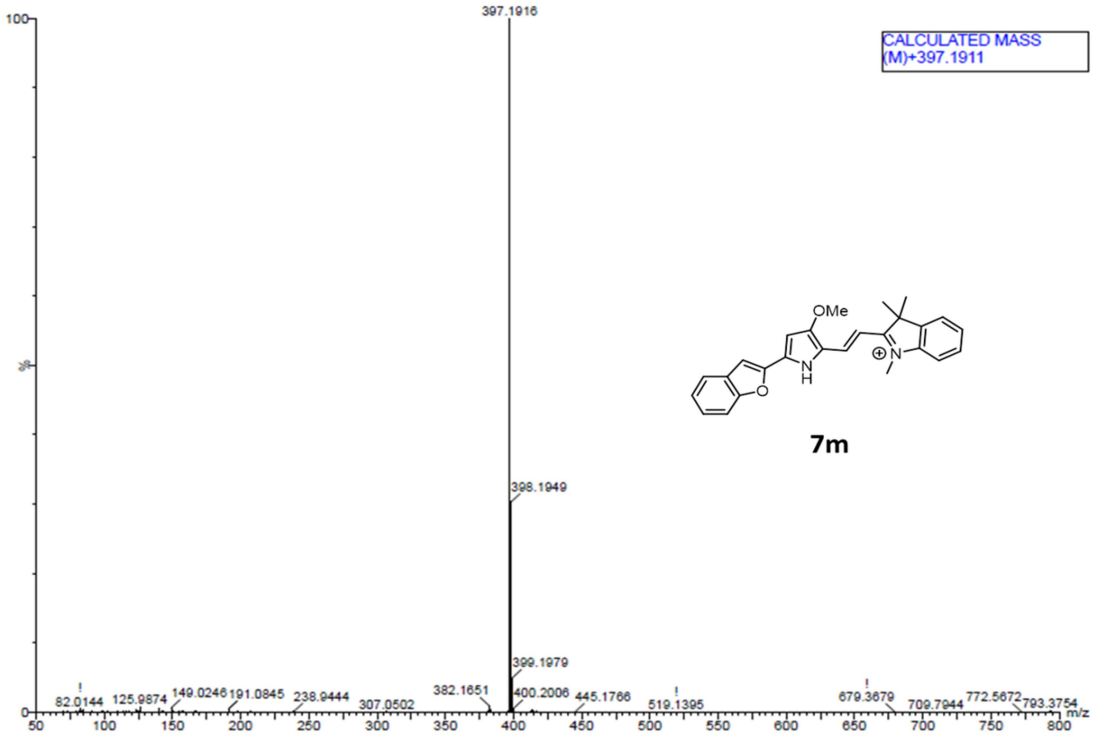


**Figure C90:** HRMS spectrum of compound **7m**

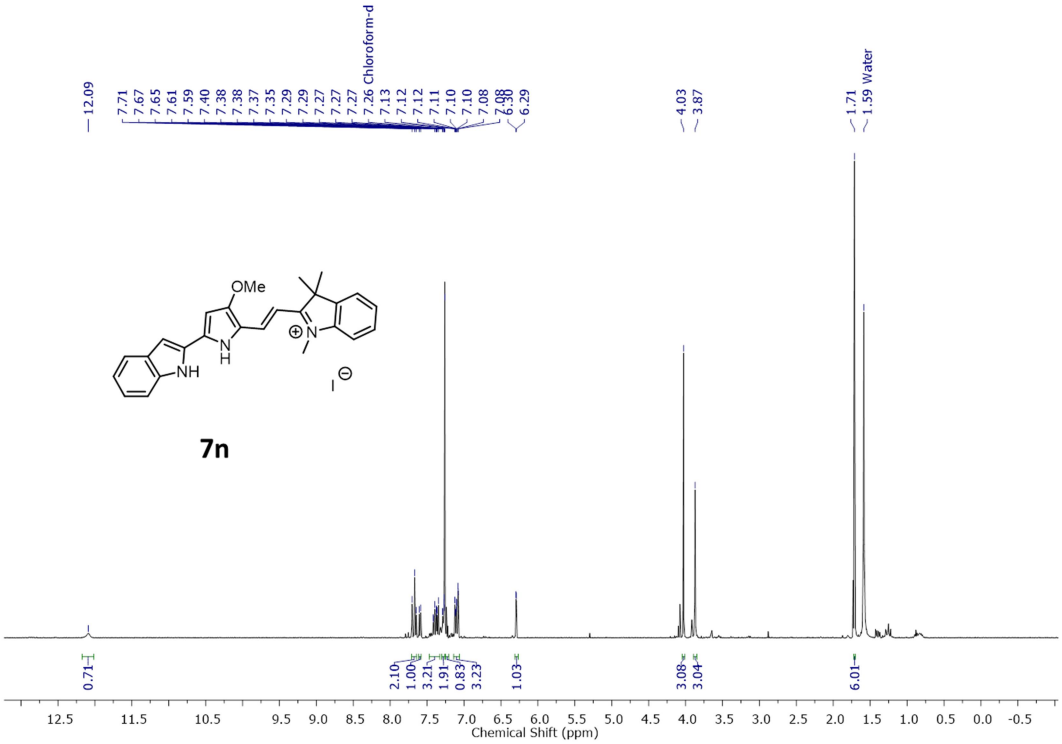


**Figure C91:** $^{1}$H spectrum of compound **7n**

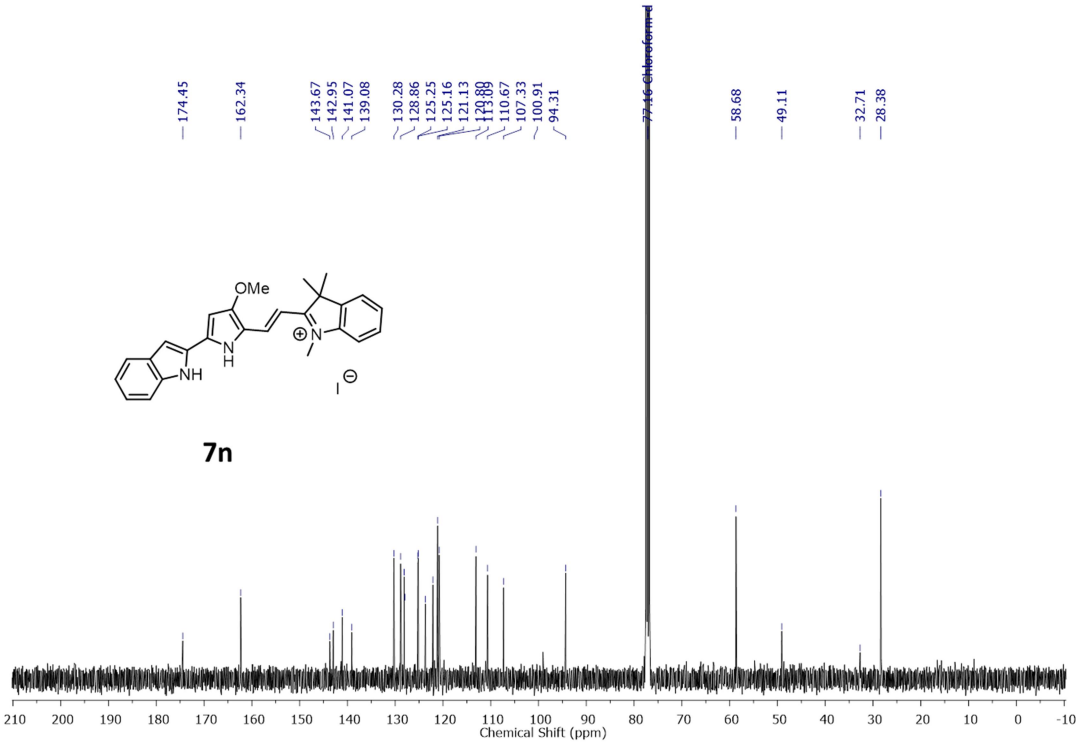


**Figure C92:** $^{13}$C spectrum of compound **7n**

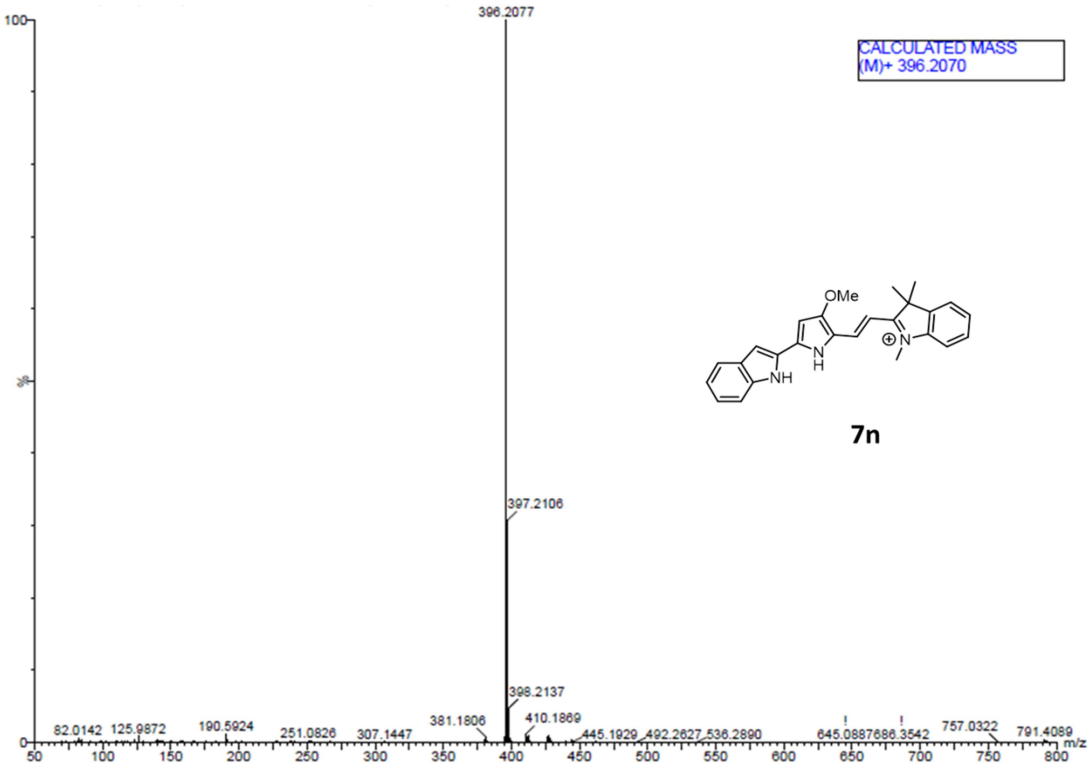


**Figure C93:** HRMS spectrum of compound **7n**

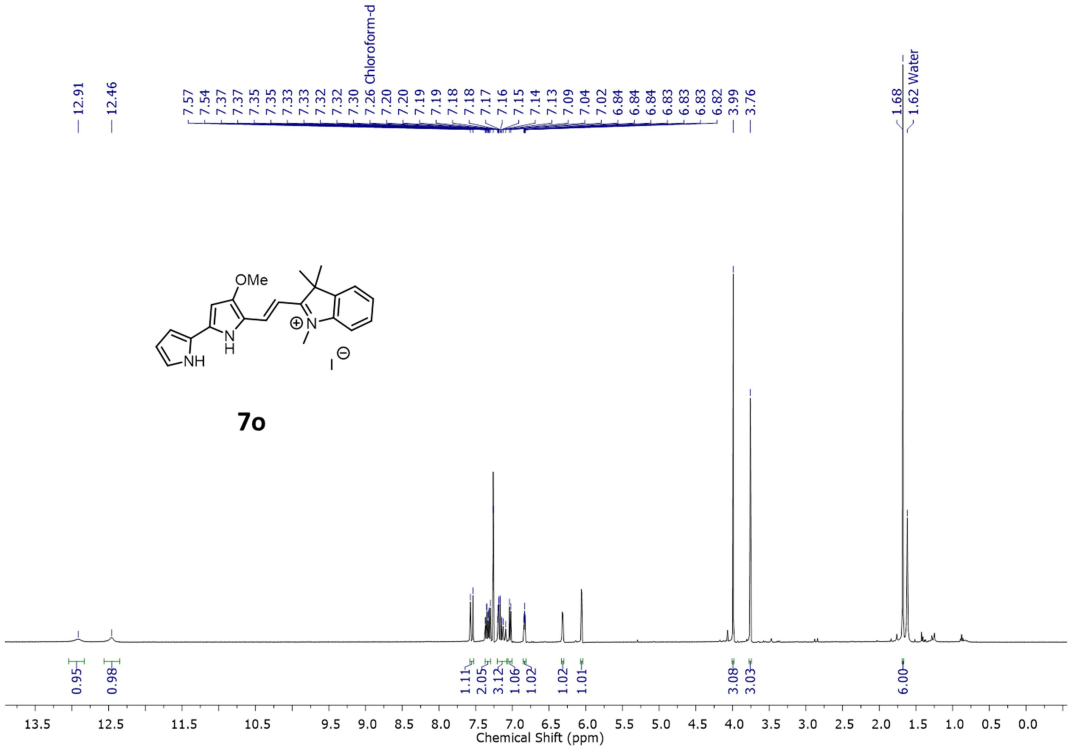


**Figure C94:** $^{1}$H spectrum of compound **7o**

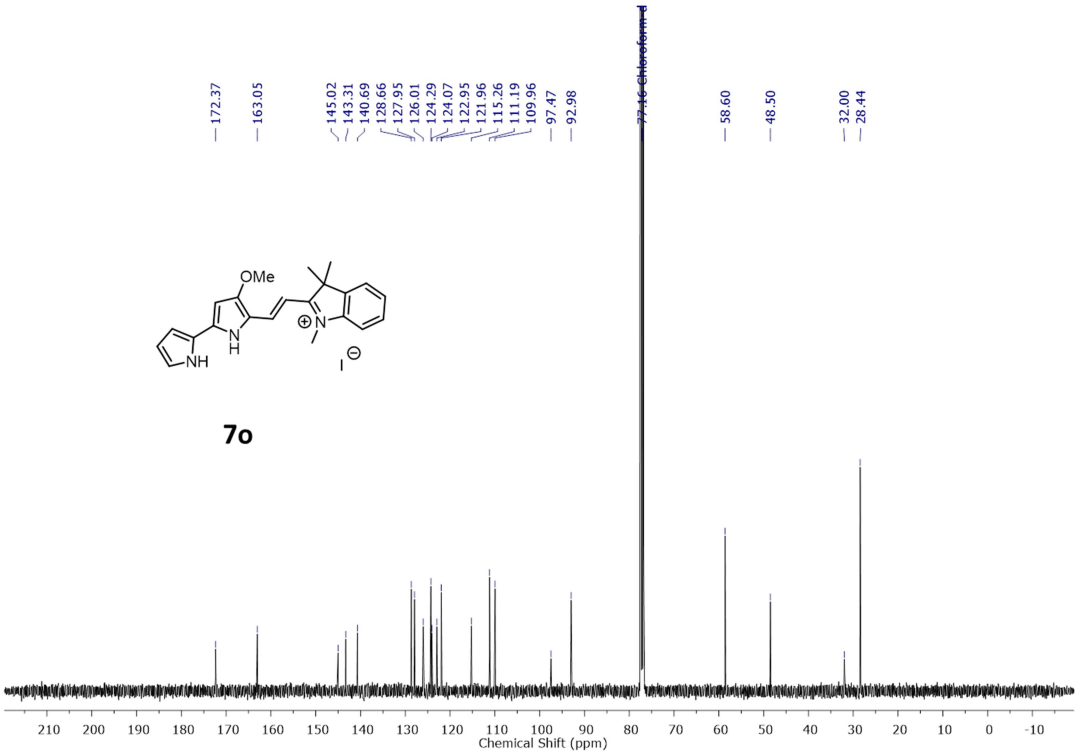


**Figure C95:** $^{13}C$ spectrum of compound **7o**

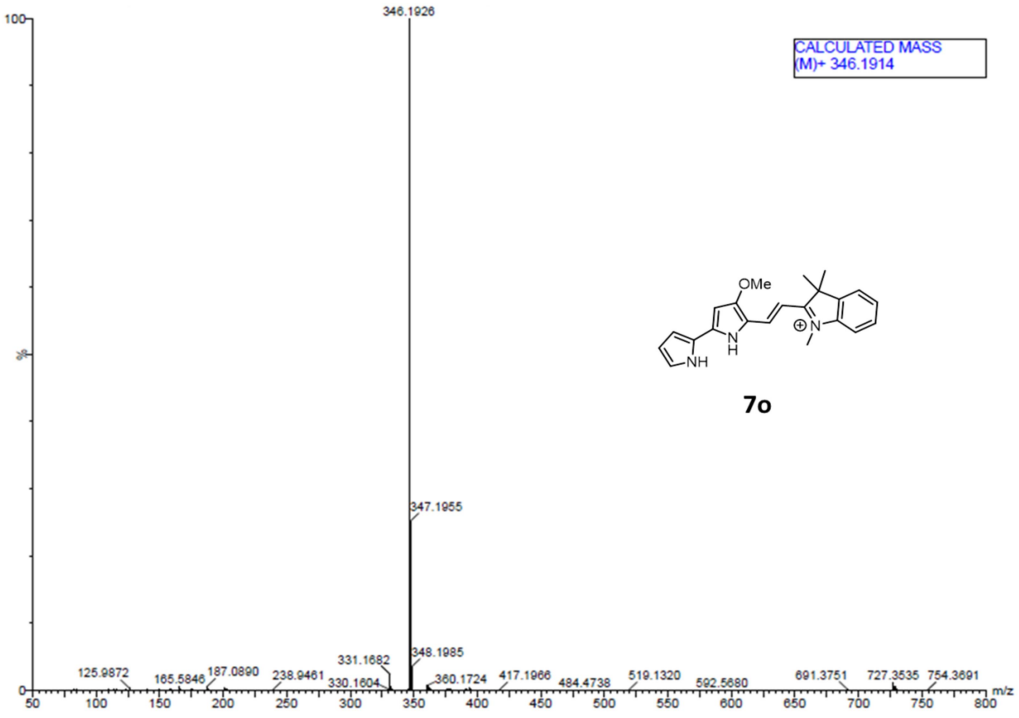


**Figure C96:** HRMS spectrum of compound **7o**

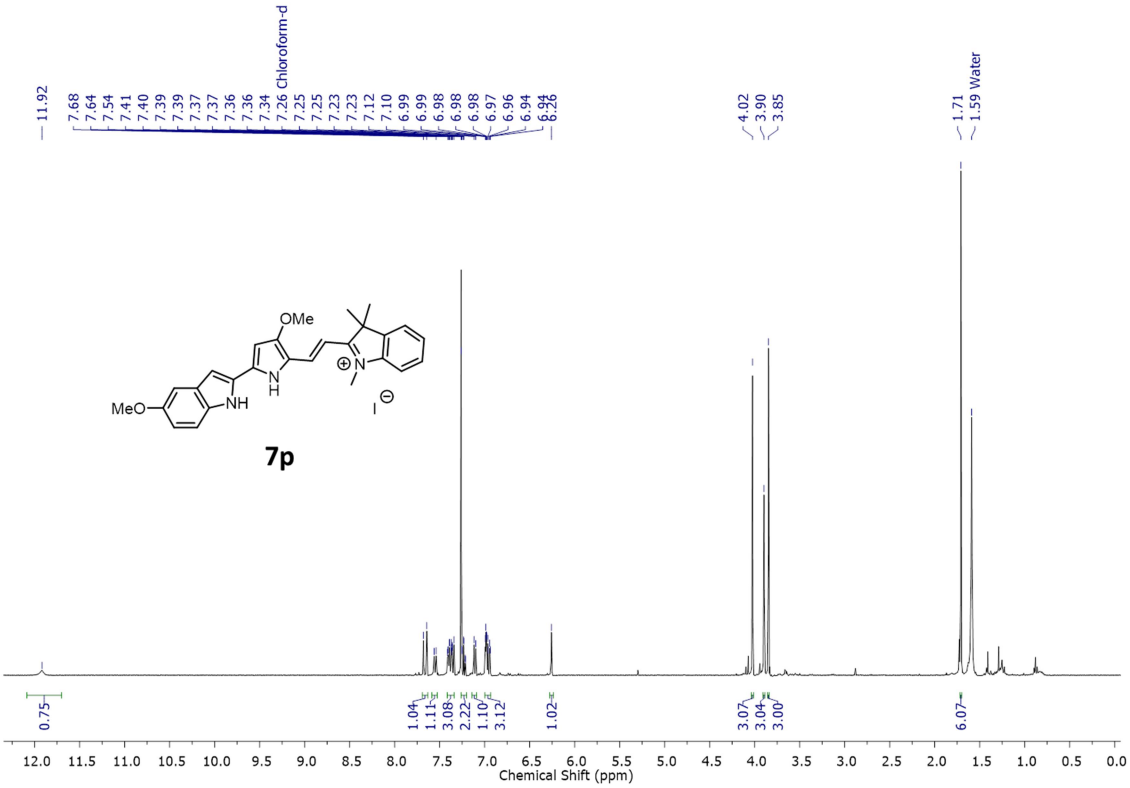


**Figure C97:** $^{1}$H spectrum of compound **7p**

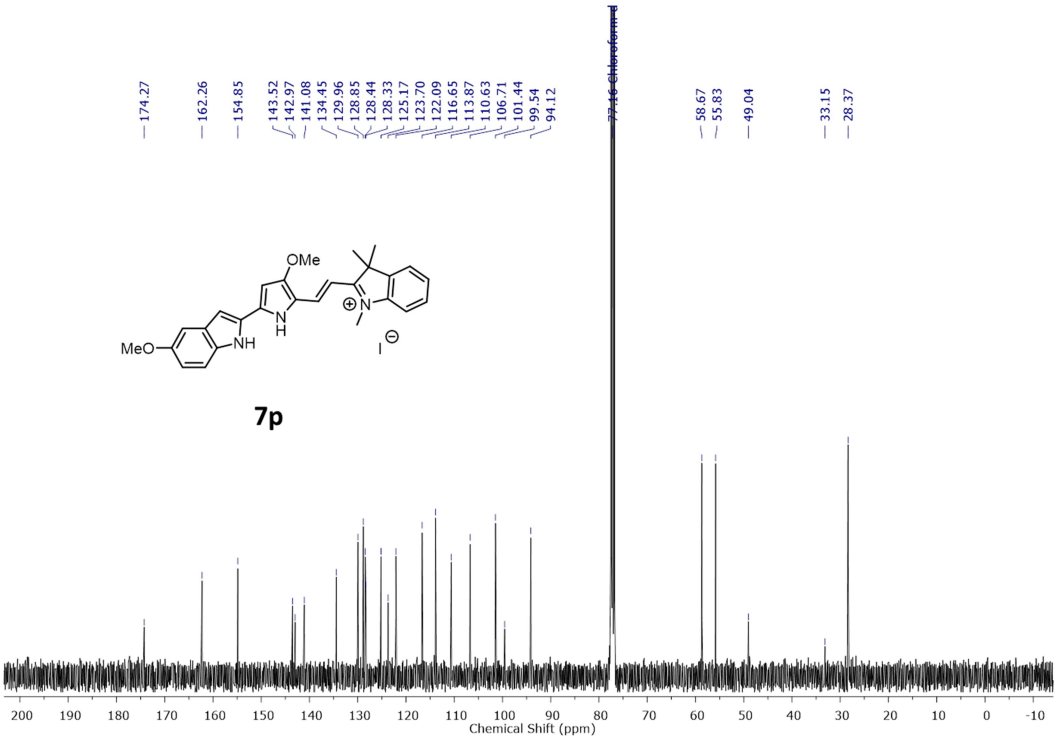


**Figure C98:** $^{13}$C spectrum of compound **7p**

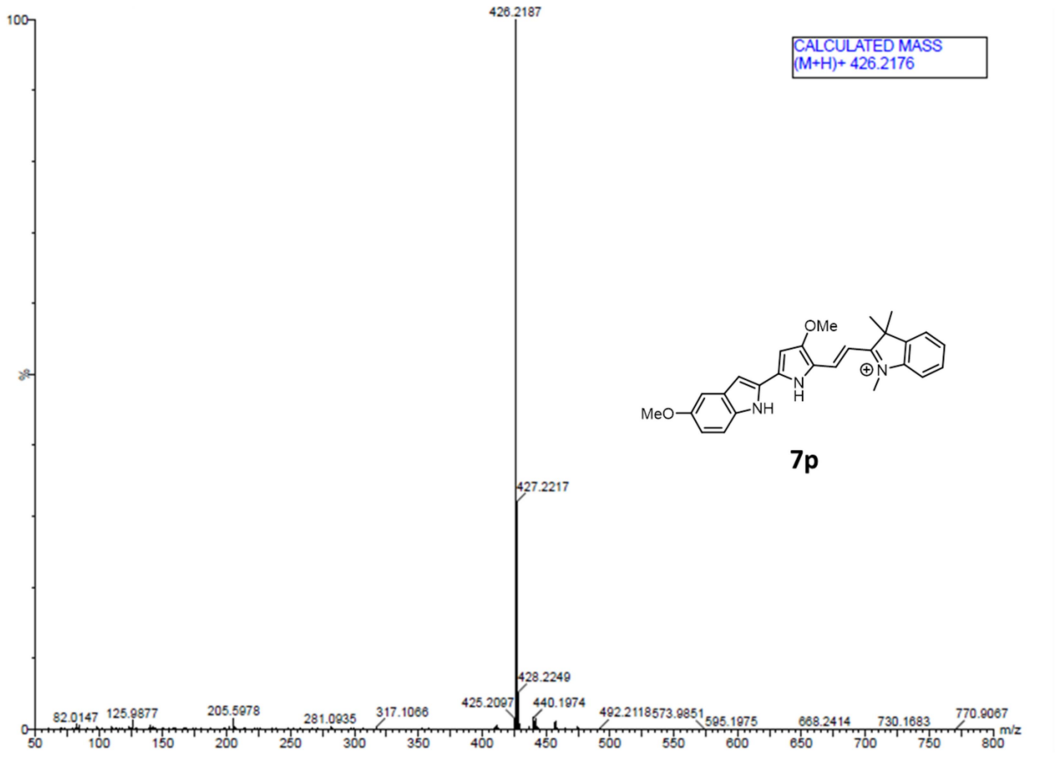


**Figure C99:** HRMS spectrum of compound **7p**